



U. S. DEPARTMENT OF  
**ENERGY**

Office of  
Science

**Technical Design Report  
for the  
FACET-II Project  
at  
SLAC National Accelerator Laboratory**

**SLAC Site Office**

**Office of High Energy Physics  
Office of Science  
U.S. Department of Energy**

**SLAC-R-1072**

**SLAC**  
NATIONAL ACCELERATOR LABORATORY

<b>1</b>	<b>Executive Summary .....</b>	<b>7</b>
<b>2</b>	<b>Overview .....</b>	<b>9</b>
2.1	Staged Approach and Level of Maturity of the Conceptual Design.....	10
2.2	Electron Injector .....	10
2.3	Bunch Compressors and Linac .....	11
2.4	Shielding and Global Control Systems .....	12
2.5	Positron Systems .....	12
2.6	Beam Tracking and Simulations .....	14
2.7	Future Upgrades .....	14
<b>3</b>	<b>Scientific Objectives.....</b>	<b>15</b>
3.1	<b>Plasma Wakefield Acceleration (PWFA) Program at FACET-II.....</b>	<b>17</b>
3.1.1	Introduction .....	17
3.1.2	The High Transformer Ratio Problem .....	19
3.1.3	Generation of super- high brightness beams .....	21
3.1.4	Determining the repetition rate of a single module for stable operation and staging of two PWFA modules.....	24
3.1.5	Summary .....	24
3.2	<b>Physics of positively charged drive beams for PD-PWFA.....</b>	<b>25</b>
3.2.1	Motivation for CERN Experiments with Protons.....	25
3.2.2	PD-PWFA Physics experiments at SLAC with electron and positron bunches .....	25
3.3	<b>PWFA Based on High Brightness Photoinjector-derived Electron Beams.....</b>	<b>28</b>
3.3.1	TV/m PWFA Using Femtosecond Beams .....	28
3.3.2	Ion Motion in High Brightness Beam Drivers .....	31
3.3.3	The Quasi-Nonlinear Regime of the PWFA .....	33
3.4	<b>Trojan Horse Under dense Photocathode PWFA and follow-up applications .....</b>	<b>34</b>
3.4.1	Introduction .....	34
3.4.2	Advantages of excellent synchronization between electron beam driver from photocathode and low-energy Ti:Sapphire laser beam ( $\sim 100 \mu\text{J}$ ) .....	34
3.4.3	Advantages of high-density electron beam driver from photocathode .....	35
3.4.4	Advantages in case of a Joule-class ( $> 10 \text{ TW}$ ) Ti:Sapphire laser beam .....	35
3.4.5	Further scenarios and light source experiments .....	36
3.4.6	Summary .....	37
3.5	<b>Dielectric Wakefield Acceleration at FACET-II.....</b>	<b>37</b>
3.5.1	Introduction to DWA.....	38
3.5.2	E-201 at SLAC FACET .....	39
3.5.3	DWA studies at FACET-II .....	40
3.5.4	Conclusion .....	42
3.6	<b>BIG: Beams of Intense Gamma-rays at FACET-II.....</b>	<b>42</b>
3.6.1	Introduction. .....	42
3.6.2	Nuclear Structure Studies: Nuclear Resonant Fluorescence (NRF), including pigmy resonances .....	47
3.6.3	Nuclear Physics near pion threshold.....	50
3.6.4	QCD with real photons: Nucleon structure.....	56
3.7	<b>Gamma-gamma collider .....</b>	<b>57</b>
3.8	<b>High intensity Positron Source studies using Gamma beam generated with Compton Beam scattering.....</b>	<b>60</b>
3.9	<b>BIG - gamma-ray source at FACET-II .....</b>	<b>63</b>

<b>3.10 Generating High-Brightness Muon Beams With High-Energy Gammas .....</b>	<b>65</b>
<b>3.11 Laboratory Astrophysics at FACET .....</b>	<b>67</b>
<b>3.12 Measurements for the CLIC study at the FACET-II facility .....</b>	<b>70</b>
3.12.1 Verification of on-line system-identification, feedback and tuning algorithms .....	71
3.12.2 Measurement of long-range transverse wakefields in industrialized accelerating structures .....	74
3.12.3 Measurement of collimator transverse wakefields .....	76
<b>3.13 FEL R&amp;D or ‘A particle beam physics research program at the FACET-II’ .....</b>	<b>76</b>
3.13.1 Introduction .....	76
3.13.2 Electron beam - brightness for next-generation FELs.....	77
3.13.3 SASE FELs and longitudinal coherence.....	78
3.13.4 Polarization control, multicolor FELs, synchronization and other special features.....	79
3.13.5 Terawatt peak power FELs .....	79
3.13.6 Seeding Methods .....	79
<b>3.14 FACET-II THz Studies.....</b>	<b>83</b>
3.14.1 THz manipulation of atoms in the solid state:.....	84
3.14.2 THz manipulation of electrons and spins.....	85
3.14.3 THz radiation to trigger surface chemical reactions .....	86
<b>3.15 National-Security and Fundamental Topics with Intense Beams of Photons of Energy 5 MeV and Greater Produced by Inverse Compton Scattering .....</b>	<b>88</b>
3.15.1 Calibration of United States Nuclear Test Gamma-Ray Detectors .....	89
3.15.2 Astrophysics and Stellar Nucleosynthesis.....	89
3.15.3 Nucleon Compton Scattering and Tests of QCD .....	90
3.15.4 Polarizing and Probing the Quantum Vacuum.....	90
3.15.5 Diffraction, Imaging, and Coherent Excitation.....	91
<b>4 Performance and Parameters .....</b>	<b>96</b>
4.1 Introduction and Overview .....	96
4.2 Scientific Requirements .....	96
4.3 Electron Requirements and Parameters .....	97
4.4 Positron Requirements and Parameters.....	98
4.5 Positron Return Line Requirements and Parameters .....	99
4.6 Positron Damping Ring Requirements and Parameters .....	100
4.7 Positron Extraction Line Requirements and Parameters.....	100
4.8 Sector 20 Chicane Requirements and Parameters .....	101
4.9 Simulated performance .....	102
<b>5 Electron Injector .....</b>	<b>103</b>
5.1 Accelerator - Introduction and Overview .....	103
5.1.1 Accelerator Requirements and Parameters.....	104
5.1.2 Accelerator Layout .....	106
5.2 Drive Laser .....	107
5.2.1 Drive Laser Specifications .....	107
5.2.2 Multiple Bunch Operation .....	111
5.2.3 Laser Room.....	111
5.2.4 Laser Controls .....	112
5.3 Electron Gun and Injector .....	112
5.3.1 Required Injector Performance Parameters.....	113
5.3.2 Scaling the Photoinjector with Beam Size .....	113

5.3.3	Thermal Emittance at the RF Cathode .....	114
5.3.4	Expected Performance of the FACET-II Injector at 2 nC .....	114
<b>5.4</b>	<b>Overview of Injector Layout and Particle Tracking Simulation .....</b>	<b>115</b>
5.4.1	Electron Injector Components .....	115
5.4.2	Simulation Tools.....	115
5.4.3	Optimization Parameters.....	116
<b>5.5</b>	<b>Emittance-Compensated Injector Design.....</b>	<b>117</b>
5.5.1	Source Distribution .....	117
5.5.2	Emittance Compensation Optimization .....	117
<b>5.6</b>	<b>Baseline Design Parameters and Tracking Results .....</b>	<b>118</b>
<b>5.7</b>	<b>Linac Injector Horizontal Bend System (DL1) .....</b>	<b>119</b>
<b>5.8</b>	<b>Injector Vacuum Systems .....</b>	<b>120</b>
<b>5.9</b>	<b>Instrumentation, Diagnostics, Feedback, and Collimation .....</b>	<b>121</b>
5.9.1	Beam Position Monitors (BPMs) and Charge Monitors (Toroids) .....	121
5.9.2	Electron Beam Profile Monitors (Screens and Wire Scanners).....	123
5.9.3	Timing Diagnostics (Beam Phase Cavity) .....	125
5.9.4	Bunch Length Diagnostics .....	125
5.9.5	Beam Energy Spread Diagnostics.....	127
5.9.6	Feedback Systems .....	128
<b>6</b>	<b>loops.Bunch Compressors and Linac .....</b>	<b>130</b>
<b>6.1</b>	<b>Main FACET-II Linac.....</b>	<b>131</b>
6.1.1	Linac Energy Management.....	132
6.1.2	Linac Optics .....	134
6.1.3	Linac Modifications and Installation Issues .....	136
<b>6.2</b>	<b>Bunch Compression .....</b>	<b>137</b>
6.2.1	Stability Requirements and System Sensitivities .....	142
<b>6.3</b>	<b>The First Electron Bunch Compressor (BC11) .....</b>	<b>147</b>
6.3.1	Overview .....	148
6.3.2	Beam Parameters for BC11.....	149
6.3.3	Layout and Optics Design.....	149
6.3.4	Electron Beam Dynamics .....	150
6.3.5	Magnets .....	150
<b>6.4</b>	<b>BC14 - Bunch Compression System for e- and e+ in Sector 14.....</b>	<b>152</b>
6.4.1	Overview .....	152
6.4.2	Beam Parameters in BC14.....	152
6.4.3	Layout and Optics Design in BC14.....	153
6.4.4	Beam Dynamics in BC14 for e+ and e- .....	155
6.4.5	BC14 Magnets .....	156
<b>6.5</b>	<b>Sector 20 W-Chicane (BC20) and Final Focus Systems.....</b>	<b>157</b>
<b>6.6</b>	<b>Radio Frequency (RF) Systems.....</b>	<b>157</b>
6.6.1	The RF System Stability Tolerances.....	157
6.6.2	Radio Frequency (RF) Distribution in the SLAC Main Linac.....	158
6.6.3	Improvements to the RF Control System.....	159
<b>6.7</b>	<b>Layout and Performance of the Present SLAC Linac RF .....</b>	<b>162</b>
<b>6.8</b>	<b>Particle Tracking .....</b>	<b>163</b>
<b>6.9</b>	<b>Instrumentation, Diagnostics, Feedback, and Collimation .....</b>	<b>167</b>
6.9.1	Beam Position Monitors and Toroid Charge Monitors .....	168

6.9.2	Electron Beam Profile Monitors.....	169
6.9.3	Wire Scanners and Transverse Emittance Diagnostics .....	171
6.9.4	Bunch Length Diagnostics .....	173
6.9.5	Relative Bunch Length Monitors.....	174
6.9.6	Beam Energy Spread Diagnostics.....	175
6.9.7	Trajectory Feedback Systems.....	175
6.9.8	Energy and Bunch Length Feedback Systems .....	175
<b>7</b>	<b>Shielding.....</b>	<b>177</b>
7.1	Introduction and Overview .....	177
7.2	Sector 10 Shielding Wall.....	177
7.2.1	Sector 10 Layout .....	178
7.2.2	Shielding Wall Requirements .....	179
7.3	Penetration Shielding.....	180
7.3.1	Layout.....	180
7.3.2	Radiological Requirements .....	181
7.3.3	Usage Requirements .....	181
<b>8</b>	<b>Positron Systems .....</b>	<b>184</b>
8.1	<b>Positron System - Introduction and Overview .....</b>	<b>185</b>
8.1.1	Requirements and Parameters .....	185
8.1.2	Brief Description of the Positron System.....	188
8.1.3	Positron Yield .....	188
8.2	<b>PRLTR – Positron Return Line to Damping Ring .....</b>	<b>192</b>
8.2.1	Overview .....	192
8.2.2	Beam Parameters.....	197
8.2.3	Beam Dynamics.....	198
8.2.4	Magnets .....	199
8.3	<b>Positron Damping Ring.....</b>	<b>201</b>
8.3.1	Introduction .....	201
8.3.2	Lattice Design.....	202
8.3.3	Beam Dynamics.....	208
8.3.4	Intra-beam Scattering .....	215
8.3.5	Impedance and collective instabilities .....	216
8.3.6	Magnets .....	220
8.3.7	RF System.....	230
8.3.8	Vacuum System.....	232
8.3.9	Synchrotron Radiation .....	235
8.4	<b>Positron Extraction and Compression.....</b>	<b>236</b>
8.4.1	Overview .....	236
8.4.2	Beam Parameters.....	237
8.4.3	Layout and Optics Design.....	237
8.4.4	Beam Dynamics.....	238
8.4.5	Magnets & RF.....	239
8.4.6	Quadrupoles.....	240
8.4.7	Sextupoles .....	240
8.4.8	Dipoles .....	241
8.4.9	RF.....	241
8.5	<b>Instrumentation, Diagnostics and Feedback.....</b>	<b>241</b>

8.5.1	PRL Diagnostics .....	243
8.5.2	Damping Ring Diagnostics.....	243
8.5.3	PEC Diagnostics .....	244
8.5.4	Feedback Systems .....	244
<b>9</b>	<b>Final Bunch Compression and Final Focus .....</b>	<b>246</b>
9.1	Overview .....	246
9.2	Beam Parameters .....	247
9.3	Layout and Optics Design .....	248
9.4	Beam Dynamics .....	250
9.5	Instrumentation, Diagnostics and Feedback.....	251
9.5.1	Feedback .....	252
<b>10</b>	<b>Scope Additions and Future Upgrades.....</b>	<b>253</b>
10.1	Future Upgrades - Introduction and Overview .....	253
10.2	Sector 20 Sailboat Chicane .....	254
10.2.1	Overview .....	254
10.2.2	Beam Parameters and Matching .....	255
10.2.3	Layout and Optics Design.....	256
10.2.4	Path-Length Tuning Chicanes.....	257
10.2.5	New magnets .....	258
10.3	Electron Injector Laser Heater .....	260
10.3.1	Overview .....	260
10.3.2	Laser Properties for Laser Heater System.....	262
10.4	X-Band RF “Linearizer” .....	263
10.5	High Peak Current Configuration with 2 nC Electrons Operating Concurrently with 1 nC Positron Bunches .....	264
10.5.1	Overview .....	264
10.5.2	Particle Tracking.....	264
10.5.3	Stability Requirements and System Sensitivities .....	268
10.6	High electron charge operation mode .....	272
10.6.1	Accelerator Requirements and Parameters.....	272
10.6.2	Bunch Compressor 1 (BC11) in Sector 11 .....	273
10.6.3	Bunch Compressor 2 (BC14) in Sector 14 .....	274
10.6.4	Sector 20 .....	275
10.6.5	Particle Tracking.....	275
10.7	Witness Bunch Injector .....	277
10.7.1	Zeroth-Order Design .....	278
10.8	Differential Pumping.....	286
10.9	Compton Source .....	289
10.10	Photon-Photon Collider Option .....	289
10.10.1	Overview .....	289
10.10.2	Laser Parameters .....	290
10.10.3	Linac Configuration .....	290
10.10.4	BC20E & BC20P Configuration .....	292
10.10.5	Final Focus and Spectrometer Configuration .....	295
10.10.6	Photon-Photon Collision Luminosity and Expected Pair Production Rate.....	296

# 1 Executive Summary

The discovery of the Higgs boson, a subatomic particle whose field is responsible for endowing all other particles with mass, is one of the major discoveries of the last decade. To unlock the mysteries of the subatomic world, physicists use the worlds' most powerful microscopes – particle accelerators. The resolving power of these microscopes is proportional to the energy of the beams they produce. Since their inception nearly 80 years ago, the energy reach of accelerators has grown exponentially due to continued breakthroughs in accelerator physics and engineering. The highest energy beams in the world are currently at the 27km circumference Large Hadron Collider (LHC) in Europe. Although it is a monument to human engineering, scientists are approaching a practical limit to the size and cost of such collider facilities. Innovation is essential for continued progress.

Electrons can “surf” on waves of plasma – a hot gas of charged particles – gaining very high energies in very short distances. This approach, called plasma wakefield acceleration, has the potential to dramatically shrink the size and cost of particle accelerators. Research at the SLAC National Accelerator Laboratory has demonstrated that plasmas can provide 1,000 times the acceleration in a given distance compared with current technologies. Developing revolutionary and more efficient acceleration techniques that allow for an affordable high-energy collider has been the focus of FACET, a National User Facility at SLAC.

FACET used part of SLAC’s two-mile-long linear accelerator to generate high-density beams of electrons and their antimatter counterparts, positrons. When fully focused, these beams were so intense, they were equivalent to focusing all the power of the sun onto a surface 10 meters square for 50 femtoseconds. This produced large electric and magnetic fields over a very short span of time – ideal for creating exotic states of matter and researching advanced accelerator technologies. FACET also produced unprecedented intensities of terahertz or “sub-millimeter” electromagnetic radiation, which has many applications in material science, semiconductor research, chemical imaging and more.

Research into plasma wakefield acceleration was the primary motivation for constructing FACET. Near the end of the first year of FACET operation, the plasma wakefield acceleration program laid out a 4-year plan of milestones to be accomplished during the FACET runs in 2013 to 2016. The goals for 2013 were to commission both the high power laser and two-beam generation and with those, demonstrate mono-energetic acceleration for the first time. The goals for 2014 were to refine the mono-energetic acceleration parameters, demonstrate acceleration with positrons, and first experiments using plasma wakefields for a high-brightness injector. The goals for 2015 were to refine the positron acceleration experiments, demonstrate high efficiency and further explore the high-brightness injector. For the last year of the program in 2016, the goals were a demonstration of a single stage with narrow energy spread, preserved emittance and high efficiency. Each of these goals was successfully accomplished as planned.

Scientists from all over the world came to FACET to do experiments aimed at improving the power and efficiency of particle accelerators used in basic research, medicine, industry and other areas important to society. Experimental proposals were peer-reviewed by the SLAC Accelerator Research Experiment Committee (SAREC), which would also review FACET-II proposals. There has been extensive outreach to the user community through three FACET User Meetings at SLAC, satellite FACET informational meetings

at IPAC and other conferences, the FACET-II Science Workshops in October, 2015 and direct involvement of the users in the FACET-II proposal.

In April 2016, FACET operations came to an end to make way for the second phase of SLAC's x-ray laser, the LCLS-II, which will use part of the tunnel occupied by FACET. With this transition, the world's only multi-GeV facility for advanced accelerator research has ceased operation. FACET-II is a new test facility to provide DOE with the unique capability to develop advanced acceleration and coherent radiation techniques with high-energy electron and positron beams. FACET-II is an opportunity to build on the decades-long experience developed conducting advanced accelerator R&D at the FFTB and FACET and re-deploy HEP infrastructure in continued service of its mission.

FACET-II represents a major upgrade over current FACET capabilities and the breadth of the potential research program makes it truly unique. It will synergistically pursue accelerator science that is vital to the future of both advanced acceleration techniques for High Energy Physics, ultra-high brightness beams for Basic Energy Science, and novel radiation sources for a wide variety of applications. Nuclear physicists have proposed using the unprecedentedly high intensity gamma beams to study the structure of nuclei and as a novel particle source for future colliders. No other test facility has attracted such broad interest across so many branches of the Office of Science.

## 2 Overview

The FACET National User Facility used part of SLAC's two-mile-long linear accelerator to generate high-density beams of electrons and positrons. These beams are so intense, they are ideal for creating exotic states of matter and researching advanced accelerator technologies. Scientists from all over the world have come to FACET to do experiments and there has been extensive outreach to the user community in the FACET-II proposal.

In 2016, the second phase of SLAC's x-ray laser, the LCLS-II, has begun to use part of the tunnel occupied by FACET, and the world's only multi-GeV facility for advanced accelerator research has ceased operation. FACET-II is a new test facility to develop advanced acceleration and coherent radiation techniques with high-energy electron and positron beams. It is the only facility in the world with high energy positron beams and it offers an opportunity to build on the decades-long experience developed conducting advanced accelerator R&D at SLAC. FACET-II represents a major upgrade over current FACET capabilities and the breadth of the potential research program makes it truly unique. No other test facility has attracted such broad interest across so many branches of the Office of Science.

The most demanding design parameters for FACET-II are set by the requirements of the plasma wakefield experimental program. To drive the plasma wakefield requires a high peak current, in excess of 10kA. The requisite transverse beam quality to be useful by the wakefield, and other, experimental programs is met with normalized transverse emittances  $<20 \mu\text{m}\cdot\text{rad}$  delivered to the Sector 20 region. The beam energy is 10 GeV, set by the Linac length available and the repetition rate is up to 30 Hz.

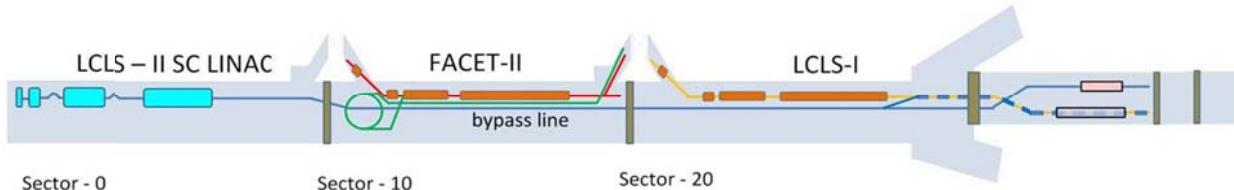


**Figure 2.1. Schematic layout of FACET-II in the middle third of the SLAC linac, downstream of LCLS-II and upstream of LCLS-I.**

The FACET-II project is scheduled to be constructed in two major stages: 1) a new photoinjector at Sector 10 and two bunch compressors in the Linac will restore operation with electrons; 2) a new positron damping ring located in the Sector 10 tunnel with injection and extraction lines will restore operation with positrons. A third stage planned as a future upgrade will construct a new final chicane in Sector 20 to provide for simultaneous delivery of positrons and electrons to the experimental area. A schematic of the layout of FACET-II in the linac is shown in figure 2.1.

For stage one, FACET-II will complete the original LCLS-II installation of the photoinjector and its auxiliary systems at Linac Sector 10. This will include installation of a gun and injector beamline in the Linac housing and power sources and control electronics in the gallery. These systems will connect the new injector at Sector 10 with the Linac, where the beam can then be accelerated and transported to the existing FACET experimental area in Sector 20. Two bunch compressor chicanes will be installed in Sector 11 and Sector 14 to provide the first two of three stages of bunch compression needed to produce the required high energy density beams in Sector 20. The third stage of compression is in Sector

20. A shield wall, similar to the existing one in Sector 20, will be constructed in Sector 10 to separate the LCLS-II and FACET-II accelerator areas.

In stage two for positron operation, FACET-II will reuse the existing positron target at Sector 19. A new small damping ring, which fits inside of the accelerator tunnel, will be installed at Sector 10. In addition to the beamlines in the tunnel, there will be power sources and control electronics in the gallery. Two new beamlines in Sector 10 will bring the positrons from the existing Positron Return Line into the new Damping Ring and from the Damping Ring back into the main linac at the last magnet of the Sector 11 bunch compressor. The Sector 14 bunch compressor will also need a second arm for simultaneous electron and positron operation.

As a future upgrade for the simultaneous delivery of positrons and electrons to the user area, a second arm of the final chicane will be installed in Sector 20. This beamline in the tunnel will be connected to power supplies and control electronics in the gallery.

## ***2.1 Staged Approach and Level of Maturity of the Conceptual Design***

Because the project is to be completed in sequential stages, the Design Report and the Work Breakdown Structure both reflect this staged approach. Chapters 5, 6 and 7 on the Electron Injector, Linac and Bunch Compressors, and Shielding and Global Control Systems describe the aspects of the project to be completed in stage one. Chapter 8 on Positron Systems describes the aspects of the project to be completed in stage two. Chapter 9 on the Sector 20 W Chicane describes the existing electron arm of the 3<sup>rd</sup> bunch compressor, which remains unchanged in stage one and two. The new positron arm of the 3<sup>rd</sup> bunch compressor which is to be built as a future upgrade is described in Chapter 10.

In this document, the description of the first stage of the FACET-II project, which will restore electron operation, is based on the existing injector built and operated for LCLS-I and the original design of a copy of that injector for LCLS-II. Since the injector and 1<sup>st</sup> two bunch compressors in the Linac are essentially identical to what was built for LCLS, the design is very mature. Because the positron systems are new, their designs are much less mature: they do not yet have the same level of engineering design. Detailed specifications for items such as power supplies, controls and vacuum systems will be included in the next release of the Design Report at CD-3b.

## ***2.2 Electron Injector***

In order to achieve the scientific goals of the experimental program at FACET-II, a high electron peak current with small transverse core beam size at the experimental IP waist,  $\sim 20\mu\text{m}$ , and a small longitudinal emittance are required. FACET-II will operate with an electron energy up to 10 GeV. The most challenging parameters are for the plasma wakefield acceleration (PWFA) experiments which require peak currents in excess of 10 kA. The RF photocathode gun and injection system is similar to that used in LCLS. This injector is capable of producing a charge of up to 5 nC in a bunch length of <10 ps, corresponding to peak currents of >120 A with transverse emittances less than 5  $\mu\text{m}$ . This implies a required compression ratio in excess of 100 to achieve the desired beam characteristics at the IP waist in Sector 20. The acceleration and compression is done in the 2nd kilometer of the SLAC linac in 3 compression stages. A schematic of the electron injector, linac and bunch compressors is shown in Figure 2.2.

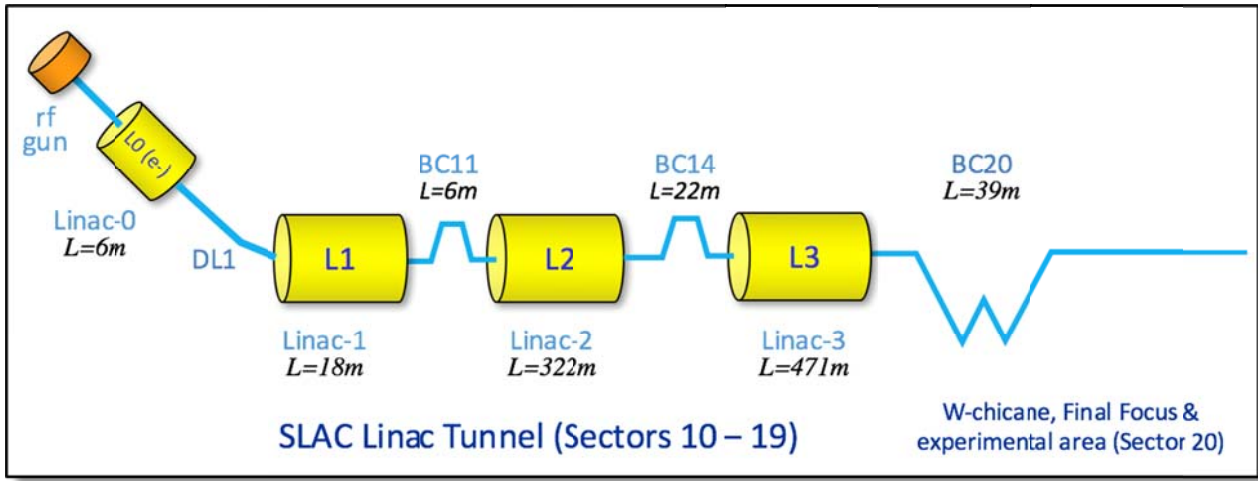


**Figure 2.2. Schematic showing injector, linac, bunch compressors, and experimental area for stage one of the FACET-II project.**

The capabilities of FACET-II vary in a non-trivial way depending on the choice of initial charge from the RF gun. The baseline design is for a 2 nC electron bunch charge from the electron gun, or a 1 nC positron bunch, generated from a 4 nC electron bunch striking the existing positron production target in Sector 19, returned and damped from a new positron damping ring. To demonstrate design flexibility and characterize the extremes of the possible parameter space, a second configuration option is considered in chapter 10 corresponding to a 5 nC pulse from the electron gun.

### 2.3 Bunch Compressors and Linac

Both electrons and positrons undergo three stages of bunch compression, the first two stages in Linac Sectors 11 and 14 and the final compression stage in Sector 20. The Sector 20 W chicane is described in Chapter 9. For positron operation, positrons produced in sector 19 are returned to the beginning of the Linac in a ceiling-mounted transfer line, their energy boosted to 335 MeV, and injected into a damping ring in Sector 10. The initial stage of positron compression takes place in the transfer line from the damping ring before injection into the main linac in the final bend of BC11 (in Sector 11). The details of the positron systems are mainly described in chapters 8. The sailboat chicane future upgrade is described in Sector 10.

The bunch compression is accomplished by a series of magnetic chicanes arranged and located such that non-linearities in the compression and acceleration process (longitudinal wakefields, RF curvature, and second order momentum compaction) are all tolerable. The goal for the Linac design is to a) achieve design peak current requirements for both positron and electron bunches, b) deliver the correct longitudinal profile into the final BC20 compression stage and c) minimize sensitivities to RF phase and amplitude variations and also to bunch charge variations. The electron energy at the first compressor is 335 MeV. This choice avoids space charge effects, while the bunch compression is still early enough in the linac to ease the effects of transverse wakefields. This energy choice is also compatible with the desired energy for damping ring operation for positrons. In the first compressor (BC11), the electron bunch length is reduced from 0.85 mm to 470  $\mu$ m (rms). For operation with positrons, the positron beam is injected into the linac at the final BC11 bend. The bunch length of the positrons, upon extraction from the damping ring, is 3.9 mm (rms). To match well into the linac compression scheme, an additional bunch compressor (2.1m S-band RF section and 4-bend chicane) is included in the damping

ring-to-linac beamline section. The positron bunch length is compressed to 276  $\mu\text{m}$  (rms) before being injected into the shared linac through a horizontal dogleg section

The second compressor (BC14 in Sector 14) produces a 94/97  $\mu\text{m}$  rms bunch length for electrons/positrons. The energy of the second compressor, 4.5 GeV, is chosen as a balance between the conflicting requirements of emittance dilution due to synchrotron radiation, and the need to generate the correct final correlated energy spread when including the final compression stage in sector 20. The design of the compressors is also impacted by the need to reduce Coherent Synchrotron Radiation (CSR) effects, which are most pronounced for short bunches. The most significant effect of CSR is to generate a time-dependent energy variation along the bunch. Designs utilizing relatively weak chicanes and larger initial correlated energy spreads for the various compression stages help control the effect CSR has on transverse emittance dilution. Additionally, adjustable collimators in the center of BC11 and BC14 can be used to cut high-energy, non-linear tails, an option explored in an alternative configuration outlined in Chapter 10. The final compression stage in sector 20 at 10 GeV is described in Chapter 9.

## ***2.4 Shielding and Global Control Systems***

In addition to construction of the FACET-II injector and bunch compressors, several modifications are needed in the Linac infrastructure before electron beams can be restored. A concrete shielding wall must be constructed in Sector 10 to separate the LCLS-II and FACET-II sections of the Linac tunnel. This allows access to the LCLS-II tunnel while there is beam in the FACET-II area. It does not permit access to the FACET-II area during LCLS-II beam operation. In addition to the wall, the Personnel Protection System (PPS) for the two areas must be separated to allow independent access. A PPS system for the injector vault will be installed, creating an Injector PPS Zone and the existing sector 19/20 PPS zone will be upgraded for Controlled Access to facilitate efficient entry to that region. Other infrastructure tasks include modifications to the control system network to restore the legacy control system post LCLS-II modifications in the first 10 sectors and a Beam Containment System for the injector and chicanes.

## ***2.5 Positron Systems***

The positrons are produced by sending an electron bunch onto the existing positron target and capture section in Sector 19. The positron bunch is transported back to Sector 11 in the existing Positron Return Line. A new beamline that starts in Sector 11 takes the positrons from the Return Line and injects them into a new Damping Ring in the Sector 10 Linac tunnel. The energy of the beam from the positron production system is 210 MeV, whilst the desired Damping Ring energy is 335 MeV, so 125 MeV of energy must be provided by S-band accelerating structures to be located in Sector 14. The accelerating structures will replace a section of the existing return line. A schematic of the positron systems for stage two of the FACET-II project is shown in Figure 2.3.

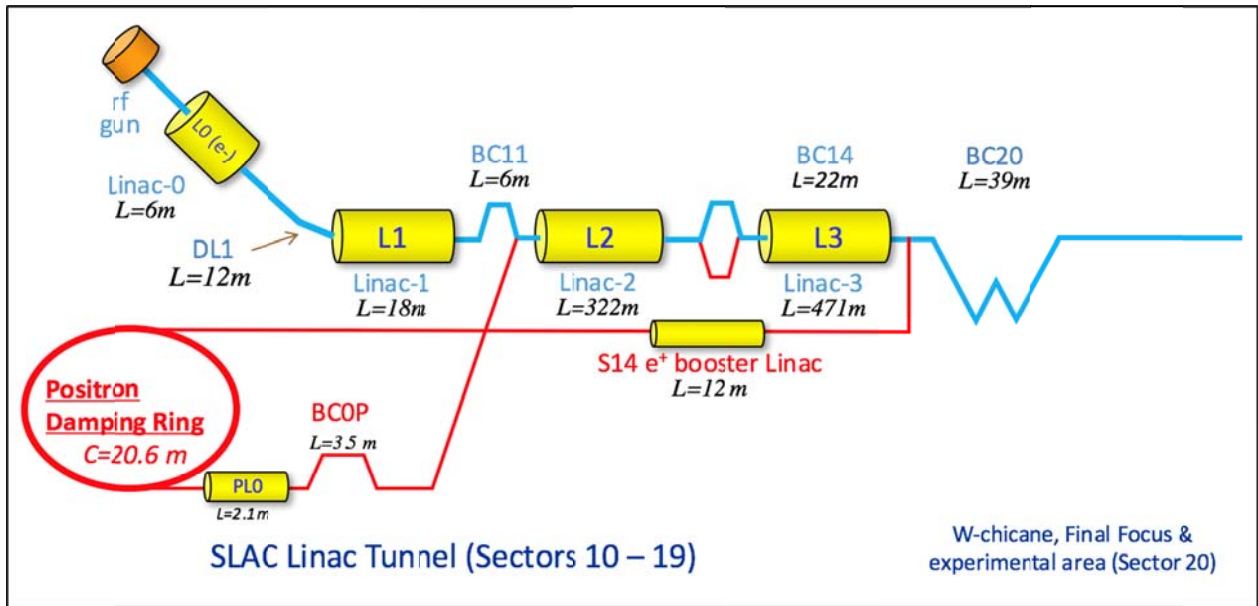


**Figure 2.3. Schematic showing positron production, return line with acceleration section, damping ring, extraction line and bunch compressors for stage two of the FACET-II project. The red sections depict positrons specific areas.**

The positron beam into the damping ring has a large transverse emittance that must be reduced by three orders of magnitude in a few milliseconds. Because the damping ring is located in the existing Linac tunnel, the diameter of the ring must be smaller than 3 meters. This constraint dictates a compact design with minimal gaps between the magnets in the arcs. The large injected beam size also dictates that the acceptance of the ring be large enough to accommodate on-axis injection. The proposed design incorporates many aspects of recent developments for diffraction-limited light sources. The beam energy is chosen to be 335 MeV which is as high as possible given the space constraints and reasonable choices of magnet technology.

Given the compact dimensions, the magnet design for the damping ring arcs is particularly challenging. As proposed, the three dipole magnets in each arc cell are wound on a single block of steel and are shaped to additionally provide quadrupole and sextupole field components. The additional arc quadrupoles have a very compact and innovative design, also incorporating sextupole field components. Designs for these magnets are described in Section 8.3.6. The straight sections contain both the injection and extraction and the RF cavities. Vacuum requirements are not particularly challenging because of the single bunch operation.

A second new positron beamline in Sector 10 takes the beam from the damping ring extraction point, performs a 1st stage of bunch compression and injects it into the last dipole magnet of the 1st electron bunch compressor (BC11) in Sector 11. All of the components of the injection and extraction lines are conventional. Once the positrons are injected into the Linac, they are accelerated to 10 GeV in the second and third Linac sections. The second stage of bunch compression is performed in a second arm of the bunch compressor in Sector 14 (BC14) and the 3rd stage in the chicane in Sector 20, which is described in Chapter 9. They are focused to a transverse size of <20 microns at the FACET Interaction Point and dumped at the end of Sector 20.

## **2.6 Beam Tracking and Simulations**

Start-to-end 6D tracking simulations have been made to model the beam transport through the FACET-II complex, including the non-linear compression and final beam focus process. The simulations include the effects of longitudinal wakefields in the 1km Linac as well as incoherent and coherent synchrotron radiation effects in the various bending magnets. Full 3d space-charge effects are modelled in the low-energy section of the injector and longitudinal space charge effects are also included for the whole machine. Simulations have also been made which calculate emittance dilution in the linac due to transverse wakefields and anomalous momentum dispersion, each of which arises from a variety of considered error sources such as RF errors, injection orbit excursions and magnetic field errors etc. Diagnostics, correction techniques, and feedback systems have also been incorporated into the design.

For the positron complex, simulations have been performed to demonstrate the performance of the transport lines and damping ring. Collective effects have been estimated analytically and appear to be controllable.

## **2.7 Future Upgrades**

To support the full breadth of the experimental program outlined in Chapter 3, several additions or upgrades will be required to expand future capabilities. These are described briefly in this chapter and in Chapter 10. They could be funded as Accelerator Improvement Projects during the operation of the FACET-II facility, but they are also available as possible scope additions should project funds be available. One such upgrade is the second arm to the existing chicane in Sector 20 (BC20), the sailboat chicane.

The Plasma Wakefield Acceleration experimental program will eventually desire a higher current electron bunch than provided in the baseline configuration. As one possible implementation, we have designed the Linac and bunch compression to be compatible with a 1nC/5nC configuration of the positron /electron beams respectively. The 1nC/5nC configuration has a large imbalance in the wakefield loading in the Linac between electron and positron bunches as well as CSR effects. This configuration would require installation of new 2nd or 4th harmonic (C- or X-band) acceleration sections in the Linac for energy equalization.

To achieve the highest possible peak currents in Sector 20 (>100 kA) would require the addition of two subsystems: 1) a 4<sup>th</sup> harmonic “linearizing” x-band RF structure in L1; 2) a “laser-heater” system in the electron injector to spoil the longitudinal phase space and control CSR emittance dilution. Both of these systems were successfully utilized during LCLS operations and could be used to aid operations at FACET-II but are not necessary for the baseline parameters initially required by the FACET-II user community.

Other upgrades considered are: 1) installation of a witness injector to provide an independent bunch to sample the plasma wakefields. This allows complete freedom to tailor the drive bunch shape for maximum transfer efficiency. 2) installation of a differential pumping system to isolate the vacuum in the experimental region from the Linac vacuum. This provides flexibility with the plasma chamber experiments and avoids the need for beryllium windows. 3) installation of a Compton source for a variety of proposed experiments. 4) operation of Compton sources in the Sector 20 chicanes to form a photon-photon collider in the final bend of BC20.

# 3 Scientific Objectives

We need to push the properties of accelerators beyond the present limits of performance and create innovative ways of applying accelerator technologies in order to advance science and further the goals of High Energy Physics and Basic Energy Science. Reaching well beyond the trillion-electron-volt (TeV) energy scale with an electron/positron collider will not be affordable without a marked improvement in accelerating gradient. Techniques developed to enable a TeV collider will also make GeV-scale light sources smaller and less expensive. Providing the luminosity required to support precision science will require significant gains in beam brightness and accelerator power efficiency. Such gains will improve the source quality and reduce the operating cost of light sources.

Developing the accelerator science necessary to make game-changing performance improvements requires significant experimentation and refinement. Such work requires a suitable test facility where machine changes can be made and significant beam time assigned to experiments without adversely impacting a scientific user community.

Decades of experience in advanced accelerator research have shown that some basic facility features are needed to support the work:

- A stable, well-diagnosed beam with broadly adjustable properties
- An extensive user-configurable beam area with a wealth of diagnostics
- An external diagnostic hutch where both electrical and optical signals can be gathered and processed
- A laser hutch, providing coherent radiation for excitation and diagnostics

Facilities at Argonne, Brookhaven, SLAC, UCLA and elsewhere cover the energy range below 1 GeV, but there is currently no planned national user beam facility above the 1 GeV range after FACET. Wakefield acceleration and coherent radiation generation are fundamentally collective effects that grow stronger with beam density and energy, and consequently the science and potential applications grow more compelling with beam energy and brightness. The wealth of attosecond-scale manipulation techniques being developed for the photon sciences (e.g. iSASE, ESASE, HGHG, and seeding) all become more robust at higher energies, where path length slippage and space charge effects can be mitigated.

An additional consideration for an advanced accelerator research facility is the pulse format. Many advanced accelerator experiments are inherently single-pulse (or single drive-witness pair) experiments because the physical process is single pass (non-resonant), or because the experiment relies on single-shot diagnostics (such as cameras), or both. Short pulse trains of <10 bunches are useful to probe long-range wakefield effects, as are pulses with widely variable spacing (perhaps out to 100 ns).

The FACET-II science program has three principle thrusts:

- High gradient acceleration techniques for the next e+/e- collider
- Radiation generation and enhancement techniques for photon science
- Physics of very high field interactions with materials

The high energy and high brightness characteristics of the FACET-II beam enables a broad class of coherent radiation and beam/matter interaction science at field strengths and energy densities not available anywhere else. A broad experimental program has been mapped out based on extensive input from the user community, in particular from a series of FACET-II Science Opportunity Workshops held at SLAC October 12-16, 2015<sup>1</sup>. While an experimental program is defined below that focuses on key challenges for discovery science, we will also seek out new opportunities to apply the unique capabilities of FACET-II to solve problems in other scientific areas, drawing in university and industrial researchers in the process.

**Table 3.1. Requirements for different experiments proposed for FACET-II. Green entries show minimum required to start experimental program. Blue entries show desired features to be used once available.**

	Experiment	Stage 1	Stage 2	Stage 3	Two bunches	High charge	Witness injector	Compton source
1	PWFA with electrons	X			X			
	High Transformer Ratio	X				X	X	
	Super-high brightness beams	X				X		
2	PWFA with positrons		X		X			
	Physics of proton driven PWFA		X					
	Physics of proton driven PWFA w electrons			X			X	
3	PWFA with low charge, high brightness electrons	X						
4	Trojan horse	X				X		
5	Dielectric WFA	X			X			
6	Beams of Intense Gamma rays	X				X		X
7	Gamma-Gamma Collider			X		X		X
8	Positrons from Compton Beam	X				X		X
9	BIG - Gamma ray source	X				X		X
10	High brightness muon beams	X				X		X
11	Laboratory Astrophysics			X				
12	CLIC studies	X		X				
13	FEL R&D	X						
14	THz & Magnetic switching	X				X		
15	National Security	X				X		X

The nominal parameters for FACET-II Phase 1 are driven by the needs of the wakefield accelerator programs. FACET-II will continue to explore the physics of plasma wakefield acceleration in regimes relevant to future collider and X-ray free electron laser applications. Specifically, experiments will operate with accelerating gradients in excess of 10 GeV/m – orders of magnitude larger than conventional accelerators. To attain these large gradients requires plasma densities on the order of

<sup>1</sup> FACET-II Science Opportunities Workshops Summary Report, Mar 29, 2016,  
<https://www-internal.slac.stanford.edu/scidoc/docMeta.aspx?slacPubNumber=SLAC-R-1063>

$10^{17}$  e-/cm<sup>3</sup>. To effectively drive large amplitude wakefields in the plasma requires the beam dimensions (radially and longitudinally) to be of the order of the plasma collisionless skin depth, or 17 μm in this case. Large amplitude wakes are achieved when the electron bunch has sufficient charge to reach peak currents on the order of the Alfvén current (17 kA). Recent experiments at FACET have demonstrated that the positron parameters to be delivered in Phase 2, similar to the above for electrons, can access regimes applicable to plasma afterburner applications [1]. A future upgrade will deliver both electrons and positron bunches to the plasma in close succession and allow studies relevant to staged collider designs with positron acceleration in the wakefields produced by an electron bunch [2]. The one kilometer-long linac produces a nominal energy of 10 GeV that ensures the required yield from the positron target and enables stable operation with these highly compressed electron and positron bunches.

Other parts of the PWFA program such as the Trojan Horse experiments benefit from the highest peak currents and can accept lower charge. The FACET-II beamline has the flexibility to produce electron peak currents in excess of 50 kA by increasing the compression and collimating the energy tails in the bunch compressors. In this configuration, the bunch charge at the IP is reduced to about 0.7 nC. At the other end of the parameter range, the Compton experiments would prefer the highest possible charge in a small transverse size, but do not require the shortest bunch. For these experiments FACET-II can deliver 5 nC with a beam size on the order of 10 μm. The full list of experiments described in this chapter use a variety of parameters within the tuning range of FACET-II.

The FACET-II scientific program will make orders of magnitude advancements in three primary areas: accelerating gradient, beam quality and photon flux. Wakefield acceleration—whether in plasma or in dielectric waveguides—is a cornerstone of the program, building on a more than 20 year history of performing groundbreaking work in GeV-scale beam-driven wakefield acceleration at SLAC. A major goal of FACET-II is to utilize gradients 1,000 times higher than current technology in a meter scale prototype plasma accelerator. The existence of such ultra-high gradients also makes it possible to trap particles and produce a beam with 1,000 times the brightness currently achievable. The combination of uniquely high energy, high density beams and the short pulse, high power FACET laser enables the generation of very high flux photon beams. In principle, 100-1000 times higher gamma flux from 10 MeV to 5 GeV and 10,000 times higher total gamma flux up to 5 GeV should be deliverable.

By offering pulse charge from pC to a nC, emittance from nm to microns, electrons and positrons, single and double bunches, tailored current profiles of up to nearly 100 kA and energy up to 10 GeV FACET-II provides experimental capabilities unparalleled anywhere in the world. By leveraging the additional infrastructure afforded by SLAC’s laser group, the FACET laser systems provide multi-terawatt peak powers with state of the art synchronization approaching 10 fs. These capabilities will draw in additional experimental programs that exploit these capabilities to their fullest generating orders of magnitude improvements in electron and photon beam brightness. The initial vision for the FACET-II science programs is described in this section, but this will certainly evolve to reflect the most pressing science issues of the time as guided by the SAREC committee.

### ***3.1 Plasma Wakefield Acceleration (PWFA) Program at FACET-II***

#### **3.1.1 Introduction**

The first phase of our beam driven plasma wakefield accelerator (PWFA) program began with the experiments in the SLAC FFTB between 1998 and 2006. These experiments demonstrated, among many other things, that a plasma can accelerate electrons with a gradient of 50 GeV/m over nearly a meter. By

April 2016, the FACET scientific program will complete the second phase of our plasma wakefield acceleration program. Upon successful conclusion we will have demonstrated several ambitious goals including a meter-scale plasma accelerator module for electrons and the first tests to identify the optimal technique to accelerate positrons in a plasma. For electrons the acceleration will be meter scale, multi-GeV/m, produce a beam with 100's pC of charge and a narrow energy spread (<10%) while preserving the incoming emittance. For positrons, The SLAC FFTB program was the first experimental investigation of the issues of accelerating and focusing positrons in a plasma. With relatively long positron bunches and low density plasmas accelerating gradients of 100MeV/m were demonstrated but the aberrations in focusing in the positron driven wake resulted in halo formation and emittance growth. FACET will make the first experimental investigation with more compressed positron bunches in tailored high-density hollow-channel plasma cells. Hollow channel plasmas are predicted to achieve an order of magnitude larger accelerating gradient compared to the FFTB experiments while being free of the focusing aberrations for positrons in uniform plasmas.

FACET-II will restart the science programs in 2019 and begin the third phase of plasma wakefield accelerator development. FACET-II will build directly on the results from FACET and investigate the issues of staging, positron acceleration, efficiency and beam quality. The first experiments will take advantage of the high-brightness beams available from the FACET-II LCLS-style photoinjector. When operated in a low charge mode, the large phase space density of these pico-coulomb beams allows them to be compressed to a few femtoseconds and to be focused to a few microns in size. In this extreme it is possible to generate TV/m fields in high-density plasmas that will break new ground for wakefield accelerators, study the threshold for ion-motion in PWFA and allow the properties of materials to be tested under extreme conditions (see Section 3.14). When operated in high-charge mode with bunch charges of 5nC or more, the compressed pulses will have peak currents approaching 100kA opening the door to new forms of plasma injectors and beam-ionized plasma sources. Harnessing the large fields and small spatial extent of the plasma wake, plasma injectors have already produced beams with state of the art micron level emittance and brightness. By controlling the injection using laser pulses and tailored plasma profiles, we will harness the flexibility of the photoinjector drive beam to produce high-energy beams from the plasma with a normalized emittance approaching a nanometer. By demonstrating the ability of compact plasma sources to function as both an energy and brightness transformer, producing multi-GeV beams with unprecedented brightness from a plasma only a meter long, we will pave the way for the first applications such as compact plasma driven XFELs.

By 2020 we will commission the new positron damping ring (see Section 8.3) and renew experiments comparing and contrasting wakefield acceleration of single species bunch(es) of either electrons or positrons in hollow channel plasmas. Using the notch collimator we will optimize the accelerating wakefield in hollow channels for an electron witness beam in an electron driven wake and for a positron witness in a positron driven wake. In 2022 the sailboat chicane (Chapter 9) will allow us to overcome the single species limitations of FFTB and FACET to demonstrate high-gradient acceleration of a positron beam in a plasma wake driven by an electron beam. This is a critical step in assessing the viability of the staged approach to a compact energy frontier electron-positron collider as exemplified in our concept recently developed prior to the 2013 Community Summer Study [2]. Staging issues common to accelerating both electrons and positron such as timing, alignment, beam combining and separation will be studied in detail using an independent witness bunch injector as described in Section 10.3. The flexibility of independent drive and witness beams will allow us to optimize the current profile of the individual pulses to maximize the energy gain and efficiency of the PWFA process.

Answering these important questions through experiments will be the main goal of the plasma wakefield accelerator research program at FACET-II.

### 3.1.2 The High Transformer Ratio Problem

The E200 experiment currently underway at FACET relies on significant beam loading to flatten the accelerating field, [3] thereby ensuring that the particles in the trailing beam gain energy uniformly. This results in a narrow energy spread. Beam loading causes local damping of the wake such that the energy of the drive beam is efficiently transferred to the trailing beam via the wake. However beam loading leads to an effective reduction of the transformer ratio, [4] which is defined as  $T = E^+ / E^-$ , where  $E^+$  and  $E^-$  are the magnitudes of the accelerating and the decelerating fields, respectively.

In the linear regime of the PWFA, the unloaded wake produced by a symmetric beam has a transformer ratio of 2. In the blowout or the bubble regime shown in Figure 3.1, for particles in the tail of the one-bunch case (blue curve)  $T$  is much greater than 1. When the wake is loaded by the trailing bunch, however,  $T$  can be reduced to 1 or less (red and green curves) as shown in Figure 3.1(b). This means that with the current 20 GeV FACET drive beam we expect the energy gain of electrons to be equal to or less than 20 GeV.

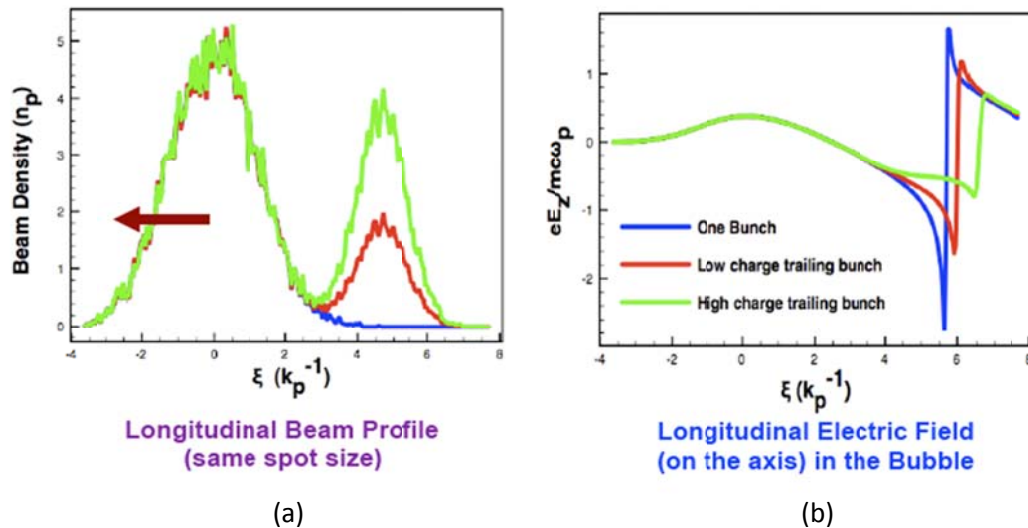


**Figure 3.1.** The wakes produced in plasma can have a dramatically different transformer ratio depending on the extent of the beam loading by the trailing bunch. (a) Shows the three pulse shapes used to produce the wakes and (b) shows the line out of the longitudinal electric field of the excited wake. The transformer ratio is the ratio of the peak decelerating (peak of the positive green curve) to the peak accelerating (peak of the spiky negative curves) field. (Courtesy Weiming An, UCLA)

Cost considerations of a future PWFA-based linear collider indicate that the primary beam should have a charge of several nC and a beam energy of several GeV. [5] This allows us to design a single PWFA stage with a beam-loaded transformer ratio of at least 3. This means that the drive linac for a future PWFA-based linear collider needs to deliver 5 or 10 GeV drive pulses with 4 or 8 nC of charge while adding 15 to 30 GeV per stage to the beam that is being accelerated. This concept requires about 20 stages to reach an energy of 1 TeV. We can accomplish this using one of two approaches.

In the first approach we break the assumption of a symmetric drive beam as shown in Figure 3.2(a). If, instead of using a temporally Gaussian current profile, we shape the beam so that it is bi-Gaussian with a longer rise and a sudden fall, then the unloaded transformer ratio can be increased to a value much greater than 2. As can be seen in Figure 3.2, if the drive beam has a linear rise over 100  $\mu\text{m}$  followed by a sharp drop over 1  $\mu\text{m}$  the fully loaded transformer ratio can be as high as 8. With a more gradual fall

time,  $T$  becomes smaller but even for a 5- $\mu\text{m}$  fall time, a  $T$  of 4 appears feasible. It is therefore possible that a 10 GeV drive beam could add up to 40 GeV per electron to the trailing beam.

There are of course many challenges to realizing such a result in practice. We need to understand how to precisely craft the drive beam pulse shape and how to produce such a high charge and transversely compact trailing beam and load it in the wake with sub-micron accuracy. We do not know whether the drive and trailing beams will be stable or if the beams will be susceptible to the hosing instability.[6] Answering these questions will be the prime goal of exploring this idea.

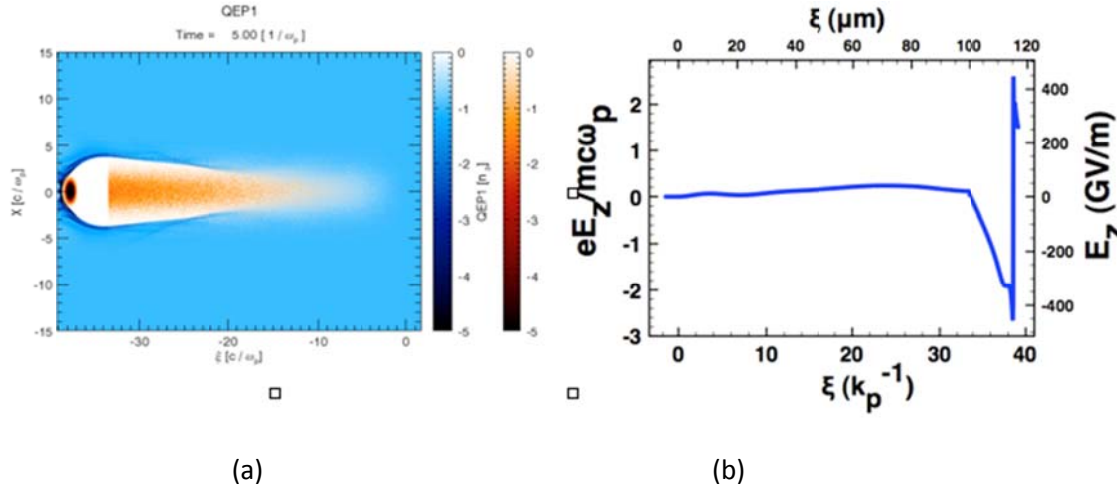


**Figure 3.2. The idea behind generating high transformer ratio wakes using a shaped drive beam. (a) beams with the wake structure and (b) the on axis electric field showing a near uniform decelerating field and a highly nonlinear accelerating spike soon after the beam has entered the plasma. In this case  $T=8$ . Drive Beam Parameters:  $Q = 6 \text{ nC}$ ,  $\sigma_r = 5 \mu\text{m}$ ,  $L_z = 100 \mu\text{m}$ ,  $\epsilon N = 5 \text{ mm mrad}$ ,  $E = 10.0 \text{ GeV}$ . Trailing Beam Parameters:  $Q = 0.288 \text{ nC}$ ,  $\sigma_r = 2 \mu\text{m}$ ,  $\sigma_z = 1 \mu\text{m}$ ,  $\epsilon N = 1.0 \text{ mm mrad}$ ,  $E = 100 \text{ MeV}$ . Distance between two beams: 12.5  $\mu\text{m}$ . Plasma Density  $n_p = 3.17 \times 10^{18} \text{ cm}^{-3}$ . The beams propagate in a pre-ionized plasma and  $k_p \cdot 1 = 3 \mu\text{m}$ . (Courtesy Weiming An, UCLA)**

Although for linear wakes that are excited by symmetric bunches  $T$  is less than equal to 2 , it can be shown that in a certain regime [7] of the fully blown-out wake,  $T = k_p \sigma_z / \Lambda^{1/2} > 2$ . Here  $k_p$ ,  $\sigma_z$  and  $\Lambda$  are wake wave number, rms bunch length and charge per unit length, respectively. Thus by appropriately optimizing the plasma density for a given charge and bunch length it is possible to achieve unloaded  $T \gg 2$  and a loaded  $T$  of  $>2$ . The goal here would be to use the 10 GeV FACET-II beam to add 30 GeV per particle to the electrons in the trailing beam over a distance of less than a meter while extracting more than 90% of the drive beam's energy. Figure 3.3 shows such a case where the loaded  $T$  is about 3. The FWHM energy spread of the trailing bunch is still a only few percent.

To load these wakes we need trailing beams to be much shorter than the drive beam and these must contain a significant amount of charge to flatten the wake so that the energy spread is narrow. The current approach to getting such a drive beam/trailing beam structure is to collimate a portion of an appropriately chirped beam in the dispersive plane and then to partially recompress the beam. [8] In this process, however, a significant amount of original beam charge is lost and the drive beam/trailing beams are tens of  $\mu\text{m}$  long. These lower charge, longer bunches require a longer and lower density preformed plasma in the current E200 experiment.

However, FACET-II would be able to supply electron bunches that contain up to 5 nC of charge. This opens the possibility of producing a drive beam/trailing beam configuration with an adequate amount of peak current in each to self-ionize the gas. We will therefore be able to produce the wake with the drive pulse and beam-load the wake with the trailing pulse. An example of such a case is discussed in detail in Ref. (2) and will in fact be one of the first experiments to do at FACET-II when the witness injector is complete. The drive beam will have an rms bunch length of 30 $\mu$ m and contain  $3 \times 10^{10}$  electrons, while the trailing bunch will have a bunch length of 10  $\mu$ m and contain  $1 \times 10^{10}$  electrons. The separation between the two bunches will be 115  $\mu$ m and both bunches will be focused to a spot size of 3.3  $\mu$ m in a  $1 \times 10^{17}$  cm $^{-3}$  Li vapor. In this case, the energy should double from 10 to 20 GeV in just 30 cm.

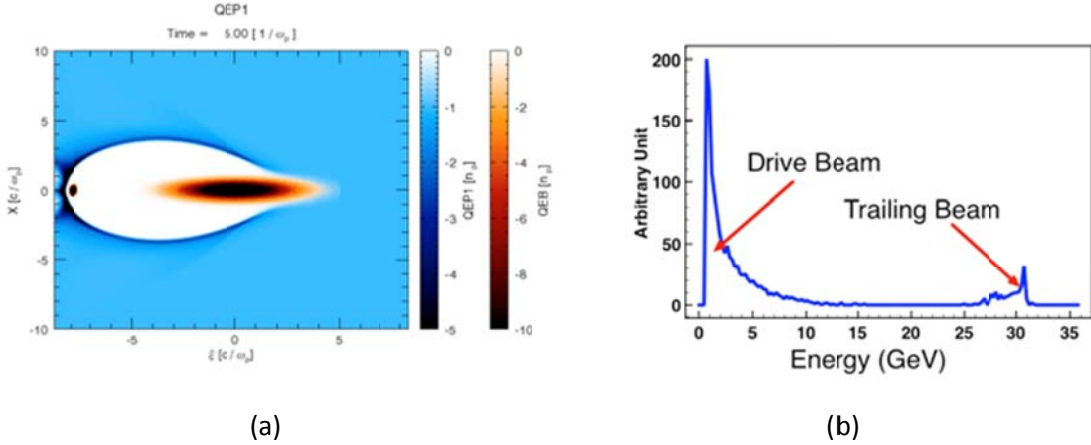


**Figure 3.3. Generation of fully loaded transformer ratio wakes of 3 using the FACET-II beam. (a) shows the beams and the wake and (b) shows the energy spectrum of the two beams after just 26 cm. Drive Beam Parameters: Q = 4 nC,  $\sigma_r = 5 \mu\text{m}$ ,  $\sigma_z = 20 \mu\text{m}$ ,  $\epsilon N = 5 \text{ mm mrad}$ , E = 10.0 GeV. Trailing Beam Parameters: Q = 0.288 nC,  $\sigma_r = 2 \mu\text{m}$ ,  $\sigma_z = 2 \mu\text{m}$ ,  $\epsilon N = 1.0 \text{ mm mrad}$ , E = 100 MeV. Distance between two beams: 93.5  $\mu\text{m}$ . Plasma Density  $n_p = 2.0 \times 10^{17} \text{ cm}^{-3}$ . The beams propagate in a pre-ionized plasma. (Courtesy Weiming An, UCLA)**

The higher transformer ratio experiments need trailing bunches on the order of 2  $\mu$ m rms with sub 100 nanometer emittance and a significant amount of charge. It is not easy to achieve all these requirements with a few femtosecond jitter between the drive and the trailing beam. Fortunately, there are other possible methods for generating such a trailing beam in situ without any loss of charge in the drive beam that can be developed at FACET-II. Below we discuss two different methods that we would like to explore on FACET-II for generating suitable beams for injection into a PWFA that is operating in the high transformer ratio mode.

### 3.1.3 Generation of super- high brightness beams

#### 3.1.3.1 Density down-ramp injection using beam parameters at FACET-II

A sudden density transition from a high-to-low-density region traps plasma electrons in the wake. [9] Even a relatively gradual density transition can trap electrons as the wavelength of the wake adiabatically increases. [10] We have examined this so-called down-ramp injection, via 3D particle-in-cell (PIC) code simulations, using the FACET-II beam driver with a charge of 5 nC, a transverse emittance of  $5 \times 5 \mu\text{m}$ , an energy of 10 GeV and a spatial size of  $10 \times 10 \times 10 \mu\text{m}$ . Plasma density is varied from  $2 \times 10^{18} \text{ cm}^{-3}$  to  $1.5 \times 10^{18} \text{ cm}^{-3}$  with a down-ramp length of 115  $\mu\text{m}$ .

Figure 3.4(a) shows the wake excited in the down-ramp and the trapped beam in this wake. The density distribution shows that the injected particles have a “head” with a relatively larger emittance that forms a halo around a beam core with a smaller emittance. To eliminate the particles of the beam halo, we just take the 95% electrons into account. The emittance of the beam core is  $\epsilon_{n,0.95} = 70 \times 100$  nm as shown in Figure 3.4(b). The beam charge, peak current and brightness are 580 pC, 47 kA and  $1.4 \times 10^{19}$  A/rad<sup>2</sup>m<sup>2</sup> respectively. The emittance of the beam head is much larger, i.e.  $\epsilon_{n,0.95}$  are  $630 \times 590$  nm. The beam charge, peak current and brightness of the particles in the beam head are 610 pC, 107 kA and  $2.9 \times 10^{17}$  A/rad<sup>2</sup>m<sup>2</sup> respectively. Clearly for these parameters, there is a trade-off between current and brightness of the core and head.

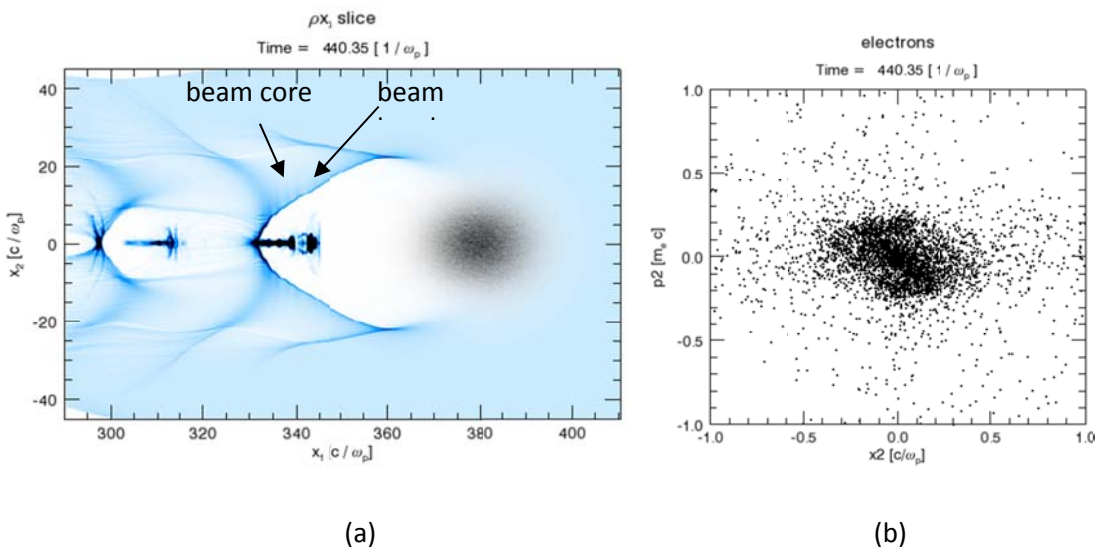


**Figure 3.4. Simulation results of density down ramp injection with a 5 nC,  $10 \times 10 \times 10 \mu\text{m}$  beam driver. (a) electron density distribution (b)  $x_2$ - $p_2$  phase space of the beam core. The unit simulation length in this figure is 1 micron. (Courtesy Fei Li and Wei Lu Tsinghua University & UCLA)**

The total emittance of the beam can be further reduced if the drive beam charge is lower. We next use a drive beam with spatial size  $10 \times 10 \times 10 \mu\text{m}$ , but with a lower charge of 1 nC. The plasma density is varied from  $2.9 \times 10^{17}$  cm<sup>-3</sup> down to  $2.2 \times 10^{17}$  cm<sup>-3</sup> and the down ramp length is 260  $\mu\text{m}$ . The results of this simulation are shown in Figure 3.5. The emittance of the total beam is now  $120 \times 120$  nm. The beam charge, peak current and brightness are 230 pC, 27 kA and  $3.8 \times 10^{18}$  A rad<sup>2</sup>m<sup>-2</sup>, respectively. Thus there appears to be a trade-off between the drive beam charge and the trailing beam brightness that is counter-intuitive and calls for experimental investigation.

How can such an experiment be realized at FACET-II? The 5 nC beam used in the first simulation is capable of field-ionizing hydrogen gas, but a 1 nC beam requires a laser-ionized column of hydrogen. At the upstream end of a tube of hydrogen at the appropriate pressure we place a thin gas cell containing higher pressure gas with an approximately 200 micron entrance and exit holes to create the necessary density ramp. [11, 12] Such cells have been successfully used in injector-accelerator experiments done with intense laser pulses. The beam trapping preferentially occurs in the down-ramp and the electrons are then accelerated in the accelerator portion of the wake excited in the approximately 30 cm long ionized gas column in the downstream tube. The attraction of this method is that it is simple and in

principle jitter free. The emittance, energy and charge of the accelerated beam can be measured by changing the length of the tube and the scale-length of the density ramp. If this technique can be perfected, it will give beam emittances that are smaller than those achieved by state-of-the art methods.

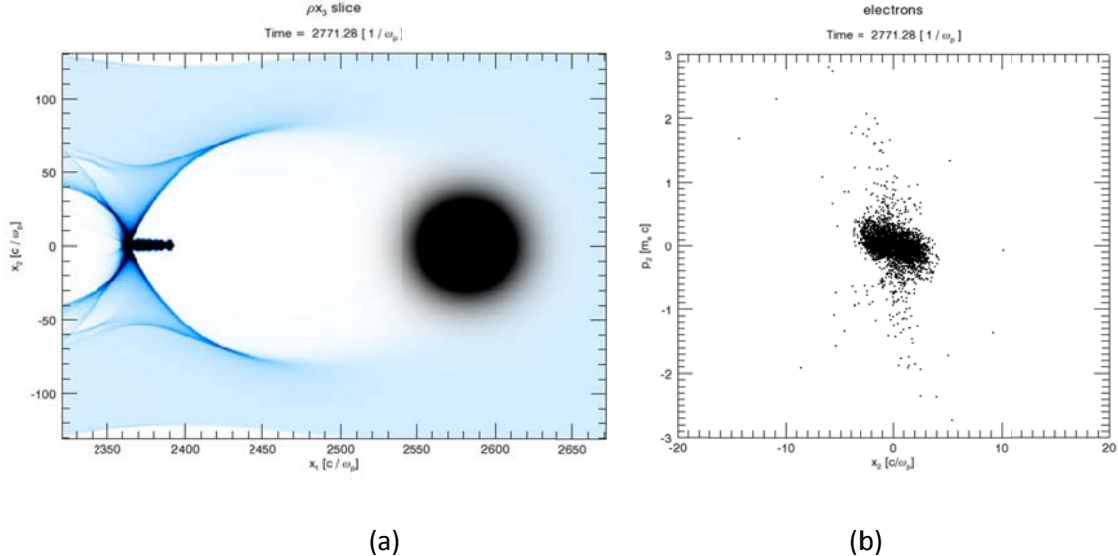


**Figure 3.5. Simulation results of density down ramp injection with a 1.1 nC, 10×10×10  $\mu\text{m}$  beam driver. (a) electron density distribution (b)  $x_2$ - $p_2$  phase space of the total bunch. The unit simulation length in this figure is 1/3 micron. (Courtesy Fei Li and Wei Lu, Tsinghua University & UCLA)**

### 3.1.3.2 Electron Injection by Transversely Colliding Laser Pulses

Generation of low emittance electron bunches will be tested at FACET using the so-called Trojan Horse scheme, [13] wherein a longitudinally co-propagating laser pulse ionizes and injects electrons inside an electron beam driven wake. At FACET-II we propose to test a variation of this scheme that has the potential to generate the highest brightness beams to-date. [14] We call this the transversely colliding laser injection method. Here ultra-bright electron bunches are produced using ionization injection triggered by two transversely colliding laser pulses inside a beam-driven wake. The relatively low intensity lasers are polarized along the wake axis and overlap with the wake for a very short time. The result is that the residual momentum of the ionized electrons in the transverse plane of the wake is much reduced and the injection is localized along the propagation axis of the wake. This minimizes both the initial “thermal” emittance and the emittance growth due to longitudinal phase mixing. This concept can be successfully tested through 3D particle-in-cell (PIC) simulations. In Figure 3.6 we show the injection process of helium electrons by two colliding laser pulses in a wake formed in a partially ionized He plasma by an electron beam. We show that ultra-short ( $\sim 8\text{fs}$ ) high-current (0.4kA) electron bunches with normalized emittance of 8 and 6 nm in the two planes and brightness greater than  $1.7\text{e}19 \text{ Amp rad}^{-2} \text{ m}^{-2}$  can be obtained for realistic parameters.

The transverse colliding pulse is inherently more complex than the density down ramp injection. We now have to deal with femtosecond synchronization of two laser ultra-short laser pulses that must overlap with one another within a micron inside the wake. In either scheme, electrons are accelerated to multi-GeV levels within roughly 10 centimeters. How does one measure the emittance of such a beam? Perhaps the most conclusive demonstration that the beam has a brightness exceeding  $10^{19} \text{ Amp}$

$\text{rad}^{-2} \text{ m}^{-2}$  is to send this beam through a section of the LCLS undulator and measure SASE gain. This is currently being studied through integrated PIC and FEL simulations.

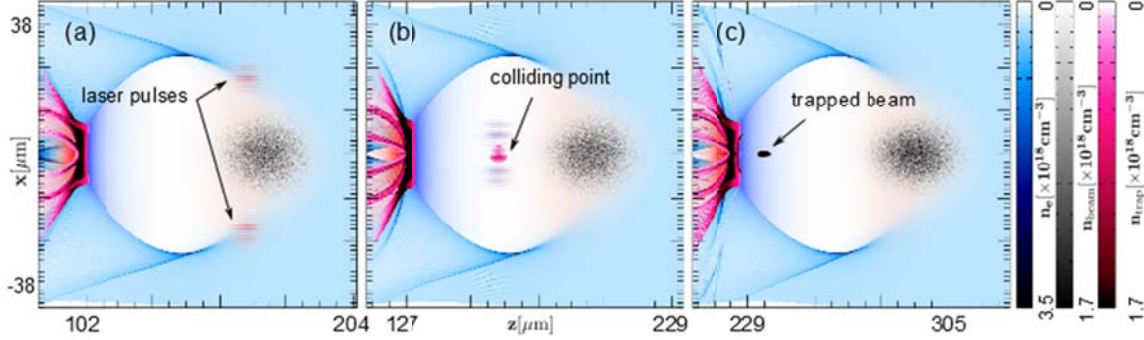


**Figure 3.6.** Snapshots from PIC code simulations illustrating the transverse colliding pulse injection of helium electrons into the ion cavity. Snapshots (a) to (c) show the charge density distribution of driver beam, wake electrons and helium electrons at three different times (a)  $\sim 80\text{fs}$  before laser pulses collision (b) around laser pulses' collision time (c)  $\sim 200\text{fs}$  after collision when the injected electrons become trapped in the wake. (Courtesy Fei Li and Wei Lu Tsinghua University & UCLA)

### 3.1.4 Determining the repetition rate of a single module for stable operation and staging of two PWFA modules.

The repetition rate requirements of a future PWFA depend on the application. [15] For instance a PWFA-based X-FEL may operate at one kHz whereas a future linear collider may need to operate at 10 kHz with a CLIC-like drive bunch structure. Different drive beam train formats can be tested at FACET-II to see what ultimate repetition rates are acceptable. FACET-II has high charge bunches compared to FACET which means that we can probably operate with field-ionized plasmas of noble gases which can be flowed and replenished in between shots. This could be tested at FACET-II.

The staging of two PWFA modules is a far more challenging problem. Any misalignment between the drive beam in the second stage and the accelerating beam from the first stage leads to strong radiation loss and emittance growth. [16] This problem has to be addressed at some point and engineering solutions have to be developed.

### 3.1.5 Summary

The PWFA program on FACET-II seeks to demonstrate a high efficiency, high transformer ratio PWFA stage that gives a 20-30 GeV energy gain while generating an electron beam with high charge, low energy spread and low transverse emittance. While working towards this goal, we will develop new beam injection and diagnostic techniques. We have considered two new injection schemes that allow for the full use of the FACET-II drive beam, as opposed to current experiments that require spoiling the FACET drive beam. One is to use the natural injection that occurs in a density down ramp and the other is to use active injection via counter-propagating laser pulses. Repetition-rate limitations have not yet been addressed in any plasma wakefield experiments. High-efficiency transfer of drive-beam energy to the trailing beam will likely be necessary for high luminosity colliders. Additionally, particle-beam-ionized plasmas can be rapidly replenished via laminar flow of fresh gas on a tens of kHz time scale. FACET-II possesses unique capabilities that enable these studies.

## **3.2 Physics of positively charged drive beams for PD-PWFA**

### **3.2.1 Motivation for CERN Experiments with Protons**

LHC proton bunches are the only plasma wakefield drivers that carry enough energy to produce an ILC type electron or positron bunch in a one or few plasma stage. Existing laser pulses and electron particle beams do not carry enough energy. ILC bunches of  $2 \times 10^{10}$  particles at 1TeV carry about 2 kJ. For reference, an LHC bunch at 7TeV and with  $10^{11}$  protons carries over 100kJ. Protons also have a large mass, can have a very high energy ( $\sim \text{TeV}/\text{p}^+$ ) and are so “stiff” that bunches can propagate over many meters of plasma without significant transverse size change. Therefore, a large average accelerating gradient (1GeV/m or more) could be sustained over the entire acceleration length without suffering from the gradient dilution arising when staging is required [17]. Gradient dilution occurs because of the drift distance necessary between stages to seed the next drive bunch into the next plasma section and to capture and re-focus the witness bunch. It can vastly exceed the length of each stage and drastically decrease the average accelerating gradient.

Operating at lower peak gradient also means at lower plasma density since the maximum accelerating field increases with the square root of electron density (that is,  $E_{\max} \sim n_e^{1/2}$ ). This also means that the size of the accelerating structure or plasma density perturbation is larger, as both scale with the inverse square root of electron density (in 3D,  $\sim \lambda_{pe}^3 \sim (n_e^{-1/2})^3$ ). This reduces the requirements in bunch longitudinal and transverse (focusing) compression ( $\sigma_r, \sigma_z < \lambda_{pe}$ ) and in temporal and spatial alignment. Matching of the bunch transverse size to the weaker plasma focusing field ( $E_r$ ), which scales with the plasma density is easier since the matched size also increases with decreasing density ( $\sigma_r \sim n_e^{1/4}$ ). This is true even for very low emittance bunches.

### **3.2.2 PD-PWFA Physics experiments at SLAC with electron and positron bunches**

Short proton bunches, on the order of 100  $\mu\text{m}$ , are suitable for driving wakefields with large amplitude (1GV/m or more), but these are not currently available. Initial experiments will be performed around 2015 at CERN with longer bunches in the self-modulation instability regime. [18] These experiments use bunches of length  $\sigma_z=12\text{cm}$  with plasma wavelength  $\lambda_{pe}=1.5\text{mm}$ .

High energy ( $\sim 20$  GeV) positron bunches are much less “stiff” and can self-modulate in only a few cm whereas CERN SPS proton bunches ( $\sim 450$  GeV) need meters of plasma.

In addition, it is well known that plasmas respond very differently to negatively and positively charged particle bunches. This was clearly demonstrated in the PWFA experiment performed at the SLAC FFTB. [19, 20, 21] Even in the self-modulation regime, plasma behavior is quite different as soon as the nonlinear, high-gradient regime is reached, as was demonstrated in numerical simulations (see Figure 3.7). [22]

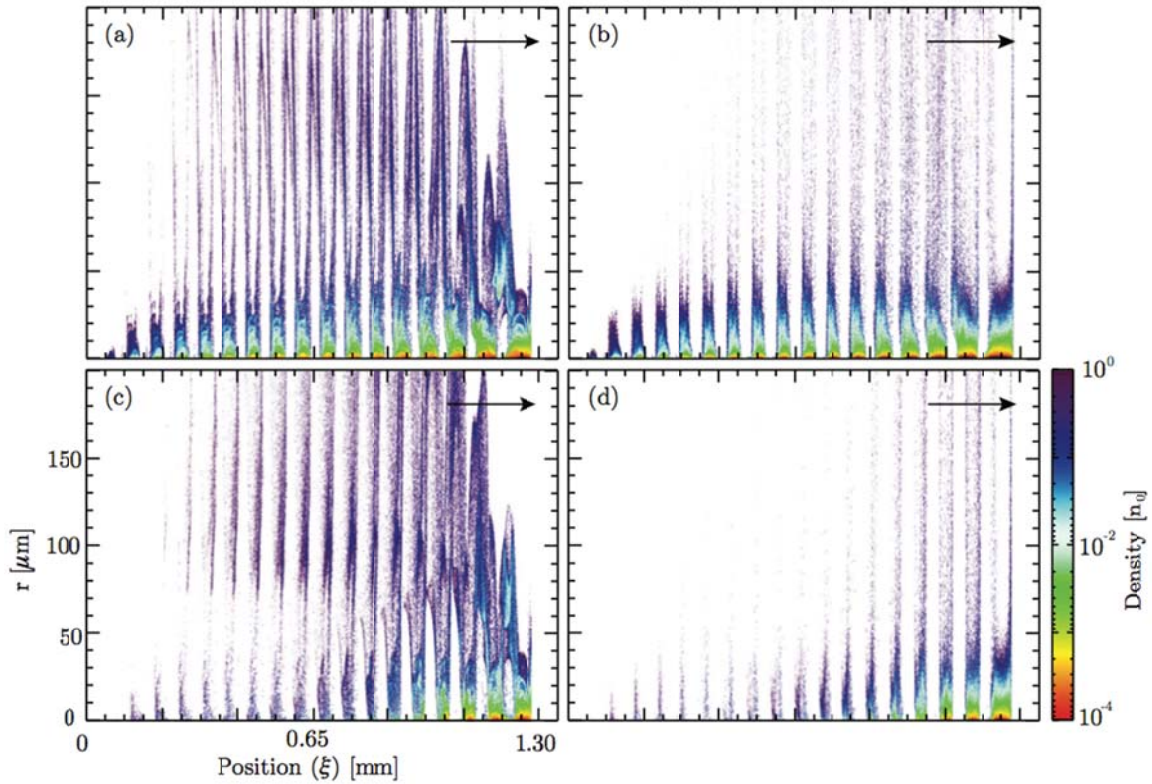


**Figure 3.7. Electron (top) and positron (bottom) bunch density after propagation of 10 cm (left) and 1 m (right) plasma with a density of  $2.3 \times 10^{17} \text{ cm}^{-3}$ .**

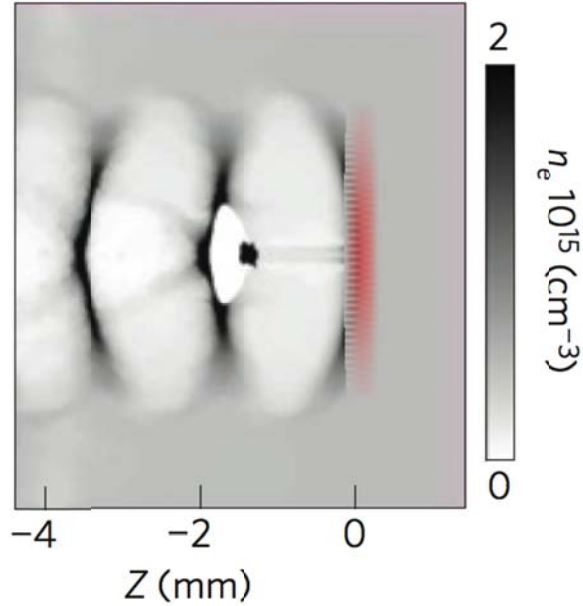


**Figure 3.8. Plasma density perturbation driven by a short ( $\sigma_z=100 \mu\text{m}$ ) and wide ( $\sigma_r=430 \mu\text{m}$ ) proton bunch. The proton bunch density is indicated in red while the witness electron bunch to be accelerated is shown in black.**

Short positron bunches can be produced at SLAC and are therefore the ideal candidate to test the concept of a PWFA stage driven by a , positively charged bunch shorter than the plasma period. In particular, the transverse evolution of the drive bunch along the plasma is a concern since there is no equivalent of the bubble regime that exists for negatively charged particle bunches. Simulations indicate that positively charged bunches need to be shaped like pancakes, in contrast to the pencil shape of electron bunches, in order to drive wakefields towards the blowout regime (see Figure 3.8 , [23]) In addition these simulations also indicate the real blowout is difficult to reach. This could lead to emittance growth of the accelerated witness bunch. The conditions appear to be much less favorable for positively charged bunches than for negatively charged bunches in the self-modulated PWFA regime (see Figure 3.7). Simulations clearly show that the loss of drive particles along the plasma is significantly larger with positively charged bunches. This leads to lower wakefield amplitudes and larger dephasing between the wakefield structure and the drive bunch and thus also with the accelerated bunch. The situation seems worse when approaching the nonlinear PWFA regime.

One to one comparisons between the case of an electron and a positron bunch could clearly show these differences and help in determining an optimum regime of operation with short, positively and negatively charged bunches. This difference will be evidenced by measuring the energy loss and gain by drive bunch particles, as well as by measuring the drive bunch self-modulation. In addition, the availability of a short, trailing electron bunch to witness the wakefields with a variable delay with respect to the drive bunch is a great asset.

Simulation of the self-modulation PWFA regime is much more challenging than that of the short bunch PWFA regime and numerical codes have not been benchmarked against experimental results.

The availability both electron and positron bunches long and short would definitely give access to a number of PWFA regimes that have never been accessed before, which will drive new discoveries in PWFA physics. Existing plasma-based PWFA designs (see section 3) use electron beams to drive the

wakefields. In order to create a next-generation electron/positron collider we need to be able to accelerate the positron bunch directly.

Therefore the availability of a witness bunch, whether electron or positron, with independently controllable parameters, would greatly enhance the relevance of the results to advanced accelerators. The actual acceleration of a witness bunch with a bunch length well below the plasma wavelength could be directly tested, both in the self-modulated and in the short bunch PWFA regime. In particular, we could test the acceleration of a positron bunch in the wakefields driven by an electron bunch. This is the favored scheme for the acceleration of a positron at high-gradient in a plasma. However, no clear parameter set that can produce a high quality positron bunch exists. The availability of a facility to test this scheme would no doubt generate the new and original ideas needed.

The availability of an electron witness bunch produced by an RF photo-injector gun would allow for exquisite and independent control of the witness bunch parameters (charge, length, timing, and transverse size), a required condition for the demonstration of beam loading producing narrow final energy spread and for optimization of the energy transfer efficiency.

Results with a positron drive bunch would bring early and important results relevant to the longer-term plans with a proton bunch as a driver. Producing suitable, short proton bunches requires very significant efforts and maybe even the design of a dedicated circular machine. Therefore, establishing the physics of this scheme with positron bunches will provide important validation.

### **3.3 PWFA Based on High Brightness Photoinjector-derived Electron Beams**

In this section, we summarize the new physics that is made possible by the introduction of very high brightness electron drivers in PWFA experiments. The scenarios presented take advantage of the improved compressibility of photoinjector beams, particularly at low charge, as well as superior focusability of low emittance systems. These attributes permit three new experimental initiatives in FACET-II: teravolt-per-meter plasma wakes with ultra-short beams; ion motion experiments (with associated implications for fusion physics); and exploration of the quasi-nonlinear regime of the PWFA. We now recount briefly the case for investigating each of these topics at FACET-II.

#### **3.3.1 TV/m PWFA Using Femtosecond Beams**

Scientists have recently proposed using low charge ( $Q$ ), in the pC range, as a path to achieving GeV-class beams that may be compressed down to hundreds of attoseconds. [24] Further, these beams are predicted to have very low transverse emittance, and thus unprecedented brightness. This proposal [25] addresses two challenges in the x-ray SASE FEL. It breaches the fs frontier in x-ray pulse length, and should also allow single-spike x-ray SASE FEL. [26] Both features are critical for resolving properties of atomic and molecular systems at the spatial and temporal scales relevant to electronic motion. Low charge operation is therefore important for advancing both FEL capabilities and fundamental beam physics.

Recent experimental work at the SLAC Linear Coherent Light Source (LCLS) focused on generating compressed beams with short pulses. In initial tests, 20 pC beams were compressed to rms duration  $\sigma_t \cong 2$  fs, while achieving transverse normalized emittances of  $\varepsilon_{n,x} = 0.14 \mu\text{m}$  and  $\varepsilon_{n,y} = 0.4 \mu\text{m}$  at an energy  $U_b = 14$  GeV. This beam, having high peak current,  $I \sim 8$  kA, and low emittance is predicted to produce nm-wavelength FEL pulses in the single-spike regime. [27] We propose to use similar beams at FACET-II to generate an extremely high field PWFA.

Beams having short duration can produce coherent excitations with frequency components up to a cut-off of  $\omega_m \sim \sigma_t^{-1}$ . Further, in the context of PWFA, as with all Cerenkov-class interactions, the amplitude  $E$  of the radiated field scales as  $\propto N_b \omega_m^2 \cong N_b / \sigma_t^2$ , where  $N_b$  is the number of particles in the beam. To maximize the wake amplitude, the maximum excitation frequency must equal the plasma frequency,  $\omega_m = \omega_p$ , giving the optimization condition  $\omega_p \sigma_t \cong 1$ . This scaling has been investigated experimentally, [28,29] theoretically and computationally, [30, 31] and its validity in application even in the nonlinear “blowout” regime [32] is well understood. PWFA operation in the blowout regime is desired, as the plasma electrons are all evacuated from the beam channel, producing acceleration dependent only on longitudinal position  $\xi = z - v_b t$  in the beam channel, where  $v_b \cong c$  is the beam  $z$ -directed velocity. Further, the nominally uniform ion density makes focusing linearly dependent on radial position  $r$  relative to the beam axis. Both of these attributes of the wake forces are deemed necessary for producing high quality beams with the phase space density demanded by advanced applications in high-energy physics and at x-ray FELs.

For the LCLS 20 pC beam scenario,  $\omega_p \sigma_t \cong 1$  yields a plasma electron density  $n_0 = [4\pi r_e (c\sigma_t)^2]^{-1} \cong 7.8 \times 10^{19} \text{ cm}^{-3}$  corresponding to a gas density of several atm. We can estimate whether this case accesses the blowout regime by evaluating the ratio of beam electrons to plasma electrons found within a volume of a cubic plasma skin-depth ( $k_p^{-1} = c/\omega_p$ ),  $\tilde{Q} \equiv N_b k_p^3 / n_0 = 4\pi k_p r_e N_b$ . [30] In our case we have  $\tilde{Q} \cong 7.4$ ; a value exceeding unity indicates the blowout regime may be achieved. To access the blowout regime we must also focus the beam to a rms size  $\sigma_x$  smaller than a skin-depth,  $k_p \sigma_x < 1$ . The self-consistent equilibrium beam size in the plasma arising from PWFA ion focusing is a function of the equilibrium  $\beta$ -function,  $\beta_{eq} = \sqrt{2\gamma}/k_p$  as  $\sigma_{x,eq} = \sqrt{\beta_{eq} \epsilon_{nx}}/\gamma$ . For our current parameters,  $\beta_{eq} = 140 \mu\text{m}$  and  $\sigma_{x,eq} = 45 \text{ nm}$ , and thus  $k_p \sigma_x \approx 0.075$ . The beam density associated with this extremely bright beam in the dense plasma is  $n_b = 6.5 \times 10^{21} \text{ cm}^{-3}$ , giving  $n_b/n_0 \approx 84$ , a highly nonlinear blowout scenario. To gauge the strength of the plasma wakes in initial particle-in-cell (PIC) simulations we use a slightly initially mismatched injected beam, to  $\sigma_x \cong 77 \text{ nm}$  ( $n_b/n_0 \approx 28$ ). These simulations were carried out using the 2D EM PIC code OOPIC, [33] with the predictions for the longitudinal plasma wake  $E_z(r, \xi)$  shown in Figure 3.9. This simulation produces unprecedented large fields, in excess of 1.3 TV/m. This field amplitude is also remarkable in that it is enormous even by internal atomic physics standards. Indeed, the collective field such beams can readily ionize matter, thus allowing both plasma formation, and a unique probe of atomic physics in an extreme field limit. The size of  $E_z$  is not surprising, however, in that the fields at the beam edge before the plasma entrance is estimated as  $E_{r,\max} \cong eN_b / 2(4\pi)^{1/2} \epsilon_0 \sigma_x \sigma_z = 1.5 \text{ TV/m}$ ; the maximum transverse field is roughly transformed to longitudinal field amplitude by the plasma response.

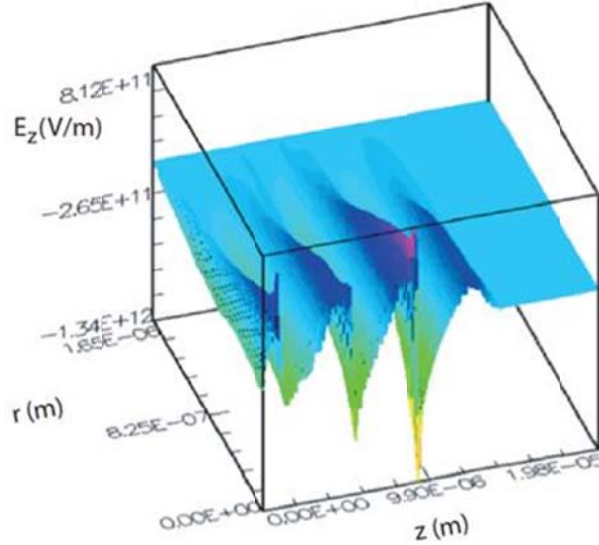


**Figure 3.9. OOPIC simulation of PWFA, 20 pC, 2 fs beam case, showing TV/m wakes.**

To produce the conditions for plasma creation and optimum plasma wake formation, we must implement an appropriate focusing scheme. Further, in order to consider implementing this experiment in a spatially-limited region such as FACET-II, we should make the focusing system as compact and easily implemented as possible. We may base the mini- $\delta$  optics on an ultra-high field gradient system based on permanent magnet quadrupoles (PMQs), similar to that developed for previous UCLA experiments on inverse Compton scattering. [34] This system, tunable by repositioning of quadrupoles, can achieve quadrupole gradients of over 700 T/m and has the further advantage of evading restrictions on performance due to geometric and chromatic aberrations without requiring complex sextupole correction schemes. With the PMQs arranged in a modified triplet configuration, [34]. ELEGANT simulations [35] indicate that we can focus the beam to  $\sigma_x = 130$  nm. This size is well suited for injection into the plasma, with a final  $\beta$  function of 1.2 mm. While this beam size is not matched to the plasma focusing, it is small enough to ionize the gas, and enter into an adiabatic focus, as shown in Figure 3.10.

The bare (no plasma) beam is compelling, as this beam allows electric field levels possibly at high as 100 V/Å, into the range that accesses the barrier suppression ionization (BSI) regime [36] in a wide variety of atomic species. This implies that the field strength at FACET-II makes it easier to create the desired plasma using the electron beam. In previous experiments at FACET that employed over an order of magnitude smaller fields, plasma formation was attributed to tunneling ionization [37, 38, 33]. Accessing BSI is an exciting possibility —a highly focused, multi-kA beam in and of itself is new instrument for performing fundamental atomic physics investigations. We will be able to use the very intense beams at FACET-II to expand upon existing research programs, such as the ultra-fast magnetic switching studies currently active at FACET, and study phenomena that have thus far been inaccessible.

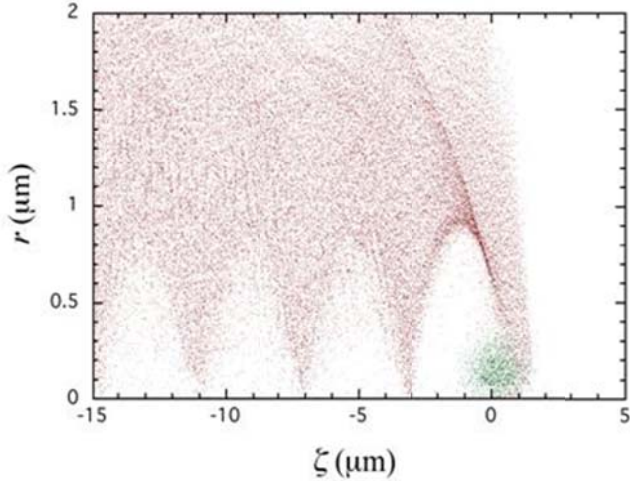


**Figure 3.10. Beam (green) and plasma (red) electrons in simulation of LCLS 20 pC beam initially focused to  $\sigma_x=130$  nm passage through 3.15 atm H<sub>2</sub> gas.**

As a practical rather than fundamental concern, the self-consistent ionization of a high pressure gas by the beam fields must occur within hundreds of attoseconds to create the plasma within the appropriate time scale to allow the full amplitude plasma wakefields to develop. The UCLA PBPL team studied this computationally and theoretically and found it to be practical with the final focus discussed above. The method is straightforward using Li gas, and is possible even in hydrogen. [39]. It should be noted that with beams well below optical wavelengths in dimension, all signals from beam profile monitors are coherent, and coherent imaging techniques should be embraced .

### 3.3.2 Ion Motion in High Brightness Beam Drivers

The condition  $n_b > n_0$  is a defining characteristic of the blowout regime. Indeed, as seen above, the density of the high brightness driving beam in a PWFA may exceed  $n_0$  by several orders of magnitude. Under these circumstances, the beam's electric field can produce relativistic plasma electron motion. [40,41] Additionally, this electric field is high enough that the ions may move significantly during the beam passage. For the parameters given by S. Lee, et al.,[42] and quoted by Raubenheimer in his discussion of the implementation of a PWFA "afterburner" to boost the energy of a linear collider (LC) by at least a factor of two, [43]the ions can collapse towards the beam axis, causing a large, non-uniform ion density spike within the beam. This *ion collapse* has disastrous implications for preserving the transverse emittance of the accelerating beam, effectively negating the oft-claimed advantage of linear transport in the blowout regime. Thus the issue of ion motion is of critical importance in evaluating the viability of using the PWFA in a collider and other high brightness beam applications. [44]

The theoretical and computational analysis of the ion collapse problem has been performed at UCLA PBPL. [45] The phenomenon of ion collapse in the PWFA can be viewed in several useful ways. First, it is a form of wakefield, with as direct as possible coupling between the beam and its environment, in this case plasma electrons and ions that lie in the beam path. The fact that linear collider beams are of unprecedented density (similar to solid matter) means that they act as a *high energy density* driver of plasma motion. As such, the study of physical effects associated with plasma wakefields in such extreme scenarios represents an unprecedented opportunity in high field plasma physics. This frontier opens up a new application to an unrelated field, as the ions are simultaneously heated and confined by the application of the beam focusing fields. Thus, with appropriate choice of ionized species (i.e. deuterium and tritium), we may envision an alternate scenario for creating fusion-relevant plasma conditions.

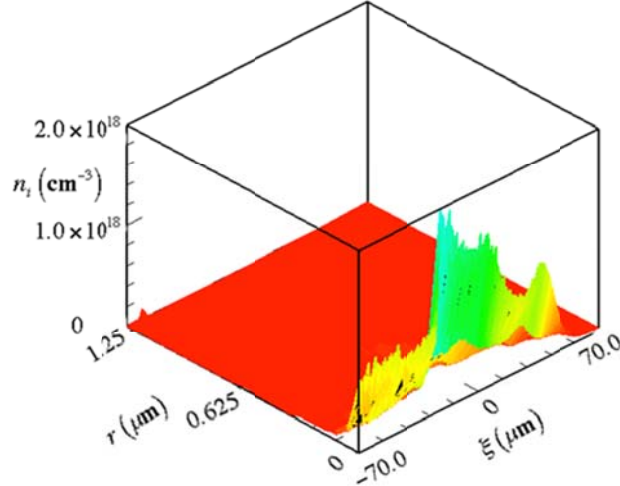


**Figure 3.11. Surface plot of ion density distribution, as simulated by OOPIC showing increase in  $n_i > 200$  due to ion collapse (from Ref. 20)**

To create the conditions for ion collapse at FACET-II, we concentrate on a large-charge scenario with the following beam parameters:  $Q = 3 \text{ nC}$ ,  $\varepsilon_{n,x} = 3 \mu\text{m}$ , with moderate compression to  $\sigma_t = 0.2 \text{ ps}$  ( $\sigma_z = 60 \mu\text{m}$ ). Using  $\omega_p \sigma_t \approx 1$  we have a relatively low plasma density,  $n_0 \approx 8 \times 10^{15} \text{ cm}^{-3}$ , and a total phase advance for small amplitude ion oscillation in the beam's potential well of

$$\Delta\phi = \sqrt{\frac{Zr_a N_b \sqrt{2\pi\gamma}}{A\varepsilon_{n,x}}} = \sqrt{\frac{Zr_a N_b}{A\varepsilon_{n,x}}} (2\pi\gamma)^{1/4} \approx \frac{\pi}{2}.$$

This phase advance indicates that the ions indeed *focus* inside of the driving beam. The first observable consequence of this ion collapse, which is illustrated in Figure 3.11, is that the transverse emittance of the trailing part of the drive beam increases dramatically.

Ion focusing not only may concentrate the ions, it may impart to them a large kinetic energy, thus providing temperatures similar to those in fusion plasmas. The maximum energy may be estimated from the potential at the beam's edge to be

$$q\Phi_{\max} = \left. \frac{Zr_a N_b m_a c^2}{2\sqrt{2\pi}\sigma_z \sigma_r^2} r^2 \right|_{\text{beam edge}} \approx \frac{Zr_a N_b m_a c^2}{2\sqrt{2\pi}\sigma_z}.$$

For our parameters, this indicates that we may achieve energies near to 100 keV in a deuterium plasma, which is adequate for achieving D-T fusion. We may observe these particles in fusion events by allowing them to collide with a tritiated wall, for example, or by using an electrostatic energy analyzer. If we wish to confine the ions for a longer time ( $\Delta\phi \gg 1$ ) we can utilize a higher density gas, with density on the order of TV/m. Then, by increasing  $n_0$  by a factor of 10,000, the phase advance for ion oscillations is augmented by a factor of 100. In this case, the ion temperature achieved is expected to be nearly the same, in the range of 100 keV, as can be deduced from the expression for the potential given above.

### 3.3.3 The Quasi-Nonlinear Regime of the PWFA

The original form of PWFA proposed exciting wakefields through the use of relativistic electron bunches, which induce a small density perturbation in the plasma. Using the linearized equations of motion, continuity and Maxwell's equations, one can readily discern the basic dynamics of PWFA in the linear regime. While the simple harmonic plasma response allows the wakefields to be driven resonantly, a small density perturbation implies that plasma electrons persist both within the volume of the driving bunch and in the beam (driving and accelerating) region. Consequently, the fields experienced by the beams are non-ideal in both the radial and longitudinal directions. In the blowout regime of PWFA, as noted above, a high intensity beam excites nonlinear plasma oscillations, having amplitude-dependent period, and thoroughly evacuates a bubble of its plasma electrons leaving behind only the ions, with associated (up to the onset of ion motion) excellent quality transverse and longitudinal fields. These distinct advantages, however, come at the expense of a nonlinear plasma response that does not permit, for example, the use of pulse trains in future linear colliders [28].

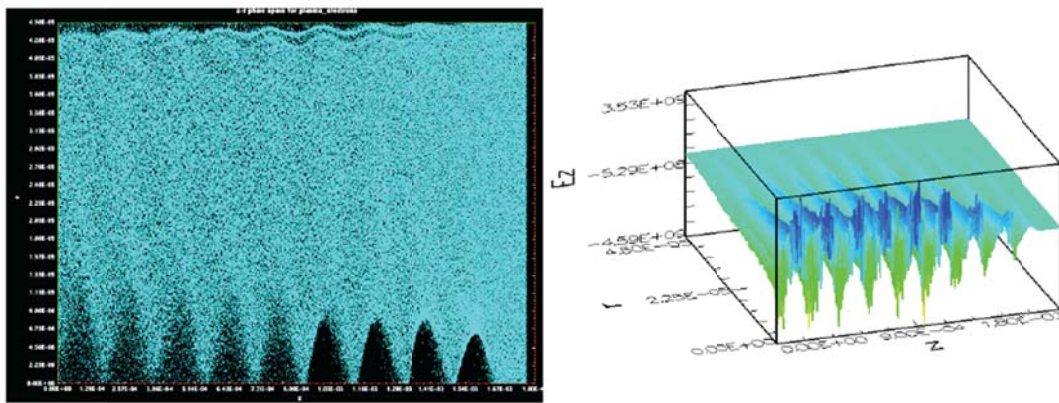


**Figure 3.12. (Left)** Plasma electron spatial ( $r, z$ ) response to a 4-beam pulse train with each beam having  $\tilde{Q} \approx 0.11$ , separated by  $\sigma p = 190 \mu\text{m}$ , and (right) the associated longitudinal electric fields.

In order to envision large total charge acceleration needed for linear colliders, we must consider how to achieve blow-out while maintaining a resonant plasma response. Such a regime is accessed with high brightness beams, by restricting pulse trains to a total charge where  $\tilde{Q} < 1$ . With very low emittance beams, the beam density may permit blow-out conditions to be accessed even with low  $\tilde{Q}$ . This scenario is termed the *quasi-nonlinear regime*, and is the subject of large theoretical [46] and experimental [47] interest, with first experiments now commencing at the Accelerator Test Facility (ATF) at Brookhaven National Laboratory. We show an example of quasi-nonlinear operation in Figure 3.12, in which a 4-pulse train with a periodicity equal to the linear plasma period resonantly excites a wave. This mode produces total plasma electron rarefaction in the region around the beam, similar to the blowout regime. In this case the normalized charge is 0.44, we have a constant plasma period of 190  $\mu\text{m}$  and beam charge per pulse is 16 pC. This is indeed an experimental design regime of interest to FACET-II. We can apply pulse-train chopping techniques to a photoinjector-enabled FACET-II to create these high brightness, low emittance, and relatively low charge beams [48]. The additional energy in the beam, and the ability to access shorter beam dimensions give FACET-II a large advantage over the present ATF configuration.

## **3.4 Trojan Horse Under dense Photocathode PWFA and follow-up applications**

### **3.4.1 Introduction**

Plasma acceleration at FACET aims for both maximized energy gain (e.g., in the E-200 experiment) as well as for dramatically increased beam quality, stability and tunability (E-210 experiment). These experiments and other advanced hybrid LWFA/PWFA strategies require a high-power laser system capable of ultra short, high-intensity pulses for preionization of the plasma, and highly controllable electron release in the wakefield to enable pump-probe measurements and many other applications.

At FACET, therefore, a ~10 TW, ~50 fs laser system is currently being installed. However, the synchronization obtainable at FACET at the interaction point between electron bunch and laser pulse is several hundreds of femtoseconds, mainly because of the thermal cathode and the large compression factor of the electron bunch. Such a jitter is unacceptable for many advanced experiments.

Installing a photoinjector and a high-power laser system at FACET-II would improve the expected jitter between electron bunch and laser pulse to probably less than 50 fs. Many experiments would profit greatly from such a reduced jitter, and others would become feasible in the first place. The proposed system would have potentially much higher maximum beam density and connected radial fields, allowing for extended self-ionization studies and extended acceleration lengths.

### **3.4.2 Advantages of excellent synchronization between electron beam driver from photocathode and low-energy Ti:Sapphire laser beam (~100 $\mu$ J)**

One experiment that would profit massively from improved synchronization would be E-210, “Trojan Horse Plasma Wakefield Acceleration”, whose name alludes to the ancient tale where the Greek soldiers are hidden in the horse’s belly. This experiment depends on the strongly localized release of electrons inside a beam-driven plasma blowout. This localized release is done by focusing a co-propagating laser pulse to an intensity slightly above the ionization threshold of an additional gaseous component (for example, helium in a lithium plasma oven or the second ionization level of rubidium in a rubidium oven). Therefore the electrons would be released only in the arbitrarily small focal region of the laser pulse. Since this laser pulse only needs a maximum density of the order of  $10^{14-15}$  W/cm<sup>2</sup> in order to ionize this component, the electrons receive a very limited transverse kick by the transversely oscillating laser fields. At the same time, the electrons are accelerated in GV/m electric plasma fields in the forward direction, which results in transversally extremely cold electrons with minimized transverse emittance down to the unprecedented level of  $10^{-4}$   $\mu$ m. This would constitute a breakthrough in plasma acceleration, for the first time providing electron bunches with much *better* beam quality when compared to state-of-the-art accelerators based on conventional technology.

The release position of electrons by the photoionization laser relative to the plasma wave determines the trapping point inside the plasma wave and therefore the electron witness bunch parameters after the acceleration. Therefore, the synchronization between the driver electron bunch and the release laser pulse should be as good as possible. It is expected that with a photoinjector and smaller compression factor, the jitter between laser pulse and driver electron bunch will be much better at FACET-II as compared to FACET. At the same time, the duration of the witness electron bunch, and consequently the energy spread of the witness bunch electrons, is strongly dependent on the laser pulse duration. Therefore, the laser pulse should be as short as possible. Fortunately, the controlled release of electrons requires a laser pulse energy of only ~100  $\mu$ J. At such energy levels, laser pulse compression to the sub-10-fs level (e.g., in a gas-filled hollow fiber via group velocity dispersion) is relatively easy.

### **3.4.3 Advantages of high-density electron beam driver from photocathode**

In addition to laser pulse duration and synchronization, the characteristics of the driving electron beam are important for the Trojan horse scheme. At FACET, the electric self-fields of the electron bunch are barely high enough to self-ionize low-alkali metal vapor media such as rubidium and lithium. The parameters eventually obtainable at FACET-II at the interaction point (i.e. 5 nC, 10x10x20  $\mu\text{m}$  beam size) allow the maximum radial self-fields of the driver bunch to approach an estimated 100 GV/m. Such unprecedented values would be enough to overcome not only the first ionization thresholds of alkali metal vapors ( $\sim 5$  eV), but also those of a variety of other gases such as hydrogen, nitrogen, oxygen, CO<sub>2</sub>, etc. Therefore, independent of the specific requirements for the Trojan horse scenario, self-ionization and other phenomena could be studied in an unprecedented parameter range. For the specific Trojan horse scenario, such large electric self-fields of the driver beam would allow for testing and optimizing the Trojan horse scheme in a fully gaseous environment at ambient conditions. For example, instead of having to use alkali metal vapors, we could use hydrogen as the beam-ionized, beam-driven plasma wave medium, and helium as the gas to be released by the injection laser pulse. Working with species that are gaseous at ambient conditions would be highly beneficial from an engineering point of view, since the optical access is easy. The gas may be contained in a glass container at room temperature, whereas alkali metal ovens need a temperature of many hundreds of Kelvin, water cooling, and a buffer gas, which prohibits easy optical access. These studies are directly relevant to future scenarios where electron bunches from laser-wakefield accelerators would be used as driver electron beams, and a small split-off fraction of the main laser pulse would be used to release the electrons in the electron beam driven wakefield. Such future systems have the inherent advantage of synchronization to the femtosecond level.

### **3.4.4 Advantages in case of a Joule-class (>10 TW) Ti:Sapphire laser beam**

A high-power ( $> 10$  TW) laser system would further allow for preionization of the low-ionization threshold component. This would decouple the acceleration process from the ability of the driver bunch to self-ionize the plasma medium. We could preionize not only alkali metal vapors, which are hard to access due to the geometry of the plasma oven, but also media which are gaseous at ambient conditions. For example, we could preionize hydrogen with the preionization laser pulse, and ionize helium with the release laser pulse. The mixture of hydrogen and helium could be stored in a glass vessel, which allows for easy access by the laser pulses, and for probing and diagnostics. In this configuration, the preionization laser pulse would ionize the helium gas a few ps before the electron beam arrives, and the release laser pulse would hit and ionize the helium gas a couple of tens of fs after the electron beam. In this configuration, it would be possible to study the Trojan horse process when the electron beam density is much weaker than in the self-ionization case. Also, it is possible to extend the total acceleration length (and thus the energy gain) by having the electron beam self-ionize during the first part of acceleration, and then have the laser pulse take over ionization in the latter part of the acceleration, where the electron beam may drop below the self-ionization threshold due to head erosion, pulse scalloping and other effects.

A high-power laser pulse capable of driving a plasma wave by itself could further be used to boost the energy of the electron beam coming from the photocathode. Such an external injection and energy boost process would be most effective at lower electron energies (i.e., at a couple of hundreds of MeV instead of 10 GeV).

Further, a high-power laser pulse could be used for Thomson scattering. The ultralow emittance of the witness beam generated by the Trojan horse process would allow for extremely large beam brightness,

which could be exploited in Thomson scattering schemes, where the high-power laser pulse would scatter with the electron witness beam.

### 3.4.5 Further scenarios and light source experiments

A currently discussed scenario for FACET-II is to ramp up the energy of the electron beam in several major radiofrequency-cavity based stages.[49] The first would accelerate to 200 to 250 MeV, the second to 4 GeV, and the final to above 7 GeV and possibly as high as 10 GeV. In any case, studies on Trojan horse acceleration could potentially be done after each of these stages, shown in Figure 3.13**Error! Reference source not found.**

**Reference source not found.** Note that while in reality, the facility setup has to be strictly linear, in the figure the three stages are drawn next to each other to indicate that in principle we may be able to insert R&D sections after each stage.

A 200-250 MeV, high-density electron bunch would be sufficient to drive a plasma wave in a low-ionization threshold medium over a limited distance, and a low-energy laser pulse could then release electrons in that plasma wave. However, since the electron energy of 250 MeV is moderate, a 10 TW+ LWFA stage could be used to substantially boost this energy to the ~1 GeV level. Then, the boosted bunch could be used as a PWFA driver in the Trojan horse stage (see 250 MeV arm of Figure 3.13). Since such a bunch with relatively high charge would be produced to generate a Trojan horse witness electron bunch with much lower charge, this witness bunch may gain several GeV of energy. The witness bunch could then be used to power a cryogenic undulator, such as the one which is currently used at the NLCTA in order to directly make use of the expected excellent witness bunch's emittance. [50] In turn, the output of the undulator could be used to definitively measure such unprecedented emittance. There may be space limitations after the first accelerator stage in the final version of the facility which would not allow us to implement a Trojan horse/LWFA booster/undulator stage. On the other hand, in case of limited funding to build FACET-II up to the 10 GeV level, we would still be able to do substantial R&D on Trojan horse E-210 follow-up experiments at 250 MeV.

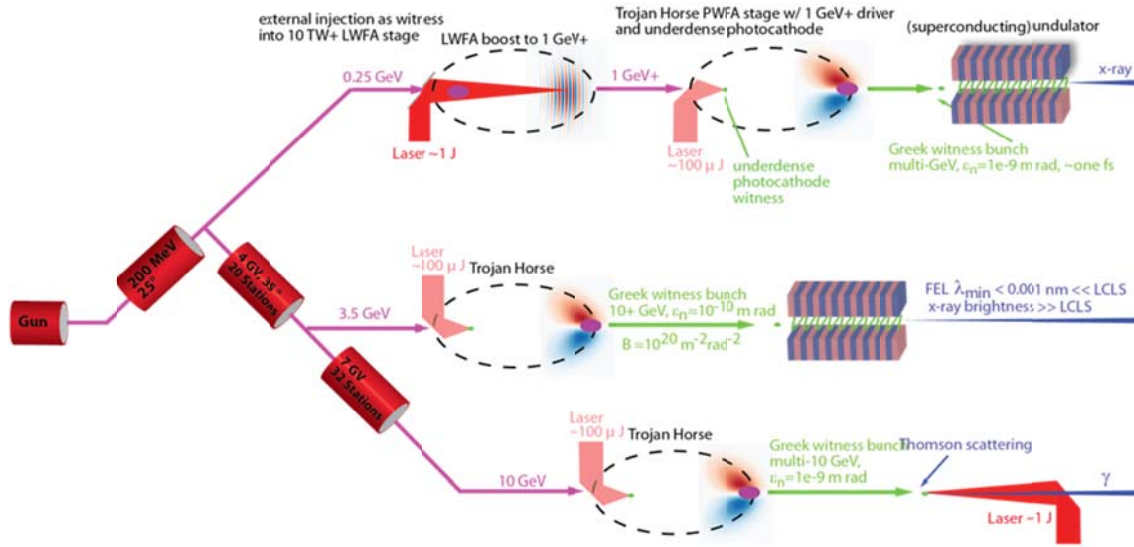


**Figure 3.13. Sketch of potential Trojan horse R&D at FACET-II**

At around 4 GeV, there would be no need to implement an LWFA booster stage. We would directly be able to conduct E-210 follow-up R&D with a beam at this energy level. While it is not shown in the figure, this stage is also attractive for Thomson scattering with a high-power laser pulse.

Note that the figure, for reasons of simplicity, does not depict the preionization laser beam, which would be highly desirable to preionize PWFA stages.

At the highest driver beam energies of 10 GeV, potentially the electron energy and flux of the driver beam and the witness beam may already be too high to use an undulator for free-electron-laser x-ray generation due to potential material damage in the undulator. A Thomson scattering light source, however, could be realized here after the Trojan horse stage.

### 3.4.6 Summary

The combination of photoinjector gun and accelerator, synchronized with a Ti:Sapphire short-pulse laser beam (30 fs, ideally less) will be ideally suited to do extended research in the context of follow-up experiments to the E-210 Trojan Horse Underdense Photocathode Plasma Wakefield Acceleration experiments. Such research at FACET-II is highly promising, since the scheme may enable the production of electron beams with highest tunability and stability, bunch durations down to the sub-fs regime and normalized emittance down to  $\varepsilon_n \approx 10^{-4} \mu\text{m}$ . One of the most intriguing applications of such a hybrid accelerator system would be to power a free-electron-laser, potentially allowing for a performance much better than at the LCLS.

The following requirements are *Essential* for such research: an electron beam driver generated by a photoinjector, an electron energy of  $> 200$  MeV, a beam density after compression such that the electric self-fields exceed 10 GV/m, and a synchronized laser pulse at the 30 fs, 100  $\mu\text{J}$  level.

Other features are *Highly Desirable*. These include an electron energy up to 10 GeV, a beam density with self-fields up to 100 GV/m, and excellent synchronization between the electron driver beam and the laser pulse. This laser pulse would be used for preionization and/or for electron witness bunch production, and therefore should have the smallest possible pulse duration, at least for the low-energy mJ-level arm. It could also be used for laser wakefield acceleration to boost the incoming electron beam energy from the photo gun prior to Trojan horse stages, which would further connect the FACET-II to laser wakefield acceleration groups worldwide.

## 3.5 Dielectric Wakefield Acceleration at FACET-II

Recent studies at Argonne, Brookhaven and SLAC have focused on large amplitude wakefields driven in dielectric structures. The primary applications focus on high-gradient dielectric wakefield acceleration (DWA) with other applications in beam energy chirp mitigation for future FEL application, and developing high-power, narrowband, tunable sources of THz radiation. Relevant, outstanding issues in DWA research include the determination of a working parameter space for this technology such as structure material and geometry optimization, effects of transverse modes and beam-break up, 1D- and 3D-periodic structures for enhanced mode confinement, and, ultimately, demonstration of high gain in acceleration through a passive dielectric lined structure.

The UCLA-led E-201 collaboration (2011-) at SLAC FACET is pursuing studies covering several of these key issues. The experimental program includes a careful parameter optimization of materials (e.g. SiO<sub>2</sub>, sapphire, diamond, alumina) to explore and identify the limits and causes of dielectric breakdown at high fields. These materials exhibit low loss tangents in THz frequencies and can thus accommodate large fields before the onset of breakdown effects. We are studying other geometries such as 1D-periodic claddings (i.e. Bragg-like alternating dielectric materials) and fully 3D photonic-like structures for enhanced mode confinement and higher breakdown thresholds compared to purely metallic boundaries. Finally, we have developed advanced autocorrelation techniques to fully characterize the

modal content of the structures using the emitted coherent Cherenkov radiation (CCR) as a diagnostic. The emitted CCR also has proven useful as a powerful, tunable THz source.

The E201 experimental program has a well-defined scope of goals to address issues in ultrahigh-gradient DWA studies today, but there are a number of open questions in the field that are not readily addressable given current electron beam limitations at FACET. These include the demonstration of high gain in acceleration, the investigation of shaped drive bunches for enhanced transformer ratios, and the exploration of beam breakup and acceleration in long structures. In order to begin to address these issues in detail, the current beam constraints, notably in beam emittance and lack of drive beam parameter flexibility, must be overcome.

The viability of a dielectric structure as a future driver for compact free-electron lasers (FEL) or colliders lies in the ability to demonstrate high-gradient DWA. The proposed parameter space of FACET-II allows such investigation of high-gradient fields. First, the ability to create a drive-witness beam pair with variable chirp and delay will allow the clear observation of acceleration. Second, the ability to shape the drive bunch (e.g. triangular ramp or multi-pulse) with a readily adaptable beam will allow the exploration of enhanced transformer ratios. Third, the photoinjector quality beam with low emittance and small spot sizes will permit the use of long structures. The effects of beam breakup due to transverse mode excitation in long structures can be investigated. Long structures also allow achieving higher energies in acceleration. Finally, the improved beam quality will permit the study of advanced 3D-photonic bandgap-like structures which have smaller beam gaps and tighter tolerances on input beams. The accelerating gradients benefit from the scalability of the wakefields with smaller dimensions of the beam. The fields are proportional to the beam charge divided by the wavelength squared, and the wavelength of the mode scales with beam dimensions. This will also allow the exploration of low emittance, low charge regimes where GV/m are more readily achieved. This exploration is also synergistic with laser-fed accelerator structures, which also demand low emittance, low charge drive beams.

### 3.5.1 Introduction to DWA

The DWA typically consists of a dielectric lined waveguide and a relativistic electron beam (drive beam) that generates a wakefield in the medium (Figure 3.14 shows a cylindrically symmetric configuration of a DWA structure). A trailing particle bunch (witness beam) can sample the wakefield and gain or lose energy depending on its phase (or delay) relative to the drive beam. The peak accelerating gradient is determined by the bunch charge, bunch length, bunch size and properties of the dielectric lined waveguide, such as the dielectric constant, and waveguide dimensions (e.g. inner/outer radii).

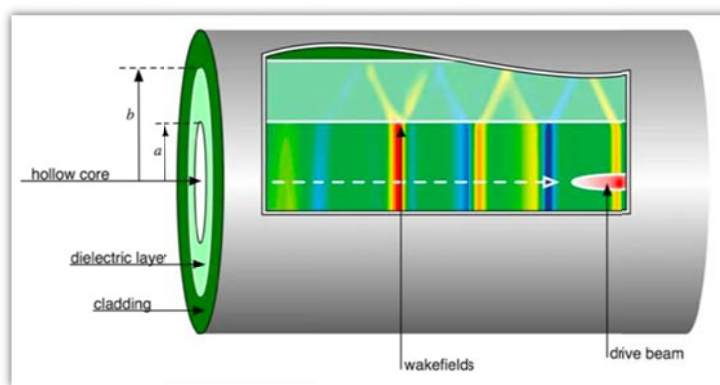


**Figure 3.14. Conceptual schematic of a generic dielectric lined cylindrical waveguide.**

### 3.5.2 E-201 at SLAC FACET

One of the flagship experiments at the SLAC FACET facility is E-201, which aims at the direct testing of DWA structures. The main goals of the experiment are the characterization of the emitted CCR and the determination of achievable field gradients. The DWA samples (cylindrical, slab, and Bragg array) are mounted on a monolithic block incorporated on a remote control 5-axis precision stage (Figure 3.15, right). A gold coated off-axis parabolic mirror is mounted coaxially at 90° to collimate and extract the CCR to a Michelson interferometer with pyroelectric detectors (Figure 3.15, left). The mirror also has a 3mm hole to allow the electron beam to propagate to a beam dump for future energy modulation measurements. A high-magnification imaging system allows for the observation of the face plane of the structures for signs of damage due to breakdown (signified by a violent flash and subsequent reduced transmission of laser light through the structure). The FACET facility has nominal parameters of  $E=28\text{GeV}$ ,  $\sigma_z=20\mu\text{m}$ ,  $\sigma_x = \sigma_y = 20\mu\text{m}$ , and  $Q=3\text{nC}$ , which allows the excitation of fields in excess of  $1\text{GV/m}$  in the THz scale DWA structures.

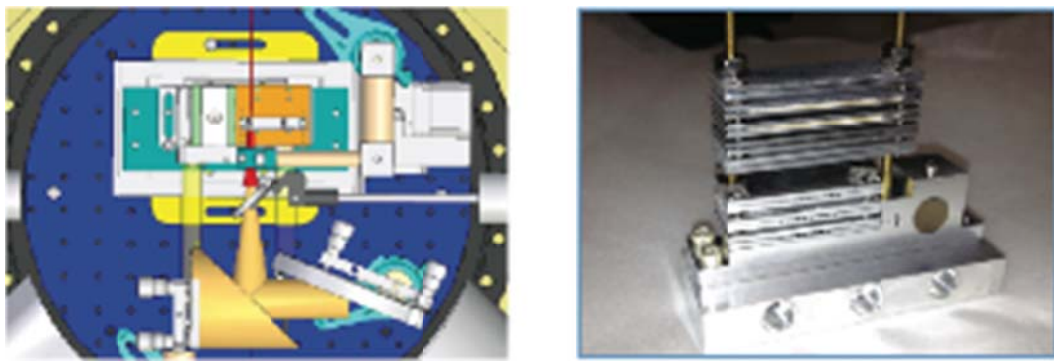


**Figure 3.15. The experimental chamber at FACET (left). Photograph of the sample holder mounting block (right).**

Preliminary results, from the experimental runs in 2012, show signs of breakdown in certain structures. In Figure 3.16, an alignment laser illuminates the inner dielectric of the cylindrical structure before the beam passes (Figure 3.16a), then again after it passes (Figure 3.16b). The cladding is not intact after the beam passes, presumably due to the heating caused by the  $>\text{GV/m}$  fields produced in the dielectric. A photograph of the sample mounting block shows clear signs of vaporization (Figure 3.16c). The cylindrical structures were characterized as darkened and brittle after exposure to the beam and the high fields. In addition, the first CCR measurements showed a weak signal at the expected fundamental mode for the cylindrical structures. The studies will continue through the next experimental runs with additional efforts placed on drive beam preparation and improved signal-to-noise in the diagnostics.



**Figure 3.16. (a) In-vacuum image of a cylindrical DWA with a laser shining through the end. (b) Image of the structure after exposure to high-fields of the beam; the cladding is no longer intact and the laser light seeps out of the side of the structure. (c) Photograph of the various cylindrical DWA structures exposed at the experiment**

### 3.5.3 DWA studies at FACET-II

The FACET-II parameter space has the potential to expose DWA research to the low emittance drive beam regime, which enables wakefields above 1 GV/m in smaller structures. Here we present several possibilities opened up by the FACET-II studies.

#### 3.5.3.1 Drive + Witness beam

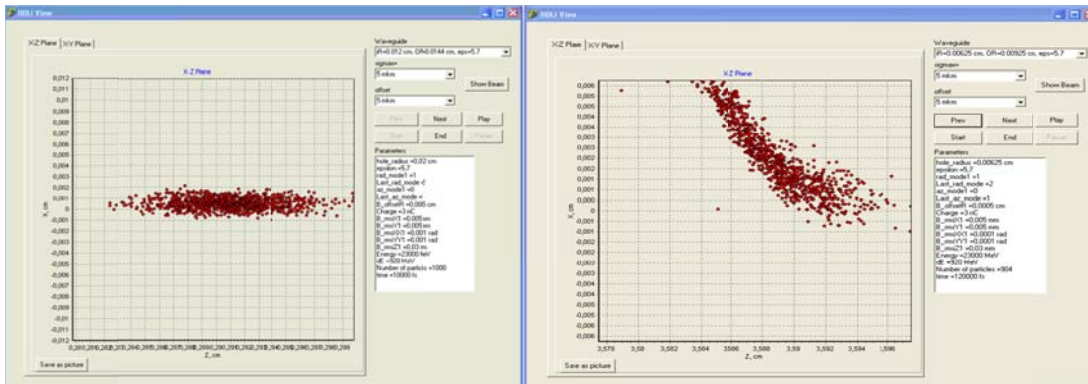
The proposed photoinjector would improve the quality of the beam, allowing the further characterization of DWA structures and the ability to unambiguously observe acceleration using a drive-witness pair. Recent experiments in THz scale slab-symmetric structures at the BNL ATF show acceleration using a chirped beam but with very modest fields (<10MV/m). The fields scale with charge and emittance, which determines the structure's dimensions and fundamental accelerating mode. With expected fields surpassing the GV/m range, FACET-II will allow the observation of near-GeV acceleration.

#### 3.5.3.2 Long structures

The improved emittance due to the photoinjector would enhance the delivery of small spot size beams (<20 $\mu$ m) with low emittance and longer collimation, allowing the use of long structures. In the current FACET setup, the structures are limited to 2.5cm in length. This is mainly due to the beam beta functions for a given beam spot size, since the gap of the structures must be five to six times the rms spot size to ensure full transport through the structure. At FACET-II, structures over ten times longer (e.g. 50cm) can be studied due to the improved emittance from the photoinjector. This allows the study of similar gap DWA structures with small beam sizes, yet much larger beta functions. Long structures are important for observing gain in acceleration and studies of beam breakup, and also will provide insight on the maximum length of the structures as it relates to multi-staged accelerating systems.

#### 3.5.3.3 Beam breakup

One of the limiting issues with long DWA structures is the undesirable effect of beam breakup within the structure. The beam dynamics due to interaction with the higher order mode excitation leads to stability issues caused by off-axis or off-angle operation. Such operation can lead to coupling to transverse modes that have adverse effects, including emittance growth, increased energy spread, and head-tail instabilities (see Figure 3.17). Beam breakup effects resulting from parasitic wakefield excitation may limit the efficacy of DWA structures as next generation drivers. Therefore these issues must be studied in detail experimentally. The FACET-II photoinjector will allow unprecedented control of a high-energy beam to purposefully excite transverse modes and develop a fundamental understanding of suppression methods and the limits of the harmful behavior of beam breakup.



### 3.5.3.4 Shaped bunches

For Gaussian beams, the transformer ratio (TR), the ratio of accelerated field to decelerated field, is limited  $<2$ . The viability of a DWA as a future driver for advanced applications and light source lies in the ability to overcome this TR limitation. Studies have shown that triangular longitudinal profiles, or ramped beams, have the potential to demonstrate  $\text{TR} > 2$ . In the FACET-II scenario, jaw collimators may be used to longitudinally shape the drive bunch while maintaining small transverse emittance. For example, in the current FACET scenario, structures of inner diameter (ID)  $200\mu\text{m}$ , and a ramped bunch produce a TR of 1.5 for a  $1\text{nC}$  beam. However, with reduced spot size, ID= $30\mu\text{m}$ , the TR increase to  $>5$  with the same ramp and charge (Figure 3.18). This is a dramatic improvement and a necessary step to demonstrate the viability of the DWA as a future compact high-brightness driver.

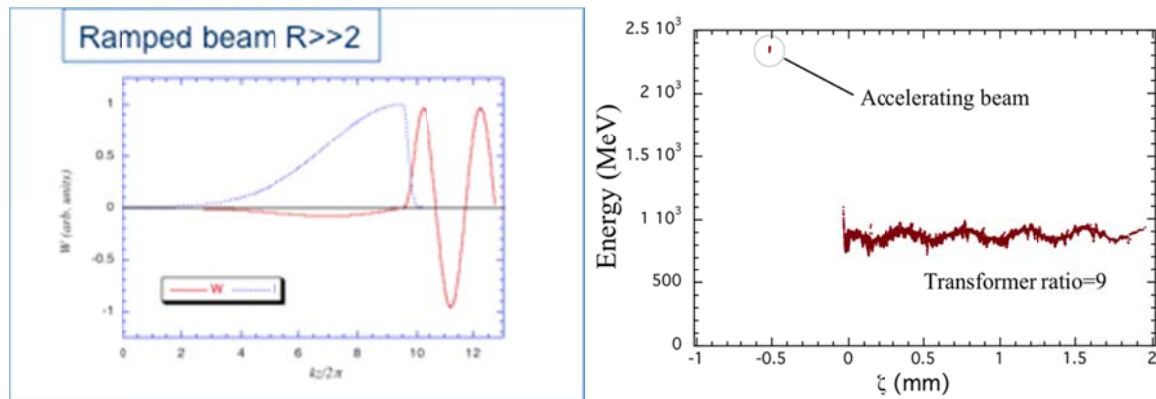


**Figure 3.18. Concept of shaped drive beam (left) and witness beam acceleration with high transformer ratio (right).**

### 3.5.3.5 Longitudinally periodic structures

With advances in nano- and micro-fabrication technology of dielectrics (e.g. ceramics and diamond) the development of 1D-periodic structures is feasible. In FACET, transversely periodic structures are being investigated for mode confinement and damage threshold measurements. However, with the introduction of multi-pulse beams, longitudinally periodic structures can be studied as well. By exploiting the position-time correlation and using a notch or rigid-mask collimator, FACET-II will be able to produce a multi-pulse drive beam.

The longitudinal DWA structures are analogous to “slow-wave” structures where the group velocity of the wakefield can be controlled by appropriate selection of dielectric constants and periodicity. One scenario under theoretical and numerical investigation is the “zero group velocity” structure, which is composed of quartz and diamond. Figure 3.19 shows the mode confinement of the structure and the field within the structure once the beam has left, where a near-standing wave is produced and confined to the structure.

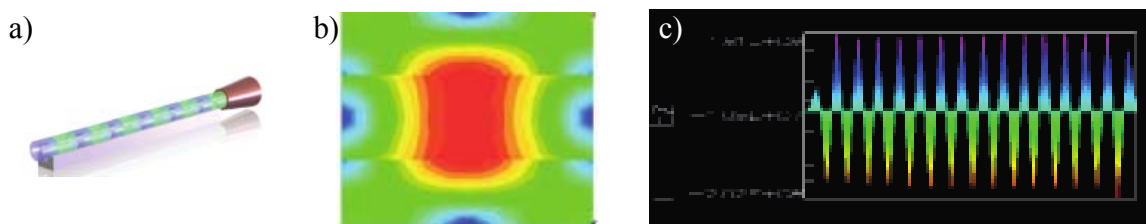


**Figure 3.19. Rendering of periodic structure (a), mode confinement of structure (b) and field (c).**

### 3.5.3.6 Photonic structures

Motivated by the need to abandon the use of metals in the presence of high fields, we have looked at a few examples of simple beam-driven all-dielectric wakefield accelerators from the perspective of bandgap photonics in 1D. However, we also gain design advantages in the ability to manipulate the modes' characteristics by examining fully 3D photonic-like structures, such as the woodpile in Figure 3.20. Control and manipulation of properties — such as modal confinement, spatial harmonic content, phase velocity and group velocity — are reasons why an all-dielectric beam-driven accelerator would be expected to benefit by borrowing from the field of optical bandgap photonics. The smaller beams and low charge operating regime afforded by FACET-II would allow further studies of these structures.

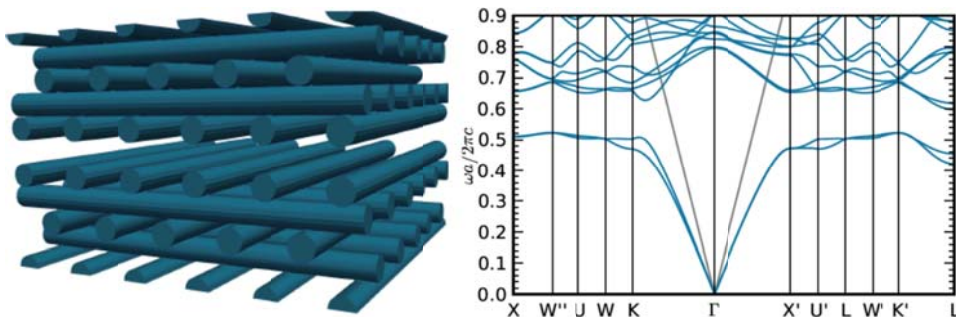


**Figure 3.20. Concept of the sapphire ( $\epsilon = 9.3$ ) woodpile (left) and simulated bandgap diagram (right).**

### 3.5.4 Conclusion

The proposed FACET-II parameter set opens up the possibilities for novel and exciting research into dielectric wakefield acceleration that is currently inaccessible due to constraints on drive beam generation and transport. These pertinent studies and demonstrations are necessary to ascertain the feasibility of the DWA as a next generation, compact accelerator for FEL and collider applications.

## 3.6 BIG: Beams of Intense Gamma-rays at FACET-II

### 3.6.1 Introduction.

Richard Feynman once wrote:

One very powerful way of experimentally investigating the strongly interacting particles (hadrons) is to look at them, to probe them with a known particle; in particular the photon (no other is known as well). This permits a much finer control of variables, and probably decreases the theoretical complexity of the interactions [51].

Indeed,  $\gamma$ -ray sources are intensely used in quantum chromodynamics (QCD) research to study structure of nuclei and nucleons. Controllable linear and circular polarization of the Compton back-scattering  $\gamma$ -ray sources opens the window of spin and parity observables in this research.

Polarized Compton back-scattering  $\gamma$ -ray sources, pioneered at ADONE and SLAC in the 1960s, [52] remain an important research and application tool. Presently there are four operational facilities covering  $\gamma$ -ray energy range from 1 MeV to 2.4 GeV.

The area of research is roughly split into low, medium and high energy ranges. Low energies,  $E_\gamma = 1\text{-}15$  MeV, are well-suited to studying the resonant structure and states in nuclei below the giant dipole

resonance. Nuclear resonant fluorescence (NRF) is the primary method for these studies. In addition, direct photon excitation and disintegration of nuclei gives access to a number important processes in astrophysics, such as  $^{16}\text{O}(\gamma, \alpha)$ . [53] Figure 3.21 indicates the richness of the nuclear structure.

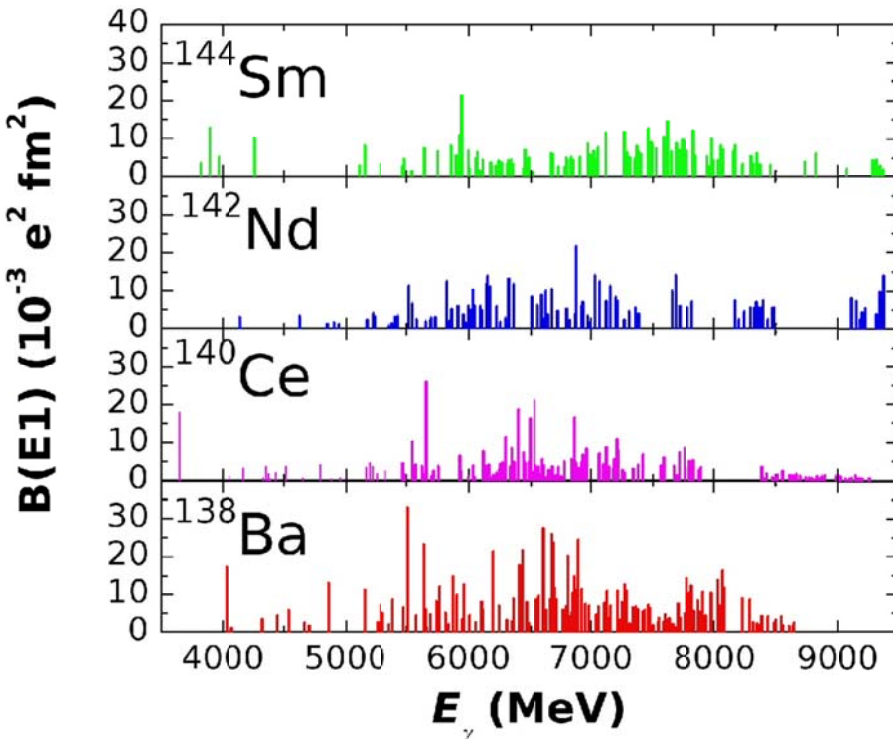


**Figure 3.21. E1 dipole strength distribution in  $N = 82$  isotones. [Courtesy of A. Tonchev, LLNL].**

Intermediate energies,  $E_\gamma = 100\text{-}200\text{ MeV}$ , are optimal for studying spontaneous breaking of QCD chiral symmetry. The main areas of interest are near threshold of pion photo-production, [54] measuring nucleon spin polarizabilities [55] and measuring the integrand of the Drell-Hearn-Gerasimov integral for the deuteron. [56].

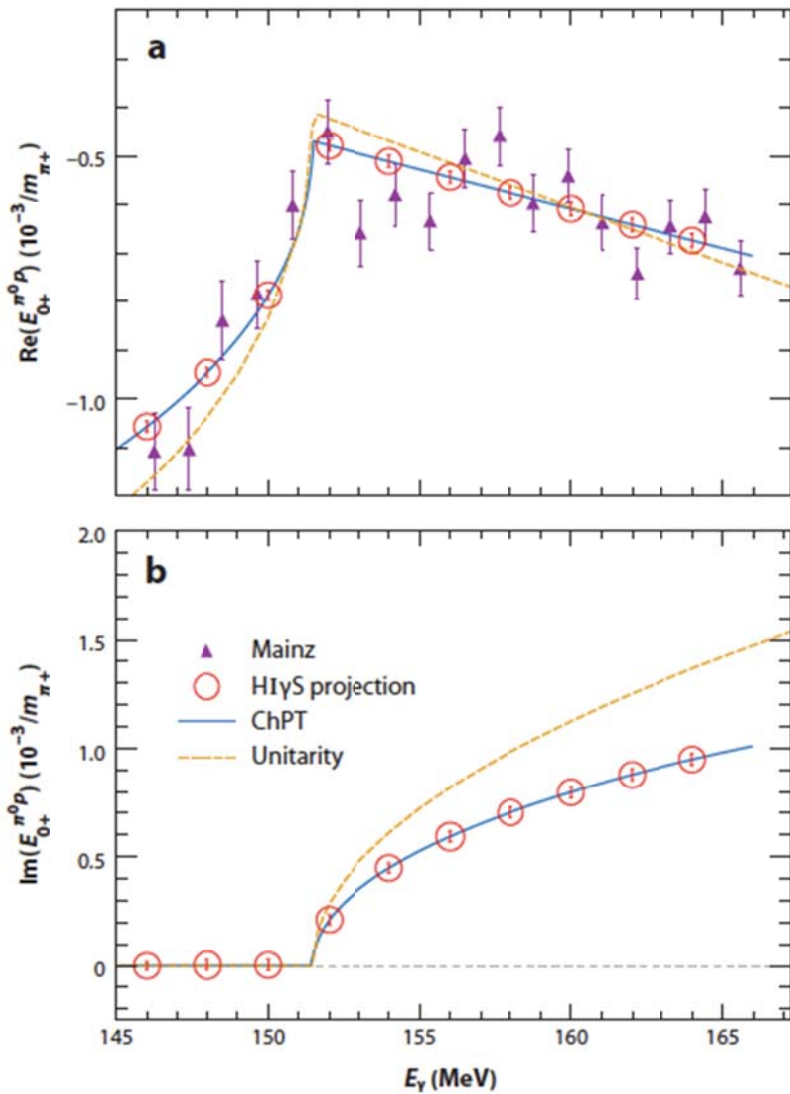


**Figure 3.22.** The  $\gamma + p \rightarrow \pi^0 + p$  reaction: (a)  $\text{Re}(E_0^+)$ , the solid blue curves represent chiral perturbation theory (ChPT) calculations, and the dashed orange curves represent the unitary fit; (b)  $\text{Im}(E_0^+)$  [Courtesy of A.M. Bernstein, MIT].

High energies,  $E_\gamma > 200 \text{ MeV}$ , are needed for studying the resonant structure and states in nucleons. The high energy reach of BIG opens the possibility of searching for light-quark + glue hybrid baryons and, probably, heavy-quark baryons. This research requires meson photo-production and direct access to gluons. These experiments are focused on a high precision extraction of pseudoscalar meson photo-production amplitudes. The most general analytic form of the cross section involves 16 spin-dependent observables, which can be reached using the flexibility of BIG in combination with a sophisticated detector. [57]. Potential discoveries include a hypothetical glue-ball [58].

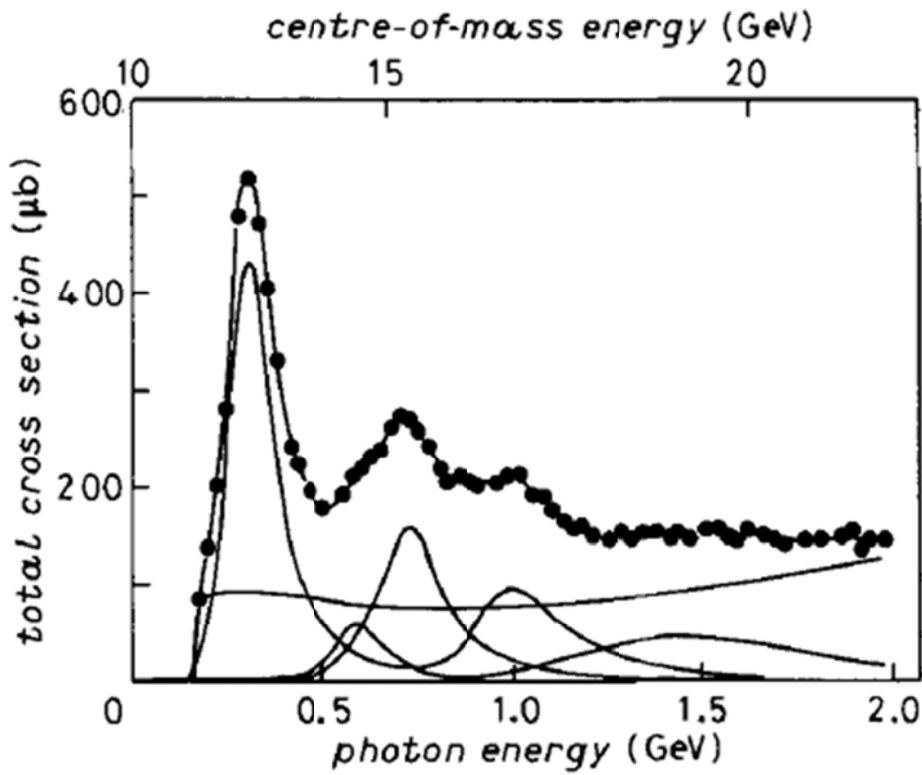


**Figure 3.23. Reach energy spectrum and structure of nucleons.** Shown is the total photo-absorption cross-section on the proton: the curves beneath the three peaks show a fit to the resonance cross-section corresponding to the M1, E1 and E2 proton excitation, respectively. The flat curve is the background; the other curves come from states with lower excitation probability. [59]

In addition to QCD experiments, the BIG can be used for R&D in generating polarized lepton (positron and muon) beams for future linear lepton and linac-ting lepton-hadron colliders. Furthermore, it can act as a test-bed for a  $\gamma$ - $\gamma$  collider. The time structure of BIG may allow us to create a textbook experiment – generating an electron-positron pair in vacuum by colliding two  $\gamma$ -ray beams.

All existing Compton back-scattering sources create  $\gamma$ -rays with a similar overall energy spectrum. The energy spread of  $\gamma$ -rays can be limited by geometrical collimation, with about 1.5% of the flux per 1% energy spread in the region near the top energy of the photons:

$$E_{\gamma \text{max}} = \hbar \omega \cdot \frac{1 + \beta}{1 - \beta + 2\hbar\omega/mc^2} \sim \frac{4\gamma^2 \hbar\omega}{1 + 4\gamma\hbar\omega/mc^2};$$

$$\gamma = 1/\sqrt{1 - \beta^2}.$$

Hence, the spectral (energy) density of the beam is determined by its total flux  $\dot{N}_\gamma$  and the maximum energy of the photons in the beam:

$$\frac{d\dot{N}_\gamma}{dE_\gamma} \sim 1.5 \frac{\dot{N}_\gamma}{E_{\gamma\max}}$$

The  $\gamma$ -ray energy resolution can be obtained either by tagging the energy of scattered electrons or by collimating the beam. The tagging approach does not create high fluxes, since only one  $\gamma$ -ray per collision can be effectively used. Collimation does not impose such restrictions. The resolution obtained by collimation depends on the quality of the electron beam.

Table 3.2 compares main parameters of existing polarized Compton  $\gamma$ -ray sources. A number of bremsstrahlung  $\gamma$ -ray sources exist as well, but these are unpolarized and in a large background of low energy photons, and are therefore not suitable for QCD experiments.

**Table 3.2. Main parameters of operational polarized Compton back-scattering  $\gamma$ -ray sources and the BIG.**

Name	ROKK	GRAAL	LEPS	HIfS	BIG
<b>Location</b>	Novosibirsk, Russia	Grenoble, France	Harima, Japan	Durham, NC, USA	Palo Alto, CA, USA
<b>Accelerator</b>	VEPP-4M	ESRF	SPRING-8	Duke SR	SLAC
<b><math>e</math>-beam, GeV</b>	1.4 - 6	6	8	0.24 – 1.2	1-10
<b><math>\gamma</math>-beam, GeV</b>	0.1-1.6	0.55-1.5	1.5-2.4	0.001-0.095	0.001-2 (5)
<b>best <math>\gamma</math>-energy resolution, %</b>	1-3	1.1	1.25	0.8-10	0.1

Note: not all parameters in the table can be obtained simultaneously

It is clear from Table 3.2 that the BIG is a superior source when compared with the other existing sources. It has a  $\gamma$ -ray energy span of more than three orders of magnitude, from MeV to GeV, about 10-fold better energy resolution than competing sources, and two to four orders of magnitude larger flux. BIG's unprecedented intensities and unique time structure open unprecedented opportunities for its utilization in fundamental and applied research.

In addition to existing Compton back-scattering  $\gamma$ -ray sources, there are a number of recent proposals for new sources. Two of them are in the USA: one is proposed at LLNL [60] and the other is the recently proposed ASTA facility at FNAL [61]. While both of these proposals promise to deliver very high fluxes of  $\gamma$ -rays, their energy reach and coverage do not match that of the BIG. The LLNL source, with its 200 MeV linac, will generate  $\gamma$ -rays with a maximum energy near 1MeV. The ASTA facility, with its proposed 800 MeV SRF linac, would be capable of generating high intensity  $\gamma$ -ray beams with a maximum energy of 15 MeV.

Hence, a large number of ground breaking experiments requiring high flux, excellent energy resolution and detailed energy scans will become possible at BIG. In short, the BIG is the dream facility for polarized photo-production and photon scattering experiments.

2007 Nuclear Physics Long Range Plan “The Frontiers of Nuclear Science” Effective Field Theory clearly indicate importance of intense polarized  $\gamma$ -ray sources for frontier QCD research. It reads:

*Effective field theories provide a powerful framework for solving physical problems that are characterized by a natural separation of distance scales. They are particularly important tools in QCD, where the relevant degrees of freedom are quarks and gluons at short distances and hadrons and nuclei at longer distances. Indeed, at energies below the proton mass, the most notable features of QCD are the confinement of quarks and the spontaneous breaking of QCD's chiral symmetry. Chiral perturbation theory is an effective field theory that incorporates both; when applied to mesons it is a mature theory. Perhaps the most striking advances in chiral effective field theory have come in its application to few-nucleon systems. This has yielded precise results for nucleon-nucleon forces and also produced consistent three-nucleon forces. This opens the way for precision analyses of electromagnetic reactions on light nuclei, e.g., the Compton scattering reactions on systems having two or three nucleons.*

The BIG would be perfectly suited for the research described above. Its energy range is ideal and its intensity is sufficient for the challenges presented by the experiments.

Another challenge where BIG may excel is studying the spontaneous breaking of chiral symmetry due to the finite quark masses. This study requires polarized photon energies between the thresholds of neutral and charged pion production (e.g. between the  $\pi^0$  threshold of 144.7 MeV and the  $\pi^+$  threshold of 151.4 MeV). As a result of the vanishing of the threshold amplitudes in the chiral limit, the experiments are difficult to perform because the cross sections are small. Furthermore, an energy scan with very narrow energy spread of the  $\gamma$ -ray (well below 1% FWHM) is needed to map this energy range. This is the reason why experts in the field call it a “dream experiment” [62]. Existing and proposed polarized  $\gamma$ -ray sources either do not have energy reach (H1 $\gamma$ S) or have very low flux: with GRAAL or LEPS it would take about 10,000 years to collect necessary statistics. The BIG’s intensity and energy resolution would allow us to perform this experiment in under one year.

The BIG’s energy reach and unprecedented intensity ( $\sim$  10,000-fold increase in the energy of interest) opens a window for studying critical details of chiral dynamics in meson photo-production. Excellent energy spread down to 0.1% FWHM in the BIG’s collimated  $\gamma$ -ray beam opens a new window into nuclear structure studies.

### **3.6.2 Nuclear Structure Studies: Nuclear Resonant Fluorescence (NRF), including pigmy resonances**

Studies of nuclear structure, some of which also have an astrophysical context, would strongly benefit from the high intensity and high quality of  $\gamma$ -ray beams at the BIG source at FACET-II. The most important parameter in any NRF or photo-induced experiment is the number of photons per eV, or the flux energy density. This is dictated by the fact that the width of nuclear states below the neutron separation energy ranges from few meV to eV depending on the nucleus and structure involved. BIG’s tunability and flux energy-density exceed any operating sources by orders of magnitude, making it a perfect choice for this application. We anticipate that dozens of scientists from the U.S. and Europe will want to take advantage of BIG for research into nuclear structure.

Studies of nuclear structure are on the forefront of low energy nuclear physics and astrophysics. The neutrino flavor transformation in the star explosions determine charged- and neutral-current interactions of supernova neutrinos. Mapping the M1 strength distributions for isotopes ranging from  $^{40}\text{Ar}$  to isotopes of Mo have been proposed for neutral-current detectors. The stable isotopes of Mo are likely to be sensitive to both  $n_e$  and anti- $n_e$  interactions [63].

The electric dipole (E1) response is a fundamental property of atomic nuclei. As with other collective multipole responses it is directly connected to the bulk properties of nuclei and nuclear matter. Recently, the E1 response (especially its low-lying part) has been shown [64, 65, 66] to provide a constraint on the isovector properties of nuclear matter, e.g., the symmetry energy, which are key ingredients in the description of exotic astrophysical objects like neutron stars. [67] Furthermore, the E1 response builds up the major part of the photo-absorption cross section and represents the dominant  $\gamma$ -ray strength function, an important quantity in determining reaction rates in different astrophysical scenarios. [68,69] Photon induced reactions are an ideal tool to investigate the dipole strength below and above thresholds in a model independent way. However, data are so far available only for a few nuclei mainly at or close to the magic shell closures. Measurements of  $(\gamma,\gamma')$  reactions at BIG will extend these studies to a wider range of masses including highly deformed nuclei.

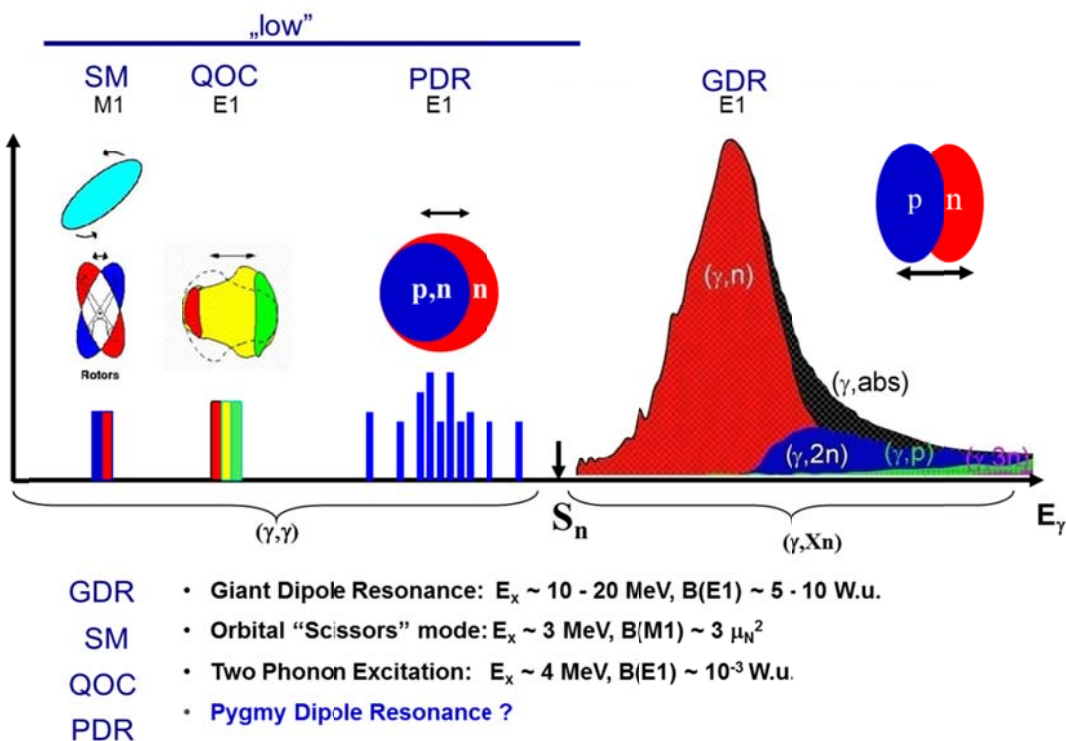


**Figure 3.24. Schematic of the dipole response over a broad range of energies, up to 10's of MeV, and related structural phenomena**

The nuclear dipole response covers a range of structural phenomena, as shown in Figure 3.24. Physics themes involving electric and magnetic dipole distributions, which can easily be separated making use of the polarization of the photon beams, range from the study of isospin purity of states, to the emergence and evolution of nuclear quadrupole and octupole collectivity, and the build-up of nucleon skins. The best-known dipole excitation is the giant dipole resonance (GDR), which is typically found at energies around 15 MeV, well above the neutron-separation threshold. On the low-energy tail of the GDR another structure has been identified in a small set of nuclei, as mentioned above. This enhancement of strength around or below the neutron-separation threshold, referred to as Pygmy dipole resonance (PDR), is typically interpreted as the effect of a neutron skin building up around a proton-neutron symmetric core. The lowest part of the electric dipole response, at few MeV excitation energy, is dominated by multi-phonon excitations involving the octupole degree of freedom. The latter requires a

short bursts of  $\gamma$ -rays natural for BIG's time structure. In either case, the enhanced, collective electric dipole strengths at low energies are a challenge to nuclear theory, since they can usually only occur due to particle-hole excitations across a major shell.

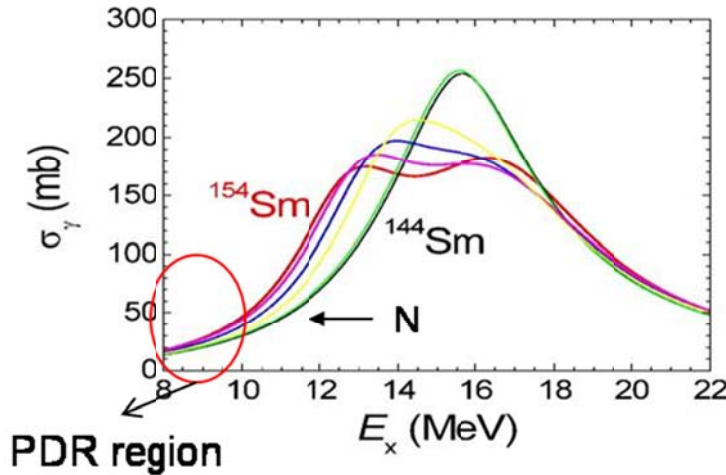


**Figure 3.25. Evolution of the GDR for all Sm isotopes calculated by the QRPA model**

Figure 3.25 depicts calculated GDR distributions for Sm isotopes across the onset of deformation. For spherical isotopes the resonance has a Lorentzian-type shape, whereas the GDR splits into two Lorentzians in deformed isotopes, corresponding to vibrations with respect to the two major axes. A similar behavior can be expected for the PDR, but has so far not been observed due to the lack of data in deformed regions. An additional complication is the disentanglements of PDR and GDR strengths, since - as indicated in Figure 3.25 - the PDR lies on the low-energy tail of the GDR.

Dipole excited states, particularly, the PDR, are at the intersection of nuclear structure and nuclear astrophysics. They are of interest to nuclear structure because they represent a weak collective mode that remains to be understood in a systematic way. The astrophysics context is clearer, since these states directly influence the rates for stellar photodisintegration reactions. Nuclear resonance fluorescence studies of the PDR show that we are missing significant (maybe most) of its excitation strength because cascades through lower-lying excited states have thus far escaped detection. Coincidence measurements, which will isolate cascades from the PDR, require the intensity and energy resolution of BIG. In addition, coincidences provide a unique way to excite other collective dipole structures, such as quadrupole-octupole coupled (QOC) states or the nuclear M1 scissors mode, and simultaneously observe their detailed decay behavior, which is the smoking gun of their nature. Such fingerprints are, for example, the one-phonon decays of QOC states corresponding to the annihilation of a quadrupole phonon, as depicted in Figure 3.26.

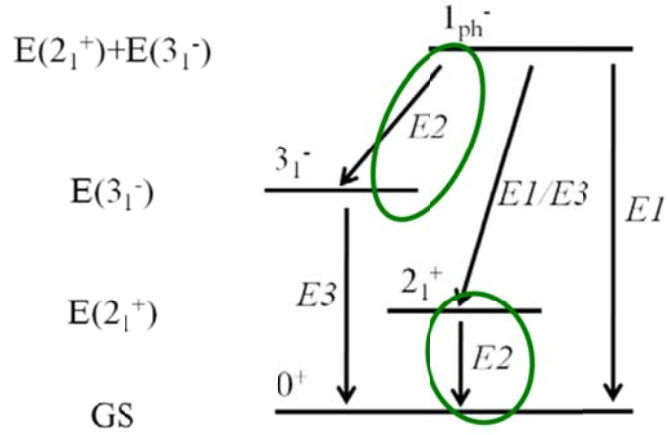


**Figure 3.26.** The  $J=1$  member of the negative-parity multiplet from coupling a quadrupole phonon to an octupole phonon is characterized by its  $E2$  transition to the octupole state, which must have the same transition probability as the quadrupole phonon to ground state decay.

Background suppression is a very big problem for this kind of experiments. Very low background to signal ratio is one of the unique aspects of BIG. BIG's geometry, e.g. a short chicane where  $\gamma$ -rays are generated, provides for bremsstrahlung-free environment. In addition, the time structure with short bursts of  $\gamma$ -rays creates an additional 30,000 fold suppression of the background to signal ratio, compared with near-CW storage ring sources, such as HlyS. Finally, a 10-fold narrower energy spread in the  $\gamma$ -ray energies provides for removing the beam-related background. Hence, BIG would open opportunities to perform experiments which are currently impossible because of the signal to background ratio being low.

In contrast to existing facilities, the very high brilliance of the beam will allow to excite specific states and study their detailed decay behavior, even in regions of high level densities. High-resolution charged particle spectroscopy has been used to map out the fission barrier landscape of many of the light actinides. [70,71] As a result, a new picture of the triple-humped fission barrier was established with an unexpected, rather deep, third hyper-deformed minimum. New photo-fission experiments could significantly improve our present knowledge on the fission resonance structure and on the potential energy landscape of the actinides, which has very important astrophysical relevance as well: the fission barrier controls the fission losses at the end of the r-process path and also the population of long-lived uranium and thorium nuclei. The improved beam energy resolution of the BIG will allow for the search and study of narrow fission resonances near the barrier.

### 3.6.3 Nuclear Physics near pion threshold

Intense beams of medium energy polarized  $\gamma$ -rays are of great interest for a variety of QCD and nuclear physics experiments. Below we describe some of new physics which can be studied with the BIG.

#### 3.6.3.1 Isospin Breaking Due to the Light Quark Masses

Chiral symmetry in QCD is both spontaneously [72] and explicitly broken due to the non-zero values of the light quark masses. Since the up and down quark masses differ by almost a factor of two, isospin symmetry is also violated. [73] Strong isospin violation is usually predicted when  $(m_d - m_u)/\Lambda_{QCD} \cong 2\%$ . However, there is one case where strong isospin breaking is predicted when  $(m_d - m_u)/(m_d + m_u) \cong 25\%$ . [74] The quantity of interest is  $a/\pi^0 p$ , the s-wave scattering length on the proton. [75]

Clearly this quantity cannot be directly measured since  $\pi^0$  beams cannot be constructed. Our present knowledge comes from data involving charged pions and constructing the isospin even s wave scattering length,  $a^+ = (a_{\pi-p} + a_{\pi+p})/2$ , measured from pionic hydrogen and deuterium, with the Coulomb contributions removed. [76, 77] If isospin symmetry holds, then  $a^+ = a(\pi^0 p)$ . To test this it is essential to measure  $a(\pi^0 p)$ . This is difficult since  $\pi^0$  beams cannot be made. However it can be measured as a final state interaction in the  $\gamma p \rightarrow \pi^0 p$  reaction with transversely polarized protons in the energy region between the  $\pi^0$  threshold of 144.7 MeV and the  $\pi^+$  threshold of 151.4 MeV. [78,79] This experiment requires a beam of  $\sim 10^9$  photons/sec with  $\approx 1\%$  energy resolution. [80] This beam is possible with the proposed FACET-II facility at SLAC. The experiment requires a time structure in which each beam burst is divided into 1000 short beam bursts. It requires an  $a \cong 4\pi$  photon detector with good energy and time resolution to observe the  $\pi \rightarrow \gamma\gamma$  decay mode, a transverse polarized proton target (butanol) and state of the art electronics due to the low duty cycle. Even with this intense beam the experiment requires  $\sim 2000$  hours of running time to measure  $a(\pi^0 p)$  with a statistical accuracy of  $\cong 10^{-3}/m_\pi$ , which is comparable with the present determination of  $a^+$ . A comparison of  $a(\pi^0 p)$  and  $a^+$  will test the predicted violation of isospin symmetry. [81] This is an ambitious and difficult experiment to test a fundamental consequence of explicit chiral symmetry and isospin breaking due to the non-zero up and down quark masses first pointed out by Weinberg over half a century ago, and will test a firm confinement scale QCD prediction.

### 3.6.3.2 Measurements of the Drell-Hearn-Gerasimov Integrand for the Deuteron

We propose measuring the integrand of the Drell-Hearn-Gerasimov integral for the deuteron from as close as possible to the maximum photon energy of 160 MeV. S. B. Gerasimov [82] and, independently, S. D. Drell and A. C. Hearn [83] showed that, using reasonable assumptions,

$$\int_{\omega_o}^{\infty} \frac{\sigma_{1/2} - \sigma_{3/2}}{\omega} d\omega = -4S\alpha\pi^2 \left( \frac{\kappa}{M} \right)^2$$

where  $\sigma_{1/2}, \sigma_{3/2}$  are total inelastic cross section when the target nucleon spin and the incident photon helicity are anti-parallel (parallel),  $\omega_o$  is the threshold photon energy for inelastic processes,  $M, \kappa$  are the mass and anomalous magnetic moment of the target, and  $S$  is the spin of the target. The equation above applies to protons, but Hosada and Yamamoto [84] and Gerasimov pointed out that these arguments could be applied equally well to the deuteron. That is, the deuteron could be treated as the object of the sum rule rather than simply as a source of neutrons. The resultant "GDH" sum rule is given by

$$\int_{\omega_2}^{\infty} \frac{\sigma_{1/2}^d - \sigma_{3/2}^d}{\omega} d\omega = -4\alpha\pi^2 \left( \frac{\kappa_d}{m_d} \right)^2$$

where  $\omega_2$  is the threshold not for pion production ( $\approx 145$  MeV) but for photo-disintegration ( $\approx 2.2$  MeV), and  $m_d$  and  $\kappa_d$  are the mass and anomalous magnetic moment of the deuteron, respectively. The sum rule values for the proton, neutron, and deuteron are given in Table 3.3.

**Table 3.3. Sum rule values for particles**

Target	$\kappa$	$\int GDH, \mu b$
p	1.79	-204.0
n	-1.91	-232.0
d	-0.14	-0.6

The GDH integral for the deuteron can be separated into three terms:

$$\int_{\omega_2}^{\infty} \frac{\sigma_{1/2}^d - \sigma_{3/2}^d}{\omega} d\omega = \int_{\omega_2}^{\omega_\pi} \frac{\sigma_{1/2}^d - \sigma_{3/2}^d}{\omega} d\omega + \int_{\omega_\pi}^{\omega_{\max}} \frac{\sigma_{1/2}^d - \sigma_{3/2}^d}{\omega} d\omega + \int_{\omega_{\max}}^{\infty} \frac{\sigma_{1/2}^d - \sigma_{3/2}^d}{\omega} d\omega = -0.6 \mu b$$

The second term, which also can be measured at BIG, has been measured at Brookhaven's Laser Electron Gamma Source and elsewhere. For the high photon energies relevant to the third (unmeasured) term we note that to the order of 0.1% the deuteron can be treated as the sum of a neutron plus a proton plus trivial corrections. The first term remains unknown. Currently there is no available source for such measurement, but BIG will be the perfect source to fill in this gap.

If the sum rule is valid then the sum of the unmeasured terms of the GDH integral for the neutron and proton must equal the unmeasured term of the deuteron. Adding these to the measured terms of the deuteron, the GDH integral should yield a value in agreement with the sum rule prediction.

If the GDH rule holds, then we can conclude that the sum rule is valid and calculating the "unmeasured" terms of the neutron and proton integrals will be a test of nucleon models. If no agreement is observed, then something is wrong with the sum rule. Perhaps the assumption of unsubtracted dispersion relations?

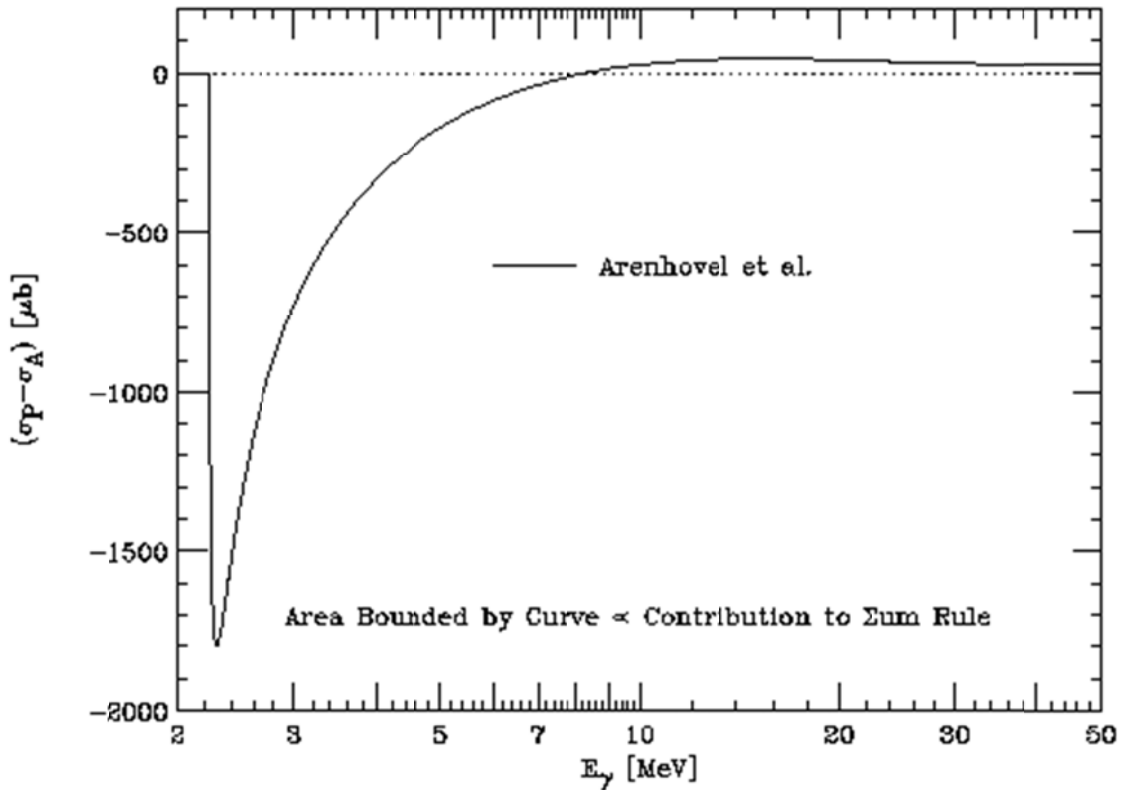


**Figure 3.27.** The cross section difference entering the GDH Sum Rule integral. Note that the abscissa scale is logarithmic so the area under the curve is proportional to the contribution to the sum rule integral.

The Blowfish detector, [85] with its associated electronics and data acquisition system, is ready for use for these measurements. The measurements require a detailed energy scan, where both the energy reach, the energy resolution and the intensity of the BIG makes it uniquely suited for this important measurement.

The experiment will involve photon energy scans from 2 MeV to about 200 MeV. The helicity of the photons should be switchable. The difference in energy between charged and neutral pion threshold is about 4.5 MeV so the energy resolution should be less than 2%. The required flux is at least  $10^7$  per MeV. BIG can achieve the required polarization, energy range, energy resolution and intensity. We expect to complete this experiment in about 2000 hours of beam-time.

### 3.6.3.3 Compton Scattering from a High Pressure Polarized 3He Target

Experimental and theoretical investigation of the nucleon structure has grown more intense in the last two decades, resulting in breakthroughs in both experiment and theory. Nucleon polarizabilities, describing the response of the nucleon in external electromagnetic fields, have attracted more attention. Significant efforts have been devoted in the last two decades to unpolarized Compton scattering measurements from the proton and deuteron to extract the nucleon electric and magnetic polarizabilities. However, very little is known about nucleon spin polarizabilities, which are fundamental quantities related to the structure of the nucleon. For a spin 1/2 target, there exist four independent spin polarizabilities. Due to the lack of free neutron targets in nature, our knowledge of the neutron polarizabilities is poor.. A theoretical calculation shows that double-polarization asymmetries from

circularly polarized photons Compton-scattering off a polarized  ${}^3\text{He}$  target elastically are expected to be sensitive to the neutron spin polarizabilities. [86]

We propose a double polarization Compton scattering experiment of circularly polarized photons from a polarized  ${}^3\text{He}$  target at the elastic kinematics. The experiment will be carried out with a photon energy of 120 MeV at a minimum photon flux of  $5 \times 10^8/\text{sec}$ . The polarized  ${}^3\text{He}$  target is a high pressure target based on the spin-exchange optical pumping technique, and the scattered photons can be detected by using a detection system such as the NaI Detector Array (HINDA). During the experiment, the double polarization asymmetry will be formed by flipping the target spin direction or the beam helicity. The proposed layout of the experiment using HINDA system is shown in Figure 3.28.

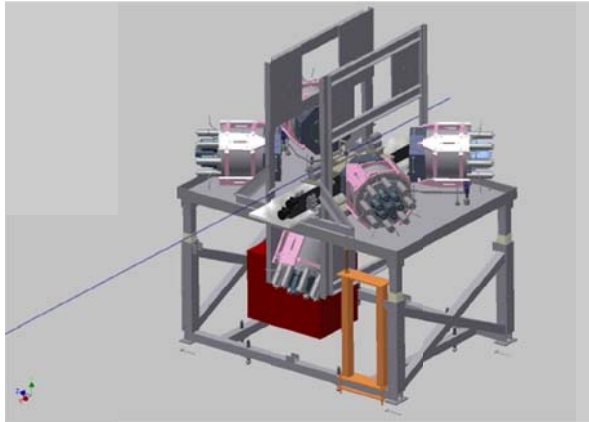


**Figure 3.28.** The proposed experimental setup for Compton scattering using NaI Detector Array (HINDA) system

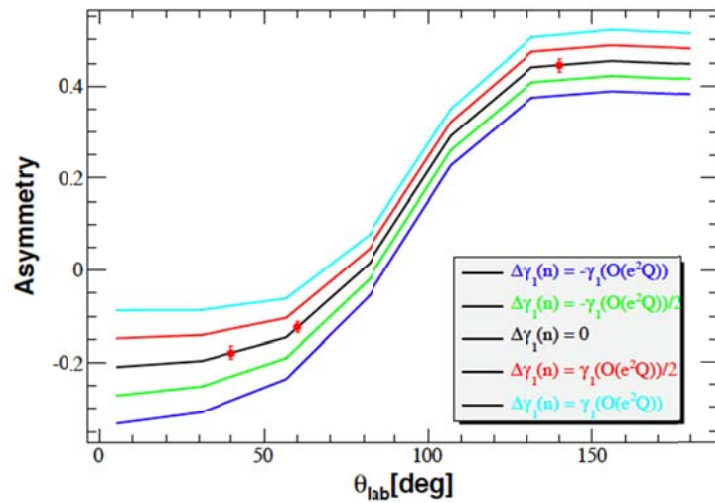


**Figure 3.29.** The projected sensitivity to the neutron spin polarizability  $\gamma_1$  from double polarization asymmetry measurement from a polarized  ${}^3\text{He}$  target as a function of photon scattering angle in the laboratory frame. The simulated results for Compton scattering (red points) are plotted along with theoretical calculations using different  $\gamma_1$  values

We propose a total beam time of 900 hours with 100% polarized photon beam and a 50% polarized  ${}^3\text{He}$  target with a target thickness of  $1.1 \times 10^{22}$  atoms/cm $^2$  and have considered possible physics backgrounds and detection efficiency. The spin-dependent asymmetry difference can be formed from the simulated events, and compared with different neutron spin polarizabilities. For example, the projected sensitivity to the neutron spin polarizability  $\gamma_1$  is shown in Figure 3.29.

### **3.6.3.4 Deuteron photodisintegration and Bethe- Heitler processes**

There is added interest in measurements of both single and double polarization observables in deuteron photodisintegration based on the discrepancy that Nath observed in the reaction  $d(\gamma\vec{n})n$ . [87] The break between theory and experiment occurs at just the energy at which measurements of other reactions suggest the existence of a narrow two-nucleon state/resonance, making the experiment especially compelling. The present indications must be treated very carefully since such a state, usually referred to as a dibaryon, has been sought for decades, and its existence has been announced and then refuted.

BIG can resolve this controversy. The  $d(\gamma\vec{n})n$  measurements involve a secondary scattering of the emitted neutron, making the high flux of the BIG essential. If the Nath data are confirmed, then a program of follow-on measurements is anticipated. These will not only expand the energy range but also address the related polarization of the neutron in the orthogonal direction. In addition, measurements of the reaction  ${}^3\text{He}(\gamma\vec{n})(np)$  would be very interesting -the presence of a narrow two-nucleon resonance should show up in this reaction. While this specific possibility is very speculative, it has discovery potential and therefore is very exciting.

Another set of experiments that can be pioneered at BIG are the Bethe-Heitler processes. [88] For low-Z nuclei which, arguably, may be the most interesting, the question of flux is paramount, as the effect is small. The energy asymmetry in wide- and medium-angle electron/ positron pair production off protons (and other targets) is caused by the interference between the first- and second-order Born diagrams and the Compton scattering diagram. It directly probes aspects of quantum electrodynamics, as well as providing a direct measurement of the real part of the Compton amplitude. The two-photon Bethe-Heitler amplitude is closely related to the two-photon exchange amplitude in  $ep \rightarrow ep'$  which is believed to cause the breakdown of the Rosenbluth separation in electron scattering. [89, 90] It may be much easier to measure two photon exchange effects to high precision in  $\gamma p \rightarrow e^+e^-p'$  than to measure the electron-positron asymmetry in  $e^\pm p \rightarrow e^\pm p'$  elastic scattering.

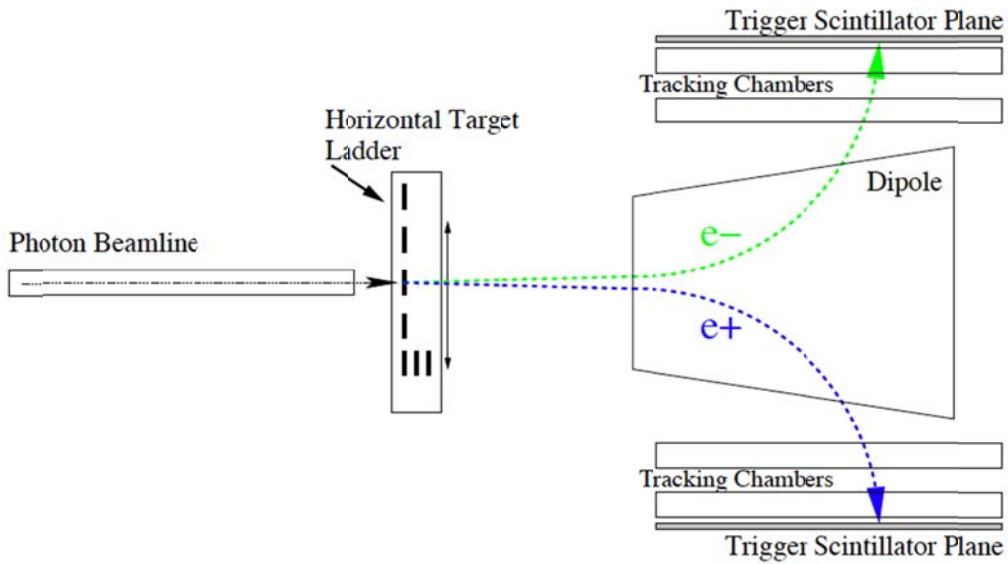


**Figure 3.30.** A schematic top-view of the proposed experimental layout showing the photon beam, the horizontal target ladder, the pair spectrometer dipole, and the tracking packages (not to scale).

### 3.6.4 QCD with real photons: Nucleon structure

The spectra of baryon resonances have been a focus of experimental and theoretical studies, both for particles composed of the light u and d quarks, and those containing one or more of the heavy c and b quarks. In the energy region available at BIG (from 300 MeV to 5 GeV) the nucleons exhibit many major and minor resonance states. There is increasing activity aimed at understanding the spectra of particles containing one or more s quarks, so-called hyperon physics. [91] At present the knowledge of the  $\Xi$  and  $\Omega$  families is particularly limited with only a few states experimentally studied, and scant knowledge as to their properties. [92] The 5 GeV energy reach of the BIG allows us to search for light-quark + glue hybrid baryons as well as for heavy-quark baryons. Figure 3.31 shows some of the recent lattice QCD predictions, showing the bands of states with alternating parities and increasing energies. [93] Each state has a well-defined spin and generally a dominant flavor content. The number of non-hybrid states of each spin and flavor in the lowest-energy bands is in agreement with the expectations based on weakly broken SU(6)O(3) symmetry. These states correspond to the quantum numbers of the quark model.

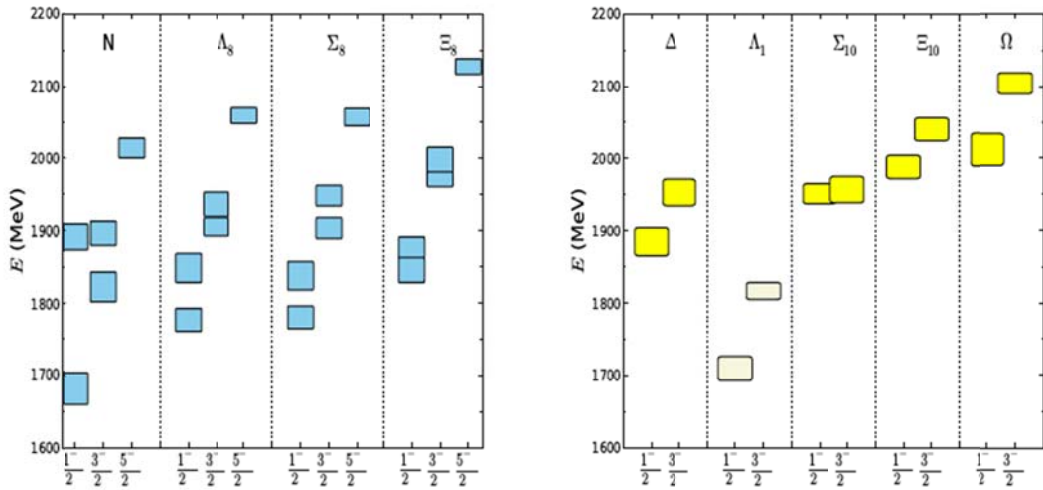


**Figure 3.31.** Lattice QCD predictions: Left, the lowest negative-parity states (flavor-octet); Right, the lowest negative-parity states that are flavor-singlet (beige) and decuplet (yellow). [93]

It would be very important to find some of these predicted states experimentally, but the experiments would be very complicated. To convincingly extract such states we would need to measure almost all polarization observables. This would require  $a \sim 4\pi$  detector to analyze recoil polarization for some channel like  $K\Lambda$  or  $K\Xi^+$ , and both linear and circular photons and one target polarization. [94] High flux  $\gamma$ -rays from the BIG and its fully controllable polarization are well suited for such studies. The extremely high intensity of the BIG, exceeding all existing Compton  $\gamma$ -ray sources by four orders of magnitude, is the key for making these experiments possible.

In addition, a precise measurements of  $d\sigma/dt$  and the meson helicity in the  $\varphi$  photo-production in the energy region of 2 to 3 GeV may reveal the existence of a  $0^{++}$  glueball, whose contribution falls off rapidly at high energies because of a negative value for  $\alpha(t=0)$ . [95] Furthermore, the study of the strangeness quark content in nucleon - which is of great relevance for modern particle physics - can be extracted from the spin observables in  $\varphi$ -photo-production. Also, photo-production of a  $\Lambda$  in  $\gamma p \rightarrow \Lambda K^+$  reactions is of great importance for a microscopic understanding of hypernuclei.

### 3.7 Gamma-gamma collider

Gamma-gamma colliders have recently attracted much interest because they would, thanks to s-channel production, probably provide the cheapest option to construct a dedicated Higgs factory. [96, 97] Such a project would require a recirculating linac and possibly energy recovery. The crucial issues for gamma-gamma Higgs factories are the realization of Compton collisions with high repetition rate, the intensity and properties of the Compton- backscattered photons, the stability and the efficiency of the Gamma-gamma Compton process.

A recent proposal for a Higgs factory gamma-gamma collider, called “SAPPHiRE” is based on a recirculating superconducting linac in possible synergy with the Large Hadron-Electron Collider [96]. Pertinent parameters are compiled in Table 3.4.

**Table 3.4. Example parameters for SAPPHiRE.**

SAPPHiRE	Symbol	Value
<b>total electric power</b>	P	100 MW
<b>e<sup>-</sup> beam energy</b>	E	80 GeV
<b>beam polarization</b>	P <sub>e</sub>	0.90
<b>bunch population</b>	N <sub>b</sub>	10 <sup>10</sup>
<b>repetition rate</b>	f <sub>rep</sub>	200 kHz
<b>bunch length</b>	σ <sub>z</sub>	30 μm
<b>crossing angle</b>	θ <sub>c</sub>	≥20 mrad
<b>normalized horizontal emittance</b>	γε <sub>x</sub>	5 μm
<b>normalized vertical emittance</b>	γε <sub>y</sub>	0.5 μm
<b>horizontal IP beta function</b>	β <sub>x</sub> *	5 mm
<b>vertical IP beta function</b>	β <sub>y</sub> *	0.1 mm
<b>horizontal rms IP spot size</b>	σ <sub>x</sub> *	400 nm
<b>vertical rms IP spot size</b>	σ <sub>y</sub> *	18 nm
<b>horizontal rms e- CP spot size</b>	σ <sub>x</sub> <sup>CP</sup>	400 nm
<b>vertical rms laser CP spot size</b>	σ <sub>y,laser</sub> <sup>CP</sup>	2800 nm
<b>laser wavelength</b>	λ	351 nm
<b>laser pulse energy</b>	E <sub>laser</sub>	5 J
<b>Rayleigh length</b>	Z <sub>R</sub>	0.3 mm
<b>horizontal rms laser CP spot size</b>	σ <sub>x,laser</sub> <sup>CP</sup>	2800 nm
<b>vertical rms laser CP spot size</b>	σ <sub>y,laser</sub> <sup>CP</sup>	2800 nm
<b>longitudinal rms laser pulse length at CP</b>	σ <sub>z,laser</sub> <sup>CP</sup>	0.15 mm
<b>distance CP-IP</b>	L <sub>CP-IP</sub>	0.6 mm
<b>e<sup>-</sup>e<sup>-</sup> geometric luminosity</b>	L <sub>ee</sub>	2x10 <sup>34</sup> cm <sup>-2</sup> s <sup>-1</sup>
<b>γ-γ luminosity (&gt;125 GeV)</b>	L <sub>γγ</sub>	6x10 <sup>32</sup> cm <sup>-2</sup> s <sup>-1</sup>

Another recent proposal for a gamma-gamma Higgs factory, submitted to the European Strategy Group Open Symposium in Cracow, uses CLIC technology [97]. There had also been an earlier proposal and study for a gamma-gamma Higgs factory “CLICHÉ” based on CLIC-1 [98]. Yet another proposal has been presented during the ICFA Higgs Factory workshop 2012 at Fermilab [99].

Gamma-gamma Higgs factories realize collisions through Compton backscattering of laser (or FEL) photons off the high energy electron beams close to the interaction point. A Higgs factory has advantages compared to a positron-electron collision scheme, in that the electron beam energy required to produce a Higgs particle is lower (about 80 GeV instead of 120 GeV), and positrons are not required. Electron beam energies of 80 GeV and a high repetition rate are the basis of the Higgs gamma-gamma collider, and are within reach of present accelerator technology. At a beam energy of 80 GeV, the laser wavelength should be 300-400 nm. For efficient conversion the total energy of the Compton-scattering laser pulse should be a few joules, e.g., 1 TW peak power and 5 ps pulse length, implying 1

MW average power at 200-kHz repetition rate. Stacking laser pulses in a high-finesse optical cavity reduces the input laser power required by two orders of magnitude, to about 10 kW. An economic way to produce the required e- energy is by means of a SC recirculating linac [97]. Operating a recirculating linac with much higher electron current in energy-recovery mode would also, or further, decrease the needed laser power [100]. The Compton IR layout with integrated optical cavity and the production of the required photon beam using a laser or FEL need strong R&D, a large part of which could be studied at FACET-II.

FACET-II can perform several important tests for future gamma-gamma colliders. Specifically, FACET-II could study the realization of multiple collisions using a multi-mirror optical stacking cavity, and the associated laser systems. Two types of such cavities, built by LAL Orsay in France and U. Hiroshima in Japan are presently being tested at the KEK-ATF2, but only with very low repetition rate. Studies of efficiency, tuning schemes, and the photon-beam parameters will be important steps towards a high-energy gamma-gamma collider.

In addition, low energy gamma-gamma collisions could directly be realized at FACET-II. A possible test involves generating electron-positron pairs using two gamma-ray beams colliding at a small angle, on the order of tens of mrad. This would be the first pair creation test using photons.

The maximum cross-section is at  $E_{cm} \sim 1.4$  MeV  $\sim 1e-25$  cm<sup>2</sup>.

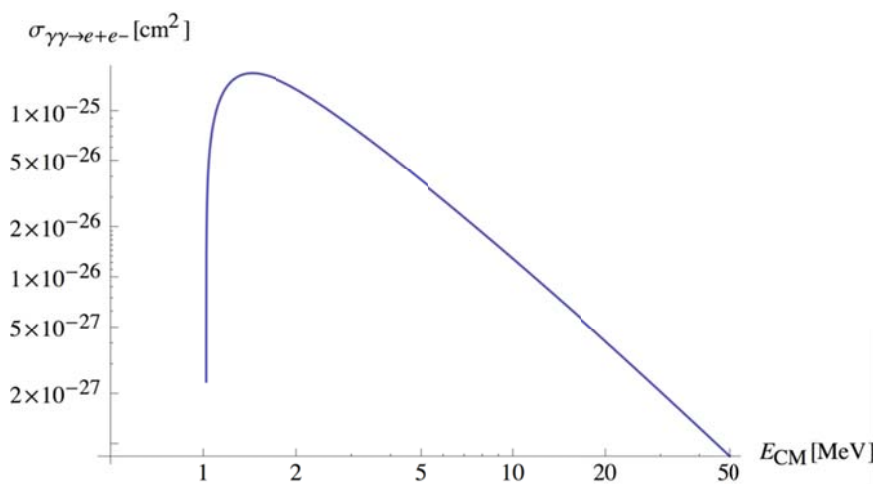


**Figure 3.32. Pair creation cross section VS. C.M. energy of colliding gamma.**

Therefore it is optimal to use a drive beam energy around 4GeV and generate 30MeV gammas using a CO<sub>2</sub> laser. In this case the C.M. energy, calculated as  $E_{cm} = 2E_g \sin \theta$ , comes to  $\sim 1.4$  MeV.. Generated positrons and electrons will have close to 30 MeV energy in the laboratory system with an energy spread of 1.4 MeV.

The trajectories of the generated particles are defined by the magnet field of the last dipole. This will allow for a very practical detection system that can detect about 30 events per minute.

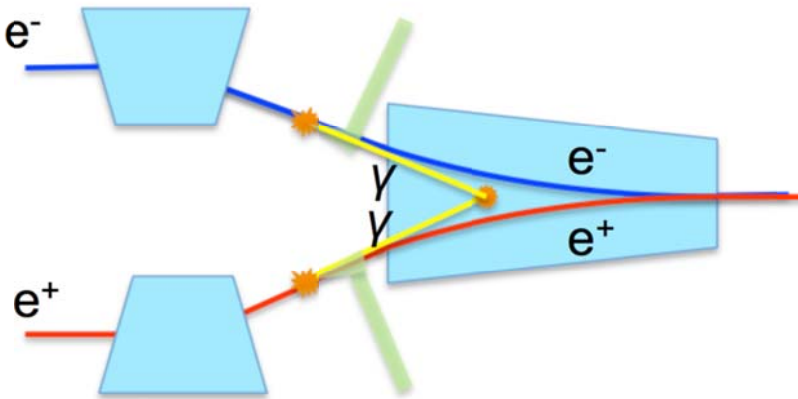


**Figure 3.33. Possible layout for gamma-gamma collider using FACET/FACET-II “sail boat” chicane.**

Another option is to generate a gamma-ray beam and a VUV beam from two consecutive electron bunches. A focusing mirror can then reflect helium VUV photons and cause them to collide with the gamma-ray head-on. There is potential of higher luminosity in this mode of operation as well as reaching energies needed for generating muon pairs. Also this scheme of self-generated gamma-rays could be of interest for a future gamma-gamma Higgs factory. The gamma-ray and VUV could be generated by an undulator, or possibly by an FEL process.

### 3.8 High intensity Positron Source studies using Gamma beam generated with Compton Beam scattering

The SLC positron source was developed in the early 1980s and successfully supported the physics needs for decades of operations. It still holds the record for highest positron flux capability of the order  $4 \cdot 10^{12} e^+/\text{sec}$ . Demands for newly proposed collider facilities exceed capabilities of the SLC type positron source by a few orders of magnitude. There are number of proposals aimed at addressing this issue, yet there is no demonstrated solution that provides a positron source that can meet the needs of ILC, CLIC, LHeC, eRHIC, and other projects [101, 102, 103, 104]. ILC needs a positron source capable of  $3 \cdot 10^{14} e^+/\text{sec}$ , and luminosity of LeHC will be limited with a source below  $4 \cdot 10^{16} e^+/\text{sec}$  (see Table 3.5). The survival of the conversion target is ultimately the limiting factor. Use of novel targets (liquid metal jet target, crystal structure target, pellets) might be necessary to address the demand on the positron beam intensity for the next generation of colliders. The gamma beam capabilities at FACET-II will open unique opportunities to study and advance the ideas on novel positron sources. In this section, we will address the generation of the gamma beams that will be of interest for the testing of novel conversion targets [105].

**Table 3.5. Positron production at the SLC source compared with the needs of future projects**

	SLC	CLIC (3 TeV)	ILC (RDR)	LHeC
<b>energy</b>	1.19 GeV	2.86 GeV	5 GeV	60 GeV
<b><math>e^+</math> / bunch at IP</b>	$40 \times 10^9$	$3.72 \times 10^9$	$20 \times 10^9$	$2 \times 10^9$
<b><math>e^+</math> / bunch before DR inj.</b>	$50 \times 10^9$	$7.6 \times 10^9$	$30 \times 10^9$	N/A
<b>bunches / macropulse</b>	1	312	2625	N/A
<b>macropulse rep. rate</b>	120	50	5	CW

<b>bunches / second</b>	120	15600	13125	$20 \times 10^6$
<b>e<sup>+</sup> / second</b>	$0.06 \times 10^{14}$	$1.1 \times 10^{14}$	$3.9 \times 10^{14}$	$400 \times 10^{14}$

Experimental programs require one of two types of gamma beams: quasi-mono-energetic photons beams or beams with a large energy spread. Optimization of the laser and electron beam parameters to achieve a narrower energy spread (and higher polarization) with angular collimation often results in many orders of flux reduction. The positron generation experiment requires maximizing gamma beam flux, possibly along with a high polarization. The laser and electron beam intensity and their focusing are pushed to the practical limits in this case.

There are many factors to consider when selecting the optimal energy of the gamma beam for positron generation. The energy dependence of the Bethe-Heitler  $e^-e^+$  pair creation process is shown in Figure 3.34.

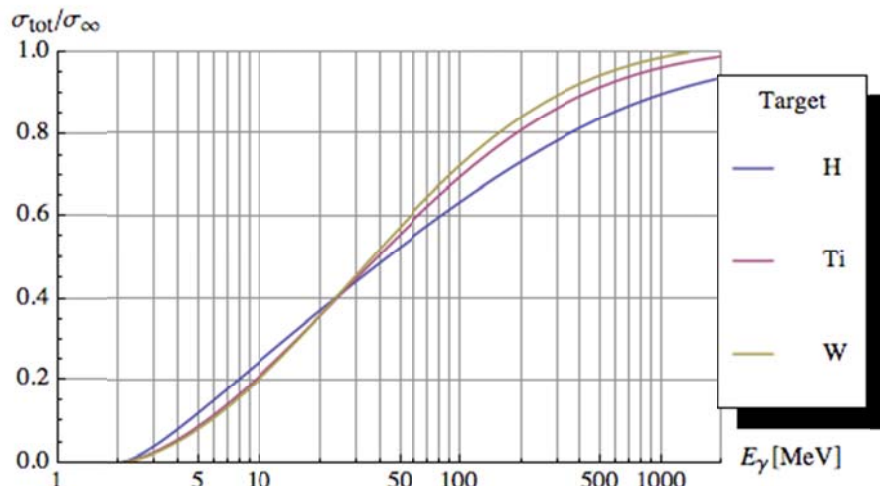


**Figure 3.34. Energy dependence for the cross section of the Bethe-Heitler  $\gamma \rightarrow e^-e^+$  process plotted as ratio of cross-sections at given energy to one at extremely high  $E_\gamma$ :  $\sigma_{tot}/\sigma_\infty$ . The dependence is plotted for hydrogen, titanium and tungsten targets.**

The energy dependence curve suggests that this process would benefit from a higher energy gamma beam. On the other hand, the longitudinal emittance of the captured beam is proportional to the energy of the generated positrons. The acceptance of the damping ring in practical designs thereby limits the energy of the gamma beam. Detailed optimization studies [102] concluded a soft optimum in the range of 30-100 MeV.

The expected efficiency of converting polarized  $\gamma$ -photons into captured positrons is between 0.2 and 2%, depending on the energy of the gamma beam [6]. Therefore, every positron requires, as precursors, more than fifty  $\gamma$ -photons assembled in the beam format (time pattern) of the  $e^-e^+$  collider beams. There are different proposals to accumulate this  $\gamma$ -flux for collider applications. A lower intensity yet more concentrated gamma beam is proposed for the conversion studies at FACET-II.

The integral efficiency of the  $\gamma$ -production in the collision can be estimated from  $\frac{N_\gamma}{N_e} = \frac{N_\phi}{S} \sigma_c$ , where  $N_\gamma$ ,  $N_e$ , and  $N_\phi$  are the numbers of  $\gamma$ -rays, electrons, and laser photons, respectively,  $S$  is the cross-sectional area of the interacting beams,  $\sigma_c = \frac{8}{3}\pi r_e^2 = 6.652 \times 10^{-29} m^2$  is the Compton scattering cross-section, and  $r_e = \frac{e^2}{mc^2} = 2.818 \times 10^{-15} m$  is the classical electron radius. With 0.1 Joule of a CO<sub>2</sub>-laser beam focused to its practical limit of 25- $\mu\text{m}$  rms radius, the efficiency is estimated as  $N_\gamma/N_e=0.1$ . It is expected that electron beam will be focused to a size smaller than laser beam, at 7.4-GeV electron energy, for the generation of the 100 MeV gammas. A similar efficiency can be achieved in the case of a Ti: Sapphire laser beam of 1.0 Joule. With the Ti:Sapphire laser only a 2.1-GeV beam will be needed for the generation of 100 MeV gammas. The laser beam can be focused much more tightly in this case, but the interaction cross section will be dominated by the electron beam size at approximately the same 25 - $\mu\text{m}$  spot. It will become more challenging to design the IP optics for Ti:Sapphire laser beam due to the small divergence of this high energy laser. Generation of gamma beams with lower than 100MeV energy will be more efficient with a CO<sub>2</sub> laser beam. The advantages of CO<sub>2</sub> laser beam for this applications as well as its excellent match to the high-energy pulse linac at SLAC were discussed in more detail in [106].

To complete the optimization of the laser parameters, such as the peak power  $P$ , pulse duration  $\tau$ , and the energy per pulse  $E$ , we note that to maintain the maximum efficiency of the laser and e-beam interactions, the laser focal spot should match the e-beam size, and its pulse length should be close to the Rayleigh length  $Z_R = \frac{2\pi\sigma^2}{\lambda}$ , where  $\sigma$  is the laser beam radius at the focal plane. For a Gaussian beam of radius 25  $\mu\text{m}$ , the Rayleigh  $Z_R \approx 0.3$  mm, and the optimum pulse length of the CO<sub>2</sub> laser is  $\sigma_\tau \cong 1$  ps.

The magnitude of the nonlinear Compton scattering is characterized by the normalized vector potential,  $a = \frac{e\sqrt{-(A_\mu A^\mu)}}{mc^2}$ , where  $e$  is the charge of the electron,  $A_\mu$  is the four-vector potential of the laser, and  $mc^2$  is the electron's rest energy. The parameter  $a$ , simply called "laser strength", can be re-written more conveniently as a function of the laser's wavelength  $\lambda$ , in  $\mu\text{m}$ , and intensity  $I$ , in  $\text{W/cm}^2$ . In this form  $a = 0.60 \times 10^{-9} \lambda I^{1/2}$ . The nonlinear Compton scattering approaches the linear process at  $a \geq 1$ , thereby putting an upper limit on the maximum laser intensity. The laser strength is not expected to exceed 0.3 for the proposed CO<sub>2</sub> laser beam parameters.

Summarizing this discussion on optimizing the IP for the Compton  $\gamma$ -source, we propose the set of parameters compiled in Table 3.6.

**Table 3.6. CO<sub>2</sub> laser- and e-beam parameters at the Compton IP.**

Parameter	Symbol	Value
Laser beam energy	$E_L$	0.1 J
Laser wavelength	$\lambda$	10.2 $\mu\text{m}$
Rayleigh length	$R_L$	0.3 mm
Laser beam length	$\sigma_t$	1 ps
Normalized vector potential	$a_0$	0.3
Electron beam size	$\sigma_e$	15-25 $\mu\text{m}$
Electron beam energy	$E_e$	4-7.4GeV
Gamma beam energy	$E_\gamma$	30-100MeV

<b><math>\gamma</math>-ray production efficiency</b>	$N_\gamma/N_e$	$\sim 0.1$
--	----------------	------------

A wide range of gamma beam energies, high peak intensities, and low divergence of the gamma beam (due to high energy and low geometrical emittance of the electron beam) make this source optimal for studying novel ideas for conversion targets.

Crystal and hybrid targets are examples of novel conversion targets. Either a gamma beam or the electron beam could be used to hit the test targets. Particles traversing at small angles along a single crystal axis experience the collective scattering force of many crystal atoms. The enormous fields inside the crystal can trap the particles along an axis or plane, a process called channeling. High-energy electrons are attracted by the positive nuclei and, therefore, can produce strongly enhanced coherent bremsstrahlung and pair production. These effects could be used in a positron production target. The target length can be shorter than for an amorphous material, which then yields a higher conversion coefficient and a lower emittance of the positron beam. This makes single crystals very interesting for positron production targets.

### 3.9 BIG - gamma-ray source at FACET-II

The BIG, based on the electron beam and lasers at FACET-II, will be a very versatile, nearly mono-energetic gamma-ray source for nuclear physics experiments. The high quality of the incoming electron beam will allow it to act as a collimator, turning BIG into a nearly mono-energetic gamma-ray beam.

We will assume that energy of the beam in FACET-II can be tuned from 1 GeV to 10 GeV. In combination with two lasers operating at 800 nm and 10  $\mu\text{m}$ , the BIG therefore has 1,000-fold tunability from about 2 MeV to 2 GeV. The high-energy reach can be increased to 5 GeV using the third harmonic of 800 nm laser, but with an accompanying 5-fold loss in the flux.

We will be able to switch lasers or select different harmonics to adjust gamma-ray energy in coarse steps, or change the electron beam energy to provide nearly continuous fine-tuning of the laser.

**Table 3.7. Main e-beam and laser parameters for the BIG**

Injectors	Beam	Energy [GeV]	$\epsilon_{\text{NX}} \times \epsilon_{\text{NY}}$ [ $\mu\text{m} \times \mu\text{m}$ ]	$\sigma_x \times \sigma_y$ [ $\mu\text{m} \times \mu\text{m}$ ]	$\sigma_z \times \Delta E/E$ [ $\mu\text{m} \times \%$ ]	The $\gamma$ -ray beam
Thermionic	3nC e <sup>-</sup>	10	30 x 3	20 x 20	40 x 1	
	1.5nC e <sup>+</sup>	10	30 x 3	20 x 20	40 x 1	
Photoinjector	20pC e <sup>-</sup>	10	0.1 x 0.1	1 x 1	2 x 1	
	1nC e <sup>-</sup>	10	1 x 1	3 x 3	5 x 1	
	6nC e <sup>-</sup>	10	5 x 5	10 x 10	20 x 1	
	3nC e <sup>+</sup>	10	30 x 3	20 x 20	40 x 1	
Witness photoinjector	0.1nC e <sup>-</sup>	0.1	1 x 1	50 x 50	20 x 0.1	
Lasers	Energy / Power [Joule / TW]		Rep rate [Hz]	T [fs]	$\lambda$ [ $\mu\text{m}$ ]	
TI: Sapphire	1 / 30		10	30	0.8	
CO <sub>2</sub> laser	0.1 / 0.1		120	1000	10.2	
Gamma beams (Inverse Compton)	Energy [GeV]	Intensity	Rep rate [Hz]	$\sigma_x \times \sigma_y$ [ $\mu\text{m} \times \mu\text{m}$ ]	$\sigma_z$ [ $\mu\text{m}$ ]	
TI: Sapphire	1.8 GeV	$10^{10}$	10	5 x 5	10	
CO <sub>2</sub> laser	150 MeV	$10^{10}$	120	5 x 5	10	

energy range comfortably covers the energy ranges of interest for users of HlyS (TUNL, Duke University) and LEPS (Spring 8, Japan). Using two set of lasers ( $\text{CO}_2$  and Ti: Sapphire) and electron beam energies from 1 GeV to 10 GeV, FACET can generate gamma rays with continuously tunable energy from 2 MeV to 1.9 GeV. This three orders of magnitude tunability is indeed unprecedented.

FACET can create gamma rays with unprecedented intensity – from  $10^{10}$  to  $10^{11}$  gammas per second. This intensity, in combination with the high brightness of the electron beam, allows us to collimate the gamma ray to a nearly mono-energetic beam with energy spread as low as 0.1%.

There is, however, a tradeoff between energy spread comes and flux: For example, a gamma-ray beam with 1% rms energy spread would have typical flux of  $10^8$  –  $10^9$  gammas per second, while increasing resolution to 0.1% will reduce the flux to  $10^7$  –  $10^8$  gammas per second. Exact numbers depend on specific choice of the gamma-ray energy, as shown in Figure 3.35.

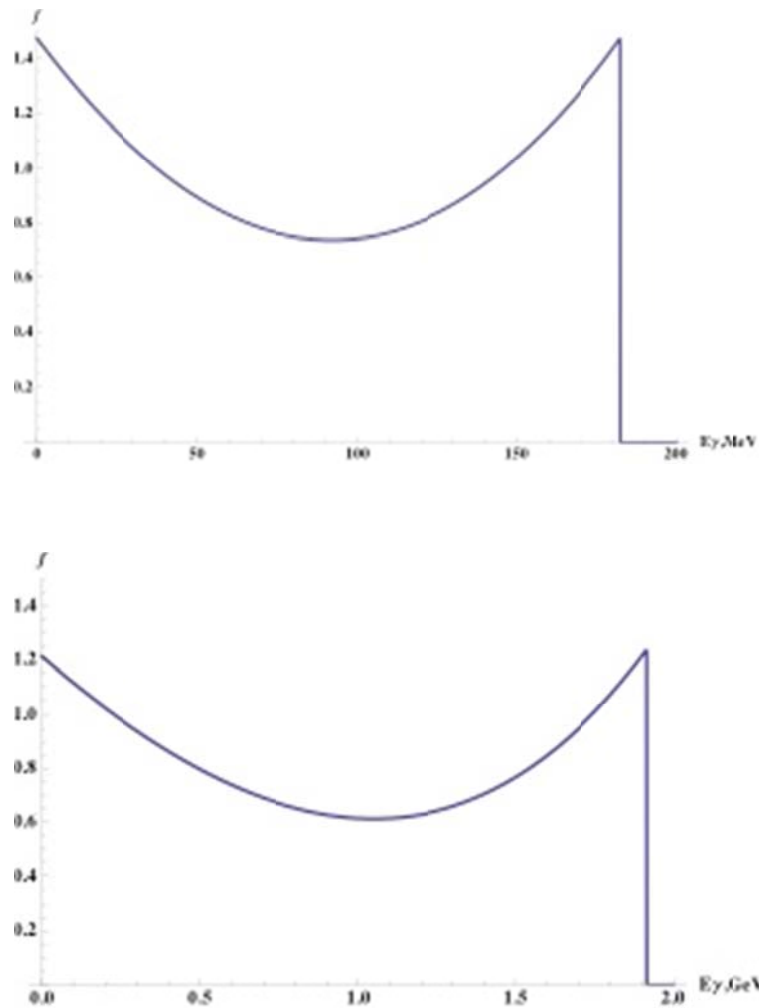


**Figure 3.35. Normalized gamma-ray distribution as function of their energy for 10 GeV e-beam: top graph is for a  $\text{CO}_2$  laser, bottom graph is for a Ti: Sapphire laser.**

The polarization of the  $\gamma$ -rays can be controlled by that of the scattered laser beam, and can be linear (vertical or horizontal), circular (left or right) or elliptical. The degree of polarization depends on the gamma-ray energy: it is very close to 100% at low energies and is 97.7% for 1.9 GeV gamma rays.

Many experiments require a fine energy resolution, and an electron beam with very low emittance provides for such possibility. A simple geometrical collimation of the  $\gamma$ -ray beam can create a  $\gamma$ -ray energy spectra with FWHM below 0.1% (see Figure 3.36). Scanning the energy of the beam will allow us, for example, to de-convolve fine structure of the spin observable at the pion threshold.

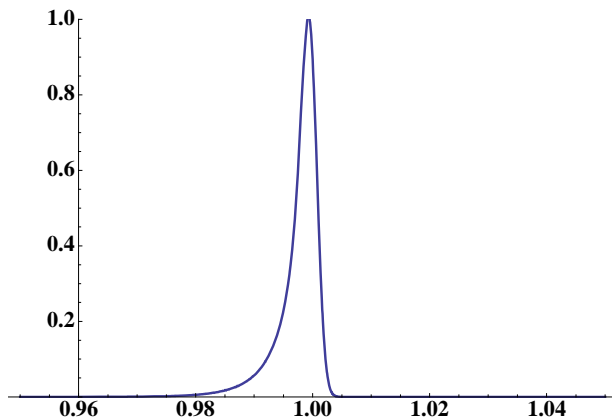


**Figure 3.36. A narrow energy spectrum of BIG's collimated beam. Energy spectrum of 0.1% FWHM or better could be obtained at BIG.**

Time structure of the gamma-ray bursts can be important for experiments. While pulsed structure with 100-120 Hz is a standard feature of BIG, the structure of each pulse can vary. The  $\gamma$ -rays can be delivered in one short picosecond duration burst, or can be distributed into as many as 1,000 ps bursts separated by 1 nanosecond.

### **3.10 Generating High-Brightness Muon Beams With High-Energy Gammas**

Hadron colliders are impractical at very high energies because effective interaction energy scales with beam energy and luminosity must rise as energy squared. Further, the prevailing gluon-gluon background radiation makes it difficult to sort out events. Positron-electron colliders are constrained at TeV energies by bremsstrahlung radiation and also by cost because long linacs are required to avoid synchrotron radiation in the rings. A muon collider will have the same advantages in energy reach as a positron-electron collider, but without prohibitive beamstrahlung and synchrotron radiation.

High-brightness polarized muon ( $\mu^+\mu^-$ ) beams are generated through gamma conversion into pairs in the nuclei field. The dominant effect in the interaction of the high-energy photons with the solid target will be the production of electron-positron pairs. The low-phase space of the resulting muon beams adequately compensates for the small probability of generating a  $\mu^+\mu^-$  pair. The probability of a  $\mu^+\mu^-$  pair creation is suppressed approximately by a factor of  $\mu_0^2/\mu_e^2$ . However, FACET-II will be able to generate extremely powerful high-energy  $\gamma$  beams through Compton backscattering, making it possible to study high brightness muon beam production. Low intrinsic emittance from the direct production of the  $\mu^+\mu^-$  pairs makes this approach competitive with the currently considered production scheme, in which a high-power proton beam generates a pion shower, and the pions, in turn, decay into muons. Indirect muon production is orders-of-magnitude more efficient in terms of the number of the muons per incident beam power. Approximately 0.2% of the drive beam power is converted into the muon beams in case of proton drivers, and only 0.001% is converted with gamma drivers. The brightness of the resulting beam, however, is much lower with protons, so that very challenging and complicated cooling schemes must be incorporated into the system. Therefore, using protons to create neutrinos may not be as cost-effective as some researchers believe. [106]

The interaction of few-GeV gamma rays with the solid target is dominated by their conversion into electron-positron pairs. At these energies, Compton scattering of the photon from the atomic electron is considerably smaller. We will consider the ratio of the  $\gamma \rightarrow \mu^-\mu^+$  to  $\gamma \rightarrow e^-e^+$  cross sections. One can split the Bethe-Heitler total cross-section, describing pair creation, into two parts: an asymptotic region at very high energies of the photon cross sections  $\sigma_\infty$ , and an energy dependent part at lower energy,  $\sigma(E_\gamma) = \sigma_{tot}/\sigma_\infty$  (Figure 3.34), that is in the range from 0 to 1. [88] It shows moderate advantage of the light nuclear targets at the lower energy range, and low efficiency for the gamma energies near the muon pair creation threshold.

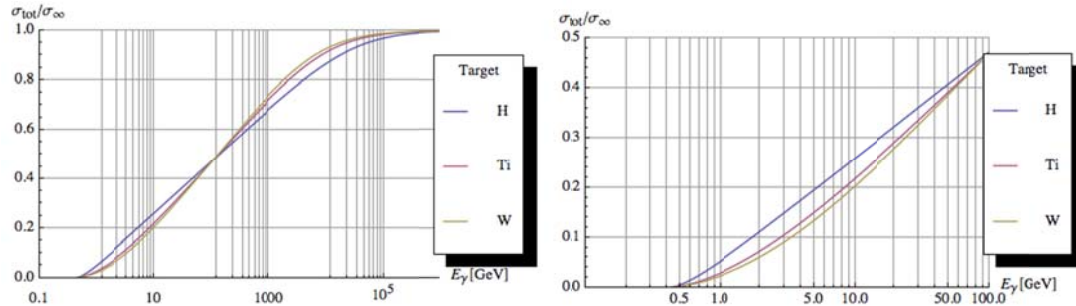


**Figure 3.37. Energy dependence for the cross section of the Bethe-Heitler process  $\gamma \rightarrow \mu^+\mu^-$  plotted as  $\sigma_{tot}/\sigma_\infty$ . The dependence is plotted for hydrogen, titanium and tungsten targets.**

The energy-independent part can be written in the following form [88]:  $\sigma_\infty = \left(\frac{7}{9}\right) 4\alpha Z^2 r_c^2 \log(W_\infty)$  where  $\alpha$  is the fine structure constant,  $Z$  is the atom charge,  $r_c$  is a classical-particle's radius,  $W_\infty \cong 136 \frac{m_{e,\mu}}{m_e}$  for hydrogen, and  $W_\infty \cong \frac{119}{A^{0.27}} \frac{m_{e,\mu}}{m_e}$  for the rest of the nuclei. The total cross section rises linearly in  $\log(E_\gamma)$  with the slope  $W_M \cong \left(\frac{1}{4}\right) \frac{1}{1.49 m_{e,\mu}}$  for hydrogen, and  $W_M \cong \left(\frac{1}{4}\right) \frac{1}{1.54 A^{0.27} m_{e,\mu}}$  for the rest of the nuclei. Therefore, the total cross-section is  $\sigma_{tot} \cong \left(\frac{28}{9}\right) \alpha Z^2 r_c^2 \log(1 + W_M E_\gamma)$ .

This derivation is valid for well above the threshold photon energy for the muon pair creation and below its saturation energies, i.e. where  $W_M E_{sat} < W_\infty$ . The gamma beams generated with Ti:Sapphire laser beam at FACET-II are within this range.

Now, the probability that the photon will create a  $\mu^+\mu^-$  pair can be estimated as  $\frac{\sigma_{tot,\mu}}{\sigma_{tot,e}} \approx \left(\frac{1}{4}\right) \frac{m_e^2}{m_\mu^2}$ , or between  $0.2 \times 10^{-5}$  and  $0.5 \times 10^{-5}$  (see Figure 3.38). Using the second or third harmonic of the Ti:Sapphire laser beam will result in a harder energy gammas (at lower beam intensity) and will improve muons pair cross section as well it will lower emittances. Some electrons and positrons will be scattered and will regenerate gamma photons with sufficient energy for  $\mu^+\mu^-$  pair production. This or other sources of correction to the assessment were not considered since they are not expected to change the result by more than tens of percents.

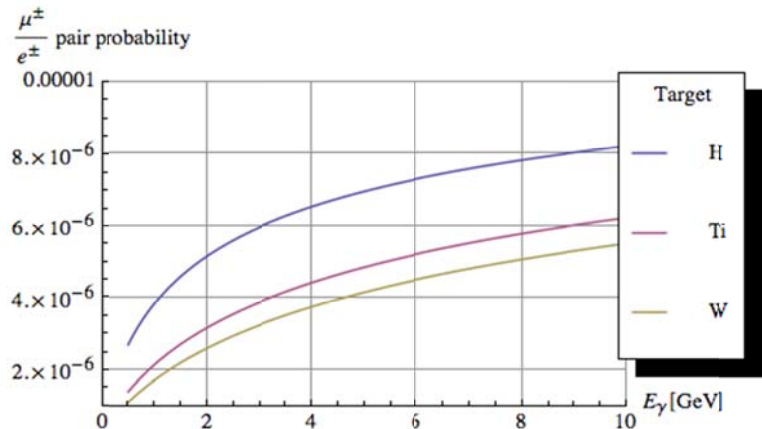


**Figure 3.38. Probabilities of creating  $\mu^+$ - $\mu^-$  pairs as a function of the incident photon energy for hydrogen, titanium and tungsten targets are plotted.**

Approximately 50% of the  $\mu^+$  and  $\mu^-$  beams will be generated with energies ranging from  $E_\gamma/2$  to  $E_\gamma$  when  $E_\gamma \gg 4m_\mu c^2$ . The duration of the  $\mu$ -beam will be similar to that of the  $\gamma$  beam, or drive electron-beam. The estimate of longitudinal emittance can be written in the form  $\varepsilon_{N\parallel} \cong c\tau_e \frac{\gamma_{max} - \gamma_{min}}{4}$ , where  $\gamma_\mu$ ,  $\gamma_{min}$ , and  $\gamma_{max}$ , are the mean, the minimum, and the maximum values for the captured  $\mu^+$  and  $\mu^-$  beams, and  $\tau_e$  is the duration of the electron bunch.

The generated muons have a divergence of  $1/\gamma_\mu$  and muon beam size at the exit of the target with length  $L_{target}$  will be dominated by the muons divergence and can be estimated as  $\sigma_{\mu min} \cong \frac{L_{target}}{2\gamma_\mu}$ .

Therefore, the normalized transverse emittance can be assessed as  $\varepsilon_{N\perp} \cong \frac{L_{target}}{2\gamma_\mu}$ . The longitudinal and transverse normalized emittances of the  $\mu^+$ - $\mu^-$  beams produced with a high-intensity 2 GeV  $\gamma$  beam from the tungsten target which is one radiation length long are calculated as 150 and 50  $\mu\text{m}$ , respectively. For comparison, it is estimated [106] that the longitudinal and transverse normalized emittances of the captured muon beam produced with proton beams are 20 cm and 18 mm, respectively. Approximately one million muons are expected to be captured per second in the 120 Hz mode with abovementioned emittances. Immersing the target into a focusing field, thereby limiting the muon beam's size expansion during the gamma ray-beam interaction, can further reduce transverse emittances. Utilizing crystal targets for pair creation will allow channeling of the created muons therefore will result in even colder beams.

Availability of the muon beams with very low transverse emittances is crucial for studies of novel muon beam cooling and acceleration techniques in the crystal lattices and nanostructures [107, 108] due to naturally low acceptance angles of such structures.

### 3.11 Laboratory Astrophysics at FACET

Ultrahigh-energy cosmic rays (UHECR) and photons have been observed, but their sources and production mechanisms in space are yet to be understood. Laboratory astrophysics experiments may contribute to the understanding of cosmic accelerators in two categories: 1) Calibration experiments for the testing and calibration of UHECR observational techniques, and 2) Dynamics experiments for the investigation of relativistic plasma dynamics to elucidate the underlying physics of cosmic acceleration.

Two calibration experiments have been carried out at the FFTB. The E-165 FLASH experiment helped shed light on the apparent discrepancies in the energy determinations of cosmic rays around  $10^{19}$  eV with precision measurements of air fluorescence yield in an electromagnetic shower. [109] The T460 experiment demonstrated the principle of a novel detection technique for ultrahigh-energy cosmic neutrinos based on radio Cherenkov signals due to the Askaryan effect. [110]

In principle FACET can provide high-energy-density particle beams at  $10^{16}$  J/m<sup>3</sup> for dynamics experiments, creating extreme relativistic plasmas in a regime relevant to cosmic acceleration studies and accessible in a terrestrial environment. A third category of lab-astro experiments involves using high intensity or high energy density particle and laser beams as a probe for fundamental physics. An example is the creation of Unruh radiation from a violently accelerated electron in a laser field due to interaction with quantum vacuum fluctuations, a process similar to Hawking radiation from the event horizon of a black hole. [111]

While the extreme astrophysical conditions can never be replicated in the laboratory, the challenge is to devise and perform lab-astro experiments that will uncover the physical principles involved that can be scaled up to understand these powerful astronomical sources. Relativistic particle outflows, commonly observed in astrophysical sources such as active galactic nuclei and gamma-ray bursts, are a key element in many models of cosmic acceleration. Their interaction with ambient plasmas is believed to give rise to particle acceleration producing the observed radiation spectrum. An understanding of their dynamics is thus crucial to the development of a theory of a cosmic accelerator. In particular, experiments seek to investigate how kinetic energy of the outflow is converted into plasma instabilities which in turn power particle acceleration and radiation.

A key difficulty is the need for overall charge-neutral beams (overlapping e+ and e- beams) to mimic astrophysical outflows. At FACET, relativistic electron-positron plasmas in the form of directed “jets” could be created by showering high-energy-density electron beams onto a solid target, analogous to the e+ e- pairs that come off the positron target. The dynamics of jet-plasma interaction can be investigated over a scale length of several collisionless skin-depths. In a collisionless plasma, the mean-free-path is long compared to the skin depth so the latter is the relevant scale. Laboratory results can be applied to astronomical collisionless plasmas and will provide important tests of simulations for magnetic filamentation, inductive, wakefield, and ponderomotive acceleration, synchrotron radiation spectra, jet-plasma instabilities, and jet propagation over long distances.

The 2001 Workshop on Laboratory Astrophysics [112], the 2003 Workshop on Quantum Aspects of Beam Physics [113], the 2003 Orion Workshop [114], and the 2006 SABER Workshop [115] all included presentations on lab astrophysics using particle beams. After the 2006 workshop, SLAC conducted a limited study of these beam-based lab-astro concepts. During the past decade, research teams around the world have instead developed astrophysics-relevant research utilizing high energy-density (HED) facilities such as intense lasers and z-pinches [116]. Research is underway in many areas, such as compressible hydrodynamic mixing, strong shock phenomena, radiation flow, radiative shocks and jets, complex opacities, equations of state, dust formation, super strong magnetic fields, and relativistic plasmas. We will not review these developments, so the reader is referred to the HEDLA Meetings, held every two years, for details. [117]

We list the presentations from the Lab-Astro, Orion and SABER workshops that are relevant to possible lab-astro experiments in Table 3.8, Table 3.9 and Table 3.10. Online workshop proceedings include further details [112, 114, 115]. The Proceedings of the 2003 “Quantum Aspects of Beam Physics” workshop [113] cover many of the same lab-astro topics, so we do not review it here. The titles in the

tables clearly indicate the preponderance of “dynamics” experiments, especially those involving charged beams, neutral beams, and lasers, in some cases with background magnetic fields superimposed to mimic astrophysical environments such as shocks, particle jets, gamma-ray bursts, supernovas, and neutron stars. Calibration experiments are the next most represented, and these can be related to dynamics experiments when code validation is required to connect simulations, laboratory results, and astrophysical observations. Beam parameters for most experiments are usually not discussed in detail, although for jet-plasma and laser-induced shock/instability experiments there is some specific information in the slide presentations. Broadly speaking, the lab-astro experiments that might use SLAC’s relativistic electron-positron beams are often flexible with respect to beam energies, which simply change the time and length scales according to the Lorentz factor. The bunch densities are usually in the range  $10^{14}$  -  $10^{18}$  /cc, bunch lengths are in the range 10 - 1000  $\mu$ m, bunch diameters are of order 10 to 100  $\mu$ m, plasma lengths are about a meter, and background magnetic fields (usually solenoidal) vary from 1 to 104 Gauss depending on the experiment.

**Table 3.8. Presentations related to possible experiments from 2001 Lab-Astro Workshop. [112]**

Presenter	Title	Experiment Type
David Cline	Primordial Black Hole Induced Plasma Instability Expt.	Dynamics
Pierre Sokolsky	High Energy Shower Expt. for UHECR	Calibration
Jasper Kirkby	CLOUD Cosmic Ray Expt. on Climate Variation	Calibration
Pisin Chen	Plasma Wakefield Acceleration Expt. for UHECR	Dynamics
K. Nakajima	Laser Driven Dirac Acceleration for UHECR Expt.	Dynamics
A. Odian	Non-Askaryan Effect Expt.	Calibration
R. Rosner	Astro Fluid Dynamics Computer Code Validation Expt.	Calibration
S. Colgate	Magnetic Flux Transport and Acceleration Expt.	Dynamics
T. Kamae	Photon Collider for Cold e + e – Plasma Expt.	Dynamics
M. Begelman	X-Ray Iron Spectroscopy and Polarization Expt.	Calibration
Johnny Ng	Relativistic e + e – Plasma Expt.	Dynamics
T. Katsouleas	Beam-Plasma Interaction Induced Photon Burst Expt.	Dynamics
R. Blandford	Beam-Plasma Filamentation Instability Expt.	Dynamics
J. Scargle	Relativistic MHD Landau Damping Expt.	Dynamics

**Table 3.9. Presentations related to possible experiments from Orion Workshop 2003. [114]**

Presenter	Title	Experiment Type
Pierre Sokolsky	Laboratory Particle Astrophysics	Calibration
Robert Bingham	Fundamental Physics using Atomic Beams and Lasers	Fundamental Physics

David Saltzberg	Neutrino Astrophysics and the Askaryan Effect	Calibration
Pierre Sokolsky	Ultra High Energy Cosmic Rays and the FLASH Expt.	Calibration
Kevin Reil	Alfven Wave Induced Wakefield Acceleration for UHECR	Dynamics
Richard Sydora	Nonlinear Alfven Wave Dynamics: Wave Dynamics Steepening and Particle Acceleration	
Johnny Ng	Cosmic Accelerators in the Laboratory	Dynamics
K. Nakajima	Intense e+e- Pair Beam Production in Superstrong Laser-Matter Interactions for LabAstro Experiments	Dynamics
A. Yashin	Wave-Packet Approach to Unruh Effect	Fundamental Physics
Richard Klein	Creation of a Neutron Star on a Petawatt Laser	Dynamics
A. Spitkovsky	Electrodynamics of Magnetized Rotators	Dynamics
Robert Bingham	Similarities between e and v Beams in Plasmas	Dynamics
R. Paul Drake	Connecting Laboratory Experiments with Astrophysical Phenomena	Dynamics

**Table 3.10. Presentations related to possible experiments from SABER Workshop 2006. [115]**

Presenter	Title	Experiment Type
Pierre Sokolsky	Some Thoughts on the Importance of Accelerator Data for UHE Cosmic Ray Experiments	Calibration
Pisin Chen	ESTA: End Station Test of ANITA	Calibration
A. Spitkovsky	Pulsars as Laboratories of Relativistic Physics	Dynamics
Johnny Ng	Astro-Jet-Plasma Dynamics Experiment at SABER	Dynamics
Kevin Reil	Astrophysical Plasma Wakefield Accelerator	Dynamics
Bruce Remington	Science Outreach on NIF: Possibilities for Astrophysics Experiments	Dynamics, Calibration
Eduardo de Silva	Can GLAST Provide Hints on GRB Parameters?	Dynamics, Calibration
G. Barbiellini	Stochastic Wakefield Particle Acceleration in GRB	Dynamics

### **3.12 Measurements for the CLIC study at the FACET-II facility**

The characteristics of the FACET-II facility at SLAC makes it an ideal test-bed for measurements of crucial importance for the CLIC study. Consequently the CLIC study is preparing a formal proposal for the approval of the following experiments to be performed at FACET-II:

- Experimental verification of the performance of system identification, feedback and on-line alignment algorithms for the linear collider and final-focus
- Direct measurement of the long-range transverse wakefields of industrialized CLIC main-linac accelerating structures
- Direct measurement of the transverse wakefields of linear collider final focus collimator geometries

More details of the experiments are presented in the following sections.

### **3.12.1 Verification of on-line system-identification, feedback and tuning algorithms**

The performance of future linear colliders depends critically on beam-based alignment (BBA) and feedback systems. ILC and CLIC will routinely undergo dispersion-free steering (DFS) in the main linacs [118, 119]. In CLIC, an option for a parasitic on-line dispersion-free correction is being studied.

DFS is a beam-based alignment technique for steering the orbit and correcting the dispersion at the same time. The technique requires accelerating one or more test beams with different gradients to evaluate the dispersion. The steering is performed by minimizing the offset of the nominal beam in the beam position monitors (BPMs) and zeroing the difference between the test beam trajectories and the nominal trajectory. The experimental verification of the DFS algorithm is essential to prove its effectiveness and to prepare the commissioning of such machines.

Knowledge of the system model is crucial for developing effective beam-based algorithms. In the CLIC main linac for example, even small changes in the acceleration gradients, the phases, or the magnet strengths can significantly change the the system model. A reliable knowledge of such a system response is very important. We propose using an adaptive system identification algorithm that measures the system response matrix dynamically and automatically [120]. We propose to test such system identification procedures and beam-based alignment algorithms for linear colliders at FACET-II. Figure 3.39 shows the results of some simulations.

The very small emittances in linear colliders require fast correction of static and dynamic imperfections, e.g. misalignment and ground motion, through beam-based alignment algorithms and feedback. The effectiveness of such algorithms is, however, limited by the knowledge of the matrix representing the response of the beam trajectory to the action of the correctors. FACET-II, with its km-long linac accelerating both electrons and positrons to a relatively high final energy, and with micro-metric emittances, offers an ideal setup for testing beam-based alignment algorithms and the system identification algorithms. We believe that this experiment will be crucial to consolidate and perfect the procedures needed to commission and operate future linear colliders.

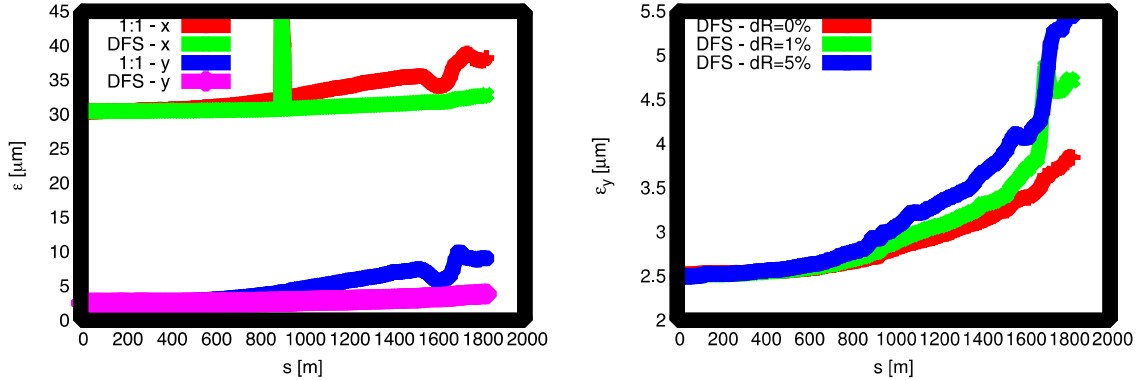


**Figure 3.39. Emittance growth in the first 2 km of SLC linac, after BBA correction. Left-hand plot shows the horizontal and vertical emittance for 1:1 corrected and DFS corrected machines. The right-hand plot shows the vertical emittance growth after DFS when the  $c$  correction is computed using an imperfect model. Each curve is the average of 100 randomly misaligned machines.**

During the first half of 2012 we have been able to perform the experiment at FACET. During this time we have installed our software on the FACET servers and performed several tests of system identification and beam-based alignment. The system identification and beam-based alignment algorithms have proven to be extremely successful, especially when dealing with orbit correction. We believe we can improve these results and test more advanced techniques such as emittance tuning bumps or dispersion bumps.

System identification results are shown in Figure 3.40. The response matrices shown in the figure were obtained automatically in about two hours of operation with no need for any human intervention, using our dedicated software.

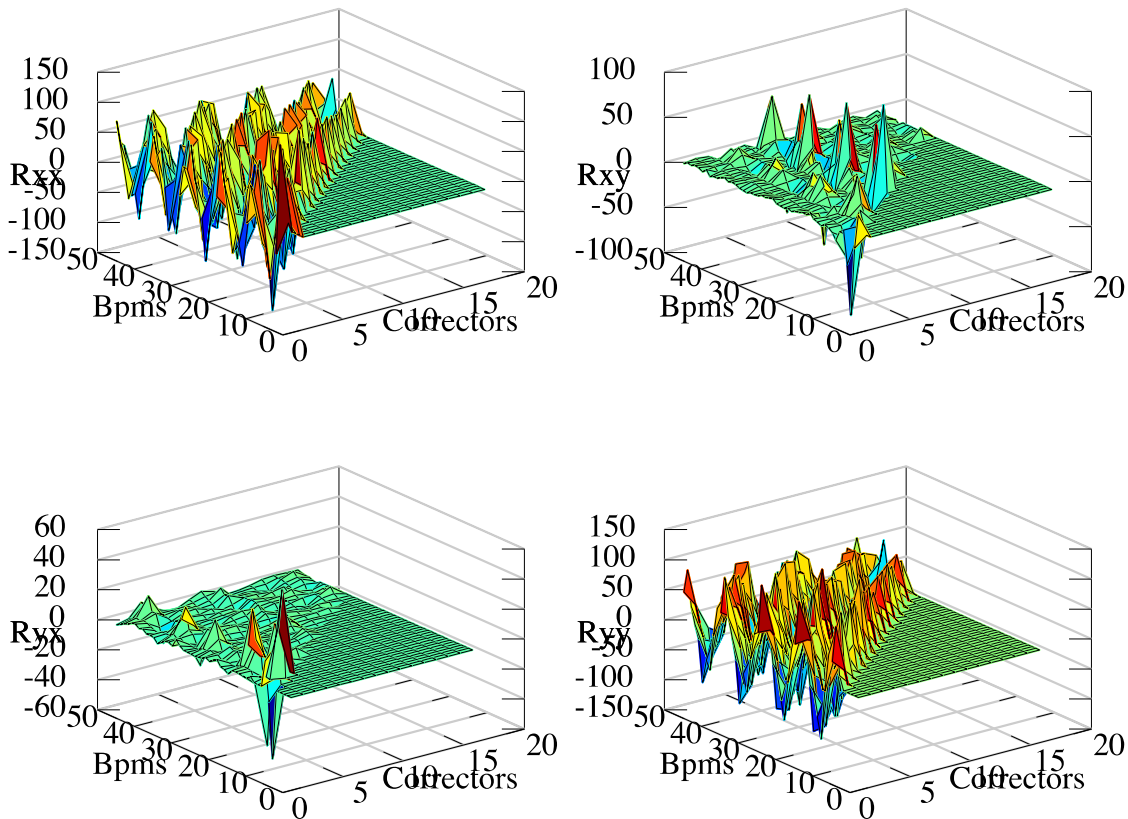


**Figure 3.40. Result of the system identification algorithm during the run in June 2012. From top to bottom, left to right, the matrices  $R_{xx}$ ,  $R_{xy}$ ,  $R_{yx}$ , and  $R_{yy}$ .**

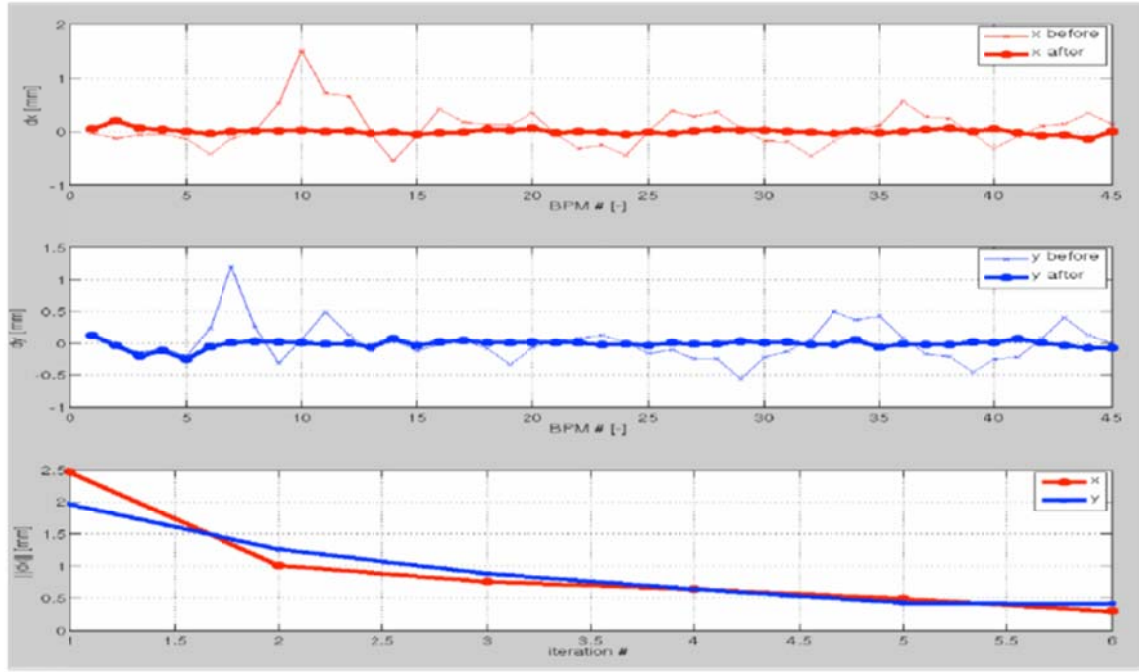


**Figure 3.41.** Result of the orbit correction algorithm during the run in June 2012. From top to bottom: the horizontal orbit, the vertical orbit, and the absolute error.

Example of results of global orbit correction are shown in Figure 3.41. An initial orbit, exhibiting an oscillation as large as about 1 mm, was steered to read zero on the BPMs, within the jitter of the machine. The orbit correction we implemented performed in an efficient and robust manner. The orbit correction software automatically performed the six iterations shown in figure in less than two minutes, with each iteration taking about 20 seconds.

### 3.12.2 Measurement of long-range transverse wakefields in industrialized accelerating structures

Manufacturing of the CLIC main linac accelerating structures will progress from the prototype phase to an industrial facility in a few years. Given the complexity of the manufacturing process, it will be crucial to suppress the long-range wakefields as effectively in the industrialized structure as in the test prototypes. Given the characteristics of its electron and positron beams, the FACET-II facility provides a unique opportunity to measure wakefield suppression.

The CLIC baseline accelerating structure is composed of a tapered chain of 26 damped cells with a double-feed coupler for the input and the output power [121]. See Figure 3.42 for a picture of a prototype. The damping suppresses the wakefields in order to reduce them to an acceptable value and to preserve small emittances during the accelerating process. It is implemented by four rectangular waveguides coupled to the main accelerating cells. The waveguides are terminated by inserting pieces of lossy dielectric loads inside. We expect to have strong long-range wakefield suppression, about a factor 50 in 6 RF cycles (15 cm). This allows us to minimize the coupling of two consecutive bunches of the CLIC train. The simulated transverse wakefield is shown in Figure 3.43.



**Figure 3.42.** High-power test structure. The overall length is 30 cm.

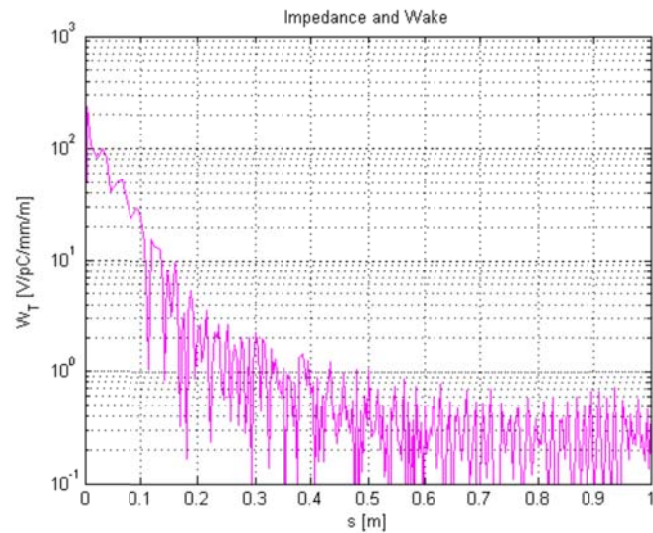


**Figure 3.43.** Simulated wakefields for the CLIC accelerating structure as a function of the distance from the driving bunch.

The x-band test structure setup will consist of six accelerating structures in a common vacuum tank. At this stage no power will be sent to the test structure and the double feed couplers will be terminated by the loads. The test structure will consist of clamped aluminum cells. We would need positrons to function as a driving bunch and electrons as a witness bunch to measure the kicks due to the drive bunch by varying the bunch separations in order to map wakefields.

We would like to measure the transverse wakefields of a fully-featured accelerating structure as a function of distance behind a driving bunch. The driving and the witness bunches must be separately positrons and electrons in order to separate trajectories and achieve sufficient resolution in the downstream beam position monitors (BPMs), which measure the deflecting angle. This angle is in inverse proportion to the energy of the witness bunch. The achievable resolution of the wakefield will depend on beam energy, driving bunch charge, beam offset and BPMs resolution. The absolute value of the wakefield can be increased by installing multiple structures. Bunch length should be ideally less than 1 mm in order to resolve the third dipole band which shows up a peak around 40 GHz in the real part of the impedance spectrum.

### **3.12.3 Measurement of collimator transverse wakefields**

Another experiment to be performed at SLAC is the measurement of collimator wakefields. Collimator wakefields in the Beam Delivery System (BDS) of future linear colliders, such as the ILC and CLIC can be an important source of emittance growth and beam jitter amplification, consequently degrading the luminosity. For this reason it is vital to understand and measure such collimator wakefields both theoretically and experimentally. Single-bunch collimator wakefields have been measured in [122, 123, 124, 125] with the aim of benchmarking theory, numerical calculations and experiments. Those studies revealed some discrepancies between the measurements and the theoretical models. Given the characteristics of such wakefields, a lower energy beam with short bunches is required. The perfect candidate for such measurements is the beam provided by the End Station Test Beam (ESTB) test facility at SLAC.

New measurements using ESTB at SLAC will help to understand the origin of the above-mentioned discrepancies. For a rigorous comparison between measurements, theoretical calculations and simulations, the precise measurement of the bunch length will be essential. We are especially interested in the regime of short bunches relevant for the CLIC studies. This experimental test uses several collimator prototypes with different materials and geometric design, with the system set up to provide bunches with longitudinal length as close as possible to the nominal CLIC bunch length. We will compare the measured wakefield kick factors with simulation and analytic calculation results.

## ***3.13 FEL R&D or ‘A particle beam physics research program at the FACET-II’***

### **3.13.1 Introduction**

Particle beam physics is at the core of the development of new instruments for the exploration of the properties and organization of matter at the sub-atomic, atomic and molecular scale with increasing space-time resolution. High energy accelerators, are the instruments that allowed the development of the standard model of elementary particles, and are now opening the exploration of atomic and molecular science with the resolution of angstroms and femtoseconds.

A strong and robust program of research in the physics of particle beams and their interaction with lasers and plasmas is critical as we continue to expand the capabilities of particle accelerators, while reducing their cost and size. The program must have a theoretical/numerical simulations component and a strong experimental component to verify calculated expectations on a large scale. National laboratories such as SLAC have the facilities needed to carry out the research and are the natural medium for this activity. The program should also have a strong university component, essential for educating the new generation of scientists in this field. The university component can and should include some smaller “university scale” experiments as well. We can prove many concepts with experiments at existing, medium size, accelerator test facilities, such as the Accelerator test facility at Brookhaven National Laboratory or NLCTA at SLAC, using beam energies in the range of 50 to a few hundred MeV.

There is a large class of important, frontier experiments requiring electron beam energies larger than a few GeV. One such class of experiments is that of laser/plasma accelerators. Another class is the acceleration and manipulation of high brightness electron beams, including manipulation with lasers, used for synchrotron radiation sources and FELs, discussed in section 3.13.2.

In the following sections we describe several experiments. It is important to notice that while these frontier experiments may vary in their primary goal, the beam physics, the required instrumentation and the theoretical/numerical tools have much in common. There is a strong synergy between the these

types of research and the facilities needed for experimental proof. The advances in laser/plasma accelerators, with the capability of producing accelerating fields of 1 GeV/m or larger, is an important step toward reducing the cost and size of hard x-rays FELs and advancing particle physics. The improved knowledge of how to transport high brightness beams while preserving their 6-dimensional phase space and measuring their characteristics will be extremely useful for advances in laser plasma accelerators and their applications.

There are four lines of research to improve the performance of existing FELs and open the way to the next generation of these photon sources:

- Quality and control of the electron bunch - the lasing medium and the 6-dimensional phase space distribution;
- Quality and control of the FEL photon pulses, including transverse and longitudinal coherence, peak power, and spectral power density;
- Special features important for experiments using the photon pulses, are tunability, synchronization, polarization control, intensity stability, pulse duration, and multicolor FELs;
- Maximization of the energy transfer from the electrons to the photon pulse. Increasing the number of coherent photons generated per electron.

### 3.13.2 Electron beam - brightness for next-generation FELs

The FEL lasing, its gain length and many other characteristics depend strongly on the electron brightness and 6-dimensional phase space distribution. The phase space distribution is determined by the electron source, the acceleration and compression process, and a variety of collective effects, including coherent synchrotron radiation, wake fields in the linac, longitudinal space charge effects and more. The present state of the art is good enough to power a SASE FEL down to a few Ångstrom wavelengths. However, the peak current is limited by CSR effects, and the distribution is not ideal for the lasing process. A typical example of longitudinal distribution of the electron bunch at the LCLS undulator is shown in Figure 3.44.

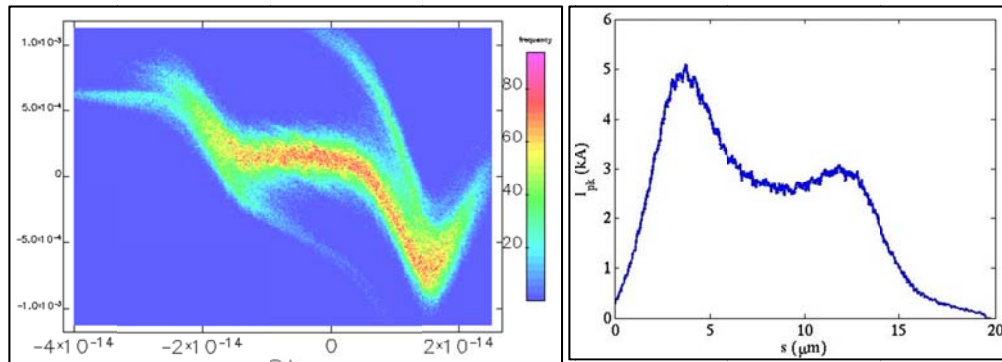


**Figure 3.44. Start-to-end simulation of the longitudinal distribution of the LCLS electron bunch.**

The current and energy spread change along the bunch, thus changing the local gain length, a situation similar to that of a conventional atomic laser where the density and temperature of the lasing medium change along its length. The less than ideal current and energy profile limit the transverse and longitudinal photon pulse coherence, and the effectiveness of seeding, self-seeding or iSASE. It also reduces the peak power obtainable when tapering the undulator.

Improving the 6-dimensional phase space distribution and making it nearer to the ideal condition for driving an FEL is a difficult task, requiring the development of new methods to: compress the beam to

achieve the high current needed to drive an FEL, better control and possibly take advantage of collective instabilities, shape the beam temporal profile, and optimize the electron current generated by the gun. Improved higher resolution diagnostics to characterize high brightness, very short (femtosecond duration) electron and photon pulses, as well as hundreds of femtoseconds long bunches needed for very small radiation line width. are also a challenge and in need of continuous development. It will also need the development of higher resolution phase space diagnostic instrumentation

Examples of possible studies include, but are not limited to: shaping the temporal and special profile of the electron current from the gun to minimize linac wakefield effects, using velocity bunching in the injector to minimize downstream magnetic compression, introducing nonlinear elements in the bunch compressors. These experiments are time consuming and require the flexibility to modify critical components such as the electron gun, linac, compressor system, thus making it impossible to execute in a user facility FEL such as LCLS. Study and proof of techniques to reduce the RF jitter from the power sources is another crucial program as jitter in the RF amplitude and phase translates to electron beam energy jitter in the accelerator and a chirp in the photons.

### **3.13.3 SASE FELs and longitudinal coherence**

Hard x-ray FELs now in operation operate in the SASE mode, the typical photon pulse line width is given by the FEL parameter,  $p$ , of about  $10^{-3}$ , and the temporal profile consists of spikes with length proportional to the cooperation length. Each spike has a transform limited line width, again on the order of  $p$ . Very short photon pulses of a few femtosecond duration, consisting of a few spikes, have been obtained at LCLS at SLAC by two methods: 1) reducing the electron bunch charge and compressing its duration to a few femtosecond; 2) filtering the electrons through a foil to spoil their emittance except for those in a very short part of the bunch.

The generation of very short photon pulses is one line of development for soft and hard x-ray FELs. However, the small number of lasing electrons limits the number of photons in a pulse. For larger bunch charges and longer photon pulses with many spikes, the longitudinal coherence is well above the transform limit.

Much attention and work has been dedicated to improving the longitudinal coherence for long bunches and reducing the line width to values between  $10^{-4}$  and  $10^{-5}$ . The methods proposed include seeding the electron beam with external lasers, and self-seeding. More recently an idea was proposed at SLAC to implement a corrugated pipe to induce strong longitudinal wakefields, which can be used to manipulate the chirp in the beam energy. [126] Calculations to prove this principle at lower energies and some experiments at about 60MeV to confirm the theory were conducted [127,128]. We need to conduct a full-scale demonstration using high brightness GeV beams with parameters similar to the beams at the entrance to the wiggler to validate the use of the technique on FEL accelerators. Another recent proposal, called the improved SASE (iSASE), is to insert electron delay lines between the undulator sections to discretely increase the photon/electron interaction instances within the bunch to increase the SASE gain [129]. This experiment also requires a full scale experimental facility. An R&D program should include experimental assessments of the most promising methods, explore the capabilities of each technique and characterize their technology requirements.

For the studies of these techniques, in particular the external laser seeding (which requires imprinting an external energy modulation on the electron beam, which then causes the beam to bunch further and using the higher harmonics of the initial bunching) it is important to have a beam of a few GeV energy, similar to that required for soft x-ray FELs and high brightness beams. The preservation of the bunching from the seeding point to the radiating undulator and the study of nonlinear effects in the harmonic

generation are important and can only be realistically studied with a beam energy not too far from that of the beam energy required for the FEL.

### **3.13.4      Polarization control, multicolor FELs, synchronization and other special features**

A GeV class test facility is needed with enough space dedicated to the undulator systems to test methods of varying and controlling the photon polarization, generating prescribed multicolor photon beams, and developing techniques to synchronize x-ray pulses with other laser pulses for pump-probe experiments down to the femtosecond level.

Multicolor pulses can be generated by using different undulators on the same electron beams or possibly with other techniques such as electron beam energy chirping by use of external lasers. The proposed facility offers the unique opportunity to utilize the beam generated by a laser/plasma accelerator to drive an FEL, possibly using undulators with a transverse magnetic field gradient to compensate for large energy spread in the electron beam generated by plasma accelerators. If successful this opportunity for a novel way to drive the FEL would have an important impact on the design of future coherent photon sources, reducing the cost and size of these facilities and making them available on a wider scale.

### **3.13.5      Terawatt peak power FELs**

Increasing the peak power and reducing the pulse duration of the x-ray pulse can have an important impact on single shot imaging experiments, making possible the imaging of a single molecules. This goal can be achieved using tapered undulator if the longitudinal coherence of the photon pulse is increased with respect to the SASE case, reducing the line width to  $10^{-4}$  or better. The studies of the longitudinal coherence, and the related longitudinal phase space distribution are critical for this possibility.

An alternative to the tapered undulator approach is to use a high charge, long, energy chirped electron bunch to drive the FEL, generating a long photon pulse with a frequency chirp. The chirp could be of the order of 1% in energy and 2% in frequency. The photon pulse, initially in the few hundred femtosecond region, can then be compressed with a double grating system to a pulse length of about 10 fs, with a corresponding increase in peak power. The large frequency band can be useful in imaging, in particular to reduce the number of diffraction patterns needed for 3-dimensional sample reconstruction. The electron energy chirp can be further enhanced with specially designed vacuum pipe as wakefield generator, which can be tested on the FACET-II beamline.

### **3.13.6      Seeding Methods**

We present several schemes for seeding that should be pursued.. These schemes each have distinctive requirements and areas for concern, and may best be studied at dedicated test facilities. We also discuss issues can apply to any FEL scheme, seeded or otherwise, although some are more relevant or suited to certain design types than to others.

#### ***3.13.6.1 Self-seeding***

Self-seeding is a straightforward extension to SASE FELs that can ideally yield coherent output, or at the minimum a significantly reduced bandwidth and thus increased spectral brilliance. Researchers at SLAC have demonstrated a self-seeding scenario [130] At the beginning of 2012 the LCLS implemented hard x-ray self-seeding with a single diamond monochromator. This scheme is currently limited to a pulse duration of the order of 10 fs. To produce x-rays with even narrower bandwidth, we can investigate different crystals and alternative self-seeding configurations, such as using two bunches.

For soft x-ray applications, R&D is focused on various monochromators that provide high resolving power, tunability, and small optical delay to reduce the electron chicane requirements. Soft x-ray self-seeding R&D efforts can be pursued at the LCLS as well. The main challenges are how to achieve tight synchronization, and how to improve the resolving power of the monochromator to yield a coherence length of 100s of fs (a bandwidth below 20 meV).

The Enhanced Self-Amplified Spontaneous Emission (ESASE) technique could resolve some of the synchronization issues by providing an alternative method to link the output to an external laser. It also provides an alternative method to changing the electron bunch length for controlling the pulse length and can be applied to generate short pulses, as described below. Cross-correlation between x-rays and experimental lasers is needed to provide the necessary time stamp.

R&D in this area has several goals. We need to improve soft x-ray monochromators by reducing bandwidth and increasing tunability, which implies R&D on optical systems. It is important to test optimal placement of monochromators, verify improved brilliance, and explore tapering. With ESASE, we can evaluate these techniques in combination and develop required laser cross-correlation technology. Most of these goals can be met at existing facilities or involve component R&D that do not need to be incorporated into a full FEL facility. However, since lower bandwidth monochromators deliver less power to the second stage of the FEL, the minimum power levels required for coherent output need to be experimentally observed. This does require a full FEL facility, although the scaling for the required power can be verified without achieving 1 nm wavelength.

### ***3.13.6.2 High Gain Harmonic Generation***

High Gain Harmonic Generation (HGHG) is a standard harmonic generation scheme and has recently been successfully implemented in the FERMI FEL operation down to 20 nm radiation wavelength. The expected effective harmonic conversion factor for a single stage HGHG is about 10. In order to go to shorter wavelengths, the concept of the “fresh bunch” cascaded HGHG has been proposed. The scheme can be sensitive to beam timing jitters and various errors can be accumulated through the cascading process.

R&D should focus on demonstrating cascaded HGHG at higher harmonic radiation wavelengths. This research can be carried out in SDUV in SINAP, SDL in BNL and FERMI FEL in Trieste.

While the HGHG operates in the nonlinear regime and does not require much FEL gain, the power radiated by the electron bunch is critical for the scheme. Thus, there are constraints on minimum current and maximum emittance for this scheme to work. While it would be preferable to observe HGHG reaching 1 nm output, a well-characterized FEL output one harmonic jump away from 1 nm, in the range of 5 to 10 nm, should be sufficient for R&D needs.

### ***3.13.6.3 Echo Enabled Harmonic Generation***

Echo Enabled Harmonic Generation (EEHG) is a novel beam manipulation concept using two seeded lasers, and is currently under intense study in several laboratories. The scheme has the potential to go directly to a higher harmonic number well beyond a factor of 10. However, going beyond a factor of 100 (to reach soft x-rays from UV laser) presents tough challenges due to physical effects such as intrabeam scattering and incoherent and coherent synchrotron radiation, as well as practical effects such as tolerance, jitter, and imperfection of laser and electron beams. R&D should focus on better understanding and modeling of these physical and practical effects. The strictest requirements are on the second seed laser with tolerances that depend on the ratio  $\lambda_2/\lambda_{x\text{-ray}}$ . Demonstrations of EEHG

beyond a factor of 10 as well as reaching shorter wavelengths are critical, and are planned at NLCTA at SLAC, SDUV in SINAP, SDL at BNL and FLASH at DESY.

EEHG involves purely external manipulations of the electron beam, with radiated power during the seeding stage actually being a deleterious effect. The manipulations themselves are very complex and produce a delicate phase space structure, so it is crucial to demonstrate bunching at the 1 nm wavelength. While FEL radiation and gain are helpful indicators of success, they could in theory be replaced by accurate slice diagnostics of the beam.

#### ***3.13.6.4 HHG (at-wavelength and cascaded)***

This direct seeding method uses a High Harmonic Generation (HHG) process in a noble gas to produce attosecond pulses with enough power at very short wavelengths to overcome incoherent shot noise. The broad bandwidth of HHG systems is not well matched to the FEL bandwidth, dropping the effective efficiency of the seeding process. Typical efficiencies for state-of-the-art systems are on the order of  $10^{-6}$  and fall significantly lower below 10 nm wavelength. Several optical elements are necessary to transport and focus the HHG source to the undulator entrance, causing further losses. As a result, power requirements for the HHG driver are daunting. Combining an Extreme Ultraviolet High Harmonic Generation (EUV HHG) source with a single-stage HGHG or EEHG in a hybrid approach may enable us to reach soft x-rays of nm wavelengths. R&D can be carried out at FLASH, SPARC and elsewhere.

Key R&D efforts include improving total efficiency from the HHG drive laser to FEL output and optimizing transport of HHG output radiation. We can either reduce HHG bandwidth at a given high harmonic, or explore filtering of the HHG source. It is important to test FEL output beam quality both at the selected HHG target wavelength and at an x-ray harmonic.

Even more so than in the HGHG scheme, radiation by the electron beam is a crucial aspect of HHG seeding. The seeding begins in the small-signal regime, requiring a large amount of FEL gain. Still, the FEL performance could be characterized in the 5 to 10 nm range and then extrapolated to a final harmonic jump to 1 nm. There might be some advantage in varying the tradeoff between bunch compression and energy spread in order to make the effect of HHG seeding on the beam more readily apparent.

#### ***3.13.6.5 FEL efficiency and high peak power***

As electron beam power is a limiting factor, improving the efficiency of energy conversion from the electron beam to the radiation pulse is a major priority. This becomes especially important when applications require pulses of short duration with a large number of photons. Typical SASE FELs have an efficiency on the order of  $10^{-3}$ , which can be modestly increased through tapering. Simulations suggest seeded FELs can be tapered much more effectively with an order of magnitude improvement. After succeeding with the self-seeding experiment, LCLS can be the ideal place to carry out R&D with increased taper strength and additional undulators, potentially producing a TW-class FEL. High power may also allow one x-ray pulse to be split and delivered to several experimental stations, increasing the capacities of x-ray FELs.

#### ***3.13.6.6 Harmonics and short wavelength optimization***

Nonlinear 3rd and 5th harmonics allow for radiation at significantly shorter wavelengths than what is practical at the fundamental resonant wavelength for a given electron beam energy. Typical measured power levels at LCLS and FLASH are 1% for the 3rd harmonic and 0.1% for the 5th harmonic, as a fraction of the fundamental power level. With a tapered undulator, simulations predict reaching a few percent of the power level in the fundamental on the 3<sup>rd</sup> harmonic under some conditions. This

potential enhancement should be explored further. Harmonic afterburners that are not effective at the FEL gain can still produce enhanced radiation at short wavelengths if placed after the saturation when a subharmonic pulse has been reached.

#### **3.13.6.7 *Polarization control***

Polarization control can be carried with an afterburner undulator, tuned to either the upstream wavelength or a harmonic, as described above. A pair of undulators in crossed geometry and a phase shifter in between is an alternative method, which may allow more rapid variation of polarization but with less control of stability. R&D can be carried out at FERMI@Elettra with APPLE undulators and is planned at LCLS with a DELTA undulator.

#### **3.13.6.8 *Pulse duration and bandwidth***

Coherent pulses are desirable for many applications. Low-bandwidth pulses with transform-limited duration of hundreds of fs are also useful, but may require a post-FEL monochromator. In the opposite limit, attosecond pulses, especially synchronized as part of a pump-probe configuration, have many applications. Various techniques have been proposed to reduce the x-ray pulse length below a femtosecond. The spoiler foil has been successfully tested. Other promising techniques include: compressing few-pC electron bunches; ESASE or ESASE-like bunch manipulation; and variants of EEHG and HHG using a few-cycled seed laser. Methods for pulse shaping and control are also important goals.

#### **3.13.6.9 *Beam quality and consistency***

Jitter in the FEL output should be reduced as much as possible. In addition to designing for low jitter in timing, pulse energy, and wavelength, diagnostics for both electron beam and radiation fields and feedback control are important areas of R&D. Many applications require longitudinal and transverse coherence. While SASE typically offers ~80% transverse coherence, seeded beamlines may yield even better results. Laser-seeded FELs must contend with the multiplication of phase variations (e.g., frequency chirp) by the total harmonic jump.

#### **3.13.6.10 *Justification and priorities***

A full scale test facility is needed to test the most promising schemes explored and developed and experimentally demonstrated at various laboratories. Such a full scale demonstration is important prior to implementing the novel schemes at user facilities.

For hard x-rays, self-seeding is likely the only viable approach for seeding. For soft x-rays, EEHG is the best risk-reward scheme, and should be aggressively pursued. Self-seeding is also a very viable option with possibly a modest loss in capabilities. R&D on hard and soft x-rays is already being pursued at LCLS and should be expanded upon. HHG seeding and other short-wavelength sources to a large part depend on external developments in the field; however, the criteria for a good laser for seeding an FEL are distinct from those for atomic physics research, and thus some guided HHG development is desirable, especially for trains of pulses with narrow bandwidth at a given harmonic. Also, HHG seeding with a single pulse is a good candidate for producing an attosecond pulse. Other ideas for generating attosecond pulses, such as using short electron bunches or variations on the EEHG scheme, are important to pursue as well. Work on an HGHG cascade is underway at FERMI@Elettra, and its requirements are essentially a subset of what is necessary for studying the EEHG scheme.

Improving the photon intensity is an important aspect to enhance the capabilities of a given FEL facility. The efforts will allow for more science to be done at a single FEL beam-line. A full FEL beamline with enough undulator to go past the conventional saturation point should be aggressive pursued for these

studies. Optimization of FEL harmonics production can improve the photon energy reach and/or reduce the linac cost.

Polarization control requires a functioning FEL but does not require going to saturation, in fact it is expected not to work well at saturation. As improvements in undulator technology may solve this concern, this is a lower priority item. Again, it is less important to operate at 1 nm for these studies.

Synchronization, generating repeatable, high-quality electron beams, measuring sub-fs pulses accurately, and other diagnostics are important issues but do not require a functioning FEL to pursue. To study repeatability and uniformity of the electron beam, a priority item is to work with an at least 2 GeV and high beam quality electron beam which is compressed to the order of 1 kA current, and to use some combinations of laser heater, third harmonic cavity, and wakefield enhancement device in order to flatten the energy profile and damp small-scale instabilities. Other desirable R&D consists of studies of independent components which will be discussed in the section on diagnostics and control systems.

### **3.14 FACET-II THz Studies**

The terahertz (THz) region of the electromagnetic spectrum represents a largely unexplored and untapped tool with respect to manipulating and controlling phases of matter using light. When we apply intense THz fields to samples we have the potential for conditioning or controlling matter, stimulating it with surgical precision, and exploring pathways to induce new phases not accessible via other means. An ultrashort single-cycle THz light pulse (see Figure 3.45) has a frequency that is resonant with the bonds that hold materials together (~1-20 THz) and is capable of biasing a material or device on time-scales of order 100 femtoseconds.

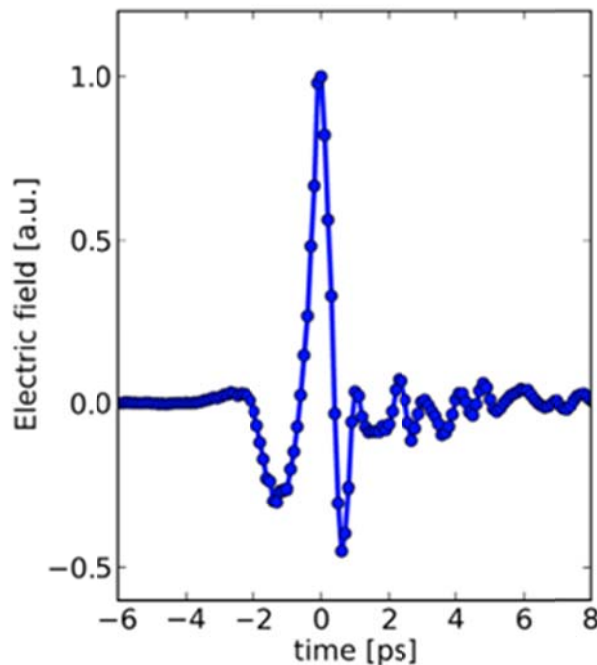


**Figure 3.45. THz electric field temporal profile**

The bonding strength of materials corresponds to energies of around 1 eV, with the spacing between atoms of a few Angstroms. The ratio of these numbers gives electric fields on the order of 0.1 - 1 V/Å (10-100 MV/cm), which sets the scale of fields that are required in order to exert a non-perturbative

influence on the structure of solids all-optically. These fields correspond to electromagnetic energy densities of 1 to 10 GPa, comparable to the pressures required to synthesize new phases of matter in diamond anvil cells.

There is a long history of using lasers and various nonlinear optical down-conversion techniques to generate single cycle THz light fields, and field strengths are now on the order of 1 MV/cm. While these approaches are being continuously improved, there is no clear pathway towards reaching the field strengths noted above in the frequency range of interest. [131] Accelerator-based sources, making use of the large electric and magnetic fields associated with a relativistic electron bunch, provide a means of reaching fields at the level of 1 V/Å. Indeed, at 0.35 nC bunch charges, experiments at using the SLAC linear accelerator have demonstrated peak fields of around 0.4 V/Å with higher fields possible . [132] Similar fields are possible at FACET now, with peak energies around 1 mJ. Recent experiments also using the SLAC linac have demonstrated that these fields can be used for switching of magnetic materials. [133, 134] Figure 3.46. shows a historical summary of the THz electric fields generated by both laser-based and accelerator-based sources.

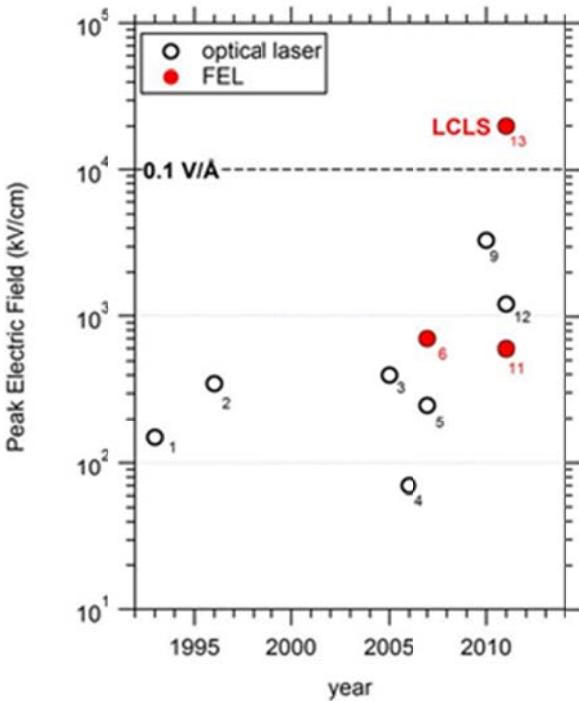


**Figure 3.46. Historical summary of peak THz electric field, comparing laser-based and accelerator-based sources.**

The interaction of THz fields in this parameter space with matter is only just beginning to be explored. The science case is broad, with opportunities spanning atomic and molecular to condensed phase systems. We described a few examples in the sections that follow.

### 3.14.1 THz manipulation of atoms in the solid state:

Whereas many nonlinear THz-driven responses associated with electron motion in materials have been observed [135, 136, 137, 138, 139] over the last decade and more, studies in which these fields are used to directly manipulate atomic positions are in their infancy. In parallel with the magnetic switching studies, the electric field of single cycle THz fields can be used to manipulate and unravel the coupled

structural and electronic degrees of freedom and the complex phase transitions that underlie the emergence of ferroelectricity and multiferroicity, in which the ferroelectric polarization is encoded through atomic displacements within the unit cell. Through vibrational excitation and all-optical application of intense single-cycle fields, [140] these measurements will enable discovery of means for programming these materials with light and controlling the microscopic pathways that the atoms and electrons follow along their potential energy surfaces, which in turn determine their functional properties. In recent experiments at the LCLS, [141] we have shown how large amplitude modulations in the internal electric fields within ferroelectric  $\text{PbTiO}_3$  nanolayers are reflected in atomic-scale motions within the unit cell, elucidating the first steps in the photovoltaic response of these materials. The THz fields generated by FACET-II may be used to directly reorient or switch the polarization, or induce specified electrical, electromechanical, or structural responses, effectively guiding these systems along well-defined atomic-scale trajectories. We will be able to couple these THz fields with absolutely synchronized probe pulses also generated by the FACET-II electron beam.

### 3.14.2 THz manipulation of electrons and spins

Relativistic electron beams at FACET-II represent a truly unique source of intense half cycle electric and magnetic field pulses that are the closest analog to an electric switch operating at THz speeds. They enable novel forms of controlling the behavior of electrons and spins in future devices relevant for information technology. While transition-metal oxide electronics based on electric field driven metal-to-insulator phase transitions is one of the most promising avenues towards energy efficient field-effect transistors, [142] switching the magnetization direction in ferromagnetic transition metals by electric fields alone, i.e. without dissipative electric currents, can be considered as the holy grail of energy efficient magnetic data storage. Both goals can be attacked using the unique x-ray and THz capabilities available at FACET-II.

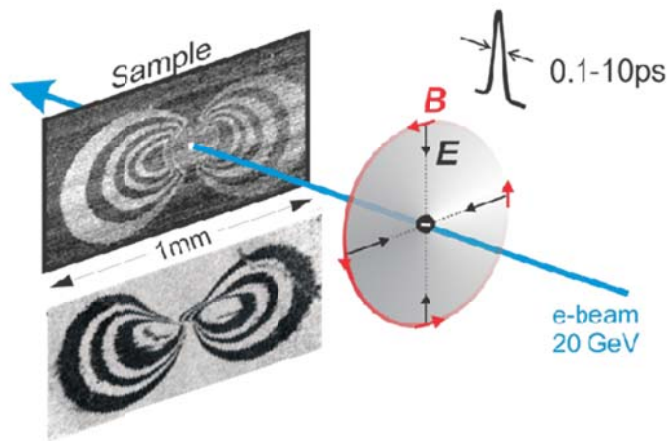


**Figure 3.47. Schematic of the magnetic switching experiment using an ultrashort electron bunch surrounded by a magnetic and electric field. [133]**

Ongoing magnetic switching experiments at FACET demonstrate the feasibility of such an approach (Figure 3.47). The high-energy electron bunch traverses the magnetic sample with an in-plane easy axis, imprinting a figure-eight magnetic pattern that depends on the number of electrons in the bunch and the temporal length of the bunch. Before exposure to the beam the sample is uniformly magnetized in-plane. When using 140 fs long pulses a characteristic deviation from an ideal figure-eight pattern (observed for ps long pulses) occurs. This deviation is ascribed to the influence of the electric field as

indicated by the simulation shown in the lower panel of the figure. Such experiments currently employ a post mortem analysis of the magnetic switching patterns.

The availability of femtosecond laser probe beams at FACET-II opens up radically new ways of probing transient electronic and magnetic states. It will enable us to study femtosecond electron dynamics in epitaxial transition metal oxide films undergoing an insulator-to-metal transition induced by THz electric-field pulses ( $\sim 0.1\text{GV/m}$ ). [143] Obtaining laser snapshots of the evolving electronic structure in a single-shot fashion is essential to the fundamental understanding of pure Mott-Hubbard-like switching of electrical conductivity without dissipative lattice transformation.

Current methods often require repetitive measurements near the damage threshold [143]. We need to go beyond that to understand the fundamental processes and develop new materials that can withstand the required electric fields. Such studies can also be extended to ferromagnetic metals, where even higher THz fields ( $>1\text{GV/m}$ ) can alter the electronic structure significantly, [133] leading to novel forms of magnetization switching. Our final goal of such switching experiments is to determine the coherence time of THz electronic excitations driven by the intense electrical field pulses. While electronic dephasing and lifetimes have been studied in detail for the optical frequency region less is known for low-energy excitations in the THz spectral range. The unique availability of electron-positron bunch pairs with variable temporal spacing at FACET-II would finally open up the possibility to study the influence of electronic coherence in the time domain. Only for a coherent electronic motion would the subsequent positron bunch restore the initial electronic and spin configuration.

### **3.14.3 THz radiation to trigger surface chemical reactions**

Many processes relevant to society, such as catalysis in chemical and energy production, the fabrication of computer chips, weathering and corrosion, the behavior of biomaterials and the fate of contaminants in the environment, rely on surface chemical reactions. . Catalytic reactions are driven thermally. These thermal excitations include phonons (substrate lattice vibration), frustrated vibrational motion of molecular adsorbates, and translational and rotational motion of molecular adsorbates (Figure 3.48A). When the excitation of these vibrations mediates the nuclear motion along the reaction coordinate, chemical reactions cause bonds to either break or form.

FACET-II provides opportunities to develop ways to stimulate chemical reactions on surfaces by triggering the motion of nuclei using THz radiation generated by an ultra short electron bunch. Assuming an electron pulse width of 100 fsec, broadband radiation is obtained with a high frequency cut-off at 10 THz, which matches the frustrated vibrational motions of adsorbed species on the surface. Both the frequency of THz radiation and the strong, directional electric field are of major interest. The coherent and broadband character of THz radiation from FACET-II generates a strong electric field,  $>1\times 10^9\text{ V/m}$  (or  $>0.1\text{ V/\AA}$ ). The quasi half-cycle pulse character of the radiation corresponds to a strong ultrashort half-cycle unipolar pulse. We envision using this strong electric field to excite frustrated vibrational motions collectively to drive a chemical reaction (Figure 3.48B). [144]

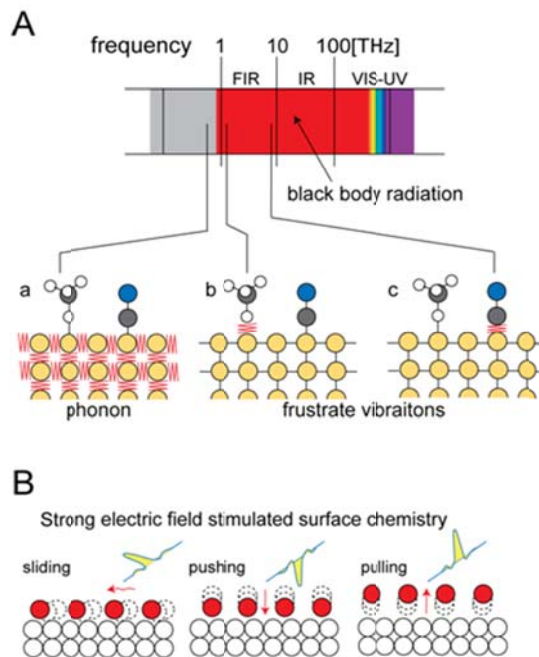


**Figure 3.48. A)** Excitation at surfaces: a) lattice vibration of the substrate (phonon), b) frustrated vibrational motion of the physisorbed (weakly adsorbed) species, c) frustrated vibrational motion of the chemisorbed (strongly adsorbed) species. The arrows indicate the maximum frequency of black body radiation at room temperature. **B)** Excitation of frustrated motions collectively using half cycle electric field pulse in different directions to the surface.

In addition to the field strengths and pulse shapes noted above, a key aspect of these studies involves generating synchronized optical or infrared probe pulses to probe the dynamics driven by the THz fields. These can be generated by a phase-locked laser or directly by the same transition radiation process that has been employed at FACET to generate coherent THz fields (Figure 3.49). Here the optical transition radiation can be separated by a dichroic mirror from the broadband THz fields and used as an absolutely synchronized probe pulse to record chemical dynamics. Nonlinear optical probes, for example, allow for direct access to the structural symmetries of a crystal and can be used as powerful probe of the underlying atomic-scale dynamics. We have carried out preliminary studies along these lines using the LCLS electron beam with high fields and observed dynamic processes at these high fields not previously observed (Figure 3.49).

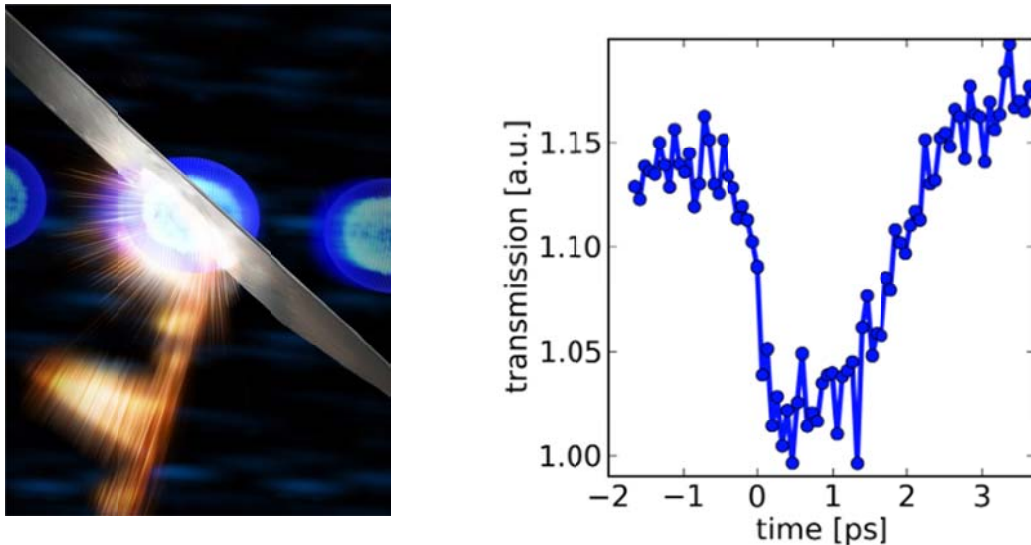


**Figure 3.49.** Schematic of coherent transition radiation process in which a femtosecond electron beam passes through a thin metallic foil in order to generate intense THz fields (left). First THz pump/optical probe studies of dynamics in GaAs in which pump and probe are simultaneously generated by the foil (right).

### ***3.15 National-Security and Fundamental Topics with Intense Beams of Photons of Energy 5 MeV and Greater Produced by Inverse Compton Scattering***

The DOE's National Nuclear Security Agency (NNSA) of the United States has instructed the nation's design laboratories to conduct full-system certification using a methodology called Science-based Stockpile Stewardship that is expressly absent any future full-scale test. In short, the Stewardship program must make the best scientific use of the cataloged data.

Were it possible, tests of nuclear weapons would include the confinement of the released energy (the yield) by a calorimeter, the temperature rise of which would provide a direct measure of the yield. Realistically, however, the yield is determined indirectly by a variety of other means. For example, the prompt yield is inferred from the output of gamma rays. [145, 146, 147] Radiochemical analyses of the atomic and isotopic constituents remaining in the aftermath of the explosion provide another, independent evaluation of the yield. Both methods of yield inference hinge on extant knowledge of instrument calibrations and photonuclear cross sections. Today, while the data may be stored and static, these methods remain active topics in search of better information on which to base their estimations.

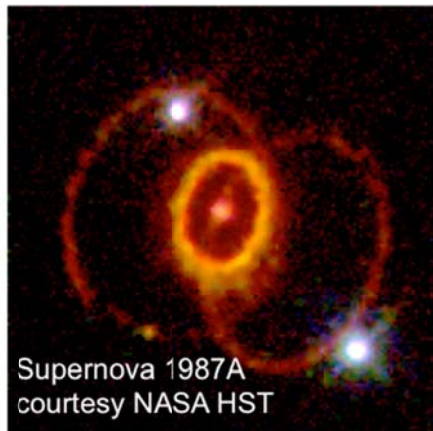


**Figure 3.50. Supernovas – the fiery death of massive stars where heavy-element nucleo-synthesis takes place – provide C, O and other elements of life.**

Our proposal for national security missions entails the use of FACET-II for reducing uncertainty in models tangible to stockpile stewardship, for example, to improve our understanding of absolute energy output. Other topics relevant to national security and undertaken with a bright, quasi-monoenergetic source of gammas of  $\geq 5$  MeV in energy include predictive capability of material damage, fundamental nuclear physics, and radiography. More advanced, if ambitious, uses of FACET-II are also of interest to the NNSA. The generation of coherent gammas for the manipulation of nuclear transitions in analogy with the coherent excitation of electronic transitions is but one example. Below, we outline some of the research areas of interest as well as introduce topics for general consideration at FACET-II.

### **3.15.1 Calibration of United States Nuclear Test Gamma-Ray Detectors**

This topic is of interest to science-based and predictive-capability Stockpile Stewardship programs at the LANL and LLNL. HFK detectors (high-frequency kinertium, the latter being a tungsten alloy) were used to measure gamma production from nuclear tests, and their data are archived. These detectors produced vital statistics that are recorded for significant events in United States Nuclear Test History, which ended in September 1992. Pulsed, spectrally-broad bremsstrahlung radiation produced at LINACS was used to calibrate the bandwidth response of HFK detectors. We remain far less certain, however, of the absolute energy calibration, or spectral response, of these detectors. To the extent that models carry uncertainties from this clouded aspect of archived data, a program in spectral calibration of HFK detectors becomes a matter of Stockpile Stewardship. For the calibration, we would chart the response of an HFK detector versus energy of an incident and reasonably monochromatic gamma beam. The gamma source at Duke University's HiS has the needed energy range but not enough flux. A gamma source at FACET-II, however, could deliver all the needed aspects of energy range, energy resolution, and flux.

### **3.15.2 Astrophysics and Stellar Nucleosynthesis**

Nuclear reactions in stars take place at temperatures between  $10^3$  and  $10^5$  eV, but the corresponding reaction rates are rarely measured below 1 MeV in the laboratory. Most rates used in stellar models thus come from severe extrapolations of the experimental data into the astrophysical-temperature regime. We offer as an example the lively controversy [148, 149] about the laboratory cross sections for  $^{12}\text{C}(\alpha, \gamma)^{16}\text{O}$  and consequences [150] of their theoretical extrapolation to the low energies at which the reaction effectively operates. As for the nomenclature of the reaction, the parenthetical  $(\alpha, \gamma)$  and ordering of nuclei means that  $^{12}\text{C}$  is the target bombarded by an alpha particle, which on collision

produces a  $\gamma$  and leaves  $^{16}\text{O}$ . The reaction affects the relative abundance of two atoms of which we are largely made, making it little wonder that the  $^{12}\text{C}(\alpha, \gamma)^{16}\text{O}$  problem is of paramount importance in nuclear astrophysics. Moreover, the ratio C/O following helium burning (of which  $^{12}\text{C}(\alpha, \gamma)^{16}\text{O}$  is a part) figures critically in the fate of massive stars, determining in some instances whether they collapse to black holes or neutron stars. The  $^{12}\text{C}(\alpha, \gamma)^{16}\text{O}$  cross section also appears in burning models and perhaps forensics of nuclear weapons.

Weller *et al.* at HlyS indicate that  $^{12}\text{C}(\alpha, \gamma)^{16}\text{O}$  cross sections are reported for energies no lower than 1.2 MeV and are in sufficient discord to make extrapolation to stellar-burning energies of 0.3 MeV treacherous. [149] The *inverse* reaction,  $^{16}\text{O}(\gamma, \alpha)^{12}\text{C}$ , however can be examined at HlyS and the cross section for  $^{12}\text{C}(\alpha, \gamma)^{16}\text{O}$  obtained by detailed balance. Calculations by Weller *et al.* showed that the then present  $5 \times 10^7 \gamma/\text{s}$  flux of HlyS at  $E_\gamma \approx 10 \text{ MeV}$  in 2009 was sufficient to inspect  $^{12}\text{C}(\alpha, \gamma)^{16}\text{O}$  at the equivalent energy of 1.5 MeV. An expected brightness upgrade for HlyS to  $\sim 10^{11} \gamma/\text{s}$  would push the equivalent energy far lower. Still greater fluxes, however, as might be produced at FACET-II, will be needed to measure the  $^{12}\text{C}(\alpha, \gamma)^{16}\text{O}$  cross sections accurately at the equivalent (incident alpha) energies of 300 keV and lower as relevant to nucleosynthesis in red giants (*cf.* Fig. 6 of Fowler [148]). In topics as diverse as stellar evolution, the nucleosynthetic origins of life's elements, and the outcome of silicon burning and the heavier elements that follow, much would be riding on such a foundational measurement.

Apart from  $^{12}\text{C}(\alpha, \gamma)^{16}\text{O}$ , there are numerous other reactions of importance in nucleosynthesis with still greater uncertainty. Weiss [151] lists ten *p*-capture processes (proton-capture nucleosynthesis, such as  $^{27}\text{Al}(p, \gamma)^{28}\text{Si}$ ) for which the uncertainties at stellar temperatures range from factors of 2 to nearly 2000. Specific isotopes of Na, Mg, and Al figure in these processes and range widely in their calculated abundances, often turning an estimated metallicity of a star into a hazardous guess. As with the  $^{12}\text{C}(\alpha, \gamma)^{16}\text{O}$  reaction, a FACET-II beam of high flux could interrogate nine of these *p*-capture processes at relevant stellar temperatures using the inverse reaction and detailed balance. Doubtless other nucleosynthetic processes are in need of similar clarifications.

### 3.15.3 Nucleon Compton Scattering and Tests of QCD

Experimental work on photo-disintegration of few-body nuclei at energies below the pion threshold (<145 MeV) probes the universal dynamics of nuclei (at low energies) and the effects specific to the nuclear force (at higher energies). With implications for the Gerasimov-Drell-Hearn Sum Rule, and their connections to quantum chromodynamics (QCD), such experiments are certain to stimulate collaborations between theorists and experimentalists, in particular toward understanding the way that QCD manifests itself in low-energy photon reactions. Weller *et al.* [149] capably motivates this area of research in the context of HlyS and conveys its excitement. We wish to call attention to the fact that HlyS is the only facility within the United States active in this nuclear-science subfield, while China, Japan, and Europe have either built new inverse-Compton gamma sources or are about to, for entry into this and other fields of photonuclear physics. It is crucial, we believe, for FACET-II to complement or exceed the capacity of HlyS in order for the U.S. to maintain an active international role in what appears to be the growing topical areas made possible by inverse-Compton gamma sources.

### 3.15.4 Polarizing and Probing the Quantum Vacuum

The vacuum is not inert. Since the beginnings of quantum electrodynamics in the mid 1930s, it has long been predicted that the vacuum in special circumstances can be a nonlinear medium through which photons interact. Strong electromagnetic fields, for example, can convert the vacuum into a birefringent and dichroic dielectric medium. Intense laser pulses available today provide high intensities of  $10^{22}\text{--}10^{24}$

$\text{W}/\text{cm}^2$  and associated strong electric fields of  $10^{12}\text{--}10^{13}\text{ V}/\text{cm}$  but are insufficient by themselves for us to witness vacuum polarization. The combination of intense lasers, a gamma photon source, and nuclear physics at FACET-II, however, could reveal the long-sought prediction of QED of elastic photon-photon interactions within the vacuum. We imagine that lasers capable of producing peak pulsed intensities of  $6\times10^{24}\text{ W}/\text{cm}^2$  are available. Propagating against this laser pulse in vacuum is a linearly-polarized gamma pulse of 10-MeV photons (generated by FACET-II). The net rotation of the beam that probes the vacuum polarization is proportional to the fluence of the intense laser pulse and the photon energy of the probe beam. The gamma energy of a probe beam can thus be a significant multiplier of rotation. Where the linear polarization of a visible-wavelength probe (<2 eV) would rotate <50 nanoradians when propagating against a  $6\times10^{24}\text{ W}/\text{cm}^2$  pulse in vacuo, the polarization of a 10-MeV beam rotates 0.25 rad (14 degrees). A probe-beam detector is necessary, and in this case involves a deuterium target. The known nuclear physics of the angular distribution of deuteron photodisintegration at 10 MeV can be used to deduce the polarization angle of the incident gammas. We offer this realizable experiment as but one example where extremes in energy and fields that exist in the separate disciplines of lasers and nuclear physics can be joined to bring about interesting and unique phenomena.

### 3.15.5 Diffraction, Imaging, and Coherent Excitation

Nuclear-resonant diffraction is not a new topic [152] but needs to re-examined for experimental use amid the coming generation of gamma sources produced by Compton laser-backscattering, as planned for FACET-II. Such sources of gammas are bright, quasi-monochromatic (energy resolution of  $\leq 1\%$ ), polarized, and tunable across the giant dipole resonances (GDRs) held by isotopes from tritium through transuranics. In analogy with visible optics, the GDRs have real and imaginary indices of refraction that can influence a diffraction pattern depending on the detuning of the gamma energy from resonance. Thus, complementary to x-ray diffraction and its sensitivity to electron density, nuclear diffraction of gammas would presumably have a tunable sensitivity to atomic constituents and positions. The gammas of Compton laser-backscattering are also expected to exhibit a partial spatial coherence, presenting the opportunity to image the structures of non-crystalline materials. Coherent diffractive imaging is applicable to spatially-coherent sources and is used, for example, at DESY and the LCLS in connection with their programs in 2-D imaging (and 3-D reconstructions) of biological molecules illuminated by x-ray, FEL light. A program in imaging would take into account the issue of pair production within the examined material and the mitigation of this problem through the latest or foreseeable advances in gamma-beam imaging or geometries. The combination of today's high-intensity lasers with advanced high-current sources such as FACET-II can also be examined for ways to produce spatially- and temporally-coherent gammas, for entry into the topic of coherent-excitation of nuclear transitions.

- 1 S. Corde et al, *Nature* **524** 2015
- 2 E. Adli et al SLAC-PUB-15426, [arXiv:1308.1145](https://arxiv.org/abs/1308.1145) (2013).
- 3 M.Tzoufras et al *Phys. Rev. Letts.* **101**, 145002 (2008).
- 4 T. Katsouleas et al, *Phys. Rev. A* 33,2056 (1986)
- 5 Seryi et al *Proceedings of PAC* May 4-8, pp. 1-3 (2009).
- 6 Huang et al *Phys Rev. Letts.* **99**, 255001 (2007).
- 7 W. Lu et al (2012). Unpublished manuscript.
- 8 M. J. Hogan et al *New Journal of Physics* **12**, 055030 (2010).
- 9 H.Suk et al *Phys. Rev. Letts.* **86**, 1011 (2007).
- 10 C.Geddes et al *Phys Rev. Letts.* **100**, 215004 (2008).
- 11 J.Shaw et al (2012). Unpublished manuscript.
- 12 C.E. Clayton et al *Phys. Rev. Letts.* **105**, 105003 (2010).
- 13 B.Hidding et al *Phys. Rev. letts* **108**, 035001, (2012).

- 
- 14 F. Li et al (2012). Unpublished manuscript.
- 15 T. Katsouleas and M.J. Hogan, Proposal to SAREC committee (2012).
- 16 D. Johnson et al *Phys. Rev. Letts.* **97**, 175003 (2006).
- 17 A. Caldwell et al., *Nature Physics* **5**, 363 (2009).
- 18 N. Kumar et al., *Phys. Rev. Lett.* **104**, 255003 (2010).
- 19 B.E. Blue et al., *Phys. Rev. Lett.* **90**, 214801 (2003).
- 20 M. J. Hogan et al., *Phys. Rev. Lett.* **90**, 205002 (2003).
- 21 P. Muggli et al., *Phys. Rev. Lett.* **101**, 055001 (2008).
- 22 J. Vieira et al., *Phys. Plasmas* **19** *Nature Physics*, 063105 (2012).
- 23 A. Caldwell et al., *Nature Physics* **5**, 363 (2009).
24. J. B. Rosenzweig, et al, *Nucl. Instrum. Method A* **593** 39 (2008).
25. R. Bonifacio, C. Pellegrini, and L. Narducci, *Opt. Commun.* **50**, 373 (1984).
26. R. Bonifacio et al., *Phys. Rev. Lett.* **73**, 70 (1994).
- 27 Y. Ding, et al., *Phys. Rev. Lett.* **102**, 254801 (2009).
28. M. J. Hogan et al., *Phys. Rev. Lett.* **95**, 054802 (2005).
29. I. Blumenfeld, et al., *Nature*, **445** 7129 (2007).
30. J.B. Rosenzweig, N. Barov, M.C. Thompson, R.B.Yoder, *Phys. Rev. ST Accel. Beams* **7**, 061302 (2004).
- 31 N. Barov, J.B. Rosenzweig, M.C. Thompson, R.B.Yoder, *Phys. Rev. ST Accel. Beams* **7**, 061301 (2004).
32. J.B. Rosenzweig, B. Breizman, T. Katsouleas and J.J. Su, *Phys.Rev. A* **44**, R6189 (1991).
33. D. L. Bruhwiler et al., *Phys. Plasmas* **10**, 2022 (2003)
34. J. K. Lim, et al., *Phys. Rev. ST Accel. Beams* **8**, 072401 (2005)
- 35 M. Borland, Advanced Photon Source LS-287 (2000).
- 36 D. Bauer and P. Mulser, *Phys. Rev. A* **59**, 569 (1999).
- 37 Calionn L. O'Connell, Stanford PhD thesis (2005).
- 38 Eric Mevel et al., *Phys. Rev. Lett.* **70** 406 (1993).
- 39 J.B. Rosenzweig, et al., *Nucl. Instr. and Methods A* doi:10.1016/j.nima.2011.01.073 (2011).
40. J.B. Rosenzweig, N. Barov, M.C. Thompson, R. Yoder, *Phys. Rev. ST Accel. Beams* **7**, 061302 (2004)
41. N. Barov, J.B. Rosenzweig, M.C. Thompson, R.B.Yoder, *Phys. Rev. ST Accel. Beams* **7**, 061301 (2004)
42. S. Lee, et al., *Phys. Rev. ST—Accel. Beams* **5**, 011001 (2002).
43. Tor O. Raubenheimer, in *11th Advanced Accelerator Concepts Workshop*, AIP Conf. Proc. 737, (AIP, New York, 2004), p. 86.
44. "Single-shot coherent diffraction imaging of microbunched relativistic electron beams for free-electron laser applications," A. Marinelli, et al, to appear in *Phys. Rev. Lett.*
45. J.B. Rosenzweig, A.M. Cook, A. Scott, M.C. Thompson, R. Yoder, *Phys. Rev. Lett* **95**, 195002 (2005)
- 46 . "The Quasi-nonlinear Regime of the Plasma Wakefield Accelerator", J.B. Rosenzweig, et al., *Proceedings of Advanced Accelerator Concepts 2010*, Annapolis, Md, USA (AIP, 2010).
47. Plasma wakefields in the quasi-nonlinear regime: Experiments at ATF, J.B. Rosenzweig, et al., to appear in *Proceedings of Advanced Accelerator Concepts 2012*.
48. P. Muggli, et al., *Phys. Rev. Lett.*, **101**, 054801 (2008)
- 49 N. Holtkamp, SAREC presentation, October 2012, <https://slacspace.slac.stanford.edu/sites/ard/facet/sarec12-2/Documents/Oct-2012-Presentations/FutureFACETTestFacilities-Holtkamp-SAR-Oct12.pptx>.
- 50 F. Oshea et al., *PRSTAB* **13**, 070702 (2010).
- 51 Richard Feynman, *Photon-Hadron Interactions*, Addison Wesley (1992).
- 52 J. Ballam, *Phys. Rev. Lett.* **23**, 498–501 (1969).
- 53 M. Gai, *Journal of Physics: Conference Series* **316**, 012033 (2011).
- 54 A.M. Bernstein et al., *Annu. Rev. Nucl. Part. Sci.* **59**, 115–44 (2009).
- 55 D. Choudhury, A. Nogga and D. Phillips, *Phys. Rev. Lett.* **98**, 232303 (2007)
- 56 K. Helbing, Proc. Third Int. Symp. On the GDH Sum Rule and its Extensions, Norfolk, USA, 28 (2004).
- 57 A. M. Sandorfi et al., *J Phys* **G38**, 053001 (2011).
- 58 Frank Close and Phillip R. Page, "Glueballs", *Scientific American*, **279: 5**, 80 (1998).
- 59 D. Babusci, *Il Nuovo Cimento*. **103**, N11, 1555 (1990).
- 60 <https://str.llnl.gov/AprMay11/pdfs/4.11.3.pdf>
- 61 [http://apc.fnal.gov/programs2/ASTA\\_TEMP/index.shtml](http://apc.fnal.gov/programs2/ASTA_TEMP/index.shtml).
- 62 Bern

- 
- 63 E. Ydrefors, *Proc. 4th International Symposium on Neutrinos and Dark Matter in Nuclear Physics*, <http://web.ias.tokushima-u.ac.jp/physics/nucl/NDM12/NDM12.html>, (2012).
- 64 J. Piekarewicz, *Phys. Rev. C* **83**, 034319 (2011).
- 65 D. Vretenar, et al., *Phys. Rev. C* **85**, 044317 (2012).
- 66 J. Piekarewicz, et al., *Phys. Rev. C* **85**, 041302 (2012).
- 67 C. J. Horowitz, et al., *Phys. Rev. Lett.* **86**, 5647 (2001).
- 68 E. Litvinova, et al., *Nucl. Phys. A* **823**, 26 (2009).
- 69 H. Utsunomiya, et al., *Phys. Rev. C* **84**, 055805 (2011).
- 70 A. Krasznahorkay, “Triple-Humped Fission Barriers,” *Handbook of Nuclear Chemistry*, Springer: Verlag, Berlin, 281 (2011).
- 71 P. Thirolf and D. Habs, *Prog. Part. Nucl. Phys.* **49**, 325 (2002).
- 72 Yoichiro Nambu, Nobel Lecture: “Spontaneous symmetry breaking in particle physics,” *Int. J. Mod. Phys. A* **24**, 2371 (2009).
- 73 S. Weinberg, *Trans. N.Y. Academy of Science, Series II* **38** (I.I.Rabi Festschrift), 185 (1977).
- 74 N. Fettes and U.G.Meiner, *Nucl. Phys. A* **693**, 693 (2001).
- 75 V. Baru et al., *Nucl. Phys. A* **872**, 69(2011).
- 76 D. Gotta, *Lecture Notes in Physics* **745**, 165 (2008).
- 77 Th. Strauch et al., *Eur.Phys.J. A* **47**, 88 (2011).
- 78 A.M. Bernstein, *Phys. Lett. B* **442**, 20 (1998).
- 79 B. Ananthanarayan, *Phys. Lett. B* **634**, 391 (2006).
- 80 A.M. Bernstein, et al. *Ann. Rev. Nucl. Part. Sci.* **59**, 115 (2009).
- 81 V. Baru et al., *Nucl. Phys. A* **872**, 69 (2011).
- 82 S.B. Gerasimov, *Sov. J. Nucl. Phys.* **2**, 430 (1966).
- 83 S.D. Drell and A.C. Hearn, *Phys. Rev. Lett.* **16**, 908 (1966).
- 84 M. Hosada and K. Yamamoto, *Prog. Theor. Phys.* **36**, 426 (1966).
- 85 B. Sawatzky, Ph.D. dissertation, “A Measurement of the Neutron Asymmetry in near Threshold,” University of Virginia (2005).
- 86 D. Choudhury et al *Phys. Rev. Lett.* **98**, 232303 (2007).
- 87 Nath, et al, *Nucl. Phys. A* **194**, 49 (1972).
- 88 H. Bethe and W. Heitler, *Proc. Roy. Soc. Lond. A* **146**, 83 (1934).
- 89 P. A. M. Guichon, M. Vanderhaeghen, *Phys. Rev. Lett.* **91**, 142303 (2003).
- 90 A. V. Afanasev, S. J. Brodsky, C. E. Carlson, Y. C. Chen and M. Vanderhaeghen, *Phys. Rev. D* **72**, 013008 (2005).
- 91 B. Aubert et al., *Phys. Rev. Lett.* **97**, 112001 (2006).
- 92 J. Beringer et al., *Phys. Rev. D* **86**, 010001 (2012).
- 93 R. Edwards et al., arXiv:1212.5236v1 (2012).
- 94 A.M. Sandorfi et al., *J Phys* **G38**, 053001 (2011).
- 95 T. Nakano et al., *Nuclear Physics* **A629**, 559 (1998).
- 96 J. Ellis et al., “SAPPHiRE: a Small gamma-gamma Higgs Factory”, arXiv:1208.2827 (2012).
- 97 G. Unel et al., “A Higgs” Factory at the Greek-Turkish Border” (2012). Manuscript submitted for publication, ESPG.
- 98 D. Asner et al., “Higgs physics with a gamma gamma collider based on CLIC I,” *Eur. Phys.J. C* **28**, 27 (2003).
- 99 T. Raubenheimer, “An SLC-Style Higgs Factory,” ICFA Higgs Factory Workshop “HF2012”, FNAL 14 November 2012.
- 100 Y. Zhang, “Design Concept of a - Collider-Based Higgs Factory Driven by Energy Recovery Linacs,” Jefferson Lab Technote JLAB-TN-12-053 (2012).
- 101 “ILC Reference Design,” <http://www.linearcollider.org/about/Publications/Reference-Design-Report>.
- 102 *The Linear Collider Physics Resource Book for Snowmass* (2001). pp. 333-345; <http://www.slac.stanford.edu/grp/th/LCBook/positron.pdf>.
- 103 CERN Report 2004-005: Physics at the CLIC Multi-TeV Linear Collider, editors; M. Battaglia, A. de Roeck, J. R. Ellis, and D. Schulte, p. 208; ISBN: 92-9083-226-6 <http://cdsweb.cern.ch/search.py?recid=749219&ln=en>.
- 104 F. Zimmermann et. al. , Positron Options for the Linac-Ring LHeC, IPAC'12, New Orleans.
- 105 V. Yakimenko, I.V. Pogorelsky, Polarized gamma source based on Compton backscattering in a laser cavity, *Phys.Rev.ST Accel.Beams* **9**, 091001 (2006).

- 
- 106 J. S. Berg, et al. “A Cost-effective design for a neutrino factory,” *Phys.Rev.ST Accel.Beams* **9**, 011001 (2006).  
107 ASTA proposal.  
108 V. Biryukov, Chesnokov Yu, V. Kotov, “Crystal Channeling and Its Application at High Energy Accelerators” (Springer–Verlag, Berlin, Heidelberg, 1997).  
109 K. Reil et al, “Measurements of the Fluorescence Light Yield in Electromagnetic Showers”, 22nd Texas Symposium On Relativistic Astrophysics, Dec. 13-17, 2004, Stanford, CA, SLAC-PUB-11068.  
110 D. Saltzberg et al., *Phys. Rev. Lett.* **86**, 2802 (2001).  
111 P. Chen and T. Tajima, *Phys. Rev. Lett.* **83**, 256 (1999).  
112 2001 Workshop on Laboratory Astrophysics, WP-020, SLAC.  
113 2003 Workshop on “Quantum Aspects of Beam Physics”, Hiroshima, Japan, P. Chen and K. Reil, editors (World Scientific Publ., Singapore, 2004).  
114 Second Orion Workshop, WP-026, SLAC, 2003.  
<http://www.slac.stanford.edu/pubs/slacwps/slac-wp-026.html>  
115 SABER Workshop, WP-070, SLAC, 2006.  
<http://www.slac.stanford.edu/pubs/slacwps/slac-wp-070.html>  
116 “HEDLA from 1996 to 2012”, R. Paul Drake, abstract for HEDLA 2012.  
[http://hedla2012.sc.fsu.edu/hedla2012/website/data/program/talk/paul\\_drake\\_t.pdf](http://hedla2012.sc.fsu.edu/hedla2012/website/data/program/talk/paul_drake_t.pdf)  
117 HEDLA 2012 meeting. <http://www.hedla2012.org/>  
118 N. Phinney, N. Toge and N. Walker (ed.), “LC Reference Design Report Volume 3 - Accelerator”, arXiv:0712.2361 [physics.acc-ph]  
119 Oh. Burrows et al., “ILPS Deliverable 2: Report on Luminosity Tuning and Control Strategies”, EUROTeV-Report-2008-090.  
120 J. Pfingstner et al., “An interleaved, model-supported system identification scheme for the particle accelerator CLIC”, *Proceedings of the 49th IEEE Conference on Decision and Control* (2010).  
121 A. Grudiev et al. “Design of the CLIC main linac accelerating structure for the CLIC conceptual design report”, *Proceedings of LINAC10*, Tsukuba, Japan (2010).  
122 P. Tenenbaum et al., “Direct measurement of the transverse wakefields of tapered collimators”, *Phys. Rev. ST-AB* **10**, 034401 (2007).  
123 S. Molloy et al., “Measurements of the transverse wakefields due to varying collimator characteristics”, *Proceedings of EPAC07*, Albuquerque, New Mexico, USA, FRPMS074 (2007).  
124 J. L. Fernandez-Hernando et al., “Measurements of collimator wakefields at End Station A”, *Proceedings of EPAC08*, Genoa, Italy, WEPP163 (2008).  
125 P. Tenenbaum et al., “Direct measurement of the resistive wakefield in tapered collimators”, *Proceedings of EPAC04*, Lucerne, Switzerland (2004).  
126 K. Bane and G. Stupakov, SLAC-PUB-14925 (2012).  
127 Emma, NGLS, 2012.  
128 S. Antipov, et. al. *Phys. Rev. Lett.* **108**, 144801 (2012).  
129 <http://accelconf.web.cern.ch/accelconf/IPAC2013/papers/weodb101.pdf>  
130 J. Amann et al *Nature Photonics* **6**, 693–698 (2012).  
131 Hirori, H., Doi, A., Blanchard, F. & Tanaka, K. “Single-cycle terahertz pulses with amplitudes exceeding 1 MV/cm generated by optical rectification in LiNbO<sub>3</sub>.” *Appl. Phys. Lett.* **98**, 091106 (2011).  
132 Daranciang, D. et al. “Single-cycle terahertz pulses with >0.2 V/Å field amplitudes via coherent transition radiation.” *Appl. Phys. Lett.* **99**, 141117 (2011).  
133 Gamble, S. J. et al. “Electric field induced magnetic anisotropy in a ferromagnet.” *Phys. Rev. Lett.* **102**, 217201 (2009).  
134 Tudosa, I. et al. “The ultimate speed of magnetic switching in granular recording media.” *Nature* **428**, 831–833 (2004).  
135 Wen, H., Wiczer, M. & Lindenberg, A. “Ultrafast electron cascades in semiconductors driven by intense femtosecond terahertz pulses.” *Phys Rev B* **78**, 125203 (2008).  
136 Hirori, H. et al. “Extraordinary carrier multiplication gated by a picosecond electric field pulse.” *Nature Communications* **2**, 594–6 (2011).  
137 Liu, M. et al. “Terahertz-field-induced insulator-to-metal transition in vanadium dioxide metamaterial.” *Nature* **487**, 345–348 (2012).

- 
- 138 Gaal, P. *et al.* “Internal motions of a quasiparticle governing its ultrafast nonlinear response.” *Nature* **450**, 1210 (2007).
- 139 Turchinovich, D., Hvam, J. & Hoffmann, M. “Self-phase modulation of a single-cycle terahertz pulse by nonlinear free-carrier response in a semiconductor.” *Phys Rev B* **85**, 201304 (2012).
- 140 Qi, T., Shin, Y.-H., Yeh, K.-L., Nelson, K. & Rappe, A. “Collective Coherent Control: Synchronization of Polarization in Ferroelectric PbTiO<sub>3</sub> by Shaped THz Fields.” *Phys Rev Lett* **102**, 247603 (2009).
- 141 Daranciang, D. *et al.* “Ultrafast Photovoltaic Response in Ferroelectric Nanolayers.” *Phys Rev Lett* **108**, 087601 (2012).
- 142 Zheng Yang, Changhyun Ko and Shriram Ramanathan, “Oxide Electronics Utilizing Ultrafast Metal-Insulator Transitions”, *Annu. Rev. Mater. Res.* **41**, 337 (2011).
- 143 M. Liu, et al, “Terahertz-field-induced insulator-to-metal transition in vanadium dioxide metamaterial”, *Nature* **487**, 345 (2012).
- 144 H. Ogasawara, D. Nordlund, A. Nilsson, SLAC-PUB-11503 (2005).
- 145 Langenbrunner, J.R., Booker, J.M. Ross, T.J., Hemez, F.M “Uncertainty Qualification: Estimating uncertainties due to Inference,” *Uncertainty Quantification and Multiscale Materials Modeling, DOE conference*, El Dorado Hotel, Santa Fe, NM, June 13-15, 2011, Technical Report LA-UR-11-03366, Los Alamos National Laboratory, Los Alamos, New Mexico.
- 146 Langenbrunner, J.R., Booker, J.M., Ross, T.J. Hemez, F.M. (2010b), “Evolving Desiderata for Validating Engineered-Physics Systems Without Full-scale Testing,” *American Institute of Aeronautics and Astronautics, Proceedings 12<sup>th</sup> Non-Deterministic Approaches Conference*, Orlando, Florida, April 12-15, 2010, LA-UR-10-01494, LA-UR-10-02167.
- 147 Langenbrunner, J.R., Booker, J.M., Ross, T.J. Hemez, F.M. (2010c), “Inference Uncertainty Quantification Instead of Full-scale Testing,” *Proceedings, American Institute of Aeronautics and Astronautics, 49<sup>th</sup> AIAA/ASME/ASCE/AHS/ASC Structures, Structural Dynamics, and Materials Conference and 10<sup>th</sup> AIAA Non-Deterministic Approaches Conference*, Schaumburg, Illinois, April 7-10, 2008; Technical Report LA-UR-08-1669, Los Alamos National Laboratory, Los Alamos, New Mexico.
- 148 W. A. Fowler, “Experimental and Theoretical Nuclear Astrophysics; The Quest for the Origin of the Elements,” in *Nobel Lectures, Physics 1981-1990*, Tore Frängsmyr, editor-in-charge, Gösta Ekspång, editor. World Scientific Publishing Co.: Singapore (1993).
- 149 H. R. Weller, M. W. Ahmed, H. Gao, W. Tornow, Y. K. Yu. M. Gai, and R. Miskimen, “Research Opportunities at the upgraded HIγS facility,” *Prog. Part. Nucl. Phys.* **62**, 257 (2009).
- 150 C. Tur, A. Heger, and S. M. Austin, “Dependence of s-process nucleosynthesis in massive stars on triple-alpha and <sup>12</sup>C(α, γ)<sup>16</sup>O reaction rate uncertainties,” *Astrophys. J.* **702**, 1068 (2009).
- 151 A. Weiss, “Stellar nucleosynthesis,” *Phys. Scr. T133*, art. no. 014025 (2008).
- 152 D. A. O’Connor, “The theory of nuclear resonant diffraction of gamma rays by perfect crystals,” *J. Phys. C* **1**, 973 (1968).

# 4 Performance and Parameters

## 4.1 *Introduction and Overview*

The FACET-II electron system design uses a copy of the LCLS-I injector system installed in the existing off-axis bunker at Sector 10. The 135 MeV beam is injected into the linac and accelerated in Sectors 11-19 (the second kilometer of the SLAC Linac) to the existing FACET experimental area in Sector 20. To achieve the required bunch length, the bunch compression is done in three stages: the first compression with a chicane in Sector 11; the second with a chicane in Sector 14; and the third in the W-chicane in Sector 20. The accelerator requirements are described below.

The FACET-II positron system takes the beam from the existing positron target, capture section and return line and transports it to Sector 10. To match the 335 MeV energy of the damping ring, four sections of S-band acceleration (each 7 feet long) will be installed in the return line at Sector 14. Starting in Sector 11, a new beamline takes the positrons from the existing return line and injects them into a small damping ring in the Sector 10 Linac tunnel. The beam extracted from the damping ring undergoes a 1<sup>st</sup> stage of bunch compression and is then injected into the Linac at the Bunch Compressor in Sector 11, BC11. The positrons have a 2<sup>nd</sup> stage of bunch compression in a 2<sup>nd</sup> arm of the Sector 14 chicane.

Sector 20 contains the final bunch compression stages for both the electron and positron beams. The existing W chicane can transport either electrons or positrons depending on its polarity. When the sailboat chicane is built as a future upgrade, the beams will be separated at the first bend magnet at the start of sector 20 and each travel through their own compression chicanes.

## 4.2 *Scientific Requirements*

The nominal parameters for FACET-II Stage 1 are driven by the needs of the wakefield accelerator programs. FACET-II will continue to explore the physics of plasma wakefield acceleration in regimes relevant to future collider and X-ray free electron laser applications. Specifically, experiments will operate with accelerating gradients in excess of 10 GeV/m – orders of magnitude larger than conventional accelerators. To attain these large gradients requires plasma densities on the order of  $10^{17}$  e/cm<sup>3</sup>. To effectively drive large amplitude wakefields in the plasma requires the beam dimensions (radially and longitudinally) to be of the order of the plasma collisionless skin depth, or 17  $\mu$ m in this case. Large amplitude wakes are achieved when the electron bunch has sufficient charge to reach peak currents on the order of the Alfvén current (17 kA). Recent experiments at FACET have demonstrated that the positron parameters to be delivered in Stage 2, similar to the above for electrons, can access regimes applicable to plasma afterburner applications [1]. A future upgrade, the sailboat chicane, will deliver both electrons and positron bunches to the plasma in close succession and allow studies relevant to staged collider designs with positron acceleration in the wakefields produced by an electron bunch [2]. The one kilometer-long linac produces a nominal energy of 10 GeV which ensures the required yield from the positron target and enables stable operation with these highly compressed electron and positron bunches.

Other parts of the PWFA program such as the Trojan Horse experiments benefit from the highest peak currents and can accept lower charge. The FACET-II beamline has the flexibility to produce electron peak currents >100 kA by increasing the compression and collimating the energy tails in the bunch compressors. In this configuration, the bunch charge at the IP is reduced to about 0.7 nC. At the other end of the parameter range, the Compton experiments would prefer the highest possible charge in a small transverse size, but do not require the shortest bunch. For these experiments FACET-II can deliver 5 nC with reduced but still useable transverse beam quality. The full list of experiments described in Chapter 3 use a variety of parameters within the tuning range of FACET-II. The baseline design is based around providing a stable beam (2 nC source electron charge, 1 nC positrons from the positron damping ring) that satisfies a broad spectrum of the experimental requirements and is presented in the parameter tables here and elsewhere in the CDR documentation.

### **4.3 Electron Requirements and Parameters**

For the FACET-II experimental program, the electron beam must meet a specific set of requirements for electron transverse beam emittance at the end of the Linac, peak current in Sector 20, energy and stability. These electron parameters are listed below in Table 4.1. Transverse emittance values are using the normal “90% emittance” definition used by LCLS. This is where the outlying 10% of the transverse distribution is removed to de-weight these from the emittance calculation and provide a more useful estimate of the beam emittance in the regime here where strong non-linear tails to the distributions necessarily exist. A schematic layout of the accelerator is shown in Figure 4.1 with beam parameters listed at various points along the accelerator.

**Table 4.1. Nominal electron beam requirements and design parameters and their operational ranges. Emittances are “90% emittance” values, beam sizes are from Gaussian fits to the core of the projected beam distributions.**

Parameter	Symbol	Unit	Requirement	Baseline Design	Range
Final energy	$E_f$	GeV	10.0	10.0	4.0 – 13.5
Bunch charge	$Q_0$	nC	2	2	0.7 – 5
Pulse repetition rate	$f_{rep}$	Hz	1	30	1 - 30
Number of electron bunches per RF pulse	$N_b$	-	1	1	1 - 2
Normalized transverse emittance input to Sector 20	$\varepsilon_{x,y}$	$\mu\text{m}\cdot\text{rad}$	<20	4.4,3.2	3-6
Spot size at Sector 20 focus	$\sigma_{x,y}$	$\mu\text{m}$	<20	18,12	6-20
Final peak current	$I_{pk}$	kA	>10	72	10-130
Final bunch length (rms)	$\sigma_z$	$\mu\text{m}$	<20	1.8	1.5 - 20
Final rms energy spread (rms)	$\sigma_E/E$	%	-	1.4	0.4 – 1.6
Max. avg. $e^-$ beam power (10 GeV, 5 nC, 1 bunch/pulse, 30 Hz)	$P_b$	kW	-	1.5	0.1 - 4.2
Dump design for avg. $e^-$ beam power	$P_D$	kW	-	5	-

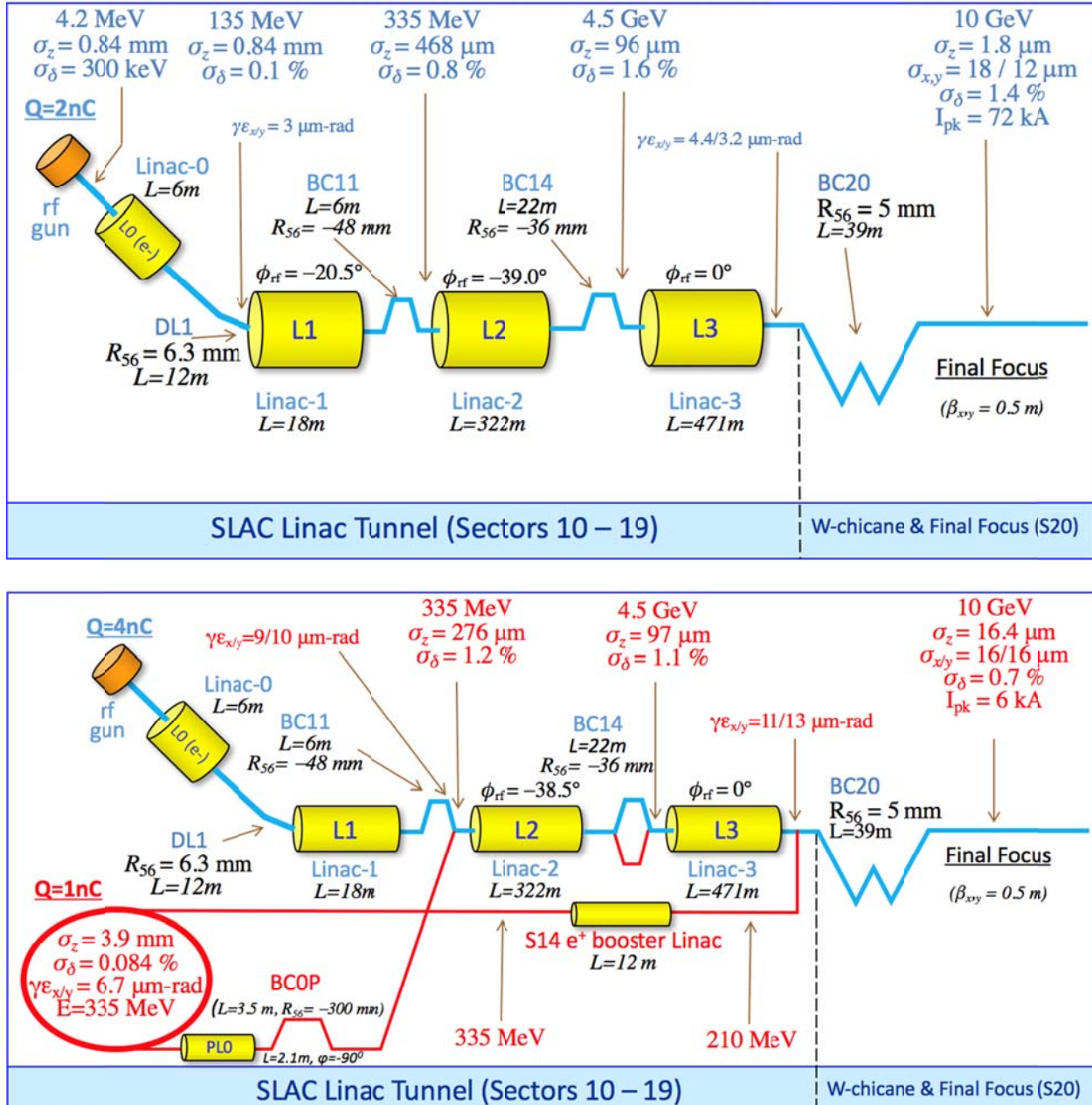


Figure 4.1. Schematic layout of FACET-II injector, linac, bunch compressors, and experimental area, with main parameters listed for operation. The blue sections depict the electron specific and common e-/e+ areas. The red sections are for positrons. The top schematic depicts the baseline design for electrons, the bottom schematic show the baseline positron design parameters.

#### 4.4 Positron Requirements and Parameters

For the FACET-II experimental program, the positron beam must meet a specific set of requirements for emittance, peak current, energy, energy spread, and stability. These parameters are listed below in Table 4.2. A schematic layout of the positron system is also shown in Figure 4.1 with beam parameters listed at various points along the accelerator.

**Table 4.2. Nominal positron beam parameters and their operational ranges. Emittances are “90% emittance” values, beam sizes are from Gaussian fits to the core of the projected beam distributions.**

Parameter	Symbol	Unit	Requirement	Baseline	Range Design
Final energy	$E_f$	GeV	10	10	4 – 13.5
Delivered bunch charge	$Q_0$	nC	1	1	0.6 - 2
Pulse repetition rate	$f_{rep}$	Hz	1	5	1 - 5
Number of positron bunches per RF pulse	$N_b$	-	1	1	1
Positron transverse core beam size (x/y, rms)	$\sigma_{x,y}$	μm	<20	16	10-20
Normalized transverse emittance input to Sector 20	$\varepsilon_{x,y}$	μm-rad	<20	10,12	10-20
Positron peak current	$I_{pk}$	kA	>5	6	6 – 15
Positron bunch length (rms)	$\sigma_z$	μm	<20	16	16 – 20
Final rms energy spread	$\sigma E/E$	%	-	0.7	0.5 – 1.5
Max. avg. $e^+$ beam power (10 GeV, 1nC, 5Hz,1 bunch/pulse)	$P_b$	W	-	50	5 - 140

#### 4.5 Positron Return Line Requirements and Parameters

The positron return line (PRL) is responsible for accelerating the positrons to 335 MeV and then transporting them (18" below the ceiling of the linac tunnel) to Sector 11, where they are matched and injected into the damping ring. To accomplish this, 4 new beamline sections are required. These accelerate the beam to 335 MeV, translate the beam horizontally 103" across the accelerator housing, then transport down vertically 74", and finally inject into the DR. This system takes the measured PRL beam parameters and existing optics and matches into the required optics at the DR injection point.

**Table 4.3. Beam parameters for beamline section injecting into DR in Sectors 10 and 11.**

Parameter	Symbol	Nominal	Min-Max	Unit
Beam Energy	$E_0$	335	-	MeV
Initial Transverse Emittance	$\gamma \varepsilon_x / \gamma \varepsilon_y$	2.0 / 2.0	-	mm.rad
Final Transverse Emittance	$\gamma \varepsilon_x / \gamma \varepsilon_y$	2.5 / 2.2	-	mm.rad
Initial Twiss (At entrance to first horizontal dogleg bend)	$\beta_x / \alpha_x$ $\beta_y / \alpha_y$	0.352 / -0.040 12.918 / 4.082	-	m
Final Twiss (At exit of injection kicker)	$\beta_x / \alpha_x$ $\beta_y / \alpha_y$	0.335 / 0.243 8.813 / -0.555	-	m
Initial Bunch Length (rms)	$\sigma_z$	3	-	mm
Final Bunch Length (rms)	$\sigma_z$	3	-	mm

Initial Energy Spread (rms)	$\sigma_E/E$	1.0	-	%
Final Energy Spread (rms)	$\sigma_E/E$	1.1	-	%
Initial Bunch Charge	Q	4		nC
Final Bunch Charge (in DR)	Q	1	1-2	nC

#### 4.6 Positron Damping Ring Requirements and Parameters

As the positron beam emerges from the target and reaches an energy of  $E=335$  MeV, it has a normalized emittance  $\gamma\epsilon$  of about 2.0 mm-rad. This emittance is three orders of magnitude larger than the electron beam out of the photo-injector. A damping ring is necessary to reduce the positron emittance to  $\mu\text{m-rad}$  level in a few milliseconds. For practical reasons, the ring is placed in sector 10 inside the existing linac tunnel. This implies that the diameter of the ring has to be smaller than 3 meters. This constraint dictates a compact design with minimal gaps between the magnets in the arcs.

**Table 4.4. Main parameters of the positron damping ring including IBS calculations.**

Parameter	Value
Energy, $E$ [MeV]	335.0
Circumference, $C$ [m]	20.57
Tune, $v_x, v_y, v_z$	4.586, 2.615, 0.0383
Normalized emittance, $\gamma\epsilon_0$ [ $\mu\text{m-rad}$ ]	7.6
Bunch length, $\sigma_{z0}$ [mm]	3.55
Energy spread, $\sigma_{\delta_0}$	$7.6 \cdot 10^{-4}$
Momentum compaction	$5.73 \cdot 10^{-2}$
Damping partition, $J_x, J_y, J_z$	2.0, 1.0, 1.0
Damping time, $\tau_x, \tau_y, \tau_z$ [ms]	16.1, 32.0, 34.0
Natural chromaticity, $\xi_{x0}, \xi_{y0}$	-6.19 -4.8
Energy loss per turn, $U_0$ [keV]	1.435
RF voltage, $V_{RF}$ [MV]	1.1
RF frequency, $f_{RF}$ [MHz]	714.0
Harmonic number	49

#### 4.7 Positron Extraction Line Requirements and Parameters

The positron extraction line starts at the entrance to the DR extraction kicker on the final extraction turn and ends at the positron injection point into the main Linac in the final bend of the BC11 electron bunch compressor. In order to match with the electron compression scheme, this system must also compress the bunch length by a factor of  $\sim 10$ . These tasks are achieved with 4 sub-systems, a vertical dog-leg to extract from the damping ring, a diagnostics section, an initial stage of bunch compression (BC0) and a horizontal dog-leg to inject into the last magnet of the first Linac bunch compressor (BC11).

This system is matched given the damping ring beam parameters at the extraction point and provides the required positron (and electron) matching conditions at the insertion point into the main FACET-II beamline.

**Table 4.5. Beam parameters for positron extraction and compression system from the entrance of the DR extraction kicker on extraction turn to injection into the main linac in the final bend of the electron BC1 chicane bend.**

Parameter	Symbol	Baseline Design	Range	Unit
Beam Energy	$E_0$	335		MeV
Initial rms Bunch Length	$\sigma_z$	3.9	3.9-4	mm
Final rms Bunch Length	$\sigma_z$	0.3	0.3-0.4	mm
Initial rms Energy Spread	$\sigma_E/E$	0.084	0.08-0.1	%
Final rms Energy Spread	$\sigma_E/E$	1.2	0.5-1.5	%
Bunch Charge	Q	1	1-2	nC

#### **4.8 Sector 20 Chicane Requirements and Parameters**

The sector 20 system is designed to deliver high peak-current (>10kA) at the IP area with <20μm transverse beam sizes for both electron beams (>5 kA for positrons). The optics match is highly constrained and must satisfy specific requirements for both electron and positron optical systems simultaneously, in order to be compatible with the sailboat chicane future upgrade. These are described in detail in Chapters 9 and 10.

**Table 4.6. Beam parameters for sector 20 chicanes and final focus system for electron and positron beams.**

Parameter	Symbol	Baseline Design	Range	Unit
Beam Energy	$E_0$	10.0	4.0-13.5	GeV
IP Swiss Parameters	$\beta_x / \alpha_x$	0.5 / 0	0.1-5 /0	m
Initial Bunch Length (rms) / peak Current	$\sigma_z / I_{pk}$ (e-)	96 / 3		μm / kA
	$\sigma_z / I_{pk}$ (e+)	97 / 3		
Final Bunch Length / peak Current	$\sigma_z / I_{pk}$ (e-)	1.8 / 72	1-20 / 10-130	μm / kA
	$\sigma_z / I_{pk}$ (e+)	16 / 6	16-20 / 6-15	
rms relative Energy Spread	$\sigma_E/E$ (e-)	1.4	0.4 – 1.6	%
	$\sigma_E/E$ (e+)	0.7	0.5 – 1.5	
rms Transverse Core Size at IP Waist	$\sigma_x / \sigma_y$ (e-)	18 / 12	6 - 20	μm
	$\sigma_x / \sigma_y$ (e+)	16 / 16	10 - 20	
Bunch Charge	Q (e-)	2	2-5	nC
	Q (e+)	1	1-2	nC
Chicane compression coef.	$R_{56}$	5	-10 - +10	mm

## 4.9 Simulated performance

Error sources were added to the tracking simulation used for the FACET-II design to assess the performance under expected running conditions. Sources such as RF phase and amplitude errors, magnet field jitter, orbit jitter etc were considered, see Chapter 6 for more details. The results of this Monte Carlo simulation are summarized in the table below.

**Table 4.7. Simulated range of delivered key performance parameters with all error parameters specified in Table 6.2 applied. Each entry shows mean and rms spread of results from a 100 seed Monte Carlo simulation. Note that the distributions are not actually Gaussian, see presented data in Chapter 6 for error distributions and breakdown of errors into independent sources.**

IP Parameter	Electron Bunch		Positron Bunch	
	Design Req.	Simulation	Design Req.	Simulation
$\varepsilon_x$ ( $\mu\text{m}\cdot\text{rad}$ )	<20	4.4 +/- 0.5	<20	10.7 +/- 0.7
$\varepsilon_y$ ( $\mu\text{m}\cdot\text{rad}$ )	<20	3.3 +/- 0.1	<20	13.0 +/- 1.2
$\sigma_z$ ( $\mu\text{m}$ )	<20	3.1 +/- 1.5	<20	16.5 +/- 0.2
$I_{pk}$ (kA)	>10	64 +/- 16	>5	5.8 +/- 0.2

---

1 S. Corde et al., *Nature* **524** 2015

2 E. Adli et al SLAC-PUB-15426, [arXiv:1308.1145](https://arxiv.org/abs/1308.1145) (2013).

# 5 Electron Injector

---

## Technical Synopsis

*In order to achieve the scientific goals of the experimental program at FACET-II, a high electron peak current with small transverse emittance at the experimental IP waist, <20  $\mu\text{m}\cdot\text{rad}$ , and a small longitudinal emittance are required. FACET-II will operate with an electron energy up to 10 GeV. The most challenging parameters are for the plasma wakefield acceleration (PWFA) experiments which benefit from peak currents in excess of 10 kA. The RF photocathode gun and injection system is similar to that used in LCLS. This injector is capable of producing up to 5 nC with bunch lengths in the range 2-10 ps with typical corresponding peak currents of up to 300 A and transverse emittances of <5  $\mu\text{m}\cdot\text{rad}$ . The acceleration and compression to reach several kA in Sector 20 is done in the 2<sup>nd</sup> kilometer of the SLAC linac in 3 compression stages.*

*The capabilities of FACET-II vary in a non-trivial way depending on the choice of initial charge from the RF gun. The baseline design is for a 2 nC electron bunch charge from the electron gun, with a 4 nC bunch required for positron generation (with no emittance quality requirements). To demonstrate design flexibility and characterize the extremes of the possible parameter space, other configuration options are considered in chapter 10 corresponding to maximum peak current operations at 2 nC and a 5 nC pulse option from the electron gun. In general, the compression scheme can be tailored more towards higher electron peak current by requiring beam collimation of dispersed energy tails or degrading the final transverse emittance. There are also stability trade-offs when operating at higher peak-current.*

*6D tracking simulations have been made to model the beam transport through the FACET-II complex including the non-linear compression and final beam focus processes. The simulations include the effects of longitudinal and transverse wakefields in the 1km linac as well as incoherent and coherent synchrotron radiation effects in the various bending magnets. Space charge effects are also simulated. Simulations have also been made which calculate emittance dilution in the linac due to transverse wakefields and anomalous momentum dispersion. Diagnostics, correction techniques, and feedback systems have also been incorporated into the design.*

---

### 5.1 Accelerator - Introduction and Overview

The FACET-II electron system design is based on the LCLS-I injector system installed in the existing off-axis bunker at Sector 10. The generated electron beam is accelerated to 135 MeV with two 3m s-band acceleration sections and injected into the main linac through a 2 bend dogleg and accelerated in Sectors 11-19 (the second kilometer of the SLAC linac) to the existing FACET experimental area in Sector 20. To achieve the required final bunch length, compression is performed in three stages: the first compression stage with a 4-bend chicane in Sector 11; the second with a chicane in Sector 14; and the third in the W-chicane in Sector 20. The accelerator requirements are described below.

Positrons are produced by a 4 nC electron bunch, accelerated to 10 GeV through Sectors 11-19 and striking the existing target station in Sector 19. Wakefield acceleration experiments require a Drive and a

Witness bunch configuration. These two bunches will be generated using the notch collimator in Sector 20 as performed during FACET-I operations. This is required for both electron and positron operations. For simultaneous operation, the electrons serve as the Drive bunch and the positrons as Witness bunch. The addition of a witness bunch injector in Sector 20 is foreseen in future to provide additional flexibility. Very recently, LCLS has successfully generated two micro-bunches in a single RF bucket. This is a potentially interesting alternative that will be also be explored in the future. Another considered operation mode is to co-accelerated electron and positron bunches on the same RF pulse for positron wakefield acceleration experiments in Sector 20. An example configuration of the FACET-II accelerator for this final option is explored in Chapter 10.

### 5.1.1 Accelerator Requirements and Parameters

For the FACET-II experimental program, the electron beam must meet a specific set of requirements for electron transverse beam size at the Interaction Point in Sector 20 (IP) waist, peak current, energy, energy spread, and stability. These electron parameters are listed below in Table 5.1. Transverse rms values are from a Gaussian fit to the core of the distribution. A schematic layout of the accelerator is also shown in Figure 5.1 with beam parameters listed at various points along the accelerator. The electron beam optics from cathode to dump in Sector 20 is shown in Figure 5.2.

**Table 5.1. Nominal electron beam parameters at the FACET IP and their operational ranges. Ranges arise from other considered compression schemes.**

Parameter	Symbol	Unit	Nominal	Range
Final electron energy	$E_f$	GeV	10.0	4.0 – 13.5
Initial electron bunch charge	$Q_0$	nC	2	2 - 5
Final electron bunch charge	$Q_f$	nC	2	0.7 - 5
Pulse repetition rate	$f_{rep}$	Hz	30	1 - 30
Number of electron bunches per RF pulse	$N_b$	-	1	1 - 2
Final Electron transverse core beam size (x/y, rms)	$\sigma_x/\sigma_y$	$\mu\text{m}$	18/12	6-20
Final electron peak current	$I_{pk}$	kA	72	10-130
Final electron bunch length (rms)	$\sigma_z$	$\mu\text{m}$	1.8	1 - 20
Final electron rms energy spread (rms)	$\sigma_E/E$	%	1.4	0.4 – 1.6
Max. avg. $e^-$ beam power (10 GeV, 5 nC, 1 bunch/pulse, 30 Hz)	$P_b$	kW	1.5	0.1 - 4.2
Dump design for avg. $e^-$ beam power	$P_D$	kW	5	-

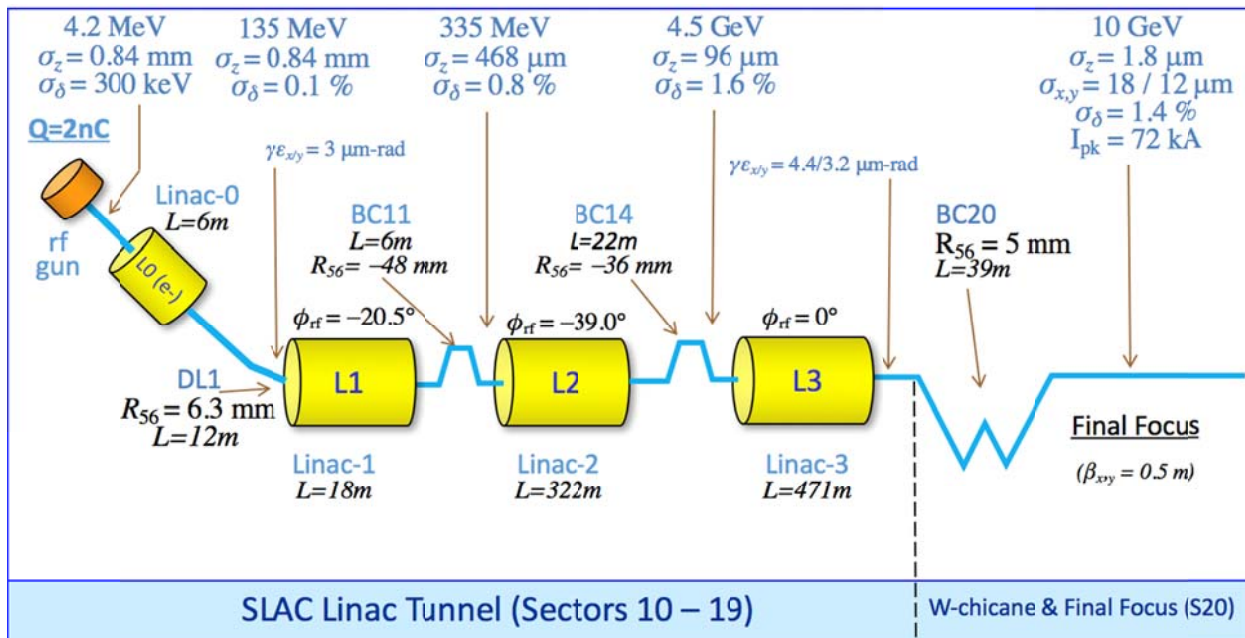


**Figure 5.1.** Schematic layout of FACET-II injector, linac, bunch compressors, and experimental area, with main parameters listed for electron operation. The linac sections and the Sector 20 W chicane and final focus are existing systems. All other components are new installations, although many will be repurposed from existing systems.

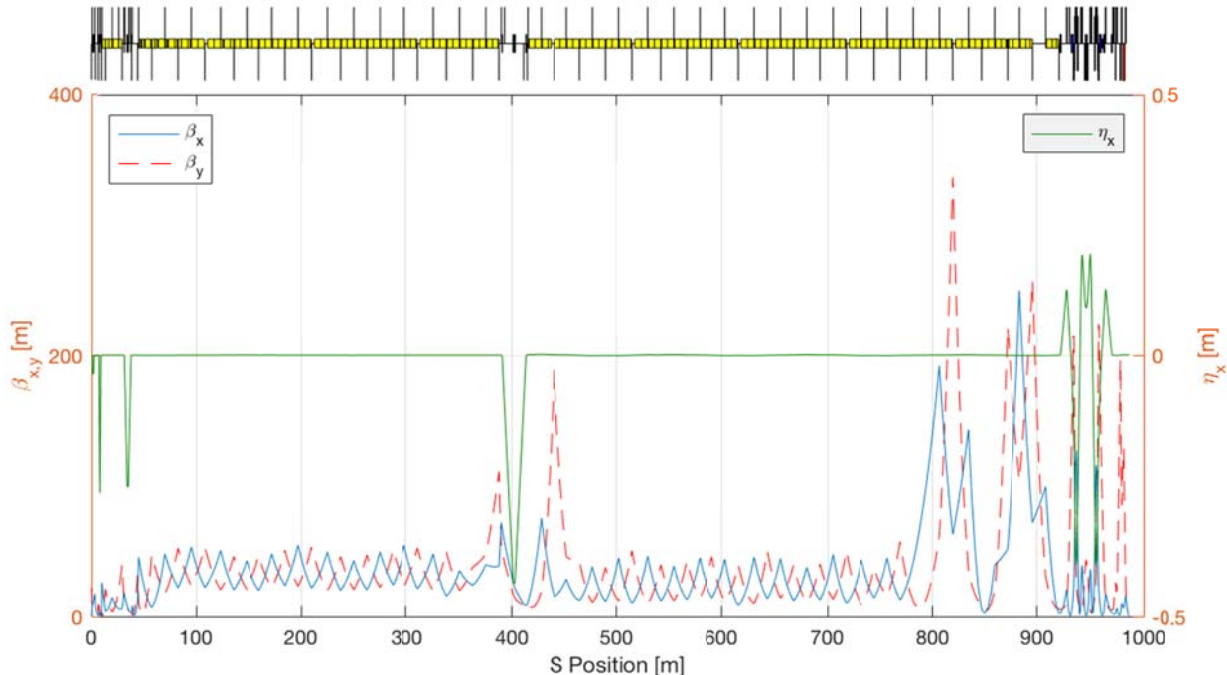


**Figure 5.2.** Linac electron optics from the exit of L0 (135 MeV point) to the IP waist in sector 20. BC11 is at  $s \approx 30$  m, BC14 is at  $s \approx 390$  m, FACET W-chicane is at  $s \approx 920$  m.

### 5.1.2 Accelerator Layout

The FACET-II accelerator layout will occupy the second kilometer of the SLAC S-band linac (2.856 GHz), from sector 11 through 20, in order to generate up to a 10 GeV electron beam at 1-30 Hz.

The injector is based on the 1 nC design of the LCLS 135 MeV electron injector with the injector parameters optimized for operation at the required 2 nC bunch charge [1]. A single bunch of electrons is generated at a 30 Hz repetition rate in an S-band (2.856 GHz) RF photocathode gun (see “rf gun” in Figure 5.1) by exciting a copper cathode with Ultra-Violet (UV) laser light from a high-power drive laser system located in the linac gallery above the existing Sector 10 off-axis injector vault. The Orion gun, currently installed in NLCTA, operating with a peak accelerating field of 90 MV/m will be used. The electrons are accelerated to 4.2 MeV in the gun, where the transverse emittance is formed by choosing an appropriate UV laser spot size on the cathode (2.68 mm radius) and using a strong focusing solenoid magnet immediately after the gun.

Further acceleration in the injector vault (see “Linac-0” in Figure 5.1) takes the beam energy up to 135 MeV where it is horizontally deflected by 35 degrees into the main SLAC Linac at the start of Sector 11 (see “DL1” in Figure 5.1). The beam is then accelerated 20.5° off of the RF crest where an energy chirp (time-energy correlation) is generated (see “Linac-1” in Figure 5.1). A 6-m long, four-dipole magnetic chicane at 335 MeV (see “BC11” in Figure 5.1) compresses the bunch length from 840  $\mu\text{m}$  to 468  $\mu\text{m}$ . More off-crest acceleration follows (see “Linac-2” in Figure 5.1) to 4.5 GeV where a second chicane (see “BC14” in Figure 5.1) compresses the bunch length to an rms bunch length of 96  $\mu\text{m}$ . The last accelerator section (see “Linac-3” in Figure 5.1) accelerates at the RF crest phase up to 10 GeV. The bunch is over-compressed in BC14, with the wakefield chirp delivered in Linac-3 further enhancing the chirp to rotate the beam in E-z phase-space to the correct orientation to allow for the final (+ve  $R_{56}$ ) compression stage in sector 20. The final compression stage is performed by the existing FACET W-chicane system in sector 20 (see Chapter 9) which compresses the beam to a bunch length below the required 20  $\mu\text{m}$ , corresponding to a peak current of 72 kA. A final focus system comprising of 7 families of quadrupole magnets forms a beta waist of equal magnitude in both transverse planes at one of several possible user areas in the beam IP waist experimental region. User requirements are for a range of possible  $\beta^*$  values, typically between 0.1 – 5 m. The nominal design is based around a representative 0.5 m  $\beta^*$  in both planes. The required final normalized transverse emittance injected into Sector 20 is < 20  $\mu\text{m}\cdot\text{rad}$  in both planes.

The electron beam is finally directed onto the dump at the end of Sector 20 through 3 quadrupoles and a vertical bend to provide high energy bandwidth energy spectrometry to the user community, as used during FACET operations.

## **5.2 Drive Laser**

The FACET-II injector drive laser provides UV output to illuminate a copper cathode, producing the electrons for acceleration. A copper cathode has been demonstrated to produce very good thermal emittance levels, long lifetimes ( $>2$  years in LCLS-I at  $<250$  pC/bunch), and does not require extreme vacuum pressure control ( $\sim 10^{-9}$  Torr), but it also can have a fairly low quantum efficiency (QE) from between  $2.4 \times 10^{-5}$  (early LCLS-I) to  $1.2 \times 10^{-4}$  (recent LCLS-I for UV light at 253 nm). The lower range of QE requires an ultra-violet (UV) laser pulse energy of 400  $\mu\text{J}$  on the cathode for a 2 nC electron bunch. The drive laser is of the same design as has been demonstrated at LCLS-I for several years [2]. In LCLS-I, the entire system has been very reliable with up-time  $>98\%$ . The drive laser system is composed of the following components:

- The laser, which produces the UV beam for electron generation and the IR beam for the heater.
- The gun transport system, which conditions the UV beam to meet the required spatial and temporal parameters, and projects the beam onto the cathode at near normal incidence.
- Diagnostics that allow all relevant beam parameters to be measured at the appropriate places in the system, integrated with feedback loops for pointing stability.
- The laser hall that provides the environmental conditions required by the laser, which serves to limit the exposure to laser hazards and includes a laser safety system that meets SLAC, DOE, OSHA, and ANSI laser safety standards.

### **5.2.1 Drive Laser Specifications**

As is the case in LCLS-I, the drive laser itself will be based on chirped pulse amplification (CPA) in Ti:sapphire, followed by harmonic conversion to the required UV wavelength. In this case we begin with a mode-locked Ti:sapphire oscillator that generates a 68-MHz train of nano-Joule level pulses in the 750-780 nm wavelength range. The 68-MHz repetition rate is important because it is commensurate with the RF timing systems of the SLAC linac, allowing the laser oscillator to be synchronized to the linac. Because these pulses are roughly 30 fs in duration the time-bandwidth limited spectral width is roughly 30 nm. In CPA systems, this large spectral width is exploited to stretch the pulse to a width of  $>150$  ps by passing the pulses through a device with significant group velocity dispersion. This stretcher expands the pulses temporally so that they can be amplified to higher energy without the risk of damaging the amplifier components. After the pulses are amplified to the desired energy, they can be compressed back to the 30-fs level in a device with group velocity dispersion that cancels that of the stretcher.

The laser consists of commercially available laser hardware with minor modifications to meet our specific needs. In the case of the laser oscillator, there are at least two companies that can provide an oscillator (Figure 5.3) that meets the FACET-II requirements. Between the LCLS-I injector and the NEH experimental laser systems, SLAC is currently operating several of these oscillators from both companies and has worked with both companies to make the required modifications.

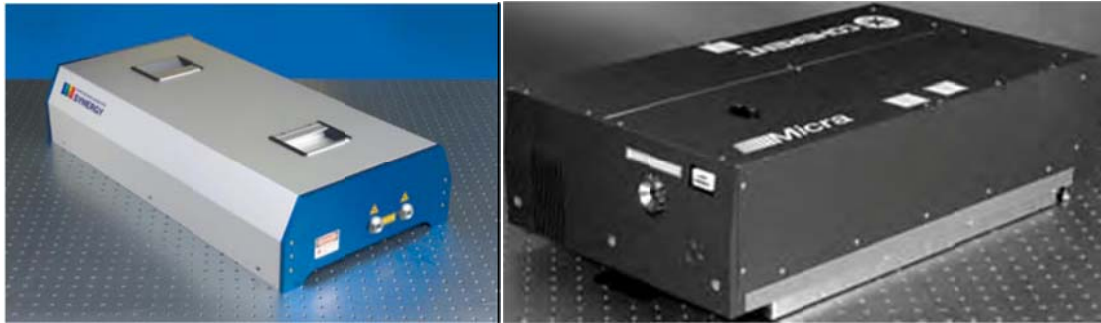


**Figure 5.3. Commercially available mode-locked oscillators that meet FACET-II requirements.**

The stretcher, amplifiers, and compressor used in LCLS-I are also commercially available devices with minor modifications. In all cases, the first stage of amplification is performed in a regenerative amplifier (regen) based on Ti:sapphire pumped by frequency doubled Nd:YAG or Nd:YLF and running at 30 Hz repetition rate. The regenerative amplifier provides very high gain in a compact space, raising the pulse energy from nJ to mJ. We are currently using regens from two different companies (Figure 5.4) with SLAC modifications to force the amplifier to operate at the desired wavelength. Following the regen, one or more multi-pass Ti:sapphire amplifiers will be used to increase the pulse energy to the required level. We currently operate multi-pass amplifiers from commercial companies as well as SLAC designed units.



**Figure 5.4. An example of a commercial regenerative amplifier (regen).**

After amplification to the desired energy and compression to the desired pulse width, the 760-nm pulse is frequency doubled and then tripled to 253 nm. The final output parameters required are shown in Table 5.2.

**Table 5.2. Parameters of the UV drive laser system (“nominal” 2 nC bunch charge).**

Parameter	Symbol	Unit	Nominal	Range
Operating wavelength (for Cu cathode)	$\lambda_{UV}$	nm	253	253-266
Pulse repetition rate	$f_{rep}$	Hz	30	1-30
Number of laser pulses per RF pulse	$N_b$	-	1	1-2
Nominal pulse energy on cathode	$U$	$\mu\text{J}$	400	100-1000
Laser spot Gaussian rms width pre-cut	$\sigma$	mm	5.0	0.2-5.0
Cut radius on transverse laser spot	$R$	mm	2.68	0.5-5.0

Pulse length (FWHM)	$\Delta t$	ps	7.0	2-10
Longitudinal pulse shape	-	-	Gaussian	-
Transverse pulse shape	-	-	cut Gaussian	-
Spatial homogeneity on cathode (peak-to-peak)	-	%	<15	-
Longitudinal homogeneity on cathode (peak-to-peak)	-	%	<10	-
Optical energy jitter (in UV, rms)	-	%	<2	-
Laser-to-RF phase jitter (rms)	-	ps	<0.2	-
Laser rms position jitter on cathode / rms spot size	-	%	<3	-

Once laser pulses are produced with these parameters, they leave the laser and move into the transport system. The transport system consists of three primary parts: The upstairs beam conditioning and transport, the transport tube down to the injector vault (evacuated for most of the distance), and the gun laser transport in the vault. Drawings of the optical components upstairs and in the vault are shown in Figure 5.5 and Figure 5.6.

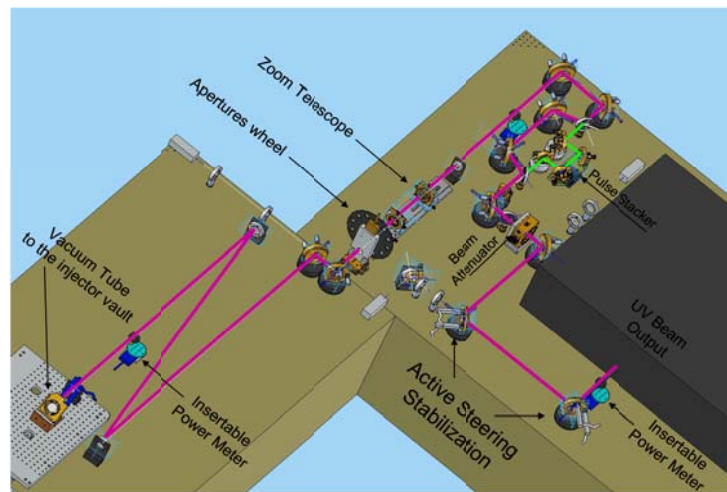
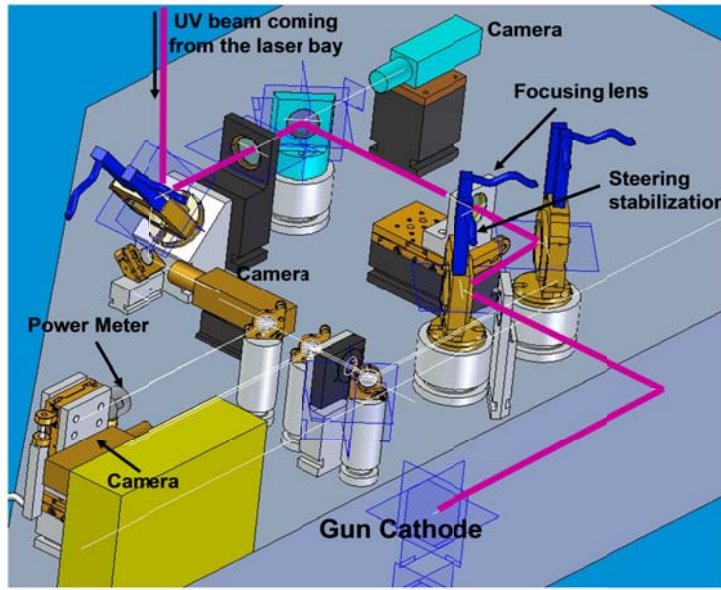
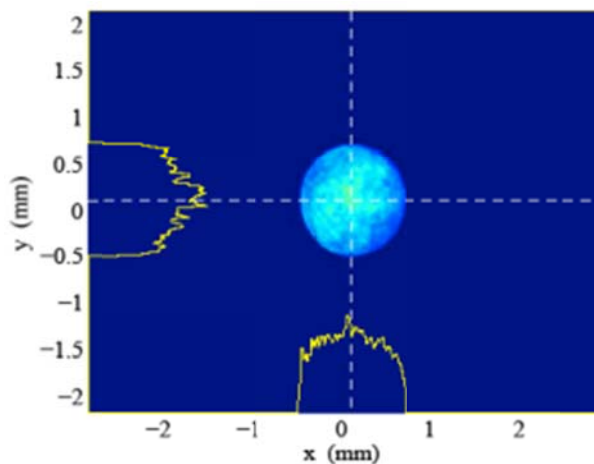


Figure 5.5. Upstairs laser beam conditioning and transport.



**Figure 5.6. Laser transport system in the vault.**

Upstairs, the beam is first propagated through a beam pointing stabilization system consisting of two cameras and two motorized mirrors. After that the beam passes through a waveplate and polarizer that allows the laser pulse energy to be controlled in a feedback loop that measures the charge produced from the gun. The pulses can then be sent into a pulse stacker that allows for more temporal control or multi-bunch production. The beam diameter is then adjusted in a zoom telescope before being spatially clipped on one of twelve apertures. This aperture is then relay imaged through the transport pipes, to the vault transport optics where the image is reformed on the photocathode. Before reaching the cathode a fraction of the pulse is sampled for another pointing stabilization system, an energy measurement, and an equivalent plane imaging system that allows the spatial profile on the cathode to be monitored on the Virtual Cathode Camera (VCC). The spatial profile for LCLS-I as seen on the VCC is shown in Figure 5.7.



**Figure 5.7. Spatial profile on cathode as recorded by Virtual Cathode Camera in LCLS-I. Yellow curves are “line-out” traces showing the instantaneous distribution along that line.**

### 5.2.2 Multiple Bunch Operation

To allow operation of FACET-II with both electron and positron bunches simultaneously as part of a future upgrade, a second laser system will be required to provide a second electron bunch in the photoinjector. This laser system will be comprised of an amplifier chain seeded by a later pulse from the same oscillator as the primary laser system, and a separate third harmonic generation (THG) stage coupled to the same spatial shaping optics and beam transport as the output of the primary laser. The amplifier and THG will be identical to those of the primary laser. An optical delay line will be used to independently control the phase of the second laser pulse relative to the RF.

### 5.2.3 Laser Room

The laser room serves several purposes. It provides a stable clean environment for the laser. It also serves to limit access to the laser hazard zone and provides the infrastructure for the Laser Safety System (LSS). The laser room is at ground level above the injector vault and the UV and IR beams are transported through 10-meter long vacuum pipes that are installed in a penetration to the injector tunnel (see Figure 5.8).

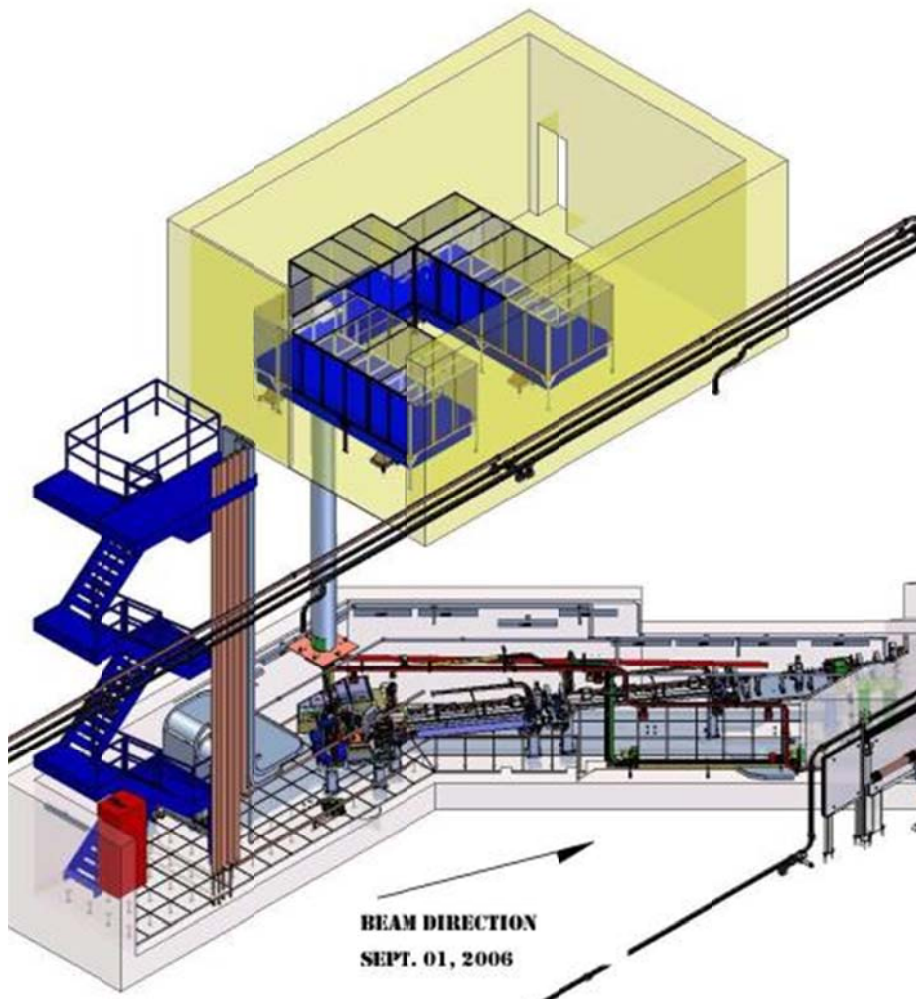


**Figure 5.8. Laser room above the LCLS injector vault. Silver pipe is UV transport to laser bench attached to ceiling. Red pipe is IR transport to heater.**

The laser room is designed to provide a temperature stability of better than  $\pm 1^{\circ}\text{F}$  at a humidity of  $50\% \pm 10\%$ . The conditioned air is filtered by High Efficiency Particulate Air (HEPA) filters, providing a clean environment for the laser system. The LSS controls the operational state as well as entry and exit to and from the room. If there are interlock faults, the LSS will insert the required shutters or turn off lasers as described in the facility Standard Operating Procedure (SOP).

#### 5.2.4 Laser Controls

FACET-II can utilize both currently supported controls components used throughout the facility, or systems under development as part of ongoing projects, given the similarity between the FACET-II electron injector and LCLS-I injector systems. Generally, these components fall into two categories, either OEM equipment which is vendor supplied and usually has specified controls interfaces, or SLAC-designed components which therefore have SLAC-maintained controls interfaces and structures.

The first category of components that will be used in the FACET-II injector include many of the optical components necessary for commissioning and maintaining operation of the laser generation and transport. Examples of such components include power meters, translation stages and motion control systems, shutters and cameras. In many cases, these are readily available from common vendors, and have well defined controls interfaces for which SLAC controls groups have already deployed support.

Examples within this first category of components are camera systems and motor control systems. Ongoing development programs at SLAC are working on high-rate, high-survivability camera systems that will mitigate some of the failure modes we've encountered maintaining camera systems on LCLS-I. Motion control systems have also been susceptible to failure when placed within the accelerator housings, necessary due to OEM equipment design. However, SLAC has active programs to address these requirements, such that we can move sensitive motion control hardware outside of the accelerator housing, increasing supportability and reducing aggregate system cost. Further, where possible, controls hardware in general will be installed outside the injector vault.

Some specific controls additions in this first category which are not available in the LCLS-I injector systems will be considered for FACET-II, due to experience commissioning and operating LCLS-I systems. First, remote monitoring of laser cooling systems will be implemented as available. Second, as available and depending on stability requirements, the laser delay stage for two pulse operation (see section 5.2.2) may be motorized for remote control.

The second category of components include those systems developed entirely at SLAC. A specific example of this category are the SLAC Laser Timing Module System (LTMS), which controls laser pulse timing. These components typically have well-delineated controls interfaces necessitating only software support to integrate with the existing accelerator systems. The LTMS system interfaces with accelerator LLRF systems and the accelerator timing system at large. FACET-II will use existing EVR/EVG style systems as used in LCLS-I and some FACET-I systems, so little development work will be needed for the LTMS system and analog/digital signal processing systems. There is little design or implementation risk, and the system is well understood.

Much of the FACET-II laser system and controls will look much like the LCLS-I injector laser systems. FACET-II will benefit from the operational experience with LCLS-I.

### 5.3 Electron Gun and Injector

The parameters of the LCLS injector are optimized for use at FACET-II for a bunch charge of 2 nC. The source laser parameters were scaled by extrapolating from the design of the Orion gun at BNL/ATF [3],

the LCLS injector [4], and measurements thereof. Simulations of the injector design were performed using IMPACT-T [10] and Lucretia [11]. Simulated performance estimates of FACET-II, constituting the baseline design, are summarized in Table 5.3. The required performance parameters, outlined in 5.3.1, were shown to have been met.

The baseline design for the injector of FACET-II is to use the Orion RF photocathode gun, currently situated at the NLCTA test facility, operating with a peak gun field of 90 MV/m.

The FACET-II injector is configured with minor configuration changes to the LCLS injector design, leveraging design and operational experience gained at BNL/ATF. Tracking simulations show expected beam quality in excess of that required for the FACET-II program and to meet the project KPP's.

### 5.3.1 Required Injector Performance Parameters

The “Key Performance Parameters” (KPP) that constitute the FACET-II design electron beam are:

- Up to 2 nC bunch charge to be transported into Sector 20
- <20  $\mu\text{m}$ -rad transverse normalized emittance to be delivered into Sector 19
- <20  $\mu\text{m}$  rms core bunch length to be delivered to the Sector 20 experimental interaction region

The requirements above are selected to enable a large fraction of the FACET-II experimental program to proceed. The most demanding beam delivery requirements into the Sector 20 FACET-II interaction region come from the beam-driven plasma experiments. These require core transverse beam sizes of <20  $\mu\text{m}$  at the interaction point in addition to the parameters listed above.

### 5.3.2 Scaling the Photoinjector with Beam Size

We follow the work of Rosenzweig and Colby [5] and K. J. Kim [6]. For this work we assume the distribution function which defines the beam is not changed from previous experience. To provide for a 2 nC bunch, we extrapolate from experience at BNL/ATF with a similar injector configuration and measurements with bunch charges in the range 120-560 pC. Since the bunch length  $\sigma_z$  is determined by the laser we assume it does not change (7 ps FWHM).

To obtain the proper operation of an LCLS injector at 2 nC, we find a relation which ensures the beam energy spread is consistent between the two cases and derive expressions for the change in emittance due to space charge and RF effects. Finally, we estimate the new parameters in the FACET-II case by scaling the laser spot size incident on the RF photocathode based on measured values at BNL/ATF.

#### 5.3.2.1 Image Charge Force Effects

When emitted from a copper cathode a beam experiences image charge forces from the cathode which depress the accelerating field  $E_0$ . The maximum beam density for a cylindrical symmetric Gaussian beam distribution which limits the maximum deceleration force due to image charge effects to one half the peak accelerating voltage  $E_0$  is [7],

$$n_b = \frac{QE_0\sigma_z}{4(2\pi)^{3/2}r_e m_e c^2 \sigma_x^2}.$$

Where  $\sigma_x$  is the rms beam size, Q is the charge and  $\sigma_z$  is the rms bunch length. To ensure these forces remain the same as the charge is increased the transverse beam size must increase as,

$$\sigma_{x,new} = \sqrt{\frac{Q_{new}}{Q_{old}}} \sigma_{x,old}.$$

### 5.3.2.2 Space Charge Induced Emittance

The emittance of the beam due to space charge effects can be estimated, for a Gaussian beam, as [6],

$$\varepsilon_x^{SC} = \frac{\pi}{4I_0} \frac{1}{\alpha k \sin \phi_0} \frac{1}{(2\pi)^{3/2} \sigma_z \sigma_x^2} \mu(A),$$

where  $A = \frac{\sigma_x}{\sigma_z}$  is the beam aspect ratio, and  $\mu(A) = \frac{1}{3A+5}$ .

The change in emittance when the beam current is increased and the bunch size scaled as shown in 5.3.2.1 is given by the scaling factor:

$$\frac{\varepsilon_{x,new}^{SC}}{\varepsilon_{x,old}^{SC}} = \frac{Q_{new}}{Q_{old}} \frac{\sigma_{x,old}^2}{\sigma_{x,new}^2} \frac{3A_{old} + 5}{3A_{new} + 5}$$

### 5.3.2.3 Emittance Due to RF Effects

The normalized emittance from RF effects can be calculated as [6],

$$\varepsilon_x^{RF} = \frac{\alpha k^3 \sigma_z^2 \sigma_x^2}{\sqrt{2}}.$$

Thus the emittance is expected to scale with charge based on,

$$\frac{\varepsilon_{x,new}^{RF}}{\varepsilon_{x,old}^{RF}} = \frac{\sigma_{x,new}^2}{\sigma_{x,old}^2} = \frac{Q_{new}}{Q_{old}}.$$

## 5.3.3 Thermal Emittance at the RF Cathode

Measurements with the LCLS injector and at BNL/ATF [4,8] indicate a normalized thermal emittance at the cathode of 0.9 um-rad / mm (rms) transverse laser spot size. For ATF measurements at 560 pC, this is 0.63 um-rad. Scaling the laser transverse spot size as in 5.3.2.1, we expect a corresponding thermal emittance of ~1.2 um-rad at FACET-II with 2 nC bunch charge.

## 5.3.4 Expected Performance of the FACET-II Injector at 2 nC

Based on the scaling in 5.3.2.1 and measurements at the BNL/ATF injector [9] we select a hard-edge laser spot size diameter of 5.36 mm and expect a peak current in excess of 300 A for FACET-II at 2 nC bunch charge (see Figure 5.9). This scaling assumes peak current remains directly proportional to total bunch charge.

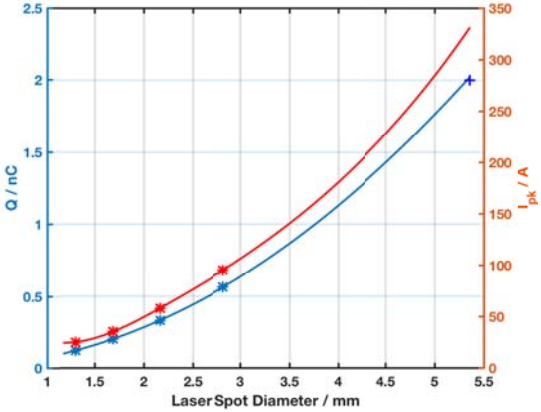


**Figure 5.9: Measurements at BNL/ATF of achieved charge vs. used laser spot size on the cathode. Solid lines show expected scaling from 5.3.2.1, the points are the ATF measurements, the cross is the selected working point for FACET-II.**

The measured normalized emittance at BNL/ATF for  $\sim 0.5$  nC bunch charge is  $1\text{--}1.5 \mu\text{m}\text{-rad}$  [9]. The emittance growth due to space charge is negligible due to the choice of laser parameters, emittance growth of  $\sim 0.8\text{--}1.1 \mu\text{m}\text{-rad}$  predominantly arises due to the gun RF. According to the scaling law in 5.3.2.2, the space charge emittance is even more negligible with the FACET-II laser parameters. Assuming a thermal emittance of  $1.2 \mu\text{m}\text{-rad}$  and the RF emittance scaling law expressed in 5.3.2.3, we would expect a normalized transverse emittance of  $\sim 3.4\text{--}4.6 \mu\text{m}\text{-rad}$  at FACET-II with a bunch charge of 2 nC.

Tracking simulations presented below show expectations consistent with the lower end of the expected emittance range, and lower than expected peak current performance for the NLCTA gun at 90 MV/m peak gun rf accelerating gradient.

## 5.4 Overview of Injector Layout and Particle Tracking Simulation

### 5.4.1 Electron Injector Components

The key components of the FACET-II electron injection system are shown in the schematic below in Figure 5.10, which also shows the simulated design parameters @ 2nC. The initial design configuration of the electron injector is based on the LCLS injector design for 1 nC [4].

The injector beamline consists of an initial s-band photocathode electron gun with peak field gradient of 90 MV/m and integrated solenoid (the Orion gun as currently installed at NLCTA). Two 3m-length travelling-wave s-band accelerating structures accelerate the beam to 135 MeV. A laser-heater chicane used in the LCLS injector system is not present in the baseline FACET-II injector design, but space is reserved for possible future inclusion ( $\Delta z = 1.32$  m) of the requisite 4-bend chicane system plus undulator. After the laser heater chicane section and an emittance measurement section, the beam is transported to the FACET-II main Linac through a 2-bend dogleg system, DL1.

### 5.4.2 Simulation Tools

The 6D tracking code IMPACT-T [10] is a fully three-dimensional program to track relativistic particles taking into account space charge forces and short-range longitudinal and transverse wakefields. The IMPACT-T model used for LCLS was used as a starting point and optimized for the 2 nC FACET-II design.

IMPACT-T tracking was used for tracking the beam representation from cathode to the exit of the L0a accelerating structure at 63 MeV.

The 6D tracking code Lucretia [11] was used for beam tracking from the exit of L0a through the rest of the injector and FACET-II acceleration, bunch compression and focusing beamlines. Lucretia implements a 1-d longitudinal space charge treatment in addition to longitudinal and transverse wakefields, ISR and CSR, similar to the beam tracking code Elegant [12].

Lucretia is a Matlab[13]-based toolbox for the design and simulation of single-pass electron machines. Scripts in the Matlab environment were used to control the overall simulation environment, including the modification and execution of the simulation decks of IMPACT-T. An initial macro-particle definition of 200,000 particles was used to describe the electron beam at the cathode. Previous experience with IMPACT-T for LCLS injector designs and with Lucretia for FACET designs have shown this to be sufficient and provide results with negligible difference to that produced by a many million macro-particle description.

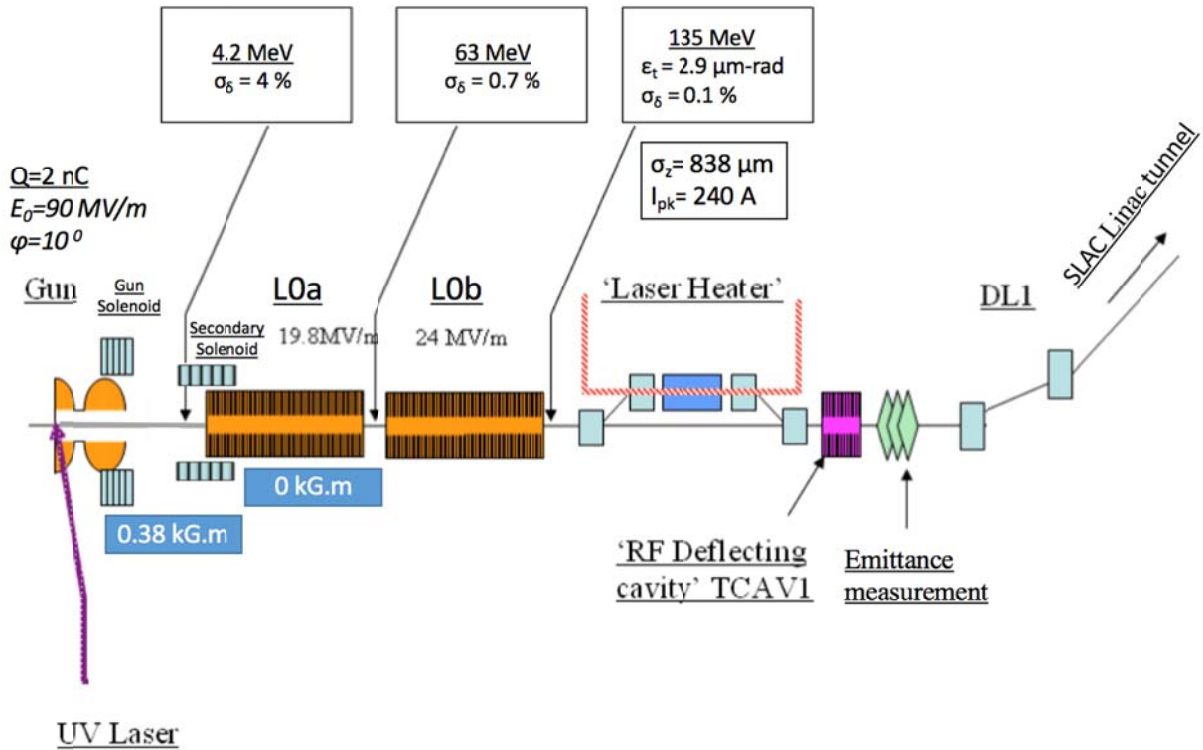


**Figure 5.10: FACET-II electron injector schematic showing key beam parameters for the design 2 nC physics bunch. Also shown here is an LCLS-style laser heater and location of a secondary solenoid which is not in the FACET-II project baseline design.**

### 5.4.3 Optimization Parameters

The following injector parameters were considered as variables in the optimization study to design an emittance compensated 2 nC source for the FACET-II machine with bunch charge of 2 nC:

- Phase of RF photocathode gun (2856 MHz) relative to uv source laser.
- Gun solenoid strength.

- Drift distance from gun cavity exit to first (L0a) acceleration section.

In each case, the RF phase of L0a is set for maximum acceleration at design gradient. The RF phase of L0b is set to de-chirp the beam and minimize the energy spread into DL1.

## 5.5 Emittance-Compensated Injector Design

### 5.5.1 Source Distribution

The design uv drive laser profile is a ~400  $\mu\text{J}$ , 253 nm wavelength pulse, with a 7 ps FWHM Gaussian longitudinal profile and a cut-Gaussian transverse distribution with a hard-edge diameter of 5.36 mm. The assumed normalized thermal emittance of the beam from the gun is 0.9  $\mu\text{m}\cdot\text{rad}$  per mm rms transverse beam size, giving an initial normalized transverse emittance of ~1.2  $\mu\text{m}\cdot\text{rad}$ .

### 5.5.2 Emittance Compensation Optimization

Using the tracking simulation, 2-d scans of gun phase vs. gun solenoid strength were performed for varying settings of cathode to L0a distance settings. A cathode to L0a distance of ~1m yields the smallest final emittance. Figure 5.11 shows gun phase and solenoid strength scans for this drift length. Figure 5.12 shows the tracked emittances through the injector for the baseline parameters. Transverse emittance is improved at lower gun phases. Peak currents are also higher at lower phase with more longitudinal compression of the bunch in the gun. The baseline design used for further simulation is based on a gun rf phase of 10 degrees (with respect to zero field crossing at the cathode surface and with respect to source laser arrival time) and integrated solenoid strength of 0.38 kG.m.

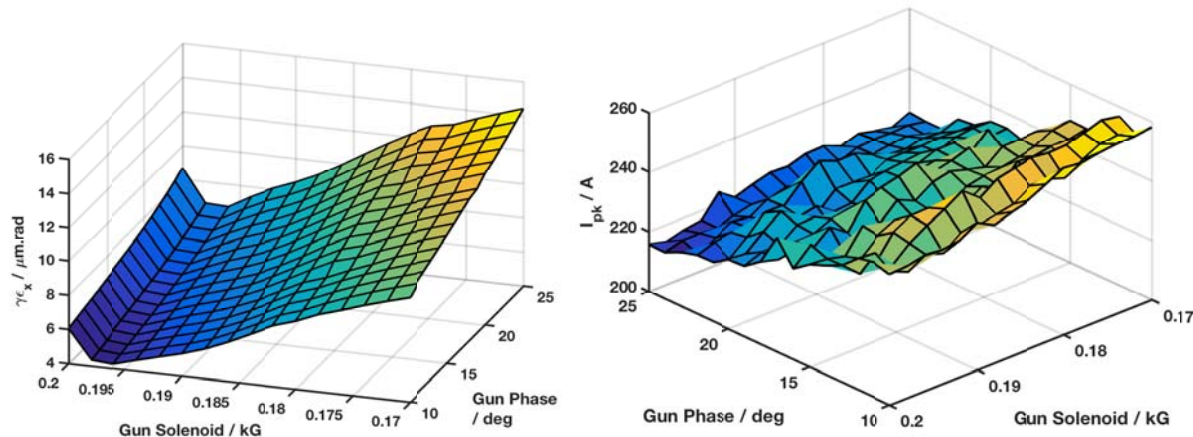


**Figure 5.11: Gun phase vs. gun solenoid strength scan. 100% Transverse emittance (left) and peak current (right) response shown. Values shown are calculated from the simulated bunch at injection into the L1 accelerating section at the exit of the injector system. Gun phase is with respect to the zero field crossing at the cathode surface. Solenoid strength is peak field / kG.**

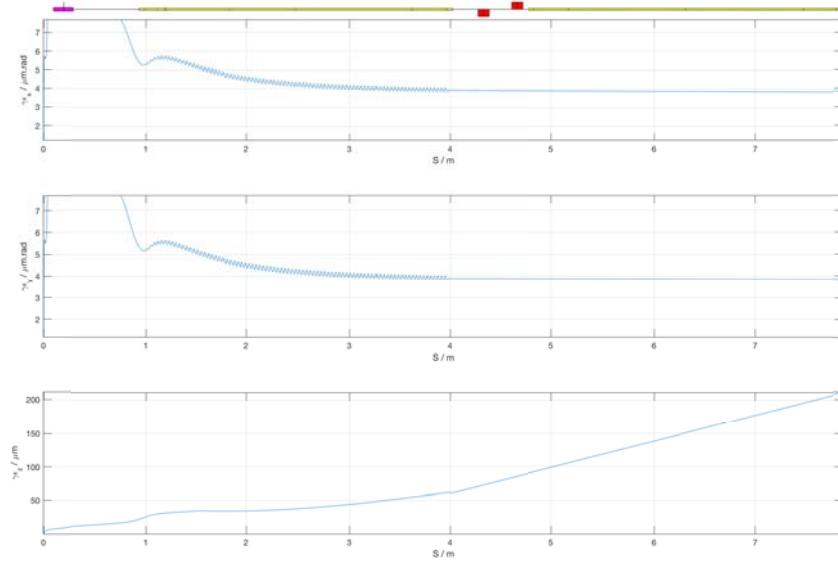


**Figure 5.12: Normalized 100% transverse and longitudinal emittance through the FACET-II injector.**

## 5.6 Baseline Design Parameters and Tracking Results

Results from particle tracking through the injector section, and then on through the FACET-II linac, bunch compressors and Sector 20 optics to the FACET-II IP are shown below. The FACET final focus system is tuned to provide beta-functions of 0.5 m in both planes at the IP. Operationally, values between 0.1 and 1.0 are typically used. Emittances are defined, as at LCLS, in terms of “90% emittance” numbers, where tails in position and angle phases are subtracted prior to calculating emittance from the macro-particle distributions in the usual way. For non-Gaussian distributions, this value more accurately represents a quality measurement for the core of the beam which is of most interest to FACET-II experimental requirements. This does not well describe the beam at the FACET IP however, where aberrations are present mainly at the IP angle phase, hence core beam sizes are better at the IP phase than suggested by the emittance. See Chapter 6, for more details of the tracking simulations for the Linac and Sector 20 of FACET-II.

Figure 5.13 and Figure 5.14 below show particle distributions tracked to the exit of the injector system at the entrance to the L1 Linac, and at the Sector 20 IP. Table 5.3 below summarizes the tracking results at these two locations. This simulation results indicate that this design exceeds the requirements for the FACET-II project requirements outlined in 5.3.1.

**Table 5.3: Tracking simulation results for baseline FACET-II design.**

Parameter	Symbol	Unit	Requirement	Simulation
Energy at injector exit (L1 entrance)	$E_0$	GeV	0.135	0.135
Energy at Sector 20 experimental region IP	$E_f$	GeV	10	10
Peak current at injector exit	$I_{pk}$	kA	-	0.24
Peak current at Sector 20 IP	$I_{pk}$	kA	>10	70
Bunch length after injector (rms)	$\sigma_z$	μm	-	838
Bunch length at Sector 20 IP (core rms)	$\sigma_z$	μm	<20	1.8
Energy spread after injector (rms)	$\sigma_\delta$	%	-	0.1

Energy spread at Sector 20 IP (rms)	$\sigma_\delta$	%	$\sim < 1.5$	1.4
Transverse emittance after injector (90%)	$\gamma\epsilon_{x,y}$	$\mu\text{m}\cdot\text{rad}$	-	2.9
Transverse emittance into Sector 19 (90%)	$\gamma\epsilon_{x,y}$	$\mu\text{m}\cdot\text{rad}$	$< 20$	3.9
Transverse beam size at Sector 20 IP (core rms)	$\sigma_x, \sigma_y$	$\mu\text{m}$	$< 20$	17.7, 12.2

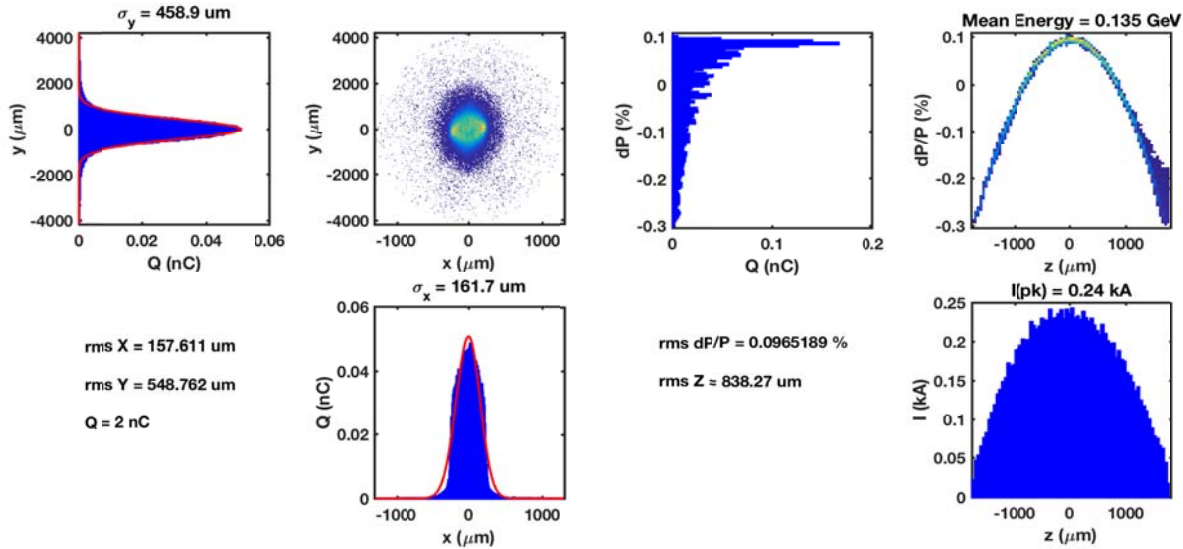


Figure 5.13: Longitudinal (right) and transverse (left) particle distributions at the end of the injector, prior to acceleration in L1.

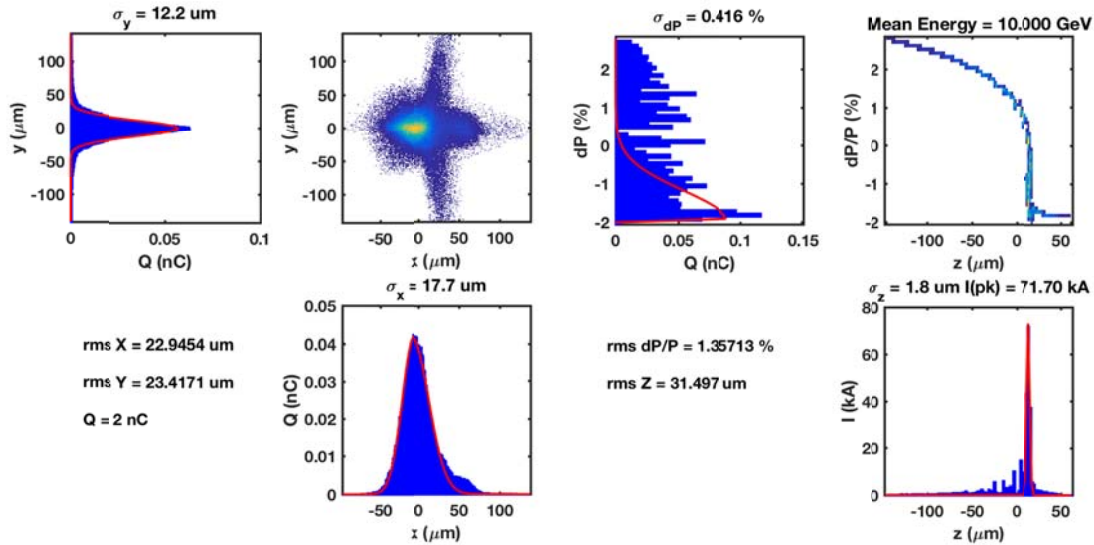


Figure 5.14: Longitudinal (right) and transverse (left) particle distributions at the FACET IP.

## 5.7 Linac Injector Horizontal Bend System (DL1)

The function of the low-energy ‘Dog-Leg’ (DL1) is to transport 135-MeV electrons from the new injector into the existing SLAC linac. DL1 is designed as a simple transport line, its design requirements are:

- Provide a horizontal beamline deflection of  $35^\circ$  over a short distance,

- Should not alter the bunch length (*i.e.*, should be nearly isochronous),
- Should introduce no significant transverse emittance dilution,
- Should provide a dispersive section for energy and energy spread measurement.

A simple system that satisfies these conditions is composed of two dipole magnets of equal strength with a quadrupole lens located between them to produce a linear achromat. The dipoles are rectangular bends. A profile monitor based on Optical Transition Radiation (OTR) and a BPM at the high dispersion point will provide energy and energy spread measurements.

**Table 5.4. Parameters of the linac injector horizontal bend system (DL1).**

Parameter	Symbol	Unit	Value
Beam energy	$E_{\text{DL1}}$	MeV	135
Total horizontal deflection (sum of 2 bends)	$\theta$	deg	35
RMS bunch length	$\sigma_z$	mm	0.8-1.6
RMS energy spread throughout beamline (at 135 MeV)	$\sigma_\delta$	%	0.11-0.35
Momentum compaction	$R_{56}$	mm	6.3
Second order momentum compaction	$T_{566}$	mm	140
Length of each of two dipole magnets	$L_B$	m	0.20
Bend angle of each dipole	$ \theta_B $	deg	17.5
Magnetic field of each dipole	$ B $	kG	6.9
Maximum horizontal dispersion	$ \eta _{\text{max}}$	mm	263

The momentum compaction,  $R_{56}$ , of such a system for ultra-relativistic electrons and small angles is

$$R_{56} \approx \frac{1}{3} \theta_B^2 L_B , \quad (1)$$

where  $\theta_B$  and  $L_B$  are the bend angle and length of each dipole, respectively. A 1.3-meter long beamline with two 17.5° bends provides the required deflection and the 20-cm long dipoles produce an  $R_{56}$  of 6.3 mm (opposite sign of a chicane). Therefore, an electron which is off energy by 1% will move axially by only 60  $\mu\text{m}$ , which is small compared to the 0.8-1.6 mm rms bunch length. The effect of the second order momentum compaction,  $T_{566}$ , is even less. Nevertheless, the non-zero  $R_{56}$  value and the second order term of  $T_{566} \approx 0.14$  m has been taken into account throughout the design and stability optimization, and in the 2D and 6D particle tracking.

## 5.8 Injector Vacuum Systems

The pressure requirements for the FACET-II gun/injector vacuum systems are listed in Table 5.5. To maintain a differential pumping regime with a vacuum gradient that is lowest away from the gun, an additional ion pump (with respect to LCLS-I) will be located immediately downstream of the RF gun at the location that was occupied by a YAG screen, which is not often used in LCLS-I. The RGA originally installed on the gun in LCLS-I will be installed at this location. A fast DAQ system will be implemented to allow detailed tracking of vacuum events. The LCLS-I injector was upgraded with such a system in 2010.

**Table 5.5. Injector vacuum system pressure requirements.**

LCLS-1 equivalent	Unit	Value
Waveguides	Torr	$<1 \times 10^{-8}$
Gun	Torr	$<5 \times 10^{-10}$
GTL	Torr	$<5 \times 10^{-9}$
L0A/B	Torr	$<5 \times 10^{-9}$

## 5.9 Instrumentation, Diagnostics, Feedback, and Collimation

Critical to the preservation of the transverse emittance and the generation of a low-energy spread electron bunch are the precise measurement techniques and correction schemes used to initially commission and maintain the machine. The FACET-II injector has diagnostics located after each functional area of the injector, with correction schemes built into the design.

Located between the L0 accelerating section and the DL1 dogleg is a drift space spanning the radiation shield wall separating the injector vault from the linac accelerator housing. This drift space contains two OTR screens and one wire scanner, which allow for emittance measurements to be made using a ‘quadrupole-scan’ technique, taking advantage of the nominal beam waist. This diagnostic station will also incorporate a wire-scanner to provide a backup emittance measurement system for operating conditions which may cause problems for an OTR screen (a larger degree of bunch compression may cause optical CSR effects to limit the resolution of the measurements for example). A charge monitoring toroid and wakefield radiation bunch length monitor are also located in the diagnostic section. An overview of the beam diagnostics is shown in Figure 5.15.

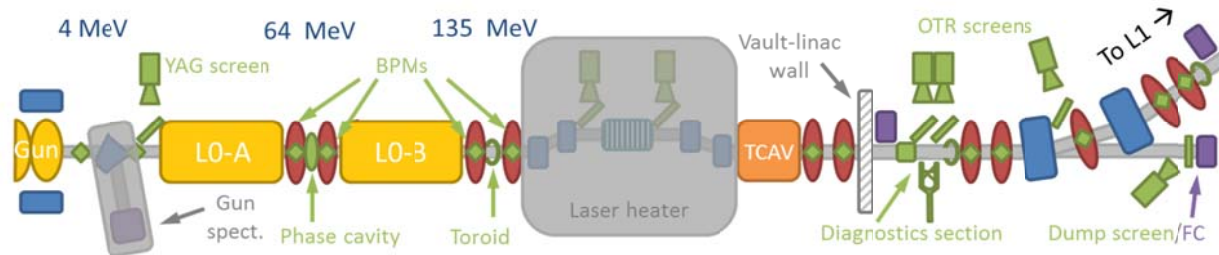


**Figure 5.15: Injector beamline diagnostics layout. Diagnostic devices are shown in green, while the gun spectrometer and laser heater chicane are shown greyed out as they are considered future upgrades for FACET-II.**

The injector diagnostics will be controlled and read out via EPICS-based hardware and software developed for LCLS and LCLS-II.

### 5.9.1 Beam Position Monitors (BPMs) and Charge Monitors (Toroids)

The FACET-II injector has 12 beam position monitors (BPMs) distributed along the injector with one in or near each quadrupole focusing magnet, as well as at high-dispersion regions for measurement and control of beam energy. Table 5.6 contains a full list of the FACET-II injector BPM specifications.

The bipolar signal pulse from the four striplines is carried on high-quality, length-matched coaxial cables to processing electronics located in the Sector 10 RF hut, where they are processed into difference and sum signals and provided to users via EPICS channel access. In the MicroTCA BPM platform developed

for LCLS-II [14], the raw signals pass through analog front-end electronics including a 300 MHz band-pass filter which produces a relatively long ringing signal that is digitized by a Struck SIS8300 digitizer clocked at 109 MHz. This system is self-calibrating and has demonstrated excellent resolution at LCLS, less than 5 microns at 250 pC. These BPM processors already built are no longer of use to LCLS-II, and FACET-II will use them in the injector if they are made available.

Otherwise, 12 CAMAC 605-style BPM processors recovered from the SLAC Sector 0-10 equipment recovery project will be installed in their place. This system designed for the SLC linac uses analog hybrid front end and three sample-and-hold 10-bit ADC circuits to directly integrate the sum and two difference signals. The 605 processors have 50 – 100 micron resolution and poor performance below 800 pC of beam charge. BPM readings will be available from the SLC control system and BPM sampler software will push the BPM readings to EPICS PVs approximately once every 3 seconds.

New BPM processors being developed under the LCLS-I Mission Readiness project on the ATCA “common platform” will be evaluated for use in FACET-II as well.

**Table 5.6: FACET-II injector BPM specifications. The “stay clear” column is the nominal  $10\sigma$  rms beam diameter from tracking simulation of the 2 nC beam.**

FACET-II Deck Name	Roll Angle	Stay Clear	BPM ID	Stripline Length	Captive Magnet
	deg	mm	mm	mm	
BPM02B	45	14.1	30	100	XC/YC01B
BPM03B	45	14.1	30	100	--
BPM05B	45	15.7	20	120	QA02B
BPM10436	45	10.6	20	120	QE10436
BPM10557	45	8.9	20	120	QE10557
BPM10572	45	6.4	20	120	QE10572
BPM10669	45	2.3	20	120	--
BPM10738	45	3.9	20	120	QM10738
BPM10759	45	7.9	20	120	QM10759
BPM10815	45	6.6	20	120	QB10815
BPM10869	0	5.1	20	120	QM10869
BPM10885	0	10.6	20	120	QM10885

Three toroids for precise measurement of non-invasive pulse-by-pulse bunch charge data are located in the injector: one just upstream of the LOA/B accelerating structures, one in the diagnostic waist section, and one just upstream of the entrance to the L1 linac. These absolute charge measurements are then used to calibrate other diagnostics which have a sensitivity to bunch charge, such as BPMs and bunch length monitors.

The 3 FACET-II injector toroids are 0.875" ID resonant toroids originally purchased for LCLS-II, which no longer requires their use. The same toroid design was originally installed at LCLS, and were limited by high noise and accuracy no better than 5-10% due to the combination of single-ended signal path and low beam charge. An upgrade to the LCLS toroids was performed in 2013, including the installation of a 10x amplifier with integrated remote calibrator located in the tunnel at the toroids, differential cables for the preamplified signal, and Caen QDC965A VME 12-bit digitizer replacing the original Acromag

IP330 ADC. This upgraded system has demonstrated better than 1% absolute accuracy [15] and will be suitable for FACET-II.

**Table 5.7: FACET-II injector toroid requirements.**

FACET-II Deck Name	Location	S from cathode	Accuracy 1 – 5 nC	Precision 1 – 5 nC	Stay Clear
			% rms	% rms	mm
IM10441	Upstream of L0A	8.6	< 5.0	< 2.0	9.5
IM10700	Diagnostic waist	15.2	< 5.0	< 2.0	2.6
IM10893	L1 linac entrance	20.2	< 5.0	< 2.0	10.4

Four additional BPMs and two additional toroids are located in the gun and injector spectrometer diagnostic lines, though those sections of the injector are not planned to be installed as part of the FACET-II project. In place of the straight-ahead spectrometer line, the Sector 1 BAS-I Faraday cup dump will be installed on a short spur of beamline, and will be instrumented with a nanoammeter to verify the toroid signals with the injector dogleg magnets turned off.

### 5.9.2 Electron Beam Profile Monitors (Screens and Wire Scanners)

Four intercepting electron beam screens and one wire scanner are used throughout the injector to measure the transverse beam size. Located between the L0 accelerating section and the DL10 dogleg is a drift space spanning the radiation shield wall separating the injector vault from the linac accelerator housing. This drift space contains two profile monitors and one wire scanner which allows emittance measurements to be made using a ‘quadrupole-scan’ technique, taking advantage of the nominal beam waist on the center profile monitor, PR10678. This profile measurement station will also incorporate a wire-scanner to provide a backup emittance measurement system for operating conditions which may cause problems for an OTR screen (a larger degree of bunch compression may cause optical CSR effects to limit the resolution of the measurements, for example).

The profile monitors are insertable screens which intercept the beam with a material that generates visible light in proportion to the local beam charge. The screens are either fluorescent YAG:Ce crystals, thin metal foils which generate optical transition radiation (OTR) at the foil surface, or plates coated with a phosphorescent material such as chromium-doped alumina (Chromox). These allow measurement and tuning of the transverse beam distribution, as well as longitudinal tuning when placed at regions of high dispersion, especially in conjunction with the transverse deflecting cavity. A schematic of the profile monitors is shown in Figure 5.16 and the specifications for each profile monitor screen is given in Table 5.8.

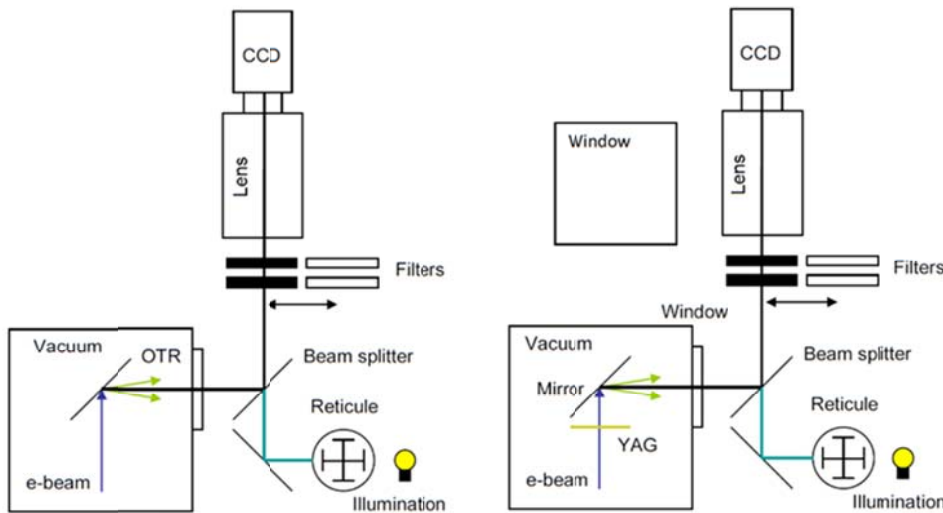


**Figure 5.16. Injector profile monitor schematic for OTR/phosphor (left) and YAG (right).**

**Table 5.8. List of injector profile monitors and their required screen type, diameter, resolution and expected beam size at 2 nC.**

FACET-II Name	Type	Location	S from cathode	Beam energy	D	T	Res	$\sigma_x$	$\sigma_y$
			m	MeV	mm	$\mu\text{m}$	$\mu\text{m}$	mm	mm
YAG02B	YAG:Ce	Upstream of L0A	1.39	6	20	100	25	0.7	0.7
PR10678	OTR AI	Diagnostic waist	14.68	135	20	1	10	0.11	0.11
PR10690	OTR AI	Diagnostic waist	15.00	135	20	1	10	0.12	0.11
PR10800	OTR AI	Dogleg bend	17.8	135	20	1	10	0.22	0.22

The YAG02B profile monitor is used for cathode imaging and gun studies. The diagnostic waist profile monitor, PR10678 is the main injector tuning diagnostic used largely in conjunction with an upstream quadrupole magnet to do quad-scan emittance measurements. The dogleg profile monitor provides energy-spread measurement due to its location in a high dispersion area. In conjunction with the upstream TCAV, time-sliced energy and energy spread measurements are possible.

OTR foils of 1  $\mu\text{m}$  aluminum were selected for LCLS-II due to higher reflectivity and OTR yield than titanium at low LCLS-II beam charge. The damage threshold for aluminum will be evaluated in the 2 nC FACET beam and titanium will be used if there is a risk of damage.

Wire scanners provide transverse beam profiles sampled over 50 – 100 pulses by moving a stretched wire across the beam path in uniform steps and measuring radiation downstream of the scattered beam. At LCLS, the wire scanner system is the main diagnostic for projected beam size measurements of the high brightness electron beam past the injector due to issues of coherent radiation from micro-bunching affecting OTR screens. It is not yet clear to what extent the COTR problem will manifest in the FACET-II injector. Therefore, a single wire scanner of the SLC design recovered from the Sector 0-10 equipment removal project, along with its associated detector, will be installed in the injector located next to the “workhorse” injector profile monitor PR10678 (formerly OTR2B). A summary of the wire scanner parameters is given in Table 5.9.

**Table 5.9. Injector wire scanner requirements.**

WS10684	Value
S distance from cathode [m]	14.9
Beam energy [MeV]	135
Nominal rms beam size $\sigma_x, \sigma_y$ [ $\mu\text{m}$ ]	120, 120
Maximum rms beam size $\sigma_x, \sigma_y$ [ $\mu\text{m}$ ]	600, 600
Minimum rms beam size $\sigma_x, \sigma_y$ [ $\mu\text{m}$ ]	50, 50
Wire diameter [ $\mu\text{m}$ ]	20
Wire material	Tungsten
Wire directions	x, y, u
Minimum scan speed [ $\mu\text{m/s}$ ]	22
Maximum scan speed [ $\mu\text{m/s}$ ]	5000

### 5.9.3 Timing Diagnostics (Beam Phase Cavity)

A beam phase monitor cavity is located between the L0-A and L0-B RF accelerating sections in the injector linac and is used to determine the electron bunch arrival time with respect to an RF phase reference signal. This measurement may be used in a feedback loop to control the timing of the drive laser for the photo-cathode RF gun to correct for slow drifts over a time scale of seconds to minutes. This slow drift requirement is based on preservation of the transverse emittance, which is increased by 5% for an error of  $\pm 4$  ps in the gun RF – laser timing.

The phase cavity system uses the same design in use at LCLS-I for the injector and undulator beam phase cavities, namely a copper clad stainless steel body cavity tuned to a resonance at 2805 MHz. The cavity RF frequency is 51MHz below the S-band RF frequency of 2856MHz. The beam-induced pulse will be mixed with a reference RF signal and the IF signal digitized by a digitizer clocked by a subharmonic of the RF reference. With careful cable temperature stabilization and noise isolation, this system has demonstrated timing resolution better than 50 fs at LCLS.

The system described above provides excellent timing resolution within a single 2856 MHz RF bucket. To resolve timing jumps larger than the 350-ps bucket, a bucket jump detector based on edge detection of a raw beam-induced signal (such as a BPM) with respect to an EVR trigger may be employed, as it currently is at the LCLS injector.

### 5.9.4 Bunch Length Diagnostics

The peak current delivered to the experimental user area in sector 20 is a critical parameter. It is determined by both the charge and the final bunch length and non-trivially dependent on the specific compression configuration employed by the various compression stages. To set up the compression, the bunch length and distribution needs to be measured and corrected before injection into the linac.

#### 5.9.4.1 Relative Bunch Length Monitor

In the injector, the bunch length range of interest is approximately 1.3-0.8 mm rms. A single-shot relative bunch length monitor based on the detection of wakefield radiation from a ceramic gap in the beam pipe will be used to provide pulse-by-pulse relative bunch length signals. The total radiated

power is roughly proportional to  $q^2/\sigma_z$ . A mounting plate surrounding the ceramic gap will hold a pair of waveguides and diode detectors and be aligned to the beam to  $\pm 1$  mm. The ceramic gap, plate, waveguides and 60/100 GHz detectors were used in FACET for monitoring the 1.5 mm bunch length injected into the Sector 2 linac, and will be recovered from the Sector 0-10 equipment removal project and reinstalled in the injector diagnostic section just downstream of the toroid IM10700. Low-loss coaxial cables will carry the diode output signal to a diagnostic oscilloscope and a charge-integrating ADC. Calibration of the bunch length monitor will be performed using the transverse RF deflecting cavity.

#### **5.9.4.2 Transverse RF Deflectors**

A very simple technique to measure the very short electron bunch is to use a transverse RF deflecting cavity. This idea has been used in the past [16], [17] and has been quite successful at the LCLS-I and also in sector 20 during FACET-I operations. The high frequency time variation of the deflecting field is used to ‘pitch’ the electron bunch, while the resulting transverse beam width is measured on a simple profile monitor. This is a reliable, single-shot measure of the absolute bunch length. The technique is completely analogous to a streak camera, but with much better potential resolution down to about 10 fs rms, depending on the energy and vertical emittance. Detailed studies have been made of this technique [18], including wakefield and chromatic effects, and beam measurements have also been made at LCLS-I and FACET-I [19], [20]. A design for a 0.55-meter long S-band RF deflecting structure is available at SLAC and is now used in the LCLS-I injector. A cut-away view of the S-band traveling-wave rf-deflector is shown in Figure 5.17. A new deflecting structure of this design will need to be fabricated.

The bunch length,  $\sigma_z$ , can be calculated from knowledge of the deflecting voltage,  $V_0$ , the RF wavelength,  $\lambda_{rf}$ , and the beam energy at the screen,  $E_s$ .

$$\sigma_z \approx \frac{\lambda_{rf}}{2\pi} \frac{E_s}{|eV_0 \sin \Delta\psi \cos \varphi|} \sqrt{\frac{\sigma_y^2 - \sigma_{y0}^2}{\beta_d \beta_s}} \quad (2)$$

Included here is the product of  $(\beta_d \beta_s)^{1/2} \sin(\Delta\psi)$ , which is the (measurable) vertical transfer matrix element from angle-to-position and deflector-to-screen. Finally,  $\varphi$  is the RF phase of the deflector ( $\varphi = 0$  at zero-crossing) and  $\sigma_y$  and  $\sigma_{y0}$  are the measured vertical beam sizes with RF on and off, respectively. The voltage of the deflector is easily calibrated using simple BPM measurements as a function of RF phase. The RF deflecting structure (55 cm long) will be located in the injector at 135 MeV, as in the LCLS-I, providing <0.1 ps resolution of the 5 ps long bunch there (see Figure 5.18).

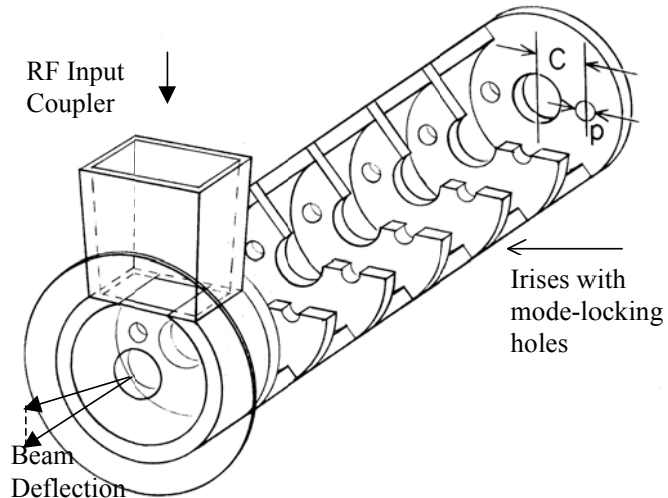


**Figure 5.17. Schematic of a SLAC S-band transverse deflecting structure. The kick is vertical here.**

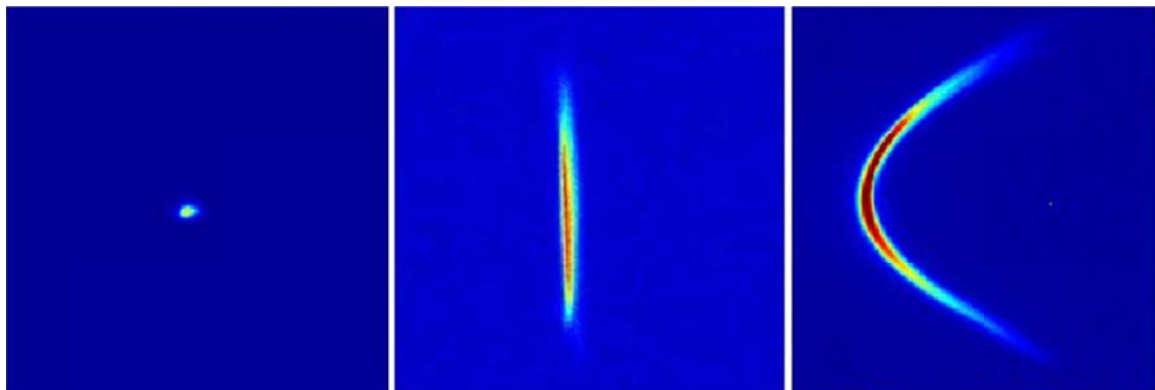


**Figure 5.18. OTR image with RF deflector “OFF” (left) and “ON” (middle), to measure slice emittance. YAG screen after a bend (right) with deflector ON, reveals longitudinal phase space directly on the screen. The horizontal axis ( $\pm 4$  mm) is the horizontal beam coordinate in the left two plots, but it becomes relative energy in the right plot ( $\pm 0.8\%$ ). The vertical axis ( $\pm 4$  mm) is the vertical beam coordinate in the far left plot, but it becomes time in the two right plots ( $\pm 8$  ps).**

The structure as shown in Figure 5.17 is approximately 55 cm and provides a maximum deflecting voltage of 1.4 MV on crest at an RF pulse power of 2 MW. The structure will be fed from the klystron located at station 10-5 in the klystron gallery.

## 5.9.5 Beam Energy Spread Diagnostics

The electron energy spread is typically measured using a profile monitor at a location with large momentum dispersion and small beta function. The key location designed into the FACET-II optics is in the DL10 dog-leg system at 135 MeV (35 degree bend from injector into the linac), where an insertable profile monitor is located a region of maximum horizontal dispersion.

### 5.9.5.1 DL1 Energy Spread Diagnostics

The energy spread measurement in DL10 is made with one of two possible profile monitors (a retractable OTR screen or a wire-scanner) located between the two dipoles of DL1 at the point where

the horizontal dispersion function reaches a value of  $|\eta_x| \approx 154$  mm (OTR) with a horizontal beta function of  $\beta_x \approx 1.4$  m. For the nominal emittance and nominal energy spread of  $\sigma_\delta = 0.1\text{-}0.35\%$  at 135 MeV, the betatron beam size is 160  $\mu\text{m}$  rms, but the dispersive size is 154-540  $\mu\text{m}$ . The statistical error depends on the profile monitor and should be 5–10%. The principal purpose of the energy spread diagnostics is to minimize the energy spread into DL10 by adjusting the phase of L0b.

### 5.9.6 Feedback Systems

Software-based feedback systems will be used throughout the injector and the whole of FACET-II using an architecture that has seen heavy use at LCLS and FACET. These feedbacks are typically implemented as either Matlab or Python scripts which use existing communications systems (EPICS channel access, AIDA control of SLC control system devices, etc) to actuate some device based on the reading of a set of diagnostics.

Trajectory feedback systems will be placed at the exit of the gun and in the injector. As at the SLC [21], and as utilized during FACET-I operations, these systems will each be composed of approximately ten BPMs which record both  $x$  and  $y$  positions, preceded by a set of two horizontal and two vertical fast dipole corrector magnets controlled by a software based feedback system.

In order to control transverse orbit variations to better than  $1/10^{\text{th}}$  of the beam size in the injector, the individual one-pulse BPM resolution for the 10 BPM feedback systems described above needs to be  $<10\text{ }\mu\text{m}$  rms. Trajectory variations which occur at frequencies below  $\sim 5$  Hz will be stabilized. Faster variations cannot be damped significantly and will need to be identified at the source. Transverse vibrations of quadrupole magnets will generate orbit variations, which if fast enough will not be damped by feedback systems. Magnet vibration tolerances in the injector are set according to LCLS experience: 0.1  $\mu\text{m}$  rms pulse-pulse transverse stability. Tolerance calculations for the Linac magnets indicate that uncorrelated random vibrations for magnets can be at the level of  $< 1.5 / 0.5\text{ }\mu\text{m}$  rms (horizontal / vertical) which corresponds to typical measurements in the SLC linac in the past. See Chapter 6 for more details of tolerance calculations.

A bunch charge feedback loop will maintain the bunch charge by reading the TMIT sum signal from BPM02B and controlling the UV laser energy per pulse with a rotating polarizer/wave plate attenuator. Tolerance studies require this system to be capable of regulating fluctuations in the injected beam charge to less than 2% of the full charge. An analogous feedback at LCLS operates well within this specification. Additionally, the measurement from the beam phase cavity will be used to delay the laser pulse timing in order to regulate the relative timing between the laser pulse and the RF reference to better than 0.2 ps.

Energy feedback systems will be placed in the bending region (DL1). A single BPM, BPM10815 at the high dispersion point of the dogleg, will be used to stabilize the beam energy by varying the amplitude of the LO-B klystron drive.

---

1 G. White, FACET-II-TN001 “FACET-II Electron Injector Optimization”

- 
- 2 R. Akre *et al.*, Phys. Rev ST – Accel. Beams **11**, 030703 (2008).
- 3 X. Wang, et al., PAC 99 Proceedings, 1999, p. 3495.
- 4 R. Akre et. al., COMMISSIONING THE LCLS INJECTOR, SLAC-PUB-13014
- 5 Rosenzweig, James, and E. R. Colby. Charge and wavelength scaling of RF photoinjector designs. No. TESLA-95-04. SCAN-9505146, 1995.
- 6 Kim, Kwang-Je. "RF and space-charge effects in laser-driven RF electron guns." Nuclear Instruments and Methods in Physics Research Section A: Accelerators, Spectrometers, Detectors and Associated Equipment 275.2 (1989): 201-218.
- 7 Rosenzweig, James, and E. R. Colby. Charge and wavelength scaling of RF photoinjector designs. No. TESLA-95-04. SCAN-9505146, 1995.
- 8 ATF Experimental Log Book 03/10/2010.
- 9 V. Yakimenko, et al., NIM A 483 (2002) 277–281 and V. Yakimenko Private communications.
- 10 J. Qiang et al., Phys. Rev. ST Accel. Beams **9**, 044204 (2006).
- 11 P. Tenenbaum, SLAC-PUB-11215, (2005). <http://www.slac.stanford.edu/accel/ilc/codes/Lucretia/>
- 12 M. Borland, Proc. of the ICAP-2000 Conference, Darmstad (2000)
- 13 <http://www.mathworks.com/products/matlab/>
- 14 C. Xu et. al, Design of an Ultra-Compact Stripline BPM Receiver Using MicroTCA for LCLS-II at SLAC, SLAC-PUB-15734 (2013).
- 15 H. Loos, LCLS Beam Diagnostics, WEIXB1, Proceedings of IBIC 2014, Monterey, CA (2014).
- 16 G. A. Loew, O. H. Altenmueller, Design and Applications of R.F. Deflecting Structures at SLAC, PUB-135, Aug. 1965.
- 17 R.H. Miller, R.F. Koontz, D.D. Tsang, The SLAC Injector, IEEE Trans. Nucl. Sci., June 1965, p. 804-8.
- 18 P. Emma, J. Frisch, and P. Krejcik, *A Transverse RF Deflecting Structure for Bunch Length and Phase Space Diagnostics*, LCLS-TN-00-12, August 2000.
- 19 P. Emma, et al., Bunch Length Measurements Using a Transverse RF Deflecting Structure in the SLAC Linac, Proceedings of the 2002 European Particle Accelerator Conference, Paris, France, June 3-7, 2002.
- 20 V. A. Dolgashev et. Al., Design and application of multimegawatt X-band deflectors for femtosecond electron beam diagnostics, Phys. Rev. ST Accel. Beams **17**, 102801 (2014)
- 21 T. Himel et al., *Adaptive Cascaded Beam-Based Feedback at the SLC*, Proceedings of the 1993 Part. Accel. Conf., Washington, DC, 1993.

# 6 loops.Bunch Compressors and Linac

---

## Technical Synopsis

*In order to achieve the scientific goals of the experimental program at FACET-II, a high peak current bunch with small transverse emittance at the end of the Linac ( $\gamma e < 20 \text{ um.rad}$ ) and small longitudinal emittance is required (<20 um rms bunch length at IP). FACET-II will operate with electron and positron bunches at an energy of up to 10 GeV. The most challenging parameters for the design of the bunch compression scheme are given by the plasma wakefield acceleration (PWFA) experiments which benefit from peak currents in excess of 10 kA. The RF photocathode electron gun and injection system is similar to that used in LCLS. This injector is capable of producing up to 5 nC with bunch lengths in the range 2-10 ps with corresponding peak currents of up to 300 A and transverse emittances of <5  $\mu\text{m}$ . Positrons are generated in the existing target in Sector 19 of the Linac, transported through existing return lines mounted on the ceiling to Sector 10 where they are damped in a new damping ring before being transported to the main Linac, injected in the final bend of the first stage electron compressor at 335 MeV.*

*Both electrons and positrons undergo three stages of bunch compression, the first two stages in Linac Sectors 11 and 14 and the final compression stage in Sector 20. The Sector 20 chicanes are described in Chapter 9. The initial stage of positron compression takes place in the transfer line from the damping ring before injection into the main Linac in the final bend of BC11 (in Sector 11). The details of the positron systems are mainly described in chapters 8 and 9.*

*The capabilities of FACET-II vary in a non-trivial way depending on the choice of initial charge from the RF gun. The baseline design is for a 2nC electron bunch charge, with a possible future upgrade configuration option of a 5 nC bunch, or co-acceleration of a 2 nC electron bunch together with a 1 nC positron bunch described in Chapter 10.*

*The bunch compression is accomplished by a series of magnetic chicanes arranged and located such that non-linearities in the compression and acceleration process (longitudinal wakefields, RF curvature, and second order momentum compaction) are all approximately compensated. The goal for the Linac design is to achieve the final bunch length requirements for both positron and electron bunches, while minimizing sensitivities to RF phase and amplitude variations and also to bunch charge variations. The electron energy at the first compressor is 335 MeV. This choice avoids space charge effects, while the bunch compression is still early enough in the linac to ease the effects of transverse wakefields. In the first compressor (BC11), the electron bunch length is reduced from 0.84 mm to 468  $\mu\text{m}$  (rms). For operation with positrons, the positron beam is injected into the linac in the final BC11 bend with a bunch length of 276  $\mu\text{m}$  (rms). The injection energy of 335 MeV is also convenient for the design of the compact positron damping ring. The bunch length of the positrons, upon extraction from the damping ring, is 3.5 mm (rms). To match well into the linac compression scheme, an additional bunch compressor (2.1m S-band RF section and 4-bend chicane) is included in the damping ring-to-linac beamline section.*

*The second compressor (BC14 in Sector 14) produces a ~100  $\mu\text{m}$  rms bunch length for electrons & positrons. The energy of the second compressor, 4.5 GeV, is chosen as a balance between the conflicting requirements of emittance dilution due to synchrotron radiation, and the need to minimize energy*

spread when including the final compression stage in sector 20. The design of the compressors is also affected by the need to reduce CSR effects, which are most pronounced for short bunches. The most significant effect of CSR is to generate a time-dependent energy variation along the bunch. Designs utilizing relatively weak chicanes and larger initial correlated energy spreads for the various compression stages help control the effect CSR has on transverse emittance dilution. The largest single source of emittance dilution is within the Sector 20 bunch compressor. The need to keep the peak current as low as possible ( $\sim 3$  kA) at the entrance to Sector 20 whilst still compressing to  $<20$   $\mu\text{m}$  bunch lengths drives the overall compression scheme design. The final compression stage in sector 20 using the BC20 chicane at 10 GeV is described in Chapter 9.

6D tracking simulations have been made to model the beam transport through the FACET-II complex, including the non-linear compression and final beam focus process. The simulations include the effects of longitudinal wakefields in the 1km linac as well as incoherent and coherent synchrotron radiation effects in the various bending magnets. Longitudinal space charge effects are also simulated. Simulations have also been made which calculate emittance dilution in the linac due to transverse wakefields and anomalous momentum dispersion, each of which arises from a variety of considered error sources such as component misalignment and magnetic field errors. Diagnostics, correction techniques, and feedback systems have also been incorporated into the design.

## 6.1 Main FACET-II Linac

The main Linac of FACET-II (sectors 11-20) is designed to accelerate the electron beam to 10 GeV using about 850 meters of S-band (2.856 GHz) radio frequency (RF) traveling-wave accelerating structures. The main Linac for the FACET-II electron system (as in LCLS-I) is segmented into three separate sections, as shown in Figure 6.1.

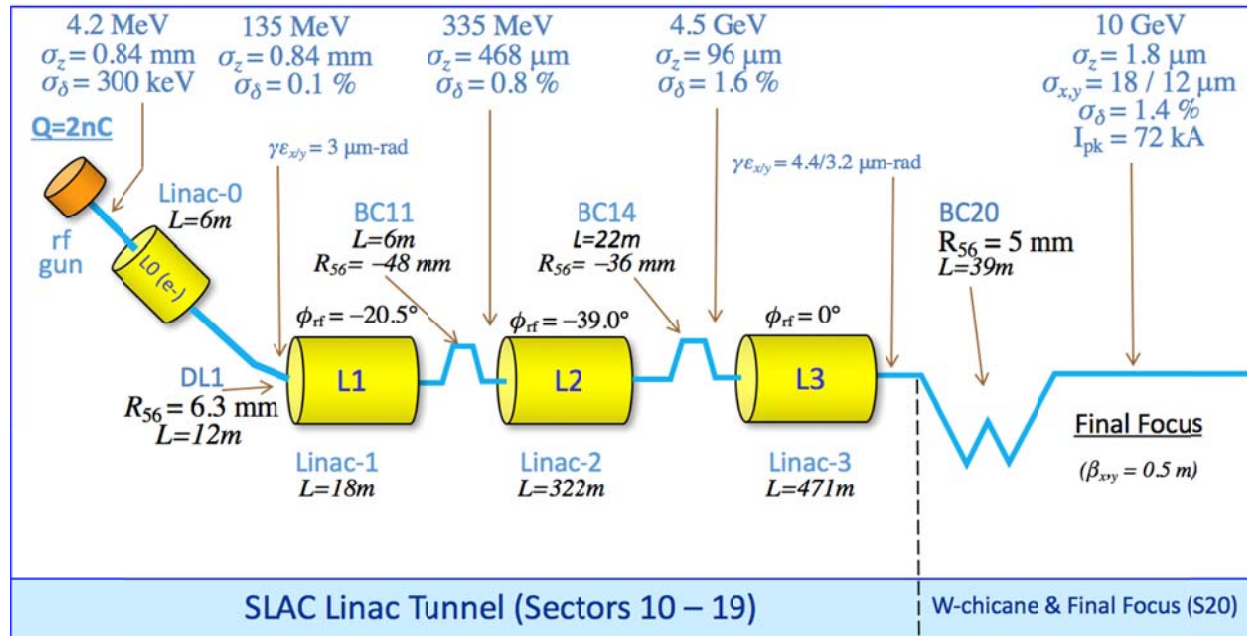
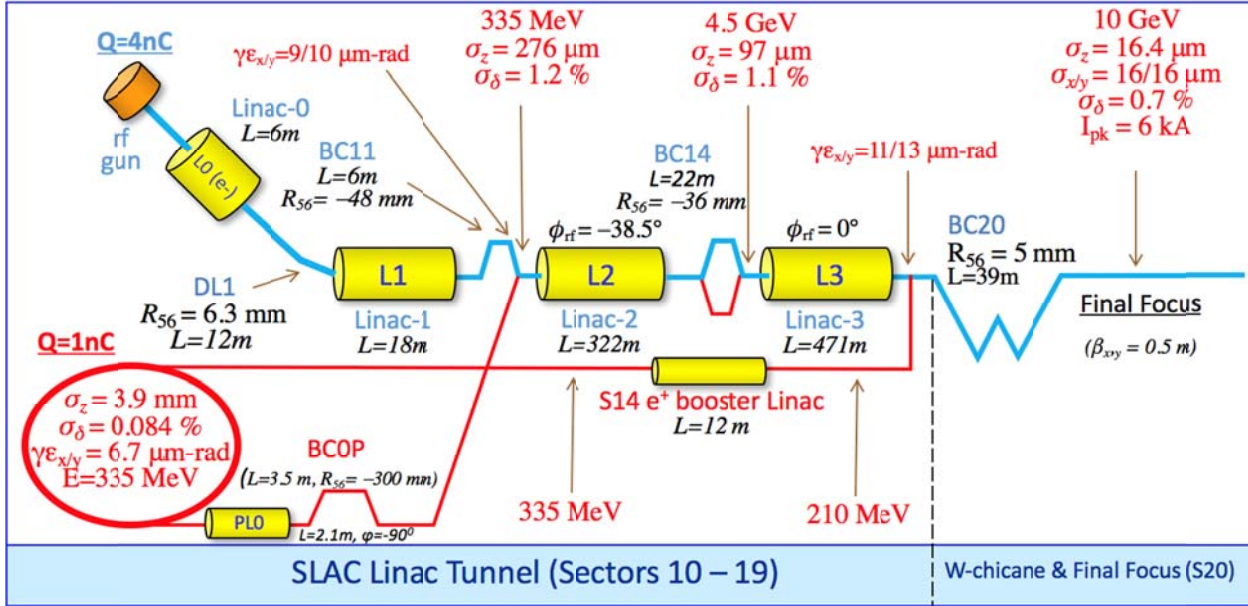


Figure 6.1. Schematic layout of FACET-II injector, linac, bunch compressors, and experimental area, with main parameters listed for electron beam operation.



**Figure 6.2. Schematic layout of FACET-II injector, linac, bunch compressors, and experimental area, with main parameters listed for positron beam operation.**

The first acceleration section after the injector is the L1-Linac (L1) composed of three 3-m long S-band accelerating structures in each of RF sections 11\_1 and 11\_2. Here the bunch is accelerated off the RF crest (-20.5 deg S-band) up to 335 MeV and then compressed partially in the BC11 chicane. The L2-Linac (~326 m) follows the BC11 chicane and also accelerates off-crest (-39 deg S-band) up to 4.5 GeV where the second Bunch Compressor (BC14) chicane executes the next stage of bunch length compression. Beyond BC14 is the L3-Linac (582 m), which accelerates on-crest to an energy of 10 GeV. To avoid excessive energy spread, the Sector 20 chicanes are designed with opposite sign  $R_{56}$  compression parameters (compared to the earlier chicanes) to compress most effectively in conjunction with the wakefield chirp imposed by L3. The positron beam on extraction from the damping ring requires an additional compression stage before injection into the final BC11 bend and is described in Chapter 9.

The transverse optics in the various Linac sections were designed to minimize transverse wakefield effects and also to loosen magnet alignment tolerances. This is done at the design stage by selection of the phase-advance per linac cell independently for the three linac sections.

### 6.1.1 Linac Energy Management

With two bunch compressor chicanes to be located within the 850 meters of main linac, and the RF phase to be set significantly off crest (-20.5° in L1 and -39° in L2), the recommended layout of the accelerating sections is summarized here, including spare klystrons in each long Linac section (L2 and L3) suggested. There is one spare klystron in L2 with the RF 39-deg off crest, and 2 klystrons are reserved for BC14 energy feedback control. With the BC11 energy as  $E_1$ , we can show the BC14 energy,  $E_2$ , and the max final linac energy,  $E_3$ , as

$$E_2 = E_1 + N_{k2} \Delta E_k \cos \varphi_2 + N_{f2} \Delta E_k \cos \varphi_{2f} \quad (3)$$

$$E_3 = E_2 + N_{k3} \Delta E_k \cos \varphi_3 + N_{f3} \Delta E_k \cos \varphi_{3f} \quad (4)$$

where  $\Delta E_k$  is the average energy gain of each klystron (taken as 231 MeV or 19 MV/m average gradient),  $N_{k2}$  as the number of powered klystrons in L2 at an RF phase of  $\varphi_2$ ,  $N_{f2}$  as the number of powered energy-feedback klystrons in L2 at a phase of  $\varphi_{2f}$ ,  $N_{k3}$  as the number of powered klystrons in L3 at an RF phase of  $\varphi_3$ , and  $N_{f3}$  as the number of powered energy-feedback klystrons in L3 at a phase of  $\varphi_{3f}$ . Choosing  $E_1 = 0.335$  GeV,  $E_2 = 4.5$  GeV,  $E_3 = 10.0$  GeV, and also choosing  $N_{f2} = 2$ ,  $\varphi_{2f} \approx 60^\circ$ , and  $\varphi_3 = 0$ , and  $N_{f3} = 6$  and  $\varphi_{3f} \approx 60^\circ$  we find that  $N_{k2} = 23$  and  $N_{k3} = 21$ . Adding in a spare klystron per linac section, accounting for the feedback klystrons, and reserving an RF station in each section for use by a transverse cavity for bunch length diagnostics, then the total number of required klystrons in L2 is 27, and 29 in L3. BC11 is placed in the location of the 11-3 and 11-4 RF structures, with BC14 taking over the space of 14-7 and 14-8. RF station 19-7 is used, as for FACET, for extracting the beam into the positron production line and station 15-2d is used for TCAV installation for bunch length measurements. There are 10 additional klystrons in L3, which would allow for a final energy up to  $\sim 13.5$  GeV if all available RF stations in L3 were to be used. The expected linac layout is shown in Figure 6.3.

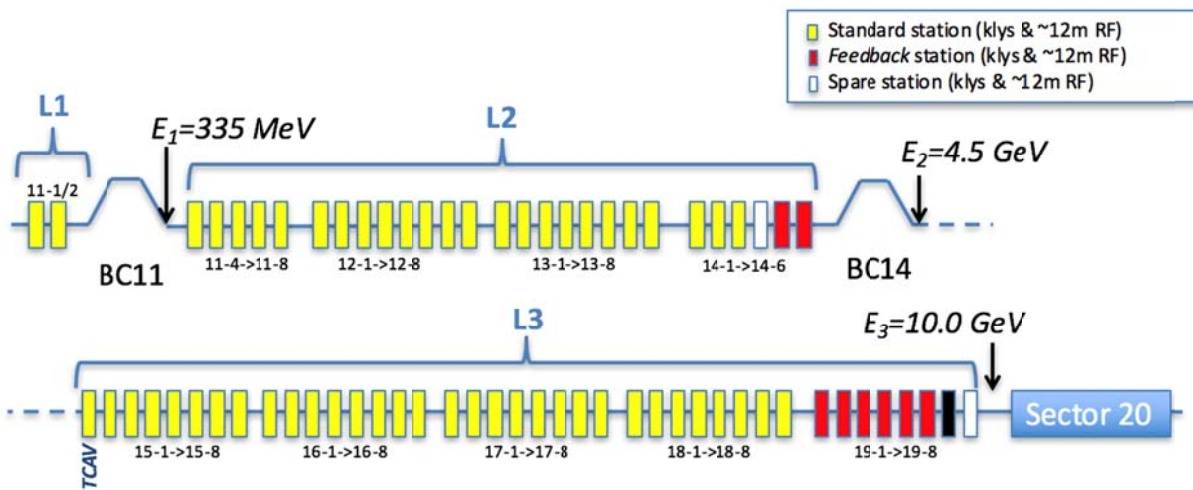


**Figure 6.3. Linac klystron distribution showing Sectors 11 through 20, where each box represents one klystron (typically 12 meters of accelerator with 231 MeV energy gain on crest).**

The yellow boxes are typical stations usually with four 3-m RF sections, the red boxes are energy-feedback stations, the white boxes are spare stations reserved for when failures arise. The black colored box indicates the removed section in 19-7 used for extraction of the positron-generating “scavenger” pulse.

Table 6.1 lists, for each FACET-II linac section, the total number of klystrons potentially available,  $N_{klys}$ , the number of klystrons held in reserve,  $N_{res}$ , the largest off-crest RF phase,  $\varphi_i$ , the on-crest average energy gain per klystron,  $\Delta E_k$ , the beam loading energy loss (+ CSR energy loss in bunch compressors) for  $Q = 1/2$  nC initial (positron/electron) charge,  $\Delta E_B$ , the nominal initial and final energy,  $E_i$  &  $E_{nom}$ , of that section, and the maximum energy,  $E_{max}$ . For L2 and L3 two numbers are presented for electron and positron beams respectively. The nominal charge, Q in each section (again for electron and positrons in L2 and L3) is shown.

**Table 6.1. Energy management parameters for the four main linac sections. L2 and L3 parameters show 2 numbers for electrons, positrons respectively. The beam loading energy losses indicated here include the few MeV energy-loss due to CSR in the bunch compressors.**

Linac	$N_{klys}$	$N_{res}$	$\phi_i$ [deg]	$\Delta E_k$ [MeV]	$\Delta E_B$ [MeV]	$E_i$ [GeV]	$E_{nom}$ [GeV]	$E_{max}$ [GeV]	$Q$ [nC]
L1	2	0	-20.5	102.5	3.1	0.135	0.335	0.44	2
L2	26	1	-39,-38	198	53,26	0.335	4.5	4.55	2,1
L3	38	1	0	148	117,63	4.50	10.0	13.5	2,1

### 6.1.2 Linac Optics

The electron optics in the various Linac sections are designed to minimize transverse wakefield effects and also to loosen magnet and RF structure alignment tolerances. Each section, with its different bunch length and energy spread values, has a different optimal configuration. Additionally, the beta functions are manipulated to be small and close to waist locations at the exit of each BC11, BC14 and Sector 20 bunch compressors in both dimensions. This minimizes the impact of CSR induced emittance growth for both electron and positron beams. The optics functions of the L1, L2, and L3 Linac sections are plotted in Figure 6.4, Figure 6.5 and Figure 6.6, respectively.

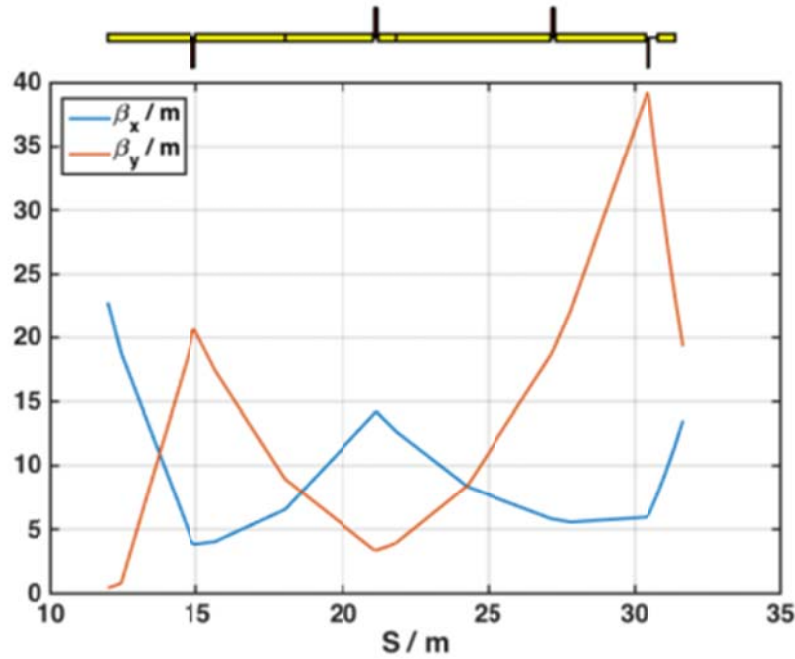


**Figure 6.4.** The optics functions of the L1-linac (11-1 and 11-2).

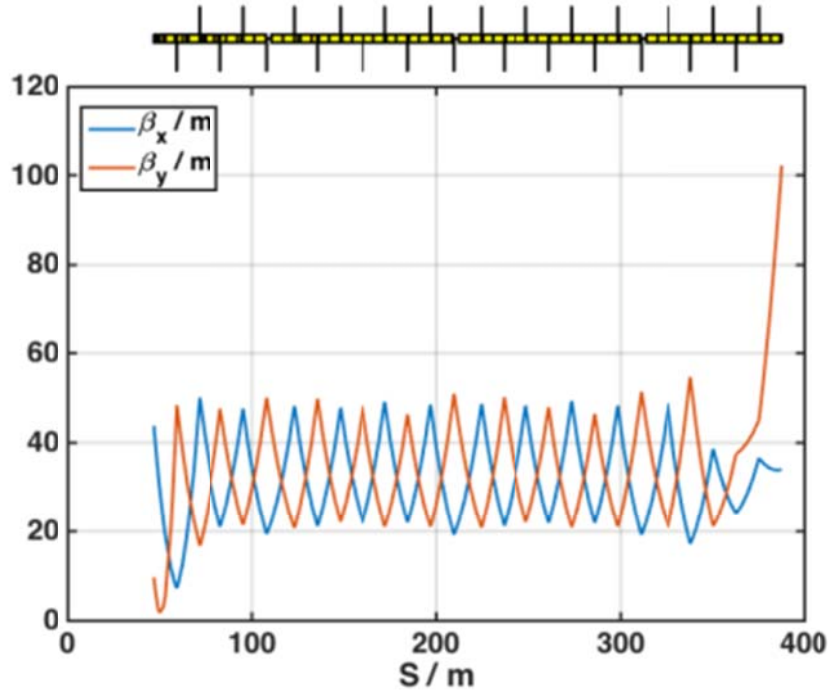


**Figure 6.5.** The optics functions of the L2-linac from 11-2 to 14-6, with a phase advance per FODO cell of 70 degrees.

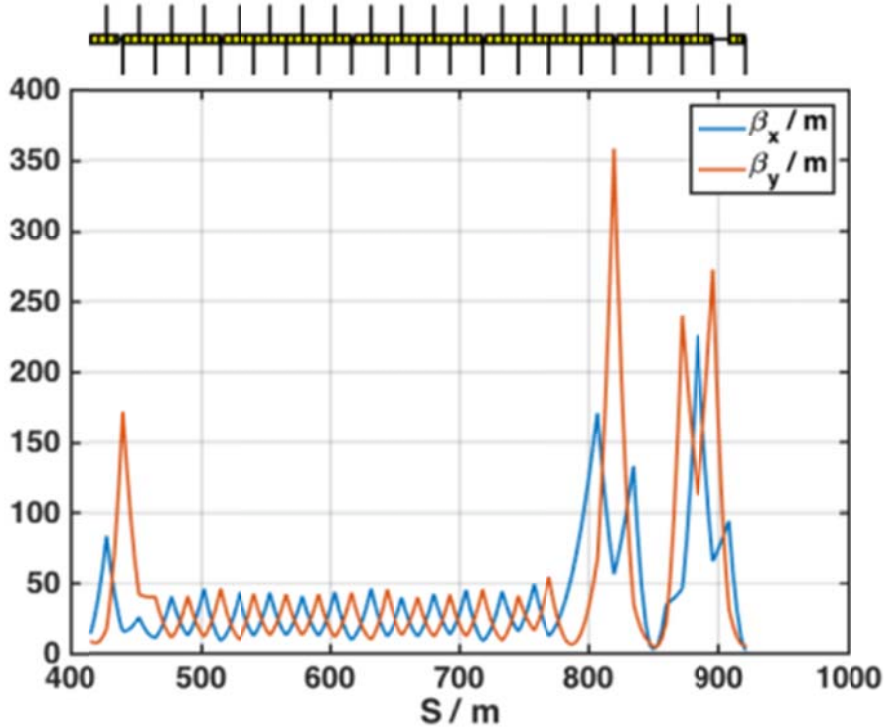


**Figure 6.6.** The optics functions of the L3-linac from 15-1 to 19-8, with a phase advance per FODO cell of 67 degrees.

### 6.1.3 Linac Modifications and Installation Issues

The SLAC Linac between sectors 11 through 19 must be modified to install the main components of FACET-II, especially considering the new bunch compressor chicanes. A list of the Linac beamline modifications follows:

- The 11-1b and 11-2b RF 10-foot sections must be replaced with 9.4-foot sections in order to insert a quadrupole magnet after each RF section in the L1-Linac (there has never been an 11-1a RF section in the linac and this will continue). Two new quadrupoles are introduced into the L1 Linac section to help with matching into BC11.
- All four of the 11-3a, b, c, and d 10-foot RF sections need to be removed to install the new BC11 compressor chicane and its associated beam diagnostics.
- All eight of the 14-7a, b, c, d and 14-8a, b, c, d 10-foot RF sections, as well as the 14-8 quadrupole magnet, will be removed to install the new BC14 compressor chicane.
- The 15-2d 10-foot RF section will be removed in order to make room for an 8-foot S-band TCAV transverse RF deflector.
- Four 10-foot RF sections at 18-1d, 18-2d, 18-3d, 18-4d will each be replaced by a 9.4-foot section in order to install four new wire scanners.

## 6.2 Bunch Compression

In order to achieve the bunch density required for the PWFA experiments, the final electron bunch must be compressed in length to several thousand amperes of peak current. The bunch compression system must meet several basic requirements as follows:

- To improve stability and to avoid significant space charge forces, two separate and independently adjustable stages of bunch compression should be included. These are in addition to the existing final compression stage in sector 20 which also provides additional non-linearity correction and diagnostic functionality.
- The two new electron compression stages (BC11 and BC14) should be based on a four-dipole magnetic chicane, which is simple and achromatic to all orders.
- The first compressor should be located as far upstream as possible, but at high enough energy to avoid space charge effects after compression. An additional constraint on the energy of BC11 is given by the requirement to inject the positron beam at the final chicane bend, the energy of the damping ring should be as high as possible to maximize the quality of the damped positron beam (given other space constraints imposed on the ring design).
- The second compressor should be located such that sufficient energy chirp can be built up, but also located so that the remnant energy chirp after compression is fully cancelled by the longitudinal wakefield of the post-BC14 linac plus the sector 20 bunch compressor with acceptable remaining energy spread at the IP. There must also be enough remaining accelerating structures to reach the desired 10 GeV Sector 20 beam energy. BC14 is shared for both e- and e+ beams (shared first and last bend magnets, independent symmetrically placed middle two bends). The compression design presented here assumes a symmetric arrangement with equal  $R_{56}$  compression coefficients for both beams.
- Transverse beam emittance is seriously degraded in Sector 20 for peak currents >1 kA entering the W-chicane due to CSR. This provides a strong constraint for the bunch compression configuration in the Linac: as much compression as possible should occur in the final Sector 20 compression stage. This requires a strong chirp in L3, but the energy spread should also not greatly exceed ~1% without seriously degrading transverse emittance due to chromatic aberrations in Sector 20. The final configuration of the chirped compression in L1, L2 and L3 reflects this balance of considerations.

Bunch compression in FACET-II is closely based both on the successful design of LCLS-I and on the experience operating FACET. The compression is accomplished by the standard method where a linear energy chirp (energy correlation along the bunch) is generated by accelerating at an RF phase,  $\varphi$ , which is a few tens of degrees away from the RF crest. With the correct sign of correlation (*i.e.*,  $\varphi < 0$  for chicane compressors), the head of the bunch (low energy particles) will travel a longer distance within a given bunch compressor's magnetic optics, while the tail of the bunch (high energy particles) will travel a shorter path, effectively compressing the bunch length. For compression of the electron bunch, there are two standard 4-bend chicane compressors in the linac. The bunch is set to 'over-compression' in the second, where compression proceeds beyond the minimum bunch length. Then the wakefield-induced energy chirp in L3 is made to add to the remnant chirp in the right way to fully compress in the sector 20 W-chicane. Unlike the negative  $R_{56}$  of the simple 4-bend chicanes (defined for a coordinate system with bunch head at  $z < 0$ ), the W-chicane has a more complex arrangement of magnets and is made to have a positive  $R_{56}$  which can be varied across the range ~0-10mm and is nominally set to +5mm.

The compression factor is encompassed in its  $R_{56}$  value, where each electron is delayed or advanced by its energy deviation with respect to the reference particle (design energy). If the relative energy deviation is expressed as  $\delta (= \Delta E/E_0)$ , then the electron delay (or advance) is written as

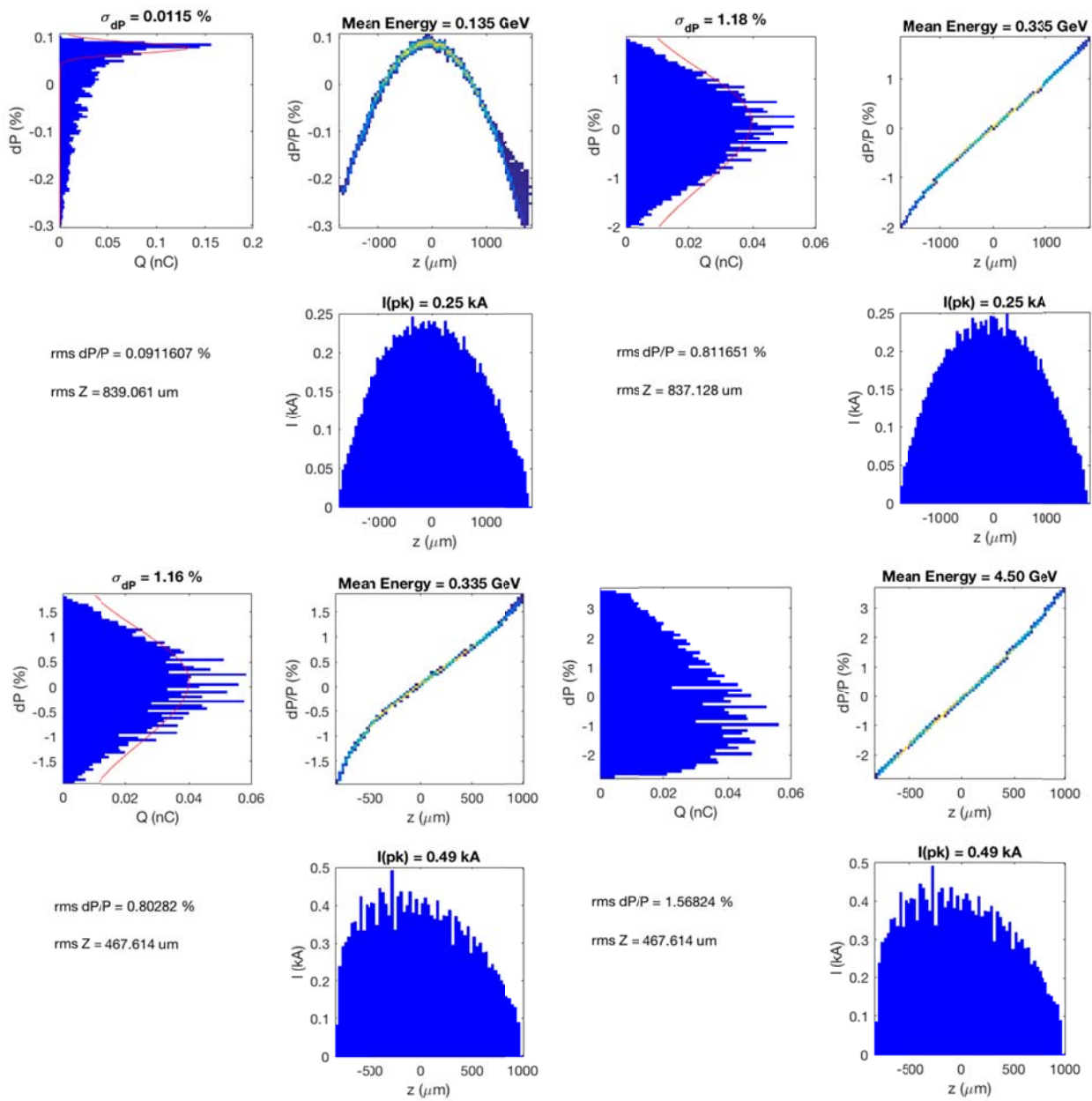
$$\Delta z = R_{56}\delta . \quad (5)$$

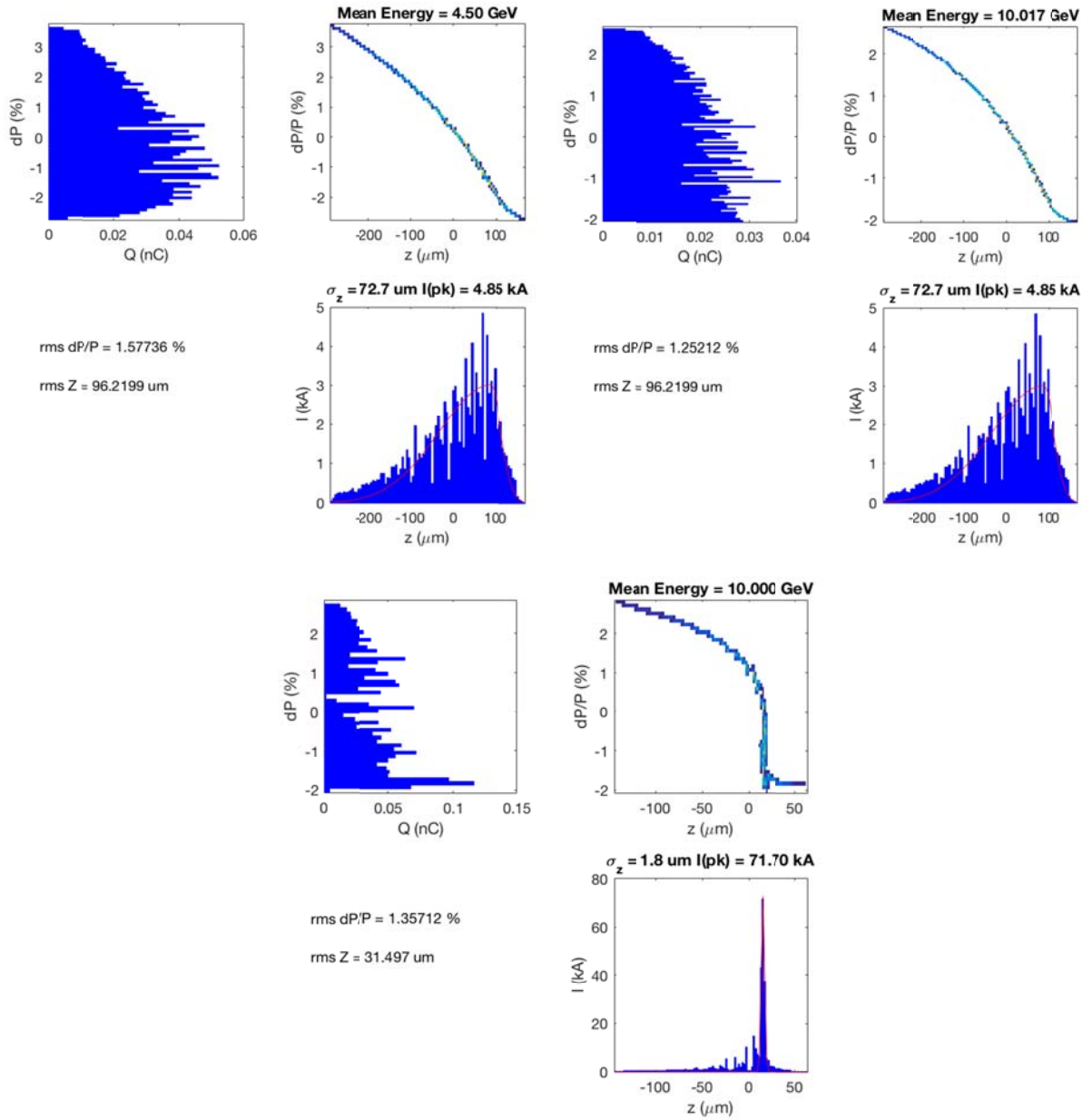
The  $R_{56}$  coefficient for simple 4-bend chicanes (BC11 and BC14) is related to the chicane strength through the following formula

$$R_{56} \approx -2\theta^2 \left( \Delta L + \frac{2}{3}L_B \right), \quad (6)$$

where  $\theta (<< 1)$  is the bend angle of each dipole magnet,  $\Delta L$  is the drift distance between 1<sup>st</sup> and 2<sup>nd</sup> (and 3<sup>rd</sup> and 4<sup>th</sup>) dipoles, and  $L_B$  is the magnetic length of each magnet. The more complex arrangement of magnets in sector 20 requires optics matching software, such as MAD8, to compute the  $R_{56}$  of that system, along with the other matching requirements for that sector.

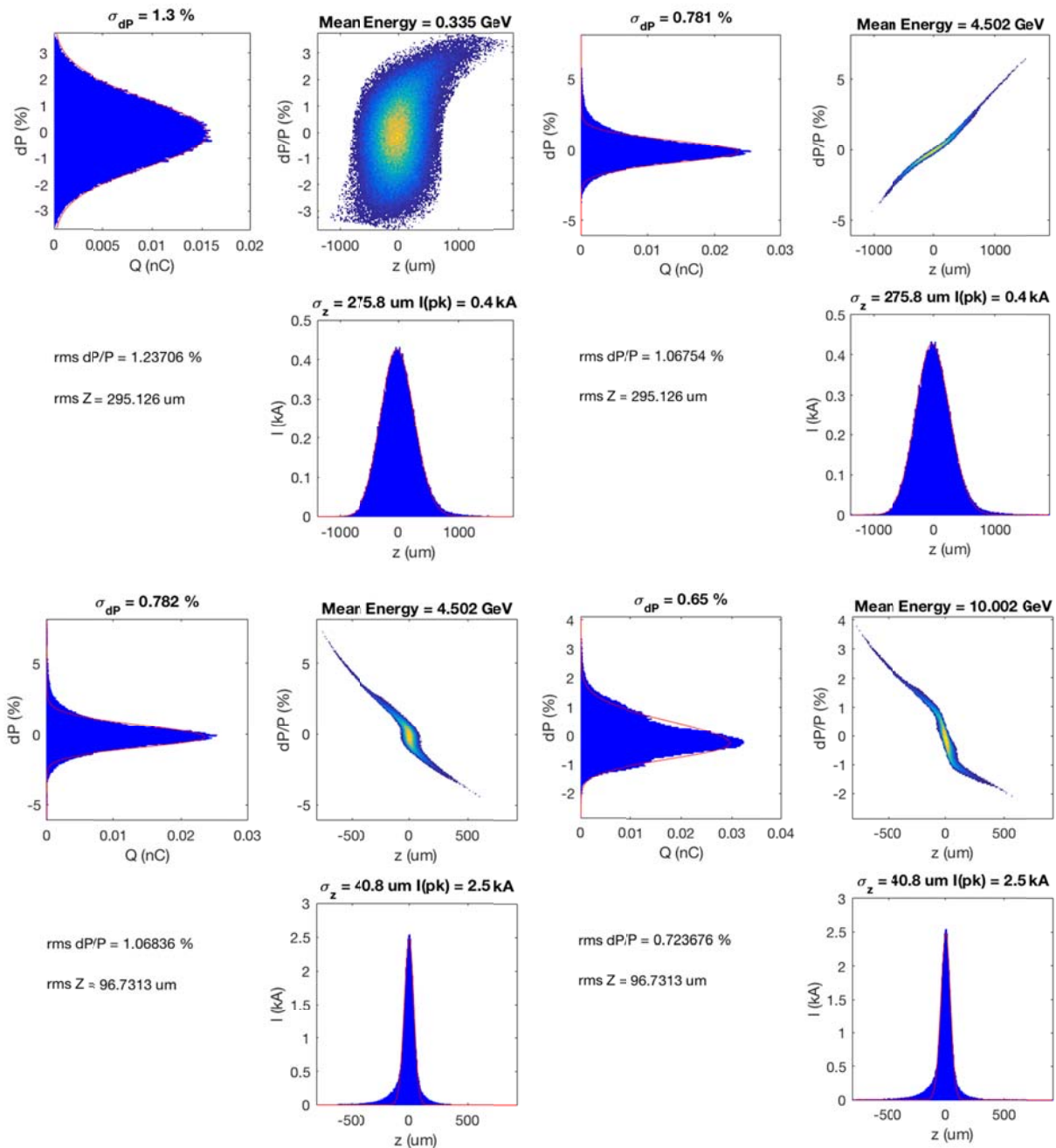
Longitudinal phase-space from a 6D particle tracking simulation of the FACET-II compression process (using *Lucretia* [1]) is shown in Figure 6.7 for the electron bunch and Figure 6.8 for the positron bunch (see Section 6.7 for full 6D tracking results and further explanation of the tracking simulation performed). Longitudinal wakefields of the SLAC S-band accelerating structures are included in addition to a simulation of the ISR and CSR effects in the bends of the bunch compressors. In the shown plots,  $z$  shows the local projected time coordinate of the macro particles (negative  $z$  particles are at the head of the bunch),  $dP$  is the relative deviation of the particle energy away from the mean energy of the bunch. Bunch lengths and energy spreads are presented for both Gaussian fits to the distributions where appropriate and rms quantities are also shown.





**Figure 6.7. Tracking simulation of the electron bunch compression process. Sigma numbers displayed above plots indicate the widths of fitted Gaussians where appropriate, the rms quantities from the distributions are shown in the text in the lower-left quadrant of each plot.**

Details pertaining to Figure 6.7: starting at the end of the L0b section at 135 MeV (top row, left), before the BC11 compression chicane at 335 MeV (top row, right), after the BC11 compression chicane at 335 MeV (2<sup>nd</sup> row, left), before BC14 at 4.5 GeV (2<sup>nd</sup> row, right), after BC14 at 4.5 GeV (3<sup>rd</sup> row, left), at the start of the W-chicane in Sector 20 at 10 GeV (3<sup>rd</sup> row, right) and at the IP experimental waist at 10 GeV (bottom row). The final plot is truncated at the 3-sigma level to show details of the beam core.



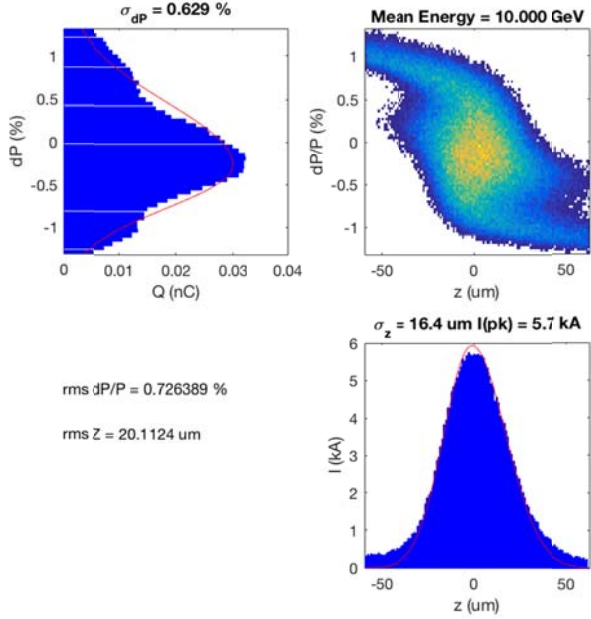


**Figure 6.8. Tracking simulation of the positron bunch compression process. Sigma numbers displayed above plots indicate the widths of fitted Gaussians where appropriate, the rms quantities from the distributions are shown in the text in the lower-left quadrant of each plot.**

Details pertaining to Figure 6.8: starting at the end of the BC11 section where the positrons are injected into the main L2 linac section along with the electron bunch at 335 MeV (top row, left), before the BC14 compression chicane at 4.5 GeV (top row, right), after the BC14 compression chicane at 4.5 GeV (2<sup>nd</sup> row, left), before the Sector 20 W-chicane at 10 GeV (2<sup>nd</sup> row, right), at the IP experimental waist location in Sector 20 (3<sup>rd</sup> row). The final plot is truncated at the 3-sigma level to show details of the beam core.

### 6.2.1 Stability Requirements and System Sensitivities

The final level of bunch compression and transverse beam quality in 3 dimensions is quite sensitive to RF phase and amplitude variations in the different sections of the machine. Orbit errors of the generated beams and magnetic field fluctuations also effect the final beam quality. The longitudinal and transverse phase spaces available for experimenters in Sector 20 have been studied using particle tracking (with *Lucretia*) while varying many of the system parameters (see Section 6.7 for further details of the tracking simulations). Table 6.2 lists the various parameters: the phase and amplitude of each major linac section, the bunch charge, drive-laser timing, magnet vibration, and bunch compressor settings. The value listed for each jitter property is either from a tolerance specification elsewhere (e.g. laser timing fluctuation from LCLS requirements and operation experience) or directly measured (magnet vibrations) or motivated from past experience operating FACET. Table 6.3 shows the impact of these jitter properties on the design key performance parameters. The tracking results show the requirements set out by the key performance parameters requested from the user-driven experimental program are met with these error parameters. These Monte Carlo simulations were performed using 100 random seeds for the jitter parameters and yield results with non-Gaussian distributions. Hence the results shown in Table 6.3 do not well describe the particular distributions of errors. Figure 6.9 through to Figure 6.14 below depict the numerical distributions, both for the total set of jitter properties and also with the parameters individually applied so the major contributions can be identified. These are statistical “box plots”: for each box, the red line indicates the median value for the distribution, the blue “box” shows

the 25<sup>th</sup> and 75<sup>th</sup> percentiles and the dotted line “whiskers” show the range of the distribution. Where there are red crosses included, these are considered outliers (if they are larger than  $q_3 + w(q_3 - q_1)$  or smaller than  $q_1 - w(q_3 - q_1)$ , where  $q_1$  and  $q_3$  are the 25th and 75th percentiles, respectively, and  $w$  is 1.5 meaning that the outliers correspond to approximately +/- $2.7\sigma$  if the distribution were Gaussian).

### 6.2.1.1 IP Timing Jitter

The relative arrival time jitter for the tracked electron and positron bunches with the error properties listed in Table 6.2 are shown in the histograms in Figure 6.15. The rms jitter on both the electron and positron bunches is 30  $\mu\text{m}$  in each case. The tolerance on the desired level of timing jitter is very relaxed: experimental programs record the actual timing using EOS techniques to retrospectively analyze data, the presence of some timing jitter is therefore actually a desired property.

**Table 6.2. Jitter properties studied and estimated achievable values. Quoted values are rms.**

Property	Value
Source Charge Fluctuation	1% (e-) 2% (e+)
Source Electron Position Fluctuation (laser spot jitter on cathode)	3 % $\sigma_{x,y}$
Source Positron Position Fluctuation (from DR extraction)	0.1 $\sigma_{x,y}$
Initial Electron Laser Timing Error	200 fs
L1 Phase Jitter	0.1 degS
L2/L3 Phase Jitter	0.25 degS
L0P Phase Jitter	0.1 degS
L1 Amplitude Jitter	0.1 %
L2/L3/L0P Amplitude Jitter	0.25 %
BC0 & BC11 Magnet Strength Jitter	1e-5 dB/B
BC14 & BC20 Magnet Strength Jitter	1e-4 dB/B
L1/L2/L3/S20 Magnet Vibration (x/y), rms	1.5/0.5 $\mu\text{m}$
PEC Magnet Vibration (x/y), rms	0.4/0.18 $\mu\text{m}$
e- injector Magnet Vibration (x&y), rms	0.1 $\mu\text{m}$

**Table 6.3. Simulated range of delivered key performance parameters with all error parameters specified in Table 6.2 applied. Each entry shows mean and rms spread of results from a 100 seed Monte Carlo simulation. Note that the distributions are not actually Gaussian, see presented data in Figure 6.9 through Figure 6.14 for error distributions and breakdown of errors into independent sources.**

IP Parameter	Electron Bunch		Positron Bunch	
	Design Req.	Simulation	Design Req.	Simulation
$\varepsilon_x$ ( $\mu\text{m}\cdot\text{rad}$ )	<20	4.4 +/- 0.5	<20	10.7 +/- 0.7
$\varepsilon_y$ ( $\mu\text{m}\cdot\text{rad}$ )	<20	3.3 +/- 0.1	<20	13.0 +/- 1.2
$\sigma_z$ ( $\mu\text{m}$ )	<20	3.1 +/- 1.5	<20	16.5 +/- 0.2
$I_{pk}$ (kA)	>10	64 +/- 16	>5	5.8 +/- 0.2

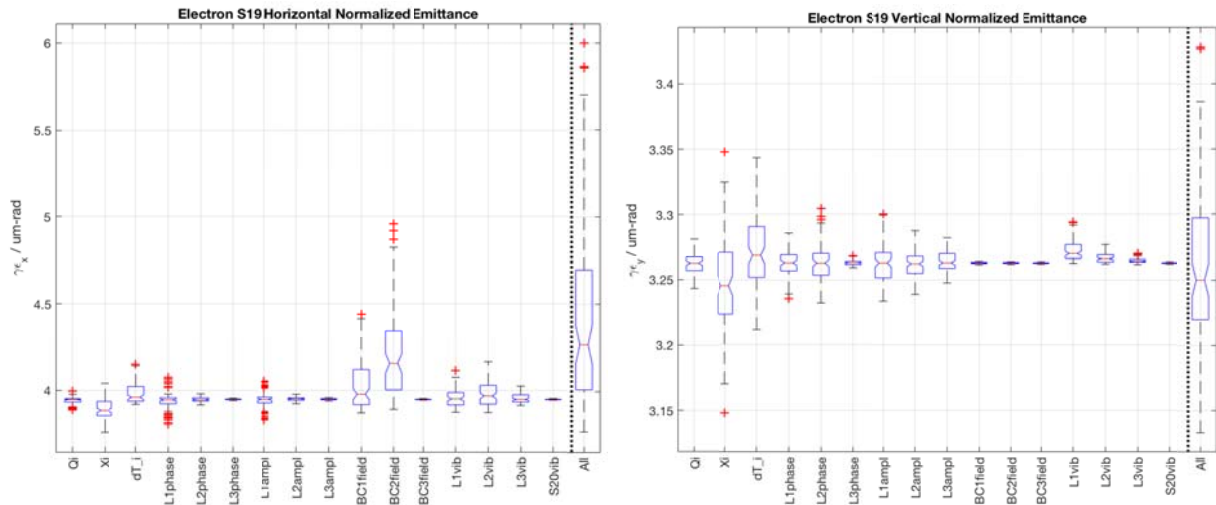


**Figure 6.9. Box plox showing electron emittance at the end of the Linac for jitter simulation properties shown in Table 6.2.**

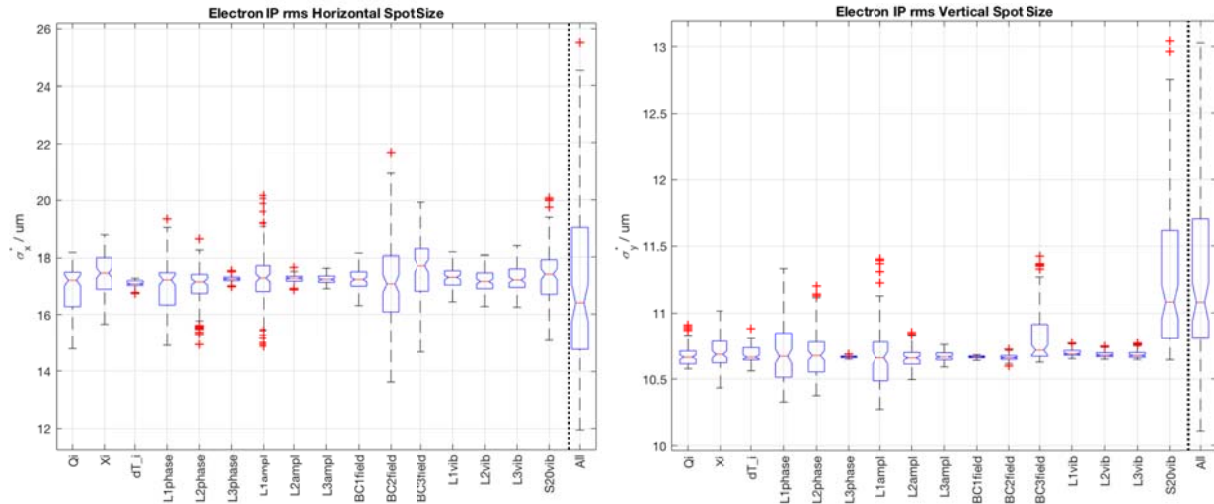


**Figure 6.10.** Box plots showing distributions for jitter simulation studies for properties shown in Table 6.2. Effect on electron horizontal and vertical spot sizes at the IP waist in Sector 20 for 0.5 m waist beta functions are shown for the nominal design parameters.

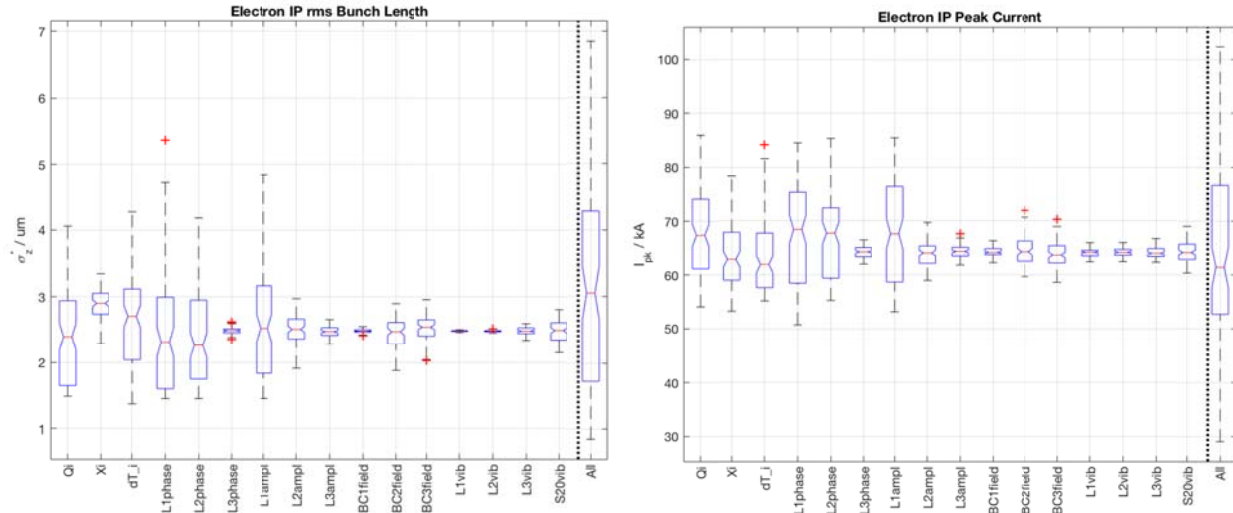


**Figure 6.11.** Box plots showing distributions for jitter simulation studies for properties shown in Table 6.2. Effect on electron bunch length and peak current at the IP waist in Sector 20 are shown for the nominal design parameters. The red dotted line shows the required design performance.

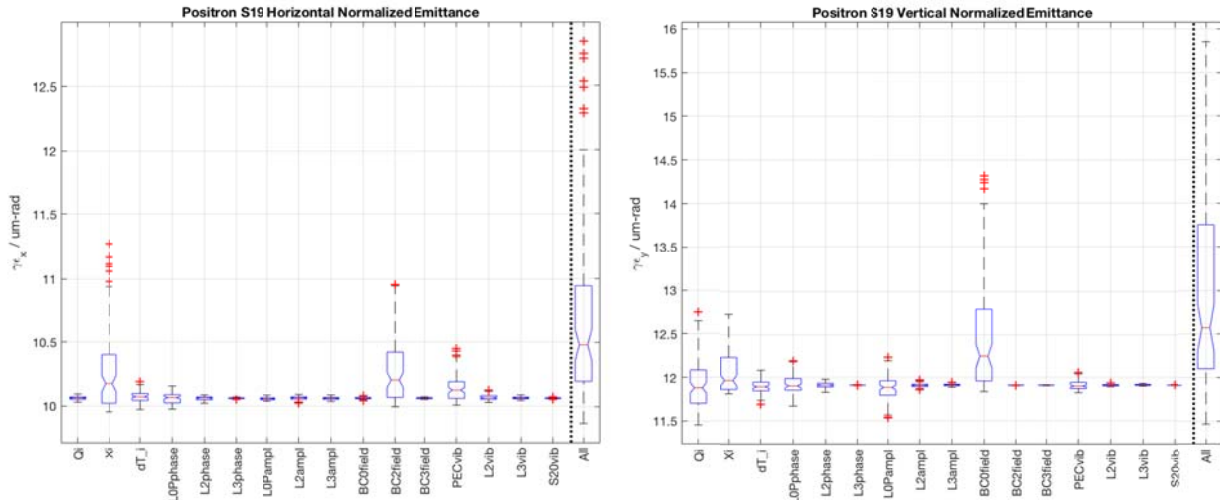


**Figure 6.12.** Box plox showing positron emittance at the end of the Linac for jitter simulation properties shown in Table 6.2.

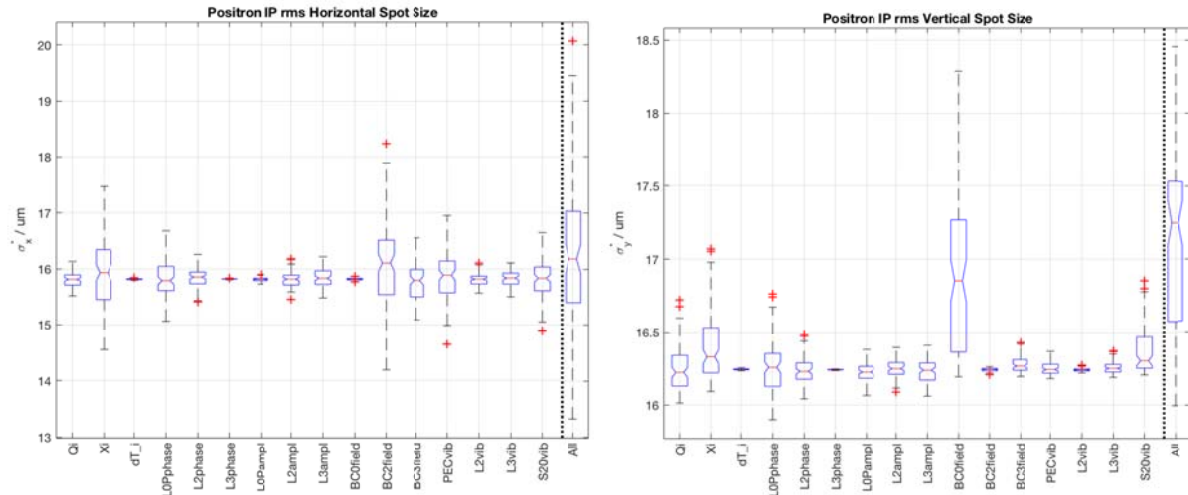


**Figure 6.13.** Box plots showing distributions for jitter simulation studies for properties shown in Table 6.2. Effect on positron horizontal and vertical spot size at the IP waist in Sector 20 are shown for the nominal design parameters.

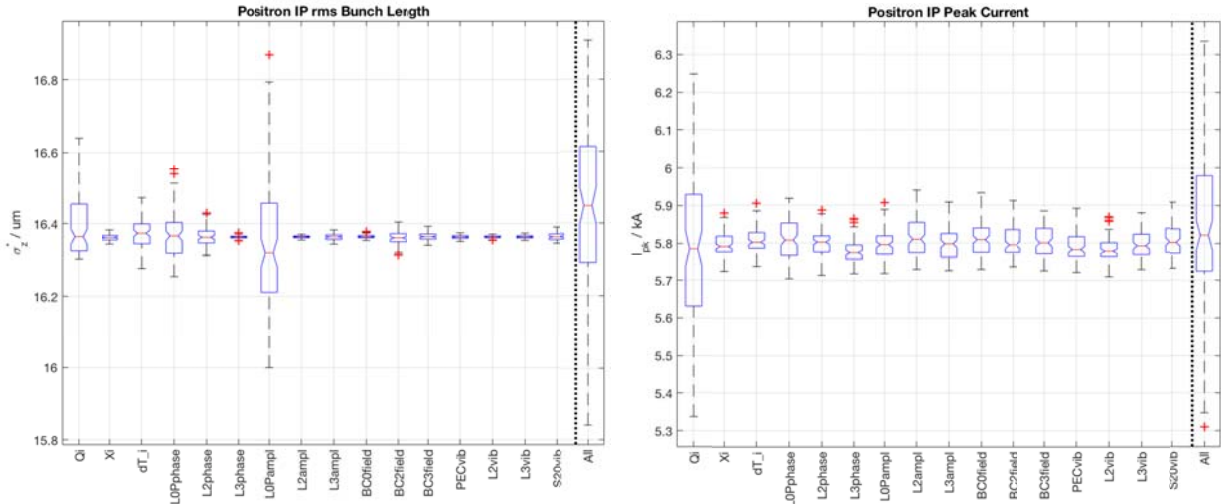


**Figure 6.14.** Box plots showing distributions for jitter simulation studies for properties shown in Table 6.2. Effect on electron bunch length and peak current at the IP waist in Sector 20 are shown for the nominal design parameters.

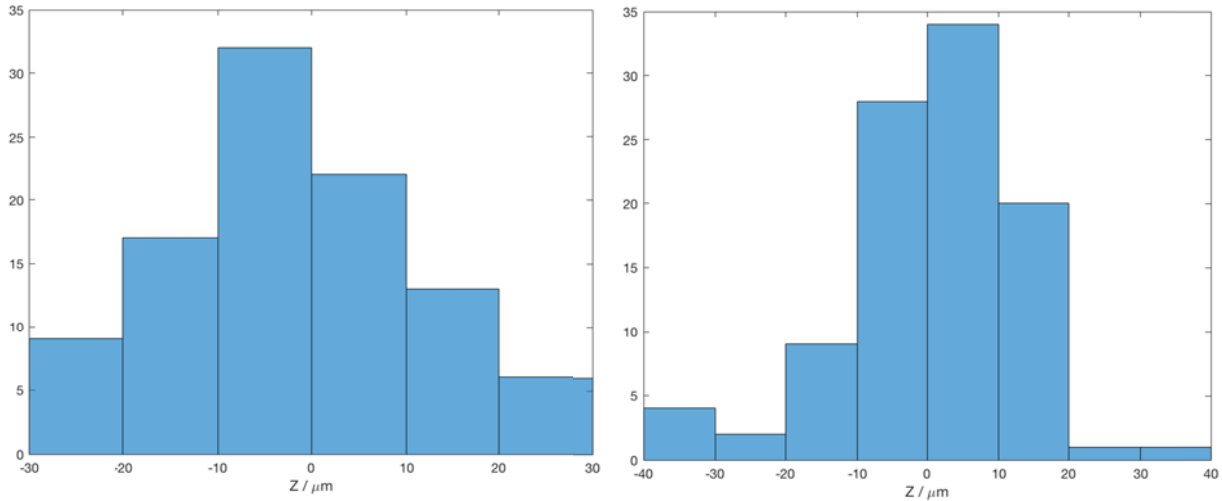


**Figure 6.15.** Arrival time (longitudinal position) jitter for electrons (left), positrons (right).

### 6.3 The First Electron Bunch Compressor (BC11)

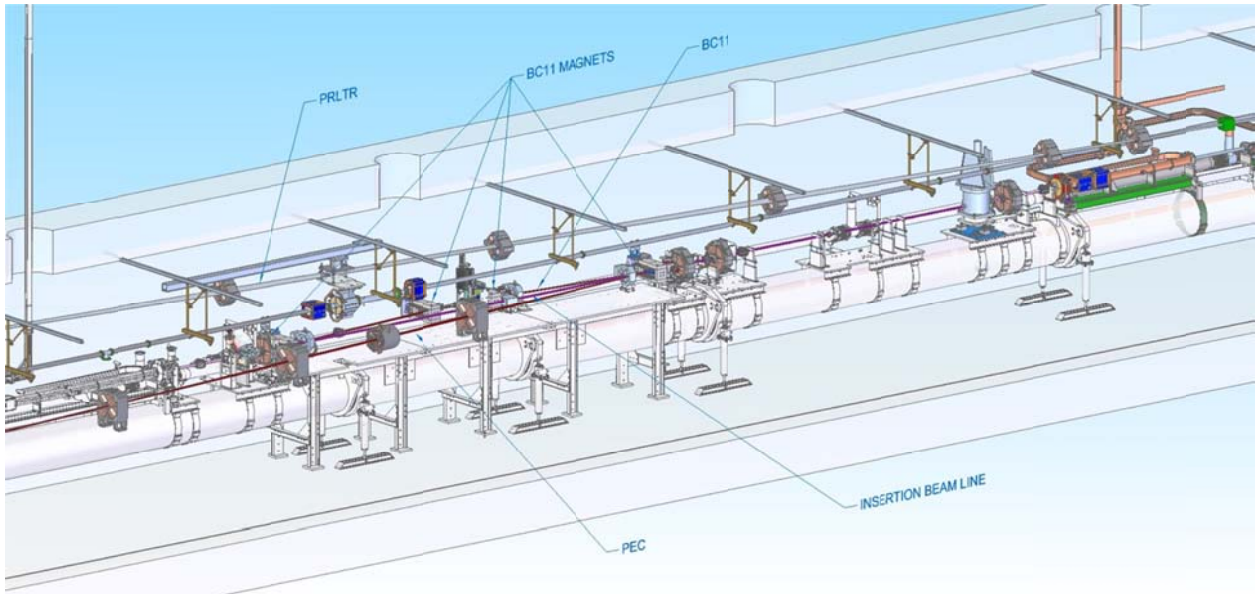


**Figure 6.16. Sector 11 region of Linac showing BC11 bunch compressor magnet locations.**

### 6.3.1 Overview

The BC11 compressor is a symmetric chicane with 4 rectangular bend magnets, dispersion tweaking quadrupole magnets and a skew-quadrupole magnet in the chicane dispersive region. It serves as the first-stage bunch length compression for the electron beam and as a location to merge in the positron beam. The BC11 compressor forms part of the integrated compression system as one of a total of 6 compression systems employed for the electron and positron beam transport systems. The BC11 system is defined by areas after the L1 RF sections and before the start of the L2 RF sections. The five quadrupole magnets before and after the chicane are required for matching purposes from the L1 linac section into L2 and require independent power supplies. The chicane is designed to provide an R56 of -48 mm. Information regarding the positron injection system is provided in Chapter 7. The positron beam is injected into the main linac in the shared final bend magnet of this chicane as can be seen in Figure 6.16 and Figure 6.17. An adjustable collimator (rectangular with independent control of each of two jaws), located downstream of the central region of the chicane, provides for the capability to selectively remove beam halo and/or non-linear energy tails which can improve the final peak current performance. A wire scanner and screen are also placed in the central chicane region to provide energy spread diagnostics. Also, a BPM in this location provides information for the energy feedback system.

### 6.3.2 Beam Parameters for BC11

These are the nominal electron design beam parameters of the BC11 subsystem.

**Table 6.4. Beam parameters for the BC11 subsystem for the electron beam between the end of the L1 Linac section to the beginning of the L2 Linac section as depicted in Figure 6.16. See Section 6.7 for details of the beam tracking simulation. No collimation is used for the nominal parameter case.**

Parameter	Symbol	Nominal Value	Unit
Beam Energy	E0	335	MeV
Transverse Emittance	$\gamma \epsilon_x / \gamma \epsilon_y$	3 / 2.8	$\mu\text{m}\text{-rad}$
Initial Bunch Length / peak Current	$\sigma_z / I_{pk}$	839 / 240	$\mu\text{m} / \text{A}$
Final Bunch Length / peak Current	$\sigma_z / I_{pk}$	468 / 490	$\mu\text{m} / \text{A}$
Relative Energy Spread (rms)	$\sigma_E/E$	0.8	%

### 6.3.3 Layout and Optics Design

The optics of BC11 is designed to match the outgoing electron and positron parameters from the L1 Linac section into the L2 Linac section. The final bend of the bunch compressor also serves as the injection point of the positron beam. The beta functions are matched to a low value in both planes in the final bend to minimize CSR effects for both the electron and positron bunches.

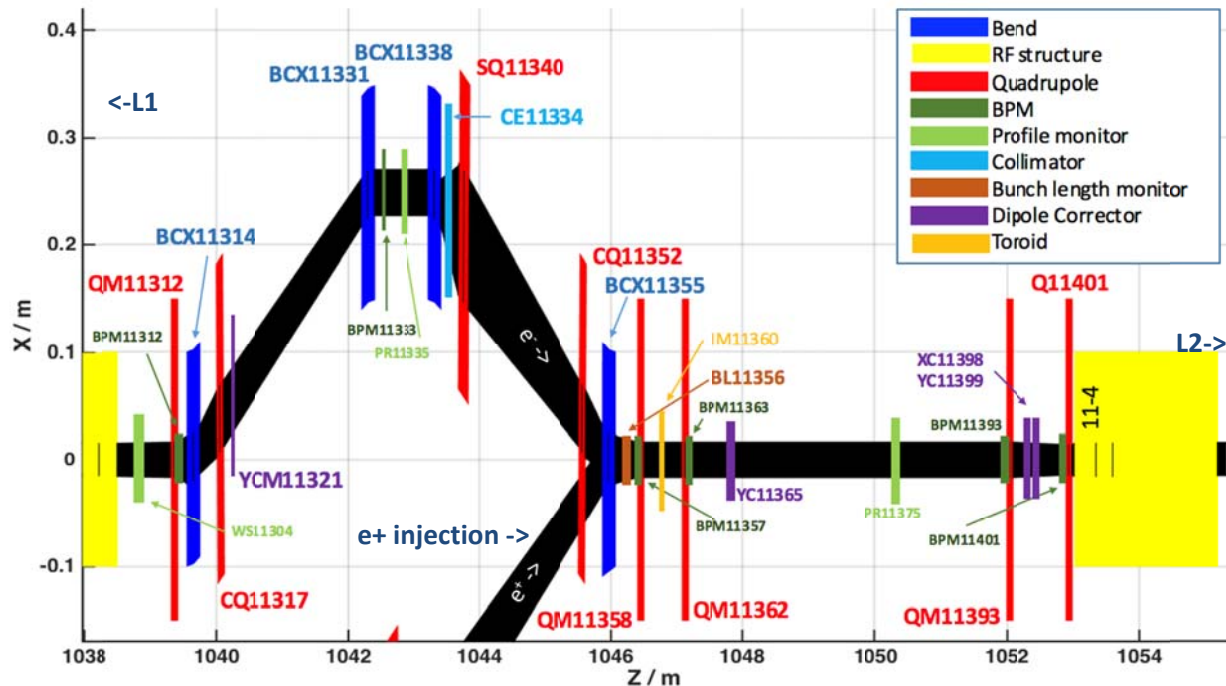


**Figure 6.17. Layout schematic of the BC11 bunch compression section showing required devices and approximate locations. K1X is a space reserved for a possible future x-band structure not part of the project baseline.**

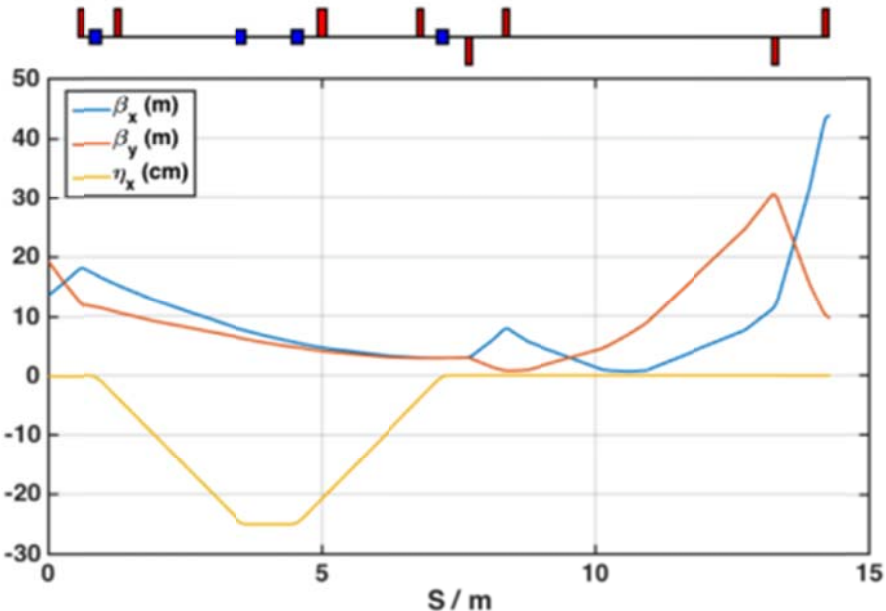


**Figure 6.18. Twiss parameters across the BC11 compression system for the electron beam.**

### 6.3.4 Electron Beam Dynamics

See Section 6.7 for further explanations of the beam tracking simulation and Figure 6.7 for the longitudinal phase space calculations across this subsystem. Figure 6.19 below shows 10X the tracked beam size through the system used as the definition of the desired beam stay-clear region.

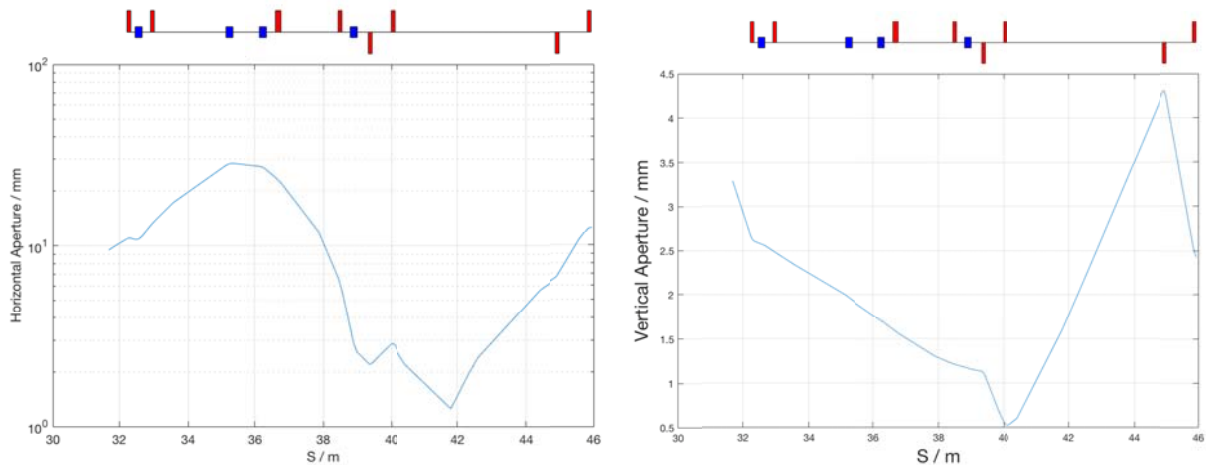


**Figure 6.19. Electron beam stay-clear envelopes calculated as 10X tracked beam sigma.**

### 6.3.5 Magnets

The BC11 section consists of 8 quadrupole magnets (7 new) of 3 engineering types (2 new) and 4 dipole magnets of 2 types (the final bend is shared with the positron ring-to-linac section). The bend magnets are standard chicane-style bends (rectangular bend magnets, with no yaw angle with respect to the reference trajectory).

### 6.3.5.1 Quadrupoles

**Table 6.5. Quadrupole magnet parameters for BC11 (at E=335 MeV). Q11401 is an existing Linac quadrupole, others are new.**

Deck Name	Effective Length / m	Design Int. Strength / T	Max. Int. Strength /  T	Design Pole Tip Field /  T	Max Pole Tip Field /  T	Beam stay-clear radius / mm
<b>QM11312</b>	0.108	0.41	0.5	0.061	0.07	11.0
<b>CQ11317</b>	0.108	0.0	0.5	0.0	0.07	13.2
<b>SQ11340</b>	0.108	0.0	0.5	0.0	0.07	12.0
<b>CQ11352</b>	0.108	0.0	0.5	0.0	0.07	6.2
<b>QM11358</b>	0.108	-0.983	1.5	0.146	0.222	2.2
<b>QM11362</b>	0.108	1.144	1.5	0.17	0.222	2.9
<b>QM11393</b>	0.108	-0.764	1.5	0.113	0.222	6.8
<b>Q11401</b>	0.108	0.41	0.5	0.061	0.07	11.0

### 6.3.5.2 Dipoles

**Table 6.6. Dipole magnet parameters for BC11 (at E=335 MeV).**

Deck Name	Effective Length / m	Bend Angle / rad	Design Int. Strength / T.m	Max. Int. Strength /  T.m	Design Pole Tip Field / T	Max Pole Tip Field /  T	Aperture (radius) / m
<b>BCX11314</b>	0.2035	-0.105	0.12	0.516	0.6	2.6	10.9
<b>BCX11331</b>	0.2035	0.105	0.12	0.516	0.6	2.0	28.2
<b>BCX11338</b>	0.2035	0.105	0.12	0.516	0.6	1.7	26.9
<b>BCX11355</b>	0.2035	-0.105	0.12	0.516	0.6	1.2	10.0

## 6.4 BC14 - Bunch Compression System for e- and e+ in Sector 14

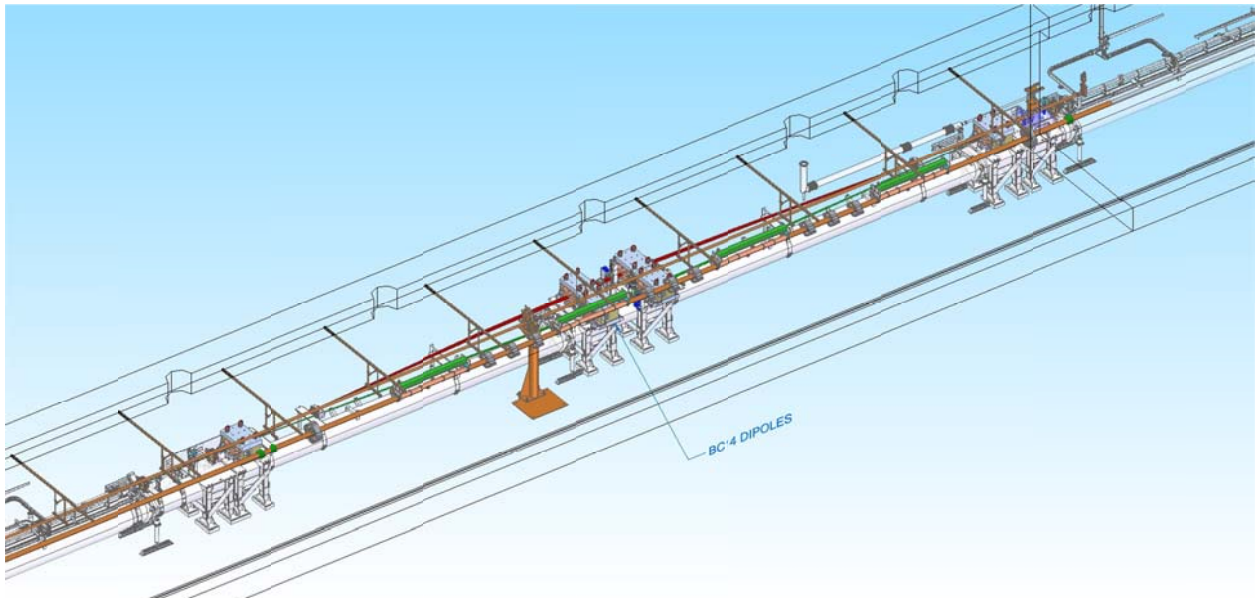


Figure 6.20. Sector 14 region of linac showing magnet locations for BC14 chicanes.

### 6.4.1 Overview

The BC14 system is defined as the region after the last L2 RF section and before the first L3 RF section. Q14701 and Q14901 quadrupole magnets are existing Linac devices, all other elements are new to this region. The BC14 compressor is a symmetric chicane comprising 6 rectangular bend magnets (4 for each e-/e+ beamline), for the purpose of bunch length compression of the electron and positron beams. The first and last bends are common to e- and e+ beams, with a symmetric arrangement for the central 2 bends, providing equal  $R_{56}$  terms for both beams with equal energy. A pair of quads before and after the chicane are included in this system for matching purposes. Each chicane (for e- and e+) contains an adjustable collimator to cut the beam halo and/or the high-energy tail portion of the compressed beam for beam quality control. The collimator can also function as a beam stopper for tune-up and commissioning. The internal edge angles of the first and last bend magnets and CQ quadrupoles are used as free parameters during the matching process to form an  $x \leftrightarrow y$  betatron exchange transfer matrix to match both electron and positron optics simultaneously. Without this adjustment, a beta mismatch of order 10% exists between e- and e+ beams due to vertical focusing in the bend magnets. Screens are placed near the center of the chicanes to provide beam energy spread diagnostics. Also, a BPM is placed in this region to provide information for the beam energy feedback system.

### 6.4.2 Beam Parameters in BC14

The optics are designed to match the outgoing electron and positron parameters from the L2 Linac section into the L3 Linac section. This is performed using a pair of quadrupole magnets before and after the chicane in conjunction with the first and last few quadrupoles in L2 & L3. The magnitude of the beta functions at the exit of the final B883 bend magnet are kept to a minimum to suppress CSR effects. Also the internal edge angles of B720 and B883 are set along with small tweaks of CQ quadrupoles to produce an optimal  $x \leftrightarrow y$  betatron transform matrix ( $M_x(e-) = M_y(e+)$ ;  $M_y(e-) = M_x(e+)$ ) between electron and positron arms. Although not perfect, this is achievable with a BMAG mismatch parameter

<1% for both particle types which is well within normal operational working accuracy for the optical matching. The dispersion match must also be completely closed at the exit of the system.

**Table 6.7. Electron beam parameters across BC14. See section 6.7 for details of beam tracking simulation. No collimation is used for the nominal parameter case.**

Parameter	Symbol	Nominal Value	Unit
<b>Beam Energy</b>	$E_0$	4.50	GeV
<b>Transverse Emittance</b>	$\gamma\epsilon_x / \gamma\epsilon_y$	3.4 / 3.3	$\mu\text{m}\cdot\text{rad}$
<b>Initial Bunch Length (rms) / peak Current</b>	$\sigma_z / I_{pk}$	468 / 0.3	$\mu\text{m} / \text{kA}$
<b>Final Bunch Length (rms) / peak Current</b>	$\sigma_z / I_{pk}$	96 / 4.9	$\mu\text{m} / \text{kA}$
<b>Relative Energy Spread (rms)</b>	$\sigma_E/E$	1.6	%
<b>Bunch Charge</b>	Q	2.0 (physics bunch) 4.0 (scavenger bunch)	nC

**Table 6.8. Positron beam parameters across BC14. See section 6.7 for details of beam tracking simulation. No collimation is used for the nominal parameter case.**

Parameter	Symbol	Nominal Value	Unit
<b>Beam Energy</b>	$E_0$	4.50	GeV
<b>Transverse Emittance</b>	$\gamma\epsilon_x / \gamma\epsilon_y$	9 / 12	$\mu\text{m}\cdot\text{rad}$
<b>Initial Bunch Length (rms) / peak Current</b>	$\sigma_z / I_{pk}$	276 / 0.4	$\mu\text{m} / \text{kA}$
<b>Final Bunch Length (rms) / peak Current</b>	$\sigma_z / I_{pk}$	97 / 2.5	$\mu\text{m} / \text{kA}$
<b>Relative Energy Spread (rms)</b>	$\sigma_E/E$	1.1	%
<b>Bunch Charge</b>	Q	1.0	nC

### 6.4.3 Layout and Optics Design in BC14

BC14 are symmetric bend chicanes with equal  $R_{56}$  for the electron and positron portions of the chicanes. The bend angles are 41.92 mrad and each arm of the compressor provides a compression factor  $R_{56}=36\text{mm}$ . For higher charge operation where CSR effects become even more pronounced in BC14 a smaller bend angle may be required for optimal emittance preservation, it is assumed that under these circumstances the chicane geometry will have to be changed, but this is not expected to be a routine procedure. Figure 6.20 and Figure 6.21 below show a schematic layout of the BC14 section and the details of the edge angle requirements for the outer bend magnets. In addition to the collimator downstream of the center of the chicanes, it is also required to have a screen for energy spread

measurements and a BPM for input to the beam energy feedback system. Figure 6.23 shows the Twiss parameters through each arm of BC14.

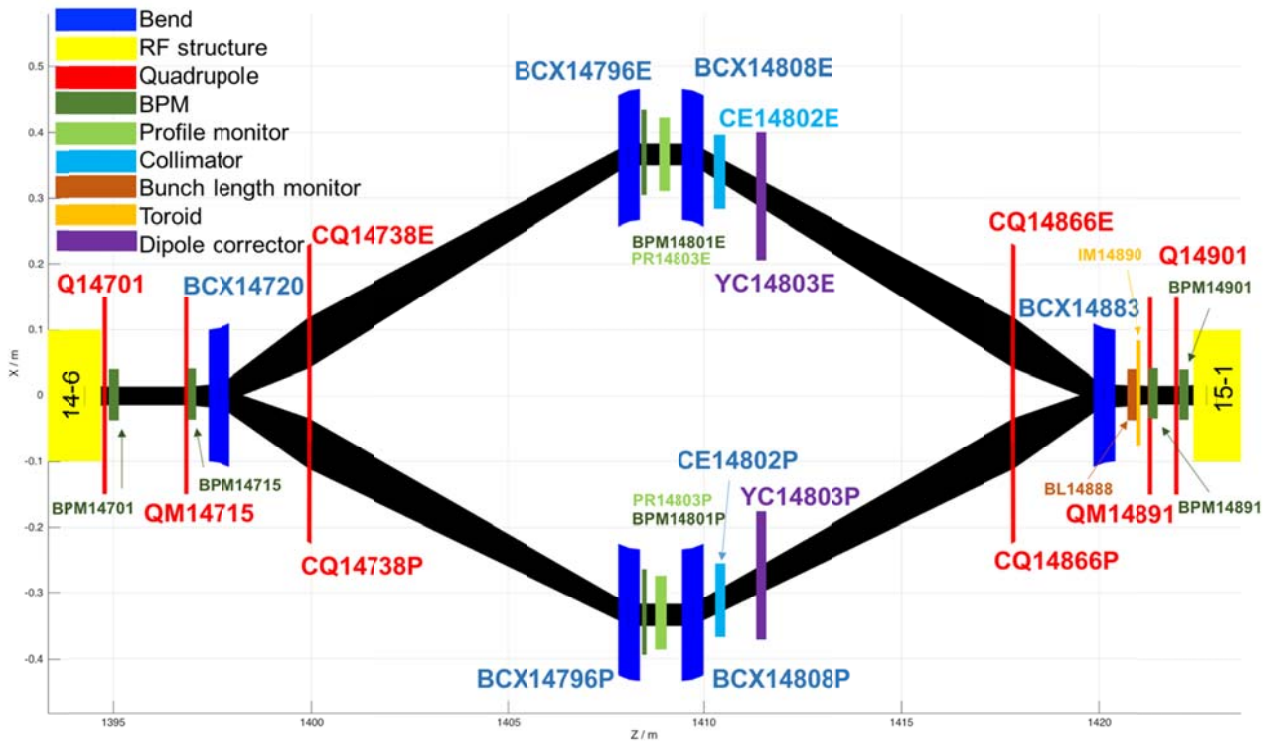


**Figure 6.21.** Layout schematic of BC14 bunch compression section showing required devices and approximate locations.

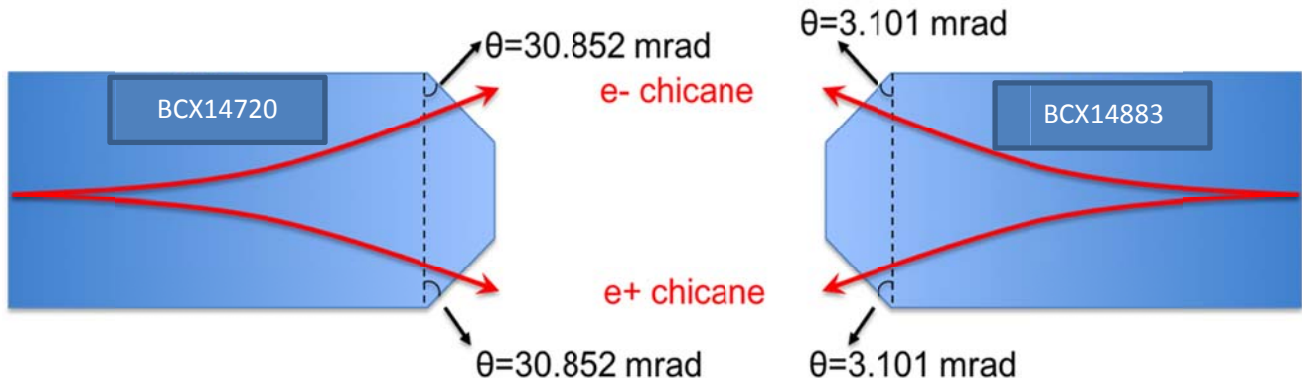


**Figure 6.22.** Design edge angles for first and last chicane bend magnets.

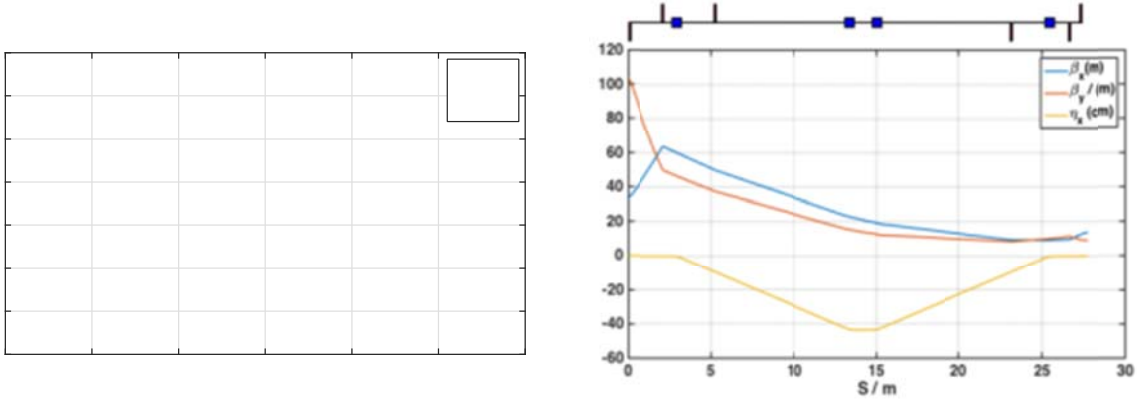


**Figure 6.23.** Twiss parameters across BC14 system for the positron beam (left) and the electron beam (right).

#### 6.4.4 Beam Dynamics in BC14 for e+ and e-

See Section 6.7 for explanation of beam tracking simulation and Figure 6.7 and Figure 6.8 for the longitudinal phase space calculations for e+ and e- beams across this subsystem. Figure 6.24 below shows 10X the tracked beam size through the system which defines the desired beam stay-clear region.

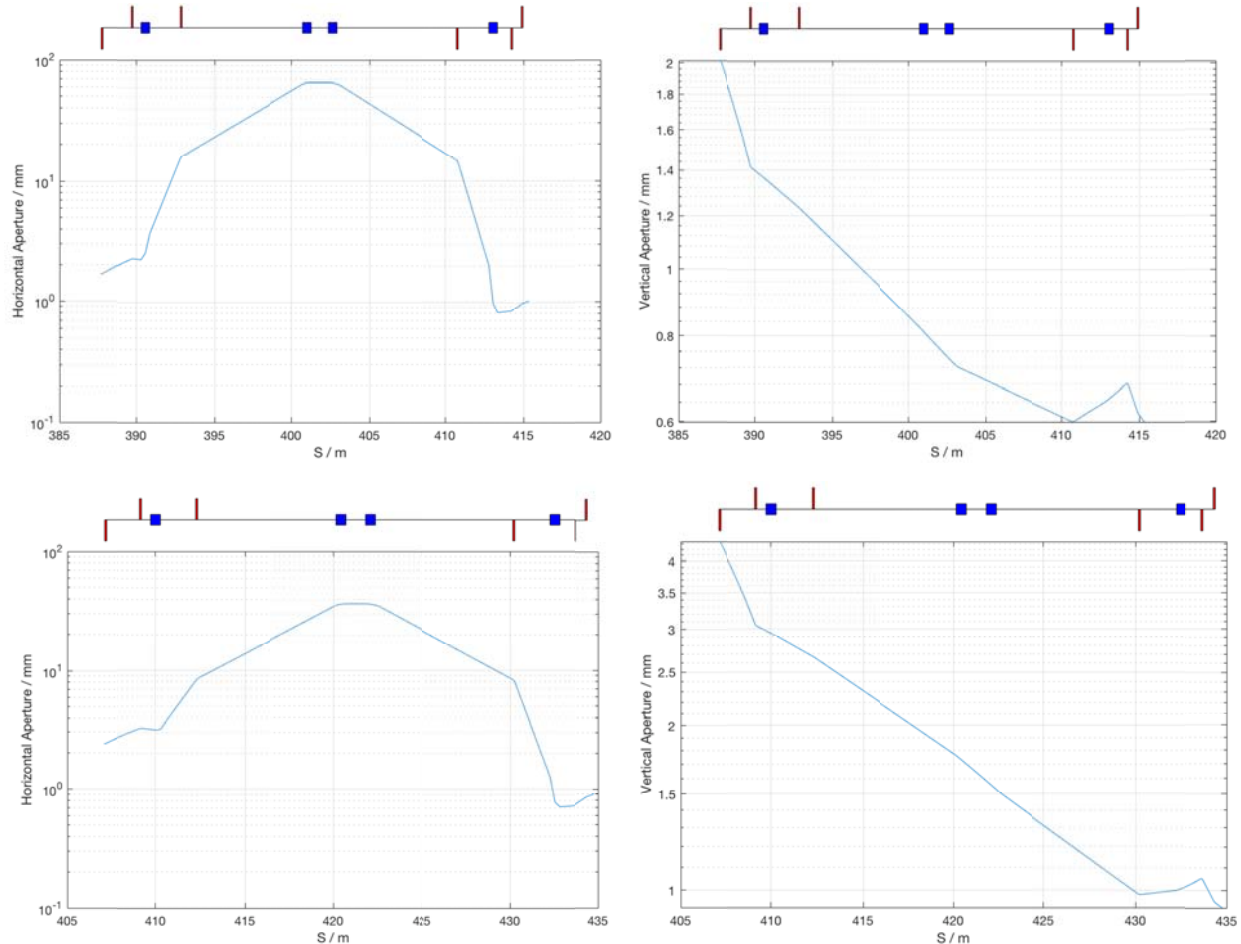


**Figure 6.24. Required horizontal (left) and vertical (right) magnet apertures in BC14 from tracked rms beam sizes (10X tracked beam sizes shown by blue curve). Top row is for the electron beam design; bottom row is for the positron beam.**

## 6.4.5 BC14 Magnets

The BC14 compressor section consists of 8 quadrupole magnets of 2 engineering types and 6 dipole magnets of 3 types. The outer bends are shared between electron and positron beams and have specially designed interior edge angles, the central bends are normal chicane-style rectangular bends.

### 6.4.5.1 Quadrupoles

**Table 6.9. Quadrupole magnets for BC2. Q14701 and Q14901 are existing Linac quads, other are new to this region.**

Deck Name	Effective Length / m	Design Int. Strength / T	Max. Int. Strength /  T	Design Pole Tip Field /  T	Max Pole Tip Field /  T	Beam stay-clear radius / mm
<b>Q14701</b>	0.1068	2.661	5.500	0.343	0.710	2.0
<b>QM14715</b>	0.1068	-2.533	5.500	0.327	0.710	2.3
<b>CQ14738E</b>	0.108	0.000	3.000	0.000	1.056	15.7
<b>CQ14866E</b>	0.108	0.000	3.000	0.000	1.056	14.5
<b>QM14891</b>	0.1068	2.970	5.500	0.383	0.710	0.8
<b>Q14901</b>	0.1068	-1.343	5.500	0.173	0.710	1.0
<b>CQ13738P</b>	0.108	0.000	3.000	0.000	1.056	8.3
<b>CQ14866P</b>	0.108	0.000	3.000	0.000	1.056	8.1

### 6.4.5.2 Dipoles

**Table 6.10. Dipole magnet parameters in BC14. BCX14720 and BCX14883 are shared between e- and e+ beams.**

Deck Name	Effective Length / m	Design Int. Strength / T.m	Max. Int. Strength /  T.m	Design Pole Tip Field / T	Max Pole Tip Field /  T	Beam Vertical stay-clear radius / mm	Horizontal good field region / mm
<b>BCX14720</b>	0.54913	0.62932	0.6500	1.1460	1.1837	1.4	11.5
<b>BCX14796E</b>	0.54913	0.62932	0.6500	1.1460	1.1837	1.0	65.2
<b>BCX14808E</b>	0.54913	0.62928	0.6500	1.1460	1.1837	1.0	65.1
<b>BCX14883</b>	0.54913	0.62922	0.6500	1.1459	1.1837	1.0	11.5
<b>BCX14796P</b>	0.54913	0.62932	0.6500	1.1460	1.1837	1.8	36.2
<b>BCX14808P</b>	0.54913	0.62928	0.6500	1.1460	1.1837	1.5	36.2

## **6.5 Sector 20 W-Chicane (BC20) and Final Focus Systems**

Sector 20 contains the final bunch compression stage for both the electron and positron beams, the existing W-chicane system is described in Chapter 9. The Sector 20 chicane has a positive  $R_{56}$  between 0-10mm (design=5mm), providing the final stage of bunch compression while also providing other measurement and aberration correction functions before delivery of either beam to the experimental IP area. The layout of BC20 is unchanged from the FACET experiment and will be operated in a similar way.

## **6.6 Radio Frequency (RF) Systems**

The RF system for FACET-II has several performance requirements as follows:

- The high-power RF system must make use of the existing Linac RF stations in an efficient and convenient configuration.
- The RF system needs to provide adjustable phase and amplitude for each main linac section (*i.e.*, Gun, L0a, L0b, TCAV0, L1, L2, TCAV1, L3, XTCAV).
- The phase and amplitude stability must meet the requirements described in this chapter.
- Several transverse RF deflectors are included in order to measure the electron bunch length at various locations.

LCLS-I has been successfully delivering beam to users since October 2009 with the stability and availability of the RF systems meeting all requirements. With this clear success, the RF systems for FACET-II will be modeled following the design and experience of LCLS-I.

The installed complement of S-band (2.856 GHz) klystrons in the SLAC Linac, from Sector 10 through Sector 19, is capable of accelerating the FACET-II beam to at least the required energy of 10.0 GeV (for both e- and e+). In addition to setting the electron beam energy, precise control of RF phase and amplitude is required to manipulate the longitudinal phase space of the beam to produce the desired short bunch in Sector 20. Specifically, the Linac RF is used to introduce an energy-time correlation along the bunch for compression, and to compensate for longitudinal wakefields generated by the accelerating structures. The success of the bunch compression and wakefield compensation schemes rely on tight tolerances for phase and amplitude control of the Linac, especially in L1. Methods used in LCLS-I to achieve this will be duplicated for FACET-II.

### **6.6.1 The RF System Stability Tolerances**

The RF system stability tolerances specify the pulse-to-pulse rms variations that are acceptable in Linac phase and amplitude, while still maintaining the desired peak current and energy at the FACET IP. These pulse-to-pulse random variations cannot be corrected by feedback and therefore place upper limits on the phase and amplitude noise level of individual components, such as klystrons. Longer timescale drifts, ranging from several seconds to several days, will be corrected by feedback systems. Beam-based diagnostics of relative bunch length and relative energy will be used to provide feedback for the RF phase and amplitude to control variations slower than  $\sim 0.5$  Hz.

Although beam-based feedback will be the final mechanism to stabilize RF phase and amplitude, there are several reasons for keeping the low-level RF distribution system as stable as possible. Some

development work on feedback tuning algorithms is to be expected before subsystems can be cascaded together. Any extension in the duration over which the beam remains stable and within tolerance makes the task of tuning easier, both during the period of commissioning the accelerator and subsequent operation. The detailed RF stability tolerances are listed in Table 6.2.

### 6.6.2 Radio Frequency (RF) Distribution in the SLAC Main Linac

The RF master signal will be generated by a stress compensated cut quartz crystal located at Sector 10, which is 50 m up-stream of the FACET-II injector. The RF from the crystal oscillator is multiplied up to 476 MHz and distributed along the final 2/3 of the 3-km linac on an air dielectric rigid coax referred to as the Main Drive Line (MDL). The timing system fiducial, which is locked to the 71.43 kHz resync frequency shared between LCLS-II, LCLS, and FACET-II, as well as the coarse 360 Hz harmonic of the AC power lines is also distributed down the MDL as a double amplitude cycle of the 476 MHz signal. A coupler will be added in Sector 11 to pick off some of the 476-MHz and generate the RF frequencies required for FACET-II.

The SLAC Linac is divided into 30 sectors, of which FACET-II will utilize RF systems in sectors 10 through 20. The RF distribution for two adjacent, nominal sectors is shown in Figure 6.25, showing how the RF power is derived for each sector and distributed to each of the eight klystrons (typical) in the sector.

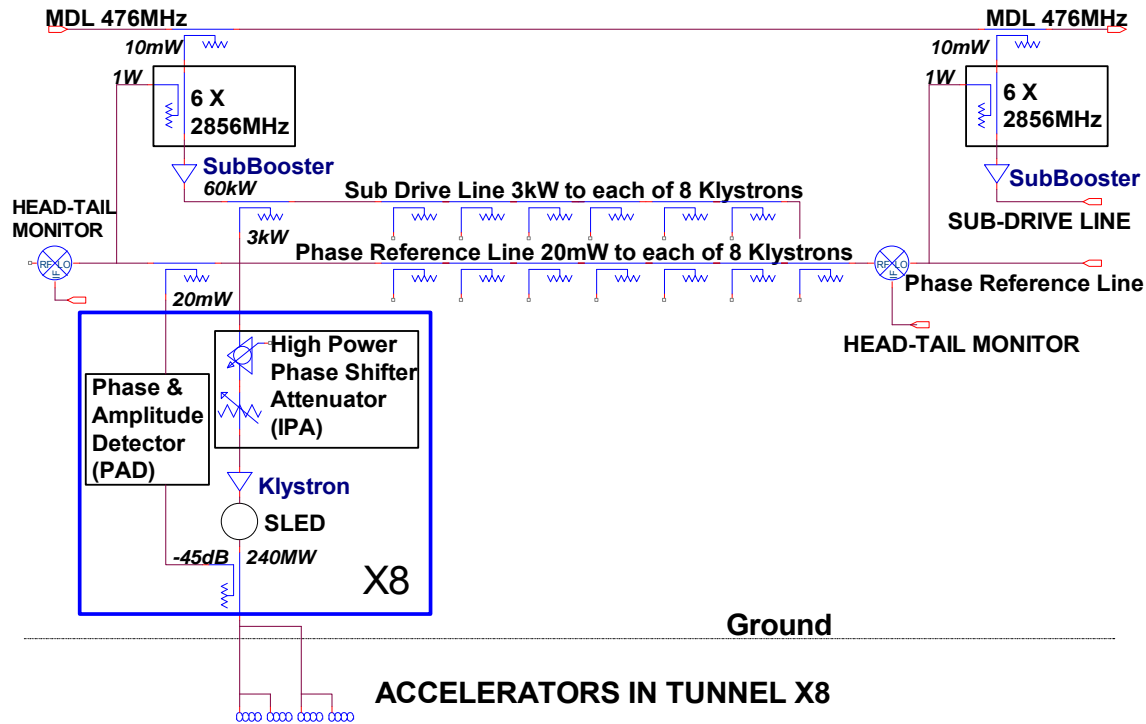


**Figure 6.25. Schematic of two adjacent, nominal linac sectors showing distribution of RF power to the 8 klystrons per sector.**

At each sector boundary, a x6-multiplier is coupled to the MDL and provides 2856-MHz power for the sector phase reference line and the sub-booster klystron. The sub-booster klystron produces 60 kW of pulsed RF power to drive the Sub-Drive Line (SDL). The SDL and the Phase Reference Line (PRL) run the length of one sector (101.6 m) and are temperature stabilized over most of their length. The SDL provides 3 kW of RF power to each klystron and the PRL provides 20 mW of RF power to the Phase and Amplitude Detector (PAD).

After the injector, when the beam enters the Linac it passes through an S-band (2.856 GHz) accelerator. The RF stability and phase in this section is critical to stable operation of FACET-II. A temperature stabilized enclosure has been built in the Linac gallery at the end of Sector 10 to provide a centrally located room to route temperature sensitive RF cables from the tunnel and electronics which measure phase and amplitude of the RF signals. This enclosure is referred to as the “RF Hut”. The routing of sensitive measurement cables and the area layout is shown in Figure 6.26.

RF cables will be run in the tunnel to Sector 14, where a second transverse deflector and the L2 energy feedback klystrons will be located. The MDL will route the RF reference from Sector 10 to Sector 15 through 20, where the existing L3 feedback klystrons, positron source klystrons and Sector 20 X-band transverse deflector klystron are located.

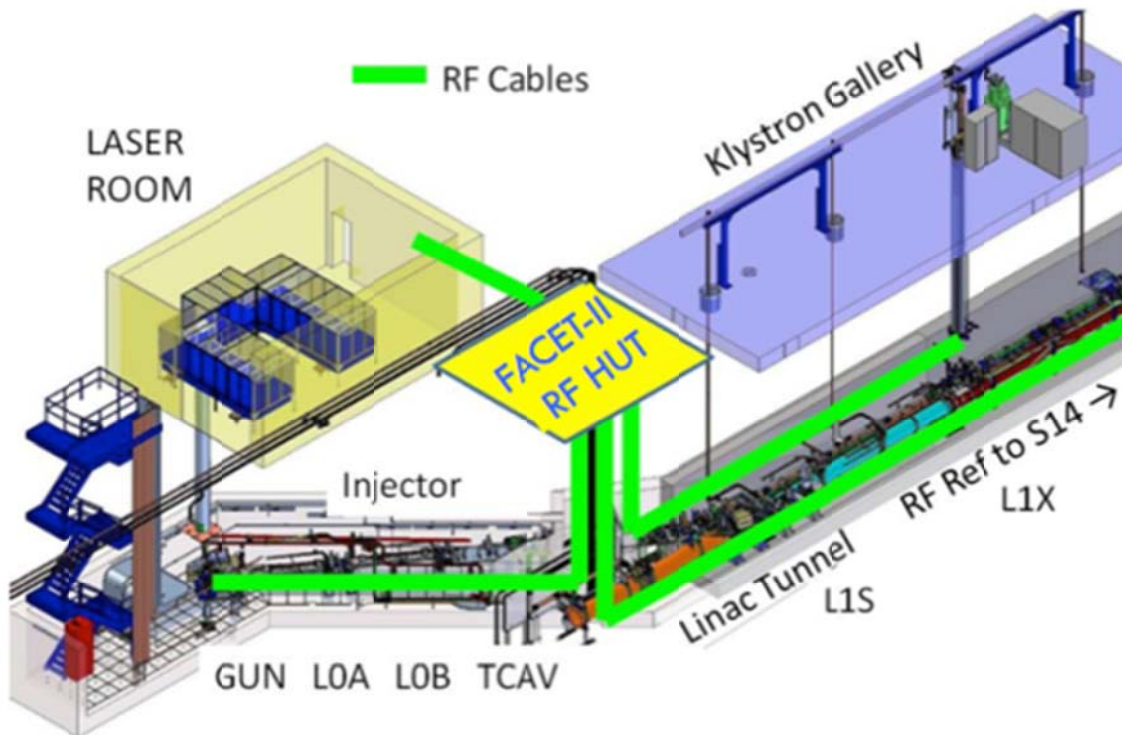


**Figure 6.26. Layout of the injector area with the new temperature stabilized FACET-II “RF Hut” at the end of Sector 10, the laser room, and the routing of temperature sensitive RF cables. L1X refers to a reserved region possibly used in a future upgrade where an X-band structure will be installed, but is not included in the project baseline.**

### 6.6.3 Improvements to the RF Control System

A low noise RF control system is required to meet FACET-II specifications for jitter and drift. The RF control system will be modeled after LCLS-I, in that it will go on top of the existing Linac system. This will add a tighter control of phase and amplitude for individual klystrons in the injector and for feedback klystrons in L2 and L3. The majority of the klystrons in L2 and L3 will use existing linac controls and not require any changes.

### **6.6.3.1 L2 and L3 RF Distribution and Control**

A separate phase reference line is used to control the phases of the klystrons in L2. This phase reference line feeds four sectors and has a Phase and Amplitude Controller (PAC) which is used to adjust the overall L2 phase based on beam measurements. In FACET-II the L2 phase reference line will need to control klystrons in four sectors, as in LCLS-I. Sectors 11, 12, 13, and a portion of the klystrons in Sector 14 will need to be controlled by the L2 phase reference line. Two energy feedback klystrons will be used in Sector 14. These feedback klystrons will require solid-state sub-boosters (SSSBs), PADs and PACs.

The L3-Linac in FACET-II will retain the existing RF distribution from the MDL, as shown in Figure 6.25. To provide control for energy feedback, pulsed 476 MHz phase shifters upstream of the sub-booster in Sector 17 and 18 will be used as in the existing FACET configuration.

### **6.6.3.2 Sub-Boosters**

The present Linac uses one klystron sub-booster per sector to provide 60 kW of drive power divided into 8 klystrons. Low power phase control is therefore only done at the input side to the sub-booster klystron and hence changes the phase of all 8 klystrons. The high power mechanical phase shifters on the individual klystrons are only capable of coarser, 0.125° steps. Also they were not designed for pulse-to-pulse operation, typically making only a few tens of phase corrections per day in the present linac operation.

The three klystrons in the injector, the two L1-Linac klystrons, the two feedback control klystrons in L2, the positron bunch compressor klystron, as well as the two RF deflector klystrons in Sector 10 and 15, will all require individual solid-state sub-boosters. This allows PACs to be used at each individual klystron, on the input side to its sub-booster, to enable pulse-to-pulse phase control with fine resolution.

### **6.6.3.3 Phase and Amplitude Detectors and Control Units**

The Phase and Amplitude Detectors (PADs) designed and built for LCLS-I are capable of measuring phase variations down to <30 fs (<0.03 degS) as shown in the plot for phase jitter on the LCLS-I Gun in Figure 6.25.

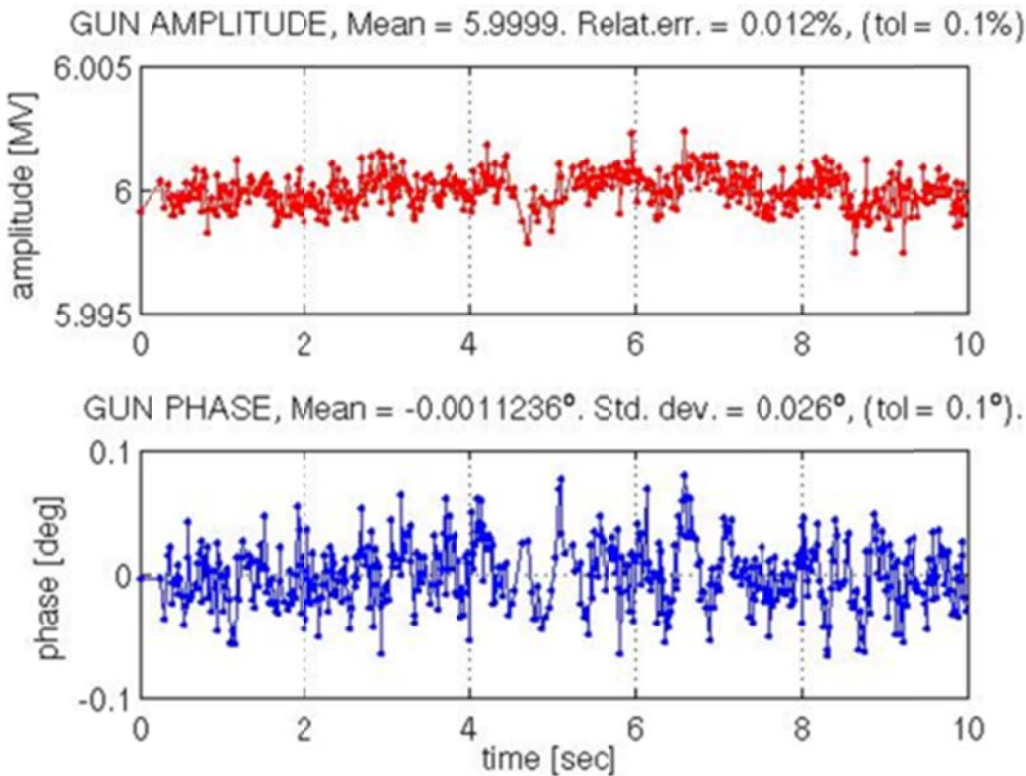


**Figure 6.27. LCLS-I gun RF phase and amplitude jitter measurements over 10 seconds at 60 Hz.**

The PADs use low noise RF and Local Oscillator signals to down-mix the RF to 25.5 MHz. The RF is then digitized at a 102-MHz sample rate and digitally down-mixed to baseband. The signals are integrated over the portion of the RF pulse of interest and made available as EPICS Process Variables (PVs) on TCPIP Ethernet. A second Ethernet, User Datagram Protocol (UDP), port sends out data at beam rate for feedback and Beam Synchronous Acquisition (BSA). Matlab programs are used to read and analyze the PVs.

The LCLS Phase and Amplitude Controllers (PACs) use high speed digital-to-analog converters (DACs) to put out a waveform that is up-converted to the RF frequency. FACET-II will use similar type electronics to control the phase and amplitude of the RF system.

#### 6.6.3.4 Timing System

The present linac timing system is based on 360-Hz fiducials superimposed on the 476-MHz RF that is distributed along the 2-mile linac. LCLS-I uses an Event Generator (EVG) which reads beam code information over a serial link and superimposes the beam code information and a 119-MHz clock on a 2.38-GHz high speed serial link. This high speed serial link is then distributed to Event Receivers (EVRs). This EVR based timing system will be used to supply FACET-II with triggers that are locked to the Linac RF. In parallel to this system, an existing SLC-era timing signal distribution scheme supplies 119 MHz timing clock and fiducial to the legacy CAMAC controls Programmable Delay Unit (PDU) modules for the generation of triggers. This system will remain in use as it is currently installed.

#### 6.6.3.5 Beam Diagnostics

Pulse-to-pulse measurements of relative bunch length after each bunch compressor will be available for feedback control of the RF phase. These will be based on CSR detectors (pyro-electric thermal

detectors). The bunch length monitors will be calibrated against the absolute bunch length measurement using the RF deflecting cavities (see Section 6.9.4).

Direct measurement of the beam phase with respect to the Linac RF is desirable from the point of view of feedback control. However, the thermal sources of phase drift that need to be compensated in the RF distribution systems are equally likely to disturb the phase measurement at the 0.1 deg S-band level required here. A technique of measuring the phase of the beam-induced signal in the accelerating structures relative to the RF drive has been studied. One accelerating structure per klystron in a typical Linac station is equipped with an output coupler on its load, where such measurements can be made. This may be a suitable technique for long-term phase control at the sub 1 deg S-band level in the L2 and L3-Linacs. This measurement requires a dynamic range of over 120 dB and has been done using the configuration shown in Figure 6.28. By using two channels of Analog to Digital Converter (ADC), one channel with a 60-dB attenuator to measure the RF and the other channel with a limiter to protect the ADC that will handle 1 kW of RF input power from the klystron, to measure the 0.5 mW of beam induced RF, we achieved 120 dB of dynamic range. The 1-kW RF and 0.5-mW beam signal from the output of the accelerator structure is split into two paths. One path has a 60-dB attenuator and the other path has a limiter. The 60-dB attenuator gives 1 mW of power from the RF. The limiter limits the RF to 13 mW to protect the circuits and allows 0.25 mW of beam power to pass. This has been tested on LCLS-I with very good results.

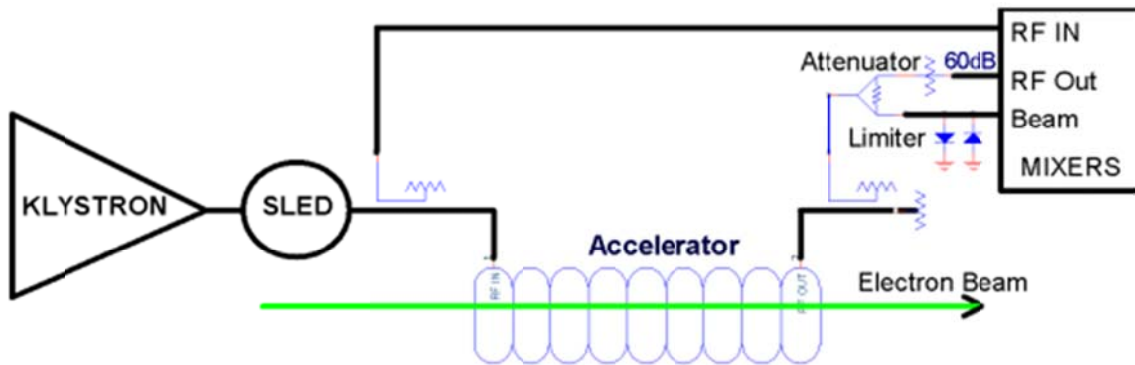


**Figure 6.28. Beam and RF phase measurement from output of an accelerator structure.**

## 6.7 Layout and Performance of the Present SLAC Linac RF

FACET-II will use the existing klystrons and their corresponding high voltage modulators installed in the klystron gallery from 10-4 to 20-4B. In the injector area, the RF Gun, L0a, L0b, and TCAV0 will be powered by 10-5, 10-6, 10-7, and 10-8 respectively, an identical configuration to that of LCLS-I. For the L1 linac (operated 20.5 degrees off-crest), the 11-1 and 11-2 klystrons will be used to drive the six accelerating structures that remain at the 11-1 and 11-2 girders. The existing 11-3A klystron will not be used, as the 11-3 accelerator structure will be removed for the installation of BC11. However, the 11-3A modulator, klystron slot, and associated support equipment in the gallery will be reserved for the possible future installation of the x-band linearizer.

The L2-linac (operating 39 degrees off crest for electrons) will be powered by the 27 klystrons from 11-4 to 14-6. 11-4 is designated as a spare, 11-5 and 11-6 are used as energy feedback stations and are operating nominally +/-60 degrees off crest. The existing 14-7 and 14-8 accelerator structures will be removed for the installation of the BC14 chicane. Therefore, klystrons 14-7 and 14-8 will be used to power the positron return line 335-MeV booster and the L3 TCAV located at 15-2d, respectively. The L3-linac (accelerating on-crest) will consist of the 39 existing klystrons from 15-1 to 19-8, with 19-8

designated as a spare, and energy feedback stations operating nominally +/- 60 degrees off crest. The 19-7 klystron is not in use as the 19-7 accelerating structure has been replaced by the scavenger beam extraction system to generate positrons as at FACET.

The FACET-II gun will be driven from klystron 10-6. The SLED cavity will be removed and enough waveguide, more than 600 ns, will be installed to provide isolation in time for the klystron from the reflected power of the standing wave gun. This method provides better isolation than a circulator and requires no sulfur hexafluoride gas.

L0a will be driven from klystron 10-7 and L0b will be driven from klystron 10-8. Both of these stations will have the SLED cavities removed and waveguide will be routed to the structures in the off axis injector bunker. These two 3-m long structures will be SLAC type structures modified with dual feed inputs, but single outputs (as in LCLS-I). Inputs and outputs of the structures will have Bethe hole couplers and new high power loads with vacuum ion pumps directly on each load.

The TCAV0 transverse deflector in the injector will be driven with klystron 10-5 using a high power 10 dB coupler to drop the power level to 0.5 MW. The SLED cavity will be removed from this station. Both input and output of the structure will have Bethe hole couplers and the output will have a new high power load.

Two of the six L1S 10-foot accelerating structures (11-1b and 11-2b) will be replaced by existing 9.4-foot structures so quadrupole magnets can be placed between them. The two L1 stations will have the SLED cavities remain as they are installed. Bethe hole couplers will be added to the input of the 11-1b section and to the outputs of all the sections. New high power loads will be installed at the outputs of the structures with vacuum ion pumps directly on each load.

Table 6.11 gives the no-load energy gain (in MeV) of the klystrons in the L2 and L3-linacs. Nominal FACET-II operational energy is 10.0 GeV.

**Table 6.11. Unloaded energy gain (MeV) of each klystron in L2 and L3.**

Sector	1	2	3	4	5	6	7	8	
L1/L2	11	102	102	--	164	164	151	164	176
	12	176	164	176	176	176	176	176	176
	13	176	176	176	176	176	176	176	176
	14	176	176	176	SPARE	108	108	--	--
L3	15	140	140	164	164	164	164	164	164
	16	164	164	164	164	164	164	164	164
	17	164	164	164	164	164	164	164	164
	18	164	164	164	164	164	164	164	164
	19	92	92	92	84	92	92	--	SPARE

## 6.8 Particle Tracking

Start-to-end particle tracking studies have been performed throughout the injector, accelerator, and Sector 20 compression and final focus systems by stringing together results from *IMPACT-T* (injector) and *Lucretia* [2] (Linac & Sector 20). Included in the tracking are longitudinal and transverse wakefields,

Coherent Synchrotron Radiation (CSR), Incoherent Synchrotron Radiation (ISR), and up to 3<sup>rd</sup>-order optics (*e.g.*, chromatic effects). 3D space charge forces are only included in the *IMPACT-T* simulation up to 63 MeV at the exit of L0a, with output particles transferred to *Lucretia*. *Lucretia* includes a model of longitudinal space-charge forces only. The results from the tracking simulation (200k macro-particles simulating the particle bunch) for the baseline machine design are shown earlier in this chapter in the relevant sections. Results from the *IMPACT-T* simulation, specific to the injector system can be seen in chapter 5.

Three machine configurations have been simulated, summarized below. Configuration (1) constitutes the baseline design and results from this configuration are shown here and in other chapters. The required key performance parameters are demonstrated with this baseline configuration. To further explore the *FACET-II* performance capabilities: results from configurations (2) and (3), outlined below, are described in Chapter 10.

1. The baseline configuration which delivers 1 and 2 nC of charge (for positrons and electrons, respectively).
2. A high peak current configuration which aims to maximize the current density at the experimental IP waist in Sector 20. This configuration uses a 2 nC source for both electrons and positrons whilst collimating the high energy spread tails within the BC0, BC11 and BC14 bunch compressors to deliver a final bunch charge of 0.6-0.7 nC. It provides peak currents of 12 and 76 nC (for positrons and electrons, respectively) and <10  $\mu\text{m}$  transverse spot sizes with 0.1 m IP beta functions.
3. A maximum electron charge configuration with 5 nC charge from the RF gun, un-collimated, together with a 1 nC positron beam. This configuration demonstrates requirements to run with the maximum envisioned beam-loading imbalance between electron and positron beams.

Beam optics for the electron and positron beam lines are shown in Figure 6.29 and Figure 6.30 and the energy profile is shown in Figure 6.31. The tracked longitudinal phase space for electron and positron beams are shown in Figure 6.7 and Figure 6.8. The final tracked transverse beam profiles for electrons and positrons at the experimental IP location are shown in Figure 6.32. All components are error free for these tracking simulations (*e.g.*, perfect alignment). Due to energy loss due to synchrotron radiation in the bunch compressors, there are steering and dispersive “errors” by design. During operation, these are ameliorated by the routine steering and dispersion correction systems. For design tracking purposes here, the orbit and dispersive “errors” are numerically subtracted after each bunch compression stage to mimic these operational corrections and to derive the expected performance for the machine. These fixed corrections are stored and used during tolerance calculations which apply additional errors (*e.g.* RF phase and amplitude errors) so the impact of those errors is properly treated.

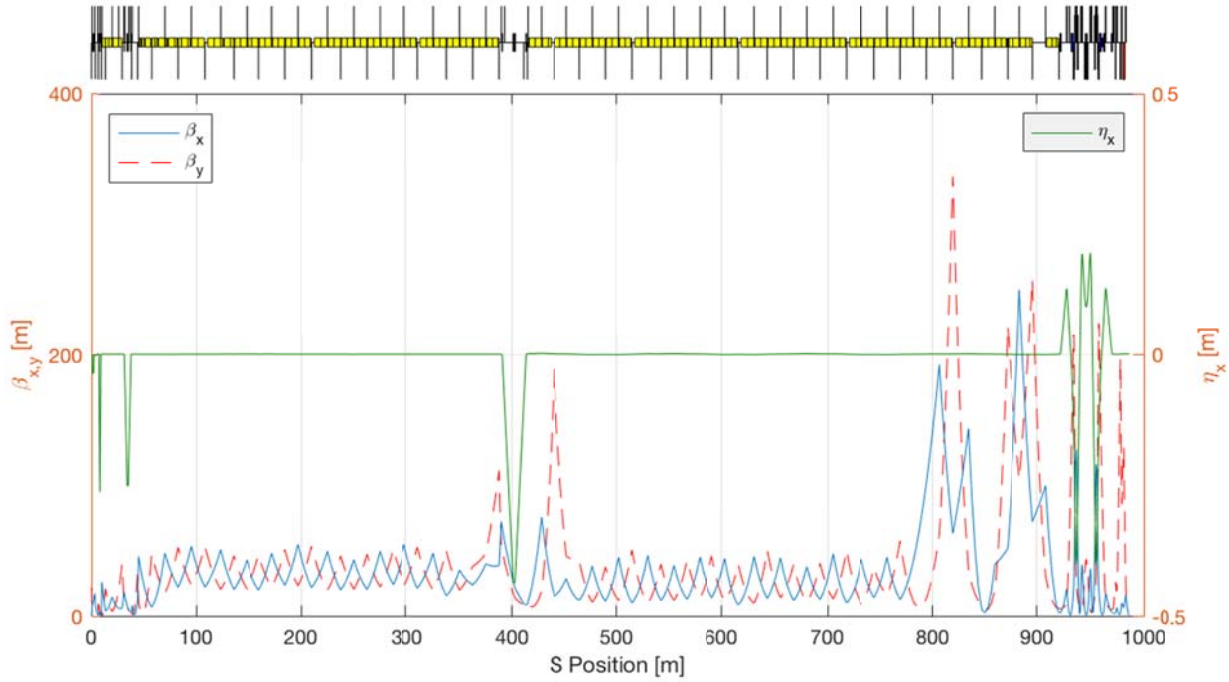


**Figure 6.29. Electron optics across entire FACET-II (using Lucretia), from exit of L0 (at 135 MeV) to the start of the experimental IP area.**

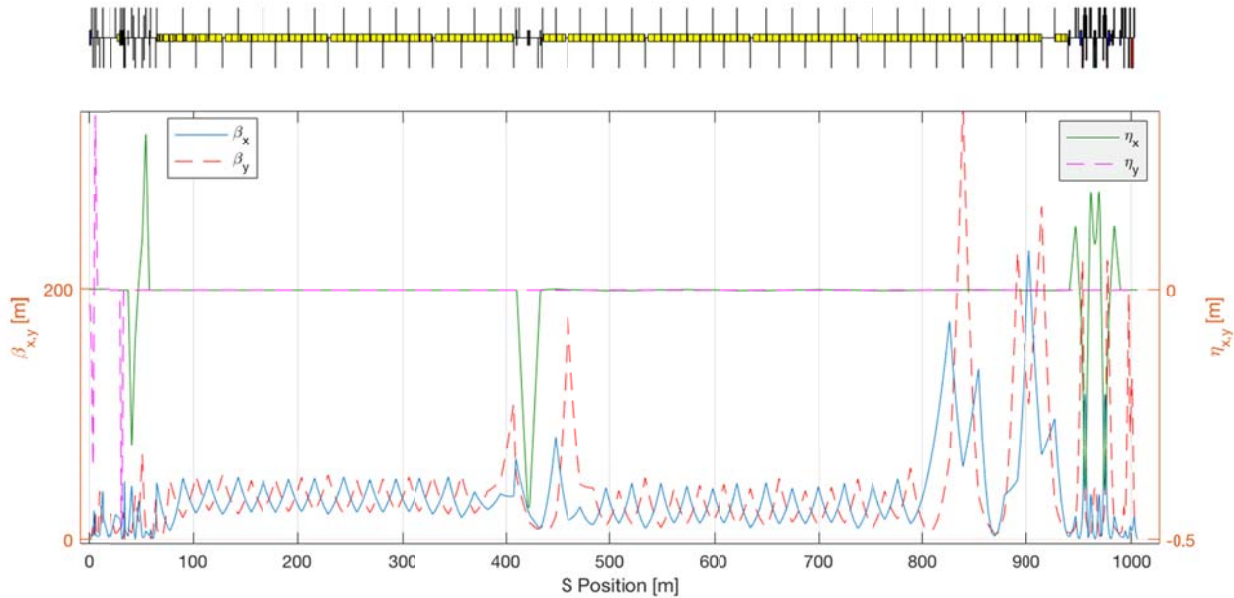


**Figure 6.30. Positron optics across entire FACET-II (using Lucretia), from exit of positron damping ring (at 335 MeV) to the start of the experimental IP area.**

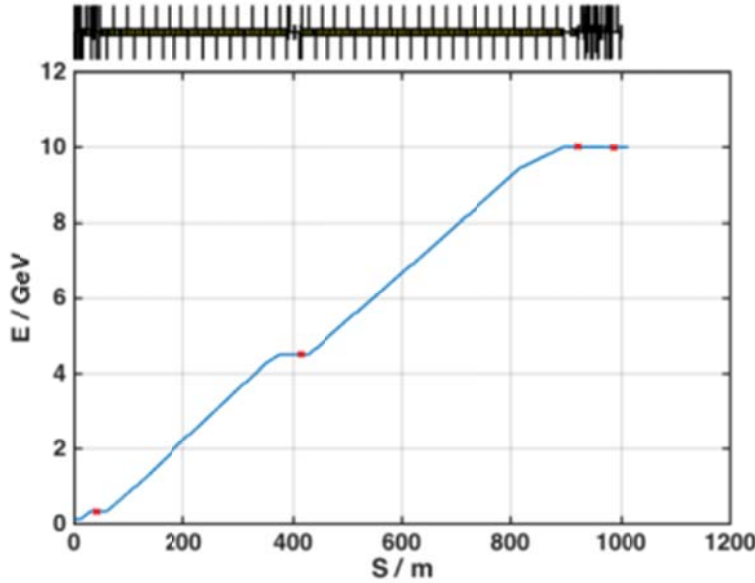


**Figure 6.31. Energy profile through FACET-II electron beamlines. Computed energy profile in blue with tracked energy marked as red crosses after each compression stage.**

The following list describes the various effects which are included in the particle tracking.

- 200k macro particles representing a 2 nC electron bunch was tracked using *IMPACT-T*, which includes 3D space charge forces, up to the exit of the L0a accelerator section at 64 MeV. The initial temporal profile, with a 0.85 mm rms bunch length, is shown in Figure 6.20.
- First to third-order optics of dipole, quadrupole, sextupole, and sinusoidal RF fields.
- Longitudinal and transverse wakefields of the SLAC S-band RF accelerating structures with 321.8 meters of structures between BC11 and BC14, and 471.0 meters after BC14.
- CSR applied to all bends and downstream drift spaces using the 1D line-charge model in *Lucretia*, which includes transient fields but ignores the transverse beam dimensions (not of major impact for the beam parameters considered here).
- ISR applied to all bends, which impacts the energy spread and beam emittance, although by small levels.
- A simulation of longitudinal space charge impedance effects is applied in the *Lucretia* tracking model.
- Collimation of the beam in BC0, BC11 and BC14 bunch compressor collimation sections.

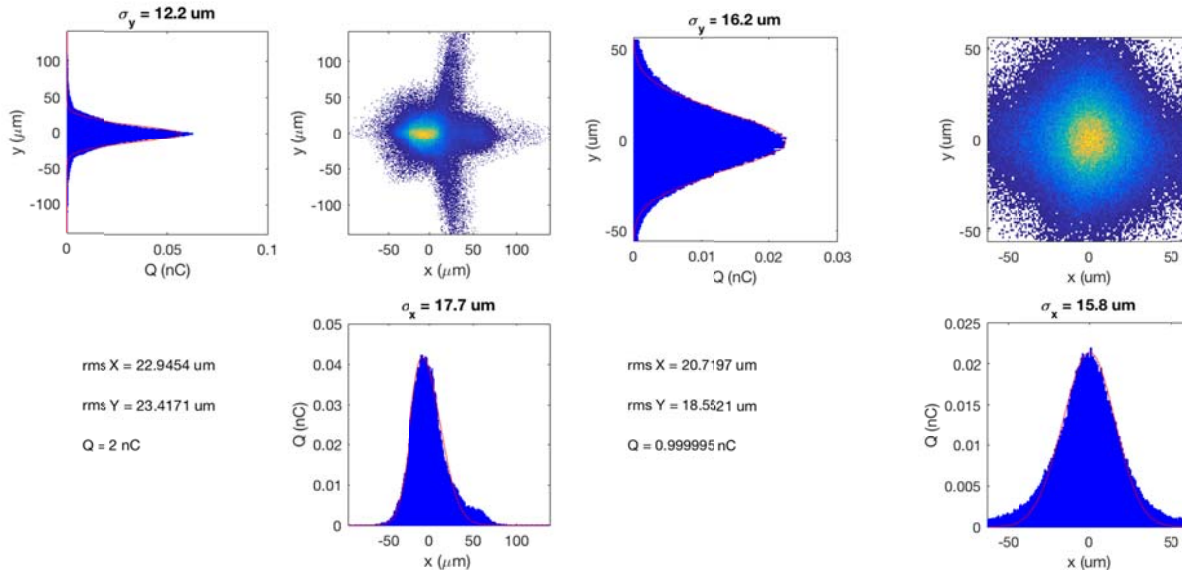
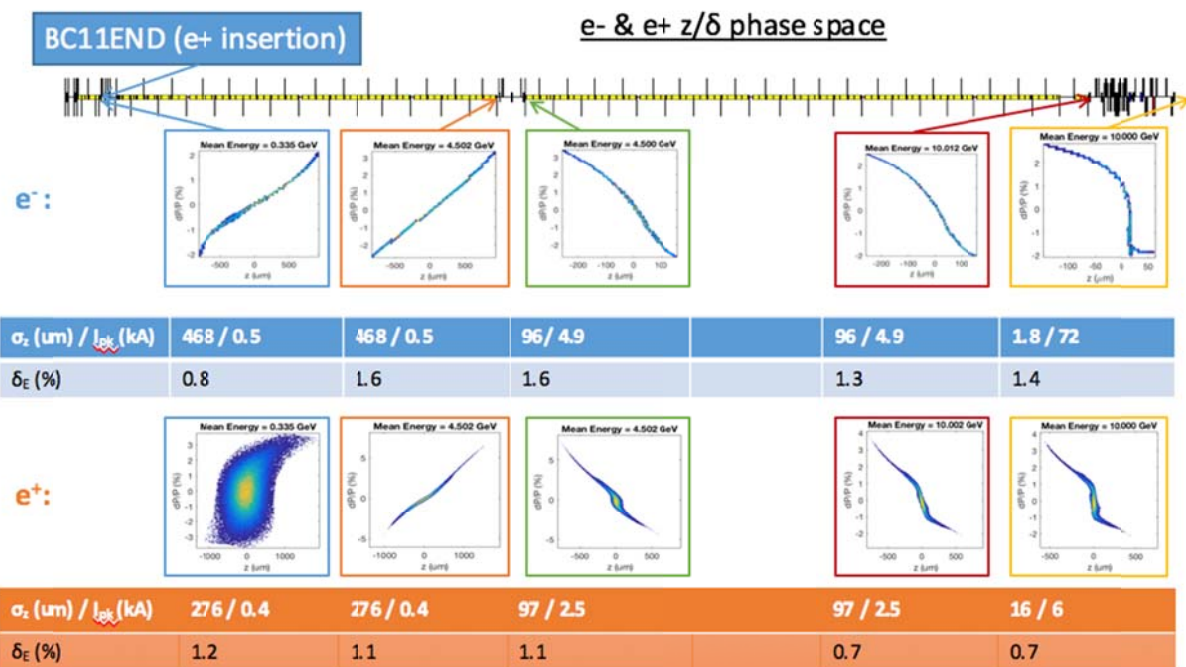


Figure 6.32. Tracked beam particles for electron (left) and positron (right) beams at the experimental IP waist in Sector 20, transverse beam dimensions shown. Tracking results are for the baseline parameter design with  $\beta^* = 0.5$  m optics matching.



**Figure 6.33. Longitudinal compression configuration of FACET-II through the Linac, to the Sector 20 IP for electrons and positrons.**

## **6.9 Instrumentation, Diagnostics, Feedback, and Collimation**

Careful measurement and correction of the transverse and longitudinal beam parameters are critical for preservation of beam emittance and the production of high peak current, small transverse beam sizes at

the experimental IP. Diagnostic devices are distributed all over the FACET-II linac in order to provide precise measurements for use both during initial commissioning and regular operation. An overview of these diagnostics is shown in Figure 6.34.

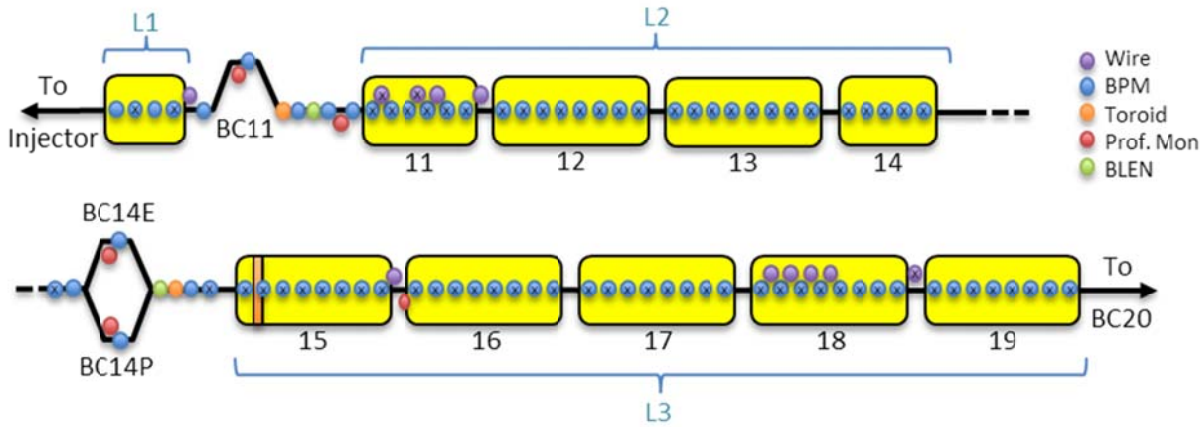


**Figure 6.34. Beam instrumentation in the FACET-II linac and bunch compressors. X's indicate the locations of existing FACET instrumentation that will be re-used.**

### 6.9.1 Beam Position Monitors and Toroid Charge Monitors

Beam position monitors (BPMs) measure the transverse beam centroid and are a primary tuning and monitoring diagnostic. Approximately 80 in total are distributed along the FACET-II linac from the beginning of Sector 11 to the end of Sector 19, located in each focusing quadrupole magnet. These BPMs are stripline assemblies with 20mm inner diameter and 120mm length captive in the pole tips of the quadrupole magnet. Most of the BPMs already exist in the linac quadrupoles and will remain in use.

New BPMs of this type will be installed in the L1 area (2), BC11 area (5), and BC14 area (2) along with their accompanying quadrupole as a single assembly. Additionally, large horizontal aperture BPMs will be located at high-dispersion points in the center of BC11 (1) and BC14 (2) to provide precise measurement of beam energy. A summary of the new BPMs that FACET-II will install as part of the linac and bunch compressor modifications is given in Table 6.12.

**Table 6.12. New BPM installations in the FACET-II linac and bunch compressors.**

FACET-II Deck Name	Area	BPM Type	Roll Angle	BPM ID	Stripline Length	Captive Magnet
			deg	mm	mm	
BPM11132	L1	L1 SA	0	20	100	QA11132
BPM11265	L1	L1 SA	0	20	100	QA11265
BPM11312	BC11	Linac QE	0	20	120	QM11312
BPM11333	BC11	BC11/14 SLA	0	90 (x), 20 (y)	120	e- chicane
BPM11358	BC11	Linac QE	0	20	120	QM11358
BPM11362	BC11	Linac QE	0	20	120	QM11362
BPM11374	BC11	Linac QE	0	20	120	--

BPM11393	BC11	Linac QE	0	20	120	QM11393
BPM14715	BC14	Linac QE	0	20	120	QM14715
BPM14801	BC14	BC11/14 SLA	0	90 (x), 20 (y)	120	e- chicane
BPM141801	BC14	BC11/14 SLA	0	90 (x), 20 (y)	120	e+ chicane
BPM14891	BC14	Linac QE	0	20	120	QM14891

The linac and bunch compressor BPMs will be read out via the legacy SLC control system using CAMAC 605-style BPM processors, which have demonstrated approximately 50 micron resolution. A BPM sampler software script will push the readings to EPICS PVs every 3 seconds, and a suite of existing software interfaces allows for extracting pulse-by-pulse measurements for use in automated tuning and analysis software.

Beam charge diagnostics provide absolute, calibrated measurements of the total bunch charge. In the FACET-II linac there are two new SLAC SLC-style resonant toroids, one after each bunch compressor chicane, which provide non-invasive pulse-by-pulse bunch charge data. The absolute charge measurements are used to calibrate other diagnostics that have a sensitivity to bunch charge, such as BPMs and bunch length monitors. A summary of the new toroids that FACET-II will install in the linac is given in Table 6.13.

**Table 6.13: Diagnostic toroids in the FACET-II linac.**

FACET-II Deck Name	Location	S from cathode	Toroid Eng. Type	Accuracy 1 – 5 nC	Precision 1 – 5 nC
				% rms	% rms
IM11360	After BC11	48.3	1" 8-turn SLC toroid	< 5.0	< 2.0
IM14890	After BC14	422.4	1" 8-turn SLC toroid	< 5.0	< 2.0

The toroids will be re-used linac toroids recovered from the Sector 0-10 equipment removal project and read out via the SLC control system interfacing to CAMAC TCM modules. These modules produce a calibration pulse of known charge that is injected into a secondary calibration winding. The signal is passed through a local preamplifier located physically nearby the toroid, typically in a lead box on the floor of the accelerator tunnel, and then up low-loss low-noise coaxial cable to the TCM module in the klystron gallery.

The toroids can also be used for monitoring beam losses along the linac as MPS interlocks to prevent damage to the various components.

## 6.9.2 Electron Beam Profile Monitors

Profile monitors (screens) and wire scanners are located throughout the accelerator to measure the transverse beam size and distribution. The screens function via either the emission of optical transition radiation (OTR) from the surface of thin metallic foils which the beam passes through, or by scintillation from cerium-doped yttrium aluminum garnet (YAG) crystals which emit visible light upon the absorption of high-energy particles. Several older phosphorescent screens also remain in use, primarily as a monitoring tool.

Experience at LCLS has proven the OTR screens downstream of the injector suffer from degraded utility due to the effects of coherent OTR (COTR) from the high-brightness beam. The FACET-II linac profile monitors are meant for longitudinal phase space diagnostics for viewing energy- or time-dispersed beam

profiles, which may somewhat reduce the coherent OTR effect. Several other methods will be used to mitigate this problem. Tilting the YAG crystal a few degrees away from normal incidence directs most of the COTR light outside the collection aperture of the camera optics; a version this technique is in use at the LCLS dump YAG screen. Additionally, the use of gated cameras allows for triggering the camera exposure to begin just after the beam passes, therefore capturing only the fluorescent emission from the crystal, which has a significantly longer lifetime than the prompt COTR pulse. One such schematic of this geometry is illustrated in Figure 6.35. Using a common screen holder design, the YAG screens can easily be replaced by plates coated with a phosphorescent material such as chromium-doped alumina (Chromox) should the COTR emission remain a problem.

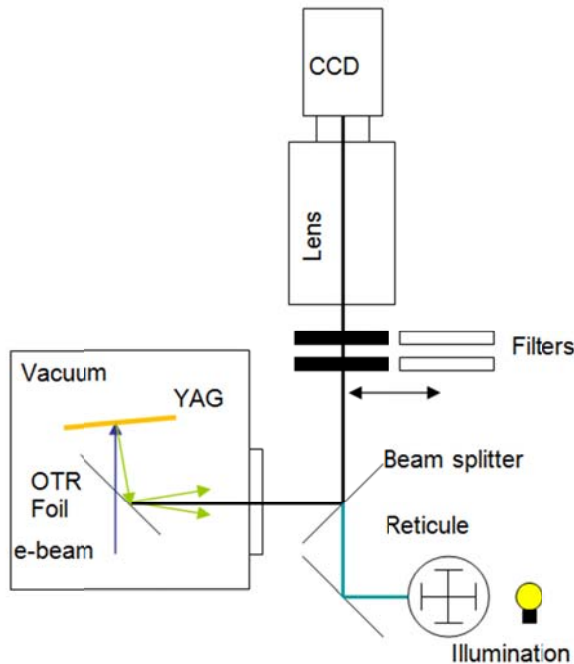


**Figure 6.35. Tilted YAG to mitigate COTR in the linac profile monitors.**

Profile monitors for measurement of electron beam energy spectrum will be installed at the center symmetry point of the BC11 chicane, as well as in both e- and e+ arms of BC14. Additionally, a profile monitor for use in combination with the Sector 15 transverse RF cavity will be installed at the 15-9 instrumentation girder to provide transverse profiles of the streaked beam after BC14. A summary of the linac profile monitor locations is given in Table 6.14.

**Table 6.14: FACET-II linac profile monitors. D is the screen diameter, T is the screen material thickness, and Res is the minimum resolution of the combined camera and optical system.**

FACET-II Name	Type	S from cathode	Beam energy	D	T	Res	$\sigma_x$ nom.	$\sigma_y$ nom.	Function	Orientation
		m	GeV	mm	$\mu\text{m}$	$\mu\text{m}$	$\mu\text{m}$	$\mu\text{m}$		
PR11335	YAG:Ce	44.3	0.335	20	100	25	2800	85	E spread	Vertical
PR11355	YAG:Ce	48.5	0.335	20	100	10	30	1500	Bunch length	Horizontal
PR14803	YAG:Ce	410.5	4.5	20	100	10	1700	35	E spread	Vertical

PR141803	YAG:Ce	410.5	4.5	20	100	10	1700	35	E spread	Vertical
PR15903	YAG:Ce	48.5	5.5	20	100	10	30	1500	Bunch length	Horizontal

All of these screens will be the standard LCLS 20 mm diameter screen geometry, mounted on pneumatic actuated holders with limit switches for position verification and interface with the MPS system. The optics will include stacked insertable ND filters for attenuation of the light and a beam splitter/reticule arrangement at equivalent optical distance as the screen for camera calibration purposes. The cameras will be digital cameras communicating over a modern interface such as Gigabit Ethernet and controlled by an EPICS IOC of standard design already in use for the FACET IP diagnostics.

### 6.9.3 Wire Scanners and Transverse Emittance Diagnostics

Wire scanners provide transverse beam profiles sampled over 50 – 100 pulses by moving a stretched wire across the beam path in uniform steps and measuring radiation downstream of the scattered beam. These wire scanners remain the workhorse tool for measuring and tuning the transverse emittance, both at LCLS and at FACET.

In the FACET-II linac there are 2 emittance diagnostic stations, each of which comprises 4 wire scanners located with optimal phase advance to provide complete measurement of the transverse beam phase space for both e- and e+ beams. In general, 4 or more wire scanners are required for each emittance measurement station to span sufficient phase advance in both planes for both beams, and to provide a measure of redundancy and improved phase-space fitting.

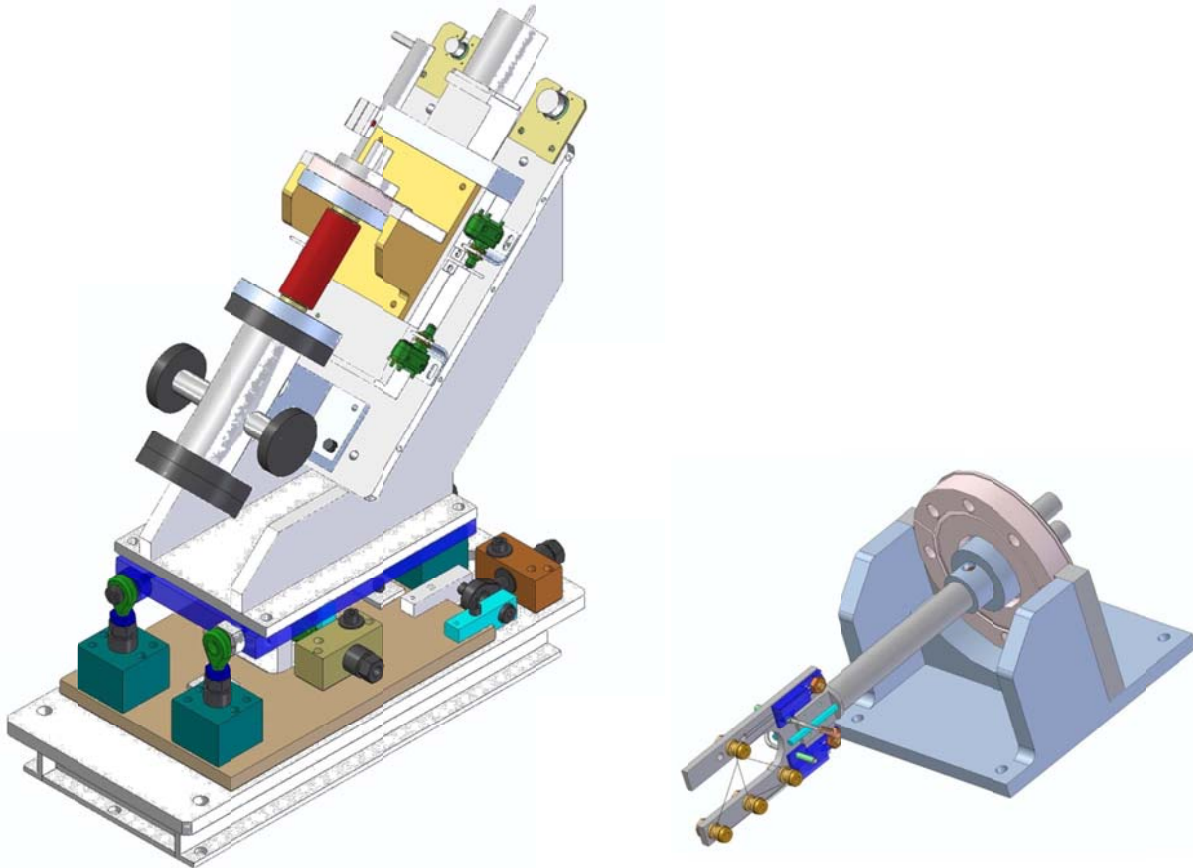


**Figure 6.36. SLC wire scanner with mount (left), internal wire holder card (right).**

Three of the four existing SLC-style wire scanners located in sector 11 will be left in place. The existing wire scanner at 11-3d will be moved to the drift space after the existing 7-foot accelerator structure at 11-7d. In Sector 18, four of the standard 10-foot accelerator sections will be replaced by 9.4-foot sections in order to make space for four SLC-style wire scanners recovered from the Sector 0-10 equipment removal and relocation project (Figure 6.36). These will comprise another 4-wire emittance measurement station. These multi-wire measurements, along with the existing single wire scanner at the 18-9 girder used for quad scan emittance measurements enables us to characterize the emittance preservation performance of the linac from start to end in a non-invasive way, allowing for regular and automated monitoring of the transverse beam quality transported into BC20. A summary of the linac wire scanners is given in Table 6.15.

**Table 6.15: FACET-II linac wire scanner installations. Wire scanners marked with an asterisk \* next to the name already exist in the locations described.**

FACET-II Name	Location	S from cathode	Beam energy	$\sigma_x$ nom.	$\sigma_y$ nom.	$\sigma_x$ min, max	$\sigma_y$ min, max	Wire diameter
		m	GeV	$\mu\text{m}$	$\mu\text{m}$	$\mu\text{m}$	$\mu\text{m}$	$\mu\text{m}$
WS11304	Before BC11	40.4	0.335	75	75	30, 300	30, 300	40
WS11444*	Sector 11	66.4	0.467	40	40	20, 400	20, 400	20
WS11614*	Sector 11	82.6	0.653	40	40	20, 400	20, 400	20

WS11744	Sector 11	103.7	0.925	40	40	20, 400	20, 400	20
WS11914	Sector 11	116.4	1.094	40	40	20, 400	20, 400	20
WS15904	After TCAV3	523.9	5.730	40	40	20, 400	20, 4000	60
WS18144	Sector 18	740.8	8.399	40	40	20, 400	20, 400	20
WS18244	Sector 18	753.2	8.556	40	40	20, 400	20, 400	20
WS18344	Sector 18	765.5	8.713	40	40	20, 400	20, 400	20
WS18444	Sector 18	777.8	8.870	40	40	20, 400	20, 400	20
WS18944*	Sector 19	833.9	9.585	40	40	20, 400	20, 400	20

The wire scanner motion is driven by a stepper motor operated in microstepping mode to minimize wire vibrations and position readback from an integrated LVDT encoder. Each grouping of wire scanners will include 2 to 4 detectors several meters downstream that detect forward scattered radiation from the beam interaction with the tungsten wire. These detectors are typically an integrated scintillator crystal with photomultiplier tube, the output of which is sampled by a charge-integrating ADC. The 90-degree detectors previously installed for the SLC wire scanner system will not be used. The motor controller, LVDT readback electronics, detector high voltage and ADC card will be implemented in a VME-based platform of standard design currently in use at LCLS.

**Table 6.16. Transverse emittance measurement stations along the FACET-II linac ( $\gamma\varepsilon_{x,y} = 6 \mu\text{m}$ ).**

Location	Station Name	Energy (GeV)	$\sigma_x$ ( $\mu\text{m}$ )	$\sigma_y$ ( $\mu\text{m}$ )	No. of Wire Scanners	Existing
Following BC11	ED11 (Sec 11)	0.335	145-215	113-215	4	Yes
At the end of Linac-3	ED19 (Sec 19)	9-10	67	85	4	3 new

### 6.9.4 Bunch Length Diagnostics

The proposed bunch compression scheme's strong sensitivity to RF drift and jitter, as described in section 6.2, requires precise measurement and control of the longitudinal bunch length and charge distribution. Each compression stage has bundled with it a pair of bunch length diagnostics, which are used in tandem to set up and maintain the desired longitudinal profile.

In the FACET-II linac the bunch lengths vary from  $\sim 400 \mu\text{m}$  rms to  $\sim 20 \mu\text{m}$  rms (4 ps to 200 fs FWHM). Transverse RF deflectors have been used at LCLS and FACET across this range and provide excellent resolution of the beam's temporal structure. These measurements are invasive, however. Non-invasive bunch length monitors using coherent dipole edge radiation allow for beam-based feedback and bunch length stabilization.

The transverse RF deflecting cavities have already been described in detail in the previous chapter, Section 5.4.4.1.

One such RF deflecting structure will be placed downstream of the BC14 chicane at 4.5 GeV. This will be located at the 15-2d location, where the existing 10-foot accelerating structure will need to be removed and replaced by a newly fabricated 2.44-meter deflecting structure. A corresponding screen will be located at the 15-9 instrumentation drift section where space is available.

### 6.9.5 Relative Bunch Length Monitors

For pulse-by-pulse monitoring and feedback stabilization, non-invasive measurement of peak current will be done by bunch length monitors (BLMs) which sample the total power the coherent diffraction or “edge” radiation emitted from the downstream face of the final bend magnet in each bunch compressor.

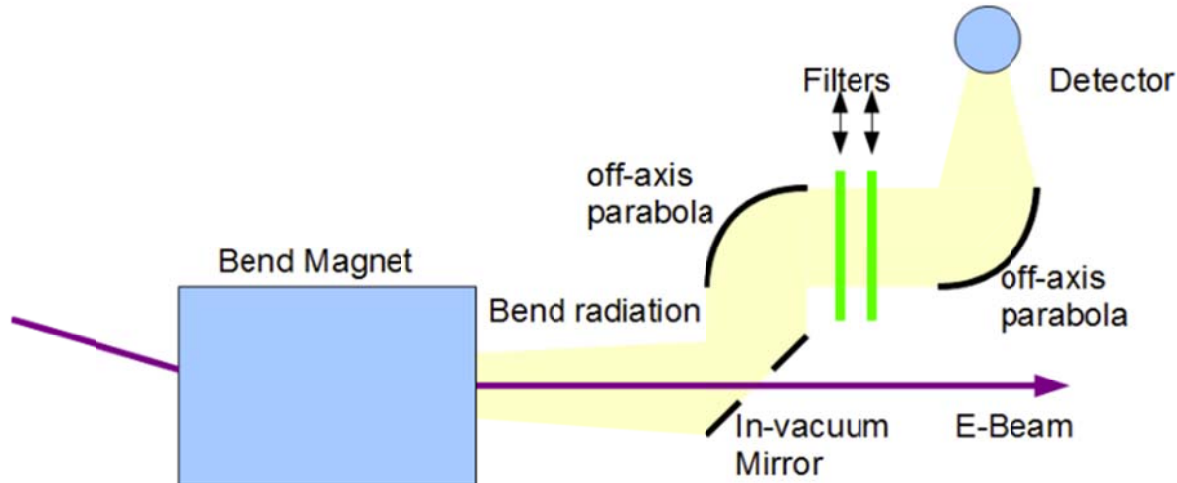


Figure 6.37. Relative bunch length monitor schematic.

The power in the coherent radiation is very sensitive to the electron bunch length with an approximate scaling of  $q^2/\sigma_z$  and typical wavelengths will be in the FIR range. For the 2 nC, 5 kA nominal configuration case at BC14, the expected FIR pulse energy is approximately 3 mJ. An in-vacuum mirror with a 1 cm diameter hole is located immediately after the last bend magnet in each chicane. This mirror directs the radiation through a vacuum window and ultimately the radiation is imaged onto a pyroelectric detector with collecting horn. Due to absorption by water vapor, the transport optics must be located within a dry gas enclosure. The arrangement is shown in Figure 6.37.

This pyrometer signal will be carried by a low-loss coaxial cable to an integrating ADC, pizza-box type digitizer or diagnostic oscilloscope. Calibration of the bunch length monitor will be performed using the transverse RF deflecting cavity.

## 6.9.6 Beam Energy Spread Diagnostics

The electron energy spread is typically measured using a profile monitor at a location with large momentum dispersion and small beta function. Several locations have been designed into the FACET-II optics in order to enable this measurement. The key locations are in the first bunch compressor, BC11, and the second bunch compressor, BC14. Each of these locations will be equipped to allow adequate energy spread measurements along the FACET-II accelerator as described below. The location of the transverse deflecting cavities after each bunch compressor precludes the ability to measure sliced energy spread at the profile monitors in the chicanes.

### 6.9.6.1 BC11 Energy Spread Diagnostics

The energy-spread after the first compressor, BC11, is made with a profile monitor located in the center of the chicane at a point where the horizontal dispersion function is  $\eta_x \approx 250$  mm and the horizontal beta function converges towards a minimum of  $\beta_x \approx 6.8$  m. For the nominal emittance and nominal energy spread of  $\sigma_\delta \approx 0.5\%$  at 335 MeV, the betatron beam size is 90  $\mu\text{m}$ , but the dispersive size is 1.3 mm. This produces a systematic error in the energy-spread measurement of <1 %.

### 6.9.6.2 BC14 Energy Spread Diagnostics

The energy-spread after the second compressor, BC14, is also made with a single profile monitor located in the center of the second chicane at a point where the horizontal dispersion function is  $\eta_x \approx 367$  mm and the beta function converges towards a minimum of  $\beta_x \approx 26$  m. For the nominal emittance and nominal energy spread of  $\sigma_\delta \approx 1.1\%$  at 4.5 GeV, the betatron beam size is 42  $\mu\text{m}$ , but the dispersive size is 4 mm. This produces no significant systematic error in the energy-spread measurement.

## 6.9.7 Trajectory Feedback Systems

Trajectory feedback systems will be placed at the entrance of the L2-Linac and the L3-Linac. As at the SLC [3], these systems will each be composed of approximately ten BPMs which record both  $x$  and  $y$  positions, preceded by a set of two horizontal and two vertical fast dipole corrector magnets controlled by a software based feedback system.

In order to control transverse orbit variations to better than  $1/10^{\text{th}}$  of the beam size, the individual one-pulse BPM resolution for the various 10-BPM feedback systems described above needs to be <10  $\mu\text{m}$  rms. Trajectory variations which occur at frequencies below  $\sim 1$  Hz will be stabilized. Faster variations cannot be damped significantly and will need to be identified at the source.

Transverse vibrations of quadrupole magnets will generate orbit variations, which if fast enough will not be damped by feedback systems. Tolerance calculations indicate that typical previously measured uncorrelated random vibrations of FACET-II quadrupoles of <1.5/0.5  $\mu\text{m}$  rms (horizontal/vertical) are sufficient to achieve the required project objective performance parameters.

## 6.9.8 Energy and Bunch Length Feedback Systems

Energy feedback systems will be placed in each bending region (BC11 and BC14). A single BPM placed at a high dispersion point will be used to determine energy variations, and the corresponding bunch length monitor will be used to determine variations in bunch length. In BC11, the phase and amplitude of L1 will be used to stabilize the energy and bunch length. In BC14, the L2 reference phase will be adjusted to modulate the bunch length, while vernier control of two klystron phases will maintain the beam energy. These operations are to be carried out by a software feedback similar in design to the 6x6

feedback loop system that has already been fully tested and operational at LCLS-I. Modifications to this design will be required to add energy and bunch length states for both electron and positron beams, making it an “8x8” feedback, as energy feedback for the injector, positron injector and Sector 20 will be split out and handled by separate dedicated feedback loops.

---

1. K. Bane, P. Emma, Proc. of the 2005 Part. Accel. Conf., Knoxville, TN, May 16-20, 2005.
2. <http://www.slac.stanford.edu/accel/ilc/codes/Lucretia/>
3. T. Himel et al., *Adaptive Cascaded Beam-Based Feedback at the SLC*, Proceedings of the 1993 Part. Accel. Conf., Washington, DC, 1993.

# 7 Shielding

---

## Technical Synopsis

*Shielding is an integral part of the Radiation Safety System (RSS), containing beam losses to prevent excessive radiation in occupied areas, minimize residual radiation levels that contribute to personnel radiation dose exposure and minimize activation of ground water.*

*FACET-II and LCLS-II introduce new shielding requirements in addition to the existing accelerator housing. A concrete shielding wall must be constructed in Sector 10 to separate the LCLS-II and FACET-II sections of the Linac tunnel. This allows access to the LCLS-II tunnel while there is beam in the FACET-II area. It does not permit access to the FACET-II area during LCLS-II beam operation. In addition to the wall, the service penetrations in sector 10 require modified shielding due to LCLS-II beam loss in the sector.*

---

### 7.1 Introduction and Overview

FACET-II is within the existing accelerator housing and greatly benefits from 25 feet of earth between the tunnel and the klystron gallery, where personnel are present to service equipment. Shielding is a vital component to the Radiation Safety System, necessary to limit dose to personnel and to the environment. The FACET-II facility introduces new beam loss points which could result in prompt dose, dose from residual radiation or tritium production.

The shielding for FACET-II needs to meet requirements as defined by beam operations foreseen for FACET-II including potential future upgrades (chapter 10). These physics requirements, derived from particle tracking studies indicating beam loss points on collimators and apertures and due to interaction with experiments, are the basis for the final Radiation Safety Systems design incorporating shielding<sup>1</sup>. Consideration is also given to access requirements.

In addition, due to the shared use of the accelerator housing by LCLS-II, LCLS-II personnel access and beam loss must also be considered<sup>2</sup>.

This chapter describes additions to the existing Linac shielding between sectors 10 and 20 due to the new usage by FACET-II and LCLS-II:

- A concrete shielding wall will be constructed in Sector 10 to separate the LCLS-II and FACET-II sections of the Linac tunnel.
- To meet requirements for personnel to be present in the klystron gallery, select penetrations through the 25 ft earth need to have additional shielding.
- Some devices installed for FACET-II will also require spot shielding to minimize dose to personnel from residual radiation and also activation of ground water forming tritium.

### 7.2 Sector 10 Shielding Wall

A shielding wall will be constructed to isolate FACET-II from LCLS-II in Sector 10.

This allows beam operation in the FACET-II area independent of LCLS-II access state. However, access to the FACET-II area is not allowed while LCLS-II is in operation.

### 7.2.1 Sector 10 Layout

The shielding wall is a solid wall starting around  $Z = 969\text{m}$  in the Accelerator Housing, downstream of Penetration 10-9 at Sector 10.

The wall will not have any means of personnel access between the LCLS-II and FACET-II regions of the accelerator housing. There will be penetrations in the wall to accommodate:

- the LCLS-II dog-leg beamline
- Accelerator Cooling System (ACS) return pipe from 10-9
- LCLS-II cables
- the alignment measurement system (normally plugged except when needed for line-of-sight between alignment monuments on each side of the shielding wall).

A small opening at floor level will permit passage of water along the linac housing.

LCLS-II will remove the existing alignment light pipe from S0 to S10-7 or 10-8. The new starting location of the light pipe will be  $Z = 993\text{m}$ , and Metrology will have a camera at 992m for use with this alignment system when needed for FACET-II and LCLS-I.

The LCLS-II dog-leg passes through the shield wall and a 2" diameter hole will accommodate this pipe.

There are LCLS-II beamline components in the area (corrector magnets, diagnostics and collimators) however there are 7.9 m between LCLS-II components within which the wall can be located.

Penetration 10-10 is not required by either FACET-II or LCLS-II and may be blocked by the shield wall.

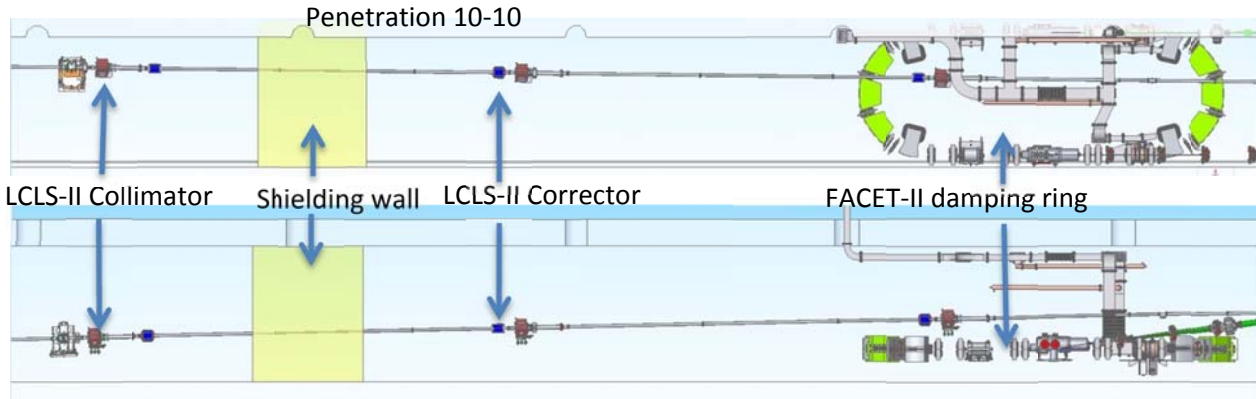


**Figure 7.1.** A conceptual drawing of Sector 10 shows a potential location for the sector 10 shielding wall (top: plan view, bottom: elevation view). The LCLS-II dogleg components (collimator, correctors) are shown. The beam pipe passes through the shielding wall. The shielding wall is depicted as 2.5 m thick with stands immediately upstream and downstream to support the LCLS-II beam pipe.

## 7.2.2 Shielding Wall Requirements

The shielding wall thickness and materials are specified to meet radiological requirements such that an individual on the LCLS-II side of the wall would not get a radiological dose in excess of 1 rem in a year during FACET-II beam operations. The shield wall will reduce the average normal dose rate to as low as reasonably achievable (ALARA) levels.

Radiation Physics (RP) perform calculations with FLUKA Monte Carlo Code based on assumptions on beam losses to estimate the dose rate on the upbeam side of a modelled shield wall. The radiation physics studies cover multiple cases: the normal operations case, the worst possible missteer case and the Maximum Credible Incident (MCI) case. Each beam loss scenario dictates a minimal width for the shield wall which must be simultaneously satisfied.

The largest contribution to the dose, and hence the driver for the radiological requirement on the thickness of the wall, is positron beam loss upon injection into the damping ring. The positron beam (3.5 W beam power) at this point is directed west, towards the shielding wall. Other radiation sources from the damping ring and positron return line include beam-interruptive diagnostics in the positron return line (PRLTR) and extraction line (PEC) (Figure 7.2). In addition, there will be a vacuum valve each at the point where the positron beam is extracted from and injected into the damping ring to isolate the damping ring vacuum from the linac vacuum. Apertures are expected to be narrow in the damping ring also contributing to a small degree of beam loss. Contributions from the eastward travelling electrons also need to be considered.

Traditionally, a mixture of material is used for a shield wall. Photon field attenuation is achieved with a high-Z material such as iron or lead which is then followed by a moderating material such as concrete with the addition of a material to capture thermal neutrons (e.g. borated polyethylene).

Using concrete only, the estimated thickness of the sector 10 shield wall, based on preliminary calculations, is of order 300 cm<sup>3</sup>. The space available in sector 10 is greater than this and such a wall would not constitute an issue. A combination of materials, however, would satisfy requirements in shorter distance. Preliminary estimates show 175 cm of concrete and 15 cm of iron can also satisfy requirements (Figure 7.3) for both expected operational losses and full beam loss in the missteer case. The final shield wall design can be optimized by what is the lowest cost of construction and the simplest design.

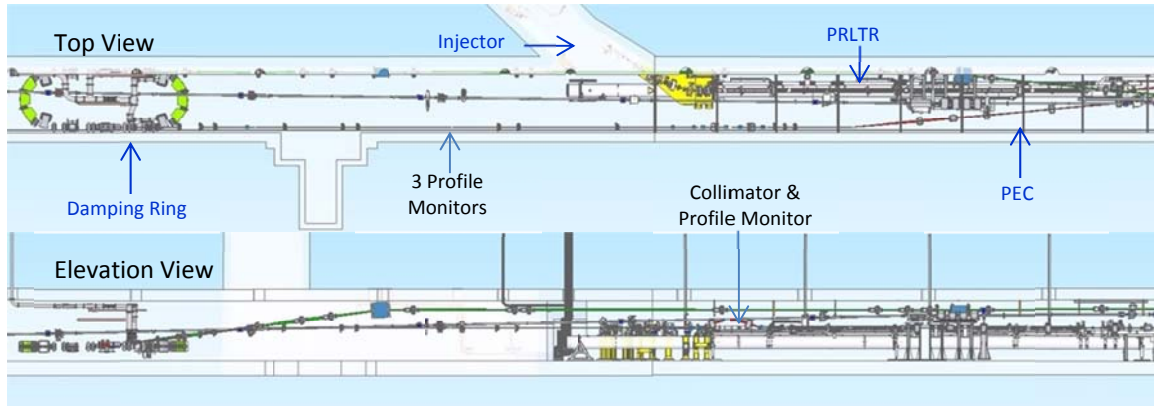


**Figure 7.2.** A preliminary layout of the damping ring, Positron Extraction and Compression (PEC), and Positron Return Line to Damping Ring (PRLTR) showing potential locations for beam-interruptive diagnostics.

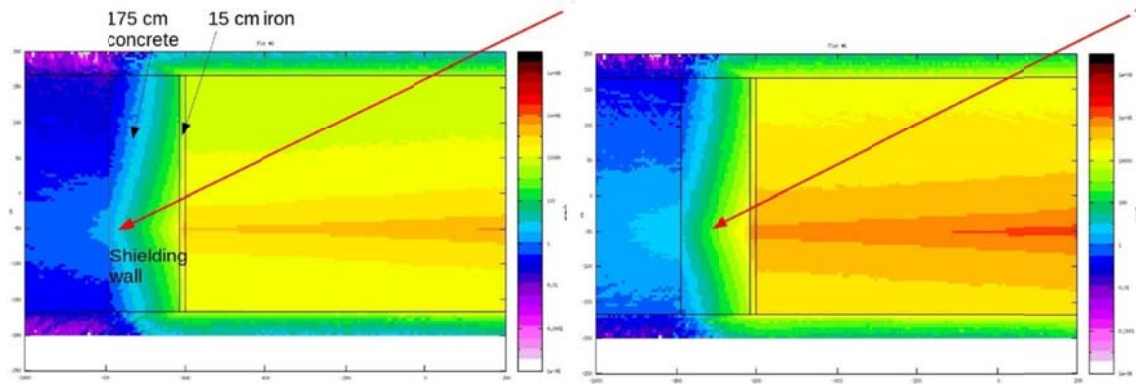


**Figure 7.3.** Preliminary calculations for dose rates due to expected positron beam losses (left) and full positron beam loss (right). The calculations were done with FLUKA Monte Carlo code. The shield wall was modeled as 15 cm iron with 175 cm concrete and was shown to satisfy the criteria for personnel to be downstream of the shield wall in both cases. The red arrow shows the contour for the dose rate criterion that must be contained within the wall for the criterion to be met.

### 7.3 Penetration Shielding

Service penetrations exist between the accelerator housing (also called beamline enclosure) and the klystron gallery, occupied by waveguides, utilities and cables. Penetrations have typically up to 60 cm of borated polyethylene beads filled in bags and places in the top end of the penetration, around installed pipes and ducts.

The accelerator housing for FACET-II is shared with the LCLS-II dog-leg and bypass line. Differences between LCLS-II and historic uses of the accelerator housing result in increased requirements for shielding on penetrations up to sector 11.

#### 7.3.1 Layout

Sector 10 and the beginning of sector 11 is a part of the LCLS-II dog-leg sections where beam is deviated both horizontally and vertically to connect the new LCLS-II beamline to the existing bypass line running

near the ceiling of the housing on the south side. The highest radiation is expected in the first part of sector 10 (up to penetration 10-8) where there is line of sight between the LCLS-II beam loss point and the klystron gallery through the penetrations (on the north side of the housing). From penetrations 10-8 up to where the dog-leg connects to the bypass line (around penetration 11-03, i.e. the third penetration in sector 11), radiation decreases gradually.

Due to this dog-leg, requirements on shielding for each penetration will be different.

FACET-II klystron gallery control racks are physically close to the penetrations in sector 10 and FACET-II requires use of the service penetrations from penetration 10-12 and downstream.

### **7.3.2 Radiological Requirements**

The penetration shielding thickness and materials are specified to meet radiological requirements such that an individual in the klystron gallery would not get a radiological dose in excess of 1 rem in a year during LCLS-II beam operations.

Radiation Physics (RP) performed calculations with FLUKA Monte Carlo Code based on assumptions on beam losses to estimate the dose rate inside the klystron gallery.

In order to estimate how much shielding is needed, dose rates were calculated for representative penetrations in sectors 10 and 11 for various beam loss scenarios for the LCLS-II beam. Three cases were considered:

- a) Normal operation with expected beam losses about 1 W/m
- b) Mis-steered beam losses limited by LCLS\_II BCS to 1 kW and
- c) Maximum Credible Incident (MCI) with beam losses up to 2 MW.

The studies showed that the design of the shielding was dictated by the MCI losses (shielding designed for MCI also fulfils requirements for normal operation and mis-steered beam). Requirements ranged from 109.65 cm concrete (penetrations 10-01 through to 10-8) to 29.56 cm concrete at penetration 10-13. Penetrations 10-14 through to 11-3 do not require a concrete solution and the shielding can be provided with between 15.2 and 76.2 cm of bags containing borax4.

### **7.3.3 Usage Requirements**

In addition to the radiological requirements, consideration is needed of both FACET-II and LCLS-II use of the penetrations for waveguides, cables and utilities. Where a penetration is not required for use by either accelerator, the penetration will be sealed with a concrete plug (Figure 7.4).

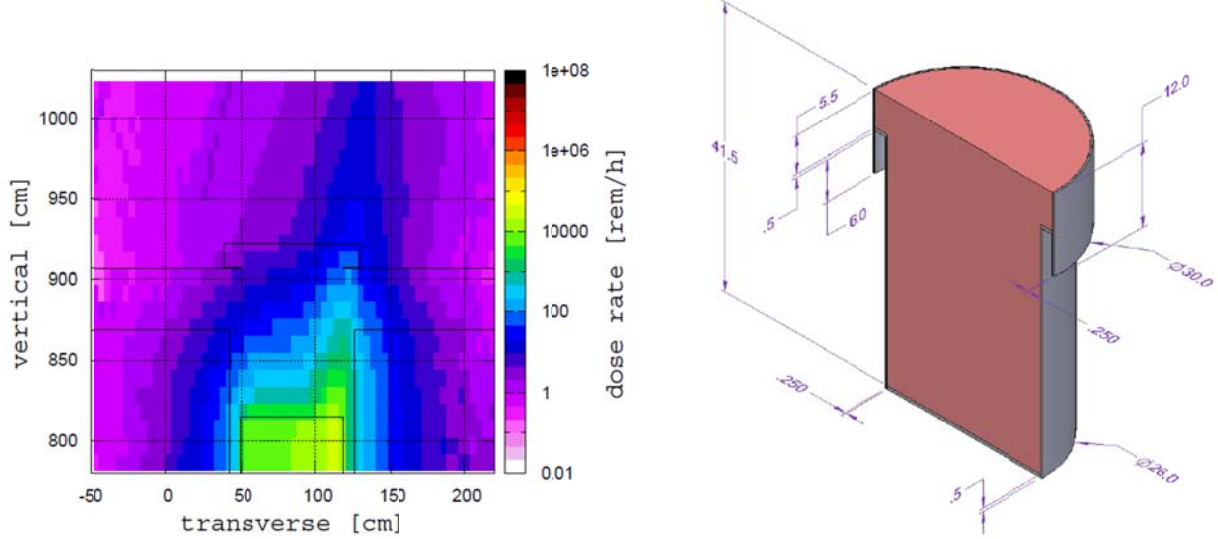


**Figure 7.4. Left:** Dose rate map for penetration with 108 cm thick concrete shielding plug (15 cm overlap between the penetration edge and shielding edge). The dose rate was calculated for 2 MW 4 GeV LCLS-II beam loss inside the linac tunnel. A black outline shows the shielding. Outside of the shielding, dose rate fulfills criteria for MCI (25 rem/h). **Right:** Engineering sketch of the concrete shielding plug used in the dose rate simulation.

Penetrations with openings require a different solution. For flexibility in future installations, up to 50% of the penetration cross-section will be kept open regardless of the cable count initially expected. The shielding for this type of penetration is also concrete with a large opening at an angle of 45° or 90° (Figure 7.5) depending on the bending radius of the cables. After cable installation, the opening shall be filled with 25 cm thick layer of bags filled with borax.

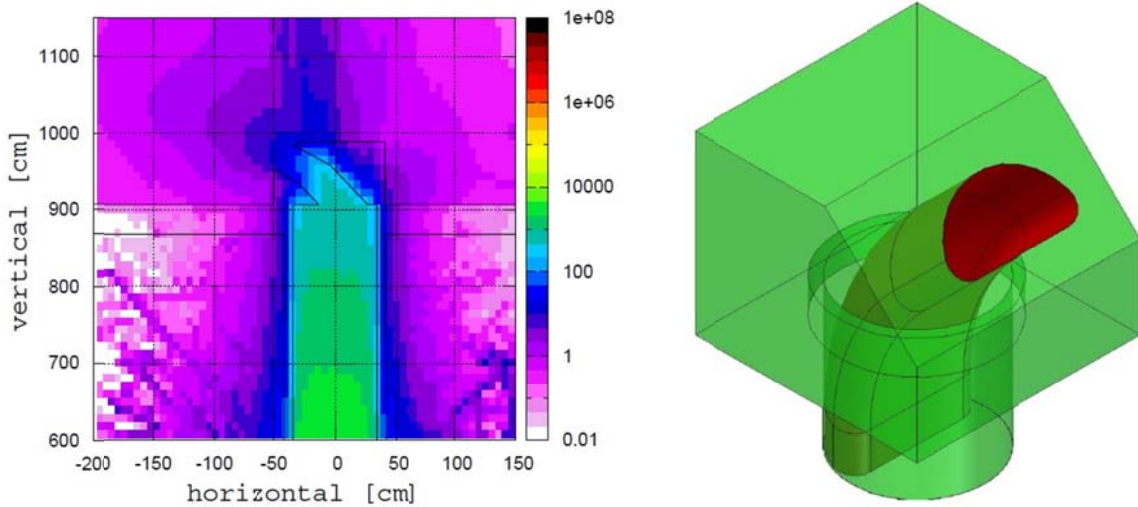


**Figure 7.5. Left:** Dose rate map for penetration with a concrete shielding cap that can accommodate cables. The dose rate was calculated for 2 MW 4 GeV LCLS-II beam loss inside the linac tunnel. A black

**outline shows the shielding. Outside of the shielding, dose rate fulfils criteria for MCI (25 rem/h). Right: Engineering sketch of the concrete shielding cap used in the dose rate simulation.**

---

1 FACET-II-PR044 *Physics Requirement Document* FACET-II Radiation Safety Systems C Clarke, G White

2 LCLSII-2.7-PR-0079 *LCLS-II Electron Beam Loss and Maximum Credible Beam* James Welch

3 RP-RPG-150818-MEM-01 *Preliminary evaluation of the FACET-II Sector 10 shielding wall thickness for cost estimates* Ludovic Nicolas

4 RP-15-22 *Shielding for penetrations in sector 10 and 11 against radiation produced during LCLS-II operation* J. Blaha

# 8 Positron Systems

---

## Technical Synopsis

In order to achieve the scientific goals of the experimental program at FACET-II, a high positron peak current with small transverse and longitudinal emittance is required. FACET-II will operate with a positron energy up to 10 GeV. The most challenging parameters are for the plasma wakefield acceleration (PWFA) experiments which require peak currents of several 1000's of amperes. Positrons are produced by sending an electron bunch onto the existing positron target and capture section in Sector 19. The positron bunch is transported back to Sector 11 in the existing Positron Return Line. A new beamline that starts in Sector 11 takes the positrons from the Return Line and injects them into a new Damping Ring in the Sector 10 Linac tunnel. The energy of the beam from the positron production system is 210 MeV and the Damping Ring energy is 335 MeV, so 125 MeV of energy must be provided by S-band accelerating structures to be located in Sector 14. The accelerating structures will replace a section of the existing return line.

The positron beam into the damping ring has a very large transverse emittance that must be reduced by three orders of magnitude in a few milliseconds. Because the damping ring is located in the existing Linac tunnel, the diameter of the ring must be smaller than 3 meters. This constraint dictates a compact design with minimal gaps between the magnets in the arcs. The large injected beam size also dictates that the acceptance of the ring be large enough to accommodate on-axis injection. The proposed design incorporates many aspects of recent developments for diffraction-limited light sources. The beam energy is chosen to be 335 MeV which is as high as possible given the space constraints.

Given the compact dimensions, the magnet design for the damping ring arcs is particularly challenging. As proposed, the three dipole magnets in each arc cell are wound on a single block of steel and incorporate both quadrupole and sextupole field components by design. Three dimensional magnet models have been produced for the damping ring, and designs for these are described in Section 8.3.6. The straight sections contain both the injection, the extraction and the RF cavities. Vacuum requirements are not particularly challenging.

A second new positron beamline in Sector 10 takes the beam from the damping ring extraction point, performs a 1<sup>st</sup> stage of bunch compression and injects it into the last dipole magnet of the 1<sup>st</sup> electron bunch compressor (BC11) in Sector 11. All of the components of the injection and extraction lines are conventional. Once the positrons are injected into the Linac, they are accelerated to 10 GeV in Linac sections 2 and 3. The second stage of bunch compression is performed in a second arm of the bunch compressor in Sector 14 (BC14) and the 3<sup>rd</sup> stage in the existing Sector 20 W-chicane (BC20), which is described in Chapter 9. The positron bunches are focused at the FACET-II Interaction Point according to user requirements, with a final transverse emittance of < 20  $\mu\text{m} \cdot \text{rad}$  required at the end of the Linac, prior to final compression and bunch length < 20  $\mu\text{m}$  at the focus point within Sector 20. The beam is dumped in the existing dump system at the end of Sector 20.

Simulations have been written to demonstrate the performance of the transport lines and damping ring. Collective effects within the damping ring have been estimated analytically and appear to be controllable.

---

## **8.1 Positron System - Introduction and Overview**

The FACET-II positron system design takes the beam from the existing positron target, capture section and return line, transporting it back to Sector 10. To match the 335 MeV energy of the damping ring, four sections of S-band acceleration (each 7 feet long and with ~20 MV/m gradient) will be installed in Sector 14 of the return line. Additional collimation is also required upstream of the Sector 14 energy booster section to shadow the S-band structure irises which otherwise would represent the first limiting aperture seen by the beam in this transport line. Starting in Sector 11, a new beamline brings the positrons from the existing return line and injects them into a small damping ring in the Sector 10 Linac tunnel. The beam extracted from the damping ring undergoes a 1<sup>st</sup> stage of bunch compression and is then injected into the Linac at the Bunch Compressor in Sector 11, BC11. One constraint on the locations of the positron beamlines and damping ring is the path of the LCLS-II bypass line, which has a dogleg section through Sector 10.

### **8.1.1 Requirements and Parameters**

For the FACET-II experimental program, the positron beam must meet a specific set of requirements for emittance, peak current, energy, energy spread, and stability. These parameters are listed below in Table 8.1. A schematic layout of the positron system is also shown in Figure 8.1 with beam parameters listed at various points along the accelerator. The positron beam optics from the target to the reinjection point in Sector 11 is plotted in Figure 8.2 and

## Positron Beam Optics

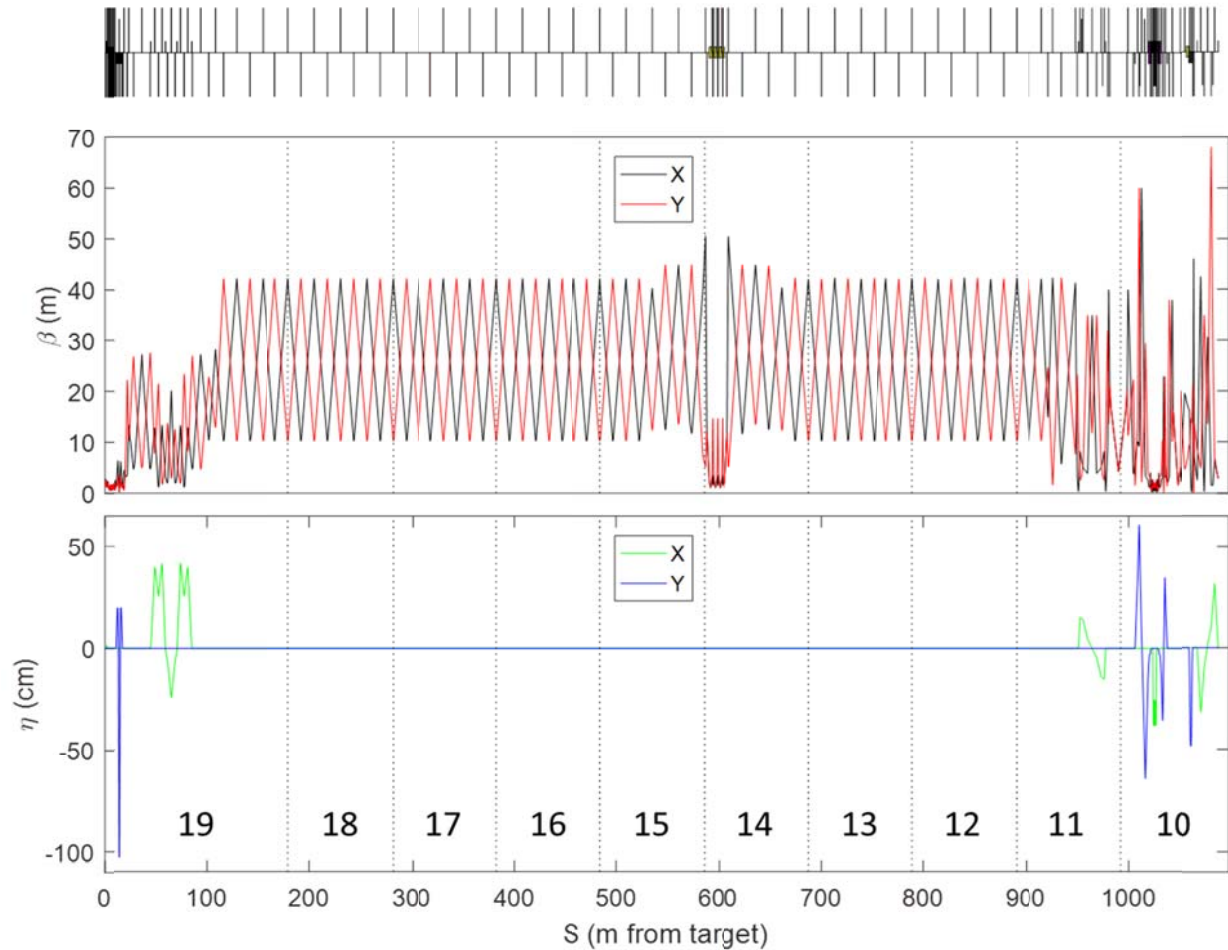
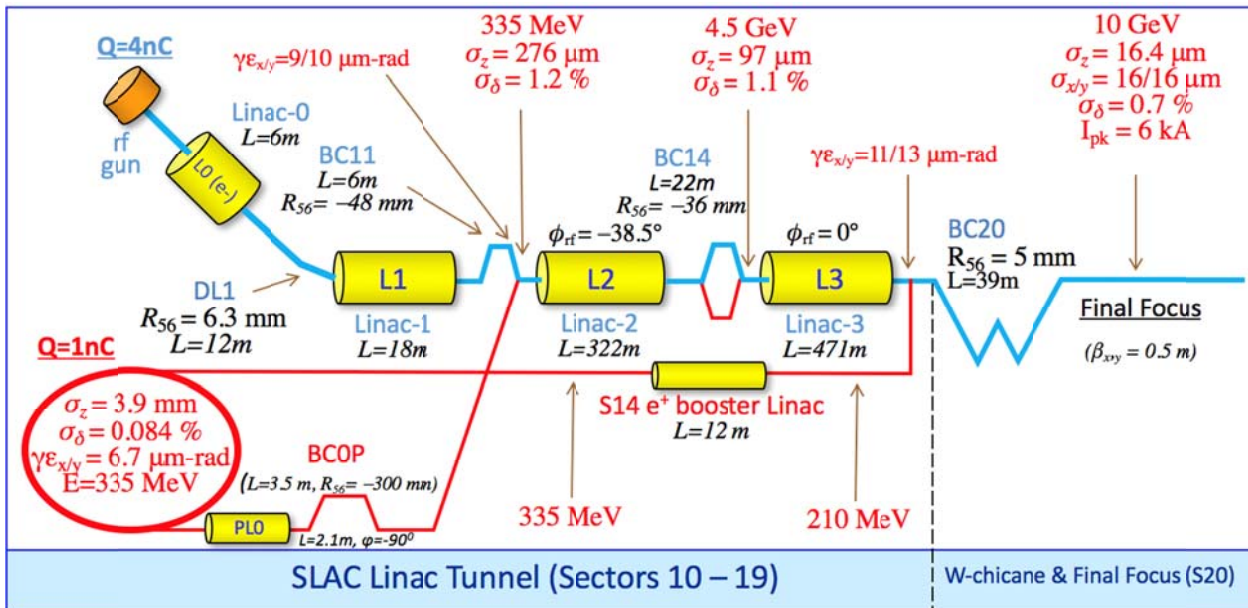


Figure 8.3.

**Table 8.1. Nominal positron beam parameters at the FACET IP and their operational ranges.**

Parameter	Symbol	Unit	Nominal	Range
Final positron energy	$E_f$	GeV	10	4 – 13.5
Initial bunch charge from PDR	$Q_0$	nC	1	1 - 2
Pulse repetition rate	$f_{rep}$	Hz	5	1 - 5
Number of bunches per RF pulse	$N_b$	-	1	1
Final Transverse core beam size (x/y, rms)	$\sigma_x/\sigma_y$	$\mu\text{m}$	18/19	10-35/7-20
Peak current	$I_{pk}$	kA	6.3	6 – 15.5
Bunch length (rms)	$\sigma_z$	$\mu\text{m}$	16.6	7 – 20
rms energy spread	$\sigma_E/E$	%	0.6	0.5 – 1.5



**Figure 8.1.** Schematic layout of FACET-II injector, linac, bunch compressors, and experimental area, with main parameters listed for operation. The blue sections depict the electron specific and common  $e^-/e^+$  areas. The red sections are for positrons.

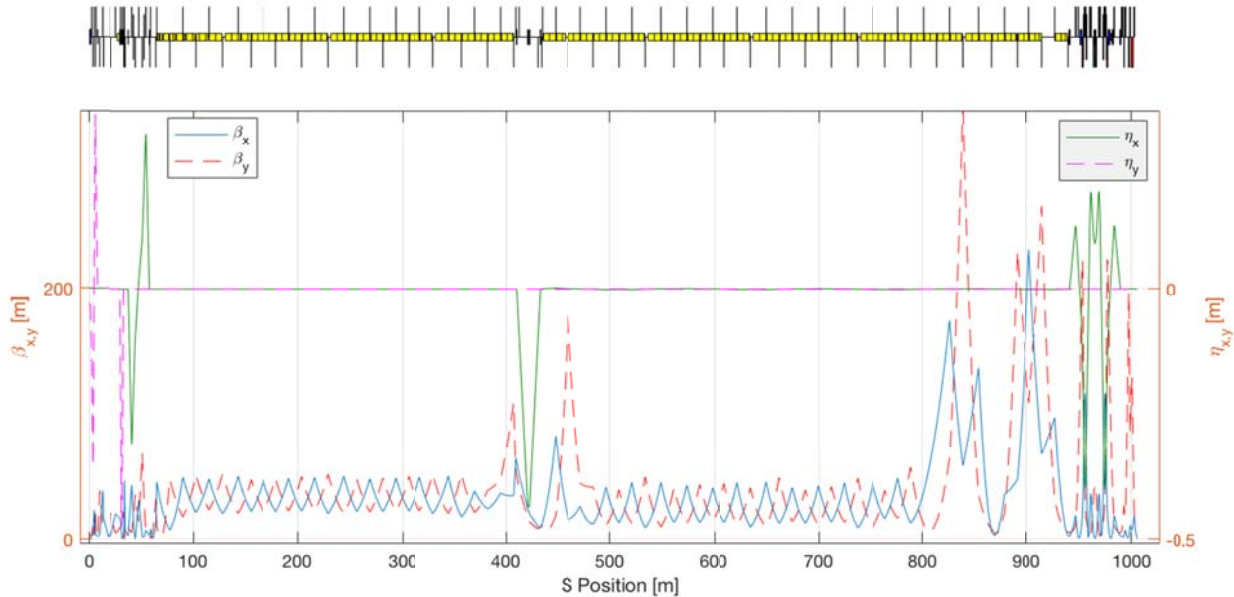


**Figure 8.2.** Positron optics from exit of positron damping ring (at 335 MeV) to the start of the experimental IP area. The positrons are injected into the existing Linac at the last bend magnet of BC11. There are three stages of bunch compression: BC0 in the extraction line; a second arm of BC14 in Sector 14; and the “W chicane” in Sector 20.

## Positron Beam Optics

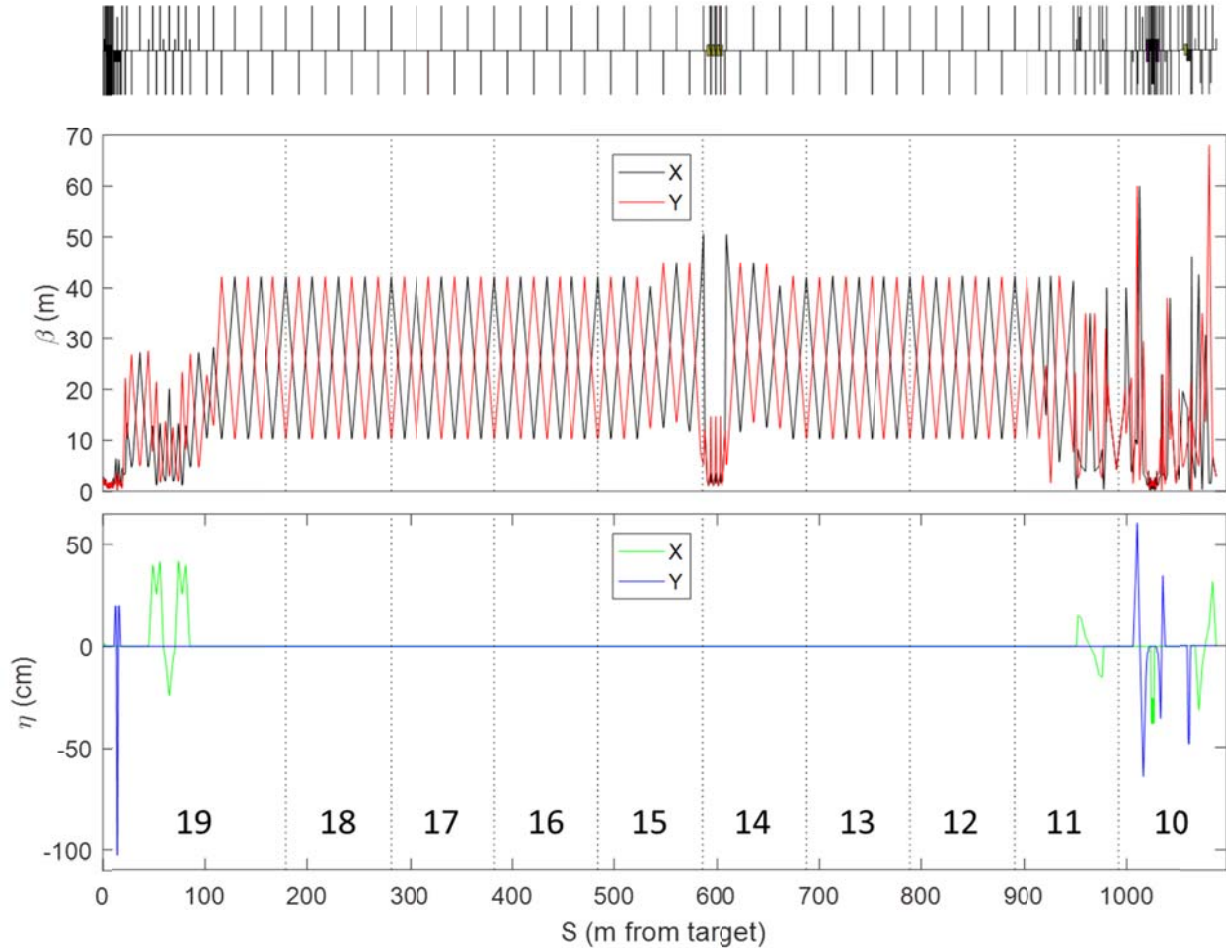


**Figure 8.3.** Positron beam optics from the target to the reinjection point in Sector 11. Sector numbers are indicated at the bottom. Note that the dispersion ( $\eta$ ) is shown in cm. This includes the existing capture section, the return line with new accelerating structures in Sector 14, (part of) the new damping ring, and the new injection and extraction lines in Sector 10.

### 8.1.2 Brief Description of the Positron System

A single bunch of positrons is generated at 5-Hz repetition rate from a 10 GeV electron bunch impinging on an existing rotating WRe target in Sector 19. The positrons are captured in a flux concentrator and capture section and accelerated to 210 MeV. They are injected into the Positron Return Line (PRL) and transported back to Sector 10, where a new injection line brings them into a new damping ring (PDR). The energy of the PDR is 335 MeV, so there will be 125 MeV of S-band acceleration installed in Sector 14 of the PRL. Collimators are placed in the PRL upstream of the Sector 14 booster to shield the S-band structure irises. A new extraction line takes the beam from the PDR, performs the first stage of bunch compression, and finally injects it into the main linac at the last magnet of the BC11 chicane in Sector 11.

### 8.1.3 Positron Yield

The positron source in Sector 19 was originally constructed for the SLC. In SLC operation, a 6.5 nC electron beam at 33 GeV had a yield of approximately 4.4 positrons per incident electron after the 210 MeV capture section. However, the ultimate yield through the system, defined by the number of

positrons exiting the damping ring per incident electron, was roughly 1:1. For FACET operation, a 20.35 GeV electron beam with 3.2 nC has a measured yield at 200 MeV of 2.5:1 positrons per incident electron. In spite of the roughly 60% reduction in yield from the target, the yield of positrons from the damping ring remains approximately 1:1 after optimization through the rest of the positron return line. For FACET-II, the incident electron beam energy is only 10 GeV. However, given the experience with positron operation in FACET, it is predicted that the final system yield should be no worse than 0.5:1.

The expected positron yield can be approximated as a function of the scavenger electron beam energy area density per pulse and rms radius incident on the positron target and the damping ring physical acceptance:

$$N^+ \sim \epsilon \sigma \rho \quad [1]$$

where,

$$\rho = \frac{N^- E^-}{\pi \sigma^2}$$

Comparing expected running conditions at FACET-II with FACET: to maintain a similar positron flux from the target while keeping the same level of energy area density (so as to not increase the risk of damaging the positron target) the rms radius of the incident electron beam should be reduced by  $\frac{\sigma}{\sigma_0} \sim 0.79$  for 4 (vs. 3.2) nC charge and 10 (vs. 20) GeV. To achieve the required 0.5:1 positron to incident electron ratio this implies a minimum relative positron damping ring (PDR) injection acceptance of  $\frac{\epsilon}{\epsilon_0} \sim 0.63$  compared to FACET. The optics and new beamline components of the positron return line and damping ring injection systems were designed to have the same total acceptance as that of the existing SLC systems used during FACET operations (40  $\mu\text{m}\text{-rad}$ ). A brief test during operations at FACET was performed to measure the positron yield for a 10 GeV beam, the results of which are shown in Figure 8.4. A relative yield of 40% compared with the incident electron beam charge was achieved. This is slightly lower than the expected 50%, but with more tuning we expect to be able to achieve closer to the design yield. Furthermore, a relative transmission of  $\sim 100\%$  was measured from Sectors 19 to 16 in the return line (a  $5\pi$  phase advance). With a 4 nC incident beam on the target for FACET-II therefore, we expect to be able to deliver up to 2 nC into the damping ring.

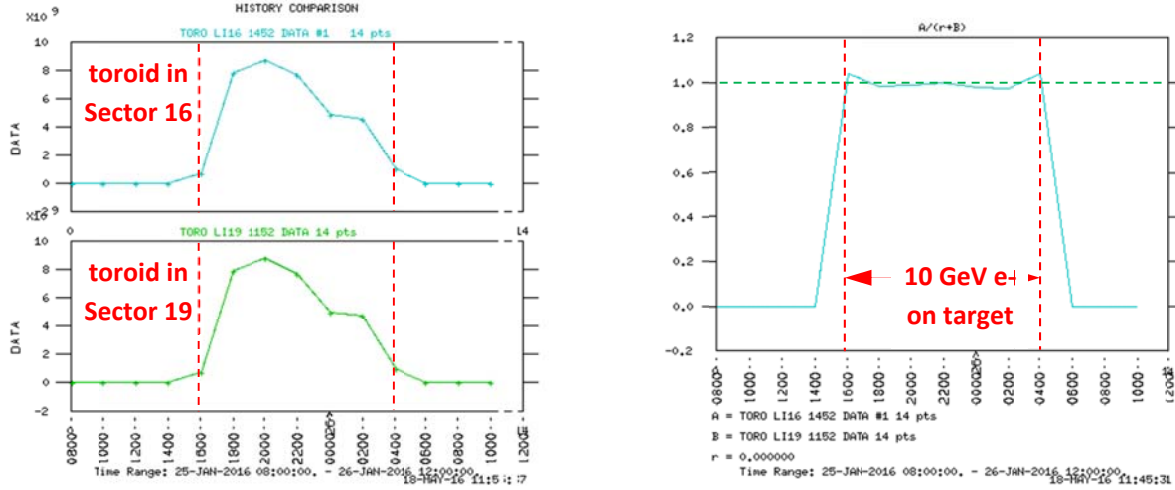


**Figure 8.4:** Positron yield tests at FACET with 10 GeV electron beam, 2E10 incident electrons on positron target over 12 hour test period. Left plots show toroid measured yeids in Sectors 16 and 19 of the positron return line. The right plot shows the relative transmission between these locations.

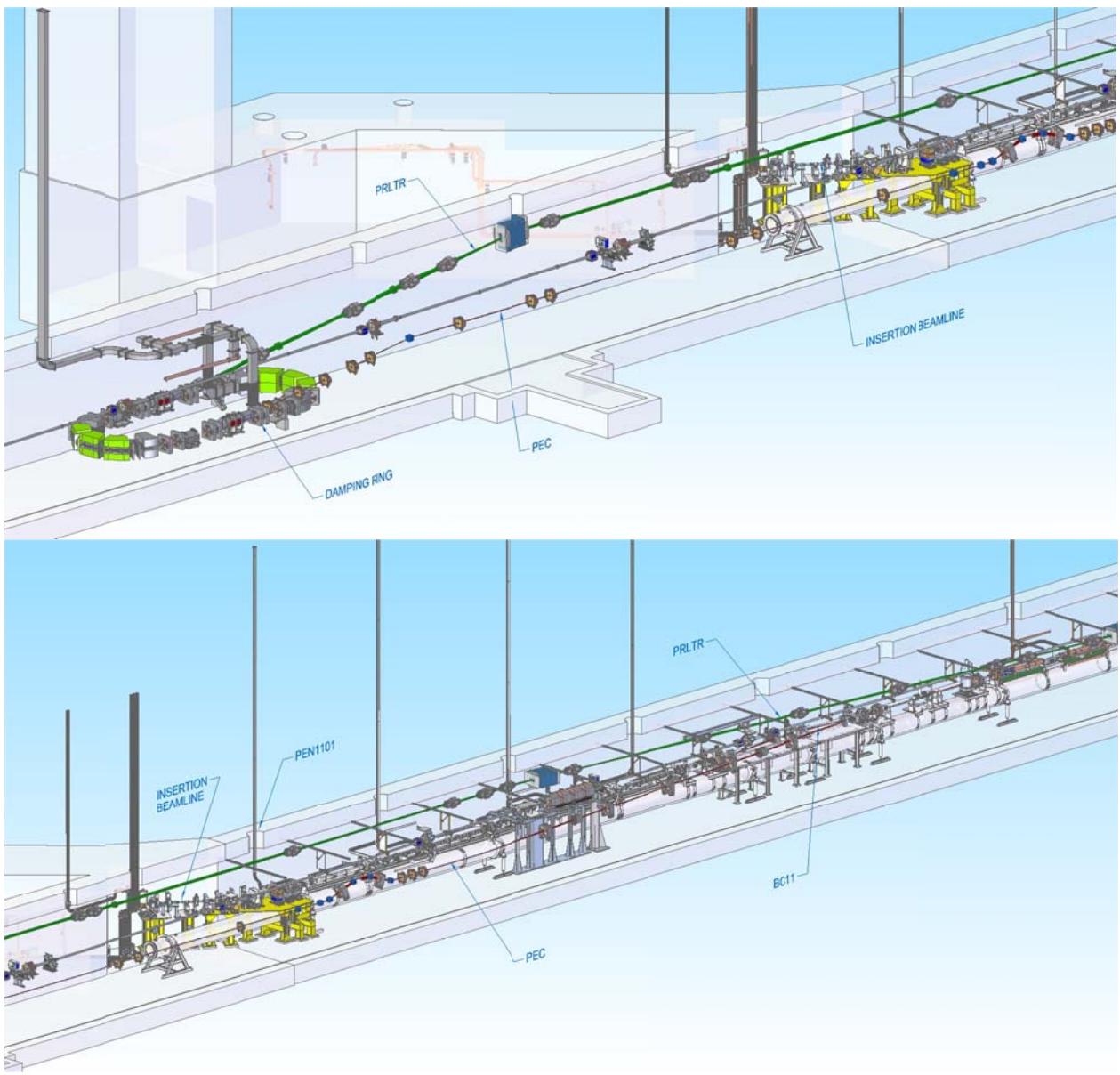


**Figure 8.5. Layout of positron damping ring and injection and extraction lines in the Sector 10 tunnel.**

## 8.2 PRLTR – Positron Return Line to Damping Ring

### 8.2.1 Overview

This beamline section is responsible for collimating the positron beam, accelerating it to 335 MeV, and transporting it to Sector 11 through the existing Positron Return Line (PRL), which is 18" below the ceiling of the Linac tunnel. The positrons are matched and injected into the damping ring (PDR) in a new beamline in Sector 10. To accomplish this, five new beamline sections are specified below and shown in Figure 8.6–Figure 8.10. These are required to collimate the beam, accelerate it to 335 MeV, translate it horizontally 103" across the ceiling of the accelerator housing, then down vertically 74", and finally into the new PDR.

#### 8.2.1.1 Collimation in Sectors 16 and 15

Beam Stay Clear (BSC) in the existing PRL is defined to be  $\pm 40$  mm. Given our assumed beam emittance ( $\gamma\epsilon = 2$  mm) and peak beta function in the PRL FODO ( $\approx 42$  m), this constitutes  $\pm 2.8\sigma$  admittance. In order to shadow the irises of the S-band accelerating sections in Sector 14 from beam halo, and to define the acceptance of the downstream PDR injection system, four fixed-aperture collimators will be added to the PRL FODO lattice in Sectors 16 and 14. Two collimators, separated by approximately  $270^\circ$  of betatron phase advance, are located at positions of large  $\beta_x$ , while two others, also about  $270^\circ$  apart, are located at positions of large  $\beta_y$ . In keeping with the defined BSC of the PRL, the collimator apertures are set to 39 mm radius. Figure 8.5 shows this system.

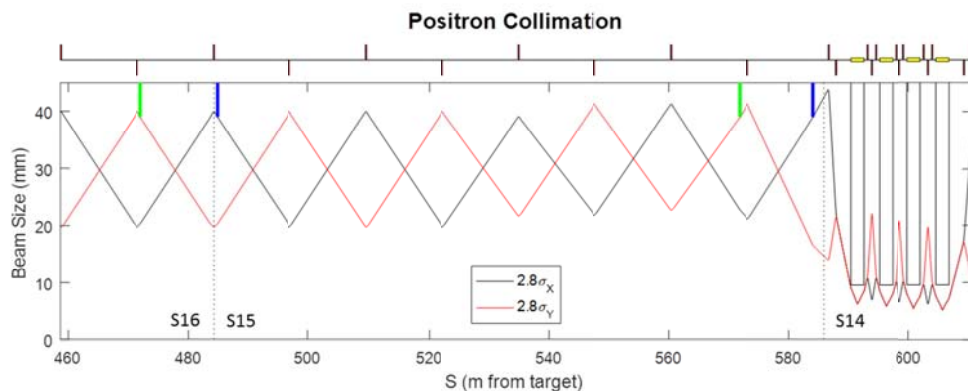


**Figure 8.6. Positron collimation optics in Sectors 15-16. Horizontal collimators are shown in blue; vertical collimators are shown in green. The accelerator iris radius (9.55 mm) is shown in black. Sector numbers are indicated at the bottom.**

#### 8.2.1.2 Acceleration in Sector 14

Four 7-foot S-band accelerating structures accelerate the positron beam in the return line on crest from 210 MeV to 335 MeV. Each structure, fed 25% of the power of a standard klystron, is capable of providing up to  $\sim 42$  MeV (19.7 MeV/m). This maintains a comfortable 25% energy overhead. RF station 14-8, made available due to the installation of BC14 at the end of Sector 14, will be used to power these four new structures. The PRL consists of 25.4 m long FODO cells (4 cells per sector) with a phase advance per cell of  $75^\circ$  in both planes, and with  $\beta$ -function peaks of  $\sim 42$  m. Because of the large emittance of the positron beam, the PRL quadrupoles have 4.625" diameters. The S-band accelerating structure, on the other hand, has a 0.75" iris diameter (minimum aperture in structure). In order to squeeze the positrons through the structures, a quadrupole doublet is first used to step the PRL  $\beta$ -functions down to  $\sim 2$  m at the entrance to the first structure. The structures are then separated by quadrupole triplets which

maintain the small beam size. After acceleration the process is reversed with another quadrupole doublet and matched back into the PRL optics. This section replaces a single PRL FODO cell. Figure 8.7 shows this rms beam size in greater detail. Table 8.3 lists the quadrupole magnet parameters.

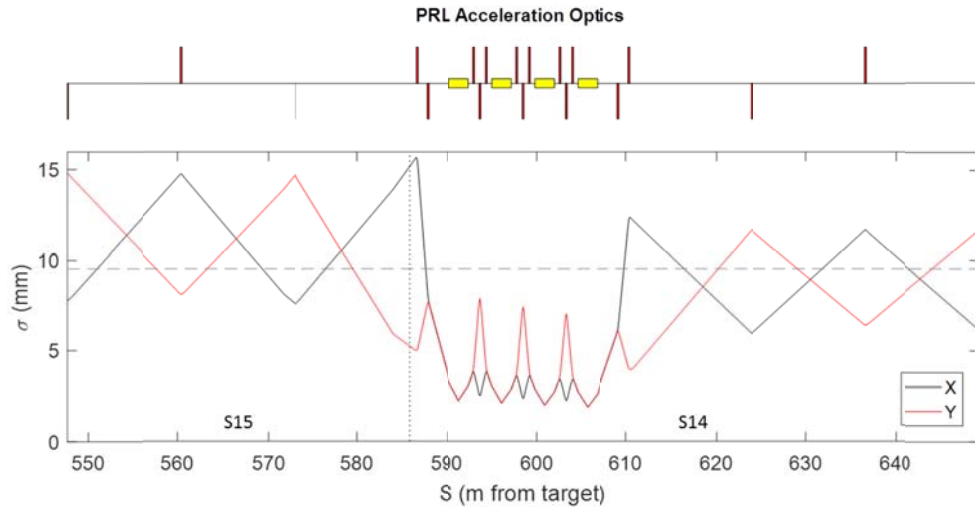


**Figure 8.7. Positron acceleration optics in Sector 14. The accelerator iris radius is indicated by a gray dashed line. The indicated rms beam sizes are  $\sqrt{\epsilon\beta}$ .**

### 8.2.1.3 Horizontal dogleg

In Sector 11, six quadrupole magnets match the beam from the PRL FODO lattice into the horizontal dogleg. A pair of rectangular bending magnets (bend angle = 100 mrad), 7 quadrupoles and 2 chromatic correction sextupoles translate the beam 103" horizontally across the accelerator housing in a z length of 86'. The upstream end of the dogleg is placed so as not to interfere with the LCLS-II "BRB2" bend magnet installation. An emittance diagnostic station is located immediately downstream of the dogleg. It is composed of three beam profile monitors located in a long (~17 m) drift. A quadrupole triplet matches the dogleg beta functions to a waist at the center profile monitor, providing 60° of betatron phase advance in both planes between profile monitors. The nominal minimum beam spot size at the second profile monitor is 3.6 mm. Figure 8.8 shows the optics of the PRL match, the horizontal dogleg, and the emittance diagnostic station. Table 8.4-Table 8.6 list the magnet parameters for the Sector 10-11 systems.

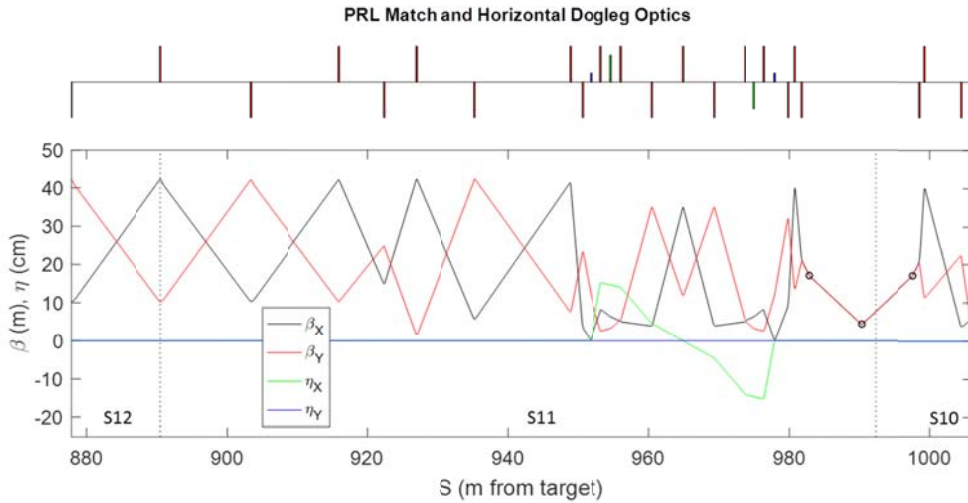


**Figure 8.8. PRL match and Horizontal Dogleg optics in Sector 11. Note that the dispersion ( $\eta$ ) is shown in cm. The emittance diagnostic station can be seen at the right-hand side of the plot (profile monitors are indicated by black circles).**

#### 8.2.1.4 Vertical inflector

Three quadrupoles are used to match the beam from the emittance diagnostic station into the vertical inflector. The angle of the inflector is set by the PDR injection trajectory at 136 mrad. A rectangular bending magnet (bend angle = 136 mrad), 5 quadrupoles and 2 chromatic correction sextupoles comprise the initial part of the inflector. The final components of the inflector, including the PDR septum and kicker, are described below. The inflector translates the beam from the PRL at a height of 36" above the Linac beamline into the PDR at a height of 38" below the Linac beamline in a length of 52'. Figure 8.9 shows the optics of the emittance diagnostic station and the vertical inflector, including PDR injection.

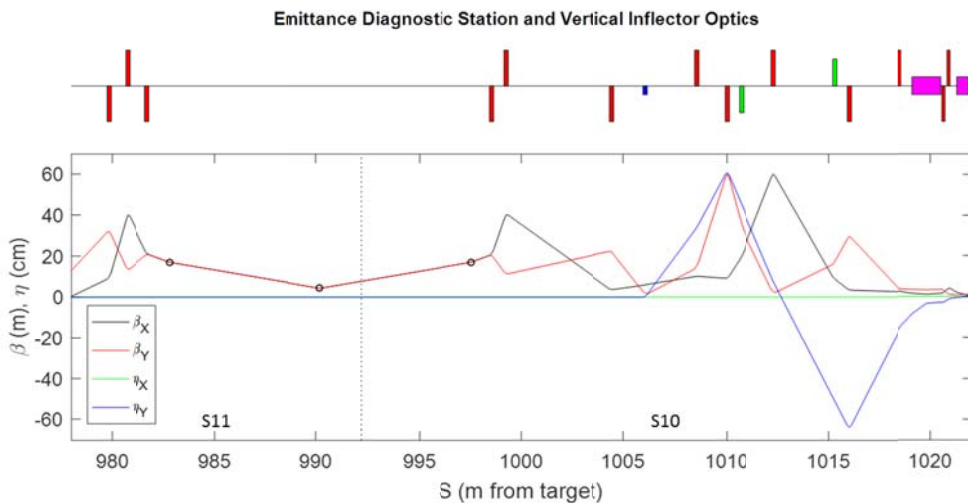


**Figure 8.9. Emittance Diagnostic Station and Vertical Inflector optics in Sector 10-11. Note that the dispersion ( $\eta$ ) is shown in cm. The PDR injection septum and kicker are shown in magenta on the right-hand side of the magnet schematic above the plot.**

### 8.2.1.5 Damping Ring Injection

As the inflector line approaches the PDR injection straight section vertically, it must first pass above the east arc of the ring. One quadrupole of the inflector is located above the magnets of the arc; the transverse size of the arc magnets and the selected inflector quadrupole type allow for this. Next is a long drift in the inflector line which allows it to clear two ring quadrupoles and pass above the edge of one of the PDR RF cavities, 9.5" above the plane of the ring. The final inflector quadrupole is installed above the space in the ring between the RF cavity and the QFI and QDI quadrupoles that are adjacent to the septum. These ring quadrupoles will be of a narrow-frame "Collins" design (full yoke height of < 200 mm) that allows the inflector line to pass above them, outside of their yokes, as it approaches the injection septum. Note that, if necessary for clearance, the final inflector quadrupole could also be of the narrow-frame design. The beam then enters the injection septum (angle = 133 mrad) at a height of 119 mm above the plane of the PDR, passes off-axis through the (large) bores of the PDR QDI and QFI quadrupoles between the injection septum and kicker, and finally is kicked vertically into the plane of the PDR by the injection kicker (angle = 16.5 mrad). Figure 8.10 shows this injection scheme.

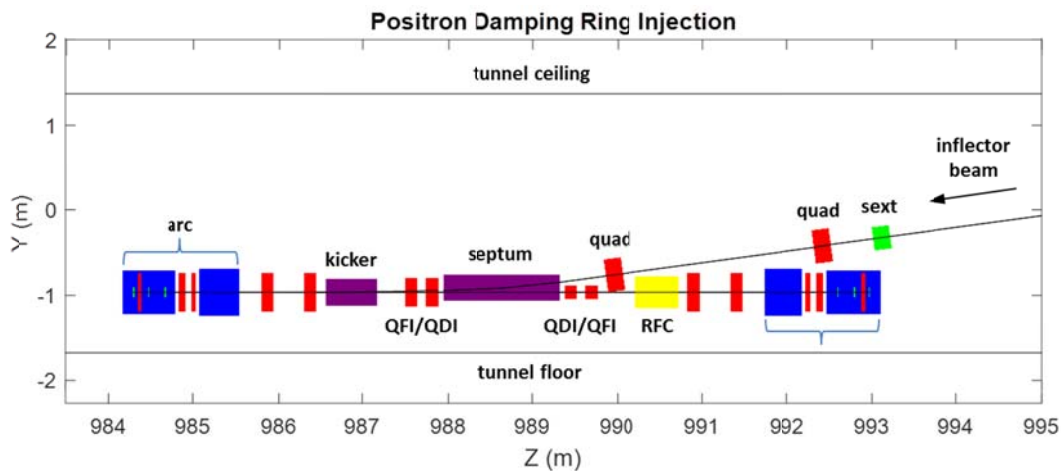


**Figure 8.10. Vertical injection into the Damping Ring. RFC is the RF cavity. The QFI and QDI quadrupoles in the ring between kicker and septum are large-bore magnets through which the injecting beam passes off-axis; the QDI and QFI quadrupoles between septum and RFC are narrow-frame "Collins"-type magnets that the injecting beam passes above.**

### 8.2.1.6 Septa and kickers

The Damping Ring injection septum will be a current-sheet device which deflects the injecting beam vertically by a total of 133 mrad, modeled after the existing SLC e+ Damping Ring injection septum; the assumed magnetic length of the septum is 1.38 m. The normalized (invariant) emittances of the injecting e+ beam are  $\gamma\epsilon_{x/y} = 2$  mm-rad; the matched beta functions of the Damping Ring optics at the kicker end of the septum are  $\beta_{x/y} = 1.529/3.472$  m. At 335 MeV, the beam size (including ~3 cm of vertical dispersion for the injecting beam) is  $\sigma_{x/y} = 2.160/3.267$  mm. The clear aperture in the septum for both the injected beam and the Damping Ring beam is approximately 1" high by 0.5" wide in order to accept  $\pm 2.8\sigma$  of the injecting beam (as defined by the PRL collimation system). The blade of the septum is assumed to be 4 mm thick. Figure 8.11 shows the proposed septum geometry at the kicker (downstream) end of the septum. The extraction septum will be identical to the injection septum.

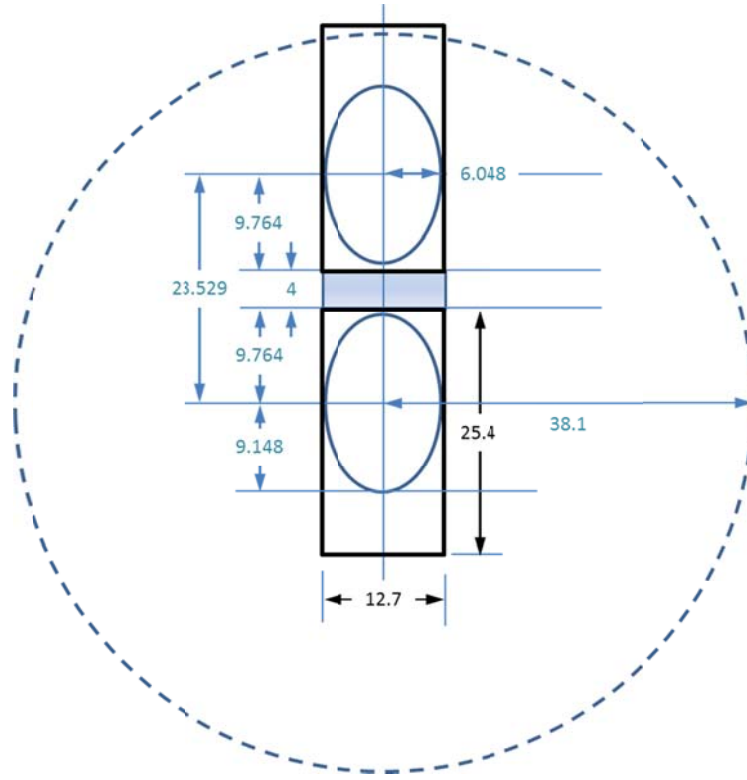


**Figure 8.11. Injection septum geometry (kicker end); drawing is to scale, and all dimensions are in mm. The beam ellipses (blue) show  $\pm 2.8\sigma$  of the injected beam, matched to the nominal e+ Damping Ring optics at this point. The black rectangles show the septum apertures. The blue shaded region shows the septum blade. The blue dashed circle represents the bore of the Damping Ring QFI and QDI quadrupoles between the septum and kicker (here assumed to be 3").**

The injection kicker will reuse the existing SLC e+ Damping Ring kicker, rotated to kick vertically. Looking at injection in reverse, the kicker must generate 23.5 mm of vertical offset at the entrance to the septum in order to allow  $\pm 2.8\sigma$  on both sides of the septum blade. Given the present FACET-II e+ Damping Ring optics, this implies a kick angle of 16.5 mrad; the magnetic length of the kicker is 0.59 m. The existing SLC Damping Ring kicker angle is 6.35 mrad at 1.19 GeV, at 335 MeV this angle would be 22.5 mrad. The kicker has a 20 mm bore, which is just adequate for the injected beam plus the vertical trajectory offset at the downstream end of the kicker (4.9 mm). Figure 8.12 shows the injected and 1<sup>st</sup> turn Damping Ring beam in the injection area, with the  $\pm 2.8\sigma$  beam envelopes shown. The extraction kicker will be identical to the injection kicker.

The QFI and QDI quadrupoles between the kicker and septum (QDI being closest to the septum) must have a bore that allows for 3x2.8 $\sigma$  of the injected beam plus the septum blade thickness, centered on the Damping Ring orbit. Here we assume a 3" bore.

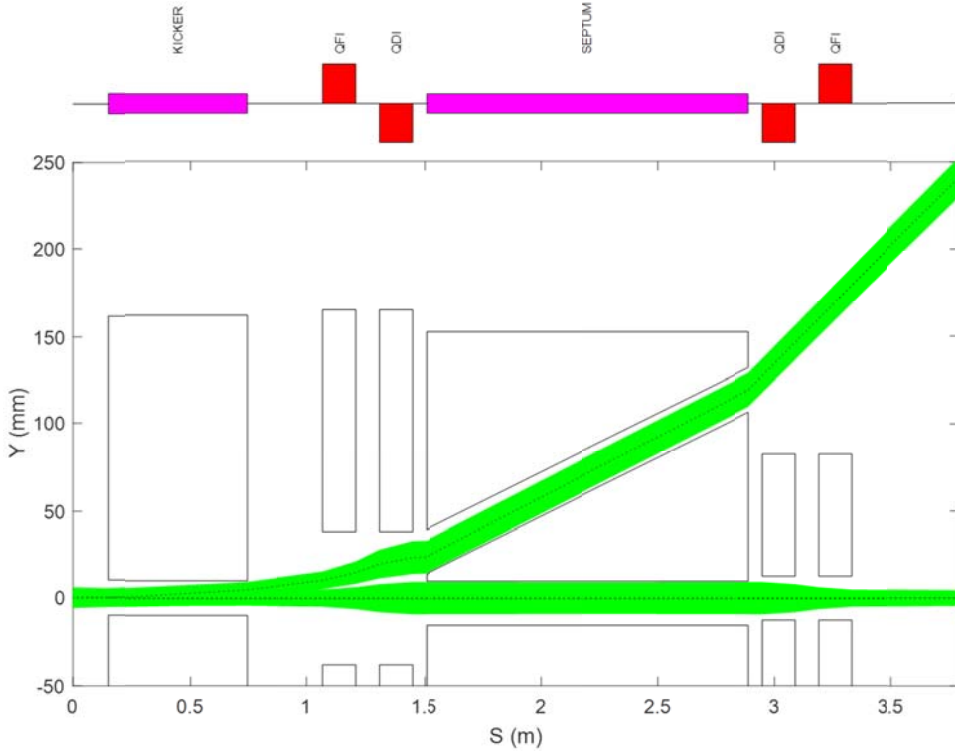


**Figure 8.12. PDR injection.** Beam injects vertically (from right to left in this figure).  $\pm 2.8\sigma$  envelopes of injecting and 1st turn beams are shown in green. Kicker and septum apertures are shown, as are apertures and yokes of the large bore quadrupoles (left side of septum in figure), and the narrow-frame quadrupoles (right side of septum in figure).

### 8.2.2 Beam Parameters

This system is designed given the measured PRL beam parameters and existing optics and matches into the required optics at the PDR injection point. A 4 nC “scavenger” electron pulse is generated in the linac specifically for positron production. For FACET operations at 20 GeV, a 1:1 ratio between scavenger electron beam charge and extracted positron beam (from positron damping ring) was routinely achieved. For operations at FACET-II at 10 GeV, a pessimistic assumption is made here where the final positron yield is reduced by a relative factor of 4 compared with FACET operations (see 8.1.3).

**Table 8.2. Beam parameters for beamline section injecting into PDR in Sectors 10 and 11.**

Parameter	Symbol	Unit	Nominal	Range
Beam Energy	E	MeV	335	-
Initial Transverse Emittance	$\gamma\epsilon_x / \gamma\epsilon_y$	mm.rad	2.0 / 2.0	-
Final Transverse Emittance	$\gamma\epsilon_x / \gamma\epsilon_y$	mm.rad	2.5 / 2.2	-
Initial Twiss ( <i>at entrance to first horizontal dogleg bend</i> )	$\beta_x / \alpha_x$ $\beta_y / \alpha_y$	m	0.344 / -0.069 12.973 / 4.202	-
Final Twiss ( <i>at exit of injection kicker</i> )	$\beta_x / \alpha_x$ $\beta_y / \alpha_y$	m	0.304 / -0.338 1.110 / 0.677	-
Initial Bunch Length (rms)	$\sigma_z$	mm	3	-
Final Bunch Length (rms)	$\sigma_z$	mm	3	-
Initial Energy Spread (rms)	$\sigma_E/E$	%	1.0	-
Final Energy Spread (rms)	$\sigma_E/E$	%	1.1	-
Initial Bunch Charge	Q		4	
Final Bunch Charge (in PDR)	Q		1	1-2

### 8.2.3 Beam Dynamics

Using a 6D tracking code (Lucretia), a 1M macro-particle representation of the positron bunch is tracked through the lattice. Figure 8.13 shows the tracked projected transverse emittance through the PRL and injection into the PDR. Some chromatic emittance growth (~5%) is present as the beta functions are reduced to fit the beam through the S-band structure iris apertures, and also within the dogleg and the inflector as the beam is injected into the PDR (<20%). Optimization of the chromatic emittance growth in this final section using sextupole magnets is envisioned before construction. Chromatic emittance dilution through the accelerating structure can also be optimized by adjusting the beta functions (quadrupole strengths) between horizontal and vertical dimensions in the focusing triplets depending on required final emittance estimates after optimizing the dogleg systems. Figure 8.14 shows the longitudinal and transverse phase space of the tracked beam at injection into the PDR.

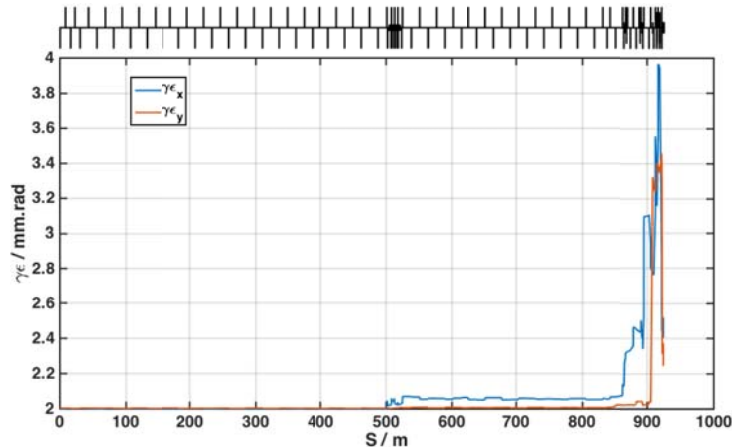


**Figure 8.13. Transverse emittance of tracked beam through PRL and injection into PDR.**

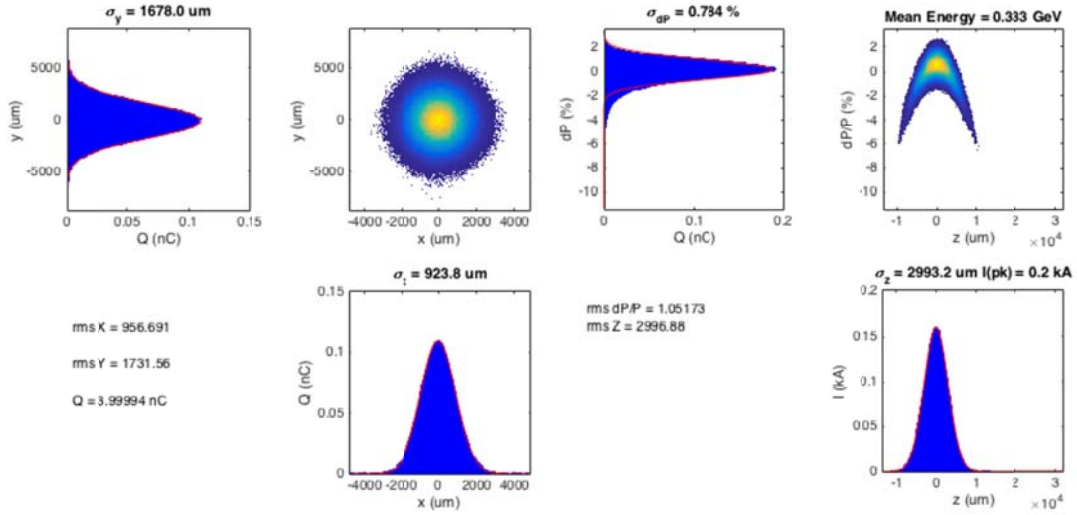


**Figure 8.14. Transverse and longitudinal phase-space of tracked macro-particle bunch at the PDR injection point.**

## 8.2.4 Magnets

The special optics in Sector 14 requires 13 new quadrupole magnets with 1 new engineering type. The remainder of the system downstream of the PRL consists of 24 quadrupole magnets with 4 new engineering types, 4 sextupole magnets with no new engineering types, and 3 dipole magnets with 1 new engineering type.

### 8.2.4.1 Quadrupoles

**Table 8.3. Quadrupole parameters for new magnets in Sector 14**

Deck Name	Engineering Type / subsection	Effective Length / m	Design Int. Gradient / T	Max  Int. Gradient / T	Design Pole Tip Field / T	Max  Pole Tip Field / T	Aperture (radius) / mm	Beam Energy / MeV
QLTRA1	4.63Q8.00	0.248	0.3307	1.6	0.0783	0.38	58.737	210
QLTRA2	C	0.2	-0.4031	2	-0.0648	0.32	32.169	210
QT11	C	0.2	0.8606	2	0.1384	0.32	32.169	241.25
QT12	C	0.2	-1.2615	2	-0.2029	0.32	32.169	241.25
QT13	C	0.2	0.8606	2	0.1384	0.32	32.169	241.25
QT21	C	0.2	0.9721	2	0.1564	0.32	32.169	272.5
QT22	C	0.2	-1.4249	2	-0.2292	0.32	32.169	272.5
QT23	C	0.2	0.9721	2	0.1564	0.32	32.169	272.5
QT31	C	0.2	1.0836	2	0.1743	0.32	32.169	303.75
QT32	C	0.2	-1.5883	2	-0.2555	0.32	32.169	303.75
QT33	C	0.2	1.0836	2	0.1743	0.32	32.169	303.75
QLTRA3	C	0.2	-0.6431	2	-0.1034	0.32	32.169	335
QLTRA4	4.63Q8.00	0.248	0.5276	1.6	0.1249	0.38	58.737	335

**Table 8.4. Quadrupole parameters for the Sector 10-11 systems.**

Deck Name	Engineering Type / subsection	Effective Length / m	Design Int. Gradient / T	Max. Int. Gradient / T	Design Pole Tip Field / T	Max Pole Tip Field /  T	Aperture (radius) / mm
QLTRM1	B	0.2	0.1295	1	0.0248	0.19	38.265
QLTRM2	B	0.2	-0.2751	1	-0.0526	0.19	38.265
QLTRM3	B	0.2	0.1972	1	0.0377	0.19	38.265
QLTRM4	B	0.2	-0.1982	1	-0.0379	0.19	38.265
QLTRM5	B	0.2	0.5387	1	0.1031	0.19	38.265
QLTRM6	B	0.2	-0.5694	1	-0.1089	0.19	38.265
QLTRH0	B	0.2	0.7847	1	0.1501	0.19	38.265
QLTRH1	B	0.2	0.1385	1	0.0265	0.19	38.265
QLTRH2	B	0.2	-0.2742	1	-0.0525	0.19	38.265
QLTRH3	B	0.2	0.3561	1	0.0681	0.19	38.265
QLTRH4	B	0.2	-0.2742	1	-0.0525	0.19	38.265
QLTRH5	B	0.2	0.1385	1	0.0265	0.19	38.265
QLTRH6	B	0.2	0.7847	1	0.1501	0.19	38.265
QLTRD1	A	0.2	-0.7024	1.5	-0.1344	0.29	38.265
QLTRD2	A	0.2	0.9948	1.5	0.1903	0.29	38.265
QLTRD3	A	0.2	-0.3507	1.5	-0.0671	0.29	38.265
QLTRD4	A	0.2	-0.5380	1.5	-0.1029	0.29	38.265
QLTRD5	A	0.2	0.6334	1.5	0.1212	0.29	38.265
QLTRD6	A	0.2	-0.5698	1.5	-0.1090	0.29	38.265
QLTRV1	D	0.2	0.1724	1	0.0277	0.16	32.169
QLTRV2	4.63Q8.00	0.248	-0.7867	1.6	-0.1863	0.38	58.737
QLTRV3	4.63Q8.00	0.248	0.5416	1.6	0.1283	0.38	58.737
QLTRV4	4.63Q8.00	0.248	-0.6969	1.6	-0.1650	0.38	58.737
QLTRV5	D	0.2	0.6549	1	0.1053	0.16	32.169

#### 8.2.4.2 Sextupoles

It is assumed that each sextupole is mounted on a remotely controllable motion stage, capable of  $\pm 2$  mm motion in x/y with  $5 \mu\text{m}$  precision. The final sextupole strengths are still being optimized.

**Table 8.5. Sextupole parameters for the Sector 10-11 systems**

Deck Name	Engineering Type / subsection	Effective Length / m	Design Int. Strength / T.m <sup>-1</sup>	Max. Int. Strength /  T.m <sup>-1</sup>	Design Pole Tip Field / T	Max Pole Tip Field /  T	Aperture (radius) / mm
SLTRH2	2.03S3.25	0.1	12.4676	16.5	0.0413	0.055	25.730
SLTRH1	2.03S3.25	0.1	-12.4676	16.5	-0.0413	0.055	25.730
SLTRV2	3.03S3.25	0.1	-5.3700	6.45	-0.0398	0.048	38.494
SLTRV1	3.03S3.25	0.1	4.1096	6.45	0.0304	0.048	38.494

### 8.2.4.3 Dipoles

**Table 8.6. Dipole parameters**

Deck Name	Engineering Type / subsection	Effective Length / m	Design Int. Field / T.m	Max. Int. Field /T.m	Design Pole Tip Field / T	Max Pole Tip Field / T	Aperture (radius) / mm
BLTRH1	E	0.203	0.1117	0.2	0.5499	0.98	30.4
BLTRH2	E	0.203	-0.1117	0.2	-0.5499	0.98	30.4
BLTRV1	E	0.203	0.1518	0.2	0.7470	0.98	30.4

## 8.3 Positron Damping Ring

### 8.3.1 Introduction

As the positron beam emerges from the target and reaches an energy of  $E=335$  MeV, it has a normalized transverse emittance  $\gamma\epsilon$  of  $2.5/2.2$  mm-rad in the horizontal and vertical planes, respectively. This emittance is three orders of magnitude larger than the electron beam out of the photo-injector. A damping ring is necessary to reduce the positron  $x$  and  $y$  emittance values to  $\mu\text{m-rad}$  level in a few milliseconds. For practical reasons, the ring is placed in sector 10 inside the existing linac tunnel. This implies that the diameter of the ring has to be smaller than 3 meters. This constraint dictates a compact design with minimal gaps between the magnets in the arcs.

Given a large injected beam size, the acceptance of the ring has to be large enough to accommodate an on-axis injection. Here, accumulation is not necessary because only a single bunch is to be damped in the ring at a given time. To provide adequate intensity for the experiment, a charge of 1 nC is required per positron bunch. The bunched beam has to be collectively stable as its emittance decreases in the ring. Moreover, the extracted emittance will include growth due to intra-beam scattering (IBS) during storage.

**Table 8.7. Main parameters of the positron damping ring including IBS calculations.**

Parameter	Value
Energy, $E$ [MeV]	335.0
Circumference, $C$ [m]	20.574
Tune, $\nu_x, \nu_y, \nu_z$	4.586, 2.615, 0.0365
Normalized emittance, $\gamma\epsilon_0$ [ $\mu\text{m-rad}$ ]	6.7
Bunch length, $\sigma_z$ [mm]	3.88
Energy spread, $\sigma_\delta$	$8.4 \cdot 10^{-4}$
Momentum compaction	$5.73 \cdot 10^{-2}$
Damping partition, $J_x, J_y, J_z$	2.16, 1.0, 0.84
Damping time, $\tau_x, \tau_y, \tau_z$ [ms]	15.6, 33.7, 40.2
Natural chromaticity, $\xi_{x0}, \xi_{y0}$	-6.19 -4.8
Energy loss per turn, $U_0$ [keV]	1.362
RF voltage, $V_{RF}$ [MV]	1.1
RF frequency, $f_{RF}$ [MHz]	714.0
Harmonic number	49

The fractional tunes are a result of the phase advances required for emittance and due to the constraints imposed by the required magnetic field strengths. Although above a half integer tunes are not preferred from a point view of instability driven by resistive-wall impedance, calculations show that the growth rate is much slower than the radiation damping rate. Moreover, ring designs with fractional tunes above a half integer were successfully used at PEP-II and KEKB.

Separation of horizontal and vertical emittance will be discussed in a later section that deals with the intra-beam scattering (IBS). The final emittance including the IBS scattering seems adequate based on the simulation from the ring to the final focusing system.

### 8.3.2 Lattice Design

In general, the choice of the beam energy in damping rings is a balancing act. On one hand, it should be higher to achieve faster damping and also to mitigate the IBS effects; On the other hand, a higher energy requires stronger magnetic fields or a larger ring. In this design, the minimum energy is determined by the existing target at 200 MeV. Given the fixed size of the ring, the highest possible energy, E=335 MeV, has been chosen to reduce the IBS growth of the beam emittance.

Given the beam energy  $E = \sqrt{m^2c^4 + c^2p^2}$  the magnetic rigidity of the ring is given by

$$B\rho = \frac{p}{e}$$

where  $m, e$  are the mass and charge of the positron respectively,  $p$  the design momentum.

$B\rho \approx 0.335 \times 10 / 2.998 \approx 1.12$  T-m. Taking the dipole field  $B=1.44$  T, the bending radius is  $\rho = 0.777$  m. So the packing factor of the dipole magnets in the arcs is  $0.777m / 1.4m \approx 55\%$ . The denominator (1.4m radius) is derived from the size of the tunnel. Here, some space has been left for the transverse dimension of the components such as RF cavities. Since these parameters are taken from the design lattice, it is not surprising to see that the packing factor is consistent with the layout of the cell shown in Figure 8.16. As can be seen from the figure, the packing factor cannot be increased further because the space is needed for quadrupoles, sextupoles, and gaps between the magnets.

#### 8.3.2.1 Scaling

Starting with these ideas about the bending dipoles and geometry of the ring, the damping times are largely determined. For example, the horizontal damping time is given by,

$$\tau_x = \frac{2\gamma C}{cJ_x} \frac{mc^2}{U_0}$$

where  $C$  is the circumference of ring,  $J_x$  the horizontal damping partition number, and  $U_0$  the energy loss per turn,

$$U_0 = \frac{2r_e mc^2 \gamma^4}{3} I_2$$

with  $I_2$  a radiation integral,

$$I_2 = \oint \frac{ds}{\rho^2}$$

and  $r_e$  the classical radius of the electron. It is worth mentioning that the damping times increase rapidly as the energy is reduced.

It is well known [2] that an equilibrium (bend plane) emittance,  $\epsilon_x$ , is a result of the balancing acts between quantum excitation and radiation damping. It can be written in terms of the radiation integrals,

$$\epsilon_x = C_q \frac{\gamma^2 I_5}{J_x I_2},$$

with

$$C_q = \frac{55}{32\sqrt{3}} \frac{\hbar}{mc}, I_5 = \oint \frac{\mathcal{H}_x}{\rho^3} ds ,$$

where

$$\mathcal{H}_x = \beta_x \eta_x'^2 + 2\alpha_x \eta_x \eta_x' + \gamma_x \eta_x^2 ,$$

$\eta_x, \eta_x'$  are the horizontal dispersion and its slope  $\beta_x, \alpha_x, \gamma_x$ , the horizontal Courant-Snyder parameters.

For a simple ring with identical arc cells, the emittance can be computed and written as,

$$\epsilon_x = C_q \gamma^2 \phi^3 \frac{F_c}{J_x},$$

where the parameter  $F_c$  depends only on the structure of the cell,  $\phi = 2\pi/N_c$  is the bending angle per cell, and  $N_c$  the number of cells. For a minimal emittance, it is therefore desired to have a large  $N_c$  and cell with a small  $F_c$  value.

For FODO cells with equal phase advances,  $\mu_x = \mu_y = \mu$ , there is an analytical expression for  $I_5$ . Knowing  $I_5$ , one can easily derive the parameter  $F_c$ ,

$$F_c^{FODO} = \frac{1 - \frac{3}{4} \sin^2 \frac{\mu}{2} + \frac{1}{60} \sin^4 \frac{\mu}{2}}{4 \sin^2 \frac{\mu}{2} \sin \mu},$$

which is plotted as a function of  $\mu$  in Figure 8.15. Although there is a minimum  $F_c^{min} = 0.15381$  at  $\mu = 2.39062$ , the rate of reduction decreases significantly beyond  $\pi/2$ . For all practical purposes of emittance reduction, it is not so efficient to choose a phase advance larger than  $\pi/2$ . For a typical value,  $F_c^{FODO}(\pi/2) = 151/480$ .

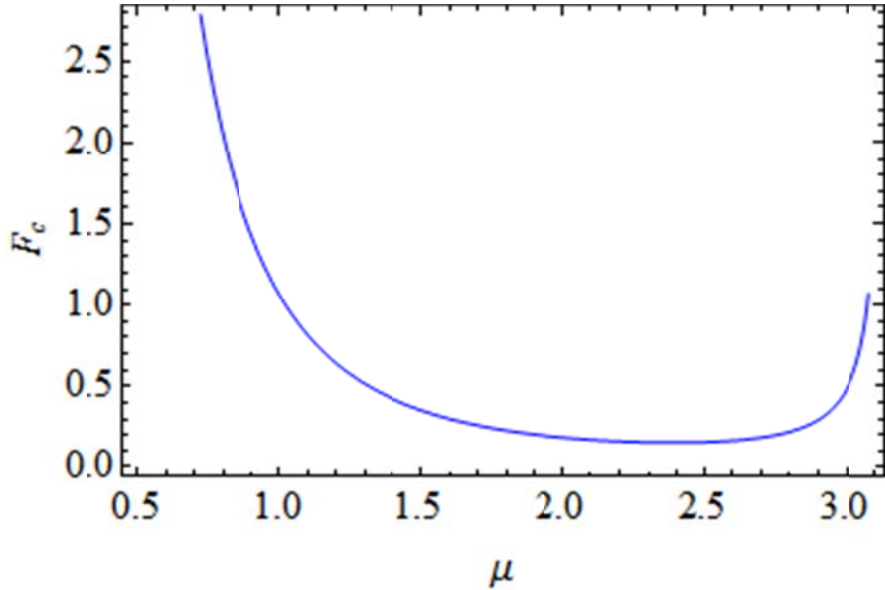


**Figure 8.15.** The emittance scaling parameter  $F_c$  a function of phase advance  $\mu$  (radians) per FODO cell.

For more efficient reduction of the emittance, the theoretical minimum emittance (TME) cell has been known [3] to yield the lowest possible emittance corresponding to the minimum value of  $F_c$ :

$$F_c^{(TME)} = \frac{1}{12\sqrt{15}}$$

This, however, requires very strong focusing which may limit dynamic aperture; hence in practical designs the TME lattice is usually set to a higher  $F_c$  value. These TME-type cells are widely used in damping rings [4,5] for linear colliders. Unfortunately, they require too much space between the magnets, especially quadrupoles. Given the size of the tunnel, there cannot be any large spaces between the magnets in the arcs; otherwise the dipole field will be too high as estimated previously. Another way to reduce the damping time and to achieve smaller emittance is using a wiggler. However, the wigglers have to be superconducting because the field of the bending magnet is already quite high at 1.44 T.

### 8.3.2.2 Cell

An alternative is a FB cell using a combined function dipole magnet with a defocusing gradient, which lowers the horizontal beta functions and dispersion inside the dipole to minimize the emittance. Moreover, it generates a high horizontal damping partition number  $J_X$  for a further reduction of emittance. From a point of view in beam dynamics, this cell is very conventional and essentially a FODO cell which was widely used in many storage rings.

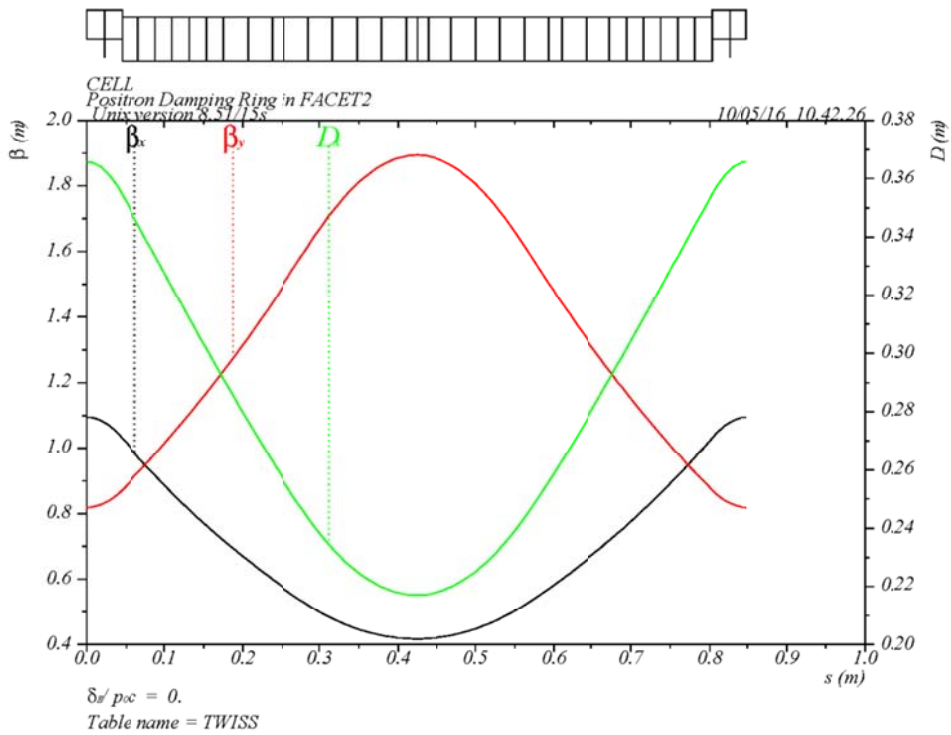


**Figure 8.16. Lattice functions of the nominal cell with a combined function dipole at the center.**

This type of cell is chosen for its compactness. The optics functions of the nominal cell are plotted in Figure 8.16. Here, the dipole and drifts are segmented into many slices so that the fringe field can be modeled accurately based on the design of the magnets. The center region is a sector bend that combines both defocusing quadrupole and sextupole gradients. It is franked by two simple sector bends. To save the space, we also combine the focusing sextupole with the quadrupole. The detailed dimensions and parameters of the magnets can be found in the magnet section later.

The phase advance values of the cell are  $\mu_x = 78.20^\circ$  and  $\mu_y = 38.36^\circ$  in the horizontal and vertical planes, respectively. Although the phase advances values are modest, the strength of the focusing quadrupole and the gradient in the dipole are quite strong because of the short length of the cell. Its scaling parameter  $F_c$  can be estimated using the equation above, provided  $\mu$  is identified as the horizontal phase advance. So for the same reason as for the FODO cell, the choice of the phase advances are reasonable and efficient.

### 8.3.2.3 Dispersion Suppressor

The dispersion in the arc has to be reduced to zero by a dispersion suppressor, such as shown in Figure 8.17 as the beam enters the straight. Leaking dispersion into the straights is not an option because of the tight aperture in the RF cavities. The bending radius of the dipoles in the dispersion suppressors are the same as those in the regular cells. The total bending angle is 95% of that in a regular cell. The first segment of the suppressor dipole is a combined function magnet. The gradient is necessary to control the vertical beta function to a reasonable value at the exit. The value of the gradient is set the same as in the gradient dipole in the regular cell to simplify the engineering effort. A pair of quadrupoles are used to adjust the dispersion and its slope to zero at the exit.

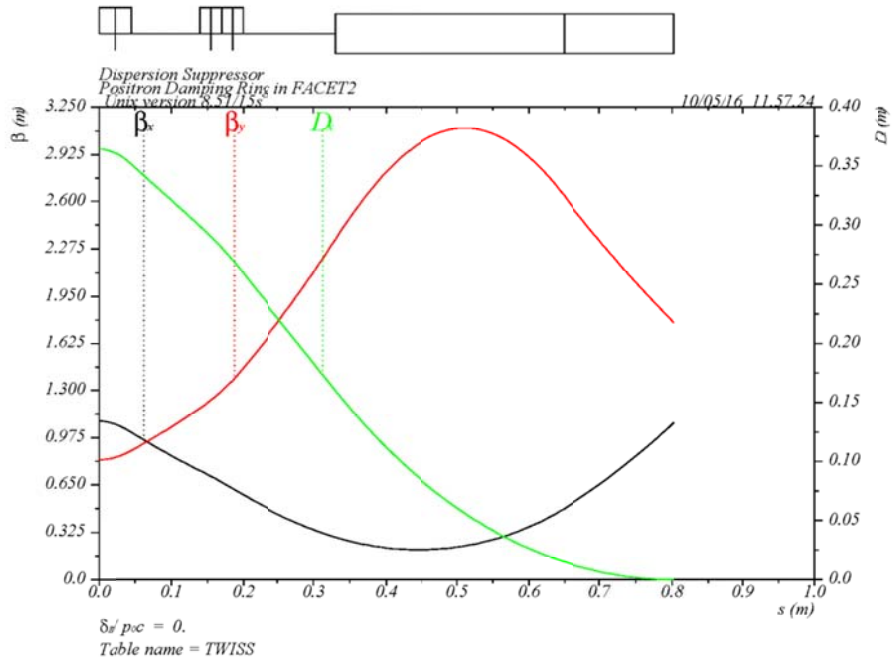


**Figure 8.17. Lattice functions of the dispersion suppressor.**

#### 8.3.2.4 Straight Sections

The straight sections contain the injection and extraction systems. Since they are dispersion free, they are also good regions in which to place RF cavities. The injection and extraction are vertical because of the limitation in the horizontal tunnel size. The injection and extraction beamlines are placed on opposite sides of the ring. The optics that meets these requirements is shown in Figure 8.18 as a part of the entire ring.

The large vertical beta function at the middle of the straight is designed to enlarge the acceptance at the septum as the beam is injected into the ring. A vertical kicker is placed at a position about 90° down stream to guide the injected beam onto the designed orbit. The large beta function is also helpful to reduce the strength of the kicker. The extraction is merely the reverse of the injection process. Because of the phase relation between the septum and kicker, the phase advance in one side of the straight is fixed. For the tune adjustment, there can be a slightly different optics in the other side of the straight. The straights are designed to be reasonably short so that the damping times are adequately fast.

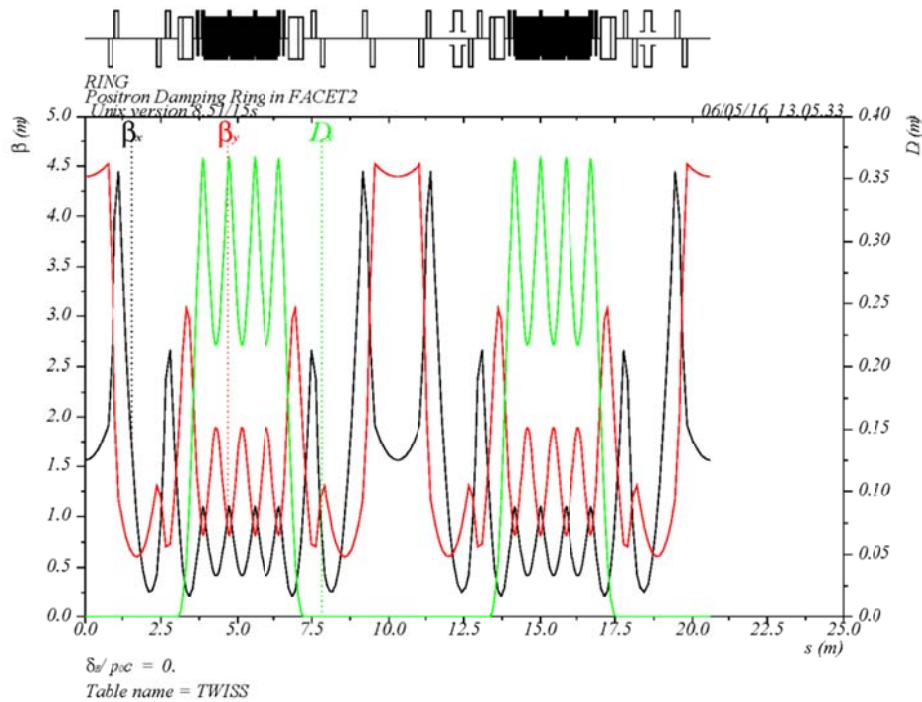


**Figure 8.18. Lattice functions of the positron damping ring in FACET2.**

### 8.3.2.5 Ring

In addition to the dispersion suppressors at the end of the arcs, it is desirable to have more cells in the arcs to reach lower emittance. To make this scheme work, more and stronger quadrupoles are required as the number of cells increases. As a result, there is not enough space left between the magnets. To leave adequate room for the ends of the physical magnets, there are only three regular cells per arc. The arcs as designed are shown in Figure 8.18.

The lattice is matched using the computer program MAD [6]. The main parameters of the ring are tabulated in Table 8.7.

For full coupling (set with tunes of  $\nu_x - \nu_y = 2$ ), the natural emittance values are  $\epsilon_{x0} = \epsilon_{y0} = 4.30$  nm-rad, and the normalized emittance  $y\epsilon = 2.88$   $\mu\text{m}$ -rad, which is three orders of magnitude smaller than that of the injected beam. The growth from IBS, covered in a later section, is not yet included. The existing RF system is the same as that used in the damping rings constructed for the SLC. Therefore, the RF parameters are fixed for the design. The betatron tunes are chosen after many iterations of maximizing the dynamic aperture of the ring.

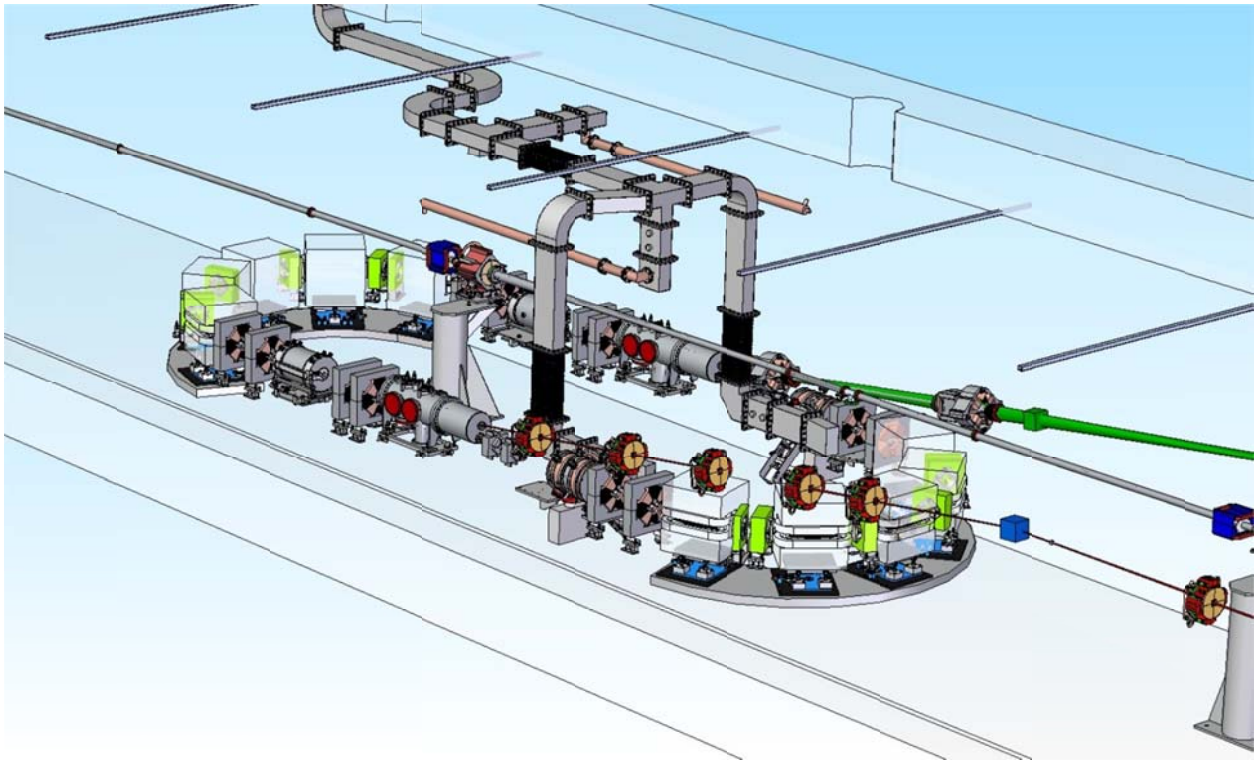


**Figure 8.19. CAD drawing of the positron damping ring for FACET-II located in Sector 10. The vertical dogleg of LCLS-II is visible overhead of the ring center, with the injection line on the wall side and the extraction beamline on the lower side of the drawing.**

### 8.3.3 Beam Dynamics

A low emittance lattice is characterized by very small beta functions and dispersion, achieved with many quadrupoles and resulting in a very large natural chromaticity. To correct the chromaticity, the chromatic sextupole magnets become extremely strong as the dispersion gets smaller and smaller. The nonlinear effects generated by such strong sextupoles result in a severe reduction of the dynamic aperture. An efficient minimization of these nonlinearities becomes essential for a successful design of storage rings.

The sextupole scheme consists of two families of sextupole magnets. The focusing sextupoles are combined with the focusing quadrupoles while the defocusing one are combined with in the sector dipoles in the regular cells or with quadrupoles in the dispersion suppressors. The two families are sufficiently separated so that they are more orthogonal and therefore their strengths are reduced accordingly. If necessary, sextupoles in the dispersion suppressors can be used as additional families to further optimize the high-order chromaticity.

#### 8.3.3.1 Normal Form Analysis

To assess the nonlinearity in the ring, a Taylor map is first extracted using a differential algebra technique [7] and then the normal form [8] is analyzed for the high-order chromaticities and the tune shifts of the ring. The computation is carried out using LEGO [9]. The result is tabulated in Table 8.8 with the sextupoles at their nominal values, setting the linear chromaticities at a half unit. Clearly, the chromaticities are well corrected with two families of sextupoles. The nonlinear tune shifts are very

modest, largely because of not much accumulation in the small ring. This analysis shows that the beam footprint in the tune space is small, so it can easily avoid nonlinear resonances.

**Table 8.8. Nonlinear chromaticities and tune shifts due to betatron amplitudes in the damping ring.**

Derivatives of tunes	Values
$\partial v_{x,y}/\partial \delta$	+0.99, +1.16
$\partial^2 v_{x,y}/\partial \delta^2$	+2, -24
$\partial^3 v_{x,y}/\partial \delta^3$	+960, +147
$\partial v_x/\partial J_x [m^{-1}]$	+349
$\partial v_{x,y}/\partial J_{y,x} [m^{-1}]$	-20
$\partial v_y/\partial J_y [m^{-1}]$	+424

### 8.3.3.2 Dynamic Aperture

For efficient injection, it is important to design a lattice that has a sufficiently large dynamic aperture. The dynamic aperture is obtained from particle tracking simulations that include synchrotron oscillations using LEGO [9]. The calculations included on- and off-momentum particles with the multipole errors up to the decapole in the sliced dipoles in the regular cells. The dynamic apertures with various momentums are shown in Figure 8.20 with sextupoles set at their nominal values. As one can see from the figures, the aperture is between 4 to 8 sigma of the injected beam, which has a normalized emittance of 2.5/2.2 mm-rad in the horizontal and vertical planes respectively. The momentum aperture is larger than 2.5%, which is 2.5 times as large as the energy spread of the injected beam. It is limited by the RF-bucket size.

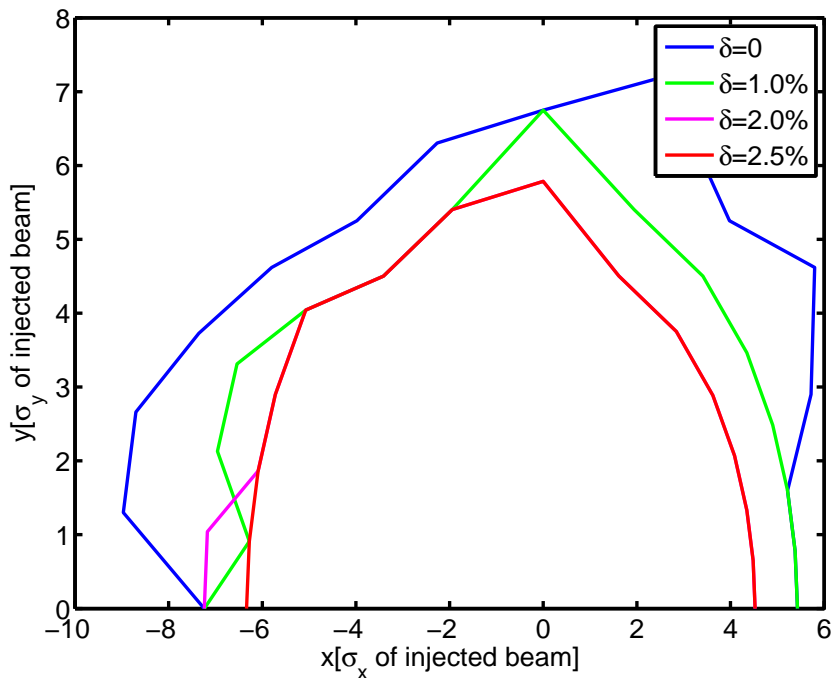


**Figure 8.20. Dynamic aperture of the lattice with errors in dipoles at various momentum deviations.**

### 8.3.3.3 Round Beam

A round beam is required not only for the plasma acceleration experiment but also as a means to mitigate the IBS growth in emittance of the positron beam while it undergoes radiation damping in the ring. The ring will operate on the linear coupling resonance  $\nu_x - \nu_y = 2$  to achieve a round beam in the damping ring. The design tunes in Table 8.7 have been chosen to be close to the resonance condition.

For a small coupling excitation can be driven by four skew quadrupoles in the straights. With this excitation, we can move the horizontal and vertical tunes close using a family of four quadrupoles to achieve a full coupling. This process of generating a round beam has been simulated. The dynamic aperture is shown in Figure 8.20 with radiation damping up to 102400 turns.

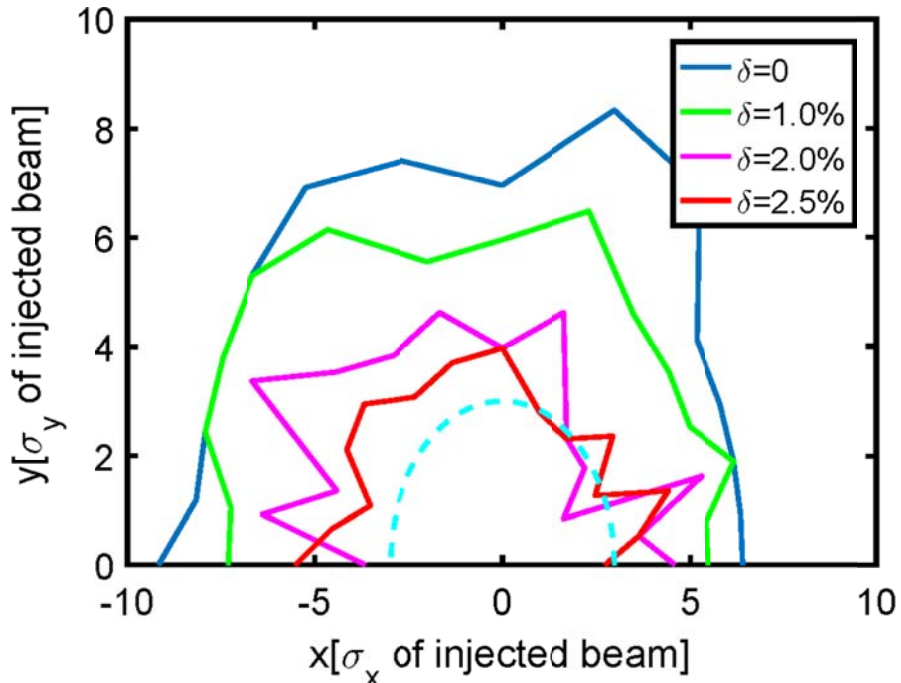


Figure 8.20. Dynamic aperture of the lattice with the dipole errors on the coupling resonance at various momentum deviations. The dashed line indicates the aperture of the vacuum chamber.

### 8.3.3.4 Magnetic Tolerances

The magnet multipole tolerance is defined relative to the field component normalized at a reference radius  $r$ :

$$\frac{\Delta B_n}{B_N} = \frac{(N-1)!}{(n-1)!} \frac{B^{(n-1)'} r^{n-N}}{B^{(N-1)'}} , B^{(n-1)'} = \frac{\partial^{n-1} B}{\partial^{n-1} x}$$

where  $N$  equals 1 represents dipole,  $N$  equals 2 represents quadrupole and  $n$  is the index of the harmonics for the magnetic errors. The measurements of dipole and quadrupole multipole field components from PEP II HER ring are shown in Table 8.9. These sets of magnetic multipole errors are applied to the damping ring. The dynamic apertures with multipole magnet errors of ten random seeds

are shown in Figure 8.21. After applying the magnet multipole errors the dynamic aperture shrinks but is still larger than 12 sigma of the injected beam size of on momentum particles. If the magnet aperture is smaller than what is used at PEPII then the multipole field error as shown in Table 8.9 may be increased and the dynamic aperture will be reduced further. The linear fringe field is included in the simulation. Nonlinear ones have to be studied once we have engineering designs of the magnets. Finally, the fringe fields should be measured and verified, and then used in future simulations.

**Table 8.9. Systematic and rms normalized multipole errors.**

Multipole errors of dipole at radius 30 mm						
multipole type	$\frac{\Delta B_3}{B_1}$	$\frac{\Delta B_4}{B_1}$	$\frac{\Delta B_5}{B_1}$	$\frac{\Delta B_6}{B_1}$		
systematic	1.0e-5					
rms	3.2e-5	3.2e-5	6.4e-5	8.2e-5		
Multipole errors of quadrupole at radius 44.9 mm						
multipole type	$\frac{\Delta B_3}{B_2}$	$\frac{\Delta B_4}{B_2}$	$\frac{\Delta B_5}{B_2}$	$\frac{\Delta B_6}{B_2}$	$\frac{\Delta B_{10}}{B_2}$	
systematic	1.03e-3	5.6e-4	4.8e-4	2.37e-3	-3.10e-3	-2.63e-3
rms	5.6e-4	4.5e-4	1.9e-4	1.7e-4	1.8e-4	7.0e-7

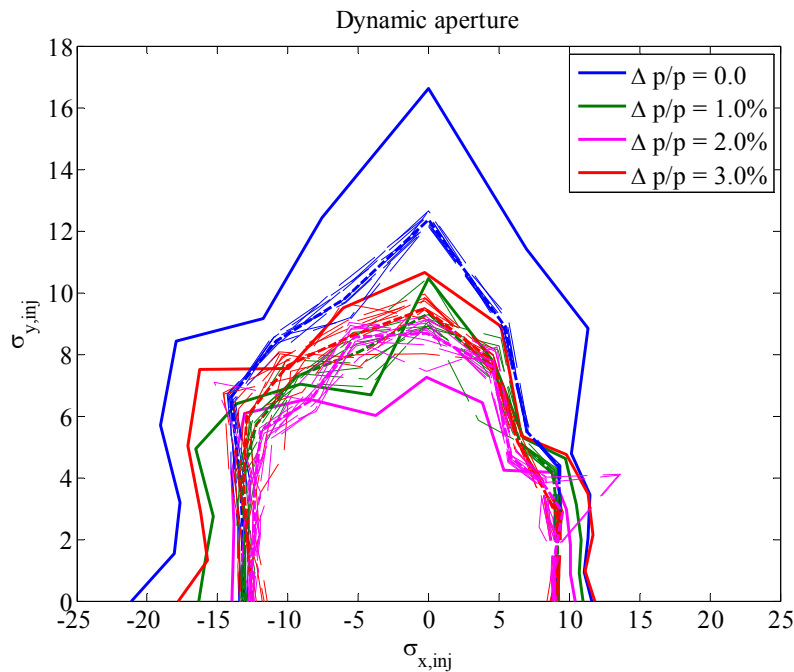


**Figure 8.21. Dynamic aperture tracking with magnet multipole field errors. Total of 10 sets of random errors are simulated. The solid line is the aperture without multipole errors and the dashed line is the dynamic aperture with multipole field errors of different random seeds. The thick dashed line is the average dynamic aperture of 10 random seeds.**

### 8.3.3.5 Alignment Tolerances and Correction System

The schematic layout of the orbit correction scheme is shown in Figure 8.22. There are 14 horizontal correctors (HCOR), 14 vertical correctors (VCOR) and 22 H/V beam position monitors (BPM) in the correction scheme. Quadrupole displacement, dipole field error and dipole rotation are the sources of errors that cause a closed orbit. The closed orbit is generated according to the closed orbit formula:

$$\Delta x, y_{co} = \frac{\sqrt{\beta_{x,y}}}{2 \sin(\pi v_{x,y})} \sum_i \sqrt{\beta_{(x,y),i}} \cos([\phi_{(x,y),i} - \phi_{(x,y)}] - \pi v_{x,y}) \Delta\Theta_{(x,y),i}$$

where  $\Delta\Theta$  is the effective kick due to different error sources. For a dipole field error,  $\Delta\Theta_x = \frac{\Delta B_1}{B_1} \theta_{\text{bend}}$ , for a dipole rotation,  $\Delta\Theta_{x,y} = \Delta\phi_{\text{rot}} \theta_{\text{bend}}$ , and for a quadrupole displacement,  $\Delta\Theta_{x,y} = \Delta x, y k_1 l_{\text{quad}}$ , where  $\theta_{\text{bend}}$  is the bending angle of the dipole,  $\phi_{\text{rot}}$  is the rotation angle of dipole,  $k_1 = \frac{B'_2}{B_1 \rho}$ . The alignment errors of the damping ring are shown in Table 8.10. The field errors are shown in Table 8.11. Dynamic aperture with alignment errors, field errors and multipole field errors of 10 seeds with corrections are shown in Figure 8.23. The corrections include linear chromaticity, orbit, beta beat, coupling and vertical dispersion. The blue solid line in Figure 8.23 is the dynamic aperture without errors. The dashed line is dynamic aperture with errors and with corrections. The red solid line is the average dynamic aperture of 10 seeds after correction. The dynamic aperture with errors after corrections gives sufficient aperture for injection. The closed orbits of 10 random seeds after correction are shown in Figure 8.24. The corrector strengths are shown in Figure 8.25. The horizontal orbit can be corrected to less than 100  $\mu\text{m}$  and the vertical orbit to less than 200  $\mu\text{m}$ . The corrector strength is less than 1 mrad.

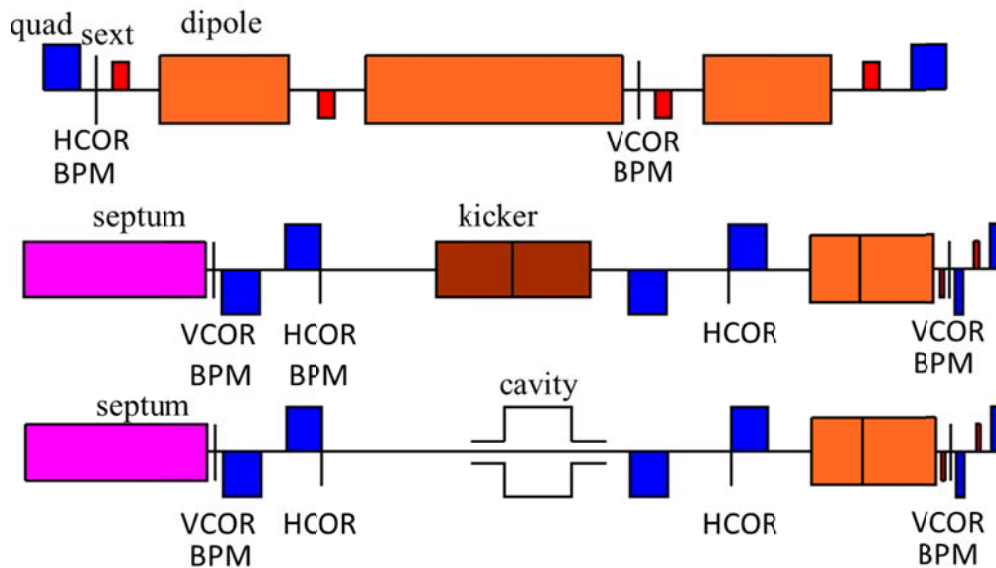


**Figure 8.22. Schematic layout of the orbit correction scheme. The correction scheme includes: 14 horizontal correctors, 14 vertical correctors and 22 H/V position monitors. The first beamline is the**

FODO cell, the second beamline is downstream of the injection septum (the reverse order applies to upstream of the extraction septum); the third beamline is downstream of the extraction septum (the reverse order applies to upstream of the injection septum).

**Table 8.10. Alignment errors**

	$\Delta x$ ( $\mu\text{m}$ )	$\Delta y$ ( $\mu\text{m}$ )	$\Delta \phi$ ( $\mu\text{rad}$ )
Dipole	50	50	100
Quadrupole	50	50	100
Sextupole	50	50	100

**Table 8.11. Field errors**

$\Delta B_1/B_1$	1.0e-3
$\Delta B_2/B_2$	1.4e-3
$\Delta B_3/B_3$	1.0e-3

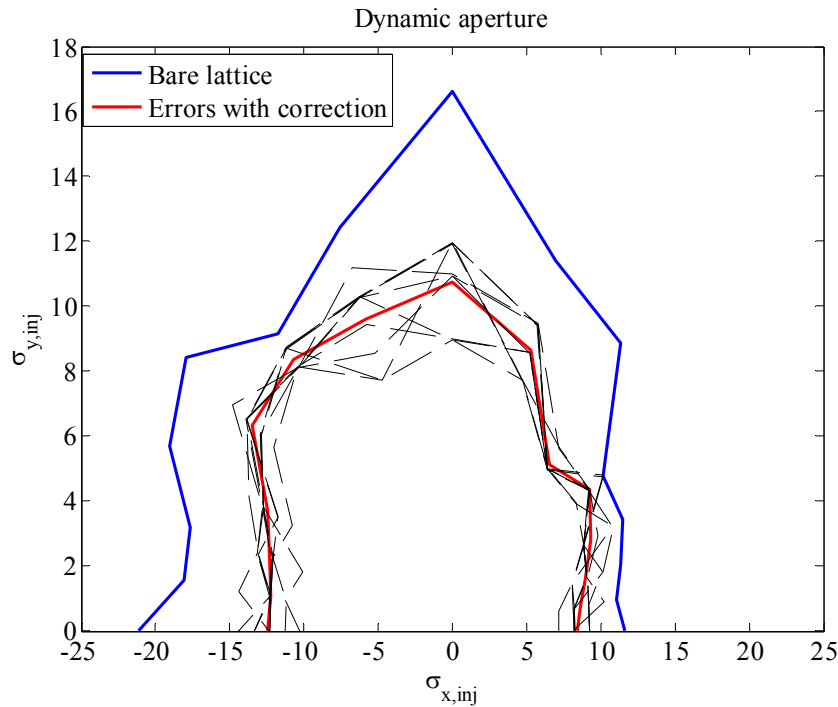


**Figure 8.23. Dynamic aperture tracking with alignment errors, field errors and magnet multipole field errors. Total of 10 sets of random errors are simulated. The blue solid line is the dynamic aperture without errors. The dashed line is the dynamic aperture with errors and with corrections. The corrections include linear chromaticity, orbit, beta beat, coupling and vertical dispersion. The red solid line is the average dynamic aperture after correction. The dynamic aperture with errors and after corrections gives sufficient aperture for injection.**

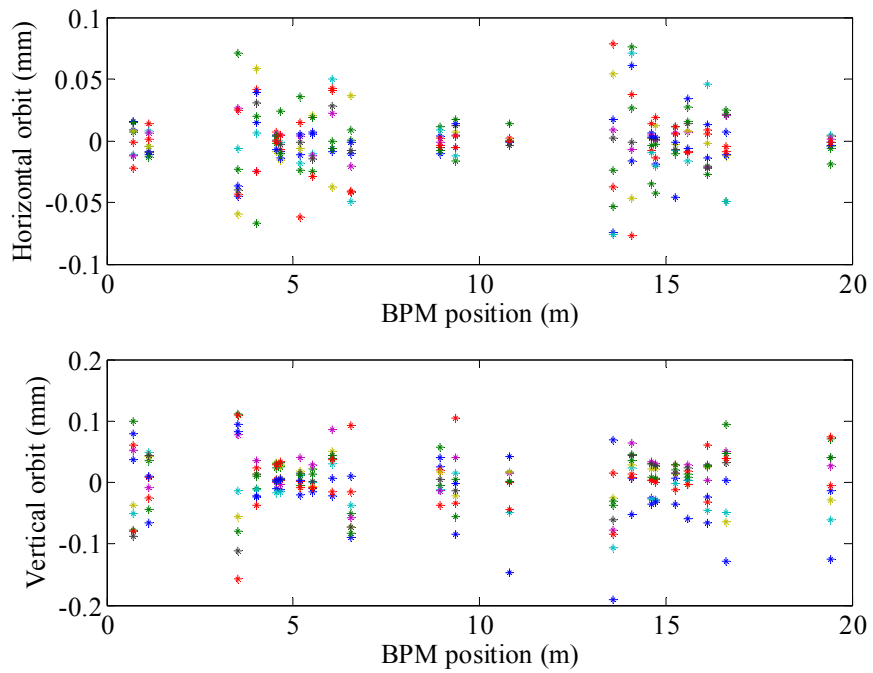


**Figure 8.24.** Closed orbits of 10 sets of random errors after correction.

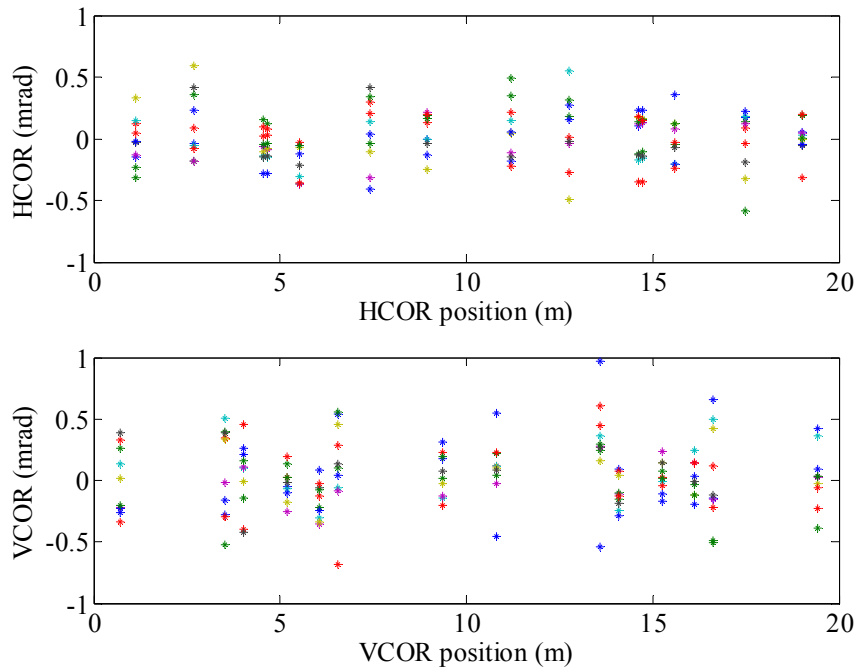


**Figure 8.25.** Corrector strengths of orbit corrections of 10 sets of random errors.

### 8.3.4 Intra-beam Scattering

Intra-beam scattering describes multiple Coulomb scattering that leads to growth in emittance and energy spread in electron machines, whereas the Touschek effect concerns large single Coulomb scattering events where energy transfer from transverse to longitudinal planes leads to particle loss. In low emittance storage rings both effects are important.

To obtain round beams in a storage ring will likely entail the use of coupling or vertical dispersion. But for simplicity here, for the purpose of IBS calculations, the vertical emittance is assumed to be primarily generated by the coupling, and the effects of the vertical dispersion can be ignored. Then the vertical emittance is proportional to the horizontal emittance

$$\epsilon_x = \frac{\epsilon}{1+\kappa} \text{ and } \epsilon_y = \frac{\kappa\epsilon}{1+\kappa},$$

with  $\kappa$  being the coupling constant between 0 and 1 and  $\epsilon = \epsilon_x + \epsilon_y$  being the sum emittance at finite current with IBS. The nominal (no IBS) horizontal and vertical emittances are given by  $\epsilon_{x0} = \epsilon_0/(1 + \kappa)$  and  $\epsilon_{y0} = \kappa\epsilon_0/(1 + \kappa)$  where  $\epsilon_0$  is the natural emittance at zero current and its value is given in Table 8.7.

It can be shown that the steady-state values of the emittance and energy spread are given by,

$$\epsilon = \frac{\epsilon_0}{1-\tau_x^*/T_x} \text{ and } \sigma_\delta^2 = \frac{\sigma_{\delta0}^2}{1-\tau_z/T_p},$$

where  $\tau_x^* = \tau_x/(1 + \kappa\tau_x/\tau_y)$ . The quantities  $\tau_x, \tau_y, \tau_z$  signify the radiation damping times in  $x, y, z$  respectively and  $\sigma_{\delta0}$  the energy spread without the IBS growth. Their values can be found in Table 8.7.  $1/T_x, 1/T_{xp}$  gives the IBS growth rate in amplitude.

For the damping ring growth rates the Bjorken-Mtingwa formulation [10] is used, using the Nagaitsev [11] algorithm for efficient calculation. Given the growth rates, the steady-state  $\epsilon$  and  $\sigma_\delta$  are obtained by solving the equations for  $\epsilon$  and  $\sigma_\delta$  simultaneously. Since the growth rates depend on the beam emittances, energy spread, and bunch length, the equations are solved by iteration using Newton's method.

For the IBS calculations for the damping using lattice parameters found in Table 8.7, it is assumed that the nominal current is below the threshold of the microwave instability and that potential well bunch lengthening is not significant (so that  $\sigma_z = \sigma_{z0}\sigma_\delta/\sigma_{\delta0}$ ). The vertical emittance is given by coupling with  $\kappa = 1$  and the beam is round.

The steady-state emittances,  $\epsilon_x, \epsilon_y$  and energy spread  $\sigma_\delta$  are calculated as a function of bunch charge. The results are summarized in Figure 8.26. There is a substantial increase in the emittances and energy spread. With 2 nC bunch charge, there is about a factor of two increase.

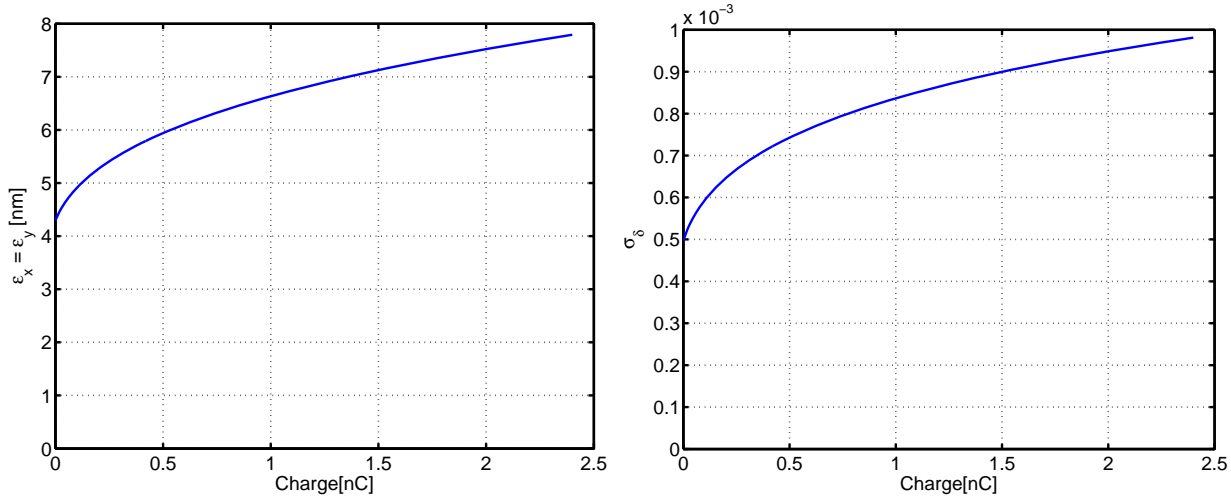


**Figure 8.26. Equilibrium emittances (left) and energy spread (right) as a function of bunch charge.**

### 8.3.5 Impedance and collective instabilities

An impedance model is required for calculations on longitudinal and transverse instability thresholds and on growth rates. Without a detailed engineering design of the vacuum chamber and its components, it is only possible to focus on a few generic types of impedance, such as the longitudinal impedance generated by coherent synchrotron radiation (CSR) and resistive-wall impedance. Here three instabilities are briefly addressed: (i) the single-bunch microwave instability driven by CSR, (ii) the single-bunch transverse mode coupling instability (TMCI) due to the resistance in the walls, (iii) the multi-turn transverse instability driven by the wall resistance and (iv) the electron cloud instability. Detailed study needs to be carried out with simulations in future as the ring components are designed.

#### 8.3.5.1 Microwave Instability due to CSR

Here the microwave threshold is estimated only due to one contributor to the impedance, shielded CSR. In the model used for the calculations the beam is assumed to be moving in a circle of radius  $\rho$  (in the plane  $y=0$ ) between two parallel plates at locations  $y=\pm h$ . In normalized units the threshold current  $S^{\text{th}}$  is given as a function of shielding parameter  $\pi$  by [12]

$$S^{\text{th}} = 0.50 + 0.12\pi$$

with

$$S = \frac{r_e N_b \rho^{1/3}}{2\pi v_s \gamma \sigma_{\delta_0} \sigma_{z0}^{4/3}}, \quad \Pi = \frac{\sigma_{z0} \rho^{1/2}}{h^{3/2}}$$

with  $N_b$  being the number of electrons per bunch and  $v_s$  being the synchrotron tune. Here  $S^{\text{th}}$  is the threshold current beyond which the energy spread of the beam starts to increase.

The vacuum chamber in the arcs is round with radius of  $r = 2$  cm and bending radius  $\rho = 0.777$  m; for these calculations  $h = r$ . With these assumptions, the effect with shielding is not significant: with  $\Pi = 0.695$ , the threshold bunch population  $N_b^{\text{th}} = 4.81 \times 10^9$ , and the threshold bunch charge 0.77 nC, which is much lower than the design bunch charge 2 nC.

Realistically, the bunch will be lengthened by the IBS scattering about 74% with 2 nC charge based on the estimate in Section 8.3.4. Using the longer bunch length and the larger energy spread generated from the IBS scattering, the threshold increases to 2.8 nC, which is significantly higher than the design value.

### 8.3.5.2 Transverse Single Bunch Instability

In most light sources with regions of small-aperture vacuum chambers, the resistive wall is the dominant contribution to the transverse single-bunch instability. The kick factor (the average kick experienced over a bunch) for a Gaussian bunch passing through a round, resistive beam pipe is given by

$$\kappa_y = (0.723) \frac{c}{\pi^{3/2} r^3} \sqrt{\frac{Z_0}{\sigma_z \sigma_c}}$$

with  $r$  the radius of the pipe,  $Z_0=377 \Omega$ ,  $\sigma_z$  the bunch length, and  $\sigma_c$  the conductivity of the beam pipe. The single bunch threshold current is given by [13]

$$I_b^{th} \approx 0.7 \frac{4\pi c v_s (E/e)}{C} \frac{1}{\sum_i l_i \beta_{y,i} \kappa_{y,i}}$$

with  $C$  the circumference of the ring. The equation above allows for several region types in the ring, each of total length  $l$ , beta function  $\beta_y$ , and kick factor  $\kappa_y$ .

Taking the conductivity of Al to be  $3.5 \cdot 10^7 \Omega^{-1} \text{ m}^{-1}$  and  $\beta_y = 5 \text{ m}$ , the threshold current is  $I_b^{th} = 49 \text{ A}$ , comfortably above the nominal current  $I_b = 28.6 \text{ mA}$ .

### 8.3.5.3 Multi-Turn Transverse Instability

Aside from HOM, the resistive wall impedance is often the dominant contributor to the transverse coupled bunch instability in storage rings. Assuming only this source of impedance, the growth rate of the instability can be estimated as [14]

$$\Gamma = \frac{c(I_b/I_A)}{4\gamma \sqrt{C(1 - [v_y])}} \langle \beta A \rangle$$

where

$$\langle \beta A \rangle = \frac{4}{\sqrt{\pi Z_0}} \sum_i \frac{l_i \beta_{y,i}}{r_i^3 \sqrt{\sigma_{c,i}}}$$

$[v_y]$  being the fractional part of the vertical tune and  $I_A = ec/r_e \approx 17045 \text{ A}$ , the Alven current. Here the beam pipe is again assumed to be round with radius  $r$ .

For the growth rate calculation, the same vacuum chamber is assumed and the total growth rate  $\Gamma = 16.68 \text{ s}^{-1}$ , which is much slower than the radiation damping rate.

#### 8.3.5.4 Electron Cloud Instability

Electron cloud studies were carried out for the FACET-II damping ring by K. Ohmi (KEK). The FACET-II damping ring stores its positron beam for several ( $\sim 6$ ) radiation damping times ( $t_x=16\text{ msec}$ ). Many positron rings which store multi-bunches have in the past suffered from electron cloud effects. This damping ring is operated with a single bunch, but the circumference is small at 20.57m. Photo-electrons are created by the synchrotron radiation of the positron beam. Most of the electrons are absorbed in the chamber wall between the bunch repetition time 20.57m (69 nsec). Accordingly, some residual electrons may be amplified by multipactoring or by being trapped in the fields of the bending magnets. Also, the use of combined bending magnets can potentially exacerbate the electron trapping issue. The study reported here was performed to confirm whether the electrons introduce any deleterious effects to the damped beam.

Firstly, the magnitude of the effect on the damped beam by electrons is calculated. Electrons oscillate in the presence of electric fields near the beam, with vertical oscillations being especially fast and having the largest contribution to beam instabilities. The frequency, with an amplitude  $\sim \sigma_y$  is expressed by,

$$\omega_e = \sqrt{\frac{\lambda_p r_e c^2}{\sigma_y(\sigma_x + \sigma_y)}}$$

where  $\lambda_p$  is the line density of a positron inside a bunch,  $\lambda_p = N_p/(2\pi)^{1/2}\sigma_z$ . The electron oscillates in the beam with a period of  $\omega_e\sigma_z/c$ . This oscillation induces instabilities within the inner bunch. The threshold is given by [15],

$$\rho_{e,th} = \frac{2\gamma\nu_s\omega_e\sigma_z/c}{\sqrt{3}KQr_0\beta L}$$

where  $K=\omega_e\sigma_z/c$  and  $Q=\min(\omega_e\sigma_z/c, 7)$ .  $\beta$  is an averaged vertical beta function. Table 8.12 shows parameters of the beam and values given by these formulae. The threshold density for electron cloud formation is given by  $\rho_{e,th}=2.9\times 10^{14} \text{ m}^{-3}$ . Electron production is also suppressed by space charge forces. The saturated electron line density should be comparable with the line density of the beam,  $\lambda_{beam}=N_p/C=3\times 10^8 \text{ m}^{-1}$ . Assuming a vacuum chamber cross-section of  $0.001 \text{ m}^2$ , the electron density neutralized is  $3\times 10^{11} \text{ m}^{-3}$ . This density is smaller than the threshold density to 3<sup>rd</sup> order.

The electron density is more quantitatively analyzed as follows. Electrons are produced by photo-emission resulting from synchrotron radiation of the positron beam. The number of photons emitted by synchrotron radiation is given by,

$$N_\gamma = \frac{5\pi}{\sqrt{3}}\alpha_{fsc}\gamma$$

per positron in one revolution. Electrons are produced by the photons with a quantum efficiency of about  $\sim 0.1$  [16]. The photon characteristic energy is sufficient to produce photo-electrons. Secondary electrons are then produced by incident electrons with a rate depending on the energy. Table 8.13 summarizes numbers related to the electron emission. In the damping ring, combined function bending magnets are used with a quadrupole component contained within the bending field. Electrons, which

predominantly move vertically in the bending fields are trapped in the combined field. This is because the field strength is stronger near the magnet pole, thus electrons are repelled by the magnetic mirror effect.

Simulation code, PEI [17], takes into account the effects of photo-emission, secondary emission, and electron motion in bending fields with combined quadrupole fields. It also incorporates beam forces and space charge forces between the electrons themselves. Figure 8.27 shows the electron line density in the vacuum chamber. The left and right pictures plot densities in the bending and combined bending magnets, respectively. Several lines are drawn for secondary emission rate,  $\delta_{2,\max}=1.8, 2.0, 2.5, 3.0$  [18]. There is no clear difference in density for the secondary rates, and also little difference between bend and combined bend results. With the arrival of the bunch, the line density jumps from  $5 \times 10^8$  to  $19-20 \times 10^8 \text{ m}^{-1}$  due to emission from a bunch with the rate  $1.3 \times 10^9 \text{ m}^{-1}$ . Since the averaged beam line density is  $\lambda_{\text{beam}}=3 \times 10^9 \text{ m}^{-1}$ , the electron line density is limited with the beam density level. The density before the jump determines the possible onset of an instability because electrons are produced after the passage of the bunch. Assuming the chamber cross-section  $0.001 \text{ m}^2$ , the volume density is  $5 \times 10^{10}-2 \times 10^{11} \text{ m}^{-3}$ . The density is smaller than the threshold density to 3<sup>rd</sup> order.

In conclusion we find electron cloud effects are negligible in FACET-II damping ring.

**Table 8.12. Parameters of beam and electron cloud instability.**

Energy	E	335 MeV
Circumference	C	20.57 m
Tune	$v_x, v_y, v_z$	4.586, 2.615, 0.0383
Emittance	$\varepsilon_x/\varepsilon_y$	5.43/5.43
Bunch length	$\sigma_z$	2.25 m
Energy spread	$\sigma_\delta$	$4.6 \times 10^{-4}$
Momentum compaction	$\alpha$	$5.73 \times 10^{-2}$
Bunch population	$N_p$	$0.625 \times 10^{10}$
Local beam line density	$\lambda_p$	$1.1 \times 10^{12} \text{ m}^{-1}$
Averaged beam line density	$\lambda_{\text{beam}}$	$3.0 \times 10^8 \text{ m}^{-1}$
Photo-electron emission rate	$Y_{1e}, N_p Y_{1e}$	$0.211 \text{ m}^{-1}, 1.3 \times 10^9 \text{ m}^{-1}$
Electron frequency	$\omega_e/2\pi$	18 GHz
Electron osc. period	$\omega_e \sigma_z/c$	0.85
Threshold electron density	$\rho_{e,\text{th}}$	$2.9 \times 10^{14} \text{ m}^{-3}$

**Table 8.13. Parameters for electron cloud production and build-up.**

Energy	E	335 MeV
Circumference	C	20.57 m
Bending radius	$r_B$	0.777 m
Bending field	$B_B$	1.44 T
Packing factor for BM		0.24
Quadrupole component of BM	$K_1$	$-4.0 \text{ m}^{-1}, -8.04 \text{ m}^{-2}$
Number of photon/turn, /m	$N_\gamma, N_\gamma/C$	$43.4, 2.11 \text{ m}^{-1}$
Characteristic energy of photon	$u_c$	107 eV
Photo-electron quantum efficiency	$\eta_{1e}$	0.1
Photo-electron emission rate	$Y_{1e}, N_p Y_{1e}$	$0.211 \text{ m}^{-1}, 1.3 \times 10^9 \text{ m}^{-1}$
Threshold electron density	$\rho_{e,th}$	$2.9 \times 10^{14} \text{ m}^{-3}$
Tune shift at threshold density	$\Delta\nu(\rho_{e,th})$	0.052

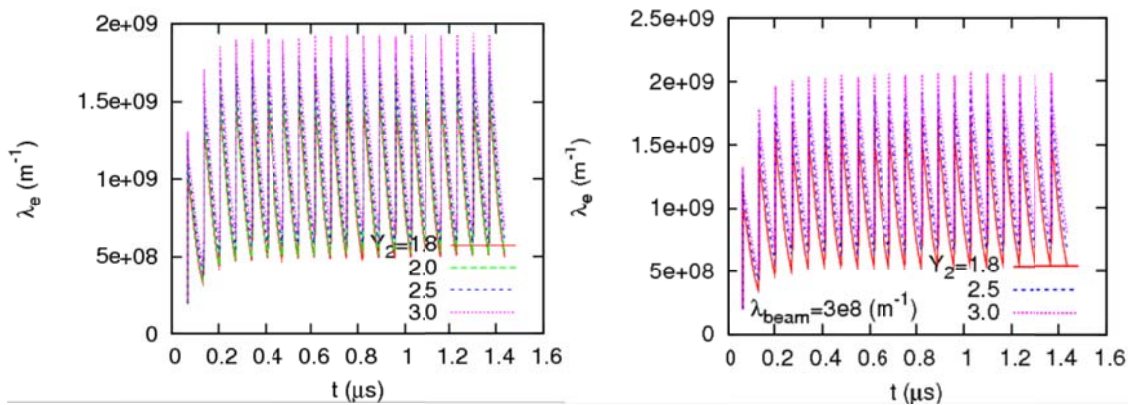


**Figure 8.27. Electron cloud line density during the beam passage. Left and right pictures plot the density in bending and combined bending magnets, respectively.**

### 8.3.6 Magnets

#### 8.3.6.1 Overview

The FACET-II damping ring magnet parameters are summarized in Table 8.14, assuming  $E_{e^-} = 335 \text{ MeV}$  and  $B_p = 1.117 \text{ T-m}$ . The designs and parameters presented in this section have evolved from the preliminary concepts presented in the FACET-II CDR (Fig. 8.27) [19] as a result of more detailed design studies and modeling. The original design concept employed dipole blocks, each having a combination of normal and gradient dipole pole surfaces machined within the single iron block that in some cases were separated by gaps to accommodate permanent magnet sextupoles. Quadrupoles, permanent magnet sextupoles and electromagnet sextupoles were located between the five dipole blocks comprising one 180-degree arc in the damping ring lattice (Fig. 8.27). As discussed in the CDR, many of the magnets in this lattice implementation were quite challenging: gradient dipoles because of high pole surface fields necessitating the use of vanadium permendur, and very short quadrupoles and electromagnet sextupoles due to the limited space between dipole blocks. No magnetic modeling was done for these

initial concepts and only approximate dimensions and coil parameters were presented in the CDR. Cross-talk between these largely fringe-field multipoles was an unanalyzed concern and the attainable field quality in all magnet concepts was uncertain.

**Table 8.14. Estimated FACET-II damping ring electromagnet parameters for baseline lattice. Only the BE-BC-BE dipole block (in bold) has been studied using 3D simulations, so its parameters are known with more certainty than the other magnets. (B = dipole, Q = quadrupole, S = sextupole)**

Magnet	Qty	Magnetic length (m)	Half gap/bore radius (cm)	Bend angle (deg)	Field (T, beam axis)	Max pole tip field (T)	Gradient (T/m, T/m <sup>2</sup> )	NI/pole (A-t) x # poles	Power (kW @ 55°C)
BC	6	<b>0.2489</b>	2.2	<b>18.37</b>	-1.44	<b>1.8</b>	<b>9.34, 112.1</b>	<b>25990 x 2</b>	24.5 per BE-BC-BE block
BE	12	<b>0.1245</b>	2.2	<b>9.18</b>	-1.44	<b>1.44</b>	-	<b>25990 x 2</b>	
BMH	4	0.3074	2.2	22.68	-1.44	1.9	9.34	25990 x 2	24.5 per BMH-BME block
BME	4	0.1655	2.2	12.21	-1.44	1.44	-	25990 x 2	
QFCHS	4	0.09	2.2	-	-	0.9	-34.47, -293.4	7050 x 4	2.4
QF2HS	4	0.09	2.2	-	-	1.14	-39.2, -293.4	7950 x 4	3.1
QDDSS	4	0.06	2.2	-	-	0.16	7.10, 358.4	1430 x 4	1
QFI	4	0.14	2.2	-	-	0.47	-21.21	4300 x 4	1
QDI	4	0.14	2.2	-	-	0.37	16.62	3370 x 4	0.6
QFI1	4	0.14	2.2	-	-	0.59	-26.82	5440 x 4	1
QDI1	4	0.14	2.2	-	-	0.42	18.98	3850 x 4	0.6

Since a more detailed magnet design study has taken place, the lattice design has been revised to include sextupole components in the gradient dipoles and inter-dipole quadrupoles (Fig. 8.28). These combined function magnets eliminate the need for the permanent magnet sextupoles and their associated gaps within the dipole blocks, allowing the dipole blocks to be shorter which, together with the elimination of permanent magnet sextupoles between dipole blocks, provides more space there for the combined quadrupole-sextupole magnets and other accelerator components such as beam position monitors (BPMs), pumping ports, etc. Another design improvement is that dipole coils have been moved from the block back-legs in the original concept to be located around to poles themselves, improving magnet efficiency and field quality as well as reducing leakage fields. This also enables the C-shaped magnets to open outwards from the ring center, facilitating access to the vacuum chamber and other components. Magnet cross-talk has been reduced with the addition of field clamps at the ends of the dipoles. As originally proposed, high quality magnet steel, such as ARMCO grade 4, will be used for the dipole blocks to achieve high magnetic permeability uniformity.

While the present combined function magnet design is simpler and more mature than the concept presented in the CDR, there remain some technical issues that have yet to be addressed. These include the detailed design of the dispersion suppressor cell BMH-BME dipole block, other quadrupoles and sextupoles, and the need to provide some independence of quadrupole and sextupole tuning and orbit correction in the arcs.

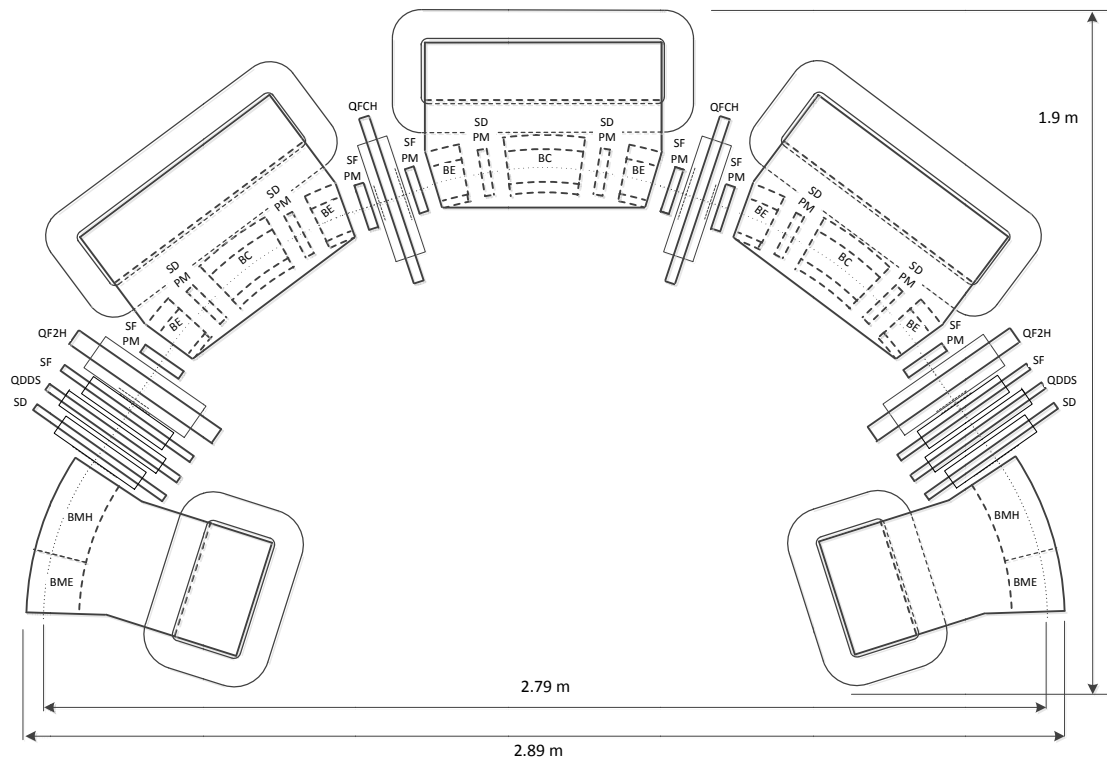


**Figure 8.28. Concept for layout of magnets in one arc of the FACET-II damping ring as presented in the 2015 CDR.**

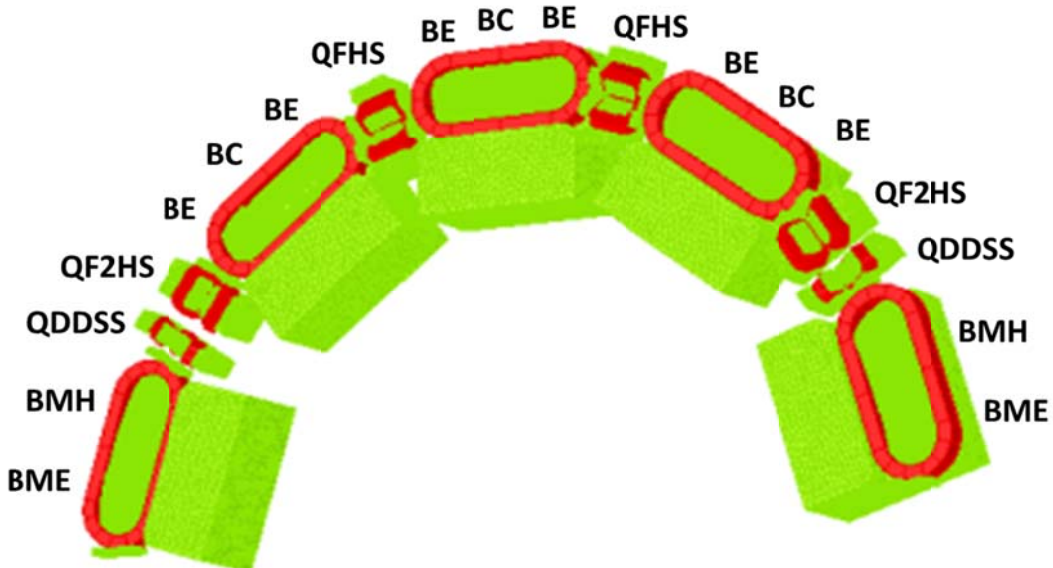


**Figure 8.28. Revised concept for layout of magnets in one arc of the FACET-II damping ring using combined sextupole-gradient dipoles and sextupole-quadrupoles.**

### 8.3.6.2 BE-BC-BE Dipole Block

A view of the bottom half of the BE-BC-BE magnet block is shown in Figure 8.29 where the three pole surfaces can be seen: normal dipole at each end and combined dipole-quadrupole-sextupole in the middle. Adding the sextupole gradient to the central pole results in a reduction of the maximum pole surface field from  $\sim 2\text{T}$  in the original design concept, which necessitated the use of vanadium permendur pole faces, to  $\sim 1.8\text{T}$ , probably eliminating the need for vanadium permendur. Field clamps are shown at each end of the dipole. It is assumed the three poles in this block would be machined with  $\sim \pm 10\text{-}\mu\text{m}$  precision.

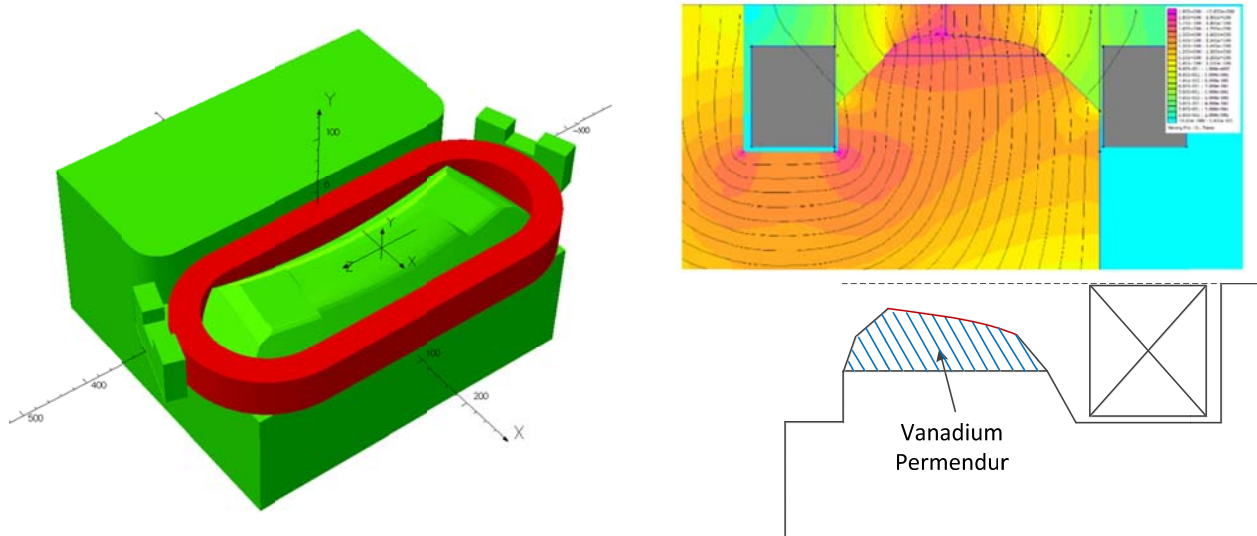


**Figure 8.29. Left:** lower half of the BE-BC-BE magnet block with field clamps. **Upper right:** cross-section of dipole-quadrupole-sextupole pole with color-coded magnet flux density at full field with 25980-A coil excitation (color scale ranges from 0 to 2T).

Eliminating the gaps for sextupoles between pole surfaces that were included in the original design concept enables the overall block length to be shortened. While it is possible to increase the block length and reduce dipole field strength, this is not beneficial since a high field is needed to minimize beam damping time.

The technical details of the Opera 3D magnetic analysis for the BE-BC-BE magnet block are given in [20]. This analysis includes an evaluation of multipole content for longitudinal slices of the magnet and adjacent straight sections (Table 8.15). The analysis indicates that multipole content is acceptable and that higher order components can be further reduced by small iterations to the pole contours. The  $B'$  content that is seen in the BE entrance slices in Table 8.5 is edge focusing, which has been set in the lattice design by using the BE entrance face angle as a free parameter in the 3D design.

**Table 8.15.** 3D simulation results of field components for longitudinal slices of the BE-BC-BE dipole block. The slices are in consecutive order from the BC center, though BE and into the adjacent straight section to the end of the next quadrupole.

magnet	slice	L [mm]	B0 [T]	B' [T/m]	B''/2 [T/m <sup>2</sup> ]	B'''/6 [T/m <sup>3</sup> ]	B''''/24 [T/m <sup>4</sup> ]
BC	-0	31.111	-1.44363	9.42031	113.363	-6.8	-1594
	-1	31.111	-1.44351	9.39214	111.592	63.3	2221
	-2	31.111	-1.44416	9.33547	110.040	-42.8	-235
	-3	31.111	-1.45079	7.65527	75.840	-332.9	570
BE	1	31.111	-1.46155	1.37077	9.408	-26.4	1625
	0	31.111	-1.45607	0.11778	0.991	0.9	594
	-0	31.111	-1.29400	1.26560	5.187	45.6	11953
	-1	31.111	-0.85089	1.95344	9.562	23.4	2251
straight	-2	21.685	-0.52819	1.21965	17.584	-12.3	1922
	-3	21.685	-0.32065	0.60785	24.252	-57.4	13
	-4	21.685	-0.13747	0.19048	23.209	-37.0	9847
	-5	21.685	-0.02640	-0.00365	14.650	-276.4	44677
	-6	21.685	-0.00211	-0.00839	3.216	-0.4	-175
	-7	21.685	0.00016	-0.00134	0.136	-1.5	-20

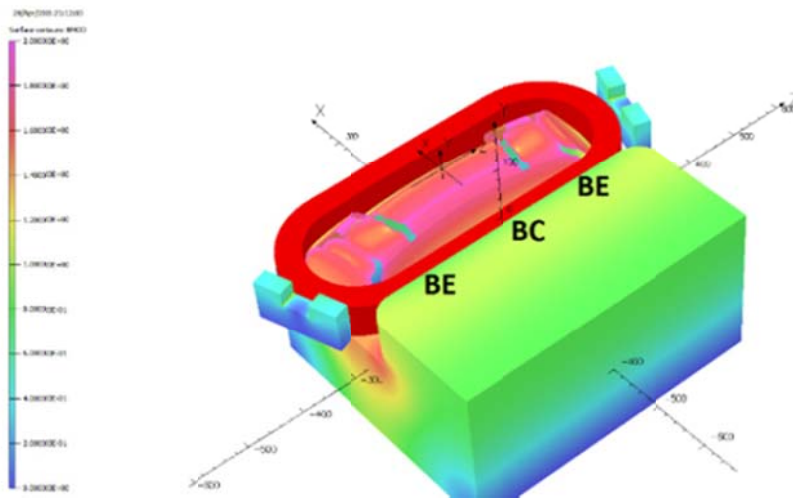


**Figure 8.30.** Field distribution in yoke surface from 3D simulation for the BE-BC-BE dipole block with 25992-A coil excitation. The color scale goes from 0 to 2T.

As seen in Figure 8.30, there is local saturation above 2 T along the sharp edges where the BE profile meets the BC profile, and at the BE outer corners, but this is expected to be easily removed by adding chamfers and smooth transitions, to be done in coming design iterations.

Also evident in Table 8.15 is the longitudinal drop-off in field components, including the sextupole component from the central pole surface towards the end pole surface and all field components extending into the adjacent straight section, aided by the field clamp. These results indicate that cross-talk between magnets, including the quadrupole-sextupoles adjacent to the dipole block, should not be an issue. This analysis indicates that it should be possible to make field measurements for the different magnets independently of each other, meaning that once the task of designing all the damping ring magnets has been accomplished, magnet production and measurement should be relatively straight forward.

As seen in Figures 8.29 and 8.30, the coil for the BE-BC-BC dipole block has a flat straight racetrack-shaped geometry, a simple design from a manufacturing point of view. Coil design parameters and analytical estimates for temperature rise, etc., are listed in Table 8.16. They are subject to future optimization of the trade-off between coil manufacturing cost, favoring small size and higher power, and power consumption. Trim coils will be added to provide  $\pm\sim 2\%$  tuning capability if the dipole blocks are powered in series with a single power supply.

### **8.3.6.3 BMH-BME Magnet Block**

The detailed design of the BMH-BME magnet block has not yet been undertaken. However, since the lattice specified length of BMH + BMH, 0.4729 m, is close to BE+BC+BE 0.4978 m length, and since the on axis-fields are the same, it can be seen the BMH-BME block will have the basically same return yoke, coils and field clamps as the BE-BC-BE, meaning that it is just the pole design that will differ. The Opera-3D BMH-BME block model shown in Fig 8.28 has been built this way, but it has not yet had free parameters of the pole shape, such as pole face length, etc., optimized in 3D (to get correct effective length, etc.). Furthermore, the BMH section does not yet have the correct quadrupole gradient, so the slice data for this magnet are not presented. The present non-finalized BMH 2D-model is shown in Fig. 8.31. This model assumes iron as pole material, but with the high side of the pole face being near 2 T, it might be necessary to add vanadium permendur instead.

The coil design data listed in Table 8.16 is valid for BMH-BME as well. It should be noted that it is possible to have all the dipole blocks series-connected with one power supply. Trim coils will be added to provide  $\pm\sim 2\%$  tuning capability if the dipole blocks are powered in series with a single power supply.

**Table 8.15. BE-BC-BE and BMH-BME coil design data.**

parameter	value	unit	comment
No. of coils /magnet	2		
conductor	OFHC copper, 9x9 mm, $\emptyset 5$ mm internal cooling channel		
No. of double pancakes /coil	3		
No. of turns in width direction	4		i.e. 8 turns / double pancake
No of turns /coil	24		
cross section width	43	mm	
cross section height	65	mm	

$I_{\text{mean}}/\text{turn}$	1.427	m	
R /coil	9.7	$\text{m}\Omega$	at 20°C, excl. exit leads
nom NI/coil	25992	A-t	
nom I	1083	A	
coil cooling	water cooled		
No of cooling circuits /coil	3		
pressure drop ( $\Delta p$ )	75	psi	
flow /cooling circuit	4.8	$\text{l}/\text{min}$	
temperature rise ( $\Delta T$ )	+12	°C	
P/coil	12.2	kW	
R /magnet	20.8	$\text{m}\Omega$	at calculated $\Delta T$ , excl exit leads
U /magnet	22.6	V	= 226 V for 10 magnets in series excl. cabling
P /magnet	24.4	kW	= 244 kW for 10 magnets in series excl. cabling
flow /magnet	28.9	$\text{l}/\text{min}$	= 289 $\text{l}/\text{min}$ for 10 magnets

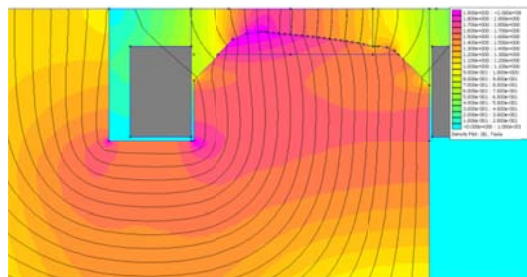
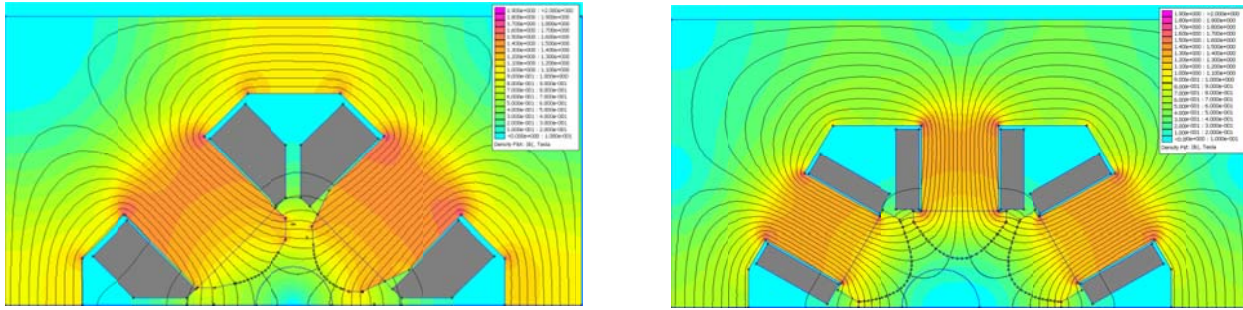


Figure 8.31. Preliminary BMH 2D-model with NI = 25992 A. The color scale goes from 0-2 T. The field in the mid-plane, by quadratic fit over  $x = \pm 20$  mm, is  $B = -1.436$ ,  $B' = 8.785$ , with residual  $<\pm 1$  G.

### 8.3.6.4 Arc Quadrupole-Sextupoles

Preliminary 2D designs for the QFCHS and QDDSS quadrupole-sextupole magnets are depicted in Fig. 8.32. QFCHS is a quadrupole with offset pole shapes creating a sextupole content, whereas for QDDSS the specified sextupole/quadrupole ratio is so high that it is easier to design this magnet as a sextupole with offset pole shapes. These 2D models both have the correct ratio of sextupole/quadrupole content but are preliminary in the sense that the pole shapes have not yet been fully optimized with respect to minimizing higher order error field terms. For QFCHS, we have extended the length from 90 mm, as specified in Table 8.14, to 110 mm, using all the space between the dipole blocks. This results in a moderate field level in the pole roots (~1.4 T) while still using a relatively simple coil design. For QF2HS, which has higher field strength specified in Table 8.14, the same design simulated at higher current has ~1.6 T in the pole roots which is acceptable. We have not made a separate QF2HS 2D design, since it was assumed that coming lattice updates would have equal sextupole/quadrupole ratio for QFCHS and QF2HS, just different strengths.



**Figure 8.32.** Preliminary quadrupole-sextupole 2D-models. Left: QFCHS at NI = 5980 A. Right: QDDSS at NI = 2400 A. The color scale goes from 0-2 T. By harmonic content evaluation at  $r = 20$  mm, the simulated fields are -28.27 T/m, -240.3 T/m<sup>2</sup> for QFCHS and 7.126 T/m, -359.6 T/m<sup>2</sup> for QDDSS.

3D models of these magnets have been built (Fig 8.28) using the 2D cross sections, but these have not yet been optimized to get correct integrated strengths, etc. However, optimization is expected to be possible within the mechanical lengths that these magnets have now so that the coil design data presented in Tables 8.17, 8.18 and 8.19 should remain valid, subject future optimization of the trade-off between coil manufacturing cost, favoring small size and higher power, and power consumption.

**Table 8.17. QFCHS coil design data.**

parameter	value	unit	comment
No. of coils /magnet	4		
conductor	OFHC copper, 5x5 mm, Ø3 mm internal cooling channel		
No. of layers	4		
No. of turns /layer	8,7,6,5		see fig. 8.32
No. of turns /coil	26		
cross section width	26	mm	
cross section height	50	mm	
$l_{mean}$ /turn	0.418	m	
R /coil	11	mΩ	at 20°C, excl. exit leads
nom NI/coil	5980	A-t	
nom I	230	A	
coil cooling	water cooled		
No. of cooling circuits /coil	1		
pressure drop ( $\Delta p$ )	75	psi	
flow /cooling circuit	1.2	l/min	
temperature rise ( $\Delta T$ )	+7	°C	
P/coil	0.6	kW	
R /magnet	45.9	mΩ	at calculated $\Delta T$ , excl exit leads
U /magnet	10.6	V	= 42.2 V for 4 magnets in series excl. cabling

P /magnet	2.4	kW	= 9.7 kW for 4 magnets in series excl. cabling
flow /magnet	5.0	l/min	= 19.8 l/min for 4 magnets

**Table 8.18.** QF2HS coils are same design as QFCHS (Table 8.17). Values listed in this table are those that differ at the higher current level for this magnet.

parameter	value	unit	comment
nom NI/coil	6760	A-t	
nom I	260	A	
temperature rise ( $\Delta T$ )	+9	$^{\circ}\text{C}$	
P/coil	0.8	kW	
R /magnet	46.2	$\text{m}\Omega$	at calculated $\Delta T$ , excl exit leads
U /magnet	12.0	V	= 48.2 V for 4 magnets in series excl. cabling
P /magnet	3.1	kW	= 12.6 kW for 4 magnets in series excl. cabling

**Table 8.19.** QDDSS coil design data.

parameter	value	unit	comment
No of coils /magnet	6		
conductor	OFHC copper, 4x4 mm, $\varnothing$ 2.5 mm internal cooling channel		
No of layers	2		
No of turns /layer	8		see fig. 8.32
No of turns /coil	16		
cross section width	12	mm	
cross section height	42	mm	
$l_{\text{mean}}/\text{turn}$	0.215	m	
R /coil	5.8	$\text{m}\Omega$	at 20°C, excl. exit leads
nom NI	2400	A	
nom I	150	A	
coil cooling	water cooled		
No of cooling circuits /coil	1/3		series connected per upper/lower half
pressure drop ( $\Delta p$ )	75	psi	
flow /cooling circuit	0.8	l/min	
temperature rise ( $\Delta T$ )	+8	$^{\circ}\text{C}$	
P/coil	0.1	kW	

R /magnet	36.5	$\text{m}\Omega$	at calculated $\Delta T$ , excl exit leads
U /magnet	5.5	V	= 22.0 V for 4 magnets in series excl. cabling
P /magnet	0.8	kW	= 3.3 kW for 4 magnets in series excl. cabling
flow /magnet	1.6	l/min	= 6.2 l/min for 4 magnets

Comparing with the CDR version design for the quadrupoles and sextupoles, incorporating the lattice sextupole gradients into the quadrupoles eliminates the need for the permanent magnet sextupoles, simplifying implementation and providing more space for combined function magnets between dipole blocks. In particular, it would eliminate the significant design challenge associated with the very close spacing of quadrupoles and sextupoles adjacent to the BMH/BME magnet blocks (Fig 8.33). These magnets must be physically short in the longitudinal dimension, significantly shorter than the magnet length defined by fringe fields, which overlap.

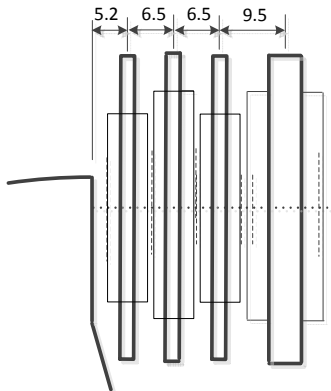


**Figure 8.33. Close spacing between quadrupoles and sextupoles in the original CDR design, with overlapping magnetic lengths determined by fringe fields. Dimensions are centimeters.**

While the combined function magnets offer this advantage, they introduce another potential problem in that they greatly reduce, and possibly eliminate, the ability to independently tune the quadrupole and sextupole settings in the arcs. Such tuning is likely to be needed to correct the lattice optics for best performance. In principle such tuning would not be needed if the actual machine parameters are very close to design values from the beginning, but there are likely to be imperfections in magnet parameters that reduce the likelihood that close matching with design is achieved at first. Further study is needed to determine if this tuning is actually needed, and if so, if sufficient independent control of the quadrupole and sextupole fields can be achieved by asymmetrically powering the four coils in the magnet [21]. This method has the drawback of inducing a dipole term as well, causing an orbit deflection that must be corrected elsewhere. If a greater tuning range than can be provided by this method is needed, independent quadrupole and sextupole magnets may be needed once again. With further study, other solutions may be possible, such as using a 12-pole magnet with independently powered coils to generate approximately independent quadrupole, sextupole and corrector dipole fields [22]. Therefore, the quadrupole-sextupole magnet design concept shown in figs. 8.28 and 8.32 above should at this point still be considered preliminary.

### 8.3.6.5 Arc Correctors

In the original CDR notional design, horizontal and vertical dipole correctors were implemented using trim windings on the back-legs of normal quadrupole magnets. In the present design, which incorporates combined function quadrupole/sextupoles, using such trim windings to generate dipole corrections will induce higher order field components as well. More study is needed to determine if this method, or using trim windings built into the main coils, would be acceptable.

An alternative solution is to add horizontal and vertical corrector windings to the “picture frame” field clamp at the end of each dipole (Fig. 8.34). ~2000 ampere-turns per coil are required to generate a 1-2 mrad corrector kick in the 50-mm aperture of the field clamp, depending on the length of the clamp. This corrector strength is sufficient to compensate for magnet field and alignment errors assuming there is individual tuning control for the dipole blocks and quadrupole/sextupoles at the few percent level, either using individual power supplies for the magnets by using trim coils for series-connected magnets. Some reduction of the length of the nearby dipole and/or quadrupole will be needed to accommodate the thickness of the corrector coils.

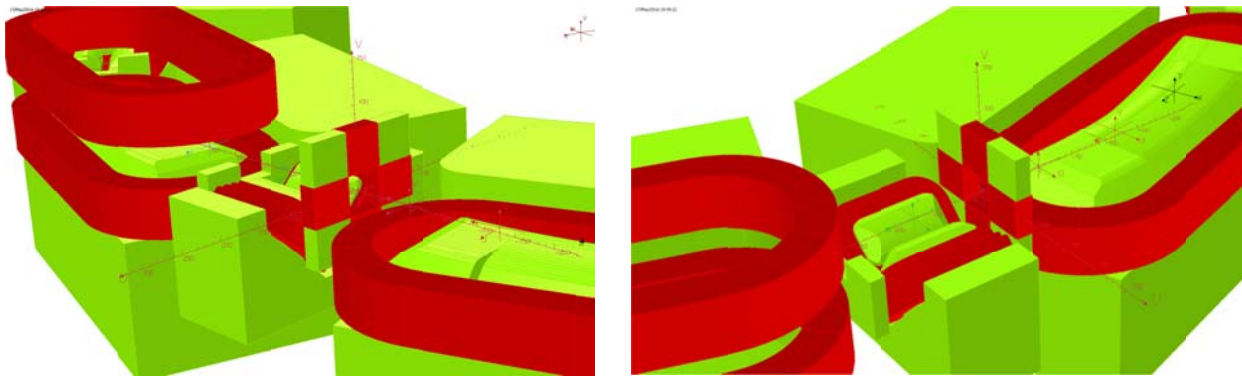


Figure 8.34. Notional horizontal and vertical corrector coils on dipole field clamps.

### 8.3.6.6 Straight Section Magnets

The QFI, QDI, QFI1 and QDI1 are all conventional quadrupoles located in the damping ring straight sections between the 180-degree arcs. Trim windings will be included either together with the main coil packs or on the back-legs of the yokes to realize horizontal and vertical corrector capability (see Fig. 8.34 for a notional concept).

## 8.3.7 RF System

### 8.3.7.1 Overview

The RF system for the positron damping ring is designed for 1.1MV of accelerating gap voltage to be provided by two RF cavities, one each in the injection and extraction straights.

### 8.3.7.2 Klystron

The two cavities will be powered by a 714MHz klystron from the current damping rings. The HVPS and klystron will be moved from the South Damping Ring and installed in the klystron gallery in Sector 10. Waveguide will be run down penetration 10-13 and power split on the ceiling of the tunnel to the two cavities.

### ***8.3.7.3 Cavities***

The two cavities will be recovered from the South Damping Ring and installed in the straight sections near the septa.

### ***8.3.7.4 LLRF***

The low-level RF and feedback system from the current damping ring will be adapted to use the new global clock. New PLC logic will be developed to interface to EPICS.

### 8.3.8 Vacuum System

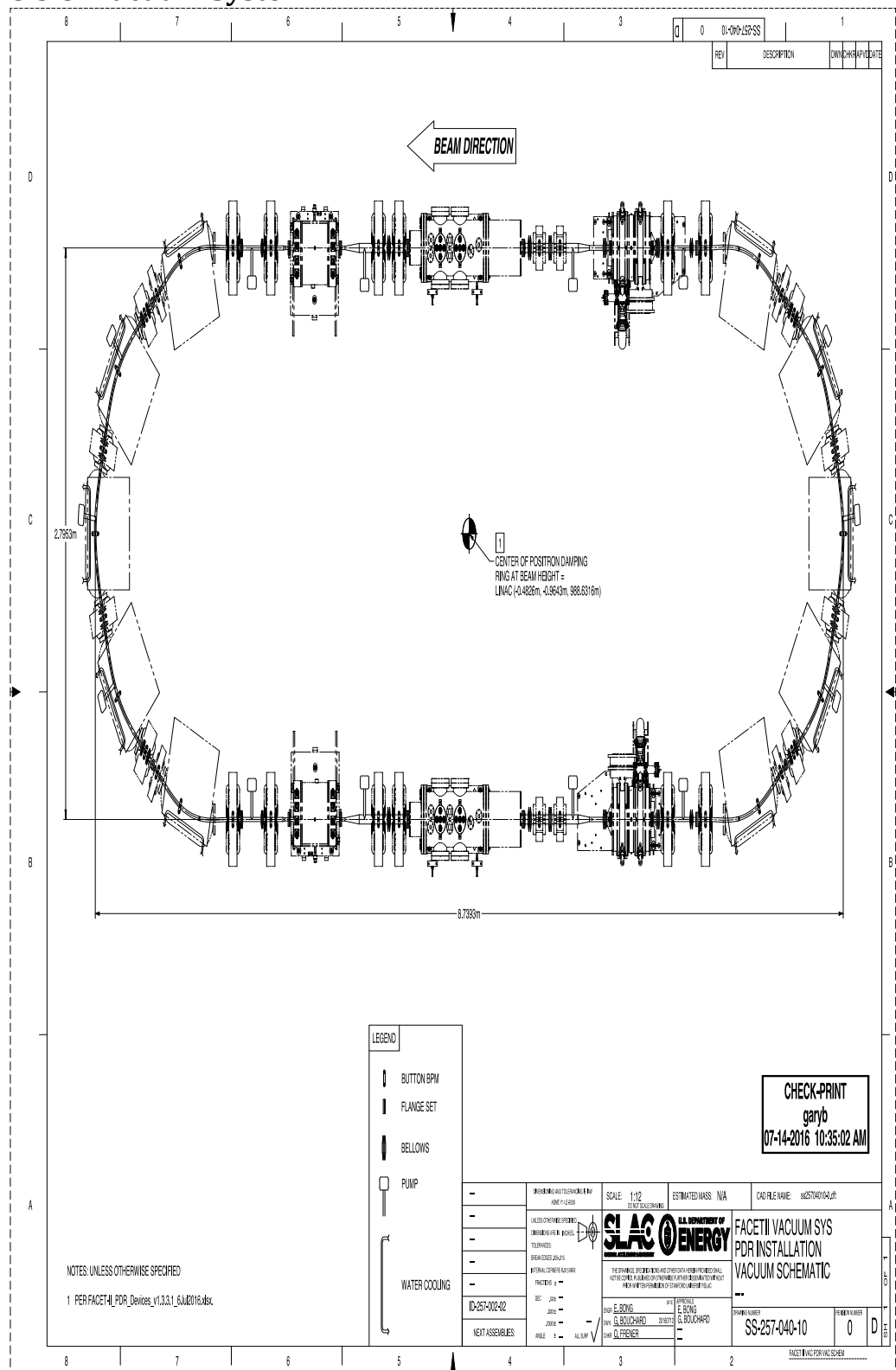


**Figure 8.29: Schematic of positron damping ring vacuum system indicating locations of BPMS, flanges, bellows, pumps and water cooling pipes.**

The ring vacuum system will be isolated from the injection and extraction beamlines by gate valves. The ring arc chambers will be machined in halves, with a circular beam cross-section. In each arc bend, the arc chamber will have a pump-port with and RF screen. Each combined-function section of the arc bend chamber will feature an RF BPM. The feedthroughs of the RF BPM will protrude horizontally to fit between the bend coils.

A single-convolution bellows will be included between each quad and bend in the arc chamber assembly. All bellows will be RF shielded. The arc vacuum chamber will be externally supported to decouple chamber thermal expansion from magnet alignment. A cooling line will be brazed to the outside edge of each bend chamber to minimize thermal excursion. Rough-down of the ring vacuum may be performed locally, or remotely in the klystron gallery through a fixed roughing line.

### 8.3.8.1 Arcs

The design of the positron damping ring arc lattice has a dense set of magnets. There is little room for vacuum pumping. The design considered here has lumped pump options for the damping ring vacuum. A program called VACCALC [23] is used to compute the pressure profile under various pumping schemes. The beam pipe in the arc is a 4 cm diameter pipe which has reasonable conductance. The length of the arc is about 4.1 m. The first case considered has lumped pumps at either end of the arc. Figure 8.30 shows the pressure profile around the arc. This assumes a thermal outgassing rate of 0.1 nTorr (l/s)/cm<sup>2</sup>. The pump speeds at the ends of the arc are 100 l/s.

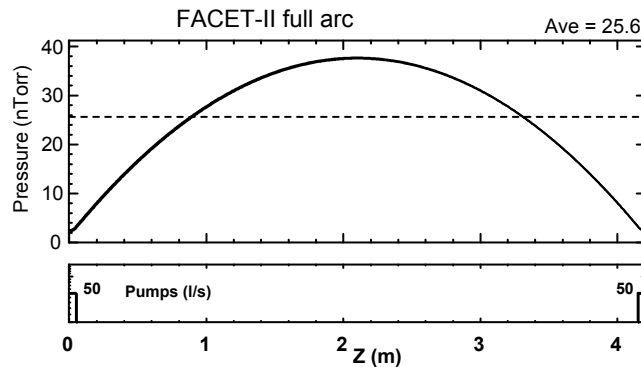


**Figure 8.30.** Plot of the arc vacuum with pumping only at the ends of the arc. The average pressure is about 26 nTorr.

To improve the pressure profile a vacuum pipe stub (4 cm dia. 10 cm long) is added to the center of the arc chamber and a pump attached to the end of the stub. Figure 8.31 shows the pressure profile of the first half of the arc (the other half is a mirror image). The pump speeds of the three pumps in this model are 50 l/s. Increasing the pump speed will lower the pressure.

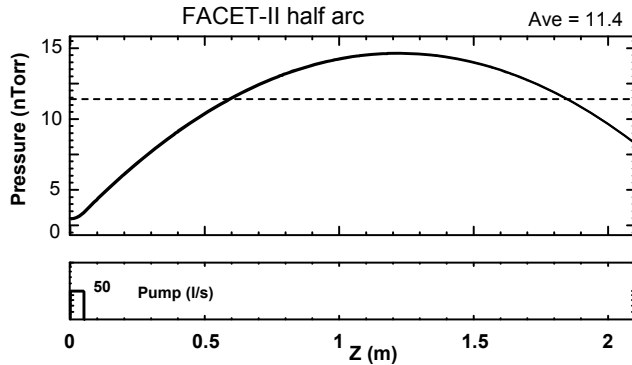


**Figure 8.31. Pressure profile of one half of the arc when a pump is added to the center point of the arc with a 10 cm pipe stub to the pump. The average pressure is 11.4 nTorr.**

One more improvement was tried where pumps were added to the arc at the 1/3 and 2/3 points. The results are summarized below in Table 8.16. The table also includes runs with higher pump speeds.

**Table 8.16. Results from various vacuum pumping scenarios for the arcs of the positron damping ring.**

Case	Description	Ave press nTorr
1	2 end pumps only (100 l/s) (Figure 8.30)	25.6
2	2 end + 1 center (50 l/s) (Figure 8.31)	11.4 11.4
3	2 end (100 l/s) + 1 at 1/3 & 2/3 pts (50 l/s)	5.8 7.5 5.8
4	2 end (100 l/s) + 1 at 1/3 & 2/3 pts (100 l/s)	5.2 6.7 5.2
5	2 end + 1 center (100 l/s)	9.4 9.4

In summary, an average pressure of 6 nTorr in the arc chambers can be achieved if 100 l/s pumps are placed at each end of the arc and at the 1/3 and 2/3 points. The pumps inside the arc are attached with a 10 cm long 4cm diameter pipe stub. This calculation does not presently account for an RF screen that might need to be placed at the junction to the main arc beam pipe. Such a screen will reduce the conductance to the pump located at the end of the stub. The pressure in the arc chamber will rise slightly but the effect should be less than 10%.

### 8.3.8.2 Straights

Next the pumping needed for the straights is considered. The RF expert [24] argues that anything less than 100 nTorr is OK for the RF cavity. However, the kicker structures for the damping ring need a

pressure that is less than 6 nTorr [25]. The following pumping scheme was developed based on the kicker requirements. Most of the beam pipe in the straight sections has a 5cm diameter, the same size as the current damping rings. However, the region between the septum and the kicker has a larger beam pipe diameter due to the larger size of the beam in this region and due to the orbit of the kicked beam. The diameter of the pipe between the septum and the kicker is 8 cm at the septum and through the quadrupole doublet. Then the pipe narrows down to a 3 cm diameter at the kicker. Also, in order to account for the extra surfaces that are inside the septum chamber, the thermal outgassing value for this pipe segment has been doubled to 0.2 nTorr (l/s)/cm<sup>2</sup>. The present septum magnet has a 440 l/s pump mounted at the center of the chamber and that pump will be located in the same place in the new damping ring. Figure 8.32 shows the pressure profile where 100 l/s pumps are installed upstream and downstream of the kicker segment and upstream and downstream of the RF cavity. This assumes no RF processing for the cavity. Processing should scrub the surfaces and hence the cavity vacuum should be lower than this estimate. There is also a 440 l/s pump in the center of the septum chamber as mentioned above. These pumps are all in addition to the previously mentioned arc pumps. The average pressure of the straight is just over 5 nTorr. The pressure at the kicker is about 4 nTorr and the pressure at the RF cavity is 10.5 nTorr.

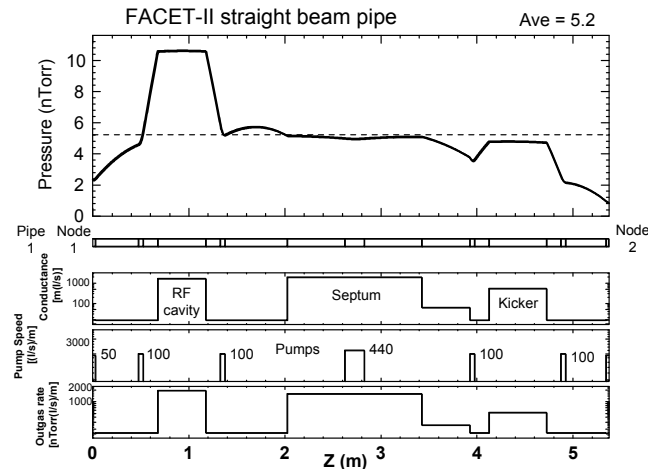


**Figure 8.32. Pressure profile of the PDR straight section. There are 2 100 l/s pumps on either side of the kicker and RF cavity. There is also a 440 l/s pump at the middle of the septum chamber.**

For case 3 in Table 8.16, the total number of pumps for the positron damping ring is 18. There are 16 100 l/s pumps and two 440 l/s pumps. The overall average base pressure for the entire ring is then about 5-6 nTorr.

### 8.3.9 Synchrotron Radiation

The beam energy of the damping ring is low (335 MeV). The bend field in the arc magnets is 1.44 T. The standard formula for synchrotron radiation gives a critical energy value of 108 eV. The ring circumference is 20.154 m. The go-around frequency is 14.885 MHz. The beam current for a bunch charge of  $2 \times 10^{10} e^+$  is 48 mA. This gives a synchrotron radiation power from the bends of 0.14186 W per cm of bending magnet length. The total length of the bending magnets in one arc is 244 cm so the total SR power is 34.6 W for each ring arc. This power is essentially spread all around the arc beam pipe which is 4.1 m long. So power per unit length is 8.4 W/m. This is a small number and can be considered to be negligible except that one may want to add an occasional cooling tube to portions of the arc chamber to

absorb the small power incident from the synchrotron radiation. The number of photons hitting the beam pipe surface is  $1.3 \times 10^{19}$  /s half of which have an energy below 10 eV. Nevertheless, there are probably enough photons to start to “scrub” the beam pipe so some initial commissioning time will likely be needed to let the SR photons “clean up” the beam pipe inner surface.

## 8.4 Positron Extraction and Compression

### 8.4.1 Overview

The Positron Extraction and Compression system (PEC) starts at the entrance of the PDR extraction kicker on the final extraction turn and ends at the positron injection point into the main linac in the final bend of the BC11 electron bunch compressor. In order to match with the electron compression scheme, this system must also compress the bunch length by a factor of ~10. Figure 8.33 gives a schematic of the PEC beamline. These tasks are achieved with the following four sub-systems:

#### 8.4.1.1 Vertical Inflector extraction from PDR.

With a linear footprint of ~9 m, the inflector extracts the beam from the damping ring at an angle of 136 mrad and raises the beam from the damping ring height by 94.1 cm to match the Linac beam height. Five quadrupole magnets provide beta matching whilst keeping the vertical dispersion reasonably small ( $|\eta_y| < 40$  cm). The extraction angle is chosen to cleanly extract the beam from the PDR, and the optical match is an optimal balance between keeping reasonably sized beta functions and keeping the dispersion function from becoming too large. The energy spread is small upon extraction from the PDR (<0.1%), so chromatic aberrations are not a problem in this section. Figure 8.34 shows the layout of this system in elevation view.

#### 8.4.1.2 Diagnostics section.

A 7 m diagnostics section is provided with a beam waist in the center for emittance measurement. Three OTR profile measurement devices will be placed across the diagnostic waist to provide fast emittance measurements and monitoring, and provide matching data to correct betatron errors from the PDR. The nominal minimum beam size at the second OTR is 130  $\mu\text{m}$ .

#### 8.4.1.3 Bunch compression (BC0).

A 2.1 m S-band accelerating section, operating at a design RF voltage of 18.6 MV, is operated at the RF zero-crossing to provide an energy chirp to the positron bunch. The bunch length is compressed across a vertical 4-bend (360 mrad per bend) chicane (BC0) providing a compression factor of  $R_{56} = -300$  mm. The chicane is designed in the vertical plane to conserve physical space in the beam tunnel. Two “dispersion-tweaker” quadrupole magnets are provided within the chicane for dispersion correction control. An adjustable gap collimator is located in the center section of the chicane for halo collimation or reduction of longitudinal non-linearities in the high-dispersion bunch tails. This can help to improve the quality of the longitudinal bunch profile throughout the machine and maximizes the possible delivered peak positron beam current.

#### 8.4.1.4 Horizontal dogleg injection.

In a z-length of 20 m, this horizontal dogleg injects the positron beam into the main FACET-II beamline at a horizontal angle of 94 mrad, matching the BC11 bend angle. The final BC11 bend magnet is shared with the electron beam. Five quadrupole magnets provide beta function matching into the main beamline and maintain a manageable horizontal dispersion function given the required injection angle and beam energy spread. After the energy chirp is added, the higher energy spread beam (compared with the vertical dogleg) requires chromatic aberration control, which is achieved by using 2 sextupole magnets in dispersive regions of the dogleg.

## 8.4.2 Beam Parameters

This system is matched, given the damping ring beam parameters at the extraction point, and provides the required positron (and electron) matching conditions at the insertion point into the main FACET-II beamline. The matched twiss parameters are shown below in Figure 8.35.

**Table 8.17. Beam parameters for positron extraction and compression system from the center of the PDR extraction septum on extraction turn, to injection into the main linac in the final bend of the electron BC11 chicane bend. Initial parameters include beam dynamics calculations performed for the damping ring (e.g. IBS growth of emittance as shown in Figure 8.26).**

Parameter	Symbol	Value	Range	Unit
Beam Energy	$E_0$	335		MeV
Initial rms Bunch Length	$\sigma_z$	3.55	3.5-4	mm
Final rms Bunch Length	$\sigma_z$	0.26	0.35-0.41	mm
Final E-z chirp	$\alpha_z$	0.14	0-0.39	
Initial rms Energy Spread	$\sigma_E/E$	0.076	0.07-0.081	%
Final rms Energy Spread	$\sigma_E/E$	1.1	0.5-1.1	%
Initial Transverse Emittance	$\gamma\epsilon_{x,y}$	7.6	10.0	$\mu\text{m}\cdot\text{rad}$
Initial Bunch Charge	Q	1	1-2	nC

## 8.4.3 Layout and Optics Design

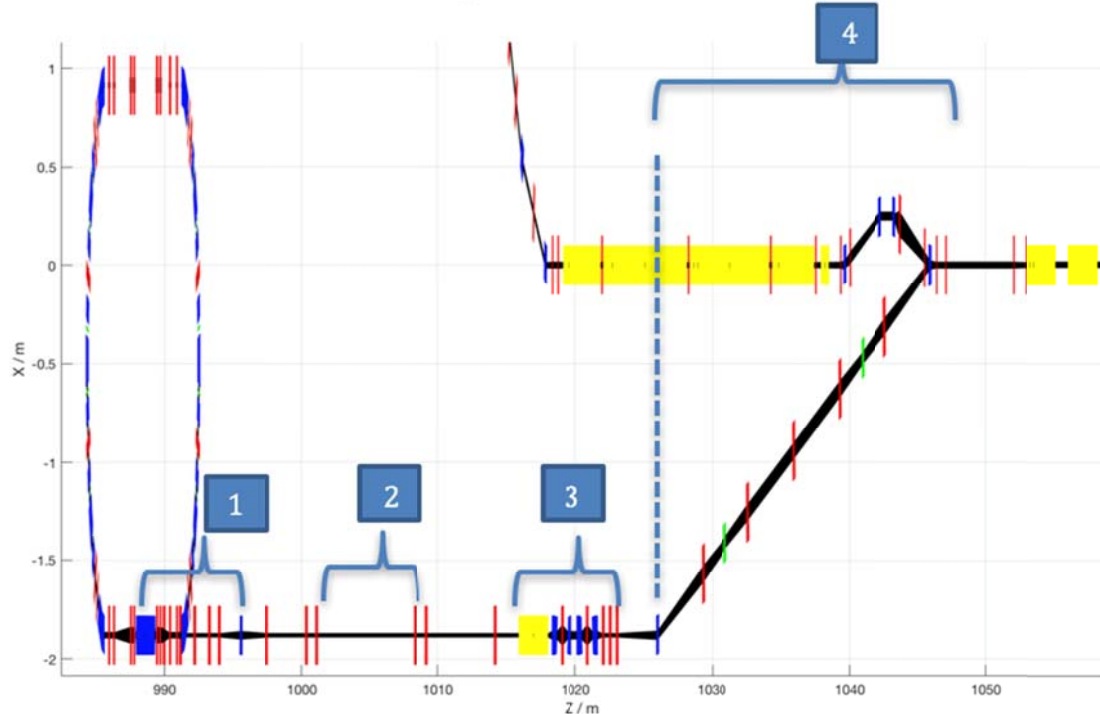


**Figure 8.33. Plan layout view of Positron Extraction and Compression system (PEC). Yellow indicates RF, blue dipoles, red quadrupoles, green sextupoles. Coordinate system is relative to SLC linac (x/y) and SLC z-reference. The numbered subsections refer to the Sections 8.4.1.1 to 8.4.1.4.**

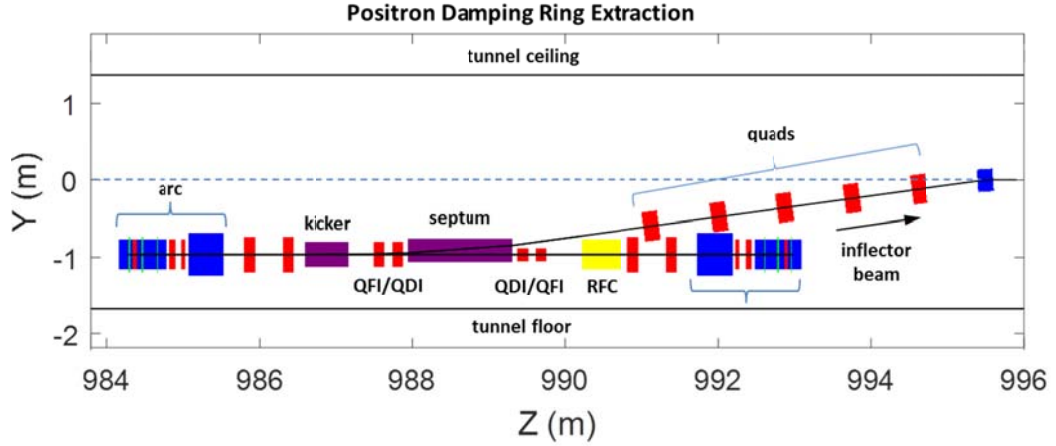


**Figure 8.34.** Vertical extraction from the Damping Ring. RFC is the RF cavity. The QFI and QDI quadrupoles in the ring between kicker and septum are large-bore magnets through which the extracting beam passes off-axis; the QDI and QFI quadrupoles between septum and RFC are narrow-frame “Collins”-type magnets that the extracting beam passes above.

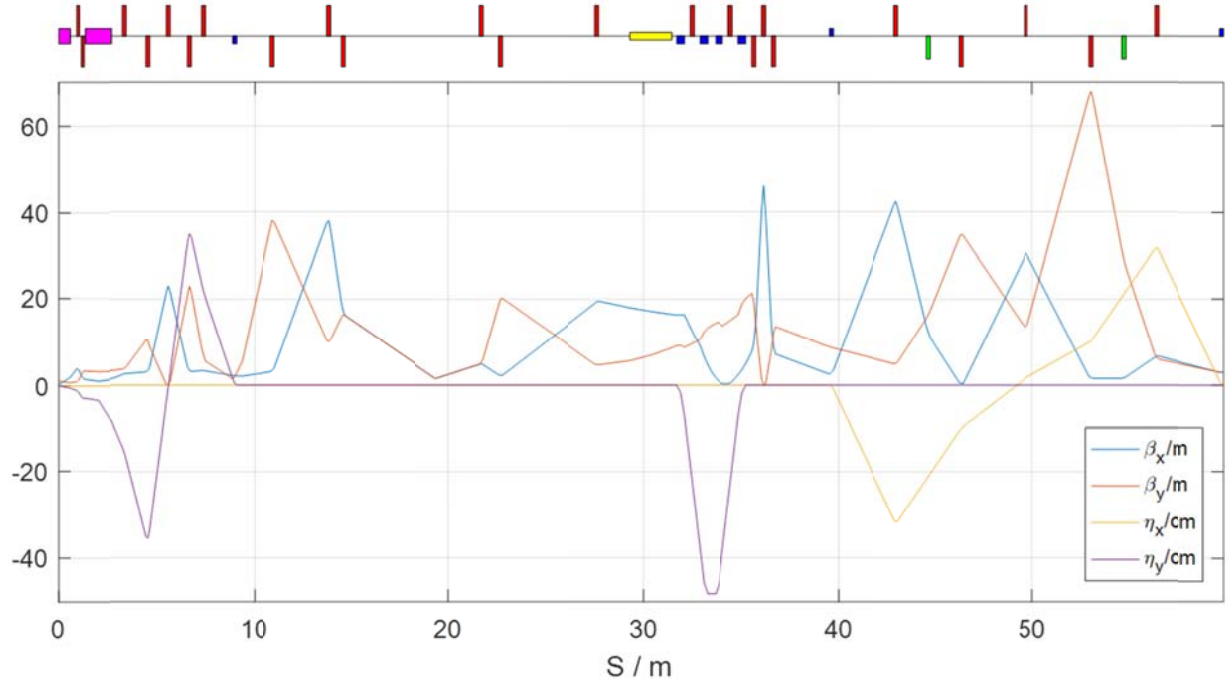


**Figure 8.35.** Twiss parameters across the PEC system.

#### 8.4.4 Beam Dynamics

Using a 6D tracking code (*Lucretia*), a 200K macro-particle representation of the positron bunch was tracked through the lattice including ISR, CSR and LSC effects as well as wakefield effects in the cavity. The final tracked longitudinal and transverse phase space of the positron beam after BC11 is shown in Figure 8.36. The sextupole magnets were set to minimize transverse emittance growth through the final

horizontal dogleg due to chromaticity and second-order dispersion. The emittance growth is controlled to  $\sim 30\%$  ( $>100\%$  without sextupole magnets).

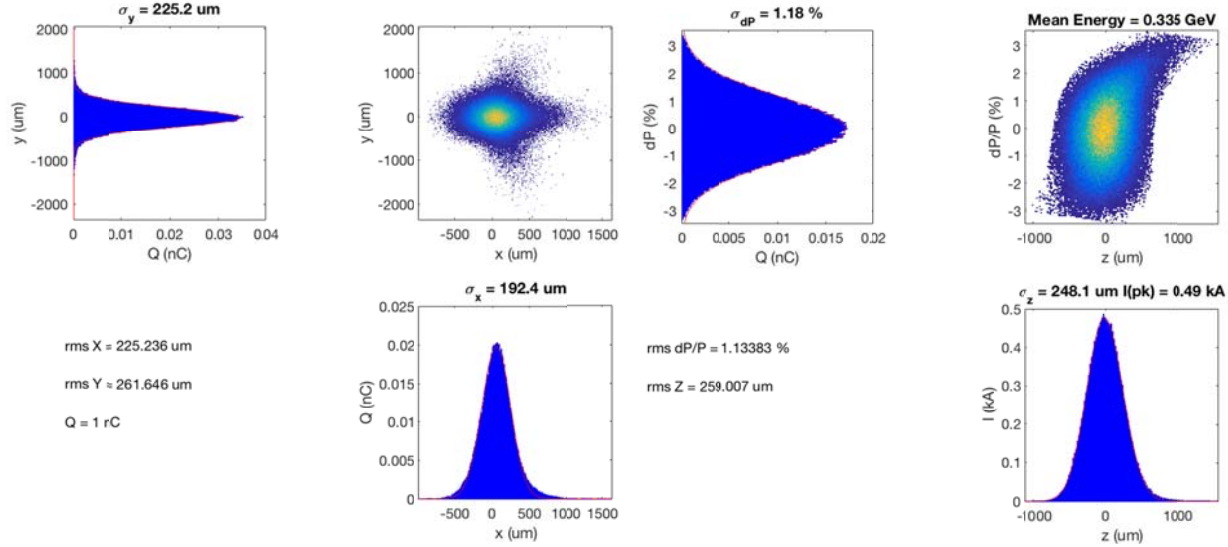


**Figure 8.36.** Transverse and longitudinal phase-space of tracked macro-particle bunch at exit of the BC11 final bend for the baseline design parameters.

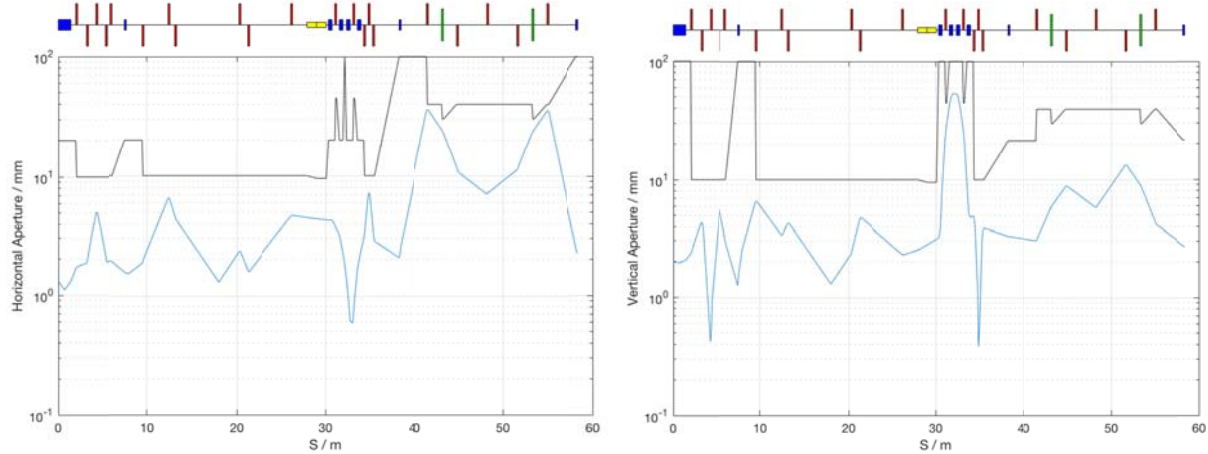


**Figure 8.37.** Required minimum horizontal and vertical magnet apertures (black) compared to tracked X10 rms beam sizes (blue) for the baseline design parameters.

#### 8.4.5 Magnets & RF

The PEC section consists of 21 quadrupole magnets of 2 engineering types, 2 sextupole magnets of 1 type, and 7 dipole magnets of 3 types (one of which is shared with the BC11 system). One S-band structure for providing bunch compression energy chirp.

## 8.4.6 Quadrupoles

**Table 8.18. Quadrupole parameters.**

Deck Name	Engineering Type / subsection	Effective Length / m	Design Int. Strength / T	Max. Int. Strength / T	Design Pole Tip Field / T	Max Pole Tip Field /  T	Aperture (radius) / mm
QPEC1	A	0.2	0.5195	5	0.0260	0.25	10
QPEC2	A	0.2	-1.6956	5	-0.0848	0.25	10
QPEC3	A	0.2	1.4317	5	0.0716	0.25	10
QPEC4	A	0.2	-1.7807	5	-0.0890	0.25	10
QPEC5	A	0.2	0.3451	5	0.0173	0.25	10
QPEC6	A	0.2	-0.6500	5	-0.0325	0.25	10
QPEC7	A	0.2	0.8291	5	0.0415	0.25	10
QPEC8	A	0.2	-0.5853	5	-0.0293	0.25	10
QPEC9	B	0.2	0.0000	1	0.0000	0.225	45
QPEC10	B	0.2	0.0000	1	0.0000	0.225	45
QPEC11	A	0.2	0.7822	5	0.0391	0.25	10
QPEC12	A	0.2	-0.7228	5	-0.0361	0.25	10
QPEC13	A	0.2	0.2079	5	0.0104	0.25	10
QPEC14	A	0.2	-2.3673	5	-0.1182	0.25	10
QPEC15	A	0.2	2.9298	5	0.1465	0.25	10
QPEC16	A	0.2	-2.6965	5	-0.1348	0.25	10
QPEC17	B	0.2	0.5752	1	0.1044	0.225	45
QPEC18	B	0.2	-0.3507	1	-0.0636	0.225	45
QPEC19	B	0.2	0.6256	1	0.1135	0.225	45
QPEC20	B	0.2	-0.4310	1	-0.0782	0.225	45
QPEC21	B	0.2	0.5722	1	0.1038	0.225	45

## 8.4.7 Sextupoles

It is assumed that each sextupole is mounted on a remotely controllable motion stage, capable of +/- 2mm motion in x/y with 5um precision.

**Table 8.19. Sextupole parameters.**

Deck Name	Engineering Type / subsection	Effective Length / m	Design Int. Strength / T.m^-1	Max. Int. Strength /  T.m^-1	Design Pole Tip Field / T	Max Pole Tip Field /  T	Aperture (radius) / mm
SPEC1	A	0.2	-12.0000	100	-0.0540	0.225	30
SPEC2	A	0.2	-0.7897	100	-0.0036	0.225	30

## 8.4.8 Dipoles

**Table 8.20. Dipole magnet parameters.**

Deck Name	Engineering Type / subsection	Effective Length / m	Design Int. Strength / T.m	Max. Int. Strength /  T.m	Design Pole Tip Field / T	Max Pole Tip Field /  T	Aperture (radius) / mm
BPEC2	A	0.2	0.15180	0.5	0.7590	2.500	20
BPEC3	B	0.4	-0.40228	0.5	1.0057	1.250	20
BPEC4	B	0.4	0.40228	0.5	1.0057	1.250	20
BPEC5	B	0.4	0.40228	0.5	1.0057	1.250	20
BPEC6	B	0.4	-0.40228	0.5	1.0057	1.250	20
BPEC7	C	0.2	-0.10504	0.2	0.5157	1.000	20
BPEC8	C	0.2	0.10504	0.2	0.5157	1.000	20

## 8.4.9 RF

**Table 8.21. RF structure parameters. Phase is with respect to on-crest acceleration (phase > 0 is defined as early with respect to synchronous particle). Voltage is un-loaded cavity gain.**

Deck Name	Freq. / MHz	Length / m	V / MV	Phase / deg	Aperture / mm
LPEC1	2856	2.1336	18.6	-90	9.5

## 8.5 Instrumentation, Diagnostics and Feedback

A standard suite of linac/transport line diagnostics will be installed in each of the functional areas of the positron system. The function of these devices – BPMs, toroids, profile monitors, bunch length monitors – is described in detail in Section 6.8 (Linac Diagnostics). In general, BPMs will be refurbished stripline BPMs retrieved from Sector 0-10, except for in the damping ring itself, where the tight conditions and aperture considerations make button-style pickups necessary.

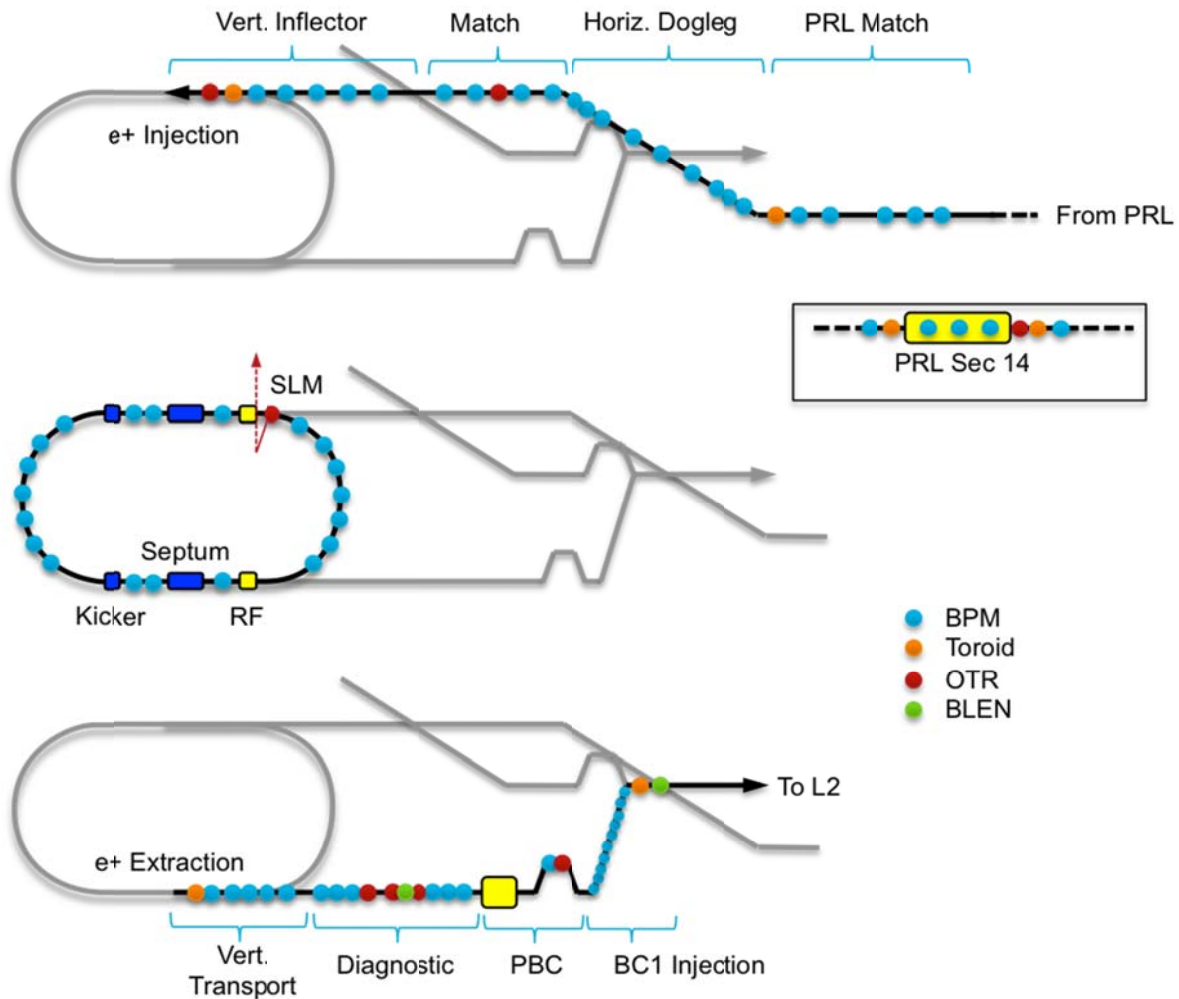


**Figure 8.38. Overview of positron system diagnostics.** Top: PRL and PDR injection; inset: accelerator structures from Sector 14; middle: damping ring; bottom: PDR extraction and PEC system. Yellow boxes indicate RF cavities or structures. Locations of diagnostics approximate only.

Toroids and ceramic gap monitors will be salvaged as well; YAG and OTR screens will receive all new hardware modeled after the diagnostics in use at FACET. OTR screens are chosen over wire scanners for beam profile measurements as the repetition rate for positrons is only 5 Hz. COTR production in these screens is not expected to be significant at the low peak currents before the linac. With the exception of the BPMs and toroids in the positron return line, EPICS controls and infrastructure will be used for all new installations.

**Table 8.22. Counts of standard diagnostics for positron system.**

New Devices	PRL	PRL	PDR	PEC
BPM	5	23	22	22
Toroid	2	1	0	2
OTR/YAG	1	2	0	4
BLEN	0	0	0	2

### **8.5.1 PRL Diagnostics**

The existing BPMs in the PRL will be retained as-is and used via the legacy controls. The exception is at Sector 14, at the 125 MeV acceleration section, where 5 additional BPMs will be installed. One will be added in each of the new upstream/downstream doublet quadrupoles and one in each of the triplets between the accelerator structures in order to center the beam in the small aperture of the disk-loaded waveguide. An insertable OTR profile monitor just upstream of the first accelerating structure will allow quad-scan measurement and correction of any incoming beta mismatch which could compromise the beam size and lead to losses. Toroids upstream and downstream of the accelerator structure will be used to monitor for beam loss.

The line connecting the PRL to the PDR has 14 BPMs in the horizontal dogleg and 9 in the vertical inflector; these will be refurbished stripline BPMs read out through new EPICS processors. An OTR profile monitor will be located in the FODO transport between the horizontal and vertical sections for quad-scan emittance measurement. Just upstream of the permanent magnet quadrupole (PMQ) triplet is a toroid for charge monitoring and another OTR screen for energy spread measurement and tuning.

### **8.5.2 Damping Ring Diagnostics**

Twenty-two BPMs are located in the damping ring as near as possible to the sextupole magnets, as space constraints due to the close proximity of magnet yokes and coils limit the BPM placement. Button-type pickups, rather than striplines, will be used to conserve aperture for the injected beam. Bandwidth limitations of the standard LCLS linac processors cause the signal to ring on a time scale of 2-3 revolutions of the stored damping ring beam. The necessary modifications to the BPM electronics to allow measurement of single turns is an area that requires further study.

Measurement of the betatron and synchrotron tunes will be done by splitting the signal from selected BPM pickups at high-beta (or high-dispersion for  $v_s$ ) locations into a networked spectrum analyzer which will be relocated from the existing NDR to Sector 10.

A synchrotron light monitor will be installed just after the final bend magnets at the beginning of the extraction straight. This consists of an in-vacuum mirror which reflects the visible portion of the synchrotron radiation spectrum through a quartz vacuum window towards the ring center. This synchrotron light will then be collected by a lens system and transported in an optical transport tube up a linac penetration to the laser prep room located adjacent to the injector laser room on the north side of the Klystron Gallery. Imaging this beam into a standard gated camera allows study of the transverse stability and damping during the store. Further, splitting the light into an optical streak camera allows for measurement of the longitudinal damping and extracted bunch length. A simplified schematic is shown in Figure 8.39.

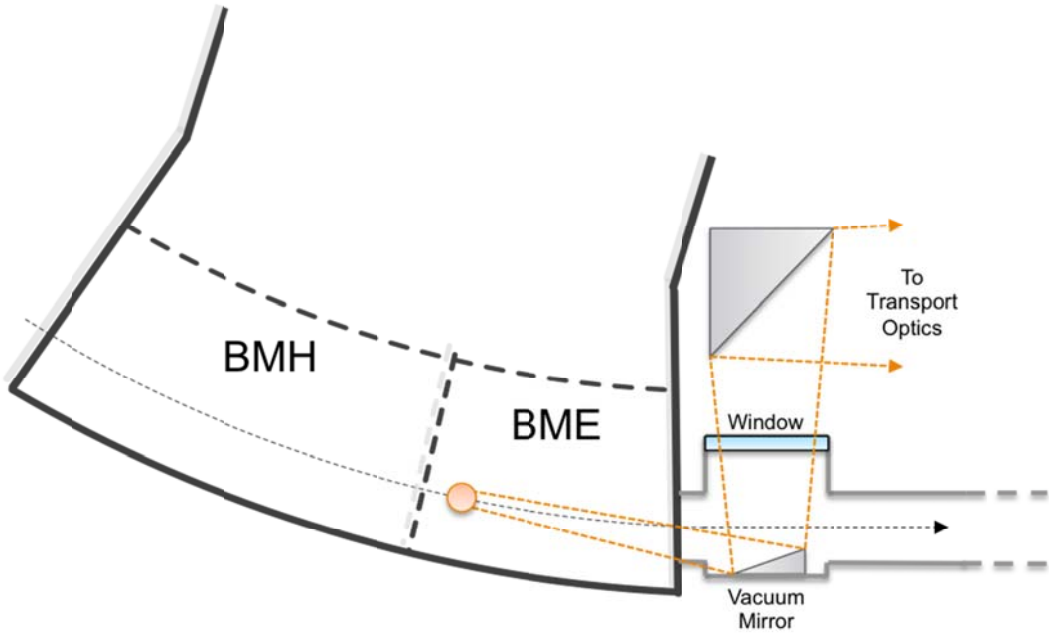


**Figure 8.39. Location of synchrotron light monitor window at arc/straight boundary.**

### 8.5.3 PEC Diagnostics

The PEC has 22 BPMs in total: 5 in the vertical extraction transport quads, 6 in the quadrupole triplets upstream and downstream of the diagnostic section, 1 for energy measurement at the center of the bunch compressor, and 10 in the horizontal dogleg into BC11 (8 in each quad plus 2 in each sextupole). Toroids for measuring the beam charge are located directly after the ring extraction and downstream of the compressor chicane. Like in the injection line, these BPMs and toroids will be refurbished from existing linac hardware and read out with new EPICS controls.

The 7-meter diagnostic drift section contains 3 OTR screens spaced symmetrically about the beam waist, allowing for fast multi-screen measurements of the extracted beam emittance. Another OTR screen at the midpoint of the bunch compressor will be installed for energy spread measurements and setting the adjustable collimator jaws. Ceramic gap bunch length monitors will be located upstream and downstream of the bunch compressor, allowing monitoring of the incoming and outgoing bunch lengths. These bunch length monitors will be calibrated with the TCAV1 transverse deflector located just after BC11 (See Chapter 6).

### 8.5.4 Feedback Systems

To correct for slow diurnally-driven drift, four-corrector ( $x, x', y, y'$ ) steering feedback loops modeled after the SLC design will be implemented at the end of the PRL, just after PDR extraction, and just before BC11 injection. If necessary, the trajectory in the ring may be stabilized by iterative application of a standard steering algorithm such as SVD or 1-to-1 over a several-minute time scale.

Energy feedback for the westbound positron beam will monitor the dispersive orbit in the vertical inflector at the end of the PRL line and vary the amplitude of the 14-8 klystron. For the extracted beam,

the energy and bunch length monitoring in the PEC chicane will feed into a “2x2” feedback that adjusts the phase and amplitude of the 2.1-m compressor klystron in a coupled fashion. This will have identical function to the BC11 – L1S feedback system for the electron beam.

These feedbacks will be implemented in the same fashion as at FACET, typically Matlab or python scripts reading inputs and writing outputs over EPICS channel access. The high-performance dedicated feedback networking used at LCLS is not applicable due to the relatively slow 5 Hz repetition rate.

- 
- 1 “A possible design for the NLC e+ source”, H. Braun et. Al., EPAC 1992
  - 2 M. Sands, “The physics of electron storage rings, an introduction,” SLAC Report No. SLAC 121, 1970.
  - 3 L.C. Teng, Fermilab Report No. TM-1269, 1984.
  - 4 Paul Emma and Tor Raubenheimer, “Systematic approach to damping ring design,” Phys. Rev. ST, Accel. Beams, **4**, 021001 (2001).
  - 5 F. Antoniou and Y. Papaphilippou, “Analytical considerations for linear and nonlinear optimization of the theoretical minimum emittance cells: Application to the Compact Linear Collider predamping rings,” Phys. Rev. ST, Accel. Beams, **17**, 064002 (2014).
  - 6 H. Grote and F.C. Iselin, “The MAD Program (Methodical Accelerator Design) Version 8.15,” CERN/SL/90-13 (AP), (1990).
  - 7 M. Berz, “Differential Algebra Description of Beam Dynamics to Very High Order,” Part. Accel. **24**, 109 (1989).
  - 8 E. Forest, M. Berz, and J. Irwin, “Normal Form Methods for Complicated Periodic Systems: A Complete Solution Using Differential Algebra and Lie Operators,” Part. Accel. **24** 91 (1989).
  - 9 Y. Cai, M. Donald, J. Irwin, Y. Yan, “LEGO: A Modular Accelerator Design Code,” SLAC-PUB-7642, August (1997).
  - 10 J.D. Bjorken and S.K. Mtingwa, “Intrabeam Scattering,” Part. Accel. **13**, 115 (1983).
  - 11 S. Nagaitsev, “Intrabeam scattering formulas for fast numerical evaluation,” Phys. Rev. ST, Accel. Beams, **8**, 064403 (2005).
  - 12 K. Bane, Y. Cai, and G. Stupakov, “Threshold studies of the microwave instability in electron storage rings,” Phys. Rev. ST, Accel. Beams, **13**, 104402 (2010).
  - 13 S. Krinsky, Brookhaven Report No. 75019-2005-IR, (2005).
  - 14 A. Wolski {\it et al.}, LBNL Report No. 59449, (2006).
  - 15 K. Ohmi, PRE65, 016502 (2001).
  - 16 Suetsugu et al., Journal of Vacuum Science & Technology A21, 186 (2003).
  - 17 K. Ohmi, PRL75, 1526 (1995).
  - 18 M. Furman, G.R. Lambertson, Proceedings of MBI97 (KEK Report, No.97-17), p. 170
  - 19 SLAC-R-1067, FACET-II Conceptual Design Report
  - 20 M. Johansson, “SLAC FACET-II Positron Damping Ring Magnet Design”, Proc. IPAC16, Busan Korea, 2016.
  - 21 V. N. Litvinenko et al., “Performance of Achromatic Lattice with Combined Function Sextupoles at Duke Storage Ring”, <http://accelconf.web.cern.ch/AccelConf/p95/ARTICLES/RAB/RAB22.PDF>.
  - 22 M. Fedurin et al., “Multipole Design for CAMD Storage Ring”, Proc. 2005 Particle Accelerator Conference, Knoxville, Tennessee, 2012.
  - 23 Sullivan, M., “A Method for Calculating Pressure Profiles in Vacuum Pipes” SLAC-PEP-II-AP-NOTE-6-94, Mar 1994. 8pp.
  - 24 Private conversation with David Steele
  - 25 The present vacuum limit for the kicker structure in the damping ring is 6 nTorr.

# 9 Final Bunch Compression and Final Focus

---

## Technical Synopsis

The existing “W-Chicane” in Sector 20 (BC20) provides the 3<sup>rd</sup> and final stage of bunch compression for either electron or positron bunches depending on the polarity of the magnets. Additionally, the existing Sector 20 optics contains: 5 sets of quadrupole magnets to form a final focus system (FFS) for demagnification of the final bunches to <20 μm in both dimensions; an extended experimental area to use the focused beam; and finally a vertical bend spectrometer for experimental use before the main dump. BC20 compresses the beam to high peak-currents in the experimental area (>10 kA for electrons, >5 kA for positrons) with experimental requirements on the bunch length of <20 μm rms.

Sextupole magnets placed in dispersive locations of BC20 control chromaticity and second-order dispersion caused by both the chicane and the final focus magnets. The sextupoles sit atop movers which can adjust their positions in 3 DOF for dispersion, coupling and waist aberration corrections at the IP. Simulations have been made which calculate emittance dilution in the chicanes due to anomalous momentum dispersion as well as geometric and chromatic aberrations and SR effects. Diagnostics, correction techniques, and feedback systems have also been incorporated into the design.

---

### 9.1 Overview

Sector 20 contains the final bunch compression stage (BC20) for both the electron and positron bunches. BC20 has quadrupole magnets included to generate a positive R<sub>56</sub> (defined for a beam coordinate system with the bunch head at z < 0), whilst also providing other measurement and corrective functions before delivery of the beam to the experimental IP area. The layout of this “W-chicane” is unchanged from the FACET experiment and it will be operated in the same way.

Sextupole magnets are included in BC20 which provide chromatic and second-order dispersion correction targeted at the experimental waist location to minimize the focused transverse spot sizes. Mover systems under the sextupoles also provide x and y dispersion correction, coupling and waist adjustment control.

A vertical wiggler section is included in BC20 (3 vertical bend magnets) to generate a vertical synchrotron radiation stripe for energy profile measurements.

An X-band (11.424 GHz) transverse, deflecting mode cavity in BC20 can measure the fully compressed bunch length.

The FACET final focus system includes 8 quadrupole magnets for final demagnification of the beam to form the small-beta waist used by experiments. During FACET, the final focus system was designed to generate beta functions at the IP with a 10:1 horizontal: vertical ratio. At FACET-II, we can provide more round beams in the x/y plane to the experimental IP. To provide additional matching capability to enable equal beta functions at the IP, an additional pair of power supplies is needed to independently power 2 extra magnets in the QFF2 and QFF4 magnet strings. The final focus system must accommodate the requirements of multiple users at different locations in the

experimental region and thus maintain the flexibility of the system used at FACET to deliver different waist sizes to different z-locations along the experimental table. Typically beta functions in the range  $\sim$ 0.1-5 m, across a range in z of  $\sim$ +/- 3.5 m are requested.

Finally, the spectrometer after the experimental region consists of a vertical bend magnet and three quadrupoles. This is the same system used during FACET operation.

## 9.2 Beam Parameters

The sector 20 optics is designed to deliver high peak-current (bunch length  $<$  20  $\mu\text{m}$ ) at the experimental area with an incoming beam of 20  $\mu\text{m}\text{-rad}$ , or less. Typical experimental requirements are for transverse beam sizes  $<$ 20  $\mu\text{m}$  in both dimensions. The optical matching in the design is highly constrained and must satisfy several requirements outlined below:

- Chicane compression ratios set in the middle of their operating range for maximum flexibility when commissioning the beamline ( $R_{56} = +5\text{mm}$ ).
- Minimize beta functions through chicane, which past experience at FACET has shown to be highly desirable for stable operation. The optics going back into Sector 18 is manipulated to help with this and other matching requirements.
- Minimize CSR effects. The horizontal beta functions in the final bend magnet are matched to be small in both planes with a waist close to the final bend exits which helps to mitigate CSR growth effects in both electron and positron beams.
- Closed dispersion at exit of chicanes.
- Correct horizontal and vertical chromaticity at the experimental IP waist.
- Minimize second-order horizontal dispersion at the IP waist.
- Enable effecting sextupole-mover based multi-knobs for dispersion, coupling and waist control.
- Waist at user-specified region in experimental area downstream of final focus system. A beta function of 50 cm is selected for the baseline design, typical user requested values during FACET operations ranged from 0.1-5 m.

Table 9.1 below shows pertinent beam parameters for this beamline section. Note that the final beam phase space is considerably non-Gaussian in shape due to both CSR and non-perfect cancellation of both second-order dispersion and chromaticity at the IP waist location. The calculated beam sizes are from Gaussian fits to the core of the beam at the IP waist which is typically the most informative measure of interest to FACET experimenters.

**Table 9.1. Beam parameters for electron and positron beams in BC20 and final focus system. Initial parameters are at the entrance to the first bend magnet of the chicane, final parameters are quoted at the default IP waist location at the entrance to the E200 experiment plasma volume.**

Parameter	Symbol	Baseline Design	Range	Unit
Beam Energy	$E_0$	10.0	4.0-13.5	GeV
IP Twiss Parameters	$\beta_x / \alpha_x$	0.5 / 0	0.1-5 /0	m
Initial Bunch Length (rms) / peak Current	$\sigma_z / l_{pk}$ (e-) $\sigma_z / l_{pk}$ (e+)	96 / 5 97 / 3		$\mu\text{m} / \text{kA}$
Final Bunch Length / peak Current	$\sigma_z / l_{pk}$ (e-) $\sigma_z / l_{pk}$ (e+)	2 / 72 16 / 6	1-20 / 10-130 16-20 / 6-15	$\mu\text{m} / \text{kA}$
rms relative Energy Spread	$\sigma_E/E$ (e-) $\sigma_E/E$ (e+)	1.4 0.7	0.4 – 1.6 0.5 – 1.5	%
rms Transverse Core Size at IP Waist	$\sigma_x / \sigma_y$ (e-) $\sigma_x / \sigma_y$ (e+)	18 / 12 16 / 16	6 - 20 10 - 20	$\mu\text{m}$
Bunch Charge	Q (e-) Q (e+)	2 1	2-5 1-2	nC
Chicane compression coef.	$R_{56}$	5	-10 - +10	mm

### **9.3 Layout and Optics Design**

Figure 9.1 shows a schematic layout of Sector 20 including BC20, the final focus optics, experimental area and vertical energy spectrometer. Figure 9.2 shows the design optics functions for this region. Note beta functions are kept small at the exit of the chicane to help to minimize CSR effects. The beta functions in the body of each chicane are kept as small as possible while maintaining compatibility with the required dispersion functions to generate a positive  $R_{56}$  and the need to set the entrance/exit parameters to the chicanes.

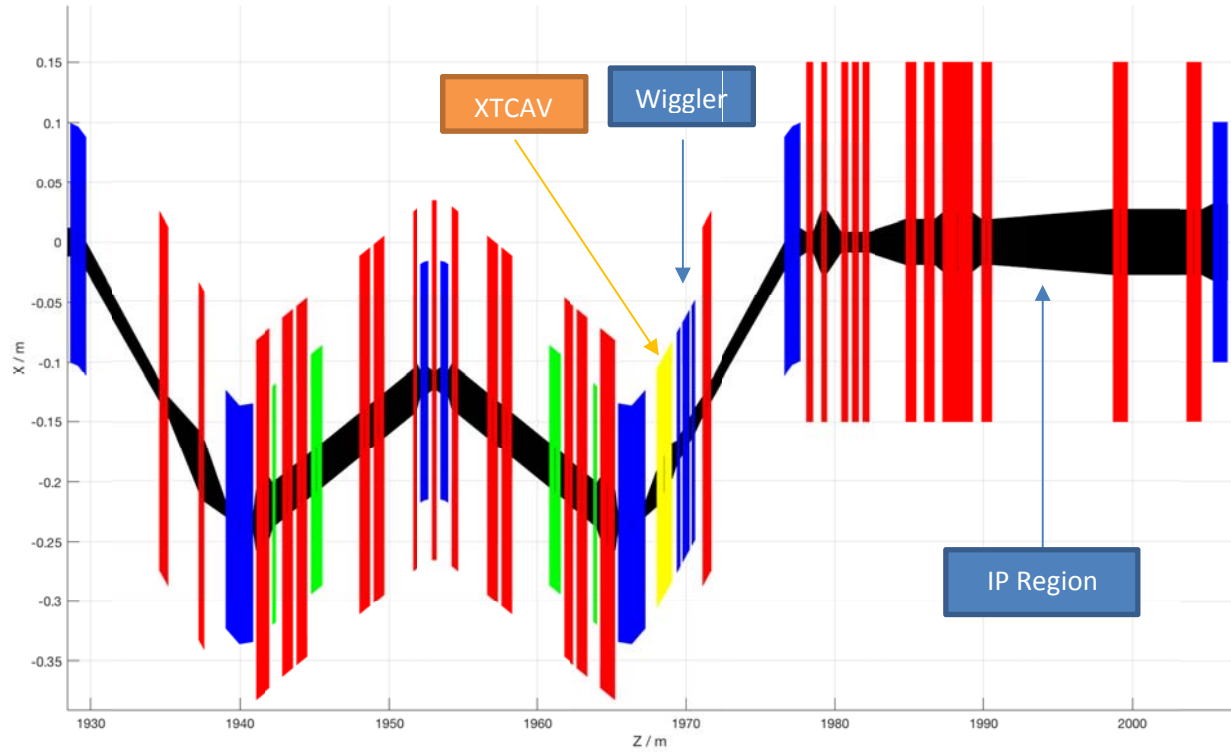


**Figure 9.1.** Plan layout view of sector 20 magnets, including BC20 horizontal chicane, final focus and vertical energy spectrometer. Yellow indicates x-band RF TCAV, blue dipoles, red quadrupoles, green sextupoles. Co-ordinate system is relative to SLC linac (x) and SLC z-reference.

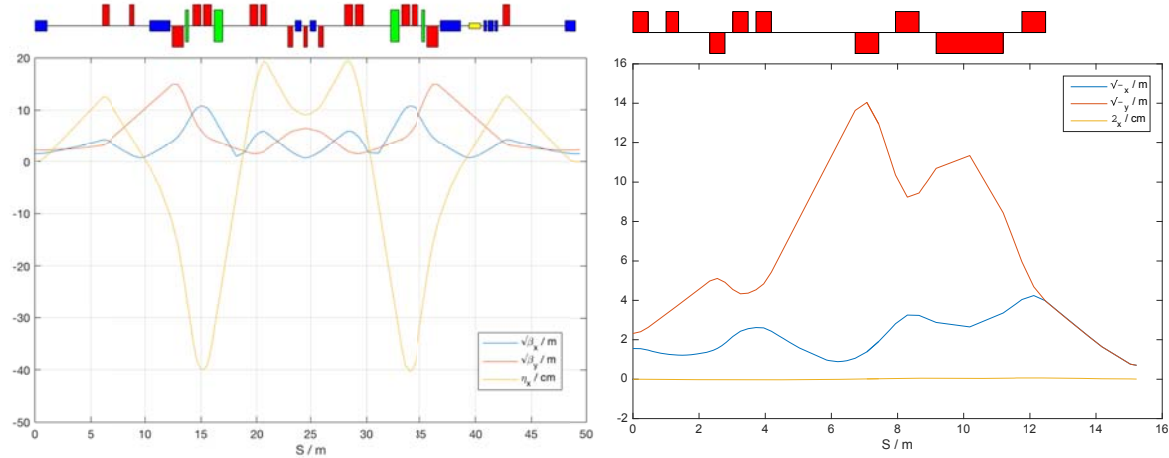


**Figure 9.2.** Twiss parameters throughout Sector 20, including BC20 and final focus systems. The IP waist is at the location of the plasma chamber experiment (E200). The left plot shows BC20, the right plot follows on immediately from the BC20 optics and shows the final focus system, where the IP is on the far right of the plot.

## 9.4 Beam Dynamics

Using a 6D tracking code (*Lucretia*), a 200k macro-particle representation of the electron and positron bunch is tracked through the entire FACET-II machine lattice including ISR, CSR and longitudinal space charge (LSC) effects as well as wakefield effects in the linac cavities. See Section 6.7 for more details of the beam tracking simulation. The longitudinal beam profiles at the end of L3 before BC20 and at the experimental IP are shown in Figure 9.3 for electrons and for positrons. The focused transverse beam profiles at the experimental IP waist are shown in Figure 9.4 for electrons and for positrons.

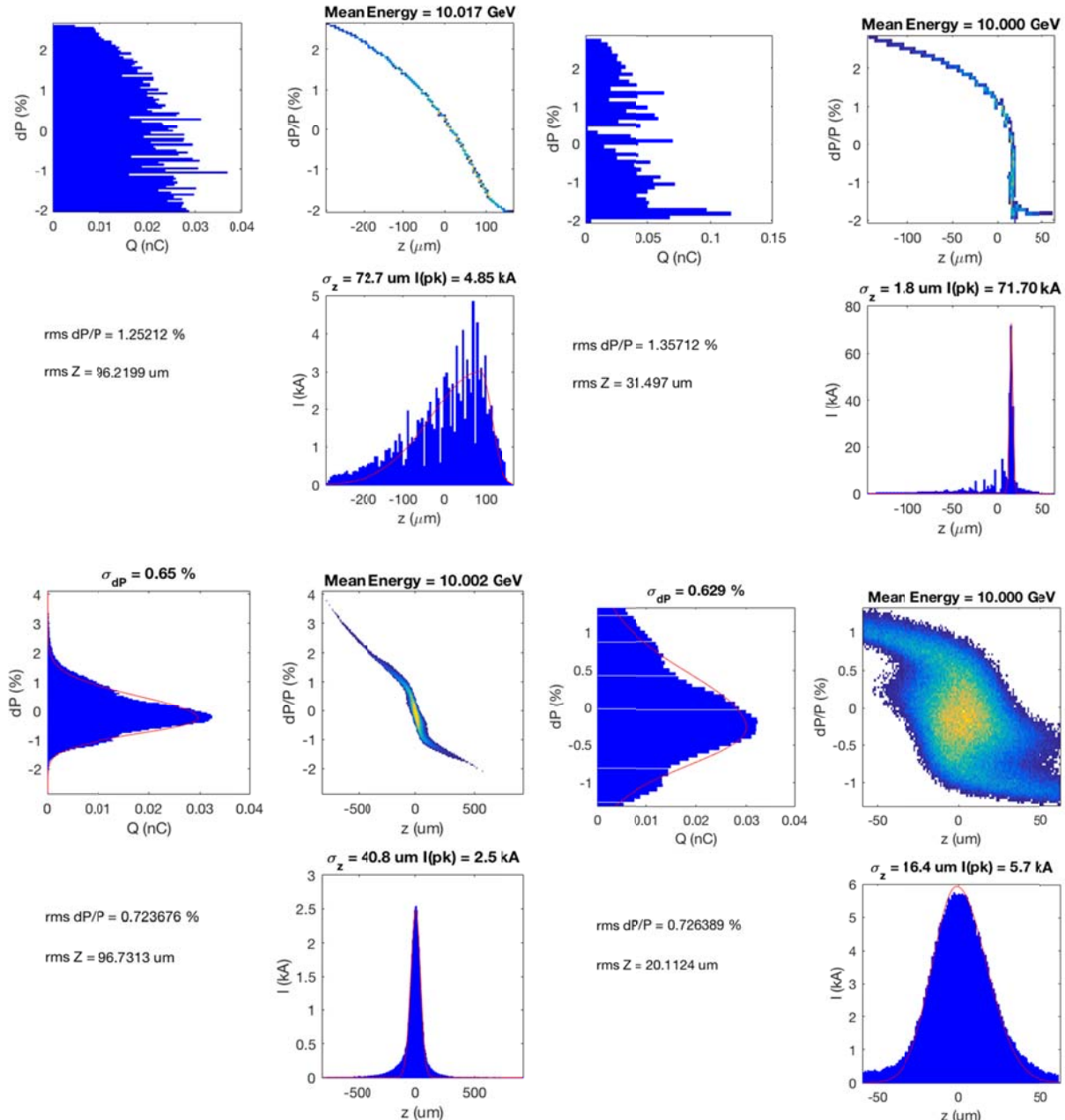


**Figure 9.3. Longitudinal phase space before (left) and after (right) the BC20 chicane. Electron beam tracking results shown on the top row, positron tracking results on the bottom.**

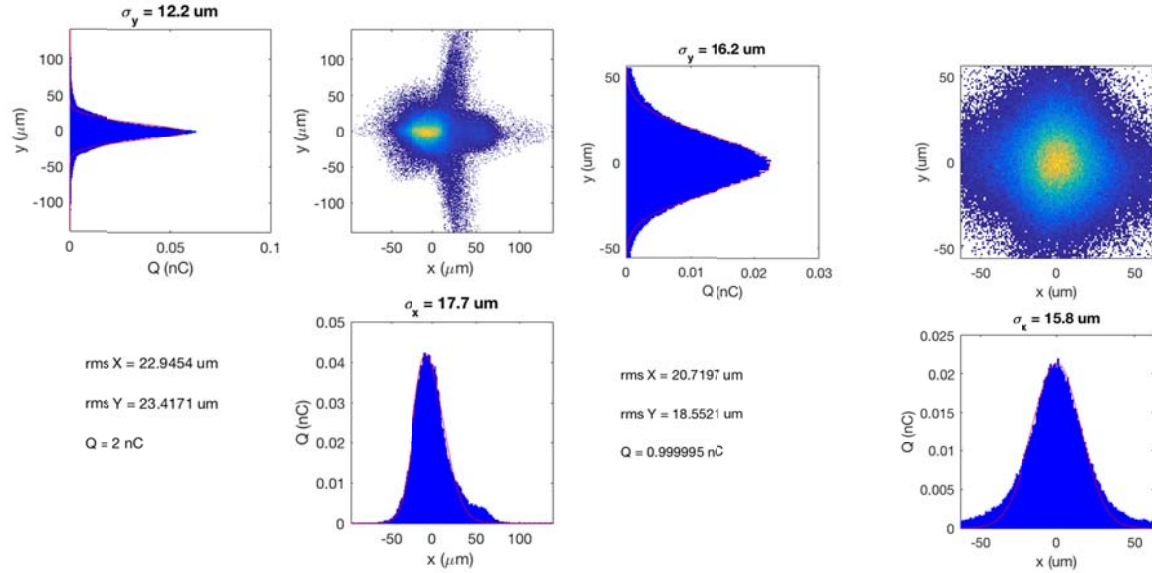


**Figure 9.4. Transverse phase space at IP waist location after final focus. Electron bunch is shown on the left, positron bunch on the right. Tracking results are for the baseline parameter design with  $\beta^* = 0.5$  m optics matching.**

The final focus and spectrometer systems are identical to those currently in use at FACET. The only change required for FACET-II operation is to allow the quadrupole pairs of QFF2 and QFF4 to have independently controllable power supplies. This is due to a greater required matching flexibility imposed by the desire to have round beams (equal beta functions) at the IP unlike at FACET which had a ~10:1 transverse emittance ratio.

## 9.5 Instrumentation, Diagnostics and Feedback

The existing FACET electron beam diagnostics located in the BC20 chicane and experimental area will be retained and used as they currently are in FACET.

Three wiresscanners are currently installed, interspersed with the experimental chambers. Also in the IP area, there are five existing insertable profile monitors (USOTR, IPOTR1, IPOTR2, IP2A, IP2B), providing final beam profile measurement at various Z locations across the experimental area. As is the case in FACET, it is expected that evolving experimental needs will require these shared diagnostics to be reconfigured frequently.

A vertical wiggler section is included in BC20 (3 vertical bend magnets) to generate a vertical synchrotron radiation stripe for energy profile measurements. Also, an X-band (11.424 GHz) transverse, deflecting mode cavity in BC20 is used to measure the bunch length, using the IP area insertable profile monitors to image the streaked beam. These are used in combination with the existing “notch” collimator in the first arm of the chicane to set up two bunch delivery.

The significantly higher 3D charge density available in the FACET-II design may compromise the performance and lifetime of intercepting beam diagnostics such as wire scanners, OTR and YAG screens in the IP area. At peak currents of ~20 kA in FACET, the highly focused electron beam has regularly burned through OTR foils and wires over several hundreds of pulses; the mechanism of this damage is hypothesized to be localized heating due to current flow driven by the radial electric field. Significantly

above this, (if configuring the machine for maximum peak current) these effects are expected to be greatly compounded. A number of mitigation schemes have been developed for FACET including multi-wire scanners, multi-screen profile monitors, and software-controlled MPS to enforce safe configurations for inserting diagnostics.

### **9.5.1 Feedback**

Several Matlab-based software loops for control of  $e^-$  energy and TCAV phase have been in use at FACET and will be retained for the FACET-II  $e^-$  beam. The existing energy feedback monitors the electron beam energy through BPM readings at the positron source extraction point in Sector 19-7 and adjusts RF phase shifters in Sectors 17 and 18 to regulate beam energy at extraction, and subsequently in Sector 20.

# 10 Scope Additions and Future Upgrades

---

## Technical Synopsis

*To support the full breadth of the experimental program outlined in Chapter 3, several additions or upgrades will be required to expand future capabilities. These are described briefly in this chapter. They could be funded as Accelerator Improvement Projects during the operation of the FACET-II facility, but they are also available as possible scope additions should project funds be available.*

*To enable the study of plasma wakefield acceleration of positrons, as driven by an electron bunch, a modification to the Sector 20 chicane has been designed. By co-accelerating the positron bunch  $\frac{1}{2}$  an s-band wavelength away from the electron bunch in the Linac and providing a separate chicane path for the positron in Sector 20, electron and positron bunches can be simultaneously delivered to the Sector 20 experimental IP with configurable bunch separations of  $\pm 200 \mu\text{m}$ . The design for this so-called “sailboat” chicane configuration is presented here. Also, additional beam dynamics studies have been performed with this configuration in the context of other enhancements detailed below.*

*The maximum achievable beam intensities in the experimental area of Sector 20 are limited by CSR driven emittance growth and non-linearities inherent in the bunch compression process. To achieve higher brightness beams than those presented in earlier chapters requires the addition of two key beamline devices utilized in LCLS: namely, a laser-heater in the electron injector and a 4<sup>th</sup> harmonic rf “linearizer” cavity in L1. A representative configuration of the FACET-II accelerator complex utilizing these devices is demonstrated here as an example of the capabilities with these enhancements.*

*The Plasma Wakefield Acceleration experimental program could eventually desire a higher charge electron bunch than provided in the baseline configuration. As one possible implementation, the linac and bunch compression have been designed to be compatible with a 1 nC / 5 nC configuration of the positron / electron beams respectively. The 1 nC / 5 nC configuration has a large imbalance in the wakefield loading in the linac between electron and positron bunches as well as CSR effects. This upgrade represents a highly “pushed” parameter set to demonstrate the performance of FACET-II with the most demanding foreseeable operating conditions for delivery of beams to the Sector 20 user area.*

*Other upgrades options are described briefly, as: 1) installation of a witness injector to provide an independent bunch to sample the plasma wakefields. This allows complete freedom to tailor the drive bunch shape for maximum transfer efficiency. 2) installation of a differential pumping system to isolate the vacuum in the experimental region from the Linac vacuum. This provides flexibility with the plasma chamber experiments and avoids the need for beryllium windows. 3) installation of a Compton source for a variety of proposed experiments. 4) operation of Compton sources in the Sector 20 chicanes to form a photon-photon collider in the final bend of BC20E & BC20P (sailboat chicane).*

---

### 10.1 Future Upgrades - Introduction and Overview

This section describes possible future upgrades to enhance the capabilities of the FACET-II facility. We start by describing the upgrade options of including an additional, so-called “sailboat”, chicane in Sector 20 for simultaneous electron-positron delivery to users of the experimental IP area. Then the laser-

heater and x-band linearizer rf structure are described. The configuration resulting from the addition of these devices then forms the machine design for the other upgrade options whose descriptions follow on later.

To present two ways in which the performance of the machine can be pushed, we present the case of a high charge electron beam (5 nC) operating with a nominal charge positron beam (1 nC). Also the case where the peak brightness of the nominal electron beam (again in conjunction with a 1 nC positron beam) is maximized through the judicious use of collimation of non-linear beam tails is presented.

Finally, the remainder of the upgrade options, as referred to in the technical synopsis, are briefly covered.

## **10.2 Sector 20 Sailboat Chicane**

### **10.2.1 Overview**

This is a full overview of the Sector 20 systems configured with additional magnets to provide an independent chicane arm for the positron bunch- the so-called “sailboat” configuration.

Sector 20 contains the final bunch compression stages for both the electron and positron bunches. The bunches are co-accelerated in the main linac with the electrons following the positrons by ~5cm, i.e.  $\frac{1}{2}$  of an S-band RF bucket. The two bunches are separated horizontally at the first B1 bend magnet at the start of sector 20 and each travel through their own compression chicanes (see Figure 10.1). In order to invert the order of the bunches for the plasma acceleration experiments, the positron chicane (BC20P) has a path length 5.27 cm longer than the electron chicane (BC20E). Each chicane has quadrupole magnets included to generate a positive  $R_{56}$  (defined for a beam coordinate system with the bunch head at  $z < 0$ ), providing the final stage of bunch compression for each beam. The chicanes also provide other measurement and corrective functions before delivery of the beam to the experimental IP area. The layout of the W-chicane (BC3E) is unchanged from the FACET experiment and it will be operated in the same way.

Sextupole magnets are included in each chicane, which provide chromatic and second-order dispersion correction targeted at the experimental waist location to minimize the focused transverse spot sizes. Transverse mover systems under the sextupoles also provide  $x$  and  $y$  dispersion correction and waist adjustment control.

A vertical wiggler section is included in each horizontal chicane (3 vertical bend magnets) to generate a vertical synchrotron radiation stripe for energy profile measurements.

An X-band (11.424 GHz) transverse, deflecting mode cavity in BC20E can measure the fully compressed bunch length. There will be a second identical structure in the second half of BC20P to perform the same function for the positron bunch. This second deflecting mode structure will be driven from the same Sector 20 X-band klystron as used for the existing electron cavity.

Operational control over the relative temporal position of the electron and positron bunches as they enter the plasma channel is required over the range  $+/- 6\sigma_z$ . A pair of 4-bend path-length adjustment chicanes are included into each half of the positron chicane which can provide up to  $+/- 100\mu\text{m}$  of  $\Delta z$  between drive and witness bunches ( $>5-10 \sigma_z$  depending on machine configuration, with larger offsets possible at the expense of degraded beam quality).

The FACET final focus system includes 8 quadrupole magnets for final demagnification of the beam to form the small-beta waist used by experiments. This system of magnets is shared by both

electron and positron beams and is adjusted in order to provide equal beta-functions at the waist to accommodate the dissimilar beta functions from the 2 chicanes at the common chicane exit bend magnet. To provide the additional matching capability, an additional pair of power supplies is needed to independently power 2 extra magnets in the QFF2 and QFF4 magnet strings. The final focus system must accommodate the requirements of multiple users at different locations in the experimental region and thus maintains the flexibility of the system used at FACET to deliver different waist sizes to different z-locations along the experimental table.

Finally, the spectrometer after the experimental region consists of a vertical bend magnet and three quadrupoles. This is the same system used during FACET operation.

### 10.2.2 Beam Parameters and Matching

The sector 20 optics is designed to deliver high peak-current (bunch length < 20  $\mu\text{m}$ ) at the experimental area with 20  $\mu\text{m}\text{-rad}$ , or less, transverse emittance simultaneously for both incoming electron and positron beams. The optics match is highly constrained and must satisfy specific requirements for both electron and positron optical systems simultaneously:

- Chicane compression ratios set in the middle of their operating range for maximum flexibility when commissioning the beamline ( $R_{56} = +5\text{mm}$ ).
- Symmetry conditions maintained across each chicane to ensure co-located waist locations and beta functions for  $e^-$  and  $e^+$  beams at the waist location.
- Minimal beta functions through chicane, which past experience at FACET has shown to be highly desirable for stable operation. The optics going back into Sector 18 is manipulated to help with this and the following match requirements.
- Minimal CSR effects. The horizontal beta functions in the final bend magnet are matched to be small in both planes with a waist close to the final bend exits which helps to mitigate CSR growth effects in both electron and positron beams.
- Closed dispersion at exit of chicanes.
- Correct horizontal and vertical chromaticity at the waist.
- Minimal second-order horizontal dispersion.
- Sextupole-mover based multi-knobs for dispersion and waist control.
- Waist at user-specified region in experimental area downstream of final focus system. A beta function of 50 cm is selected for the baseline design, typical user requested values during FACET operations ranged from 0.1-1 m.
- Due to different beam loading in L2 and L3, there is a ~90 MeV energy imbalance between electron and positron bunches entering Sector 20. The chicanes and final focus are matched to the positron energy of 10 GeV due to the tighter chromatic bandwidth of BC20P. Sextupole magnets within BC20E are offset horizontally to re-center the waist due to off-energy propagation through the common final focus magnets.

### 10.2.3 Layout and Optics Design

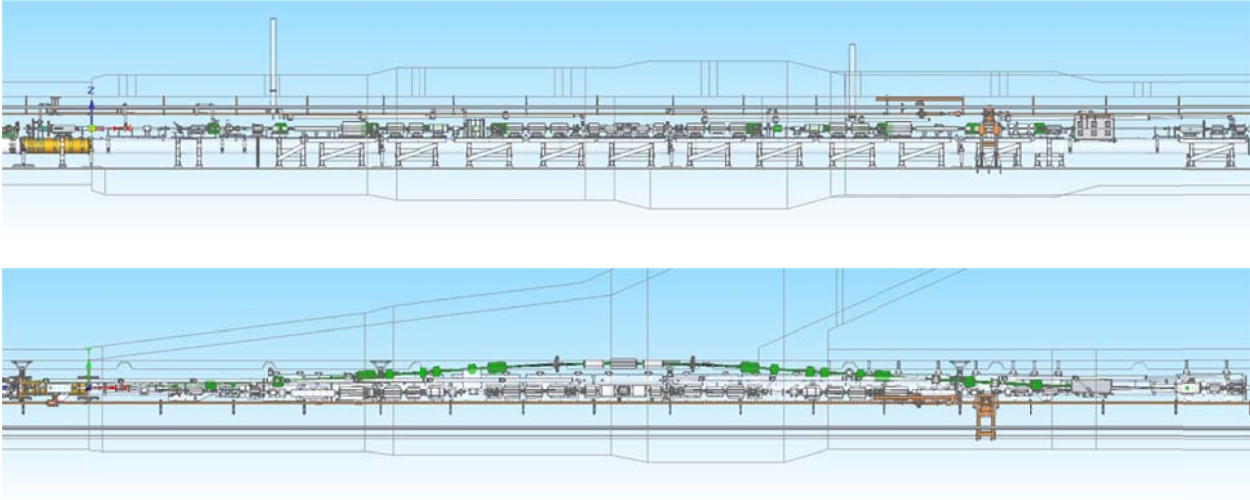


**Figure 10.1.** Layout of Sector 20 sailboat (new) chicane magnets.

Figure 9.1 shows a schematic layout of Sector 20 including both arms of the BC20 chicane with the sailboat configuration, the final focus optics, experimental area and vertical energy spectrometer. The positron chicane is new and the other magnets and associated diagnostics are existing from the FACET User Facility. Figure 9.1 shows the optics functions for both the existing electron system and the new positron BC20P chicane and final focus. Note beta functions are kept small at the exit of the chicanes in both planes to help to minimize CSR effects. Although only the horizontal function needs to be kept small for this purpose, both planes are matched in order to handle both electron and positron beams simultaneously. The beta functions in the body of each chicane are kept as small as possible while maintaining compatibility with the required dispersion functions to generate a positive  $R_{56}$  and the need to set the entrance/exit parameters to the chicanes.

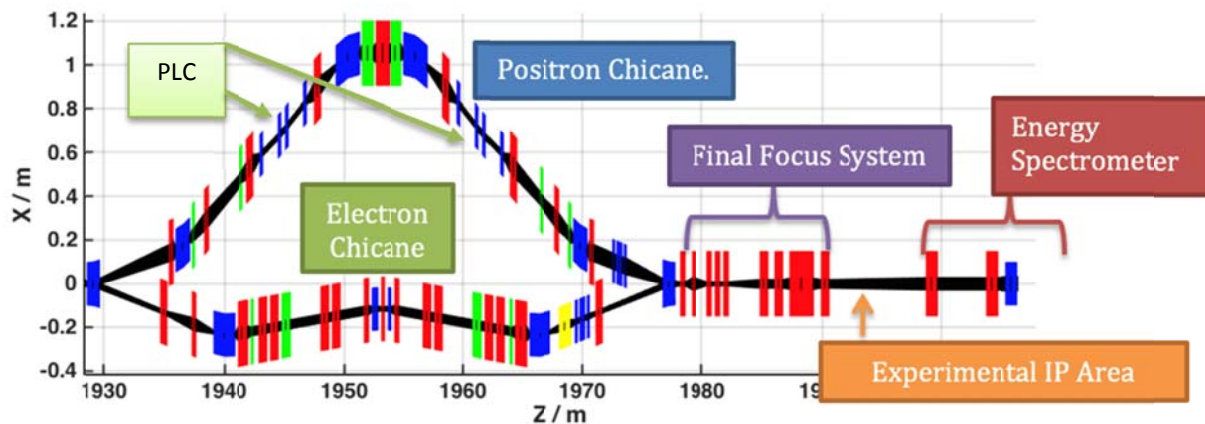


**Figure 10.2.** Plan layout view of sector 20 magnets, including e- and e+ horizontal chicanes, final focus and vertical energy spectrometer. Yellow indicates x-band RF TCAV, blue dipoles, red quadrupoles, green sextupoles. Co-ordinate system is relative to SLC linac (x) and SLC z-reference. The “PLC” label indicates the locations of the 2 path-length adjustment chicanes.

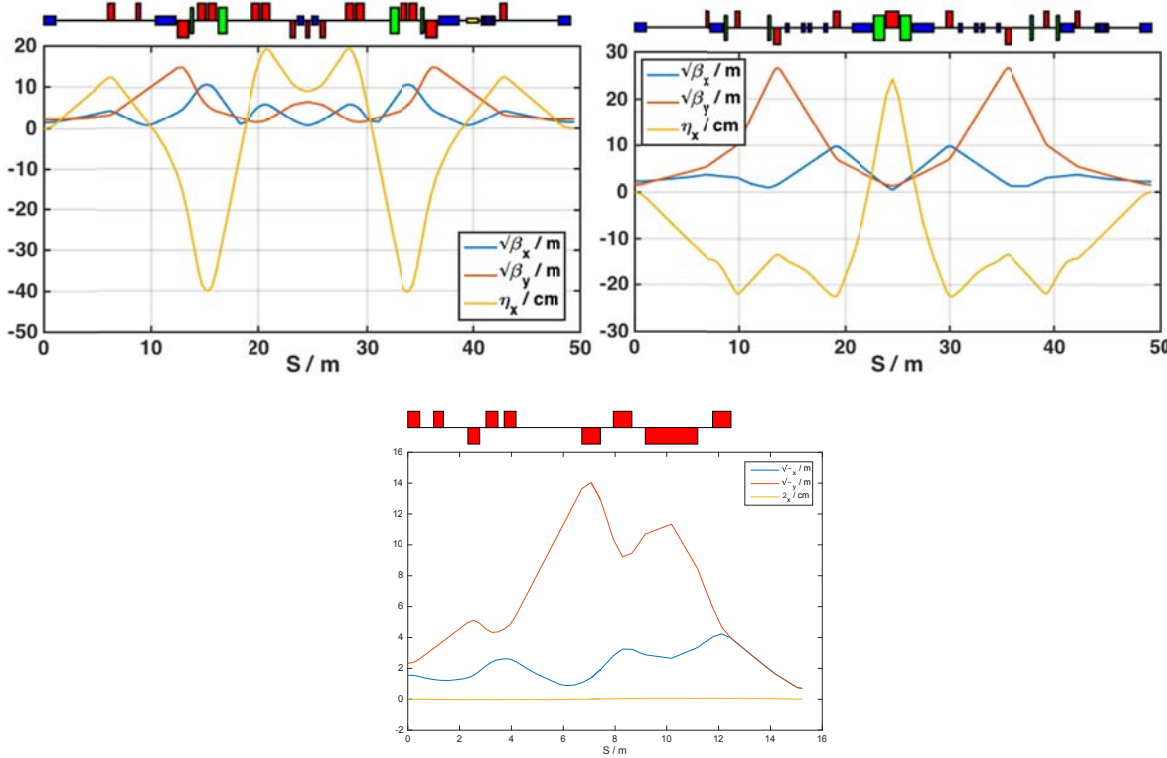


**Figure 10.3.** Twiss parameters across sector 20 electron and positron systems, including final focus. IP waist is at location of plasma chamber experiment. Top plot, left, shows BC3E electron chicane, top plot, right, shows for BC20P positron chicane. The bottom plot follows on immediately from the BC20E/P optics and shows the final focus system for the electron beam ( $x$  and  $y$  beta functions are reversed for positron beam), where the IP is on the far right of the plot. The first and last bend magnets of each chicane are shared for the positron and electron beams.

#### 10.2.4 Path-Length Tuning Chicanes

Two 4-bend horizontal chicane systems (bend length=30cm, total length=3.9m each, distance between first and second pair of bends in each chicane=1.2m) in each half of the positron chicane provide path length adjustability between electron and positron bunches of  $\pm 100\mu\text{m}$ . The default chicane configuration provides half the total path-length adjustment range. The rest of the main positron chicane is configured to deliver the design 52.7mm path length difference between electron and positron bunch to compensate for the  $\frac{1}{2}$  S-band bucket spacing in the linac. This provides for a nominal 215 $\mu\text{m}$  longitudinal separation between electron and positron bunches at the IP.

To minimize the impact on the total positron system  $R_{56}$ , the distance between the central bends in the path length adjustment chicanes was minimized as a fraction of these chicane lengths.

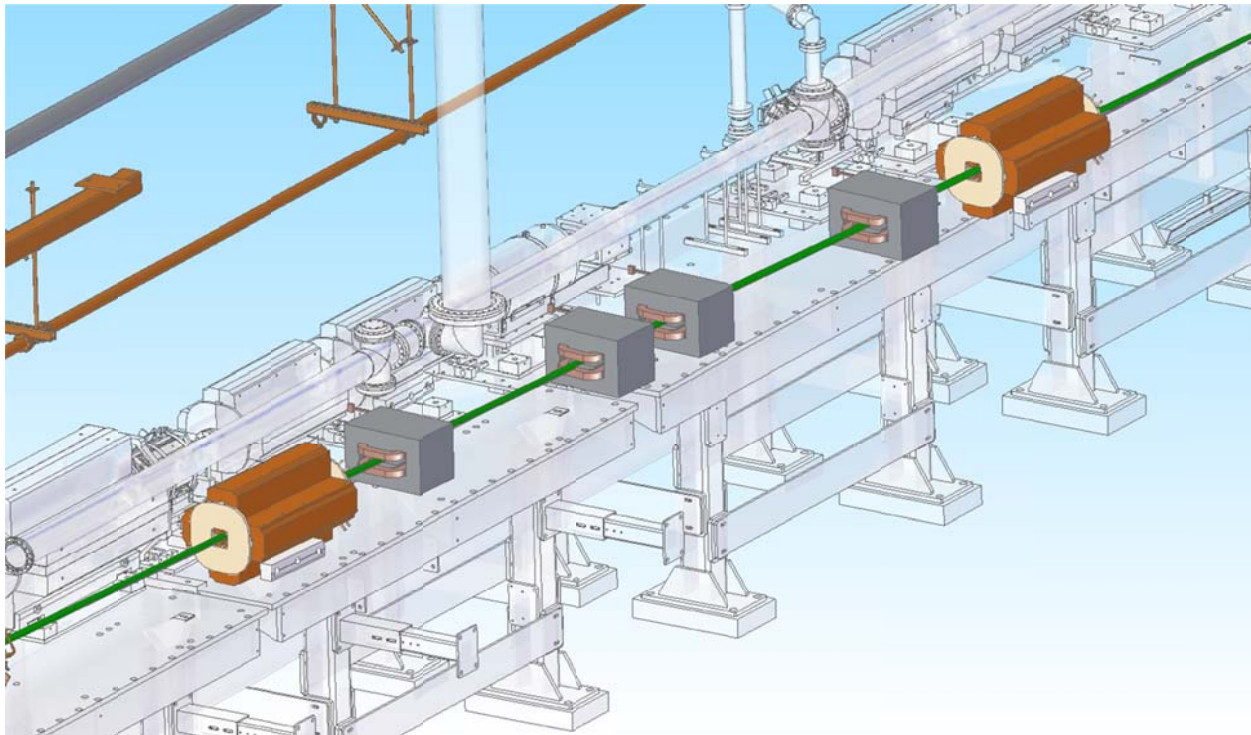


**Figure 10.4.** CAD drawing of downstream section of Sector 20 BC20P chicane showing second path length adjustment mini-chicane bend magnets.

**Table 10.1.** Operating parameters of path-length adjustment chicane system. The BMAG parameter shown is the betatron mismatch caused by edge focusing effects from the chicane bends.

Bend angle / mrad	$\Delta S$ (path length change) / um	$\Delta R_{56}$ / mm	$\Delta BMAGY$ / %	Change in horizontal beam position in central chicane bends / mm
0	-100	-0.23	-1.3	-9.7
6.45	0	0	0	0
9.14	+100	+0.23	+1.3	+4.0

## 10.2.5 New magnets

### 10.2.5.1 BC20P Chicane

Construction of the new BC3P chicane requires 9 quadrupole magnets of 3 engineering types; 6 sextupole magnets of two engineering types; 17 dipole magnets of 5 types (two of which already exist and are shared with the electron W-chicane system).

### 10.2.5.2 Quadrupoles

Table 10.2. Quadrupole magnet parameters at 10 GeV.

Deck Name	Engineering Type	Effective Length / m	Design Int. Gradient / T	Max. Int. Gradient /  T	Design Pole Tip Field /  T	Max Pole Tip Field /  T	Aperture (radius) / m
Q1PL	A	0.4	5.569	15	0.278	0.75000	0.02
Q2PL	A	0.4	9.943	15	0.497	0.75000	0.02
Q3PL	B	0.6	-10.436	20	0.348	0.66667	0.02
Q4PL	B	0.6	11.631	20	0.388	0.66667	0.02
Q5P	C	1.2	35.965	50	0.599	0.83333	0.02
Q4PR	B	0.6	11.629	20	0.388	0.66667	0.02
Q3PR	B	0.6	-10.433	20	0.348	0.66667	0.02
Q2PR	A	0.4	9.941	15	0.497	0.75000	0.02
Q1PR	A	0.4	5.567	15	0.278	0.75000	0.02

### 10.2.5.3 Sextupoles

Each sextupole is mounted on a remotely controllable motion stage, capable of +/- 2mm motion in x/y with 5µm precision.

Table 10.3. Sextupole magnet parameters at 10 GeV.

Deck Name	Engineering Type	Effective Length / m	Design Int. Field / T.m <sup>-1</sup>	Max. Field /  T.m <sup>-1</sup>	Design Pole Tip Field / T	Max Pole Tip Field /  T	Aperture (radius) / m
S1PL	A	0.25	-301.002	320	0.2408	0.512	0.02
S2PL	A	0.25	187.001	320	0.1496	0.512	0.02
S3PL	B	1	289.329	1500	0.0579	0.600	0.02
S3PR	B	1	289.329	1500	0.0579	0.600	0.02
S2PR	A	0.25	187.001	320	0.1496	0.512	0.02
S1PR	A	0.25	-301.002	320	0.2408	0.512	0.02

### 10.2.5.4 Dipoles

**Table 10.4. Dipole magnet parameters at 10 GeV. All are rectangular type dipole magnets. B1LP and B1RP are shared with B3E chicane first and last bend magnets.**

Deck Name	Engin g Type	Effecti ve Lengt h / m	Bend Angle / radians	Bend Plane	Design Int. Field / T.m	Max. Int. Field /  T.m	Design Pole Tip Field / T	Max Pole Tip Field /  T	Apertur (radius)
<b>B1LP</b>	A	1.063	-0.0226	X	-0.754	0.8	0.709	0.7525	0.0115
<b>B2LP</b>	B	1.2	-0.0418	X	-1.393	1.45	1.161	1.2083	0.0115
<b>BPA1L</b>	C	0.3	0.0065	X	0.215	0.3	0.717	0.9999	0.0115
<b>BPA2L</b>	C	0.3	-0.0065	X	-0.215	0.3	0.717	0.9999	0.0115
<b>BPA3L</b>	C	0.3	-0.0065	X	-0.215	0.3	0.717	0.9999	0.0115
<b>BPA4L</b>	C	0.3	0.0065	X	0.215	0.3	0.717	0.9999	0.0115
<b>B3LP</b>	D	2.0	0.0643	X	2.147	2.2	1.073	1.1000	0.0115
<b>B3RP</b>	D	2.0	0.0643	X	2.147	2.2	1.073	1.1000	0.0115
<b>BPA1R</b>	C	0.3	0.0065	X	0.215	0.3	0.717	0.9999	0.0115
<b>BPA2R</b>	C	0.3	-0.0065	X	-0.215	0.3	0.717	0.9999	0.0115
<b>BPA3R</b>	C	0.3	-0.0065	X	-0.215	0.3	0.717	0.9999	0.0115
<b>BPA4R</b>	C	0.3	0.0065	X	0.215	0.3	0.717	0.9999	0.0115
<b>B2RP</b>	B	1.2	-0.0418	X	-1.393	1.45	1.161	1.2083	0.0115
<b>WIGP1</b>	E	0.244	-0.0025	Y	-0.083	0.2	0.342	0.8196	0.035
<b>WIGP2</b>	E	0.488	0.005	Y	0.167	0.2	0.342	0.4098	0.035
<b>WIGP3</b>	E	0.244	-0.0025	Y	-0.083	0.2	0.342	0.8196	0.035
<b>B1RP</b>	A	1.063	-0.0226	X	-0.754	0.8	0.709	0.7525	0.0115

## 10.3 Electron Injector Laser Heater

### 10.3.1 Overview

The injector system can incorporate a laser/electron beam heater system (an inverse free electron laser) in order to generate an increased intrinsic energy spread in the electron beam [1]. This produces damping in the bunch compressor chicanes which suppresses the micro-bunching instabilities driven by Coherent Synchrotron Radiation (CSR) in the bunch compressors, and Longitudinal Space Charge (LSC) forces in the linac. The heater system is located just down-beam of the L0b accelerator section at 135 MeV in the off-axis LCLS injector housing (see Figure 10.5).

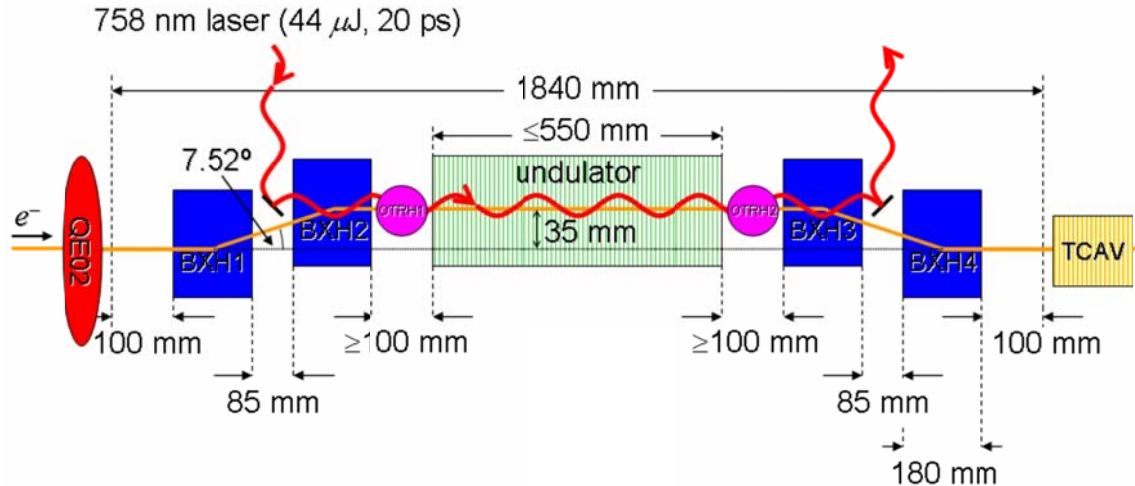


**Figure 10.5. The laser-heater system in a weak chicane with co-propagating laser beam. The blue squares represent chicane magnets and the green rectangle represents the 9-period undulator.**

Two OTR screens with photo-diodes are included to aid in achieving spatial and temporal overlap of the co-propagating laser and electron beams. Dimensions and laser power are approximate.

The electron beam (3 ps long) propagates collinearly with the Ti:sapphire laser pulse (~10 ps long, 760 nm wavelength) through a 55-cm long, 9-period, adjustable gap, planar, permanent magnet undulator located within a magnetic chicane. The laser-electron interaction modulates the electron energy along its bunch length with a period equal to that of the laser (760 nm). The chicane provides convenient injection of the laser beam and, more importantly, an effective time-smearing of the energy-modulation due to the path length dependence (through the last two chicane bends) on each electron's horizontal angle in the undulator (finite transverse emittance). This smearing erases all time-structure on the bunch and produces an effective ‘thermal’ local energy spread [1]. The available laser power and system parameters given in Table 10.5, can produce a 500-keV rms local energy spread, rather than the very small level expected from the RF gun. The heated energy spread of 500 keV is small enough to have a minimal impact on the available peak current deliverable at 10 GeV, whilst the heating of the electron longitudinal phase-space helps to mitigate transverse beam quality degradation due to CSR and LSC effects. The heater’s system parameters are listed in Table 10.5, while its laser parameters are below. The laser heater electron optics functions are shown in Figure 10.6.

**Table 10.5. Laser-heater electron beam, chicane, and undulator parameters for FACET-II.**

Parameter	Symbol	Unit	Nominal	Range
Electron energy	$E$	MeV	135	135
Electron bunch length (FWHM)	$\Delta t$	ps	7	7-12
Electron transverse beam size (rms)	$\sigma_{x,y}$	mm	0.35	0.35-0.53
Undulator period	$\lambda_u$	cm	5.4	-
Undulator parameter	$K$	-	1.385	1.047-2.229
Undulator minimum gap	$g$	mm	34	25-100
Number of undulator periods	$N_u$	-	9	-

Chicane magnet eff. length	$L_B$	m	0.18	-
Bend angle of each chicane magnet	$\theta$	deg	7.52	0-7.52
Beam offset in chicane center	$ \eta_x $	mm	35	0-35
Required spatial overlap of laser and $e$ -beam	$ \Delta x  =  \Delta y $	mm	<0.2	-
Total rms energy spread induced	$\sigma_E$	keV	500	0-500

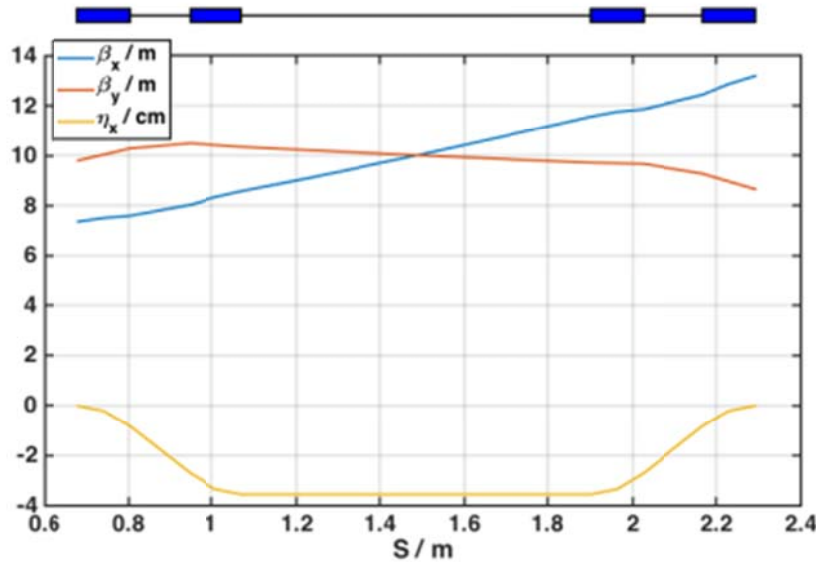


Figure 10.6. The laser heater electron optics in the FACET-II injector at 135 MeV.

### 10.3.2 Laser Properties for Laser Heater System

The IR beam used for the heater is extracted from the drive laser as the spent beam which is left over after the frequency tripler crystal- therefore it is well synchronized to the electron beam. The requirements for the laser in the heater system are listed in Table 10.6.

Table 10.6. IR laser parameters of the laser-heater system for FACET-II.

Parameter	Symbol	Unit	Nominal	Range
Maximum IR pulse energy in the undulator	$u$	$\mu\text{J}$	200	0-4000
IR wavelength	$\lambda_{IR}$	nm	760	760-800
Max. IR pulse rate	$f_{rep}$	Hz	30	1-30
IR beam size at center of the undulator (rms)	$\sigma_{x,y}$	$\mu\text{m}$	400	200-600
IR pulse length in undulator (FWHM)	$\Delta\tau_{FWHM}$	ps	12	10-20
Laser beam Rayleigh range	$L_R$	cm	50	42-1600
Laser pulse energy in the undulator	$P_E$	$\mu\text{J}$	50	0-1500
Laser power in undulator	$P_L$	MW	1.0	0-17

Laser rms beam size in undulator	$\sigma_{L-x,y}$	mm	0.4	0.4-0.55
Position stability of IR beam in und. (rms)	$\Delta x/\sigma_x$	%	<20	-
Timing stability of IR beam in und. (rms)	$\Delta t/\Delta \tau_{FWHM}$	%	<30	-



**Figure 10.7. (Left)** Optical bench attached to the ceiling of the LCLS vault and relay imaging lens and tube that transports the beam to the heater. **(Right)** Laser heater optical table with diagnostics and controls.

IR light for the laser heater is taken from the residual IR that comes out of the tripler. Because the tripler efficiency is roughly 10%, we have roughly 10 times the UV energy ( $>10$  mJ) left in the IR which is more than the required amount shown in Table 10.6. The IR is sent through a parallel grating pulse stretcher to produce the required temporal width and is then relay imaged first to an optical bench that is attached to the ceiling (see Figure 10.7) in the vault and then to the heater interaction region. There are pointing stability lock loops and diagnostics included as part of this optical transport system.

#### 10.4 X-Band RF “Linearizer”

To compensate for non-linear tails imparted during the s-band energy chirping and subsequent magnetic compression of the beam, LCLS introduced a 4<sup>th</sup> harmonic cavity into the L1 accelerating section. A similar 60cm length 11.424 GHz x-band rf structure (L1X) can be considered for use at FACET-II, placed immediately upstream of the first bunch compression chicane (BC11). The location is marked in the schematic shown in Figure 10.17. The 11-3 RF modulator would need to be modified and used to power L1X using an X-band klystron. The L1X structure would take the place of the slot currently occupied by 11-2d. Note that the existing design leaves the slot for the L1X structure spare, no sacrifices in beam energy are required.

The x-band structure would be powered at the decelerating phase (-180°), with a strength dependent on the compression configuration employed (See below sections).

Transverse wakefield are higher in the x-band cavity than the other s-band cavities, and care must be taken to both align L1X and maintain fine control over orbit excursions in its vicinity. It would be envisioned to place a mover system with O(1 μm) level control under the structure, and also to read out the HOM port for use in alignment.

## **10.5 High Peak Current Configuration with 2 nC Electrons Operating Concurrently with 1 nC Positron Bunches**

### **10.5.1 Overview**

This configuration makes use of the laser heater, x-band linearizer and sailboat chicane options detailed above to simultaneously deliver 2 nC (at source) electron bunches and 1 nC (at damping ring source) positron bunches to the user IP area in Sector 20. Here we make full use of the collimation systems in the BC11 and BC14 bunch compressors to remove a significant fraction of the high energy tail portion of the longitudinal beam profile. Beam tracking results as performed for the baseline design detailed in Chapter 6 were performed with additional features required due to the 2-bunch tracking mode of operations. Simulation details specific to this mode of operation and particle tracking results are shown below.

### **10.5.2 Particle Tracking**

Particle tracking studies have been performed throughout the injector, accelerator, and sector 20 compression and final focus by stringing together results from *IMPACT-T* (injector) and *Lucretia* as described in Chapter 6. Included in the tracking are longitudinal and transverse wakefields, Coherent Synchrotron Radiation (CSR), Incoherent Synchrotron Radiation (ISR), and up to 3<sup>rd</sup>-order optics (e.g., chromatic effects). 3D space charge forces are only included in the *ImpactT* run up to 135 MeV at the exit of L0, with output particles transferred to *Lucretia*. *Lucretia* also includes a model of longitudinal space-charge forces. The results from the tracking simulation ( $10^5$  macro-particles simulating the particle bunch) for the baseline machine design are shown in earlier chapters and results from the IMPACT-T tracking model can be seen in chapter 5.

Three machine configurations in total were simulated, listed below. Configuration (1) constitutes the baseline design and results from this configuration are shown in earlier chapters. Results from (2) and (3) are shown here.

4. The baseline configuration which delivers 1 and 2 nC of charge (for positrons and electrons, respectively).
5. A high peak current configuration which aims to maximize the current density at the experimental IP waist in Sector 20. This configuration uses a 2 nC source for both electrons and positrons whilst collimating the high energy spread tails within the BC0, BC11 and BC14 bunch compressors to deliver a final bunch charge of 0.6-0.7 nC. It provides peak currents of 12 and 76 kA (for positrons and electrons, respectively) and <10  $\mu$ m transverse spot sizes with 0.1 m IP beta functions.
6. A maximum electron charge configuration with 5 nC charge from the RF gun, un-collimated, together with a 1 nC positron beam. This configuration demonstrates requirements to run with the maximum envisioned beam-loading imbalance between electron and positron beams.

The electron beam tracking is first performed through to the end of BC11. The positron beam is tracked from the design parameters at the extraction point of the positron damping ring, through the positron ring to linac beam optics including the BC0 compressor, to the common injection point at the exit of BC11. Both electron and positron macro-particle bunch definitions are then merged with the appropriate  $\frac{1}{2}$  s-band wavelength (5.25cm) separation and tracked through L2, BC14 and L3. This allows the simulation to properly treat the transverse wake deflection imparted on the electron beam by the positron beam in the accelerating structures. Each bunch is then tracked through BC20E and BC20P,

through the common final focus system in Sector 20 to the common interaction point in the experimental area.

Figure 6.33 shows the longitudinal phase space through the machine for configuration (2). The final tracked transverse beam profiles for electrons and positrons at the experimental IP location for the high peak current parameter case (2) are shown in Figure 10.9. All components are error free for these tracking simulations (e.g., perfect alignment). Due to energy loss due to synchrotron radiation in the bunch compressors, there are steering and dispersive “errors” by design. During operation, these are taken care of by the routine steering and dispersion correction systems. For design tracking purposes here, the orbit and dispersive “errors” are numerically subtracted after each bunch compression stage to mimic these operational corrections and to derive the expected performance for the machine. These fixed corrections are stored and used during tolerance calculations which apply additional errors (e.g. RF phase and amplitude errors) so the impact of those errors is properly treated.

Collimators within the BC0, BC11 and BC14 bunch compression chicanes are used to selectively collimate the high and low energy offset tails of the beam for the high peak current parameter configuration (2). Figure 10.10 and Figure 10.11 below show how the transverse and longitudinal beam sizes at the experimental IP waist vary as a function of final beam charge (initial beam charge is 2nC) for the positron and electron beam. The beam charge is varied by symmetrically adjusting the bunch compressor collimators. Treating each beam independently it can be seen that there is an optimal collimator setting in each case in terms of maximum achievable peak current: around 1.5 nC for electrons and 1.7 nC for positrons. Due to increasing energy spread generating larger aberrations through BC20E, BC20P and the final focus, and also due to CSR effects (which become more pronounced for larger peak currents and shorter bunch lengths), the horizontal spot size at the IP is also strongly correlated to the final bunch charge. The collimation is determined by the positron beam which is most sensitive to the bunch charge. The configuration presented here corresponds to a positron bunch charge of just over 0.6 nC which meets the requirements of  $< 10 \times 10 \times 10$  um bunch dimensions at the experimental IP, and the requirement of > 10 kA peak current, whilst leaving a small overhead for operational errors etc. The electron collimation is then set to provide a similar final electron bunch charge which tracks to the same final energy when taking into account beam loading in the linacs. The electron bunch in this configuration also meets the required final bunch parameters. In principal, an additional 50% peak current is achievable if the chromatic aberrations and CSR effects can be further mitigated (mainly in BC20) to suppress the horizontal beam spot size growth. Further studies should be carried out to optimize the Sector 20 optics with this in mind. e.g. the principle of CSR-matching will be investigated.

The following list describes the various effects which are included in the particle tracking.

- $10^5$  macro particles representing a 2 nC electron bunch was tracked using *IMPACT-T*, which includes 3D space charge forces, up to the exit of the L0 accelerator section at 135 MeV.
- First to third-order optics of dipole, quadrupole, sextupole, and sinusoidal RF fields.
- Longitudinal and transverse wakefields of the SLAC S-band RF accelerating structures with 321.8 meters of structures between BC1 and BC2, and 471.0 meters after BC2.
- CSR applied to all bends and downstream drift spaces using the 1D line-charge model in *Lucretia*, which includes transient fields but ignores the transverse beam dimensions which do not play an important role here.

- ISR applied to all bends, which impacts the energy spread and beam emittance, although by insignificant levels.
- A simulation of longitudinal space charge impedance effects is applied in the Lucretia tracking model, although the effect is negligible.
- An increased slice energy spread (130 keV rms) at 135 MeV is produced by the laser heater system. This reduces instabilities due to micro-bunching through CSR and LSC.
- Collimation of the beam in BC0, BC11 and BC14 bunch compressor collimation sections.

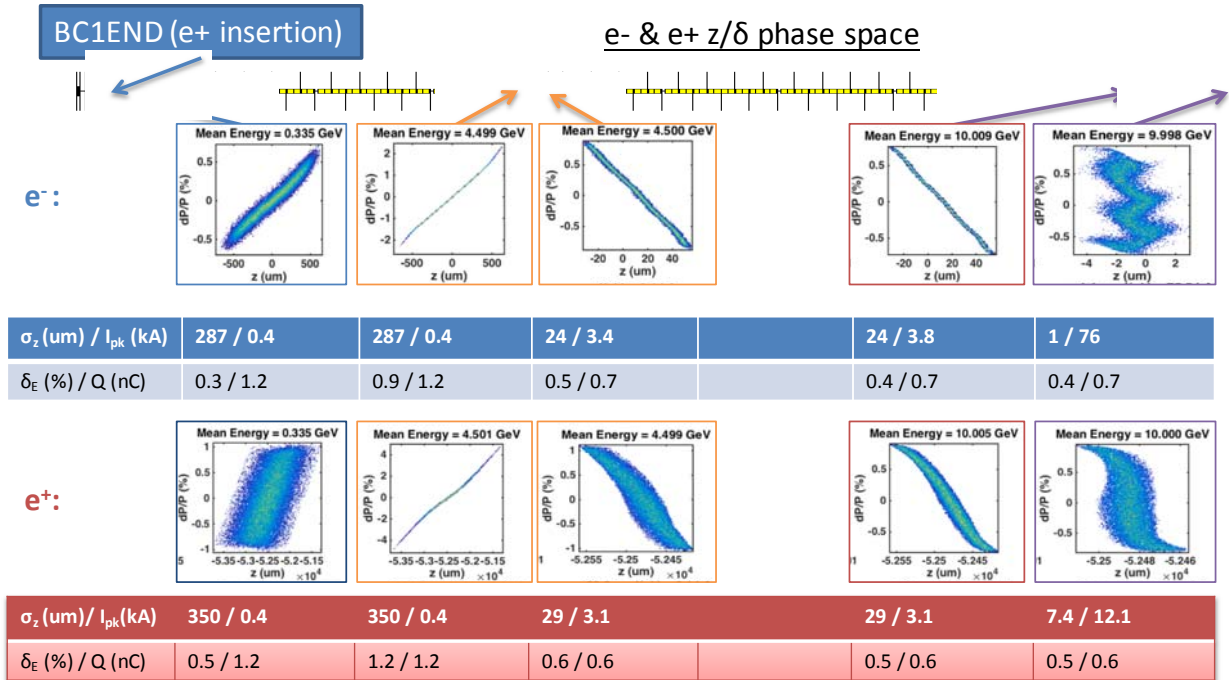


**Figure 10.8. Longitudinal configuration of FACET-II for high peak current at the IP experimental waist location.**

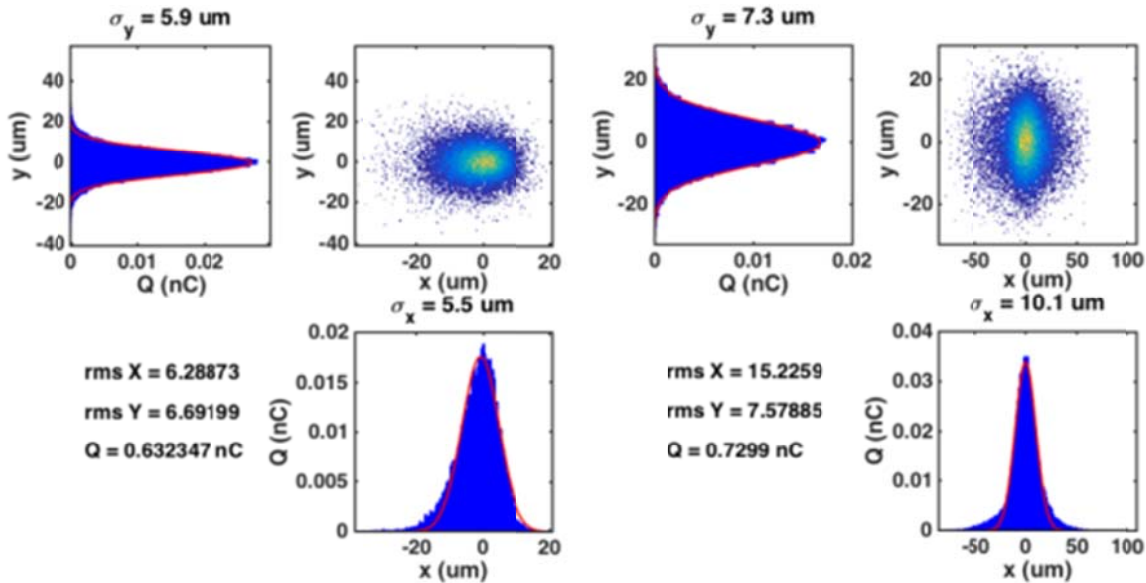


**Figure 10.9.** Tracked beam particles for electron (left) and positron (right) beams at the experimental IP waist in Sector 20, transverse beam dimensions shown. Tracking results are for the high peak current parameter design with  $\beta^* = 0.1$  m optics matching.

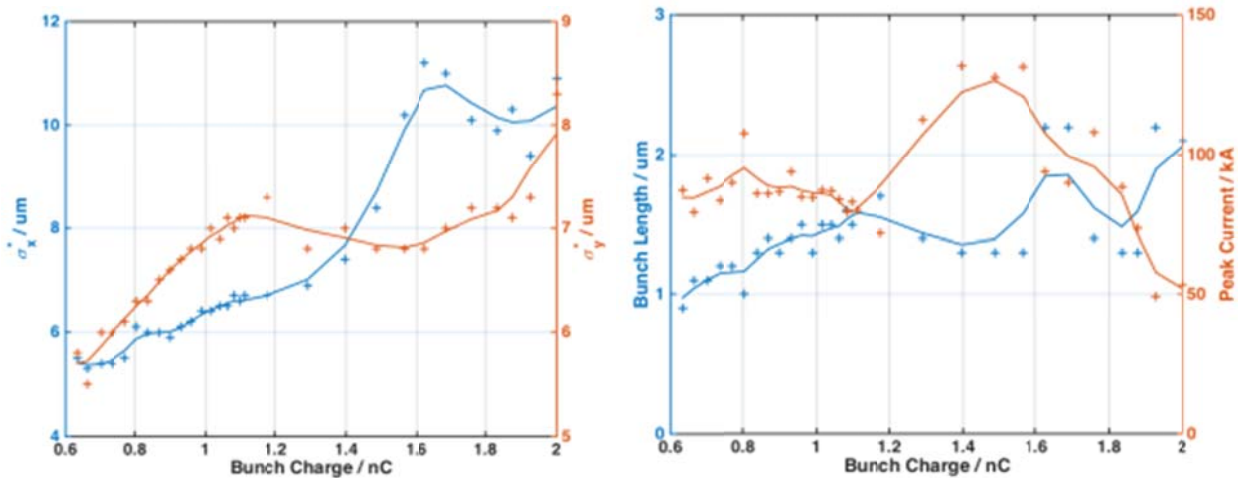


**Figure 10.10.** Transverse and longitudinal bunch sizes at Sector 20 waist for Electrons as a function of bunch charge. Lines are smoothed data values. Bunch charge is varied using BC11 and BC14 collimators.

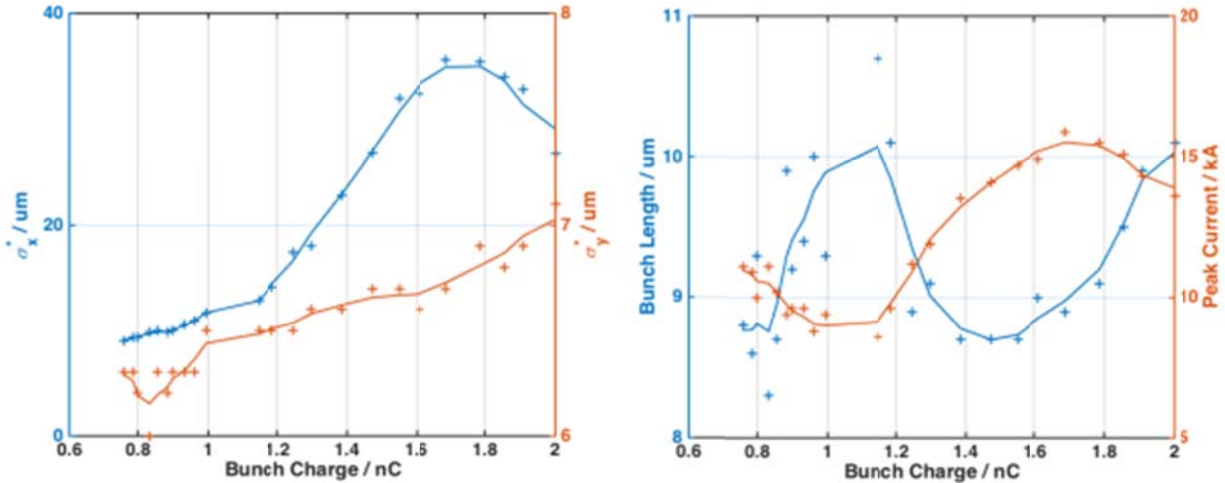


**Figure 10.11.** Transverse and longitudinal bunch sizes at Sector 20 waist for Positrons as a function of bunch charge. Lines are smoothed data values. Bunch charge is varied using BC0 and BC14 collimators.

### 10.5.3 Stability Requirements and System Sensitivities

The final level of bunch compression and transverse beam quality in 3 dimensions is quite sensitive to RF phase and amplitude variations in the different sections of the machine. The simulated final beam spot sizes for delivery to users in the Sector 20 IP region have been studied using particle tracking (with *Lucretia*) while varying many of the system parameters. Sensitivities have been evaluated here for the high peak current case (2). Table 6.2 lists the various parameters (mostly phase and amplitude of each major linac section), plus the bunch charge, drive-laser timing, magnet vibration, and bunch compressor settings. The value listed for each jitter property is either from a tolerance specification elsewhere (e.g. laser timing fluctuation from LCLS requirements and operation experience) or directly measured (magnet vibrations) or motivated from past experience operating FACET. Table 10.8 shows the machine performance including errors for configuration (2). These Monte Carlo simulations were performed using 100 random seeds for the jitter parameters and yield results with non-Gaussian distributions. Hence the results shown in Table 10.8 do not well describe the particular distributions of errors. Figure 10.13 through Figure 10.16 show results for the high peak current parameter design and depict the numerical distributions from the simulations both for the total set of jitter properties and also with the parameters individually applied so the major contributions can be identified. These are statistical “box plots”: for each box, the red line indicates the median value for the distribution, the blue “box” shows the 25<sup>th</sup> and 75<sup>th</sup> percentiles and the dotted line “whiskers” show the range of the distribution. Where there are red crosses included, these are considered outliers (if they are larger than  $q_3 + w(q_3 - q_1)$  or smaller than  $q_1 - w(q_3 - q_1)$ , where  $q_1$  and  $q_3$  are the 25th and 75th percentiles, respectively, and  $w$  is 1.5 meaning that the outliers correspond to approximately  $\pm 2.7\sigma$  if the distribution were Gaussian).

For these high peak current parameters, the jitter properties mostly contributing to the observable errors are vertical laser spot jitter, laser timing fluctuations and L1 S-band phase and amplitude jitter for the electrons, and BC3P magnet field jitter for the positrons.

The sensitivity of the vertical electron beam size to the laser spot position jitter is largely due to the transverse wakefields in the L1X X-band linearizer structure. If desired, the sensitivity due to this property can be reduced by either choosing to use a C-band cavity for the linearizer function or by re-optimizing the optical functions in L1 to lower the beta functions in the L1X structure (e.g. by relocating the structure further upstream in the L1 section). Sensitivity due to L1 S-band RF phase and amplitude

was expected and has been an area of concentrated effort for the operation of LCLS. Also during FACET-II operations, special attention needs to be applied to this RF system to achieve the required tolerances. In the case of the positron horizontal spot size the particular sensitivity to the magnet field fluctuations in BC3P have been noted. Further study will be applied to this area in the future to identify the specific magnets which we are sensitive to and to specify targeted tolerances for these magnets to reduce the sensitivity in this region to acceptable levels.

#### **10.5.3.1 IP Timing Jitter**

The relative arrival time jitter for the tracked electron and positron bunches with the error properties listed in Table 6.2 are shown in the histograms in Figure 6.15. The rms jitter on both the electron and positron bunches is 27.0um in each case, the rms relative jitter between the electron and positron bunches is 11.1 um. The relative timing jitter is smaller due to many common jitter sources (L2 and L3 RF systems). The main tolerance on the desired level of timing jitter is very relaxed, coming from a desire to easily distinguish between electron and positron signals, the relative jitter should then be small compared to the nominal separation ( $\sim < 100$  um). Experimental programs record the timing using EOS techniques to retrospectively analyze data, the presence of some timing jitter is therefore actually a desired property.

**Table 10.7. Jitter properties studied and estimated achievable values.**

Property	Value
Source Charge Fluctuation	1% (e-) 2% (e+)
Source Position Fluctuation	$0.05 \sigma_{x,y}$ (e- & e+)
Initial Electron Laser Timing Error	200 fs
L1X Phase Jitter	0.25 degX
L1 Phase Jitter	0.1 degS
L2/L3 Phase Jitter	0.25 degS
L0P Phase Jitter	0.1 degS
L1X Amplitude Jitter	0.25 %
L1 Amplitude Jitter	0.1 %
L2/L3/L0P Amplitude Jitter	0.25 %
BC0 & BC1 Magnet Strength Jitter	$1e-5$ dB/B
BC2 & BC3 Magnet Strength Jitter	$1e-4$ dB/B
L1/L2/L3/S20 Magnet Vibration (x/y)	1.5/0.5 $\mu$ m
PEC Magnet Vibration (x/y)	0.4/0.18 $\mu$ m

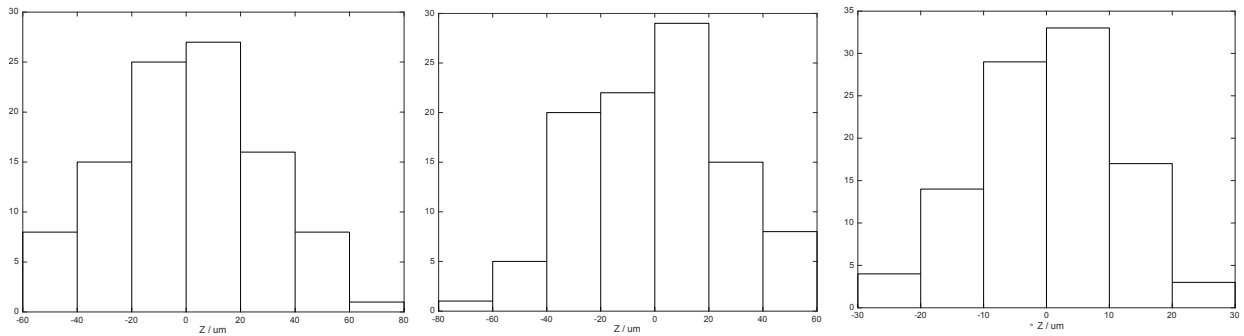


**Figure 10.12 Absolute arrival time (longitudinal position) jitter for electrons (left), positrons (center) and relative electron-positron jitter (right).**

**Table 10.8.** Simulated range of delivered beam parameters at Sector 20 IP waist with all error parameters specified in Table 6.2 applied for the high peak current parameters (~0.6 nC final bunch charge). Each entry shows mean and rms spread of results from a 100 seed Monte Carlo simulation. Note that the actual distributions are not actually Gaussian, see presented data in Figure 10.13 to Figure 10.16 for error distributions and breakdown of errors into independent sources. The design comparison is the tracked beam without errors.

IP Parameter	Electron Bunch		Positron Bunch	
	<i>Design</i>		<i>With Errors</i>	
	<i>Design</i>	<i>With Errors</i>	<i>Design</i>	<i>With Errors</i>
$\sigma_x$ (μm)	8.5	7.9 +/- 3.1	9.0	13.7 +/- 5.4
$\sigma_y$ (μm)	6.9	7.6 +/- 1.9	6.0	7.4 +/- 0.3
$\sigma_z$ (μm)	1.1	3.5 +/- 2.2	7.4	7.4 +/- 0.9
$I_{pk}$ (kA)	76	37 +/- 20	12	11.7 +/- 1.8

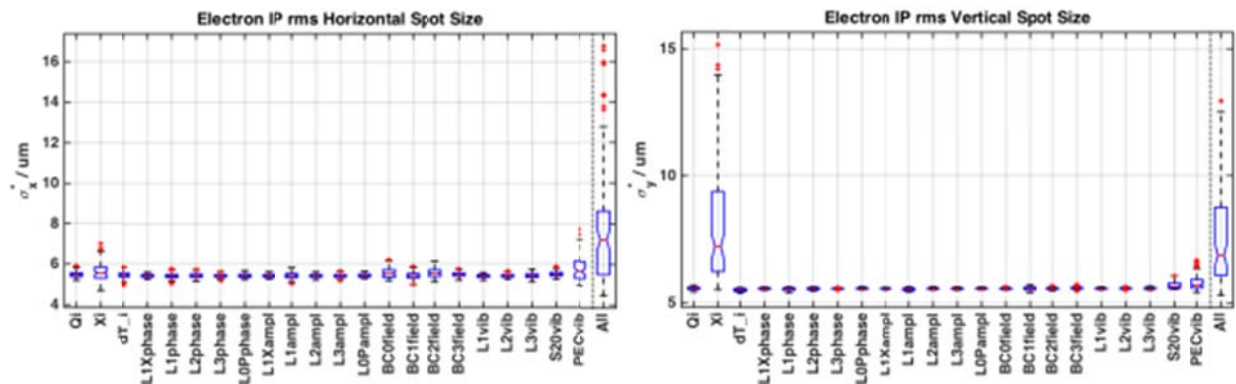


**Figure 10.13.** Box plots showing distributions for jitter simulation studies for properties shown in

**Table 6.2.** Effect on electron horizontal and vertical spot sizes at the IP waist in Sector 20 are shown for the high peak current parameter design.

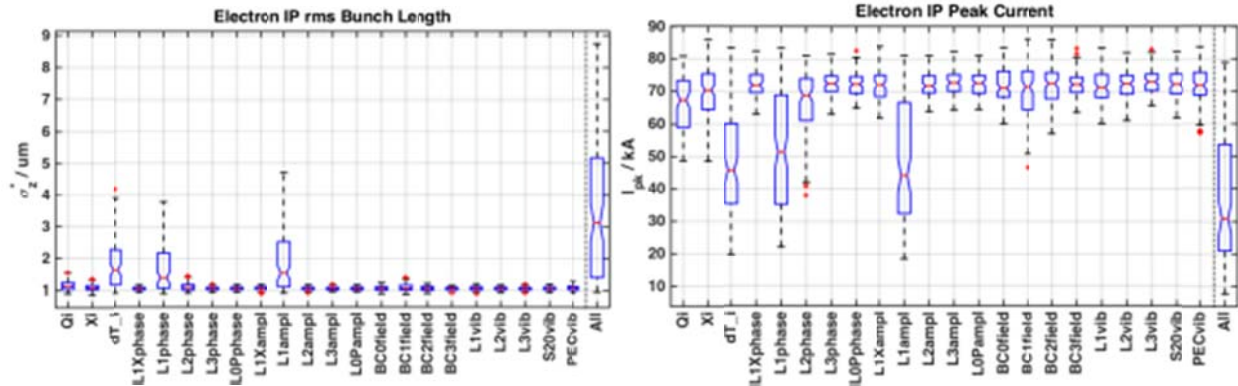


**Figure 10.14.** Box plots showing distributions for jitter simulation studies for properties shown in Table 6.2. Effect on electron bunch length and peak current at the IP waist in Sector 20 are shown for the high peak current parameter design.

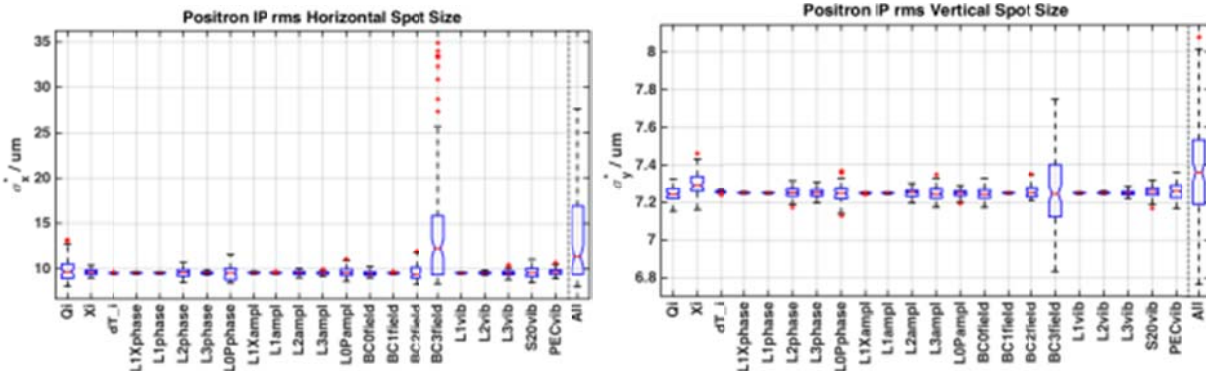


**Figure 10.15.** Box plots showing distributions for jitter simulation studies for properties shown in Table 6.2. Effect on positron horizontal and vertical spot size at the IP waist in Sector 20 are shown for the high peak current parameter design.

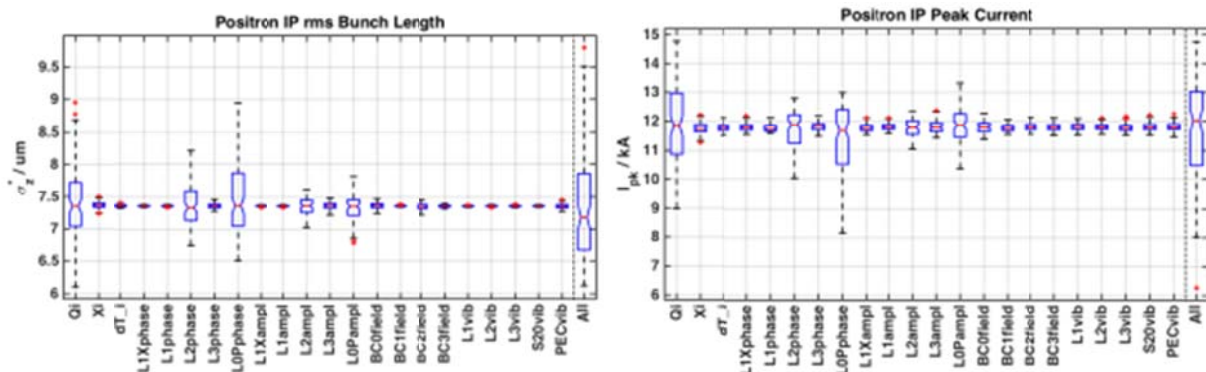


**Figure 10.16.** Box plots showing distributions for jitter simulation studies for properties shown in Table 6.2. Effect on positron horizontal and vertical spot size at the IP waist in Sector 20 are shown for the high peak current parameter design.

## **10.6 High electron charge operation mode**

### **10.6.1 Accelerator Requirements and Parameters**

For the FACET-II experimental program, the electron beam must meet a specific set of requirements for the electron transverse and longitudinal beam sizes at the experimental IP waist locations as well as requirements for peak current, energy, energy spread, and stability. These electron parameters are listed in earlier chapters which shows both the design parameters and the ranges expected. The high charge option discussed here corresponds to the 5 nC parameters included in the ranges shown. Positron parameters are listed in Chapter 8. Nominal initial bunch charge operation for positrons is 1 nC out of the damping ring. This presents the most pushed configuration for the linac imaginable, a 5 nC electron bunch co-accelerated along with a 1 nC positron bunch (additionally with a 4 nC scavenger pulse to generate the positron bunch). A schematic layout of the accelerator for the high electron charge configuration is shown in Figure 10.17 below, with beam parameters listed at various points along the accelerator. The electron beam optics from cathode to the dump in Sector 20 for the electron and positron beam is similar to that shown in Chapter 6.

No collimation is applied in BC0, BC11 or BC14 for the tracking studies presented below. The corresponding calculated apertures are then a worst-case which should be considered safe for all planned FACET-II operation modes.

There are differences between the parameters studied in the previous chapters and those simulated here. For asymmetric charges, there is considerable difference in beam loading between the electron and positron bunches, as summarized in Table 10.9. To equalize the energy between the two bunches, a set of 2<sup>nd</sup> or 4<sup>th</sup> harmonic accelerating structures are required which accelerate the electron bunches (1/2 s-band wavelength behind the positron bunch in L2 and L3) while decelerating the positrons by a total of +/- 207 MeV. Due to the increased wakefield chirp imparted to the electron bunch in L3, the L2 S-band structures are operated with maximum chirp (while still achieving 4.5 GeV beam energy at BC14) so as to achieve optimal compression after BC20. This requires sacrificing both the spare RF station and the 2 feedback RF stations. This may not be practical; and the configuration outlined here may need re-optimization later if the 5 nC option is needed.

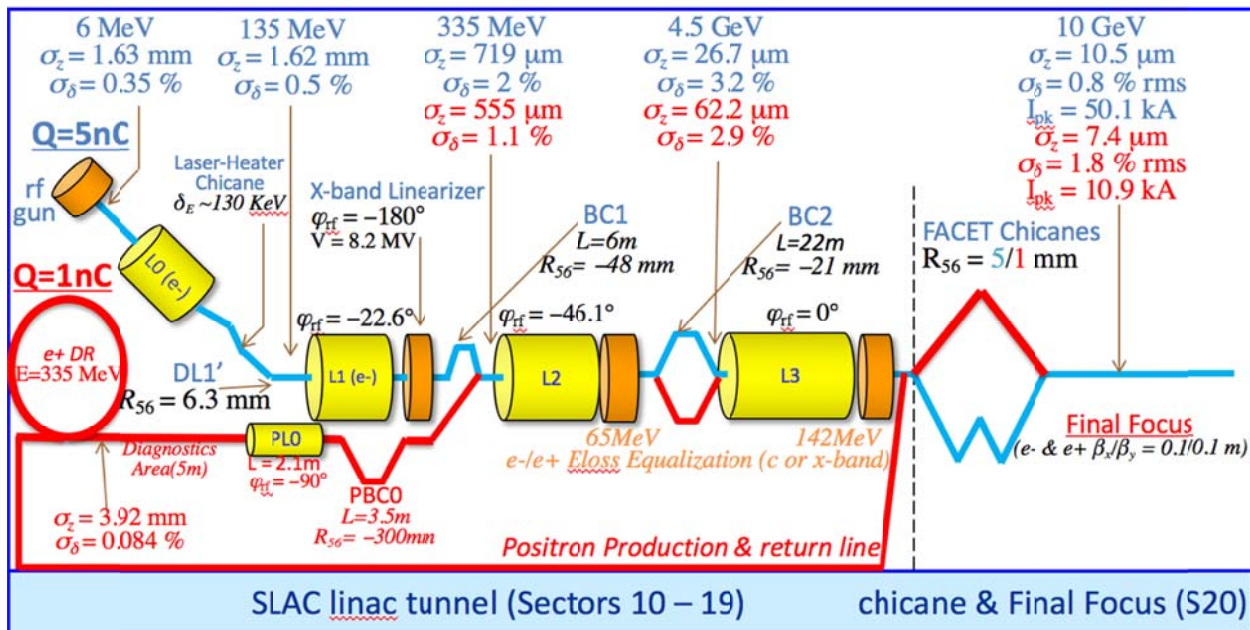


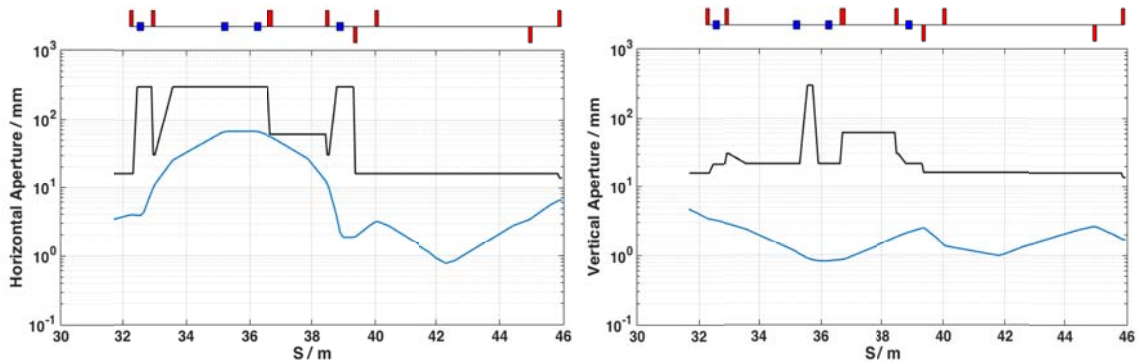
Figure 10.17. Schematic layout of FACET-II injector, linac, bunch compressors, and experimental area, with main parameters listed for operation. The blue sections depict the electron specific and common e-/e+ areas. Configuration is for the 1/5nC (e+/e-) charge option. Note: BC1 == BC11 in earlier chapters and BC2 == BC14.

Table 10.9. Energy loss for electron and positron bunches in linac sections L2 and L3 due to beam loading, and in BC14/BC20 due to ISR/CSR energy loss. Required total c or x-band RF gradient to balance the electron and positron beam energies is also shown.

E Loss Section	Positron E Loss / MeV	Electron E Loss / MeV	V <sub>x-band</sub> / MV
L2 + BC14	26.2	155.7	64.75
L3 + FACET	53.5	337.0	141.75

### 10.6.2 Bunch Compressor 1 (BC11) in Sector 11

The layout of BC11 is identical as that described in Section 6.3. The tracked longitudinal beam phase space with the 1/5 nC configuration can be seen in Figure 10.21 below. The BC11 apertures and 10X tracked beam sizes are shown in Figure 10.18.



**Figure 10.18. Horizontal and vertical magnet apertures from tracked rms beam sizes. Black curve shows design magnet apertures; blue curve shows 10X tracked rms transverse beam sizes.**

### 10.6.3 Bunch Compressor 2 (BC14) in Sector 14

The layout of BC14 is similar to that described in Section 6.4. The electron and positron tracked longitudinal phase space is shown below in Figure 10.21. The tracked beam size and required apertures are shown in Figure 10.19.

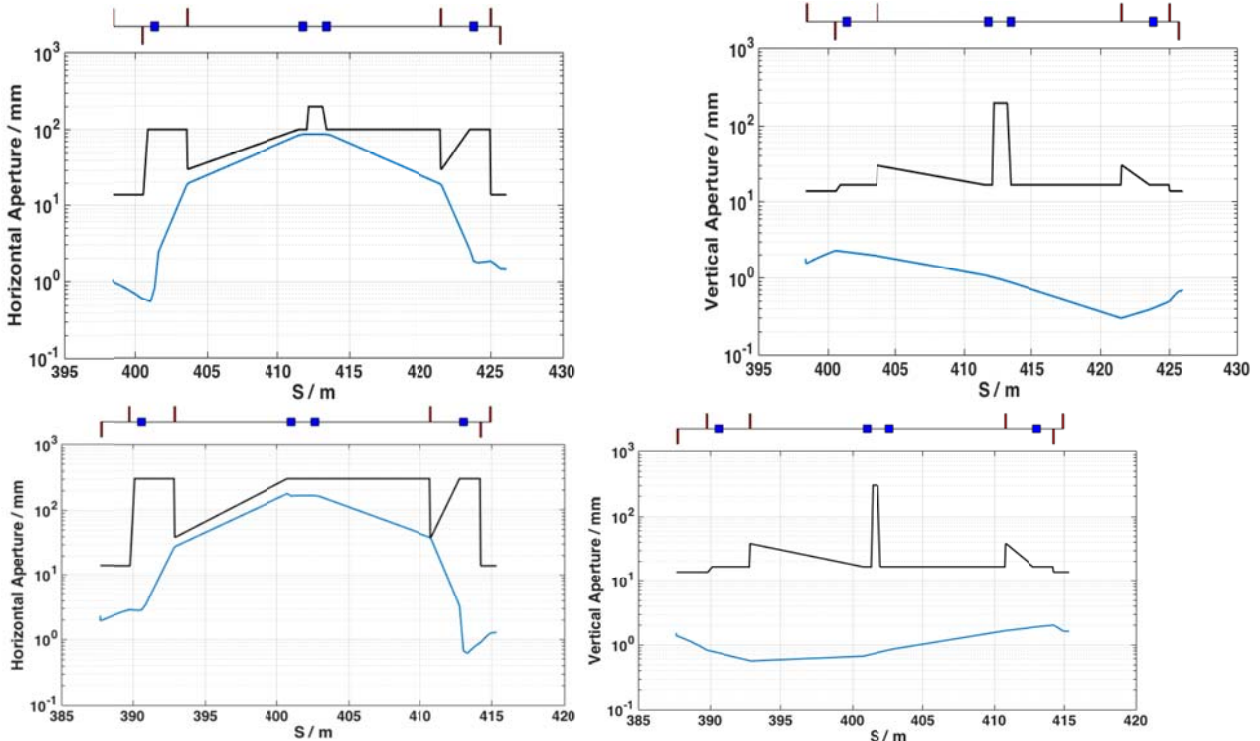


**Figure 10.19. Horizontal and vertical magnet apertures from tracked rms beam sizes. Black curve shows design magnet apertures; blue curve shows 10X tracked rms transverse beam sizes. Top row is for the positron beam design; bottom row is for the electron beam.**

## 10.6.4 Sector 20

Sector 20 is described for both the positrons and electrons in Chapter 9 and in the sailboat chicane section above in this chapter. The layout is the same here, the final tracked longitudinal and transverse phase spaces of the electron and positron beams at the experimental IP waist location are shown in Figure 10.22 and Figure 10.23 below. Beamline apertures and tracked transverse beam sizes are shown in Figure 10.20. As can be seen, the 10X beam sigma envelope encroaches on some of the horizontal beam apertures in this high charge configuration. Careful beam orbit control is required and some beam loss (as experienced at FACET) may be experienced in this region.

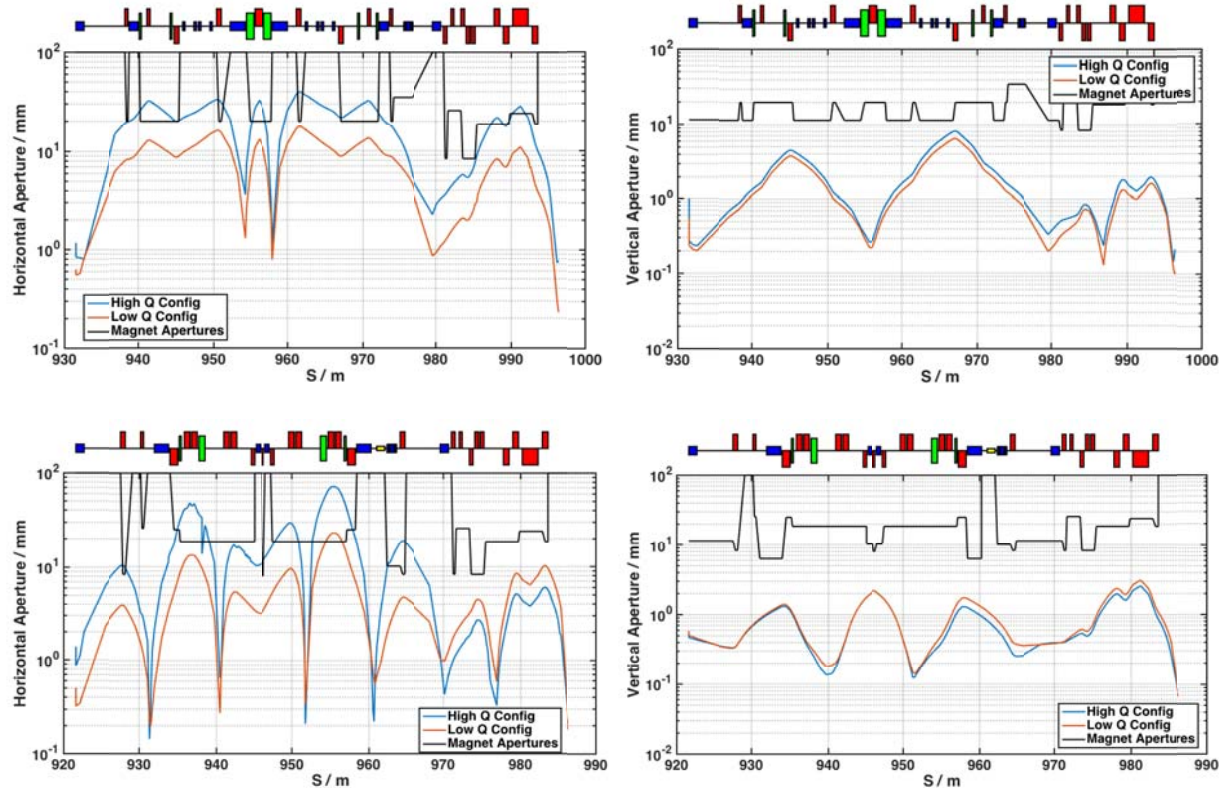


**Figure 10.20. Beamline apertures in Sector 20 and 10X tracked transverse beam sizes. Top plots are for BC20P and the positron beam, bottom plots are for BC20E and the electron beam. The "High Q config" refers to the 1/5 nC ( $e^+/e^-$  beam) configuration, the "Low Q configuration".**

## 10.6.5 Particle Tracking

Figure 10.21 shows the longitudinal configuration of the electron and positron bunches as they are tracked through FACET-II from gun or damping ring extraction through to the IP waist location in Sector 20. Figure 10.23 and Figure 10.24 show the longitudinal and transverse phase space for electron and positron bunches at the IP waist in detail. Note the longitudinal configuration is constrained by having to successfully transport and compress both electron and positron beams simultaneously. Due to the larger initial longitudinal emittance of the positron beam, the positron transport is the most challenging. If just the electron beam is required, an alternate L2 and L3 phase configuration makes it possible to deliver beams with >100 kA peak current.

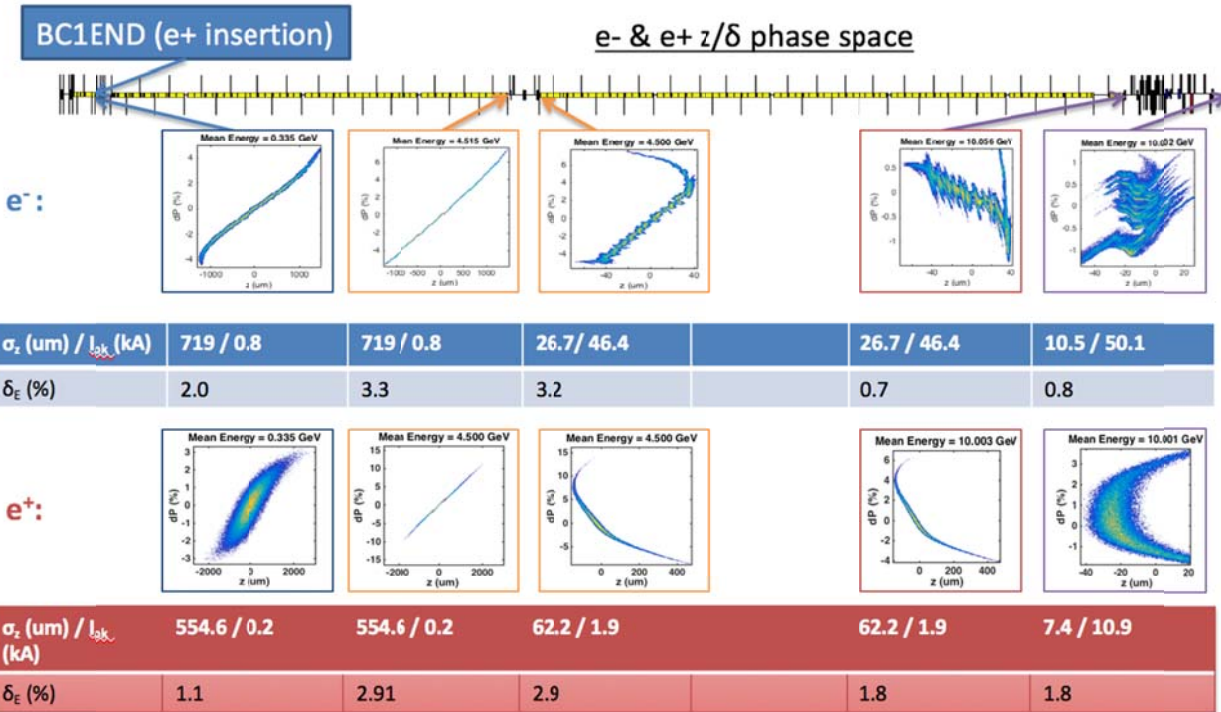


**Figure 10.21.** Longitudinal phase space of electron (top) and positron (bottom) beam as it is transported through L2, L3 and BC20 plus the final focus system to the experimental IP waist location in Sector 20. Also shown are the bunch length, peak current and relative energy spread after BC11, before and after BC14 and before and after BC20.

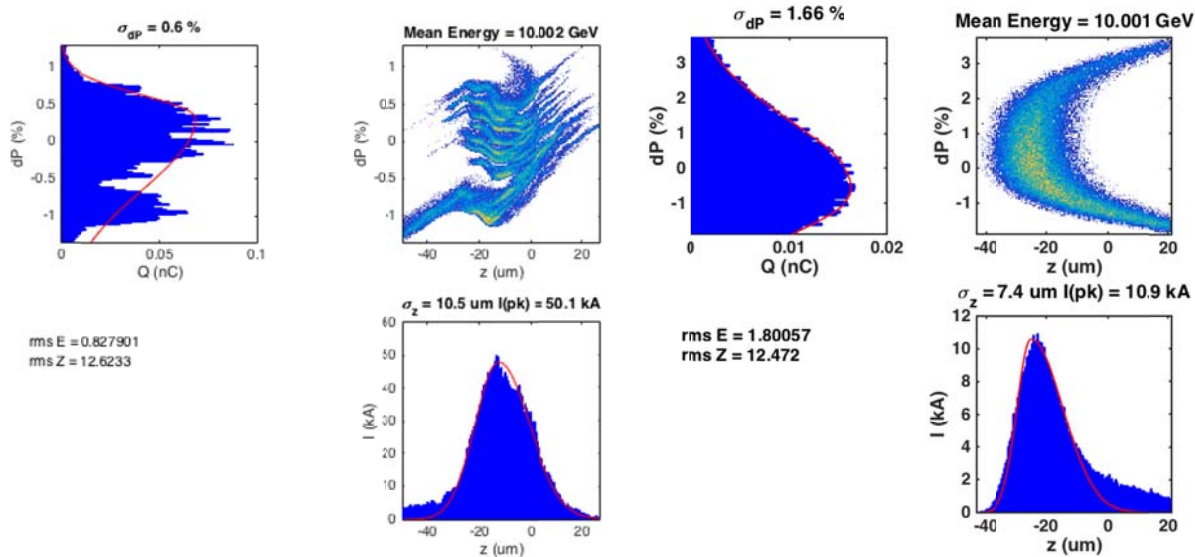


**Figure 10.22.** Longitudinal phase space of the electron beam (left) and the positron beam (right) at the Sector 20 experimental IP waist location.

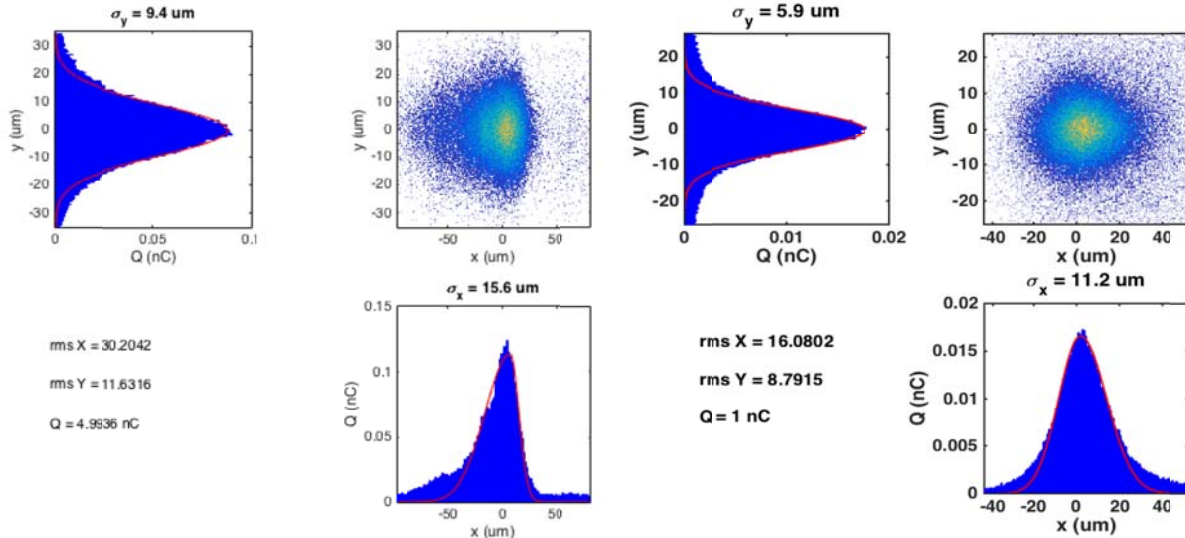


**Figure 10.23. Transverse phase space of the electron (left) and positron (right) bunches at the Sector 20 experimental IP waist location.**

### 10.7 Witness Bunch Injector

The addition of an independent witness bunch injector close to the experimental area will be a powerful tool for the plasma wakefield and dielectric wakefield programs, allowing independent control of the drive and witness bunch parameters (for example, current and energy profiles and bunch separation). The witness bunch injector will use a laser (the witness drive laser) to generate a high quality electron beam from a photocathode located inside a high field RF gun.

The witness drive laser includes a Coherent Astrella laser and a tripler to generate the 266 nm pulse for photoelectron production from a copper cathode. If needed, a multipass amplifier can be used to increase the pulse energy and electron yield. The laser system would be located in the existing FACET laser room which would be modified to house both this new laser and the FACET laser for plasma formation. An additional evacuated transport line would bring the laser a distance of approximately 50 m from the laser room to the photocathode.

The RF photocathode gun would be located in the sector 20 housing. The electrons from the gun output are accelerated to 100 MeV with two 3 meter long S-band structures.

The electron bunch needs to be compressed to meet requirements for wakefield experiments. The two accelerating sections also provide the chirp for subsequent bunch compression. The bunch is then compressed in a dogleg and injected co-linear into the main 10 GeV beamline.

Focusing of the witness bunch is provided by a final electromagnet doublet and permanent magnet quadrupole triplet located within the experimental area. The distance between the final triplet and the focus will be approximately 0.5 m. Wakefield experiments need to position their medium (whether plasma or dielectric) at the focus. The coexistence of the focusing magnets and the experiment can be achieved with a large vacuum chamber that can accommodate both the magnets and experimental apparatus. The FACET experimental area currently has two such large chambers and can reconfigure the beamline to position these at this location.

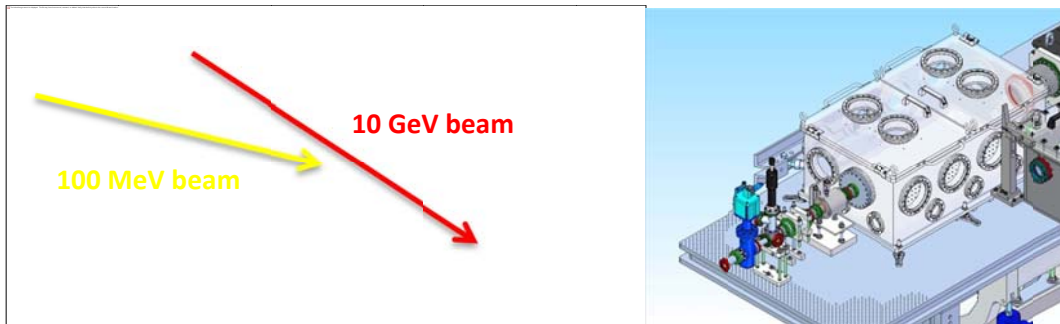


**Figure 10.24. Dogleg and focusing magnets for independently injected witness bunch. The final triplet is optimally 25 cm from the focus and can occupy the same vacuum chamber as is used for laser optomechanics (right).**

The design work to be completed includes locating the RF injector, subsequent accelerating sections and the dogleg magnets in such a way that still permits access to the experimental area. The optics need to be designed in coordination with the design of the experimental apparatus to make them compatible with the plasma source (lithium or hydrogen). The system needs to be tied into the Personnel Protection System and Beam Containment System.

### 10.7.1 Zeroth-Order Design

Below is presented a zeroth-order design of a system which has a performance approaching what is desired for the witness bunch injector. Ideally a factor  $\sim 3$  more in peak current would be preferred for the final design. The specifics of the integration within the Sector 20 main beamline environment: the physical placement, the arrangement of final focus magnets and integration into the Sector 20 experimental area etc. will need further design iterations to meet the specific user requirements outlined above.

### 10.7.1.1 Overview

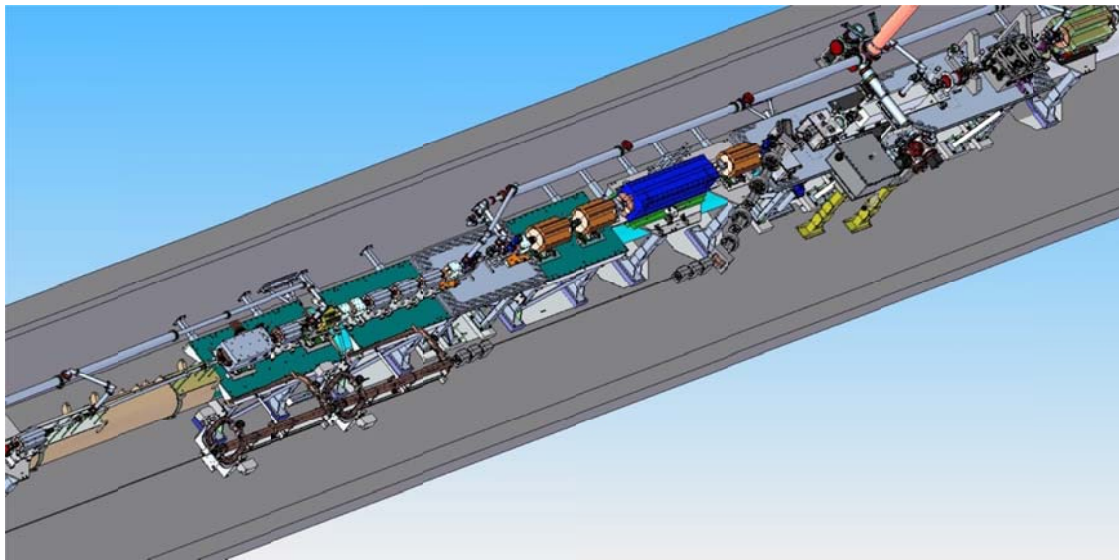


**Figure 10.25. Example integration layout of witness bunch injector components into Sector 20.** The gun (not shown) and injector RF are placed to the aisle side of the last BC20 bend, the diagnostics line runs alongside the main beam final focus optics, the horizontal dogleg injects the beam after the last QFF6 final focus magnet and is focused into the E200 plasma chamber with an insertable permanent magnet final triplet set of quads.

The key parameters and features of the witness bunch injector system are shown in Table 10.10 below. The example source parameters used in this design are presented in Table 10.11. The gun portion of the injector is not directly modeled here. The compressed beam must be directly injected into the main beamline, a short distance ( $\sim 100\text{-}200 \mu\text{m}$ ) following the main 10 GeV FACET-II “drive” beam. Hence the beam must be injected after the last main final focus quadrupole magnet (QFF6).

**Table 10.10. Key parameters and features of the witness bunch injector design**

Parameter	Symbol	Value
Drive Beam Energy	$E_d$	10.0 GeV
Witness Bunch Final Energy	$E_w$	100 MeV
rms Transverse Final Spot Size	$\sigma_x / \sigma_y$	< 10 / 10 $\mu\text{m}$
rms Longitudinal Final Bunch Length	$\sigma_z$	< 10 $\mu\text{m}$
Final Bunch Charge	$Q_f$	100 pC
Final Peak Current	$I_{pk}$	3,000 A
Final Beta Functions	$\beta_x / \beta_y$	5 x 5 mm
System Length	s	18 m

Injection Bend Angle	$\Phi$	25.78 degrees
----------------------	--------	------------------

**Table 10.11. Electron Source Parameters for witness bunch injector.**

Parameter	Symbol	Value
Initial Bunch Charge	$Q_i$	350 pC
Normalized Transverse emittance	$\gamma \epsilon_x / \gamma \epsilon_y$	1 / 1 um.rad
FWHM Bunch Length	$\Delta t_b$	1.0 ps
Peak Bunch Current	$I_{pk}$	300 A

The layout of the system is shown in the schematic in Figure 10.26, with a CAD implementation shown in Figure 10.25. The system consists of two ten-foot SLC S-band accelerating structures which are each operated at an unloaded accelerating gradient of 57.3 MV and at a phase 30.24 degrees of S-band off crest to provide the required chirp to longitudinally compress the bunch. A pair of quadrupole triplets then form a 5 m length beam diagnostics section and match the beam optics into the horizontal dogleg. The horizontal dogleg consists of a pair of bend magnets, five quadrupoles and four chromatic correction sextupoles. A quadrupole doublet immediately following the second bend magnet is shared with the drive beam, and a (removable) triplet of permanent magnet quadrupoles perform the focusing of the witness bunch just upstream of the E200 experimental plasma acceleration chamber. The L\* is designed (drift space downstream of final triplet quad to common (with drive beam) focus waist) to be 25 cm.

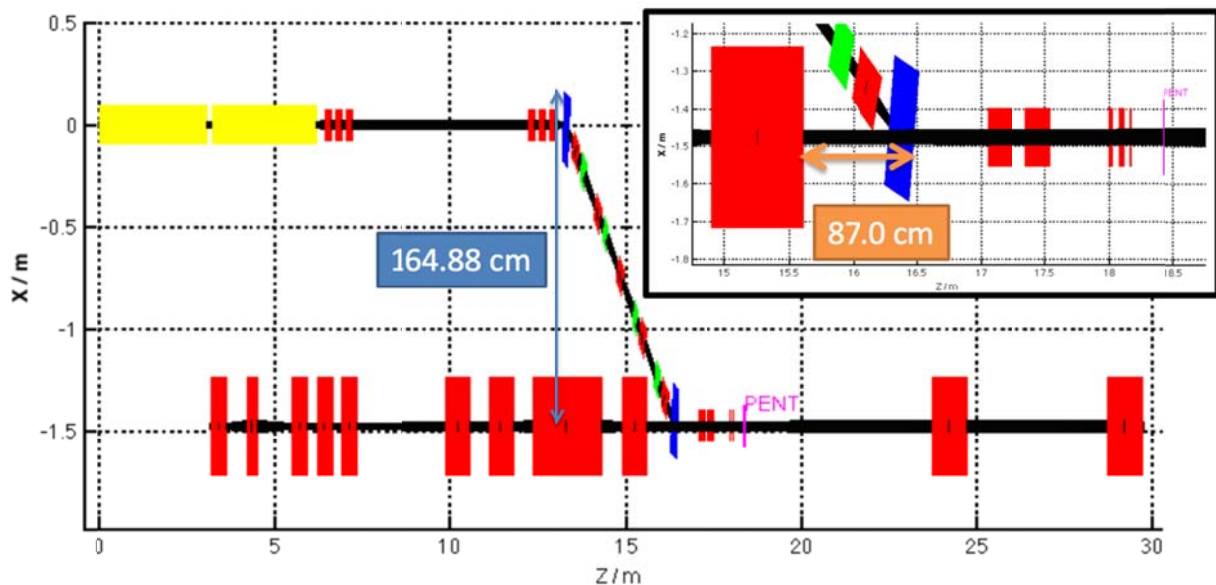


**Figure 10.26. Schematic of witness bunch injector components and implementation into FACET-II drive beam line in Sector 20. “PENT” shows the entrance location to the E200 experimental plasma**

acceleration chamber. Yellow boxes show S-band RF structure, red shows quadrupole magnets, blue are bend magnets and green are sextupoles. The black line shows the required stay-clear aperture.

### 10.7.1.2 Optics Design

The design for the witness bunch injector meets the parameter requirements set out in Table 10.10 in a compact layout which can fit alongside the main FACET-II beamline in Sector 20 and injects the bunch directly behind the drive bunch. A simple dogleg design fulfills these requirements. Using a bend angle of about 26 degrees, the witness bunch can be brought into the main beam line immediately downstream of the last final focus magnet (QFF6) leaving room to focus the beam before the E200 plasma chamber. This choice of bend angle allows for enough magnet elements to be included into the dogleg to generate a substantial compression factor ( $R_{56}=13.6$  mm) and control the optics parameters through the dogleg while fitting horizontally within the confines of the SLC tunnel.

Figure 10.27 shows the design optics functions for the witness bunch injector system. A diagnostics waist is included upstream of the dogleg to provide emittance diagnostics and matching capabilities. A moveable jaw collimator located where the high dispersion to beta ratio is high (as shown with the dashed line in Figure 10.27) allows for fine-grained control over the longitudinal bunch profile. Four sextupole magnets at dispersive locations within the dogleg compensate for chromatic aberrations and second-order dispersion inherent in the design. If placed on mover systems, they can also be used to provide correction of errant dispersion, coupling or waist shifts at the IP focus. Longitudinal compression of the beam is achieved by running the two S-band RF structures off crest by ~30 degrees which provides an energy chirp to the bunches so that they then compress in z as they travel through the dogleg. A doublet of quadrupole magnets and a final permanent magnet quadrupole triplet just before the E200 plasma chamber entrance provide the final focusing of the witness bunch. These can be shared with the main drive beam, because the upstream optics seen only by the drive beam can be matched to take these comparatively weak quadrupole fields into account. The witness bunch final focus provides beta functions at the waist of 5 mm, which for an expected 1  $\mu\text{m} \cdot \text{rad}$  normalized emittance should produce a 5  $\mu\text{m}$  transverse beam size. This allows for a factor 2 additional beam size growth due to uncorrected errors while still meeting the requirements set out in Table 10.10.

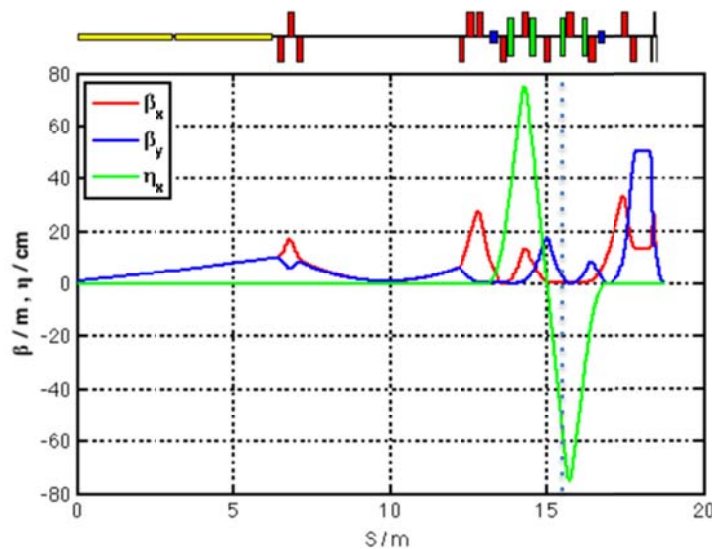


**Figure 10.27. Twiss parameters for witness bunch injector design showing RF acceleration to 100 MeV, diagnostics waist, horizontal dog leg injection into main beamline and final focus doublet and triplet**

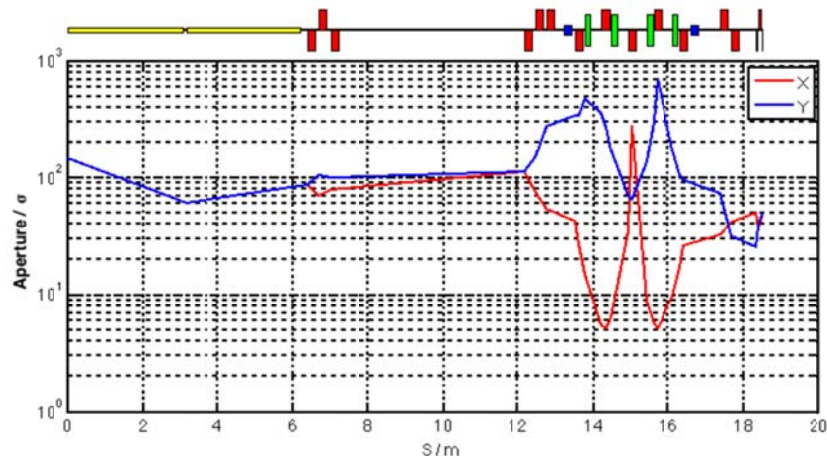
system. The beam waist in the E200 plasma chamber is the right-most point on the figure. The dashed line shows the location of the moveable jaw collimator within the dogleg.

#### 10.7.1.3 Particle Tracking

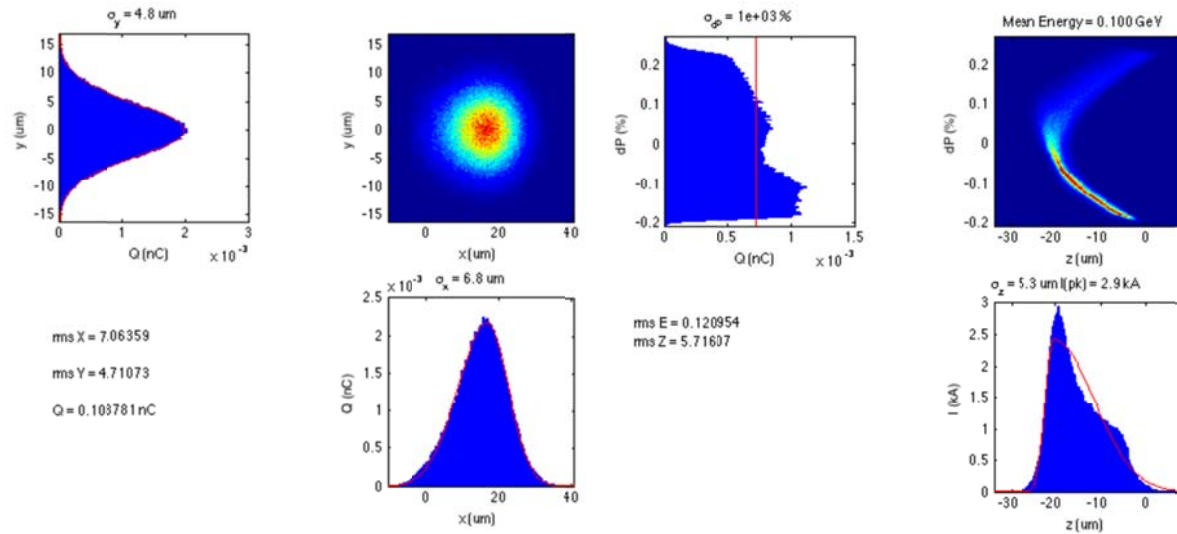
Using a 6D tracking code (*Lucretia*), a 1M macro-particle representation of the beam was tracked through the design optics including the effects of ISR and CSR, but not space-charge. Figure 10.28 shows the beam clearance for the planned magnets as a function of their aperture sizes. As can be seen, the limiting apertures are in the horizontal in the high dispersion regions of the dogleg. Here the aperture is restricted to about  $\pm 5$  sigma. In these key locations, wider aperture magnets may be required.

Figure 10.29 shows the tracked beam at the IP waist location within the plasma volume (no attempt is made here to model the interaction with the plasma) where the required parameters are met. The jaw collimators within the dogleg were set to  $\pm 2$ mm to limit the non-linear high energy-spread tails to achieve this profile.

To estimate the maximum longitudinal contrast of the delivered beam, the core of the beam was cut with one jaw of the collimator and an asymmetric Gaussian function fitted to the beam at the IP waist. A minimum resolvable length scale of about 1.9  $\mu\text{m}$  rms looks feasible (see Figure 10.30).



**Figure 10.28. Beam clearance calculation from tracked beam through witness bunch injector optics. Lines show aperture widths of beamline elements as a factor of rms transverse beam sizes at those locations.**



**Figure 10.29. Tracked transverse and longitudinal phase space of witness bunch at IP focus point. Collimator jaws are set to +/- 2mm.**

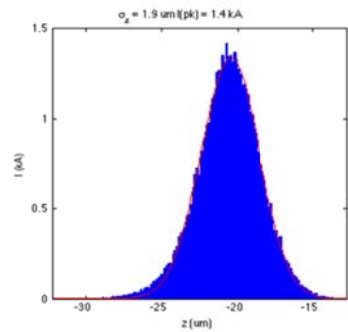


**Figure 10.30. Longitudinal contrast- the longitudinal profile of the beam at the IP waist with one jaw collimator cutting into central core region of the beam. Shown is an asymmetric Gaussian fit to the longitudinal distribution.**

#### 10.7.1.4 Magnets

This design for the witness bunch injector requires 13 quadrupole magnets, one permanent magnet quadrupole triplet installation, 2 rectangular bends and 4 sextupoles. Most of the required magnets could come from the existing positron system in Sector 1 which will be decommissioned during the construction of LCLS-II. The magnet requirements are given in Table 10.14, with some further magnet details shown in Figure 10.31 through Figure 10.34 and Table 10.12 and Table 10.13. An example design for the final permanent quadrupole magnet was provided by an external vendor (see example in Figure 10.34).

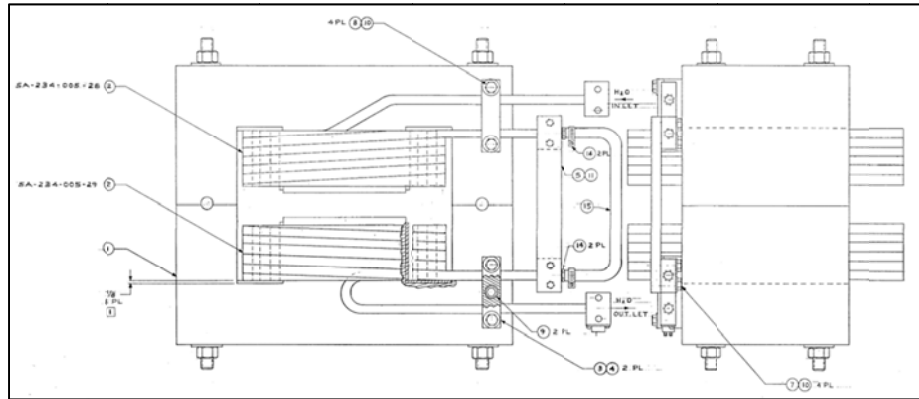


**Figure 10.31. SLC "5D7.1" style bend magnet used in Sector 1 positron re-injection section.**

**Table 10.12. Parameters of selected existing bend magnets for use in witness bunch injector design.**

Parameter	Value
Effective Length	0.2032 m
Design Bend Angle @ 200 MeV	12 deg
Half-Aperture	0.0133 m
Width	0.3556 m
Height	0.292 m
Max Integrated Strength @ I=290A	1.5 kG.m

**Table 10.13. Parameters of selected existing quadrupole magnets for use in witness bunch injector design.**

Parameter	Value
Effective Length	0.197 m
Half-Aperture	0.0192 m
Width	0.1588 m
Height	0.292 m
Max Integrated Strength @ $ l =90^\circ$	31 kG

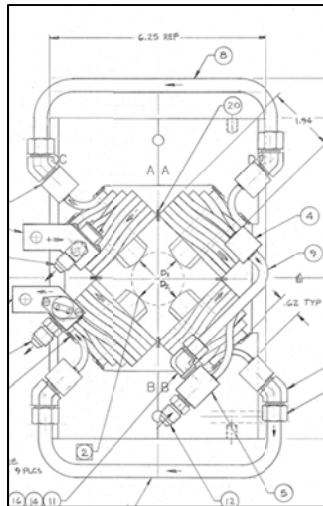


**Figure 10.32. SLC "1.57Q7" style quadrupole magnet used in Sector 1 positron re-injection section.**

**Table 10.14. Magnet properties for witness bunch injector design.**

ELEMENT	Eng_Name	L_EFF	APER	Integrated_Field_Gradient_GL	SLAC Drawing #
		m	m	kG	
<b>QWBM1</b>	1.57Q7	0.197	0.038354	-3.499954304	SA-902-708-54
<b>QWBM2</b>	1.57Q7	0.197	0.038354	6.644913243	SA-902-708-54
<b>QWBM3</b>	1.57Q7	0.197	0.038354	-3.499954304	SA-902-708-54
<b>QWBM4</b>	1.57Q7	0.197	0.038354	-5.929464018	SA-902-708-54
<b>QWBM5</b>	1.57Q7	0.197	0.038354	1.199656258	SA-902-708-54
<b>QWBM6</b>	1.57Q7	0.197	0.038354	7.345447701	SA-902-708-54
<b>BXWBDL1</b>	5D7.1	0.2032	0.02667	1.5	SA-234-005-26
<b>QWBDL1</b>	1.57Q7	0.197	0.038354	-11.39898197	SA-902-708-54
<b>SWBDL1</b>	1.625SX3.53	0.1	0.041275	6.50E+02	SA-235-037-30
<b>QWBDL2</b>	1.57Q7	0.197	0.038354	9.669975057	SA-902-708-54
<b>SWBDL2</b>	1.625SX3.53	0.1	0.041275	79.99895551	SA-235-037-30
<b>QWBDL3</b>	1.57Q7	0.197	0.038354	-8.999882494	SA-902-708-54
<b>SWBDL3</b>	1.625SX3.53	0.1	0.041275	79.99895551	SA-235-037-30
<b>QWBDL4</b>	1.57Q7	0.197	0.038354	9.669975057	SA-902-708-54
<b>SWBDL4</b>	1.625SX3.53	0.1	0.041275	6.50E+02	SA-235-037-30
<b>QWBDL5</b>	1.57Q7	0.197	0.038354	-11.39898197	SA-902-708-54
<b>BXWBDL2</b>	5D7.1	0.2032	0.02667	1.5	SA-234-005-26
<b>QWBFF1</b>	1.57Q7	0.197	0.038354	7.661553482	SA-902-708-54
<b>QWBFF2</b>	1.57Q7	0.197	0.038354	-6.87604884	SA-902-708-54
<b>QWBFF3</b>	PMQ	0.029704	0.0254	-19.69349488	

<b>QWBFF4</b>	PMQ	0.048826	0.0254	32.37121536
<b>QWBFF5</b>	PMQ	0.01773	0.0254	-11.75483653

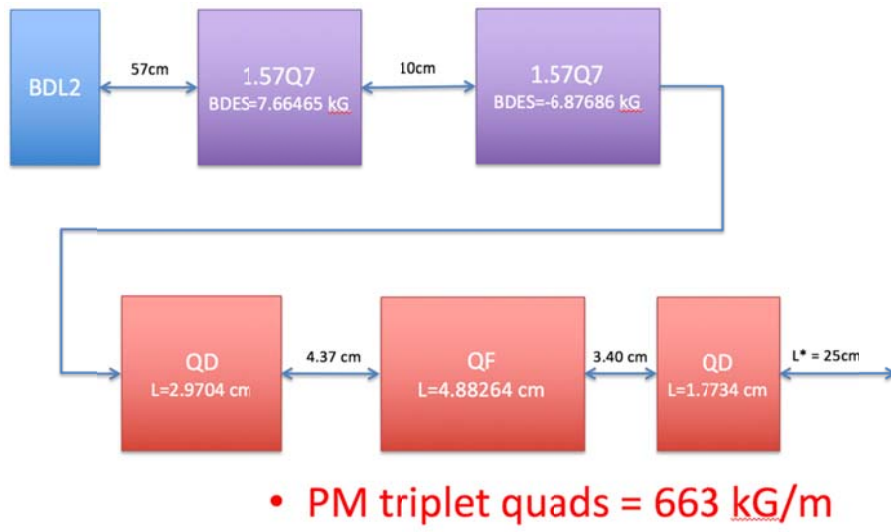


**Figure 10.33.** Schematic of design and placement of witness bunch injector final focus doublet and triplet quadrupole magnets.

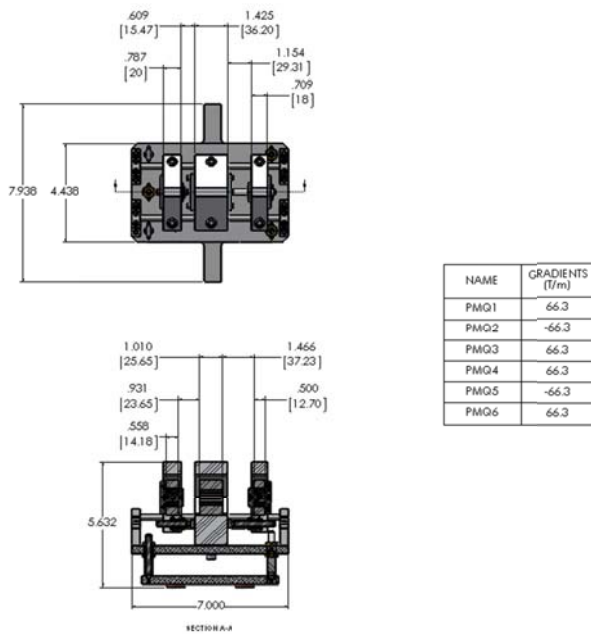


**Figure 10.34.** Vendor-sourced permanent quadrupole magnet triplet example.

## 10.8 Differential Pumping

The beam parameters for FACET-II force a new solution for isolating experimental vacuum from the main linac vacuum. To date, thin, low Z vacuum tight windows have been used (typically 50  $\mu\text{m}$  beryllium) to isolate the vacuum of the experimental systems (which by necessity include materials not suitable for the ultra-high vacuum systems needed in accelerating structures) from the linac. The

windows need to be replaced every few months as part of general maintenance as sublimation from the powerful electron beams reduces the thickness and eventually leads to hole formation. Temporary mitigations include a series of vacuum windows on valves so there is redundancy if one gets damaged. The full solution of differential pumping reduces the down time of replacing these windows and also improves the quality of the beam that is delivered to the experiments as the beam does not get scattered by solid material.

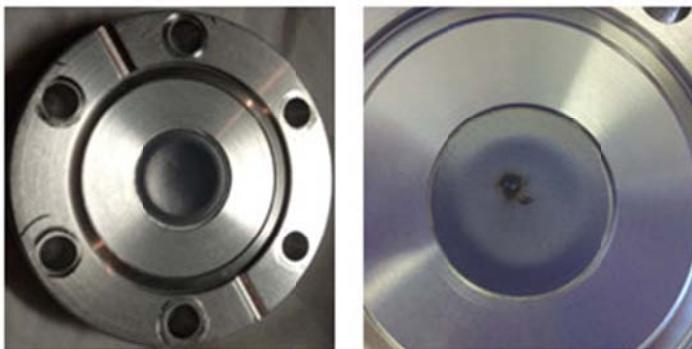


**Figure 10.35. New beryllium window, unused. Right: This beryllium window was used in the FACET beamline. Discoloration surrounds a microscopic hole.**

Differential pumping has been designed for the XTES SXR gas attenuator, part of the LCLS-II project. The requirements for this instrument are similar to those needed for the FACET-II experiments and a similar design will be used. The XTES SXR differential pumping design has undergone Preliminary Design Review.

The principal function of the gas attenuator for LCLS-II is to provide variable attenuation to the FEL beam. They will use argon or nitrogen gas with variable pressure between 0.1 Torr and 50 Torr. Experiments at FACET have to date used between 1 Torr and 40 Torr of gas species such as hydrogen, helium, neon and argon. The gas is ionized with a high power laser or by the beam to form plasma for plasma wakefield experiments or it is used as a buffer to contain a column of alkali metal vapor.

The major components of the differential pumping for XTES SXR are shown in Figure 10.36. The differential pumping is symmetric about the center of the gas cell. For FACET-II, ultra-high vacuum requirements exist upstream of the gas cell but not downstream and aperture requirements for the beam passage are larger downstream so a symmetric design is not needed.

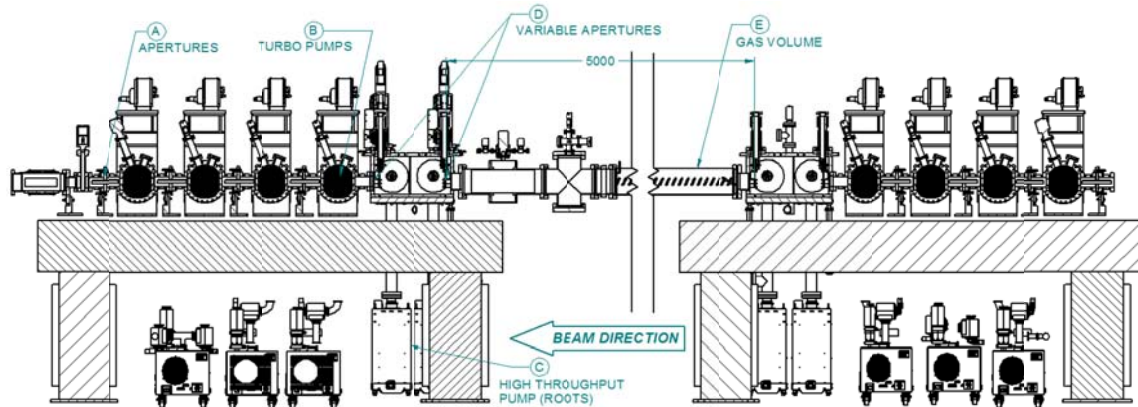


**Figure 10.36. Differential pumping design for the XTES Gas Attenuator for LCLS II. The requirements for the differential pumping are close to those needed for FACET experiments.**

On SXR, the two highest pressure apertures are variable apertures and at the lower pressures, fixed tubes. The variable apertures (labeled D in Figure 10.36 and shown in detail in Figure 10.37) are required to satisfy the variable “beam stay clear” for different x-ray energies and variable gas cell pressure. FACET-II will take advantage of variable apertures to most efficiently reduce viscous or transitional gas flow to the differential pumping system. The aperture can also be moved to the beam position remotely making alignment tolerances in installation less of an issue. The smallest aperture in the SXR design is 4 mm (pressure is approximately 10 Torr of nitrogen gas for effective attenuation of 1.2 keV x-rays). Further from the gas volume, in the molecular flow regime, tubes (labeled A) are better at limiting flow than thin plate apertures and are approximately 12 mm in diameter in the SXR model.

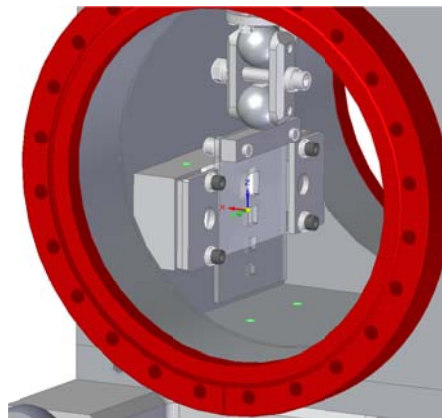


**Figure 10.37. Variable aperture plate concept for XTES SXR.**

The first stage of pumping will be high throughput pumps ( $>70$  Torr /s) such as roots type pumps (labeled C). Attention needs to be paid to the first turbomolecular pump (labeled B in Figure 10.36). With increased pressure in the gas cell and the increase in the gas flow that follows, the first turbo is the most affected. The roots pumps that precede them can pump up to atmospheric pressure, but most turbos see an exponential degradation in speed when pressures are above  $10^{-3}$  Torr. The first turbo needs high throughput at high pressures (in the range  $10^{-2}$  to  $10^{-1}$  Torr) and will need to be carefully selected. If all turbos however are the same type, this reduces operations costs by saving money with the number of spare units and in maintaining systems. After the differential pumping stages, the final pressure is  $10^{-9}$  Torr, matching requirements for operating RF cavities.

The pressure management of the gas volume will be handled with capacitance manometers and a feedback system with a variable aperture valve on the gas input.

The XTES SXR design manages the decrease from approximately 50 Torr to  $10^{-9}$  Torr in 5 meters. FACET-II can afford to use more beamline for the differential pumping system. On the up-beam side, there are 20 meters between the final RF structure and the start of the gas cell. This beamline will however be shared with magnets that are part of the sector 20 final focus.

Turbo pumps similar to those needed for this installation are commonly used in FACET for the vacuum systems in the experimental area and are reliable in the FACET environment.

## **10.9 Compton Source**

Compton experiments collide electrons on photons. FACET can provide both using existing infrastructure but to reach the required luminosity, the FACET laser needs to be upgraded in energy. Additional flash lamp YAG pump lasers (SAGAs) will be purchased and integrated as part of the FACET II project but run at low voltage so as to provide overhead for laser delivery, ensuring that the energy delivered to experiments remains nominal.

To run the SAGAs at their peak output and increase the energy of the FACET laser to 1 J at the delivery point, existing optics need to be replaced with larger ones.

The Compton Source experiments are statistical and benefit hugely from increased repetition rate. Current repetition rate of the FACET laser system is 10 Hz. This can be upgraded to 20 Hz by temporally interleaving two 10 Hz pulses. This requires an additional three SAGAs. Installation in the FACET laser room can be achieved by stacking the SAGAs vertically.

Theoretically, FACET II can operate an electron beam at 120 Hz. To upgrade the laser to 120 Hz involves the construction of a new laser facility and is not captured in this preliminary description. If 20 Hz SAGAs become available commercially, this project would also cover the upgrade of all FACET SAGAs to 20 Hz operation providing 40 Hz laser repetition rate after temporally interleaving the SAGAs.

## **10.10 Photon-Photon Collider Option**

### **10.10.1 Overview**

Section 3.7 proposes a gamma beam program that provides a test of pair creation by colliding Compton photons generated in the final sections of BC3E and BC3P. Given the geometry imposed by the final bend angles in BC20 (22.6 mrad), an optimal beam energy for this option is 4 GeV, where 30 MeV Compton photons collide inside the final BC20 bend magnet with a center of mass energy close to the maximum pair production cross-section at  $\sim$ 1.4 MeV.

Figure 10.38 below shows a sketch outlining a possible configuration for the laser interaction with the electron and positron beams in the second part of the BC20E and BC20P chicanes. A laser waist is formed as close as possible to the upstream face of the bend magnet (0.4m is assumed here) where it interacts with the electron/positron bunch. Compton photons collide at a point 0.93 m downstream within the bend magnet.

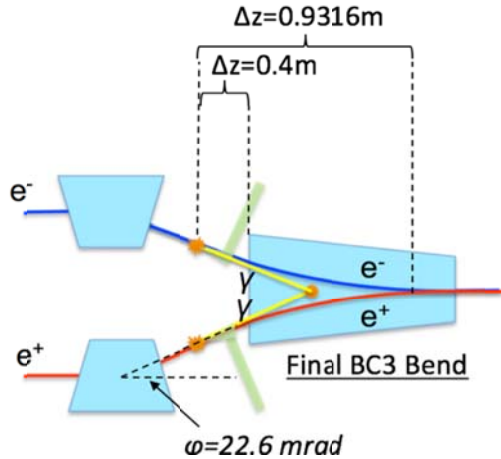


**Figure 10.38.** Sketch of photon-photon collider option in the final BC20 (labelled in figure as ‘BC3’) bend magnet.

### 10.10.2 Laser Parameters

The laser parameters at the interaction point with the electron/positron beam upstream of the final BC20 bend magnet are shown in Table 10.15.

**Table 10.15.** Parameters of CO<sub>2</sub> laser at waist location 0.4 m upstream of final BC3 bend magnet.

Parameter	Symbol	Value
Beam Energy / pulse	$E_l$	0.3 J
Wavelength	$\lambda_l$	10.2 μm
Rayleigh Length	-	300 μm
Beam Length	$\sigma_{z,l}$	300 μm
Beam Radius	$\sigma_l$	25 μm

### 10.10.3 Linac Configuration

The compression configuration for the FACET-II linac for 4 GeV beam energy operations in Sector 20 is summarized in Figure 10.39 below. For this configuration, the energy of the BC2 chicanes are lowered to 2.0 GeV, while the compression setting ( $R_{56}$ ) is the same as for nominal FACET-II operation. The beam is fully compressed by the end of L3 with a bunch length below 300 μm and final energy spread below 0.1%. Beam tracking is performed as described in Section 6.7. Figure 10.40 and Figure 10.41 show the tracked longitudinal and transverse beam phase space for the electron and positron bunch entering Sector 20. As the beam is fully compressed, without an energy chirp entering Sector 20, the  $R_{56}$  of the BC3E and BC3P chicanes is not a design parameter, see Section 10.6.9 below for details of the BC3 chicane design.

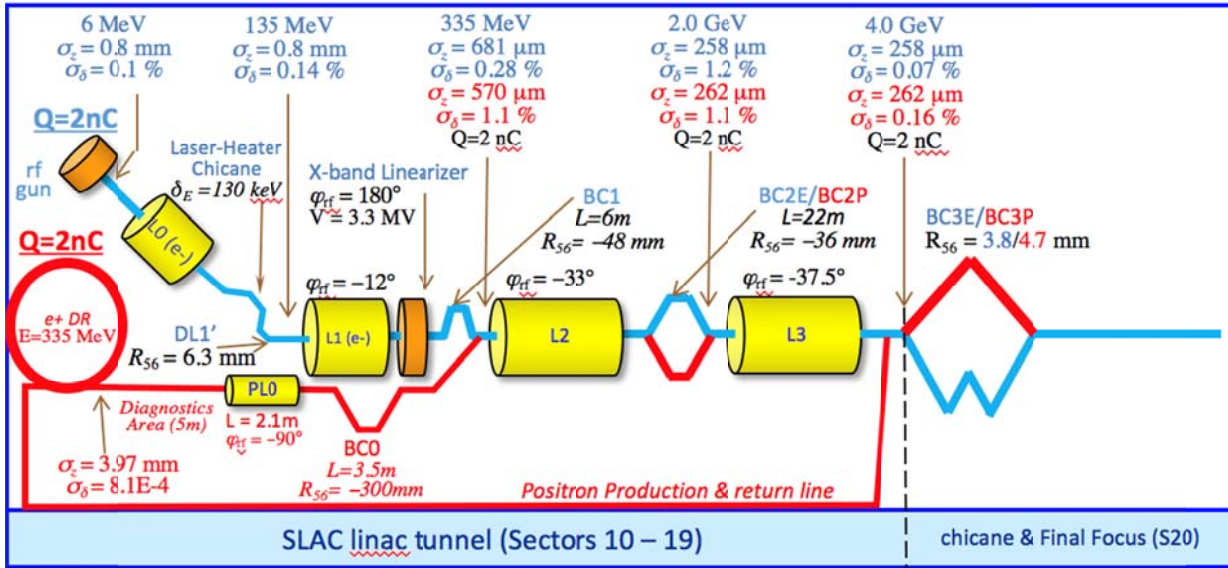


Figure 10.39. FACET-II configuration and longitudinal beam parameters for Photon-Photon collisions in Sector 20.

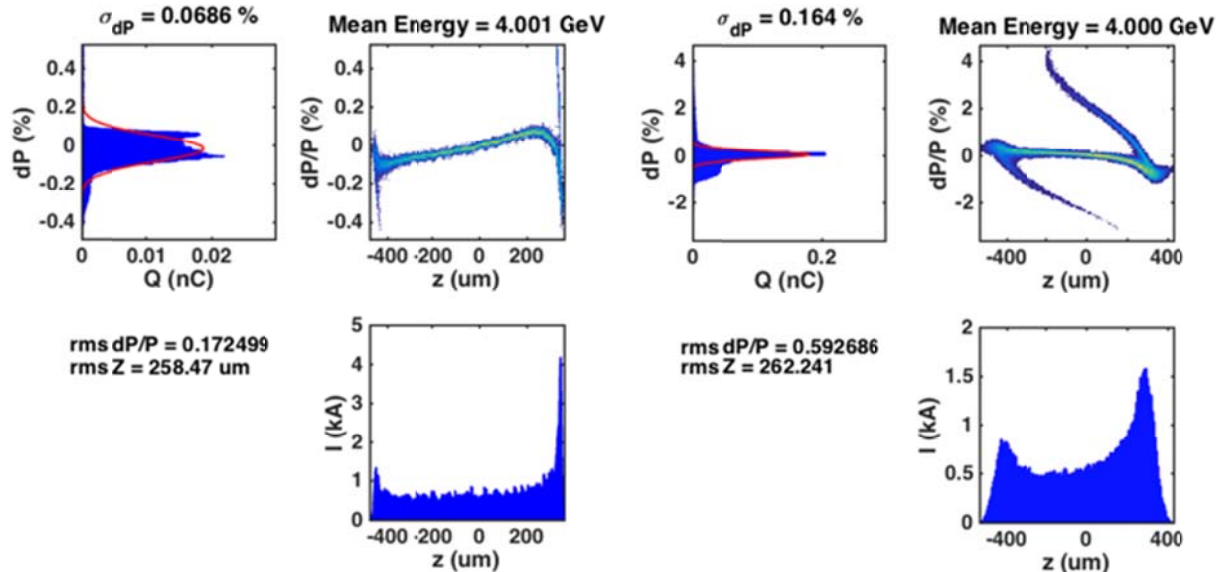
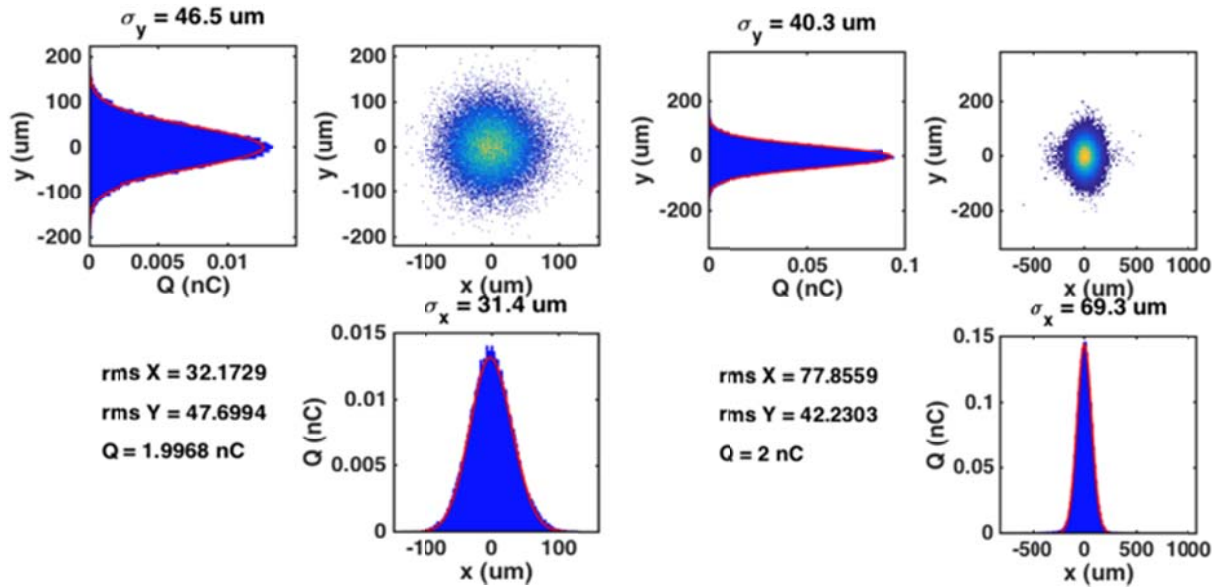


Figure 10.40. Longitudinal phase space of beam tracked to entrance of Sector 20. The 2 nC electron beam is shown to the left and the 2 nC positron beam on the right.



**Figure 10.41.** Transverse phase space of beam tracked to entrance of Sector 20. The 2 nC electron beam is shown to the left and the 2 nC positron beam on the right.

### 10.10.4 BC20E & BC20P Configuration

The BC3E and BC3P chicanes are re-matched to maximize both the Compton photon production rate at the laser waist location 40 cm upstream of the final bend and the gamma-gamma luminosity at the collision point within the bend. The following match conditions are imposed while constraining the beam size to remain within the chicane magnet apertures at the 10-sigma level:

- Electron and positron transverse spot sizes at the Compton waists consistent with laser waist sizes at those locations (25  $\mu\text{m}$ ).
- Electron and positron transverse spot size at projected photon collision point within final bend small compared to projected photon waist size at that location (119  $\mu\text{m}$ ).
- Photon waist size at collision point given by  $(1/\gamma)*L$ , where  $\gamma$  is the relativistic factor of the particle beams and  $L$  is the drift distance to the collision point in the final bend magnet (0.93 m).
- Horizontal momentum dispersion of electron and positron beams canceled at Compton laser waist location.

Figure 10.42 and Figure 10.43 below show the re-matched optics for BC3E and BC3P. To keep the changes to the normal operating system to a minimum, only the magnets within Sector 20 are adjusted. The matching solution here assumes that all magnets within the BC3E and BC3P chicanes have independently controllable power supplies. The beam spot sizes at the Compton laser interaction waist and the photon beam size at the collision point are shown in Table 10.16. Figure 10.44 and Figure 10.45 show the magnet apertures in the two bunch compressor chicanes and the 10 sigma tracked beam envelope. The calculated beam clearance is considered generally acceptable, with one tight spot around the BC2ER bend in the vertical plane. This is however compatible with current operating FACET conditions.

**Table 10.16. Electron/positron beam sizes at interaction waist with Compton laser source and projected photon beam sizes at gamma collision point in final bend magnet.**

rms Transverse Beam Size	Electron		Positron	
	Beam @ Laser Waist	y IP	Beam @ Laser Waist	y IP
$\sigma_x^*$	8.8 um	130 um	43.0 um	131 um
$\sigma_y^*$	21.6 um	123 um	22.0 um	133 um

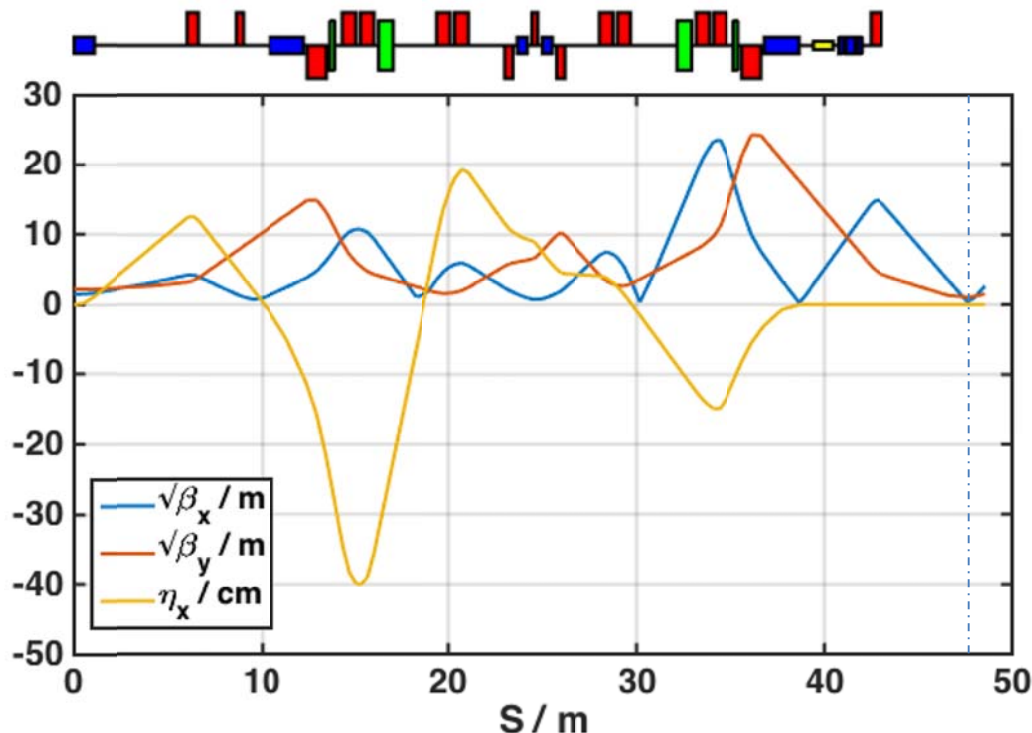


**Figure 10.42. Optics functions for BC20E chicane (electron beam) for gamma-gamma collider configuration. Dashed line shows Compton laser waist location.**

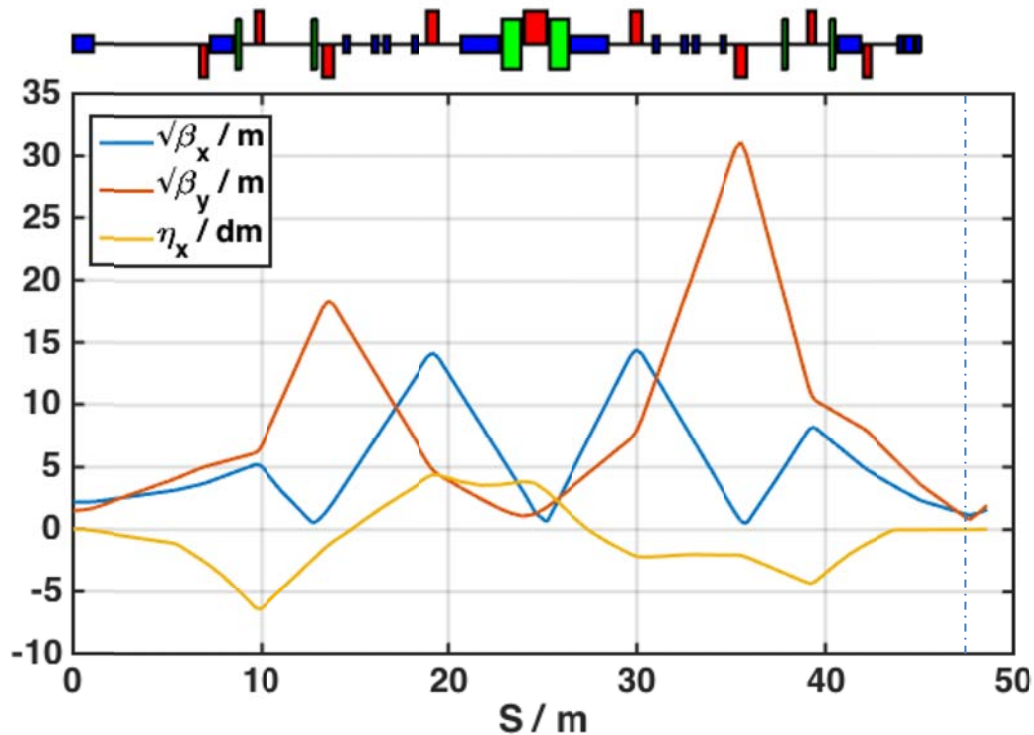


Figure 10.43. Optics functions for BC20P chicane (positron beam) for gamma-gamma collider configuration. Dashed line shows Compton laser waist location

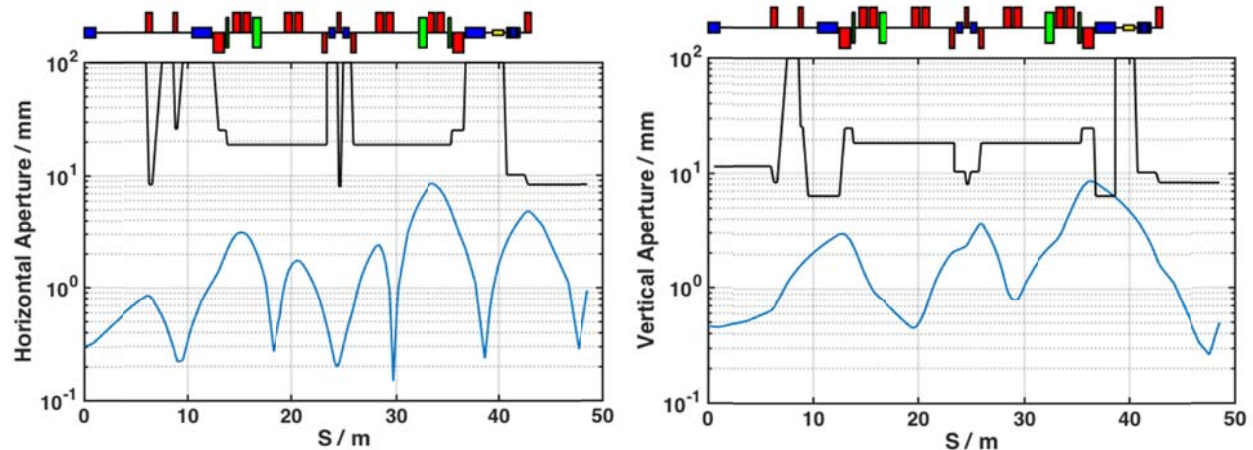
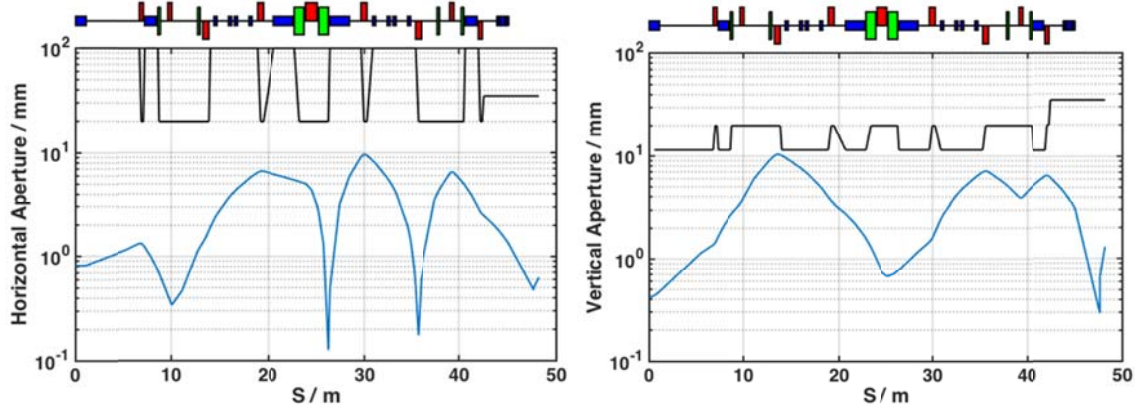


Figure 10.44. Horizontal and vertical beam apertures in BC20E (black line) and 10X tracked transverse beam envelope (blue curve). For BC20E (electrons).



**Figure 10.45. Horizontal and vertical beam apertures in BC3E (black line) and 10X tracked transverse beam envelope (blue curve). For BC3P (positrons).**

### 10.10.5 Final Focus and Spectrometer Configuration

The only requirements for the downstream final focus and spectrometer magnets is that the beam remain contained within existing apertures and extract cleanly to the dump. The optical functions are shown in Figure 10.46 and the 10 sigma beam envelope and magnet apertures are shown in Figure 10.47 and Figure 10.48 which shows adequate beam clearance.

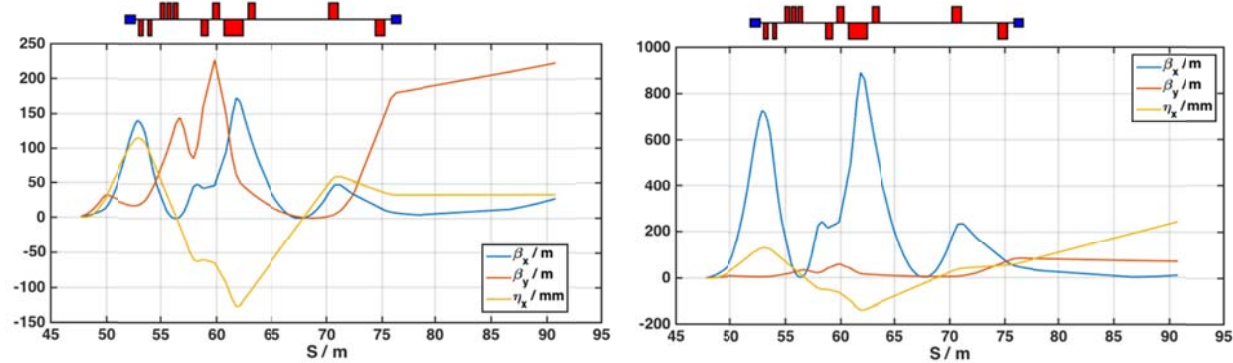


**Figure 10.46. Optics functions for the final focus and spectrometer section following the BC3E and BC3P chicanes. Positrons are shown on the left and electrons on the right.**

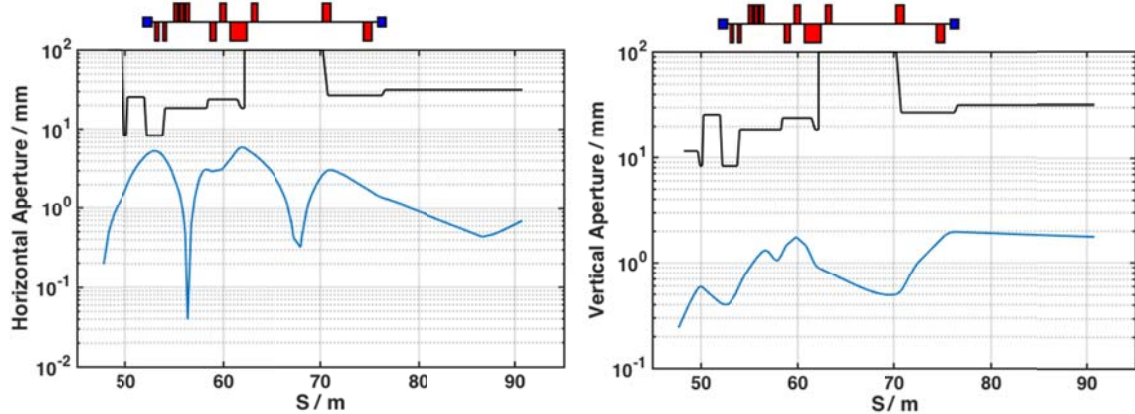


**Figure 10.47.** Electron beam 10 sigma beam envelope (blue) and final focus and spectrometer apertures (black). Horizontal dimension shown on the left, vertical shown on the right.

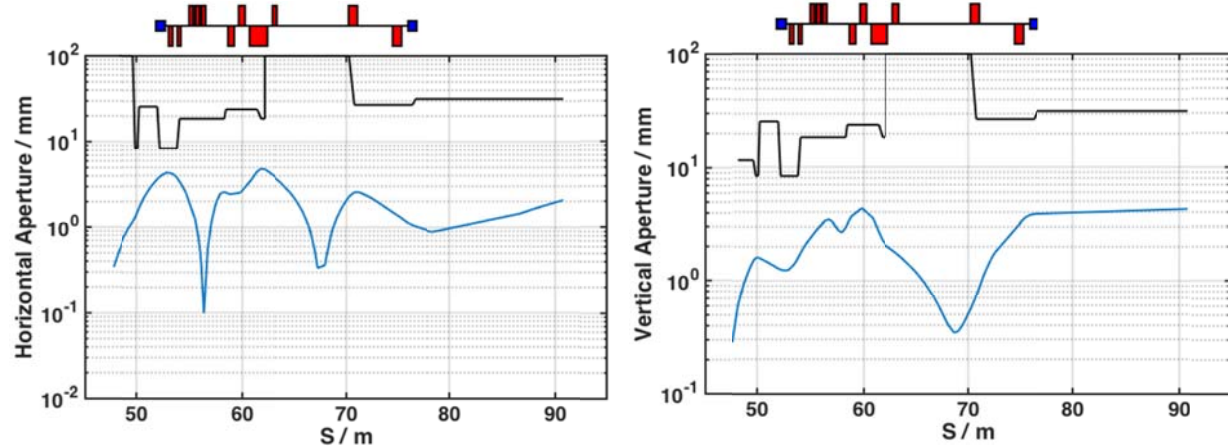


**Figure 10.48.** Positron beam 10 sigma beam envelope (blue) and final focus and spectrometer apertures (black). Horizontal dimension shown on the left, vertical shown on the right.

### 10.10.6 Photon-Photon Collision Luminosity and Expected Pair Production Rate

Using the proposed design and beam and laser parameters, the expected Compton photon luminosity per pulse is given by,

$$\mathcal{L}_\gamma = \frac{N_e N_\gamma^l}{2\pi \sqrt{(\sigma_x^2 + \sigma_l^2)(\sigma_y^2 + \sigma_l^2)}},$$

where,  $N_e$  and  $N_\gamma^l$  are the number of electrons (or  $N_p$  positrons) and number of laser photons per pulse, respectively.  $\sigma_{x,y}$  are the transverse beam spot sizes at the laser interaction waist of the electrons or positrons, and  $\sigma_l$  is the transverse spot size of the laser beam at the interaction point given in Table 10.10.

The number of laser photons per pulse is given by,

$$N_\gamma^l = \frac{E_l}{(h.c)/\lambda_l},$$

with  $E_l$  the laser energy per pulse and  $\lambda_l$  the laser wavelength given in Table 10.10.

The number of Compton photons generated per pulse (for each of the electron and positron source beams) is then given by the product of the calculated luminosity from above with the Compton cross section, which at these energies is closely approximated by the Thomson scattering cross section ( $\sigma_T = 6.65E-29 \text{ m}^2$ ):

$$N_\gamma = \mathcal{L}_\gamma \sigma_c,$$

The expected gamma-gamma collision luminosity is then given by:

$$L_{\gamma\gamma} = \frac{N_\gamma^e N_\gamma^p f_{rep}}{2\pi \sqrt{(\sigma_{x,e}^2 + \sigma_{x,p}^2)(\sigma_{y,e}^2 + \sigma_{y,p}^2)}} \cdot R_L,$$

where  $N_\gamma$  is the above calculated Compton photon rate (for electrons (e) and positrons (p)),  $f_{rep}$  is the machine repetition rate of 5 Hz,  $\sigma$  values represent the projected Compton photon transverse beam sizes at the collision point determined by the divergence of the electron/positron beams at the laser interaction waist and the opening angle of the photon radiation cone.  $R_L$  is a modification factor applied to the luminosity to account for the angle between the colliding photon beams given by:

$$R_L = \left[ 1 + \left( \frac{\sigma_z}{\sigma_x^*} \tan \phi \right)^2 \right]^{-1/2},$$

for the values shown in Table 10.11 the expected gamma-gamma luminosity is calculated to be  $\sim 7 \times 10^{21} \text{ cm}^{-2} \cdot \text{s}^{-1}$ . Given a pair creation cross section of  $\sim 10^{-25} \text{ cm}^2$  for the 30 MeV photons (see Section 3.7), this implies a pair production rate of  $\sim 7 \times 10^{-4} \text{ s}^{-1}$ , or about one  $e^+ e^-$  pair every 24 minutes.

The principal limitations to the pair production rate are given by the positron horizontal spot size at the laser waist and the distance of the Compton source to the gamma interaction point. The laser waist optimal location will be further studied in future and can be considerably closer to the final bend magnet (also a shorter bend magnet may be used). Then the gamma spot size might be reduced by as much as half. By adding additional parameters to the optics matching (e.g. by changing the incoming matching from the linac and/or trading off some dispersion control), the positron horizontal beam size could be reduced to close to the electron horizontal beam size. Combined with running at the highest electron bunch charges as outlined earlier in this chapter, these changes could increase the pair production rate by as much as a factor 10 ( $\sim$  one pair every 2.5 minutes).

<sup>1</sup> Z. Huang *et al.*, Phys. Rev ST – Accel. Beams **13**, 020703 (2010).